Preparation of diblock copolymer nano-objects via polymerization-induced self-assembly in non-polar media
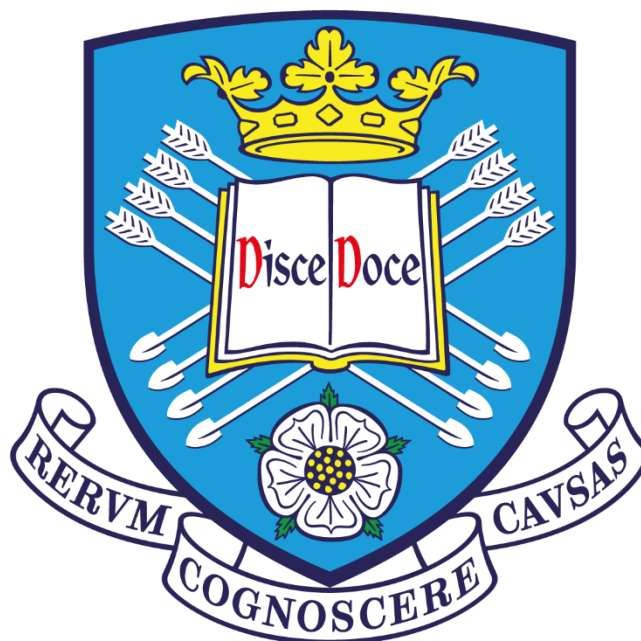
Csilla György

Department of Chemistry
University of Sheffield

Submitted to the University of Sheffield in fulfilment of the requirements for the award of Doctor of Philosophy

September 2022

Declaration

The work described in this thesis was undertaken at the University of Sheffield under the supervision of Professor Steven P. Armes between October 2018 and September 2022 and has not been submitted, either wholly or in part, for this or any other degree. All the work is the original work of the author, except where acknowledged.

Signature:

Csilla György

September 2022

Acknowledgements

First and foremost, I would like to thank God who has given me health, enthusiasm, joy and encouragement throughout all the challenging moments of completing this Thesis.

I feel so blessed that I have received the support of many people over the past few years.

I am forever grateful to my supervisor, Prof. Steve Armes FRS for giving me the opportunity to carry out my PhD studies in his fantastic research group in the UK. Thank you very much for all your advice, support and proofreading over the years. Many thanks for all the travelling opportunities to attend international conferences. I could not wish for a better supervisor!

I would like to thank my industrial sponsor Lubrizol for funding my PhD project. Many thanks to my industrial supervisors Dr. Tim Smith and Dr. David Growney for their continuous support throughout these last four years. A special thanks to Dr. Paul Kirkman for his kind help with the QCM-D and MTM studies. Megan Williams is also thanked for the MTM experiments and our discussions about these data.

I would like to thank all the past and present Armes Group members - I really enjoyed working with everyone. In particular, a big thank you to Dr. Joe Lovett and Dr. Nick Penfold who supported me when I first joined the Armes group as an Erasmus student. A massive thank you goes to Dr. Matt Derry who introduced me to non-polar PISA, helped me with the SAXS analysis and continuously supported me during the first half of my PhD. Similarly, Dr. Erik Cornel is thanked for all the fruitful discussions during my first year. Many thanks to Dr. Tom Neal for his help with SAXS analysis in the past two years and Dr. Derek Chan is thanked for his SEM analysis of my adsorbed nanoparticles.

I would like to thank all the staff in the Chemistry Department who have been immensely helpful during my PhD. Special thanks go to Dr. Sandra van Meurs and Dr. Khalid Doudin for their assistance with the *in situ* NMR experiments and both Chris Hill and Dr. Svet Tzokov for their TEM support and advice. Denise Richards and Louise Brown-Leng are also thanked for helping me to organize all my conference trips and my CDT summer placement in the USA.

I would like to acknowledge Prof. Brent Sumerlin for allowing me to do a three-month summer placement in his research group at the University of Florida. Many thanks to the members of the Sumerlin Group for being so welcoming and making me feel like home.

I am extremely thankful to my Mom, Dad and Brother for their unconditional love and support.

A huge thanks to my best friend, Noemi, for the endless phone conversations in which we shared our thoughts about our PhD experience.

Publications

1. György, C.; Hunter, S. J.; Girou, C.; Derry, M. J.; Armes, S. P. Synthesis of Poly(Stearyl Methacrylate)-Poly(2-Hydroxypropyl Methacrylate) Diblock Copolymer Nanoparticles *via* RAFT Dispersion Polymerization of 2-Hydroxypropyl Methacrylate in Mineral Oil. *Polym. Chem.*, **2020**, *11*, 4579−4590.

2. György, C.; Derry, M. J.; Cornel, E. J.; Armes, S. P. Synthesis of Highly Transparent Diblock Copolymer Vesicles *via* RAFT Dispersion Polymerization of 2,2,2-Trifluoroethyl Methacrylate in N-Alkanes. *Macromolecules*, **2021**, *54*, 1159−1169.

3. Rymaruk, M. J.; O'Brien, C. T.; György, C.; Darmau, B.; Jennings, J.; Mykhaylyk, O. O.; Armes, S. P. Small-Angle X-Ray Scattering Studies of Block Copolymer Nano-Objects: Formation of Ordered Phases in Concentrated Solution During Polymerization-Induced Self-Assembly. *Angew. Chem., Int. Ed.*, **2021**, *60*, 12955− 12963.

4. György, C.; Verity, C.; Neal, T. J.; Rymaruk, M. J.; Cornel, E. J.; Smith, T.; Growney, D. J.; Armes, S. P. RAFT Dispersion Polymerization of Methyl Methacrylate in Mineral Oil: High Glass Transition Temperature of the Core-Forming Block Constrains the Evolution of Copolymer Morphology. *Macromolecules*, **2021**, *54*, 9496−9509.

5. György, C.; Neal, T. J.; Smith, T.; Growney, D. J.; Armes, S. P. Tuning the Glass Transition Temperature of a Core-Forming Block during Polymerization-Induced Self-Assembly: Statistical Copolymerization of Lauryl Methacrylate with Methyl Methacrylate Provides Access to Spheres, Worms, and Vesicles. *Macromolecules*, **2022**, *55*, 4091-4101.

6. György, C.; Smith, T.; Growney, D. J.; Armes, S. P. Synthesis and Derivatization of Epoxy-Functional Sterically-Stabilized Diblock Copolymer Spheres in Non-Polar Media: Does the Spatial Location of the Epoxy Groups Matter? *Polym. Chem.*, **2022**, *13*, 3619-3630.

7. Calabrese, V.; György, C.; Haward, S. J.; Neal, T. J.; Armes, S. P.; Shen, A. Q. Microstructural Dynamics and Rheology of Worm-like Diblock Copolymer Nanoparticle Dispersions under a Simple Shear and a Planar Extensional Flow. *Macromolecules*, **2022**, *55*, 10031-10042.

8. Brotherton, E. E.; Josland, D.; György, C.; Johnson, E. C.; Chan, E. H. H.; Smallridge, M. J.; Armes, S. P. Histidine-Functionalized Diblock Copolymer Nanoparticles Exhibit Enhanced Adsorption onto Planar Stainless Steel. *Macromol. Rapid Commun.*, **2023**, 2200903.

9. György, C.; Kirkman, P. M.; Neal, T. J.; Chan, D. H. H.; Williams, M.; Smith, T.; Growney, D. J.; Armes, S. P. Enhanced Adsorption of Epoxy-Functional Nanoparticles onto Stainless Steel Significantly Reduces Friction in Tribological Studies. *Angew. Chem., Int. Ed.*, **2023**, https://doi.org/10.1002/anie.202218397.

Conferences

May 2019	Oral presentation at *POLY 2019: Sixth International Symposium Frontiers in Polymer Science* Budapest (Hungary)
March 2022	Oral presentation at *ACS National Meeting, Spring 2022, Bonding through Chemistry* San Diego (USA)
August 2022	Oral presentation at *ACS National Meeting, Fall 2022, Sustainability in a Changing World* Chicago (USA)
September 2022	Oral presentation at *ECIS 2022: 36th European Colloid & Interface Society Conference* Chania, Crete (Greece)

Abstract. This Thesis focuses on the synthesis, characterization and potential use of sterically-stabilized diblock copolymer nanoparticles prepared in non-polar solvents *via* polymerization-induced self-assembly (PISA). This involved chain extension of an oil-soluble poly(*n*-alkyl methacrylate) precursor *via* reversible addition-fragmentation chain transfer (RAFT) dispersion polymerization of a carefully selected methacrylic monomer. The growing second block becomes insoluble at a critical degree of polymerization (DP), which leads to *in situ* self-assembly to form spherical, worm-like or vesicular nanoparticles. Firstly, a poly(stearyl methacrylate)-poly(2-hydroxypropyl methacrylate) [PSMA-PHPMA] formulation was examined using mineral oil as the solvent. ^{1}H NMR kinetic studies conducted during the synthesis of PSMA$_9$-PHPMA$_{150}$ vesicles confirmed that the polar nature of the HPMA monomer leads to a relatively fast polymerization (94% conversion within 40 min) compared to the corresponding poly(stearyl methacrylate)-poly(benzyl methacrylate) PSMA$_9$-PBzMA$_{150}$ vesicles, for which only 37% BzMA conversion was achieved within the same timescale. PSMA$_9$-PHPMA$_{70}$ worms underwent degelation on heating, with transmission electron microscopy (TEM) analysis indicating an unexpected partial worm-to-vesicle transition. Replacing HPMA with 2,2,2-trifluoroethyl methacrylate (TFEMA) enabled ~240 nm diameter PSMA$_9$-PTFEMA$_{300}$ vesicles to be obtained at 25% w/w solids in *n*-dodecane as highly transparent dispersion (97% transmittance at 600 nm). This was attributed to the relatively low refractive index of PTFEMA, which matches that of the *n*-alkane at 25 °C. By varying the type of *n*-alkane, highly transparent vesicles could also be obtained at either 50 or 90 °C. Examining the synthesis of highly transparent PSMA$_{16}$-PTFEMA$_{86}$ spheres *via in situ* visible spectroscopy in *n*-hexadecane at 90 °C indicated the premature loss of dithiobenzoate end-groups under such conditions. A more industrially-relevant PISA formulation utilized a poly(lauryl methacrylate) PLMA precursor for the RAFT dispersion polymerization of methyl methacrylate (MMA) in mineral oil at 90 °C. However, only spheres and short worm-like particles could be accessed when using this commodity monomer: targeting higher PMMA DPs unexpectedly produced colloidally unstable spherical aggregates. This morphological constraint was attributed to the high glass transition temperature (T_g) of the PMMA core-forming block and could not be overcome by conducting the synthesis above the T_g of PMMA (115 °C). According to TEM and dynamic light scattering (DLS) analysis, PLMA$_{22}$-PMMA$_{69}$ short worms underwent a partially reversible worm-to-sphere transition on heating. Either long worms or vesicles could be accessed by statistically copolymerizing just 10 mol% lauryl methacrylate (LMA) with MMA at 115 °C. This LMA comonomer enhances solvent plasticization of the core-forming copolymer chains. Moreover, differential scanning calorimetry (DSC) studies indicate a significant reduction in the effective T_g to well below the synthesis temperature. The resulting worms and vesicles exhibited thermoreversible worm-to-sphere and vesicle-to-worm transitions on heating. Epoxy-functional spheres were prepared in mineral oil by using glycidyl methacrylate (GlyMA) to grow the core-forming block from a PLMA precursor. Alternatively, a P(LMA-*stat*-GlyMA) precursor prepared *via* statistical copolymerization of LMA with GlyMA was used for the RAFT dispersion polymerization of either MMA or BzMA. The potential post-polymerization modification of such spheres was assessed using benzyamine, water or 50% v/v aqueous acetic acid using ^{1}H NMR or Fourier transform infrared spectroscopy (FT-IR) spectroscopy. The surface adsorption of such epoxy-functional spheres onto stainless steel from *n*-dodecane was compared to non-functional PLMA-PMMA or PLMA-PBzMA spheres using quartz crystal microbalance with dissipation (QCM-D) at 20 °C. Placing epoxy groups within the steric stabilizer chains enhances the extent of adsorption significantly. For example, the adsorbed mass (Γ) obtained for ~50 nm P(LMA$_{50}$-*stat*-GlyMA$_9$)-PBzMA$_{245}$ nanoparticles is more than five-fold higher than that achieved when using the corresponding non-functional PLMA$_{63}$-PBzMA$_{245}$ nanoparticles (Γ = 31.3 *vs*. 6.4 mg m^{-2}). SEM analysis confirmed a comparable enhancement in surface coverage for the epoxy-functional spheres. Furthermore, QCM-D studies performed at 40 °C led to a higher adsorbed mass for the former type of nanoparticles, which suggests that the epoxy groups react with the hydroxyl groups present at the surface of the stainless steel to form covalent bonds. Mini-traction machine (MTM) tribological experiments confirmed that stronger nanoparticle adsorption led to a significantly lower frictional coefficient.

Nomenclature

4VP	4-Vinylpyridine
AIBN	2,2′-Azobisisobutyronitrile
ARGET	Activators regenerated by electron transfer
ATRP	Atom transfer radical polymerization
BIEE	1,2-Bis(2-iodoethoxy)ethane
BPO	Benzoyl peroxide
BuMA	n-Butyl methacrylate
BzMA	Benzyl methacrylate
CDB	Cumyl dithiobenzoate
CGC	Critical gelation concentration
CGT	Critical gelation temperature
CMC	Critical micellization concentration
CNC	Cellulose nanocrystals
CNF	Cellulose nanofibrils
CPDB	2-Cyano-2-propyl dithiobenzoate
CTA	Chain transfer agent
D	Dissipation
D4	Octamethylcyclotetrasiloxane
D5	Decamethylcyclopentasiloxane
DAAm	Diacetone acrylamide
DCP	Dicumyl peroxide
DLS	Dynamic light scattering
DMAC	N,N-Dimethylacrylamide
DMF	N,N-Dimethylformamide
DP	Degree of polymerization
eATRP	Electrochemically-mediated ATRP
EGDMA	Ethylene glycol dimethacrylate
EHCETTC	S,S′-bis[1-(2-ethylhexyloxycarbonyl)ethyl] trithiocarbonate
ESR	Electron spin resonance spectroscopy
f	Frequency
FRP	Free radical polymerization
G'	Storage modulus
G''	Loss modulus
GlyMA	Glycidyl methacrylate
GMO	Glyceryl monooleate
GPC	Gel permeation chromatography
HMDS	Hexamethyldisiloxane
HPMA	2-Hydroxypropyl methacrylate
ICAR	Initiators for continuous activator regeneration
ICI	Imperial chemical industries
LAM	Less-activated monomer

LAP	Living anionic polymerization
MAM	More-activated monomer
MCDP	Methyl 4-cyano-4(dodecylthiocarbonothioylthio)-pentanoate
MMA	Methyl methacrylate
M_n	Number-average molecular weight
MTM	Mini-traction machine
M_w	Weight-average molecular weight
MWD	Molecular weight distribution
nBA	n-Butyl acrylate
NMP	Nitroxide-mediated polymerization
P(2-EHA)	Poly(2-ethylhexyl acrylate)
PAA	Poly(acrylic acid)
PBzA	Poly(benzyl acrylate)
PDI	Polydispersity index
PDMA	Poly-(2-(dimethylamino)ethyl methacrylate)
PDMAEMA	2-(Dimethylamino)ethyl methacrylate
PDMAPMA	Poly(N-[3-(dimethylamino)propyl] methacrylamide)
PDMS	Poly(dimethylsiloxane)
PEG	Poly(ethylene glycol)
PEGDMA	Poly(ethylene glycol dimethacrylate)
PET	Photo-induced electron-transfer
PETTC	4-Cyano-4-((2-phenylethanesulfonyl)thiocarbonylsulfanyl)pentanoic acid
PFPMA	Pentafluorophenyl methacrylate
PGlyMA	Poly(glycidyl methacrylate)
PGMA	Poly(glycerol monomethacrylate)
PhBD	Poly(hydrogenated butadiene)
PHEA	Poly(2-hydroxyethyl acrylate)
PHPMA	Poly(2-hydroxypropyl methacrylate)
PISA	Polymerization-induced self-assembly
PLA	Poly(lauryl acrylate)
PMA	Poly(methyl acrylate)
PMMA	Poly(methyl methacrylate)
PNAM	Poly(N-acryloylmorpholine)
PNAT	Poly(N-acryloylthiomorpholine)
PnBMA	Poly(n-butylmethacrylate)
PNIPAM	Poly(N-isopropylacrylamide)
POAA	Poly(*tert*-octyl acrylamide)
PPPMA	Poly(3-phenylpropyl methacrylate)
PRE	Persistent radical effect
PS	Polystyrene
PSiMA	Poly(3-[tris(trimethylsiloxy)silyl]propyl methacrylate)

PSMA	Poly(stearyl methacrylate)
PTFEMA	Poly(2,2,2-trifluoroethyl methacrylate)
RAFT	Reversible addition-fragmentation chain transfer polymerization
RDRP	Reversible deactivation radical polymerization
S	Styrene
SAXS	Small-angle X-ray scattering
SIPLI	Shear-induced polarized light imaging
SMA	Stearyl methacrylate
SPTP	Phenyl-2,4,6-trimethylbenzoylphosphinate
SRR	Slide-to-roll ratio
T21s	*Tert*-butyl peroxy-2-ethylhexanoate
TBDB	*Tert*-butyl dithiobenzoate
TEM	Transmission electron microscopy
TEMPO	2,2,6,6-Tetramethylpiperidine-1-oxyl
TFEMA	2,2,2-Trifluoroethyl methacrylate
T_g	Glass transition temperature
THF	Tetrahydrofuran
TIPNO	2,2,5-Trimethyl-4-phenyl-3-azahexane-3-nitroxide
TPO	(2,4,6-Trimethylbenzoyl)diphenylphosphine oxide
TR-SANS	Time-resolved small angle neutron scattering
UCST	Upper critical solution temperature

Contents

Chapter 1. Introduction

1.1. Polymers

Polymers are long-chain molecules that comprise small molecule repeat units, or monomers. The number of repeat units per chain is denoted the degree of polymerization (DP). The wide range of commercially available monomers and polymerization techniques provide many opportunities to design polymers with bespoke physical and chemical properties for diverse applications ranging from mechanical engineering[1] to the pharmaceutical industry.[2–4]

While small molecules are characterized by a single unique molecular weight, all synthetic polymers possess a molecular weight distribution (MWD). Any given polymer sample contains a distribution of chains of varying DPs. M_n is a number-average molecular weight that is defined by **Equations 1.1** and **1.2**. This parameter depends on the probability of selecting a polymer chain with i number of repeating units (x_i) when a molecule is randomly chosen from this sample (**Equations 1.1-1.2**).[5]

$$x_i = \frac{n_i}{\sum_i n_i} \tag{1.1}$$

$$M_n = \sum_i x_i \cdot M_i = \frac{\sum_i n_i \cdot M_i}{\sum_i n_i} \tag{1.2}$$

Where n_i denotes the number of polymer chains with i repeat units, M_i is the molecular weight of that chain and $\sum_i n_i$ is the total number of chains within the sample. M_n is biased towards the shorter chains (and small molecule impurities such as unreacted monomer). It can be determined by end-group analysis if the polymer chains have suitable end-groups.

In contrast, M_w is defined according to **Equations 1.3** and **1.4**, where the weight fraction is denoted by w_i and $\sum_i i \cdot n_i$ indicates the total number of monomer units within the sample.[5] M_w is biased towards the longer chains and can be determined by static light scattering.[6,7]

$$w_i = \frac{i \cdot n_i}{\sum_i i \cdot n_i} \tag{1.3}$$

$$M_w = \sum_i w_i \cdot M_i = \frac{\sum_i i \cdot n_i \cdot M_i}{\sum_i i \cdot n_i} = \frac{\sum_i n_i \cdot M_i^2}{\sum_i n_i \cdot M_i} \tag{1.4}$$

The polydispersity index (PDI) or dispersity ($Đ$) is a crude measure of the width of the MWD: it is defined by the weight-average molecular weight (M_w) divided by the number-average molecular weight (M_n) as indicated in **Equation 1.5**.

$$\text{PDI} = Đ = \frac{M_\text{w}}{M_\text{n}} \tag{1.5}$$

If M_w is equal to M_n, then the polymer is said to be monodisperse. Certain biopolymers such as proteins may possess a unique molecular weight.[8] However, all synthetic polymers exhibit MWDs of finite width (*i.e.*, $Đ = M_w/M_n > 1.0$). A $Đ$ value below 1.50 indicates a relatively narrow MWD: (pseudo-)living polymerization techniques are required to produce such well-defined polymers (see **Section 1.2.3**).

Polymers can possess various architectures (see **Figure 1.1**). For a simple homopolymer, the polymer chains contain just one type of repeat unit. In contrast, copolymers comprise two or more comonomers. Depending on the spatial arrangement of such repeat units, we can distinguish between alternating, statistical, block, graft and star copolymers. Alternating copolymers have repeat units that are strictly alternating along the polymer chain, while statistical copolymers have a random distribution of repeat units, which is determined by the relative comonomer reactivities and polymerization mechanism. Block copolymers comprise spatially separated sequences of two or more comonomers. Graft copolymers possess both a main chain and side-chains formed by a second monomer. In the case of star copolymers, multiple linear homopolymer or block copolymer chains are connected together at one central junction.

This Thesis involves the synthesis and characterization of homopolymers, diblock copolymers and statistical copolymers.
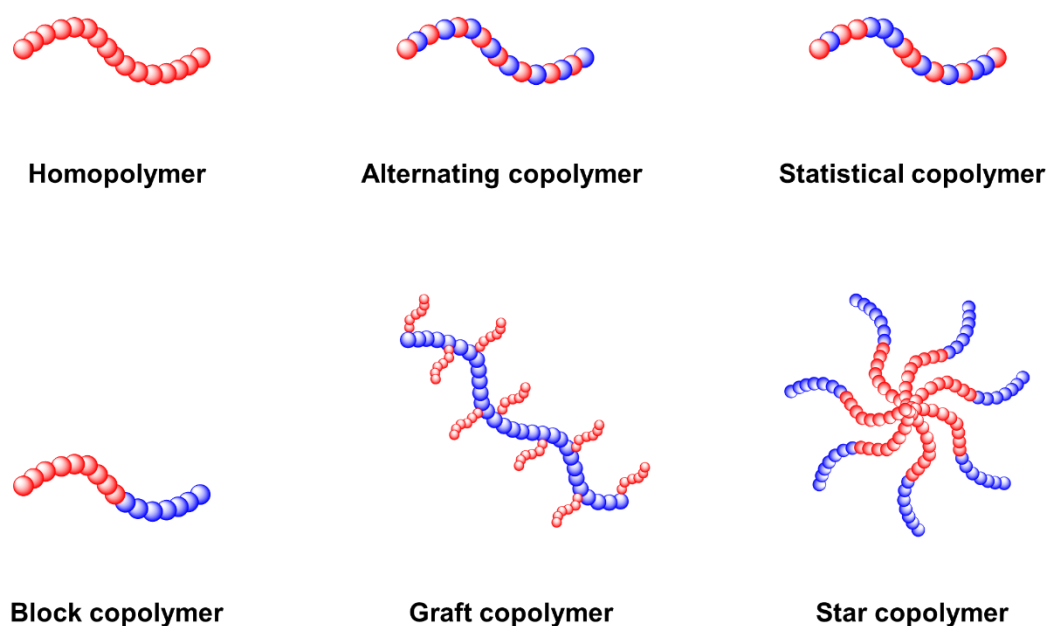
Figure 1.1. Well-defined copolymer architectures: homopolymer, alternating copolymer, statistical copolymer, block copolymer, graft copolymer and star diblock copolymer.

1.2. Chain-growth polymerization

Synthetic polymers are typically prepared by either step-growth polymerization or chain-growth polymerization. Step-growth polymerization involves using bifunctional or multifunctional monomers. Monomers react to form firstly dimers, then trimers, tetramers, oligomers etc. until high molecular weight polymer chains are eventually formed towards the end of the polymerization. In contrast, chain-growth polymerization involves the multiple addition of individual monomer units. Vinyl monomers are commonly polymerized by this method. Chain-growth polymerization normally comprises three distinct reaction steps: initiation, propagation and termination. This technique is used exclusively in this Thesis and is discussed in more detail below.

1.2.1. Free Radical Polymerization (FRP)

Free radical polymerization (FRP) is a type of chain-growth polymerization that is widely utilized in industry to produce vinyl polymers, e.g. polyethylene, poly(vinyl chloride) or polystyrene, under various reaction conditions.[9]

The active chain-end in FRP is a free radical, which contains an unpaired electron. Initiation involves two steps. Firstly, free radicals (I•) are generated from an initiator molecule (I_2) by homolytic bond cleavage (see **Figure 1.2**). This can be triggered by either heat or UV radiation, or by using redox chemistry if the polymerization requires a relatively low reaction temperature (see **Scheme 1.1**).[5,10] Secondly, such free radicals react rapidly with monomer to produce a monomer-radical adduct (I−M•) (see **Figure 1.2**).

Initiation

$$I_2 \xrightarrow{k_d} 2\,I\bullet$$

$$I\bullet + M \xrightarrow{k_i} I{-}M\bullet \;\;(= P_1\bullet)$$

Propagation

$$P_n\bullet + M \xrightarrow{k_p} P_{n+1}\bullet$$

Termination

$$P_n\bullet + P_m\bullet \;\xrightarrow{k_{tc}}\; P_{n+m}$$

$$\xrightarrow{k_{td}}\; P_n{=} + P_m{-}H$$
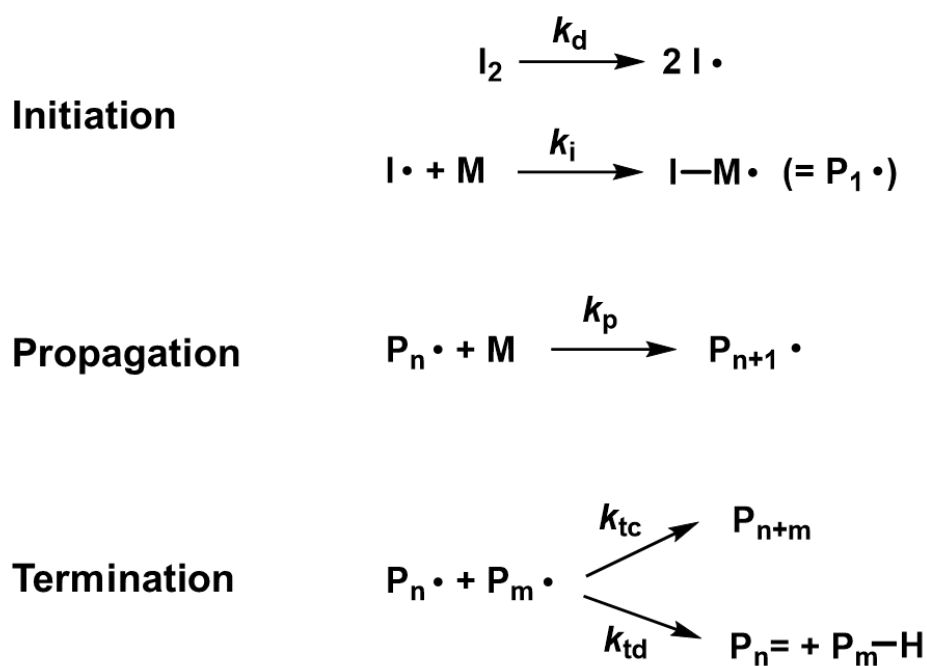
Figure 1.2. The three main steps in FRP: initiation, propagation and termination (*via* either combination or disproportionation).

(a) Initiator decomposition

Thermal initiator
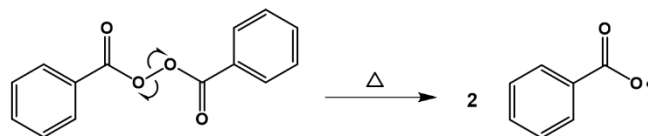
Photoinitiator

Redox initiator

$$Fe^{2+} + H_2O_2 \longrightarrow Fe^{2+} + OH^- + \bullet OH$$
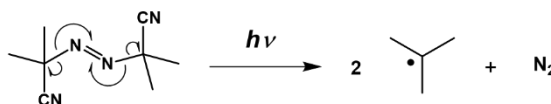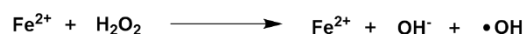
(b) Monomer initiation and head-to-tail propagation
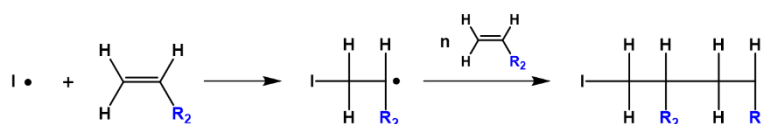
(c) Termination

Combination
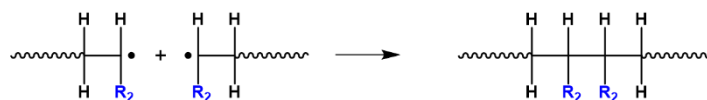
Disproportionation

Scheme 1.1. (a) Mechanism for the generation of free radical from initiator molecules during FRP: thermal decomposition of benzoyl peroxide (BPO); photochemical decomposition of 2,2'-azobisisobutyronitrile (AIBN) and the redox reaction of Fe^{2+} with H_2O_2 (Fenton's reagent).[11] **(b)** Monomer initiation followed by head-to-tail propagation for FRP of a vinyl monomer. **(c)** Termination of polymer radicals during FRP either by combination or disproportionation.

Thermal decomposition of the initiator is relatively slow and is the rate-limiting step for the overall kinetics of polymerization (see below).[12] Propagation proceeds relatively fast, with polymer chains being formed *via* head-to-tail addition reactions between each active center and

many monomer units (P$_{n+1}$•) (see **Figure 1.2** and **Scheme 1.1**). High molecular weight polymer chains are typically formed even at relatively low monomer conversions (5-10%) and the mean lifetime of any individual polymer chain is less than microsecond.

Termination prevents further chain growth. It can occur by combination, where two polymer radicals react to form an inactive chain (P$_{n+m}$) (see **Figure 1.2** and **Scheme 1.1**). Alternatively, termination by disproportion involves one polymer radical abstracting a hydrogen atom from a second polymer radical to produce an inactive polymer chain (P$_m$−H) and a macromonomer (P$_n$=), see **Figure 1.2** and **Scheme 1.1**. During FRP, both termination mechanisms can occur to some extent, with the dominant mechanism depending on the reaction conditions and the monomer type.[5] For example, styrene and acrylic monomers mainly undergo termination by combination, whereas methacrylic monomers favour disproportionation.[13,14]

To consider the kinetics of FRP, we must first recognize that the rate of initiator decomposition ($k_d \sim 10^{-5}$ s^{-1}) is much slower than the rate of formation of the monomer-initiator adduct ($k_i \sim 10^4$ M^{-1} s^{-1}). Thus, the former process is the rate-determining step for the overall rate of initiation (R_i), as described by **Equation 1.6**:

$$R_i = \frac{d[\text{I} \cdot]}{dt} = 2 \cdot f \cdot k_d \cdot [\text{I}_2] \qquad (1.6)$$

where k_d is the rate constant for the thermal decomposition of the initiator, [I$_2$] is the initiator concentration, and f is the initiator efficiency. The latter parameter is defined as the fraction of the initiator radicals that actually react with monomer, as opposed to undergoing side-reactions such as recombination (the so-called 'cage effect').[12]

In FRP, monomer is consumed during both initiation and propagation. Therefore, the rate of monomer consumption, which is equivalent to the rate of polymerization, can be described by **Equation 1.7**.[15]

$$-\frac{d[\text{M}]}{dt} = R_i + R_p \qquad (1.7)$$

Where R_i and R_p are the rates of initiation and propagation, respectively. Assuming that the number of monomers consumed during initiation is much less than that consumed during propagation (which is indeed the case when targeting high molecular weight polymers), the

rate of propagation is approximately equal to the rate of polymerization. The former parameter is given by **Equation 1.8**.[15]

$$R_p = -\frac{d[\text{M}]}{dt} = k_p \cdot [\text{P}_\text{n} \cdot] \cdot [\text{M}] \qquad (1.8)$$

Where k_p is the rate constant for propagation ($k_p \sim 10^2 - 10^4$ M^{-1} s^{-1}), [M] is the monomer concentration and [P$_\text{n}$·] is the polymer radical concentration.

Equation 1.8 indicates that the polymer radical concentration must be determined to obtain R_p. However, [P$_\text{n}$·] ($\sim 10^{-8}$ mol dm^{-3}) is experimentally challenging to determine and appropriate techniques such as electron spin resonance (ESR) spectroscopy are not widely available. Fortunately, this parameter can be excluded from the rate equation by invoking the steady-state assumption.[15] This assumes that [P$_\text{n}$·] initially increases but attains a constant value within a fraction of a second. Thereafter, there is no significant change in [P$_\text{n}$·] during the polymerization. Thus the rate of initiation (R_i) is equal to the rate of termination (R_t), which leads to **Equation 1.9**.[15]

$$R_t = R_i = 2 \cdot k_t \cdot [\text{P}_\text{n} \cdot]^2 \qquad (1.9)$$

Where k_t is the overall rate constant for termination ($\sim 10^8$ M^{-1} s^{-1}).

Rearranging **Equation 1.9**, [P$_\text{n}$·] can be expressed as follows.[15]

$$[\text{P}_\text{n} \cdot] = \left(\frac{R_i}{2 \cdot k_t}\right)^{\frac{1}{2}} \qquad (1.10)$$

Using **Equation 1.10** to eliminate [P$_\text{n}$·] in **Equation 1.8** affords **Equation 1.11**.[15]

$$R_p = k_p \cdot \left(\frac{R_i}{2 \cdot k_t}\right)^{\frac{1}{2}} \cdot [\text{M}] \qquad (1.11)$$

Substituting for R_i (see **Equation 1.6**) into **Equation 1.11**, the rate of polymerization, R_p, is now given by **Equation 1.12**.[15]

$$R_p = k_p \cdot [\text{M}] \cdot \sqrt{\frac{f \cdot k_d \cdot [\text{I}_2]}{k_t}} \qquad (1.12)$$

Equation 1.12 indicates that either increasing [M] or [I$_2$] leads to a faster polymerization. Another important parameter is the kinetic chain length (D_k), which is the mean number of monomer units per chain. D_k is simply equal to R_p divided by R_i. Since $R_i = R_t$ under steady-state conditions, this expression can be further modified to afford **Equation 1.13**:[15]

$$D_k = \frac{R_p}{R_i} = \frac{R_p}{R_t} = \frac{k_p \cdot [\text{M}] \cdot [\text{P}_\text{n} \cdot]}{2 \cdot k_t \cdot [\text{P}_\text{n} \cdot]^2} = \frac{k_p \cdot [\text{M}]}{2 \cdot \sqrt{f \cdot k_d \cdot k_t \cdot [\text{I}_2]}} \qquad (1.13)$$

If there are no side-reactions during FRP, D_k is directly related to the degree of polymerization (DP). More specifically, D_k is equivalent to DP when the polymer chains terminate exclusively *via* disproportionation. If the chains only undergo combination, DP is equal to $2D_k$.[15] Inspecting **Equation 1.13**, it is clear that targeting higher molecular weight polymers by FRP at constant (high) [M] requires a reduction in [I$_2$] to increase the kinetic chain length. However, this approach inevitably leads to a concomitant reduction in the rate of polymerization according to **Equation 1.12**.

It is well-known that most FRP syntheses usually suffer from chain transfer. Such side-reactions typically involve transfer from a polymer radical to solvent, monomer or polymer. Chain transfer to either solvent or monomer leads to a reduction in M_n, whereas chain transfer to polymer usually leads to branched polymers and hence a higher M_w (see **Scheme 1.2**).[5,10]
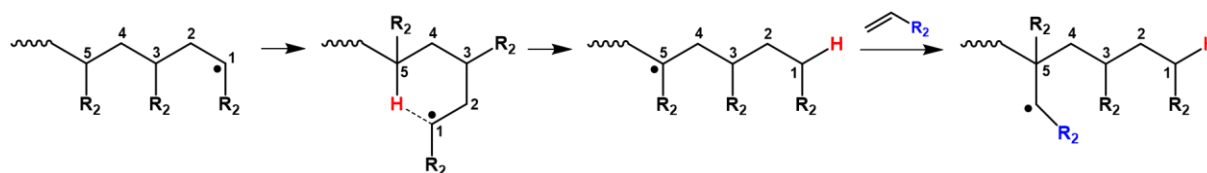
Scheme 1.2. Chain branching introduced by propagation of a tertiary radical generated by intramolecular hydrogen transfer reaction (1:5 backbiting).[16]

Unfortunately, FRP provides only rather limited control over the target M_n and the MWD. Typical M_w/M_n values for FRP-synthesized polymers range from 1.50 to 5.0, depending on the

monomer type, final conversion and reaction conditions. This is in part because the relatively slow rate of initiation means that there is substantial overlap between the initiation and propagation intervals. Thus radicals continue to be generated towards the end of the polymerization. Under such monomer-starved conditions it is inevitable that only relatively short chains can be formed. Moreover, targeting a specific M_n by FRP requires prior knowledge of various rate constants and kinetic parameters (see **Equation 1.13**), which are typically not known for the system of interest. Furthermore, the intrinsic nature of the termination mechanism and relatively short lifetimes for the propagating polymer radicals prevents the synthesis of well-defined diblock copolymers by FRP. Thus this technique is not suitable for the synthesis of the various copolymers targeted in this Thesis.

1.2.2. Living Anionic Polymerization (LAP)

The concept of living anionic polymerization (LAP) was introduced by Szwarc *et al.,* who reported the polymerization of styrene in 1956.[17,18] LAP is a chain-growth polymerization technique used to prepare polymers with specific M_n values and narrow molecular weight distributions ($M_w/M_n < 1.10$). The 'living' character simply means that such polymerizations proceed in the absence of any termination or chain transfer reactions. This leads to a linear increase of M_n with conversion (see **Figure 1.3a**). Ideally, initiation occurs rapidly and is complete prior to any propagation: if all the chains are initiated at the same time and propagate at the same rate, this results in a polymer with a narrow molecular weight distribution (see **Figure 1.3b**).[5,19] Furthermore, as $k_i \gg k_p$ and the concentration of the active chain-ends (P⁻) is equivalent to the initiator concentration [I_2], the rate of polymerization is simply given by the rate of propagation, see **Equation 1.14**.

$$R_p = -\frac{d[\text{M}]}{dt} = k_p \cdot [\text{P}^-] \cdot [\text{M}] = k_p \cdot [\text{I}_2] \cdot [\text{M}] \tag{1.14}$$

Where k_p is the rate constant for propagation and [M], [P⁻] and [I_2] are the monomer, active chain-ends and initiator concentrations, respectively.[12]
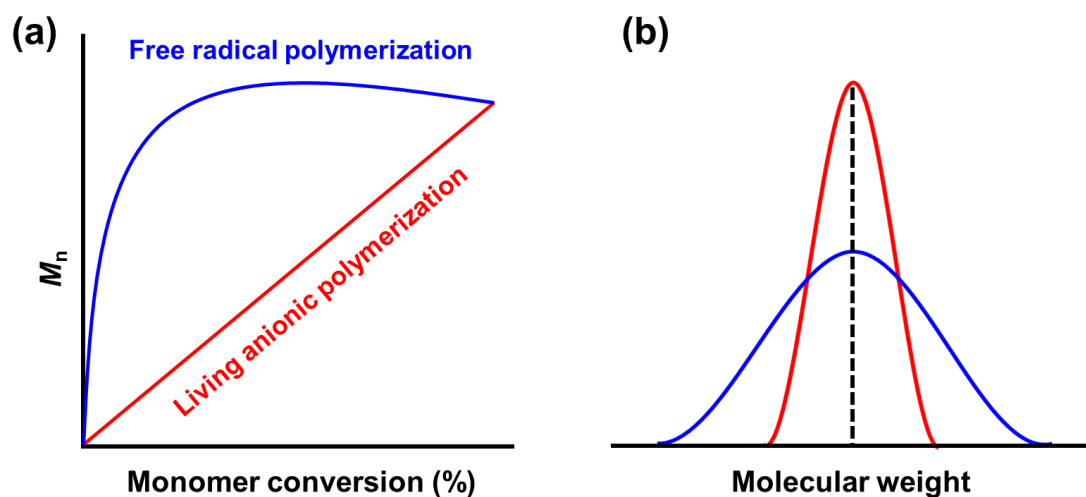
Figure 1.3. Schematic cartoons of **(a)** the evolution of M_n with monomer conversion and **(b)** the molecular weight distribution curves obtained for polymers prepared either *via* FRP (blue) or LAP (red).

Assuming 100% initiator efficiency and full monomer conversion, the target DP of the polymer chains is simply given by the molar ratio of the monomer to the initiator (see **Equation 1.15**).[19]

$$DP = \frac{[M]}{[I]} \qquad (1.15)$$

Where [M] and [I] are the monomer and initiator concentrations, respectively.

The general mechanism for LAP of a vinyl monomer using *n*-butyllithium as a typical initiator is shown in **Scheme 1.3**. Throughout the polymerization, the active chain-ends comprise carbanions stabilized by counterions (e.g. Li$^+$). [19]
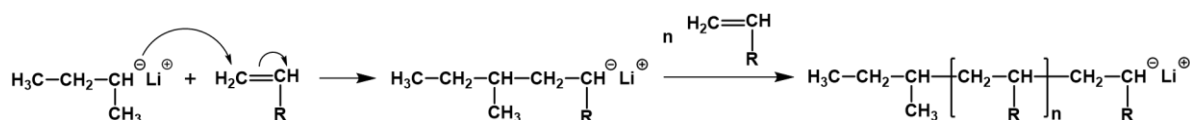
Scheme 1.3. General mechanism for the living anionic polymerization (LAP) of a vinyl monomer with an electron-withdrawing functional group (R) using *n*-butyllithium as an initiator.

Termination by combination cannot occur owing to mutual electrostatic repulsion between the anionic polymer chain-ends (see **Scheme 1.3**). Instead, extrinsic termination is conducted by introducing an acidic proton source (e.g. methanol or water) to quench the carbanion, thus producing non-reactive neutral polymer chains.[19] As a corollary, LAP must be conducted in

the absence of any water, which requires stringent purification of the monomer, solvent and reaction vessel.

Various vinyl monomers with electron-withdrawing groups (e. g. –CN, –NO$_2$, –phenyl) can be polymerized by LAP, whereas functional monomers bearing acidic protons (e. g. –OH, –NH$_2$, –COOH) require protecting group chemistry prior to polymerization.[5] Typical examples of polymers that can be prepared by LAP include polystyrene, polybutadiene, polyisoprene and poly(2-vinylpyridine).[20–25] Importantly, unlike FRP, LAP enables the synthesis of well-defined block copolymer architectures *via* sequential monomer addition. However, LAP is much less widely used on an industrial scale than FRP because it is much more synthetically demanding to ensure rigorously anhydrous conditions. Nevertheless, various companies such as Kraton Chemicals use LAP to prepare styrene-based diblock, triblock and star diblock copolymers for applications as soot dispersants, thermoplastic elastomers and viscosity modifiers for automotive engine oils.[26–29]

1.2.3. Reversible Deactivation Radical Polymerization (RDRP)

Reversible deactivation radical polymerization (RDRP) techniques (formerly known as 'controlled' or 'pseudo-living' radical polymerization) were developed to overcome the limitations of FRP and produce polymers of controlled molecular weight and narrow MWD *via* radical chemistry. RDRP methods are based on a dynamic equilibrium established between propagating radicals and dormant polymer chains.[30] In principle, termination can be suppressed throughout the polymerization by ensuring that the majority of the propagating polymer radicals in their dormant unreactive form. This can be achieved by two different methods. Firstly, propagating radicals can be reversibly deactivated by reacting with a stable radical species such as a nitroxide (for nitroxide mediated polymerization, NMP) or a halogen atom (for atom transfer radical polymerization, ATRP). Alternatively, a suitable chain transfer agent (CTA) can be utilized to ensure rapid exchange between active and dormant polymer chains. This latter method is known as reversible addition-fragmentation chain transfer (RAFT) polymerization.[5,31]

Like LAP, RDRP techniques enable design of specific copolymer architectures, such as block, star or graft copolymers (see **Figure 1.1**). However, RDRP is much more tolerant of monomer functionality and is compatible with a wide range of reaction conditions. In this regard, it is much more similar to FRP than LAP.[32]

1.2.3.1. Nitroxide-Mediated Polymerization (NMP)

In NMP, the dynamic equilibrium between propagating radicals and dormant alkoxyamine species is provided by nitroxide radicals. The aminoxyl functionality of such radicals confers relatively high stability owing to the unpaired electron delocalized in a π_{NO} three-electron bond (NO• and N^{+}•O^{-}).[33]

NMP relies on the so-called persistent radical effect (PRE).[34,35] Initially, the alkoxyamine molecule decomposes to form a transient radical and a persistent radical (see **Scheme 1.4a**). Transient radicals are carbon-based radicals which initiate the polymerization by reacting with monomers to yield active chains. Nitroxides are persistent radicals that are capable of reversible termination. Shortly after initiation, the radical concentration is sufficiently high to enhance bimolecular reactions between radical species. Transient radicals can either react with nitroxide radicals to produce dormant chains or undergo termination by either combination or disproportionation. However, nitroxide radicals prefer to react with propagating radicals rather than undergo termination. The resulting dormant chains can be activated again thermally before either propagating further or undergoing termination, which leads to the irreversible accumulation of persistent radicals over time. As polymerization proceeds, the concentration of active chains is reduced while that of the persistent radicals increases. Hence the dynamic equilibrium is shifted to the left-hand side, which significantly reduces the probability of termination (see **Scheme 1.4b**) and results in the controlled growth of polymer chains.[31,36]

NMP offers some important advantages over other RDRP techniques. For example, both initiation and control over the ensuing polymerization can be provided by a unimolecular species. Polymers can be simply purified *via* precipitation.[37] Moreover, NMP is compatible with many vinyl monomers, including styrene, acrylate, acrylamide or diene derivatives. One limitation of NMP is that 2,2,6,6-tetramethylpiperidine-1-oxyl (TEMPO)-based alkoxyamines require a relatively high reaction temperature (> 100 °C) because of the highly stable nature of the dormant alkoxyamine species. Thus, polymerization in low boiling point solvents such as water requires pressurized equipment. To overcome this problem, novel nitroxides such as 2,2,5-trimethyl-4-phenyl-3-azahexane-3-nitroxide (TIPNO) have been developed, which enable polymerizations to be conducted at lower temperatures.[31,33] However, only a few of such nitroxides are commercially available. Furthermore, the homopolymerization of methacrylic monomers by NMP is problematic owing to side-reactions and slow recombination

of the corresponding polymer radical with nitroxide. However, introducing a small amount ($\leq$ 10% mol) of styrene[38] or acrylonitrile[39] as a comonomer is sufficient to provide good control.[31]
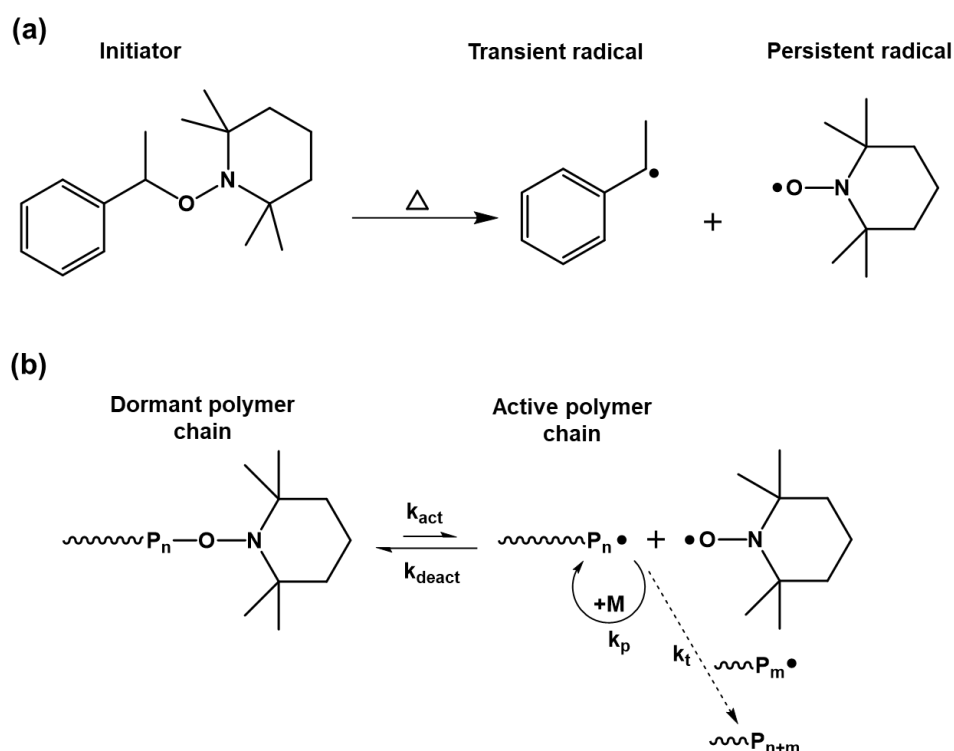
Scheme 1.4. General NMP mechanism: **(a)** initiation using a unimolecular TEMPO-based initiator; **(b)** dynamic activation-deactivation equilibrium of NMP in the presence of TEMPO, which acts as a persistent radical.[31]

1.2.3.2. Atom Transfer Radical Polymerization (ATRP)

ATRP involves using a suitable transition metal such as Cu, Fe, Ru or Ni as a catalyst. At the beginning of the polymerization, the transition metal-ligand complex is in its lower oxidation state. This species then reacts with an alkyl halide initiator to produce radicals by increasing its oxidation state *via* single electron transfer, see **Scheme 1.5a**. Such radicals react with monomer to form polymer radicals, which are converted into unreactive dormant chains by the metal complex in its higher oxidation state. Thus the dynamic equilibrium between the active and dormant polymer chains is facilitated by the transition metal catalyst (see **Scheme 1.5b**).[40]

(a)

(b)
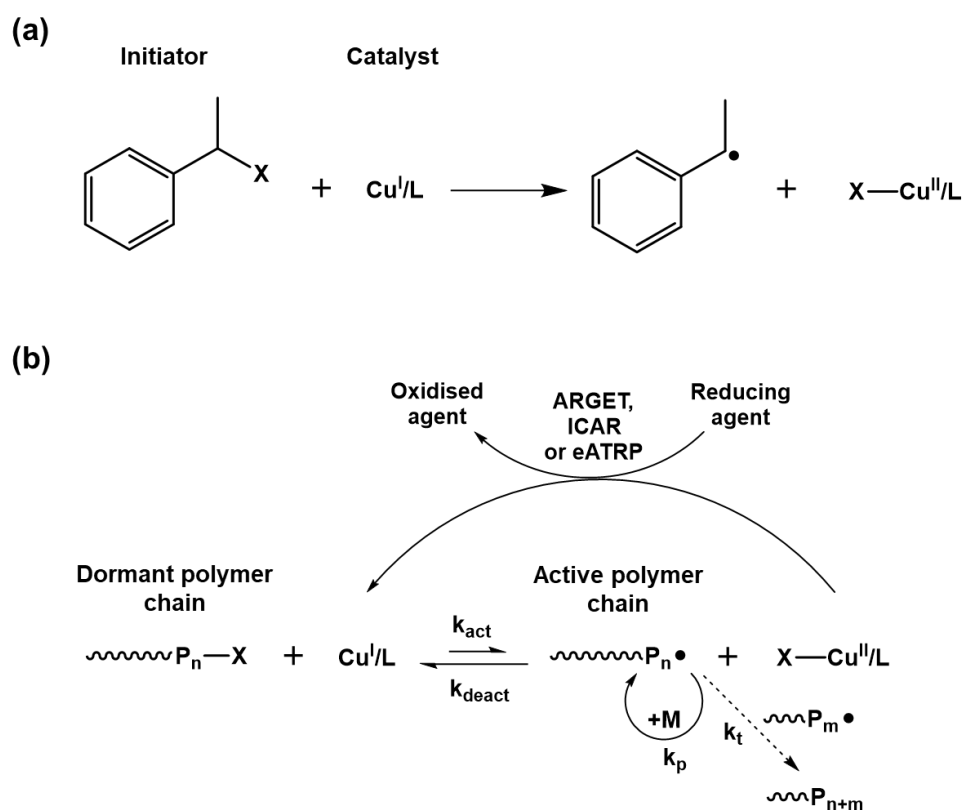
Scheme 1.5. General ATRP mechanism using a copper-based catalyst: **(a)** the initiation step; **(b)** dynamic activation-deactivation equilibrium for ATRP.[40]

ATRP is widely used by many academic groups to produce well-defined functional copolymers from various types of monomers. Indeed, the halogen-based chain-ends can be exploited to introduce desired functionality *via* post-polymerization modification.[40] However, the relatively high concentration of the transition metal catalyst makes this technique relatively expensive and complete removal of the toxic catalyst residues would be essential for many industrial applications. Furthermore, the copolymerization of monomers of differing reactivities requires judicious selection of both the metal catalyst and the alkyl halide initiator.

In order to reduce the amount of metal catalyst, various new ATRP formulations have been developed in recent years to enable the continuous regeneration of Cu^I throughout the polymerization. For example, initiators for continuous activator regeneration (ICAR) ATRP requires only ppm levels of copper catalyst and employs conventional free radical initiators to produce excess radicals that reduce the Cu^{II} species to Cu^I. Activators regenerated by electron transfer (ARGET) ATRP employs either organic or organometallic reducing agents (e.g. ascorbic acid or tin(2-ethylhexanoate)) to promote the regeneration of Cu^I. Alternatively, electrochemically-mediated ATRP (eATRP) offers a route to regenerate the Cu^I without using

a reducing agent by simply applying a suitable potential.[31,41] Nevertheless, academic interest in ATRP appears to be waning relative to RAFT polymerization (see below).

1.2.3.3. Reversible Addition-Fragmentation Chain Transfer (RAFT) Polymerization

RAFT polymerization utilizes a chain transfer agent (CTA) to mediate the conventional free radical process *via* a two-step addition-fragmentation mechanism, see **Scheme 1.6**. A RAFT CTA typically possesses a carbon-sulfur double bond, which is highly reactive towards radical addition, a Z group which governs this reactivity and stabilizes the intermediate radical (hence reducing the number of active polymer chains) and an R group. The latter must be a good radical leaving group that not only promotes the formation of CTA-capped dormant polymer chains but also reinitiates the polymerization (see **Scheme 1.6**).[42]

In an ideal RAFT polymerization, most of the polymer chains are in their dormant state and only a small fraction of chains is growing at any given time, as illustrated in **Figure 1.4**. Owing to the rapid equilibrium between the active and dormant polymer chains relative to the rate of propagation, all chains have an equal probability of growth, which ensures the formation of polymers with narrow MWDs.[43,44]

Initiation

Reversible chain transfer / propagation
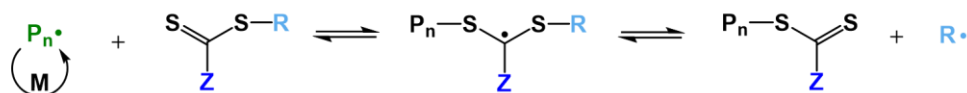
Reinitiation
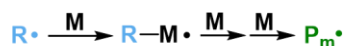
Chain equilibration / propagation

Termination

$P_n\bullet + P_m\bullet \longrightarrow$ **Dead polymer**
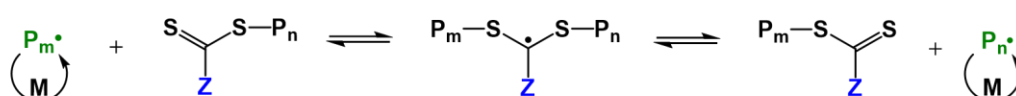
Scheme 1.6. General mechanism for RAFT polymerization.[43] First, the initiator decomposes to produce free radicals. These radicals react with monomer similarly to the FRP mechanism. The propagating radicals subsequently undergo a reversible-addition reaction with the chain transfer agent to produce an intermediate radical species, which then undergoes fragmentation to produce a new radical and a dormant polymer chain. The new radicals reinitiate the polymerization. Termination occurs just like for FRP, but the rate of termination is substantially suppressed relative to the rate of propagation owing to the relatively large fraction of dormant chains. This mechanism ensures a rapid equilibrium between the propagating and dormant polymer chains.
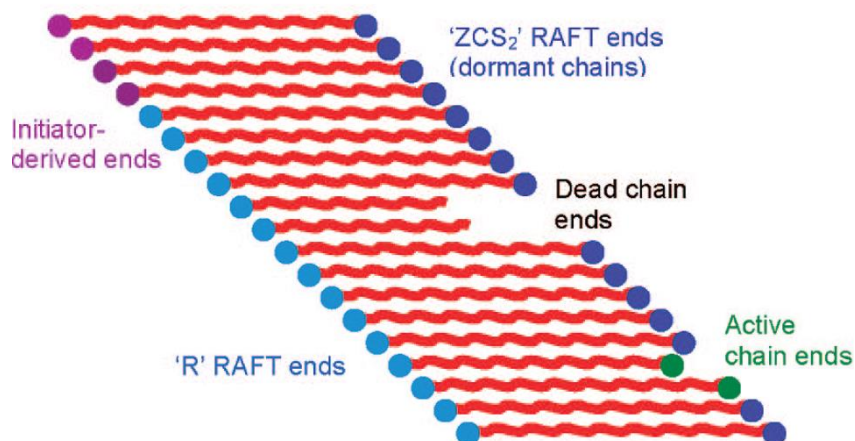
Figure 1.4. Schematic representation of the active (green) and dormant (dark blue) polymer chains present during a well-controlled RAFT polymerization. Most of the polymer chain-ends bear R groups (light blue) with only a small fraction being initiated by initiator-derived radicals (purple). For a well-controlled RAFT polymerization, there is a much higher proportion of dormant chains than it is possible to show here. The equilibration between the active and dormant chains ensures that all active chains grow simultaneously, resulting in polymer chains with approximately the same DP.[43]

RAFT can be either thermally initiated using diazo compounds (e.g. AIBN)[45] or peroxides (e.g. *tert*-butyl peroxy-2-ethylhexanoate (T21s))[46] at elevated reaction temperatures or *via* redox reactions using metal-free oxidizing and reducing agents (e.g. *tert*-butyl hydroperoxide/ascorbic acid) at ambient temperatures.[47] Alternatively, either UV[48–53] or visible light[53–59] can be used to induce initiation. In this case, polymerization can also occur at room temperature, but this approach provides an 'on/off switch' for the polymerization by simply turning the light radiation on or off.[52,60,61] Light-induced initiation can be achieved using a photoinitiator, such as (2,4,6-trimethylbenzoyl)diphenylphosphine oxide (TPO)[50,61] or phenyl-2,4,6-trimethylbenzoylphosphinate (SPTP).[62] Another approach involves a photoiniferter mechanism.[52,53,63,64] This does not require the use of any initiator since the RAFT agent acts not only as a regulator of the polymerization *via* addition-fragmentation but also as the source of the initiating radicals produced by light irradiation. Finally, there is also photo-induced electron-transfer (PET) RAFT method, whereby a photoredox catalyst can be activated by visible light. This proceeds *via* a radical anion and has expanded the applicability of light-induced RAFT because it can be conducted using either metallocomplexes (e.g. $Ru(bpy)_3Cl_2$ or chlorophyll A)[65,66] or organic catalysts (e.g. Eosyn Y dye or 10-phenylphenothiazine).[47,67,68]

To design a well-controlled RAFT polymerization, many factors need to be considered beyond the initiation step. For example, the choice of CTA, CTA/initiator molar ratio, polymerization temperature and type of solvent can each play a role.[69] Careful selection of the R and Z groups of the CTA is critical for a successful outcome and this is usually determined by the monomer class (e.g. methacrylic, acrylic, styrene etc.). Moad *et al.* reported some helpful guidelines to decide which RAFT agent can be used to control the polymerization of a given type of monomer (see **Figure 1.5**).[42,70] Accordingly, monomers can be classified as either more-activated monomers (MAMs) such as vinyl aromatics, methacrylics, and acrylics or less-activated monomers (LAMs), such as vinyl esters and vinyl amides. The phrases 'more-activated' or 'less-activated' indicate the reactivity of the monomer towards radical addition. MAMs react more easily with radicals, since the latter can be stabilized by conjugation of the unsaturated vinyl group to neighboring aromatic or carbonyl groups. However, MAMs are less reactive towards the CTA, so they require dithiobenzoate or tritihiocarbonate CTAs to enhance propagation because the aryl (dithiobenzoate) or S-alkyl (trithiocarbonate) groups can stabilize the intermediate radical. On the other hand, LAMs react more readily with the CTA but they are relatively poor leaving groups so xanthates (O-alkyl) or carbamates (N-alkyl) are employed to destabilize the intermediate radical and enhance fragmentation *via* delocalization of lone

pairs within the thiocarbonyl group. This suggests that the synthesis of diblock copolymers comprising a MAM and a LAM is problematic *via* RAFT polymerization. However, so-called 'universal' RAFT agents have been developed by Moad and co-workers that are able to provide reasonable control for both monomer classes, as well as pH-switchable RAFT agents, which can facilitate the synthesis of such MAM-LAM diblock copolymers by adjusting the solution pH.[47,69]
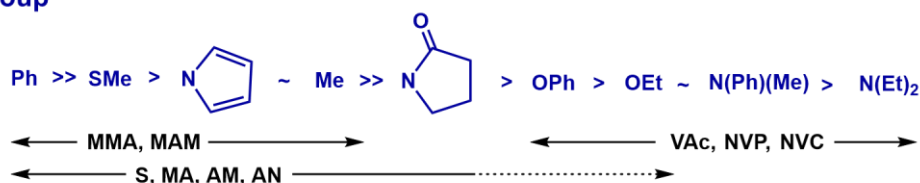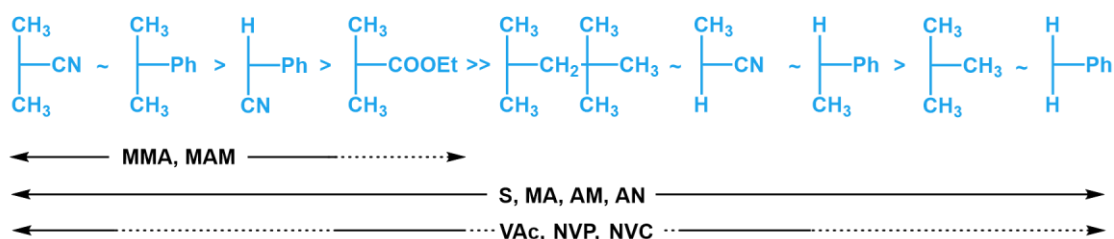
Figure 1.5. Guidelines for the selection of appropriate Z and R groups on a RAFT CTA for a given type of monomer. (**a**) For Z groups, addition rates decrease from left to right while fragmentation rates increase. (**b**) For R groups, fragmentation rates decrease from left to right. The dashed line indicates only partial control can be achieved during RAFT polymerization.[42,70] This Figure was reproduced from ref. 70.

RAFT is a versatile polymerization technique that can be used to polymerize a wide range of monomers. It is highly tolerant of monomer functionality and is compatible with various reaction conditions. Furthermore, its ease of implementation and similarity to FRP makes this technique more amenable to industrial scale-up. According to the patent literature, global chemical companies such as DuPont, Lubrizol, L'Oréal, Ashland and Unilever own IP based on RAFT polymerization formulations.[47] It is important to emphasize that polymers produced by RAFT possess a thiocarbonylthio-based end-group. In principle, this is a useful synthetic handle for introducing new functionalities *via* post-polymerization modification (see **Figure 1.6**).[71,72] For example, thiocarbonylthio groups can be directly converted into thiols by reacting with nucleophiles (e.g. amines) or ionic reducing agents such as sodium borohydride. Such thiols can be further modified *via* click chemistry.[73] On the other hand, thiocarbonylthio end-groups confer intense color, malodor and potential toxicity. In recent years, various chain-end

removal techniques have been developed. Such RAFT end-groups can be readily removed *via* thermolysis, UV-radiation, reaction with an oxidizing agent (e. g. H_2O_2, tBuOOH or O_3), or radical-induced reduction (e.g. hypophosphite salts) (see **Figure 1.6**).[71,72,74,75]
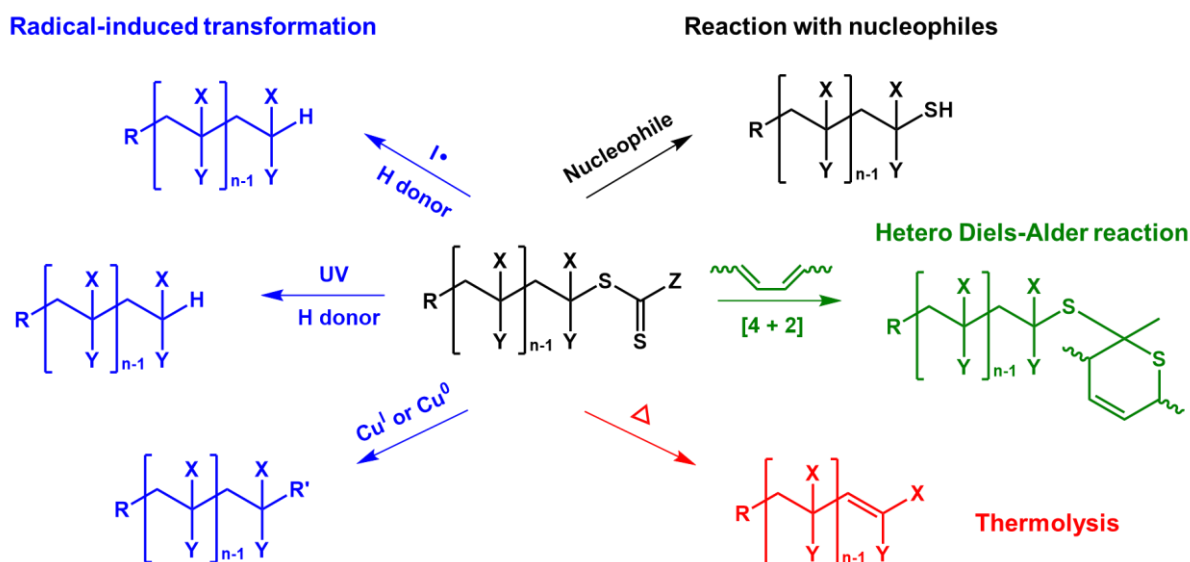
Figure 1.6. Schematic representation of various RAFT end-group modification and removal techniques, including radical-induced transformation, reaction with nucleophiles, hetero Diels-Alder reaction and thermolysis.[47,71]

Moreover, there are at least some industrial applications for RAFT-synthesized polymers that do not require end-group removal. For example, a series of star copolymers have been commercialized by The Lubrizol Corporation for use as viscosity modifiers in automotive engine oils.[76,77] Since such applications effectively involve a closed system, the color and malodor associated with the organosulfur end-groups is irrelevant.

1.3. Physical forms of polymerization

In terms of physical forms of polymerization, we can distinguish between homogeneous and heterogeneous formulations. Homogeneous formulations include bulk and solution polymerization, while precipitation and dispersion polymerization are examples of heterogenous formulations.

1.3.1. Bulk polymerization

Bulk polymerization is the simplest method to produce polymers as it only requires the monomer and a monomer-soluble initiator (or catalyst). Chain polymerization of vinyl monomers is highly exothermic so efficient heat dissipation can be problematic during bulk polymerization. Moreover, in the case of FRP the viscosity of the reaction mixture increases rapidly as high molecular weight chains are produced, which may cause stirring problems and local 'hot spots' within the reaction vessel. Thus, chain-end degradation and discoloration can occur, and the resulting polymers typically possess broad MWDs. Removal of unreacted monomer after the polymerization may also be problematic.[6,12]

1.3.2. Solution polymerization

To avoid the problem of heat dissipation, solution polymerization can offer a useful alternative to bulk polymerization. In solution polymerization, a suitable solvent is selected that dissolves the monomer, initiator and the target polymer. This approach also leads to lower solution viscosity for the reaction mixture, which aids efficient stirring. However, one disadvantage of solution polymerization is that chain transfer to solvent can occur, which results in a lower M_n. Depending on the intended application (and the final monomer conversion), the final polymer solution can be either used as is, or the polymer can be isolated and purified by removing the solvent and any unreacted monomer.[6,12]

1.3.3. Precipitation polymerization

Precipitation polymerization involves an initial homogeneous reaction mixture comprising the monomer, initiator (or catalyst) and solvent. The latter is chosen so that the target polymer precipitates during its synthesis. Both initiation and polymerization occur within the continuous phase. Nucleation of the insoluble polymer chains immediately produces nascent particles, which then aggregate over time to form a macroscopic precipitate. Consequently, it is difficult to obtain high molecular weight polymers by this technique, which can also suffer from incomplete monomer conversions.[78,79]

1.3.4. Dispersion polymerization

Dispersion polymerization essentially involves conducting a precipitation polymerization in the presence of a suitable soluble polymeric stabilizer.[78] The mechanism for a typical FRP-based dispersion polymerization is shown in **Figure 1.7**. First, a homogeneous reaction mixture of the monomer, initiator, polymeric stabilizer and solvent is produced (1). The next step involves initiation, followed by propagation to produce soluble oligomers/polymers or graft copolymers (2). When a certain critical chain length is achieved, phase separation occurs because the growing polymer chains are no longer soluble in the reaction mixture. This leads to the formation of nascent particle nuclei (3). These nascent particles aggregate and grow in size and become coated with the soluble polymeric stabilizer *via* either physical adsorption or chemical grafting (4). This confers steric stabilization, which prevents further particle growth. No further nucleation occurs, and polymerization continues within the monomer-swollen particles until all the remaining monomer is consumed (5). The final product is a colloidally stable dispersion of sterically-stabilized polymer latex particles.[80,81]
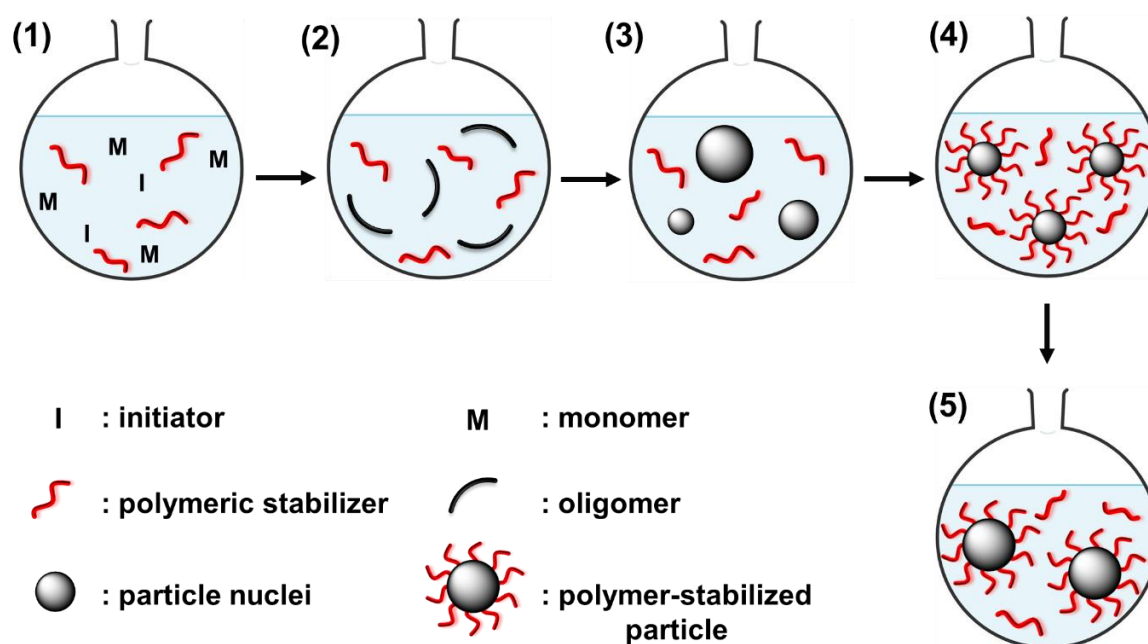
Figure 1.7. Schematic representation of the five main steps in an FRP-based dispersion polymerisation: (1) initial homogeneous phase, (2) initiation and formation of soluble oligomers, (3) nucleation to form nascent particles, (4) particle stabilization by polymer adsorption and (5) particle growth.[80]

This method usually produces uniform spherical particles with mean diameters ranging from 0.1 to 15 μm.[81] The particle size can be tuned by adjusting the monomer and polymeric stabilizer concentration, the polymerization temperature and the solvent composition.[80,81] The first example of dispersion polymerization was developed by Osmond *et al*. at Imperial Chemical Industries (ICI), who produced latex particles by copolymerizing acrylic monomers in the presence of an oil-soluble polymeric stabilizer in a hydrocarbon solvent.[82] Since then, various dispersion polymerization formulations have been developed to produce well-defined latex particles in water,[83,84] alcohols[85–87] and non-polar solvents.[80,82,88,89]

In this Thesis, either bulk or solution polymerization was employed to produce oil-soluble homopolymers or statistical copolymers, while dispersion polymerization was utilized to obtain a series of sterically-stabilized diblock copolymer nanoparticles in various non-polar solvents.

1.4. Self-assembly

Molecular self-assembly is a well-known natural phenomenon. For example, mammalian cell membranes are the result of phospholipid self-assembly. Similarly, soap molecules undergo micellar self-assembly, with the micelles being used to remove hydrophobic soils and hence produce clean laundry. Such self-assembly is driven by the amphiphilic nature of such molecules, which typically comprise a hydrophilic head-group and one or more hydrophobic tails. In aqueous media, such amphiphiles form micelles above the critical micelle concentration (CMC) to allow the hydrophilic head-groups to remain in contact with the water molecules while enabling the hydrophobic tails to 'escape' from the aqueous solution by forming the micelle cores (see **Figure 1.8**). Micelle formation occurs because the net gain in enthalpy outweighs the loss in entropy. The CMC usually depends on the size of the amphiphilic molecule.[90] Increasing the amphiphile concentration above its CMC results in the formation of more micelles, while the unimer concentration remains constant (see **Figure 1.8**). In the case of small molecule surfactants, the micelles are in dynamic equilibrium with mean unimer exchange frequencies ranging from ms to μs. In contrast, such exchange typically occurs on much longer timescales for amphiphilic block copolymers.
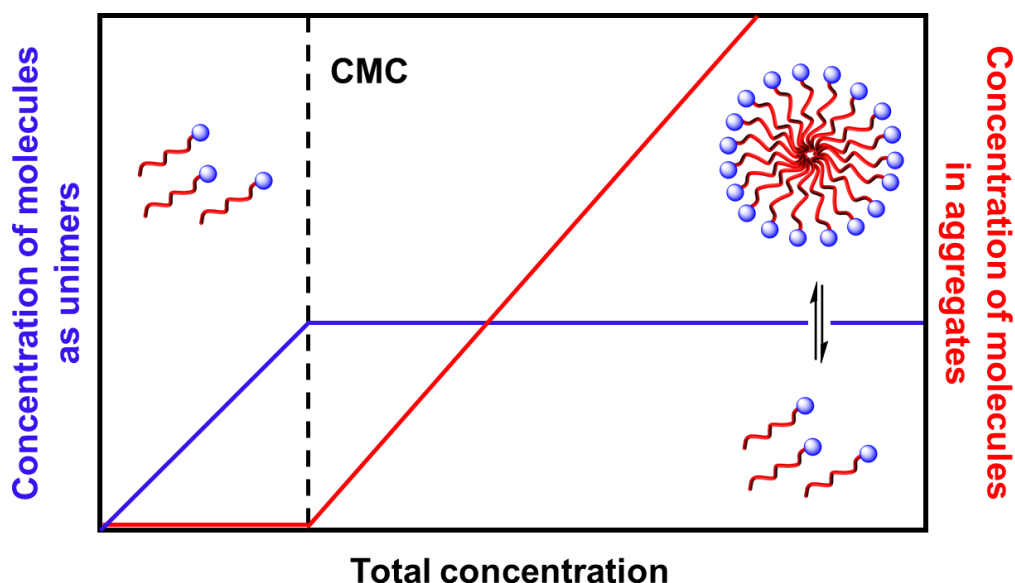
Figure 1.8. Graphical representation of the variation in concentration of a small molecule surfactant in the form of unimers and micelles on increasing the total surfactant concentration. The vertical dashed line represents the critical micelle concentration (CMC), above which surfactant molecules self-assemble to form micelles. A schematic cartoon of individual surfactant unimers and a micelle is shown, with unimer exchange between these two species also being indicated.[91]

In dilute solution, surfactant molecules typically form spherical micelles. However, higher order structures such as worms, vesicles, bilayers or inverted micelles are formed on increasing the surfactant concentration.[91] Surfactant self-assembly can be rationalised in terms of the dimensionless fractional packing parameter (P),[92] see **Equation 1.16**.

$$P = \frac{V}{a_0 l_c} \qquad (1.16)$$

P depends on the surface area occupied by the head group (a_0), the volume occupied by the hydrophobic chains (V) and the effective length of the hydrophobic chains (l_c), see **Figure 1.9**. Typical values for P for various morphologies are indicated in **Figure 1.9**.[92,93]
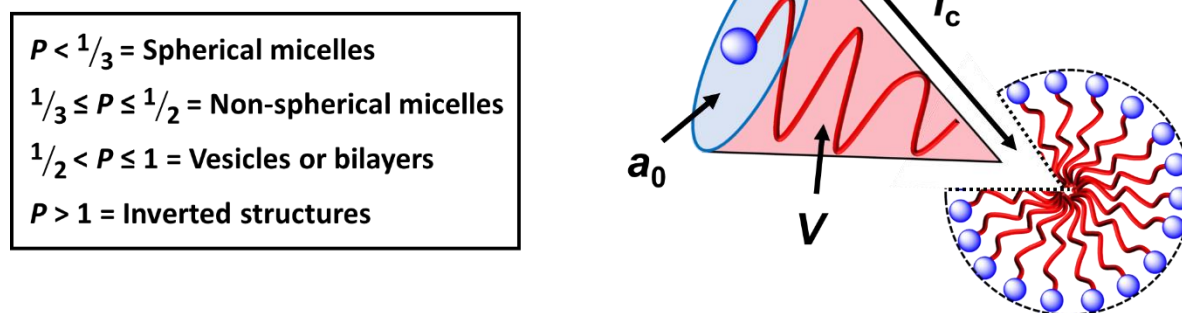
Figure 1.9. Schematic illustration of a spherical micelle with an expanded surfactant molecule shown to indicate a_0, l_c and V terms. Typical values for P for various morphologies are also provided.

Amphiphilic diblock copolymers can also undergo self-assembly either in the bulk[94–96] or in solution.[97–99] In this case, self-assembly occurs as a results of the enthalpic incompatibility between the two blocks (in the bulk) or between one of the two blocks and the solvent (in aqueous solution). Typically, block copolymer micelles exhibit significantly higher stability than surfactant micelles, with the former amphiphiles undergoing much less frequent exchange with the micelles.[100–103] Indeed, there are many literature examples of kinetically frozen (non-ergodic) block copolymer micelles in which there is effectively no exchange between the micelles and the individual chains.[104–108]

1.4.1. Block copolymer self-assembly in the bulk

Unlike blends of two or more homopolymers, diblock copolymers cannot undergo macrophase separation owing to the covalent bonds between the two blocks. Instead, block copolymers with enthalpically incompatible blocks undergo microphase separation in the bulk to form various morphologies such as spheres, cylinders, bicontinuous gyroids or lamellae.[94,96,109] The preferred microphase morphology can be tuned by adjusting the chemical composition of the copolymer. The self-assembly of an AB diblock copolymer depends on three parameters: (i) the relative volume fraction of each block (f_A and f_B; $1 = f_A + f_B$); (ii) the overall degree of polymerization ($N = N_A + N_B$) and (iii) the Flory-Huggins parameter (χ_{AB}).[110] χ_{AB} is a temperature-dependent parameter that indicates the relative incompatibility between the two blocks and hence dictates the extent of microphase separation. The relationship between χ_{AB} and temperature is described by **Equation 1.17**:[95,96]

$$\chi_{AB} = \left(\frac{z}{k_B \cdot T}\right) \cdot \left[\varepsilon_{AB} - \frac{1}{2} \cdot (\varepsilon_{AA} + \varepsilon_{BB})\right] \tag{1.17}$$

Where z is the number of nearest neighbours per repeat unit in the copolymer chains, $k_B T$ is the thermal energy (where k_B is the Boltzmann constant and T is the absolute temperature), and ε_{AB}, ε_{AA} and ε_{BB} are the interaction energies between the respective pairs of repeat units (*i.e.*, A-B, A-A and B-B).

The degree of microphase separation is equal to the Flory-Huggins parameter multiplied by the overall degree of polymerization, which is also known as the segregation product (χN). A higher χN indicates greater incompatibility between the two blocks at a given temperature, which increases the probability of self-assembly. In contrast, a sufficiently low χN value leads to no self-assembly. As shown in **Equation 1.17**, the enthalpic incompatibility between the two blocks can be reduced by increasing the temperature. A sufficiently high temperature (known as the T_{ODT}) can lead to an order-to-disorder transition (ODT) at which microphase separation no longer occurs – under such conditions the two blocks become fully miscible.[96]

A theoretical phase diagram for an AB diblock copolymer in the bulk was constructed by Matsen and Bates (see **Figure 1.10**).[111] As shown in **Figure 1.10b**, increasing f_A (when $f_A \leq f_B$) at a fixed χN above the ODT (χN > ~10.5) results in various self-assembled structures, including close-packed spheres (CPS), body-centred cubic spheres (S), hexagonally-packed cylinders (C), bicontinuous gyroids (G) and lamellae (L). When $f_A > f_B$, morphological inversion is observed (from L to G'to C' to S'). Furthermore, only a disordered melt can be obtained below χN ~10.5, which indicates that microphase separation does not occur for sufficiently low molecular weight diblock copolymers.[95,96] This theoretical phase diagram is in remarkably good agreement with the experimental morphology map obtained for a series of polyisoprene-polystyrene AB diblock copolymers reported by Khandpur *et al.* (see **Figure 1.10c**).[96,112]
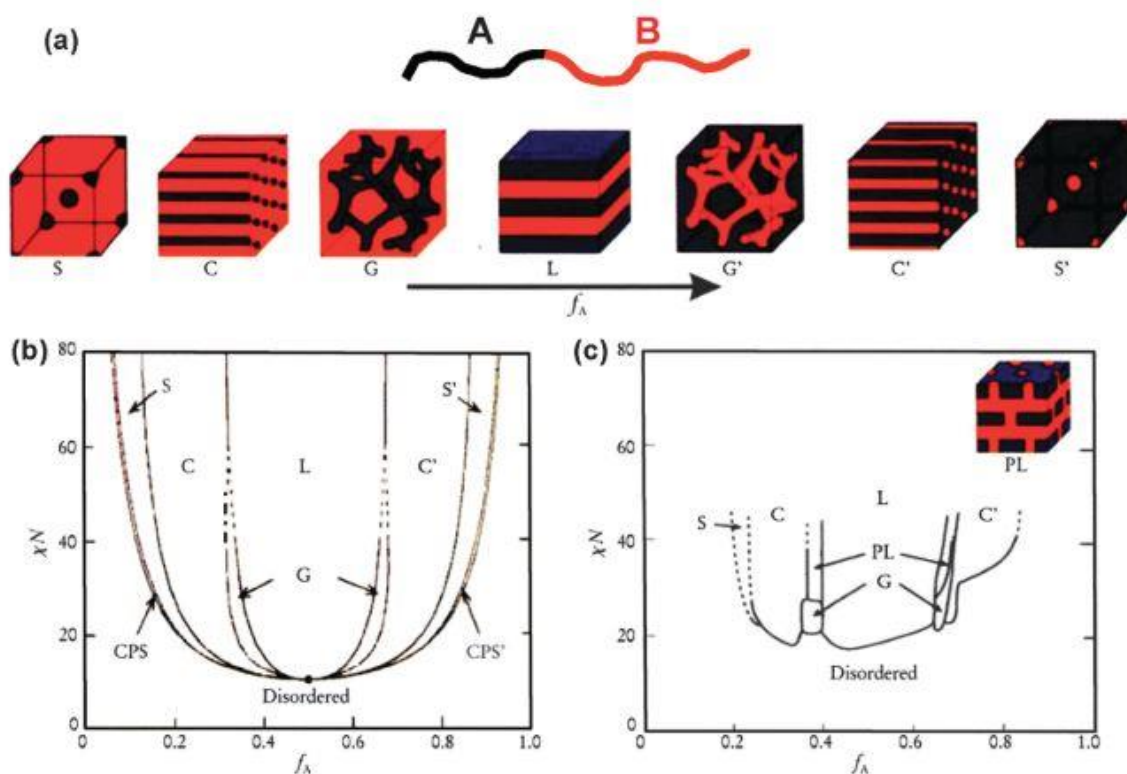
Figure 1.10. (a) Various morphologies observed for a series of AB diblock copolymers in the bulk. S and S' represent body-centered cubic spheres, C and C' are hexagonally-packed cylinders, G and G' are bicontinuous gyroids and L indicates lamellae. **(b)** Theoretical phase diagram obtained for a series of AB diblock copolymers predicted by self-consistent mean field theory by systematically varying the volume fraction (*f*) of the blocks and the segregation parameter, χN. CPS and CPS' denote close-packed spheres. **(c)** Experimental phase diagram obtained for a series of polyisoprene-*block*-polystyrene copolymers, in which f_A represents the volume fraction of polyisoprene. PL denotes perforated lamellae.[110]

1.4.2. Block copolymer self-assembly in solution

The self-assembly of an AB diblock copolymer in solution is more complicated because introducing a solvent (S) produces two additional interaction parameters between the solvent and each block (χ_{AS}, χ_{BS}). This becomes even more complex when a binary solvent mixture is utilized.[103,110]

Block copolymer aggregates are usually prepared in solution *via* post-polymerization processing. A typical protocol is the so-called 'solvent-switch' method, which involves three steps. Firstly, the amphiphilic diblock copolymer is molecularly dissolved in a suitable solvent that is a good solvent for both blocks. In the literature, DMF, dioxane or THF are commonly used. Next, a solvent (typically water) that is selective for one of the blocks is slowly added to

the copolymer solution. This induces self-assembly, where the core is formed by the block for which the selective solvent is a non-solvent while the other block remains solvated and hence acts as a steric stabilizer. After addition of sufficient selective solvent, the common solvent can be removed by either dialysis or vacuum to afford a dispersion of diblock copolymer micelles.[110,113,114]

Many copolymer morphologies can be accessed using this protocol. For example, eight different morphologies (including spheres, rods, lamellae and vesicles) were reported for polystyrene-poly(acrylic acid) (PS-PAA) diblock copolymers when using a binary mixture of DMF (which acts as a common solvent) and water (which is a selective solvent for the PAA block), see **Figure 1.11**.[103] In this case, the block copolymer morphology depends on the relative volume fraction and degree of stretching of the core-forming block and the interfacial tension between the core and the solvent, as well as electrostatic interactions between the ionized stabilizer chains.[113,114] Therefore, any conditions which affect one of these parameters can influence the final copolymer morphology.[110]
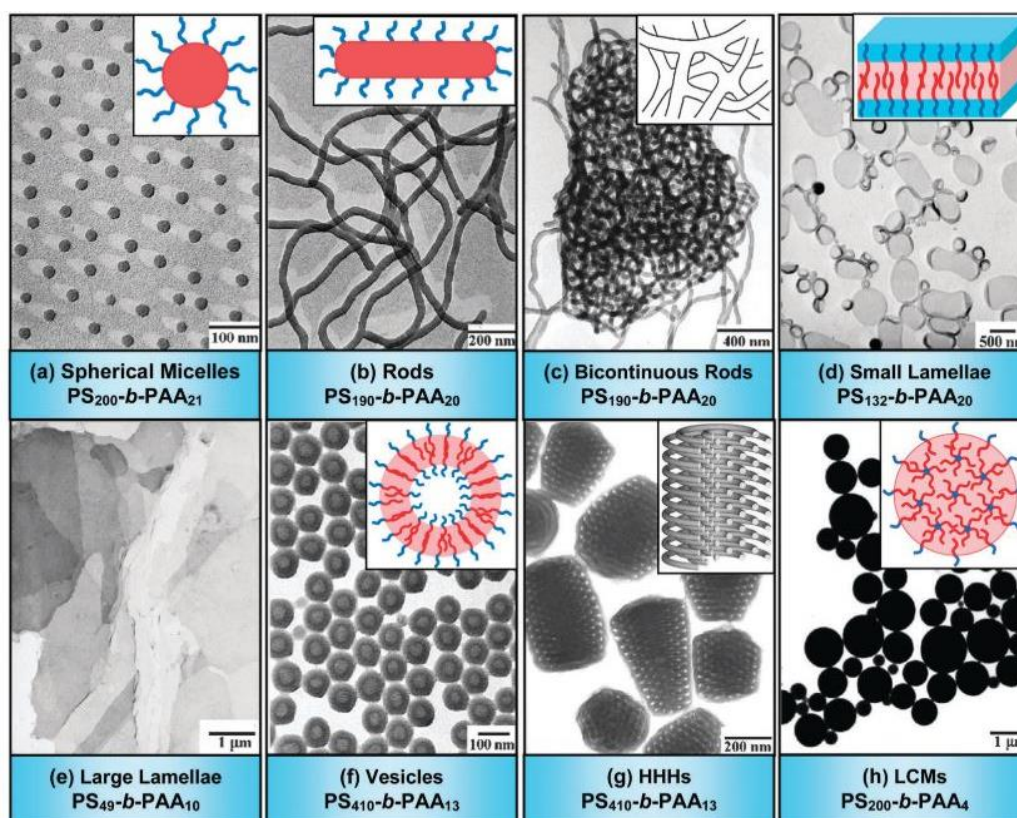
Figure 1.11. Transmission electron microscopy (TEM) images obtained for various polystyrene-poly(acrylic acid) (PS-PAA) diblock copolymer morphologies prepared in aqueous solution using DMF to ensure initial molecular dissolution. Inset: red indicates the hydrophobic PS core-forming block while blue denotes the hydrophilic PAA stabilizer block. HHHs and LCMs denote hexagonally-packed hollow hoops and large compound micelles, respectively.[103]

For example, the morphology obtained for an AB diblock copolymer is highly dependent on the relative volume fraction of each block. Thus, varying the mean DP for the core-forming PS block leads to a series of PS-PAA morphologies (see **Figure 1.11a-d**).[103] Another important parameter is the copolymer concentration. For example, the morphology evolves from spheres to rods for PS_{310}-PAA_{52} in a dioxane-water mixture at a constant water content of 10% w/w when the copolymer concentration is increased from 0.1 to 10 w/w% (see **Figure 1.12**).[115,116] This is because the copolymer concentration (c) is directly related to the aggregation number (N_{agg}), see **Equation 1.18**.

$$N_{agg} = 2 \cdot \sqrt{\frac{c}{\text{CMC}}} \tag{1.18}$$

This equation was originally derived for small molecule surfactants,[91] where the CMC indicates the critical micellization concentration. However, according to Eisenberg and co-workers the CMC should be replaced by the critical water content (CWC) required for the onset of self-assembly. According to this relationship, a higher copolymer concentration leads to a larger N_{agg}, which promotes the formation of higher order morphologies.[110]
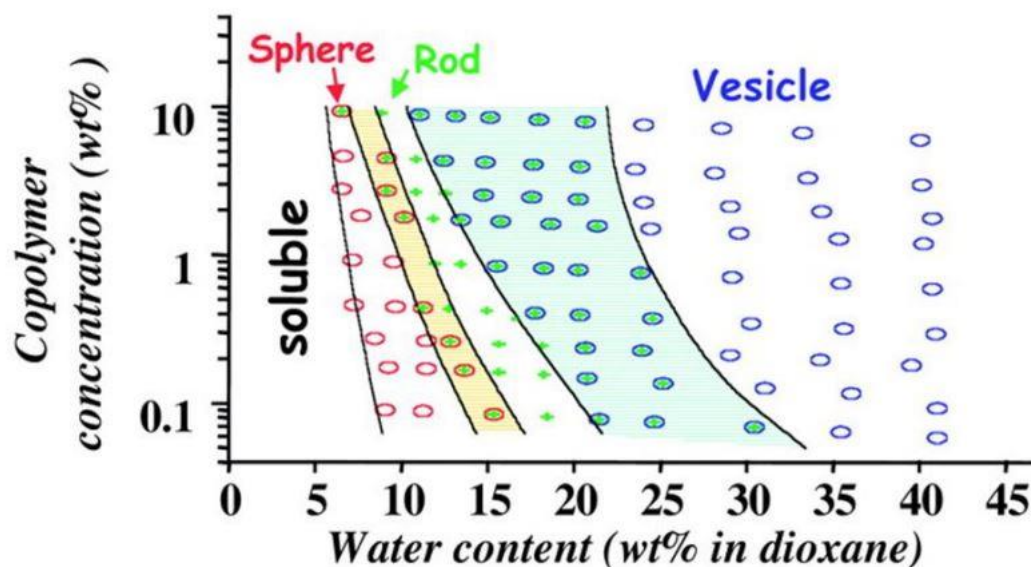
Figure 1.12. Phase diagram constructed for the self-assembly of a polystyrene-poly(acrylic acid) (PS_{310}-PAA_{52}) diblock copolymer in dioxane–water mixture when systematically varying the copolymer concentration and water content. The coloured intermediate regions indicate mixed phases: the yellow region corresponds to a mixture of spheres and rods while the green region indicates a mixture of rods and vesicles.[115]

The concentration of the selective solvent, in this case water, can also influence the copolymer morphology. As shown for a PS_{310}-PAA_{52} diblock copolymer in a series of dioxane-water binary mixtures, the copolymer morphology can evolve from spheres to rods to vesicles when increasing the water content from 10 to 40% w/w at a constant copolymer concentration (e.g., 0.1% w/w), see **Figure 1.12**.[115,116] Spherical micelles are formed at the CWC. Further addition of water causes a gradual reduction in the mobility of the core-forming PS block. If this reduced mobility is sufficient then the number of particles is reduced *via* a particle fusion mechanism, which leads to an increase in N_{agg} and the volume fraction of the core-forming PS block. This also leads to a reduction in the interfacial energy between the PS cores and water and results in the formation of higher order morphologies. If the mobility of the core-forming block is reduced significantly before N_{agg} reaches a critical point, the spherical morphology can be become kinetically frozen or non-ergodic.[110,115]

Selection of an appropriate common solvent is also important because it influences the effective volume fraction of each block. For example, a PS_{200}-PAA_{18} diblock copolymer forms spheres when DMF is used as a common solvent, whereas large compound micelles are formed when THF is employed. Using a binary mixture of these solvents can provide access to rods and vesicles. When self-assembly occurs, the common solvent diffuses into the micelle cores to provide solvation. Since THF is a better solvent for the PS chains than DMF (which is only a θ solvent), higher solvation leads to a larger effective volume fraction for the core-forming blocks, which results in higher order morphologies.[110,117]

Finally, if the stabilizer block can acquire polyelectrolytic character, the resulting charge density and counter-ions can also influence the aggregate morphology. In the case of the PS-PAA system, the PAA block becomes partially ionized at either neutral or basic pH. Thus mutual electrostatic repulsion between the anionic stabilizer chains results in a higher relative volume fraction occupied by this block. Addition of HCl lowers the effective anionic charge density and hence reduces the electrostatic repulsion: as expected, this reduction in volume fraction for the stabilizer chains promotes the formation of higher order morphologies.[110,118]

Unfortunately, the post-polymerization processing route to block copolymer nano-objects suffers from several disadvantages. It involves using a co-solvent, which usually requires removal prior to the intended application. Moreover, it is a relatively slow process (purification *via* dialysis typically requires several days) that is almost invariably performed in dilute solution (typical copolymer concentrations are no higher than 1-10% w/w solids). Such

problems have hitherto proven to be an insurmountable barrier with regard to potential commercial applications.

1.5. Polymerization-Induced Self-Assembly (PISA)

In principle, polymerization-induced self-assembly (PISA) offers a highly convenient synthetic route for the efficient production of diblock copolymer nano-objects at high copolymer concentrations (up to 50% w/w solids).[119–127] Typically, RAFT polymerization is used to prepare a soluble precursor block.[43,47,70,128] This precursor is then chain-extended using a suitable monomer/solvent pair such that the growing second block becomes insoluble in the reaction mixture once it reaches a certain critical degree of polymerization (DP). This causes micellar nucleation, and the ensuing self-assembly eventually leads to the formation of sterically-stabilized diblock copolymer nanoparticles, see **Figure 1.13**. Depending on the relative volume fractions of each block (as defined by the fractional packing parameter, P)[92,129] − and providing various other conditions are also fulfilled − the final copolymer morphology can be adjusted to obtain spheres, worms, vesicles, or lamellae.[121,122,124,130,131]
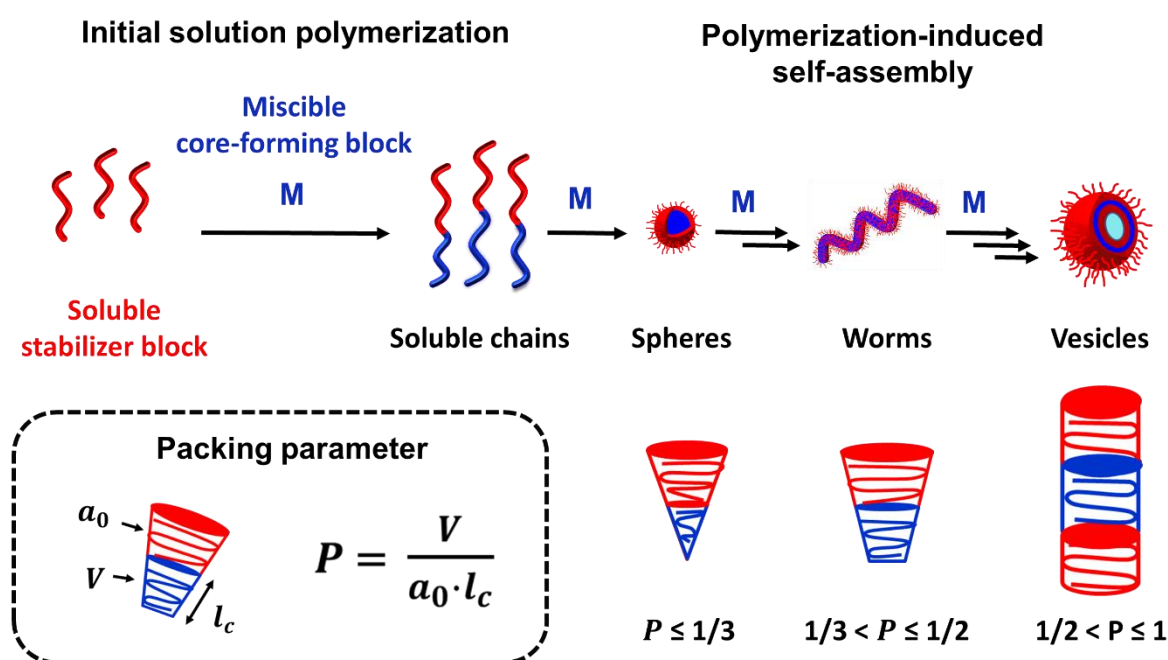
Figure 1.13. Schematic representation of the synthesis of diblock copolymer nano-objects *via* polymerization-induced self-assembly (PISA). V and l_c denote the volume and the length of the core-forming block and a_0 is the effective interfacial area of the block junction.

A wide range of aqueous and alcoholic PISA systems have been studied and various potential commercial applications have been suggested.[121,123,124,126,130,132–137] For example, spheres could be utilized as model particulate emulsifiers for the formation of oil-in-water Pickering nanoemulsions,[138,139] effective dispersants for either aqueous pigments[140] or micrometer-sized organic crystalline fungicidal microparticles for agrochemical formulations.[141] Worm-like particles have been employed for the long-term storage of human stem cells without loss of pluripotency[142] and vesicles can be used for various therapeutic applications.[143,144] In addition, over the past decade there have been many reports describing the synthesis, characterization and applications for block copolymer nano-objects prepared in non-polar media (e.g. *n*-alkanes, mineral oil or silicone oil).[45,46,122,145–158]

In this Thesis, a series of diblock copolymer nano-objects were prepared exclusively in non-polar media. Hence the relevant PISA literature in this sub-field will be discussed in detail.

1.5.1. PISA in non-polar media

1.5.1.1. Reagents used for PISA in non-polar media

Recently, PISA formulations in non-polar media has attracted attention from industrial companies such as Lubrizol, L'Oréal and Ashland to produce nanoparticles for lubrication[156,159] or personal care products.[160,161] Diblock copolymer nanoparticles can be prepared *via* PISA using either a two-pot[46,152,162] or a one-pot protocol.[152,163,164] In the former approach, the first block is synthesized in an organic solvent such as THF or toluene, purified, then chain-extended in a suitable non-polar solvent. The alternative one-pot synthesis protocol involves using the same non-polar solvent for the synthesis of the first block and its subsequent chain extension. In this case, no purification steps are required. Depending on the solubility of the monomer employed to produce the insoluble block, such syntheses can be conducted under either RAFT dispersion polymerization[46,160] or RAFT emulsion polymerization conditions.[165]

Various RAFT CTAs have been employed for preparing nanoparticles in non-polar solvents, including dithiobenzoates[46,145,152,153,162] [e.g. 2-cyano-2-propyl dithiobenzoate (CPDB) or cumyl dithiobenzoate (CDB), see **Figure 1.14a**] and trithiocarbonates,[146–148,155,160,162,164] [e.g. 2-(dodecylthiocarbonothioylthio)-2-methylpropionic acid (DDMAT) or 4-cyano-4-((2-phenylethanesulfonyl)thiocarbonylsulfanyl)pentanoic acid (PETTC), see **Figure 1.14b**]. Furthermore, acrylic[160,162,163,166], methacrylic[46,152,153,156] or acrylamide monomers[164] have been

utilized as steric stabilizer and core-forming blocks (see **Figure 1.15**). A series of alkanes [e.g. *n*-heptane,[46,164,166] *n*-octane,[164,167] *n*-decane,[164] *n*-dodecane,[147,148] *n*-tetradecane,[155,168] *n*-hexadecane,[164] *iso*-dodecane[160,162] or *iso*-hexadecane[163]] have been employed as solvents, as well as industrially-relevant solvents such as poly(α-olefin) (PAO),[152] mineral oil[152,153,156] or low-viscosity silicone oil.[157,158,169]

(a) Dithiobenzoates
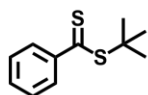
Tert-butyl dithiobenzoate
(TBDB)
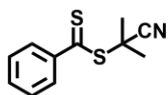
2-Cyano-2-propyl dithiobenzoate
(CPDB)
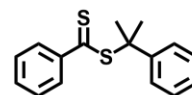
Cumyl dithiobenzoate
(CDB)

(b) Trithiocarbonates
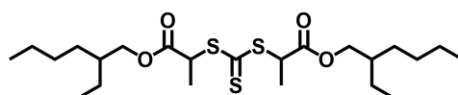
S,S′- Bis[1-(2-ethylhexyloxycarbonyl)ethyl] trithiocarbonate
(EHCETTC)
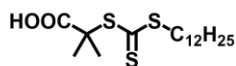
2-(Dodecylthiocarbonothioylthio)-2-methylpropionic acid
(DDMAT)
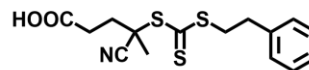
4-Cyano-4-((2-phenylethanesulfonyl)thiocarbonylsulfanyl)pentanoic acid
(PETTC)

Figure 1.14. Chemical structures for **(a)** dithiobenzoate-based and **(b)** trithiocarbonate-based chain transfer agents (CTAs) used for RAFT PISA syntheses in non-polar media.

(a) Stabilizer blocks

Poly(lauryl methacrylate)
(PLMA)

Poly(stearyl methacrylate)
(PSMA)

Poly(hydrogenated butadiene)
(PhBD)

Poly(dimethylsiloxane)
(PDMS)

Poly(3-[tris(trimethylsiloxy)silyl] propyl methacrylate)
(PSiMA)

Poly(lauryl acrylate)
(PLA)

Poly(2-ethylhexyl acrylate)
(P(2-EHA))

Poly(tert-octyl acrylamide)
(POAA)

(b) Core-forming blocks

Poly(methyl methacrylate)
(PMMA)

Poly(glycidyl methacrylate)
(PGlyMA)

Poly(2,2,2-trifluoroethyl methacrylate)
(PTFEMA)

Poly(2-hydroxypropyl methacrylate)
(PHPMA)

Poly(benzyl methacrylate)
(PBzMA)

Poly(3-phenylpropyl methacrylate)
(PPPMA)

Poly(2-(dimethylamino)ethyl methacrylate)
(PDMA)

Poly(N-2-(methacryloyloxy)ethyl pyrrolidone)
(PNMEP)

Poly(methyl acrylate)
(PMA)

Poly(phenyl acrylate)
(PPhA)

Poly(benzyl acrylate)
(PBzA)

Poly(N,N-dimethylacrylamide)
(PDMAC)

Poly(N-(2-acryloyloxy)ethyl pyrrolidone)
(PNAEP)

Figure 1.15. Summary of the chemical structures of the various polymers employed as either **(a)** the steric stabilizer or **(b)** the core-forming block for RAFT PISA syntheses in non-polar media.

In the following Section, we will discuss specific literature examples of non-polar PISA syntheses, classified according to the resulting copolymer morphologies (spheres, worms or vesicles).

1.5.1.2. Spherical nanoparticles

The first examples of the PISA synthesis of spherical diblock copolymer nanoparticles in non-polar media were reported by Charleux *et al.* in 2007[162] and 2010.[160,170] An all-acrylic formulation was employed in which poly(2-ethylhexyl acrylate) (P(2-EHA)) served as the steric stabilizer block in *iso*-dodecane and poly(methyl acrylate) (PMA) was used as the core-forming block.[160,162,170] Solely spherical nanoparticles were obtained within the size range of 30-300 nm at up to 40% w/w solids.[160,162] The dispersion polymerization of methyl acrylate using a dithiobenzoate RAFT agent (*tert*-butyl dithiobenzoate (TBDB), see **Figure 1.14**) at 28% w/w solids led to strong rate retardation, poor RAFT control ($Đ = 6.00$ at the highest MA conversion of 85% within 24 h) and ill-defined nanoparticles with bimodal distributions as judged by DLS studies. In striking contrast, using a trithiocarbonate-based P(2-EHA) stabilizer block (S,S′-bis[1-(2-ethylhexyloxycarbonyl)ethyl] trithiocarbonate or EHCETTC, see **Figure 1.14**) led to 100% conversion within 4 h when targeting 39% w/w solids. Moreover, a relatively narrow MWD ($Đ = 1.21$) and near-monodisperse nanoparticles (unimodal distribution, PDI ≤ 0.10) were obtained according to GPC and DLS studies, respectively.[162] According to the authors, the low glass transition temperature (T_g) of PMA makes these particles potentially useful for cosmetics formulations (e.g. nail varnish).[160]

In 2013, an all-methacrylic PISA formulation was reported by Fielding *et al.*[46] More specifically, poly(lauryl methacrylate)-poly(benzyl methacrylate) (PLMA-PBzMA) nanoparticles were prepared *via* the RAFT dispersion polymerization of benzyl methacrylate (BzMA) using a dithiobenzoate-capped PLMA stabilizer block in *n*-heptane. High BzMA conversions (≥ 97%) were achieved within 5 h at 90 °C. In this case, spherical nanoparticles were produced using a PLMA$_{17}$ precursor and targeting relatively low DPs for the PBzMA core-forming block (DP ≤ 38) at 12.5-25% w/w solids. Reasonably good RAFT control over the polymerization ($Đ < 1.38$) was achieved for such syntheses. Furthermore, employing relatively long PLMA stabilizer blocks (DP ≥ 37) invariably resulted in the formation of kinetically-trapped spheres. Such observations were consistent with prior studies of aqueous PISA formulations.[171,172] Using a relatively long stabilizer block (PLMA$_{37}$), the nanoparticle

diameter increased systematically from 41 nm (PDI = 0.01) up to 139 nm (PDI = 0.01) when increasing the target DP of the core-forming PBzMA block from 100 to 900 at 15% w/w solids.[46] Subsequently, Derry and co-workers used the same PLMA-PBzMA system to produce well-defined spheres (and also worms or vesicles) in more industrially-relevant solvents such as poly(α-olefin) (PAO) or mineral oil. Furthermore, a highly efficient one-pot synthesis method was devised to produce such spheres at up to 50% w/w solids.[152]

According to Zheng *et al.*, diblock copolymer nanoparticles may be useful as lubricity modifiers for automotive engine oils.[173] In a related work, Derry *et al.* prepared core-crosslinked poly(stearyl methacrylate)-poly-(benzyl methacrylate)-poly(ethylene glycol dimethacrylate) (PSMA$_{31}$-PBzMA$_{200}$-PEGDMA$_{20}$) triblock copolymer nanoparticles of approximately 48 nm diameter in mineral oil *via* RAFT PISA (see **Figure 1.16a**).[159]
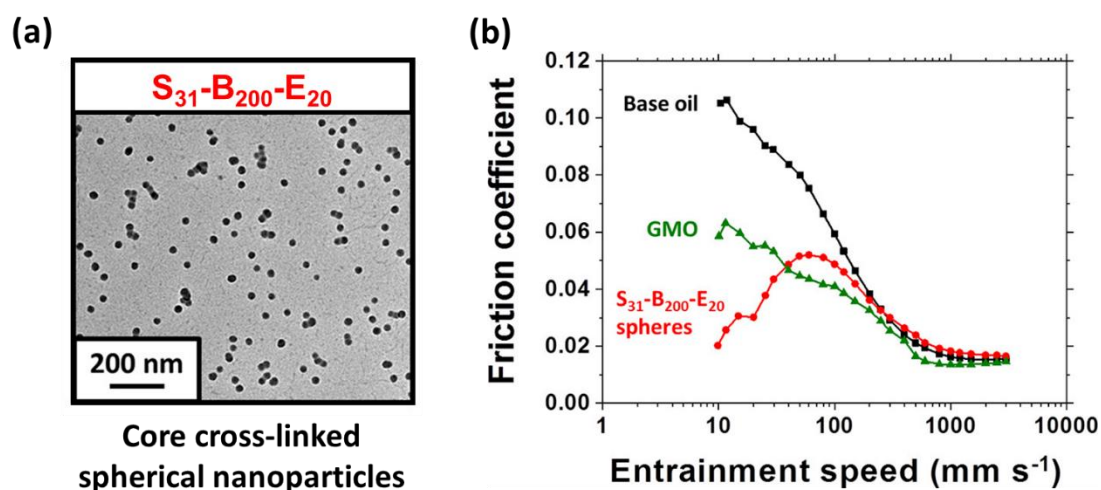
Figure 1.16. (a) Representative transmission electron microscopy image recorded for the poly(stearyl methacrylate)-poly(benzyl methacrylate)-poly(ethylene glycol dimethacrylate) (PSMA$_{31}$-PBzMA$_{200}$-PEGDMA$_{20}$) spheres. **(b)** Stribeck curves showing the change in friction coefficient with entrainment speed observed for a lubricating base oil alone (black squares), 0.50% w/w glyceryl monooleate (GMO, green triangles) in the same base oil, and a 0.50% w/w dispersion of 48 nm diameter core-crosslinked PSMA$_{31}$-PBzMA$_{200}$-PEGDMA$_{20}$ spheres dispersed within the same base oil (red circles). Data were recorded at a 20% slide-to-roll ratio (SRR) under an applied load of 35 N at 100 °C.[159] Figure adapted with permission from ref. 159.

Using PSMA instead of PLMA as a stabilizer block provided higher blocking efficiencies and improved control over the copolymer MWD, especially when targeting higher PBzMA DPs.[46,153] Incorporating only 9 mol% EGDMA into the core-forming block proved to be sufficient to obtain core-crosslinked spheres.[159] Tribology experiments conducted using a mini-

traction machine (MTM) confirmed that just 0.50% w/w of such nanoparticles can dramatically reduce the friction coefficient of engine base oil within the boundary lubrication regime compared to a traditional friction modifier, glyceryl monooleate (GMO) employed at the same concentration, see **Figure 1.16b**. Given the relative ease of production of these nanoparticles on an industrial scale, this PISA formulation offers an excellent opportunity for the design of next-generation ultralow-viscosity engine oils.[159]

Another important contribution to this field involved the preparation of nanoparticles with highly reactive functional groups. For example, the synthesis of epoxy-functional poly(stearyl methacrylate)-poly(glycidyl methacrylate) (PSMA-PGlyMA) diblock copolymer spheres in mineral oil was reported by Docherty *et al*.[156] A series of spherical nanoparticles were prepared *via* the RAFT dispersion polymerization of GlyMA using either $PSMA_{13}$ or $PSMA_{18}$ as a steric stabilizer block. The particle diameter could be tuned between 21 and 86 nm by simply varying the DP for the core-forming PGlyMA block between 50 and 400. A long-term chemical stability study revealed that only 9% of the epoxy groups reacted over a 16-week period when stored at ambient temperature. This was significantly less than that previously reported for the poly(glycerol monomethacrylate)-poly(glycidyl methacrylate) (PGMA-PGlyMA) in aqueous media (27% over a 12-week period).[174]

Another interesting example of preparing functional spherical nanoparticles in *n*-alkanes was reported by Pei *et al*., who introduced reactive pentafluorophenyl methacrylate (PFPMA) units into the steric stabilizer chains of $P(SMA_{36}$-*stat*-$PFPMA_2)$-$PPPMA_{79}$ spheres, where PPPMA denotes poly(3-phenylpropyl methacrylate) (see **Figure 1.15**).[168] The post-polymerization modification of such nanoparticles *via* nucleophilic acyl substitution was studied using excess benzylamine, tetrahydrofurfuryl amine, *N,N*-dimethylethylenediamine or methyl red amine in the presence of *n*-butyl acrylate, which acted as a Michael acceptor.

The upper size limit for sterically-stabilized spherical nanoparticles in non-polar media was examined by Parker *et al*., who studied the PSMA-PBzMA system in mineral oil.[146] Well-defined kinetically-trapped spherical nanoparticles of up to 459 nm diameter were obtained at 20% w/w solids when targeting PBzMA DPs up to 3500 by using a relatively long $PSMA_{54}$ precursor (see **Figure 1.17**). To date, these are the largest spherical nanoparticles accessed *via* RAFT-mediated PISA in non-polar media. A double-logarithmic plot indicated a linear

evolution in the DLS diameter when targeting PBzMA DP of up to 2500 (see **Figure 1.17b**). However, deviation from this linear relationship was observed when targeting higher DPs, which also produced nanoparticles with relatively broad size distributions. Moreover, RAFT control was gradually lost when targeting higher PBzMA DPs, with $Đ$ increasing from 1.14 (DP = 50) up to 3.41 (DP = 3500).
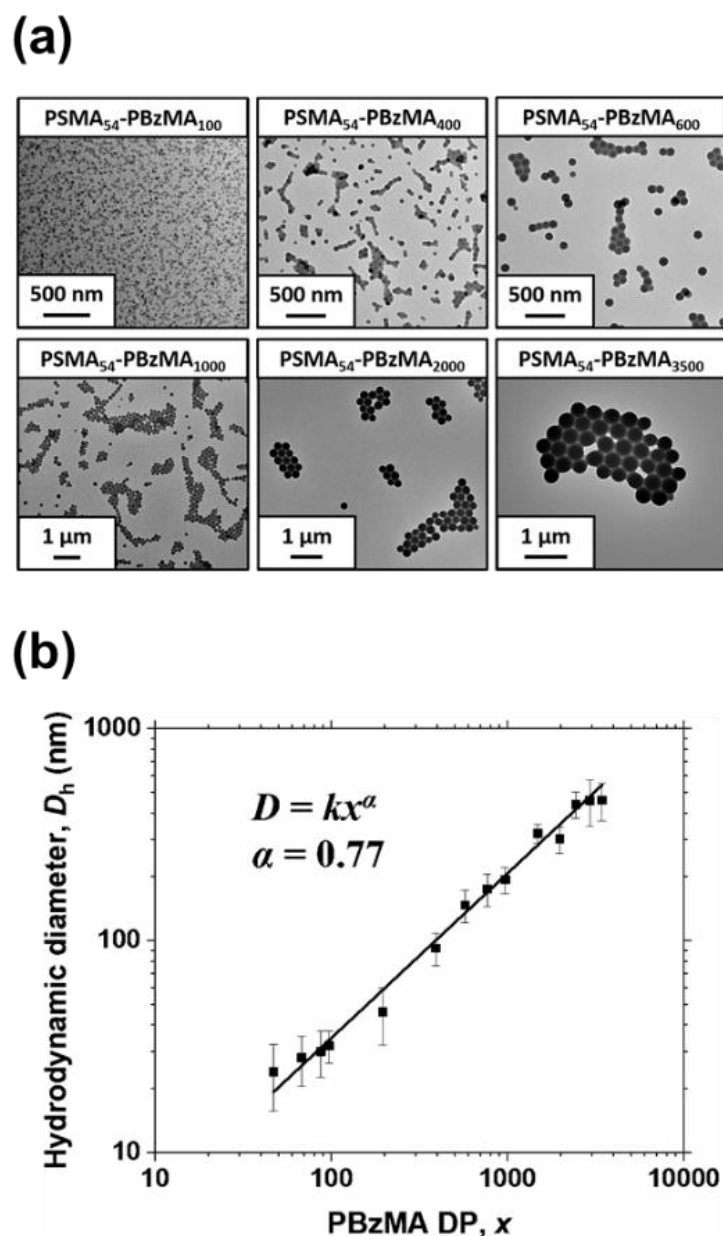
Figure 1.17. **(a)** Representative TEM images recorded for selected PSMA$_{54}$-PBzMA$_x$ spherical nanoparticles. **(b)** Hydrodynamic DLS diameter (D_h) *vs.* PBzMA DP (x) obtained for a series of PSMA$_{54}$-PBzMA$_x$ spheres (x = 50−3500) prepared *via* RAFT dispersion polymerization of BzMA in mineral oil at 90 °C when targeting 20% w/w solids. Error bars represent the standard deviation in D_h as calculated from the DLS polydispersity index.[146] Figure adapted with permission from ref. 146.

Cornel *et al*. reported a fundamental study to gain a better understanding of the behavior of PLMA$_{39}$-PBzMA$_{x}$ spherical nanoparticles during thermal annealing.[147] Small-angle X-ray scattering (SAXS) studies confirmed that heating a 1% w/w dispersion comprising a binary mixture of relatively small PLMA$_{39}$-PBzMA$_{97}$ spheres (core diameter = 21 ± 2 nm) and relatively large PLMA$_{39}$-PBzMA$_{294}$ spheres (core diameter = 48 ± 5 nm) up to 150 °C led to the formation of spherical nanoparticles of intermediate size (core diameter = 36 ± 4 nm) on cooling to 25 °C, see **Figure 1.18a**. These observations were confirmed by transmission electron microscopy (TEM) analysis (see **Figure 1.18a**). However, when the two types of initial nanoparticles were separately exposed to the same thermal annealing conditions, no size change occurred. For the smaller nanoparticles, solvation of the PBzMA cores owing to ingress by hot solvent occurred at 150 °C. In contrast, no solvation of the larger particles was observed. Furthermore, thermal annealing of the smaller particles at 150 °C resulted in a significant reduction in their aggregation number, which suggests partial dissociation under such conditions. A two-stage mechanism was proposed to account for the formation of the intermediate-sized spheres (see **Figure 1.18b**). During the first stage, the smaller PLMA$_{39}$-PBzMA$_{97}$ spheres undergo partial dissociation and the resulting free copolymer chains then become incorporated into the larger PLMA$_{39}$-PBzMA$_{294}$ spheres which leads to an increase in their size. The second stage involves fusion of the remaining smaller spheres with the new larger 'hybrid' spheres, which results in the formation of weakly anisotropic transient species that subsequently undergo fission – most likely because of further incorporation of PLMA$_{39}$-PBzMA$_{97}$ chains – to produce spheres of intermediate size.[147]
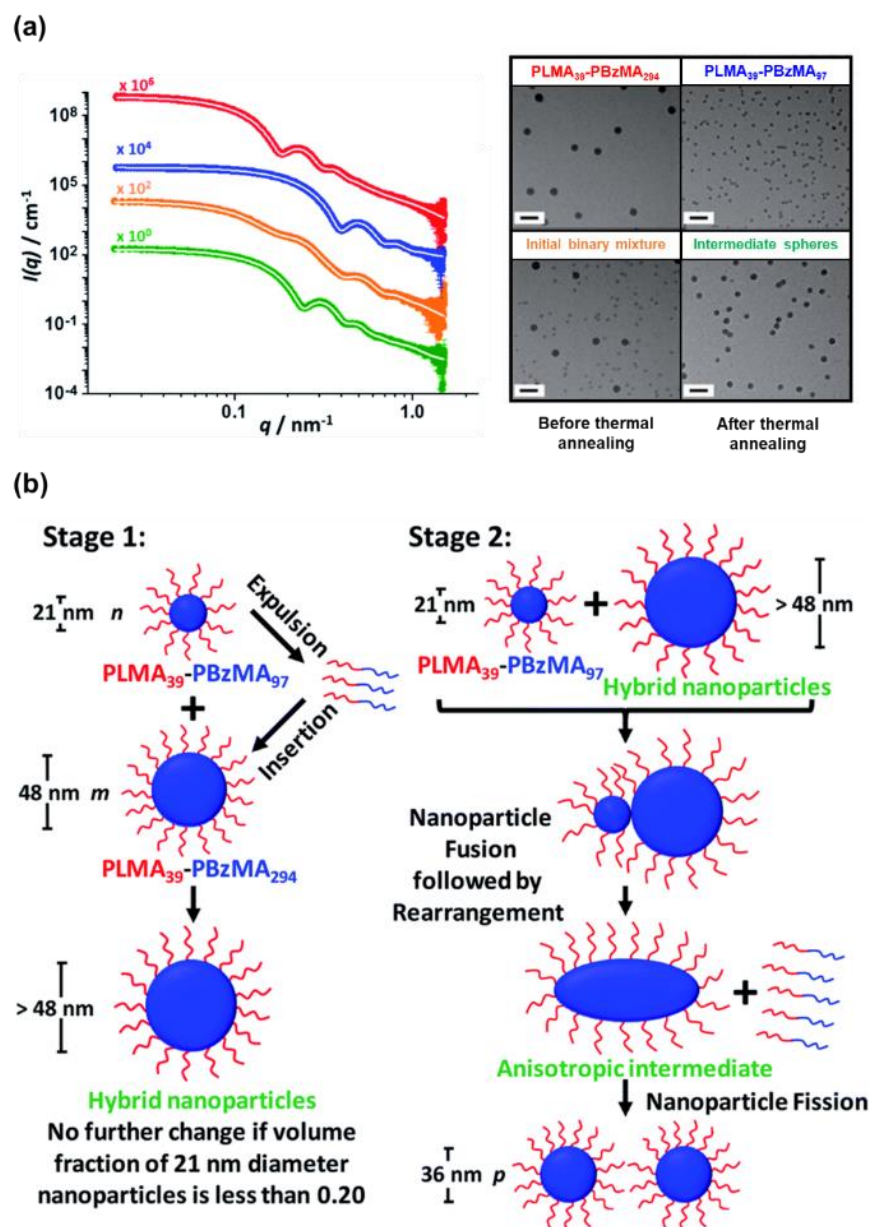
Figure 1.18. (a) SAXS patterns (and corresponding TEM images) recorded at 25 °C for 1.0% w/w dispersions of: PLMA$_{39}$-PBzMA$_{294}$ spheres (red data) and PLMA$_{39}$-PBzMA$_{97}$ spheres (blue data); a 1.0% w/w equivolume binary mixture of these two initial dispersions prior to thermal annealing (orange data) and the final hybrid nanoparticles formed after thermal annealing of the same binary mixture at 150 °C for 1 h (green data). White traces indicate the best fits to the data obtained when using a spherical micelle model.[175] Scale bars shown in TEM images correspond to 100 nm. **(b)** Schematic representation of the two-stage mechanism proposed for the changes in copolymer morphology that are observed during thermal annealing of a binary mixture of 21 ± 2 nm and 48 ± 5 nm diblock copolymer spheres at 150 °C. Here, the *n*, *m* and *p* values refer to the number density of each type of nanoparticle. In Stage 1, the smaller PLMA$_{39}$-PBzMA$_{97}$ spheres undergo partial dissociation to form copolymer chains, which then become incorporated into the larger spheres to produce hybrid spheres with a mean diameter greater than 48 nm. If the volume fraction of these smaller spheres is less than 0.20, this is the final copolymer morphology. However, using higher volume fractions of this component leads to Stage 2, whereby the 21 nm spheres undergo fusion with the larger hybrid spheres to form weakly anisotropic transient species. The latter then undergo fission – most likely mediated by incorporation of further PLMA$_{39}$-PBzMA$_{97}$ chains – to form spheres of intermediate size (e.g. 36 nm diameter).[147] Figure adapted with permission from ref. 147.

Cornel and co-workers reported direct experimental evidence for the rapid exchange of individual copolymer chains between sterically-stabilized spherical nanoparticles at elevated temperature.[148] More specifically, time-resolved small angle neutron scattering (TR-SANS) was used to analyse a binary mixture of fully hydrogenous poly(lauryl methacrylate)-poly(methyl methacrylate) (PLMA$_{39}$-PMMA$_{55}$) and core-deuterated PLMA$_{39}$-d$_8$PMMA$_{57}$ spherical nanoparticles (each with a mean core diameter of ~ 20 nm) after heating at 150 °C for 3 min. The TR-SANS data revealed that mixed core spheres comprising both the PMMA$_{55}$ and d$_8$PMMA$_{57}$ blocks were obtained after this heating protocol. Moreover, a similar mixture of PLMA$_{39}$-PMMA$_{94}$ and PLMA$_{39}$-d$_8$PMMA$_{96}$ required a longer annealing time (8 min) to produce mixed core spheres, which suggests that the rate of copolymer exchange depends on the DP of the core-forming block. Furthermore, relatively slow copolymer exchange was observed even at 80 °C, which is below the T_g of the core-forming PMMA block.[148] These findings are consistent with previous TR-SANS studies of block copolymer micelles reported by Lund *et al*. and Bates, Lodge and co-workers.[148,176–179]

Gibson *et al*. reported the RAFT dispersion polymerization of *N,N*-dimethylacrylamide (DMAC) using a poly(*tert*-octyl acrylamide (POAA$_{85}$) precursor.[164] This is the first all-acrylamide PISA formulation reported for non-polar media. High DMAC conversions and reasonably good RAFT control ($M_w/M_n \leq 1.42$) were achieved and a series of well-defined spheres with DLS diameters ranging from 23 nm to 91 nm were obtained when systematically increasing the PDMAC DP (x) from 50 to 250. Interestingly, the colloidal stability of such nanoparticles depends on the type of *n*-alkane solvent used for the PISA synthesis. Colloidally stable spherical nanoparticles were obtained at 20 °C in *n*-heptane, *n*-octane or *n*-decane, whereas employing *n*-dodecane, *n*-tetradecane or *n*-hexadecane led to nanoparticle flocculation on cooling from the synthesis temperature (70 °C) to 20 °C. This is because the POAA$_{85}$ steric stabilizer chains exhibit upper critical solution temperature (UCST)-type behavior in higher *n*-alkanes, which leads to the loss of steric stabilization at 20 °C.

Finally, it is also well-known that block copolymer spheres can be utilized as effective Pickering emulsifiers.[138,180–182] Hydrophobic particles, prepared in non-polar media usually produce water-in-oil (w/o) emulsions[183184] but examples for forming complex emulsions such as Pickering double emulsions using hydrophobic particles have also been reported.[165,185]

1.5.1.3. Worm-like nanoparticles

The synthesis of worms and vesicles in non-polar media was first reported by Fielding *et al.*[46] These workers found that the PISA synthesis of highly anisotropic $PLMA_{17}$-$PBzMA_y$ worms in *n*-heptane required a sufficiently high copolymer concentration ($\geq 17.5\%$ w/w). Presumably, this aids the stochastic fusion of multiple spheres to generate the worm-like morphology within the timescale of the BzMA polymerization. According to the pseudo-phase diagram constructed by Fielding *et al.*, the pure worm-like morphology was restricted to a rather narrow PBzMA DP range (see **Figure 1.19a**).[46] In a follow-up study, a pseudo-phase diagram for essentially the same PLMA-PBzMA formulation in *n*-dodecane was constructed by systematically varying the mean DP for each block while targeting 20% w/w solids. This approach demonstrated that a sufficiently short PLMA stabilizer block (PLMA DP ≤ 21) was required to access a pure worm phase (see **Figure 1.19b**).[45]
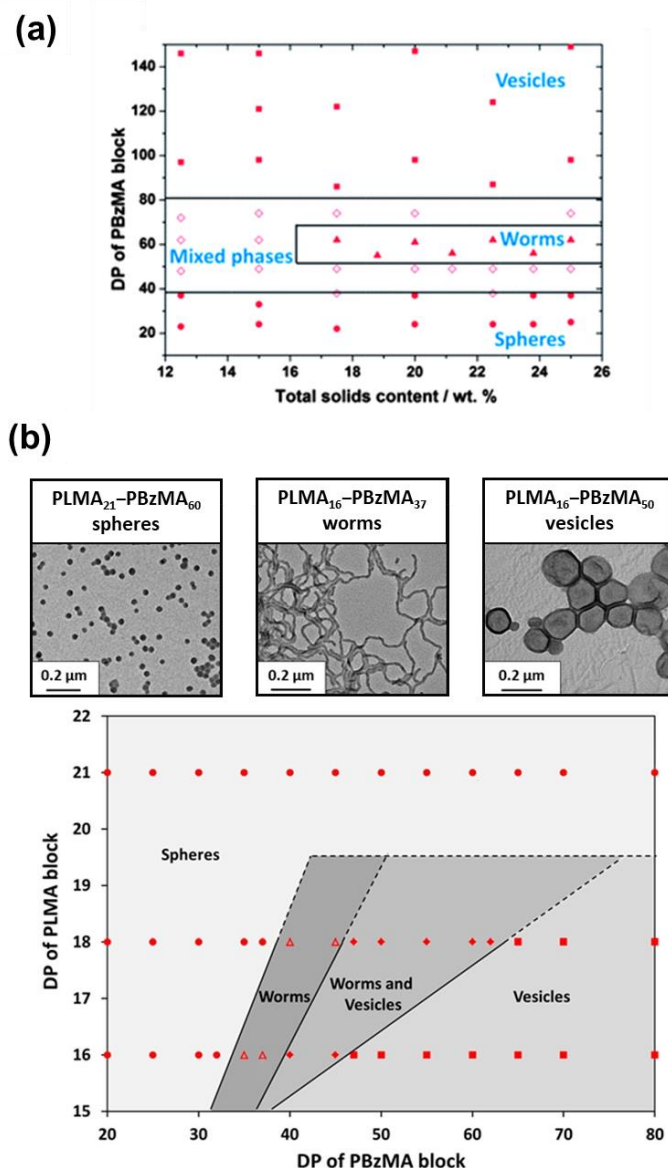
Figure 1.19. (a) Phase diagram constructed for **(a)** PLMA$_{17}$-PBzMA$_y$ diblock copolymer nanoparticles prepared by RAFT dispersion polymerization of BzMA in *n*-heptane at 90 °C using a PLMA$_{17}$ precursor and a T21s initiator when systematically varying the PBzMA DP and the total solids content.[46] **(b)** PLMA$_x$-PBzMA$_y$ diblock copolymer nanoparticles prepared by RAFT dispersion polymerization of BzMA in *n*-dodecane using an AIBN initiator at 70 °C when targeting 20% w/w solids and systematically varying the PLMA and PBzMA DPs.[45] In both cases, the *post mortem* copolymer morphologies were assigned by TEM analysis. Figures are adapted with permission from refs. 46 and 45, respectively.

The thermoresponsive behavior of such anisotropic nanoparticles was subsequently examined.[45] PLMA$_{16}$-PBzMA$_{37}$ worms prepared in *n*-dodecane (which has a higher b.p. than *n*-heptane) underwent a reversible worm-to-sphere transition upon heating from 20 to 90 °C (see **Figure 1.20**). A 20% w/w dispersion of PLMA$_{16}$-PBzMA$_{37}$ worms formed a transparent free-standing gel at 20 °C but degelation occurred at 90 °C. This is because isotropic spheres

interact with each other much less efficiently than highly anisotropic worms, which form a percolating 3D network at a relatively low copolymer concentration.[186] Moreover, the worm-to-sphere transition proved to be more or less reversible at 20% w/w solids but irreversible behavior was observed at ≤ 5% w/w solids. This difference was explained in terms of the reduced probability of interparticle fusion to reconstitute the original worms, which is a highly cooperative process.[45] Variable temperature rheology studies revealed that degelation actually occurred at ~47 °C. Interestingly, SAXS studies indicated that a purely spherical morphology was only obtained after heating the copolymer dispersion up to 160 °C. Thus, a complete worm-to-sphere transition is not required to induce degelation – simply producing a mixed phase of shorter worms and some spheres is sufficient. Variable temperature SAXS studies indicated a gradual reduction in the mean contour length on heating, which reduces the multiple inter-worm contacts that cause gelation. SAXS and TEM studies also revealed that a mixture of short worms and spheres is formed at intermediate temperatures. A mechanism for the worm-to-sphere transition was proposed that involved sequential budding of spheres from worm ends, rather than random worm scission.[45] Variable temperature ^{1}H NMR studies on a 5% w/w dispersion of PLMA$_{16}$-PBzMA$_{37}$ worms diluted in d$_{26}$-dodecane confirmed that partial solvation of the PBzMA block occurred on heating, which provided further insight regarding this thermally-induced morphological transition. If *uniform* plasticization of the core-forming block occurred at elevated temperature this would increase its effective volume fraction and hence result in a *higher* packing parameter. This scenario incorrectly predicts a worm-to-vesicle transition. Instead, a worm-to-sphere transition occurs owing to *surface* plasticization of the worms. This means that only the BzMA repeat units located nearest to the PLMA stabilizer block become solvated. Thus the effective volume fraction of the stabilizer block increases, which *lowers* the packing parameter and hence accounts for the observed morphological transition.[45]
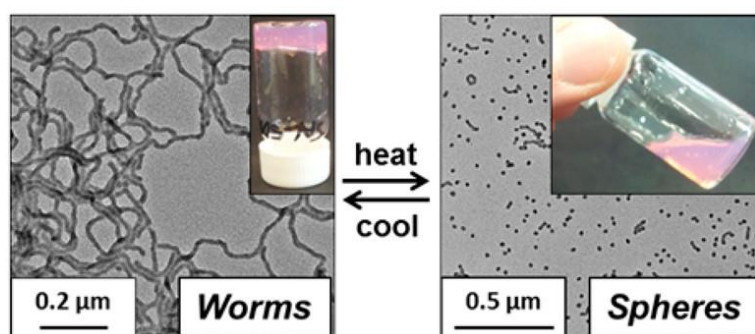
Figure 1.20. Worm-to-sphere transition observed on heating a 20% w/w dispersion of PLMA$_{16}$-PBzMA$_{37}$ worms up to 90 °C in *n*-dodecane. TEM analysis indicated reversible behavior, with reconstituted worms being formed on cooling to 20 °C.[45] Figure adapted with permission from ref. 45.

Subsequently, a similar worm-to-sphere transition upon heating was reported by Lowe *et al*. for PSMA-PPPMA worms prepared at 30% w/w solids in *n*-octane (for PSMA$_{18}$-PPPMA$_{71}$)[167] or at 20% w/w solids in *n*-tetradecane (for PSMA$_{19}$-PPPMA$_{85}$).[187] Similarly, Rymaruk *et al*. observed a worm-to-sphere transition for poly(dimethylsiloxane)-poly-(2-(dimethylamino)ethyl methacrylate) (PDMS$_{66}$-PDMA$_{100}$) worms prepared in decamethylcyclopentasiloxane (D5) silicone oil.[158]

An important aspect of the highly anisotropic worm-like nanoparticles is their distinctive rheological behavior. Rymaruk *et al*. found that PDMS-PDMA worm gels can be used as efficient viscosity modifiers for either *n*-dodecane or low-viscosity silicone oils such as decamethylcyclopentasiloxane (D5), octamethylcyclotetrasiloxane (D4) or hexamethyldisiloxane (HMDS).[169] In this case, a commercially available monohydroxy-terminated polydimethylsiloxane (DP = 66) was esterified using a carboxylic acid functionalized trithiocarbonate RAFT agent (PETTC) to yield a PDMS$_{66}$ precursor. Various methacrylate monomers (e.g. BzMA, 2,2,2-trifluoroethyl methacrylate (TFEMA), MMA, 2-hydroxypropyl methacrylate (HPMA) or DMA) were employed to chain-extend this precursor *via* PISA syntheses performed in silicone oil. However, only kinetically-trapped spheres were obtained in most cases. Exceptionally, DMA polymerizations provided access to worms and vesicles, which was attributed to the relatively low T_g of PDMA ($\sim$ 18 °C). Interestingly, rotational rheology experiments indicated that a 5% w/w dispersion of PDMS$_{66}$-PDMA$_{100}$ worms produced a sixty-fold increase in solution viscosity relative to that for the corresponding pure solvent (see **Figure 1.21**).[169] In a subsequent study, Rymaruk *et al*. reported that the same worms could be crosslinked using 1,2-bis(2-iodoethoxy)ethane (BIEE).[158] This bifunctional reagent quaternizes the tertiary amine groups on the DMA residues within the worm cores, thus introducing cross-links *via* the Menshutkin reaction. Oscillatory rheology studies of 25% w/w gels formed by the linear and core-crosslinked PDMS$_{66}$-PDMA$_{100}$ worms revealed that using a BIEE/DMA molar ratio of 0.15 increased the worm gel strength (G') dramatically from 94 to 7855 Pa. Such derivatization also reduced the critical gelation concentration (CGC) from 12% for the linear worms to just 2% for the core-crosslinked worms. This was attributed to the much greater stiffness of the latter worms. Moreover, such worm gels no longer exhibited any thermoresponsive behavior after core-crosslinking, which enables their use as a viscosity modifier over a wide temperature range. A similarly low CGC (2.5%) was determined for poly(lauryl acrylate)-poly(benzyl acrylate) (PLA$_{14}$-PBzA$_{60}$) worms, which could be prepared at up to 40% solids in *n*-dodecane using a convenient one-pot protocol.[163] This was the first

all-acrylic PISA formulation in non-polar media to provide access to higher order morphologies.
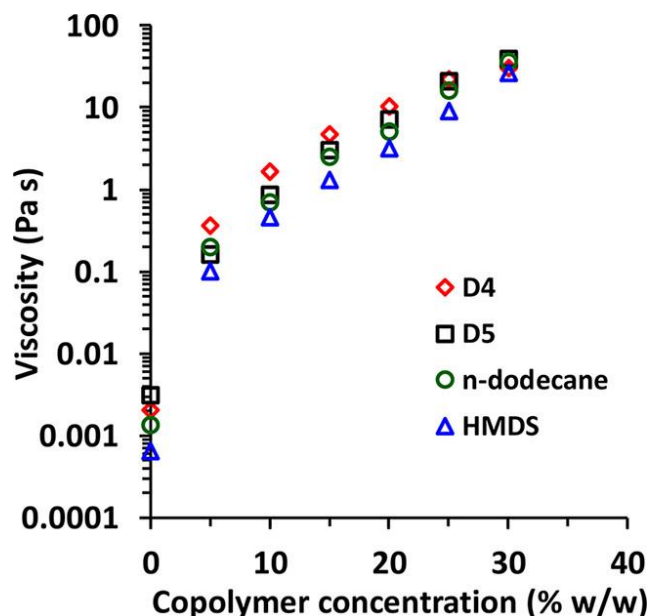
Figure 1.21. Concentration dependence of the solution viscosity (at a fixed shear rate of 10 s^{-1}) for PDMS$_{66}$–PDMA$_x$ diblock copolymer worms prepared in either D5 silicone oil (open black squares), D4 (open red diamonds), HMDS (open blue triangles), or *n*-dodecane (open green circles), where x varies between 91 and 110 depending on the solvent type. In each case, worms were prepared at an initial copolymer concentration of 30% w/w solids and then sequentially diluted using the same solvent for viscosity measurements.[169] Figure adapted with permission from ref. 169.

In related work, poly(3-[tris(trimethylsiloxy)silyl]propyl methacrylate)-poly(benzyl methacrylate) (PSiMA-PBzMA) diblock copolymers have been prepared *via* PISA syntheses conducted in silicone oil.[157] According to the pseudo-phase diagram constructed for PSiMA$_{12}$-PBzMA$_x$ nanoparticles (x ≤ 200) when varying the solids content between 5% w/w and 20% w/w, a pure worm morphology could be accessed even at the lowest copolymer concentration (5% w/w). This is rather unusual: this morphology usually requires somewhat higher copolymer concentrations.[46,152,167,168,187,188] For example, Darmau *et al*. reported that poly(hydrogenated butadiene)-poly(benzyl methacrylate) (PhBD-PBzMA) worms could only be accessed at either 40 or 45% w/w solids in *n*-dodecane.[188] For this latter system, *in situ* SAXS analysis during the synthesis of PhBD$_{80}$-PBzMA$_{40}$ worms at 40% w/w solids enabled identification of intermediate lyotropic phases such as body-centered cubic (BCC) and hexagonally close-packed (HCP) sphere phases prior to the formation of a final hexagonal cylinder phase (HEX).[189]

Another example of the synthesis of pure worms at 5% w/w is the PSMA-PBzMA system in mineral oil.[153] Potential application of such highly anisotropic nanoparticles as rheology modifiers was examined by Derry *et al.*, who studied the alignment of $PSMA_{13}$-$PBzMA_{64}$ worms in non-polar media using shear-induced polarized light imaging (SIPLI).[149] Highly anisotropic particles tend to align in the direction of flow above a certain critical shear rate, which results in shear-thinning. In this study, worm alignment was examined as a function of temperature. A worm-to-sphere transition occurs on heating from 20 to 150 °C. Thus the initial shear-thinning anisotropic worms are converted into isotropic spherical nanoparticles, which behave like Newtonian fluids. A 20% w/w dispersion of $PSMA_{13}$-$PBzMA_{64}$ nanoparticles was monitored by SIPLI during a thermal cycle from 20 °C to 150 to 20 °C to determine the relationship between dispersion viscosity and shear alignment. Between 20 and 60 °C, the dispersion had a relatively high viscosity owing to the presence of worms. Aligned linear worms were obtained at 80-110 °C and further heating up to 150 °C produced a low-viscosity dispersion of spheres. The same PSMA-PBzMA formulation was also used to design hydrogen-bonded worm gels in *n*-dodecane.[150] This was achieved by using carboxylic acid-functional PETTC for the synthesis of a PSMA precursor (HOOC-$PSMA_{11}$) *via* RAFT solution polymerization. Half of this precursor was then subjected to Steglich esterification with excess methanol to produce H_3COOC-$PSMA_{11}$. When targeting the same $PSMA_{11}$-$PBzMA_{65}$ worms in turn, the HOOC-$PSMA_{11}$ precursor produced a much stronger physical gel ($G' \sim 114$ kPa) than that obtained when using the H_3COOC-$PSMA_{11}$ precursor ($G' \sim 4.5$ kPa). This substantial difference was attributed to the formation of carboxylic acid dimers between neighbouring worms within the percolating network. Moreover, a series of worm gels with tunable gel strength can be readily prepared by either (i) using binary mixtures of acid- and ester-capped PSMA precursors during PISA or (ii) using a post-polymerization processing strategy to exploit the reversible worm-to-sphere transition exhibited by such worms to create binary mixtures of acid- and ester-functionalized spheres at 110 °C that reform 'hybrid' worms on cooling to 20 °C (see **Figure 1.22**).[150]
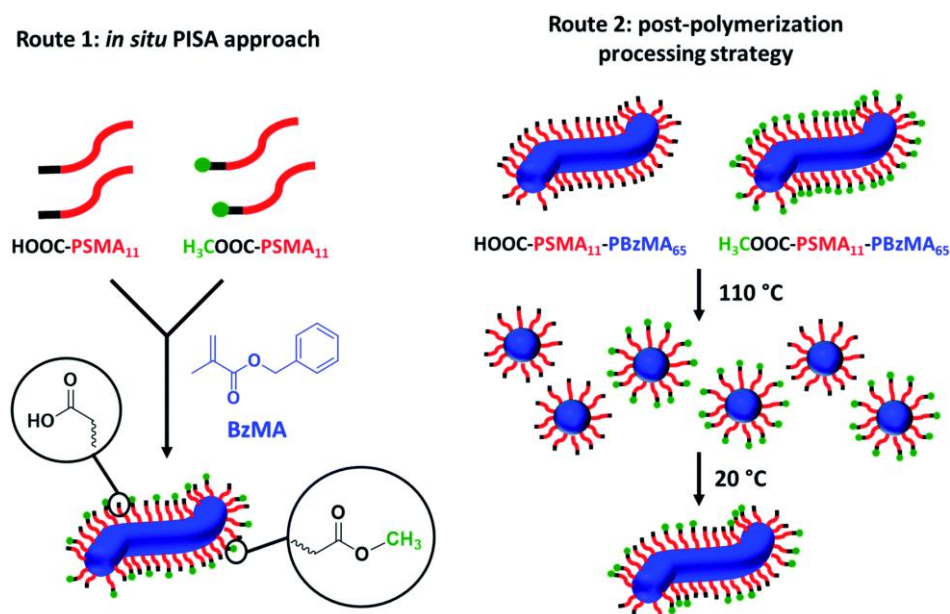
Figure 1.22. Schematic representation of the two synthetic routes used to prepare two series of PSMA-PBzMA worms containing varying proportions of carboxylic acid end-groups. Both routes are based on the principle of entropic mixing. **Route 1** utilizes a binary mixture of HOOC-PSMA$_{11}$ and H$_3$COOC-PSMA$_{11}$ precursors during the RAFT dispersion polymerization of BzMA; this approach results in a statistical distribution of carboxylic acid end-groups located at the outer surface of each sterically-stabilized worm. **Route 2** involves heating two 'masterbatch' 20% w/w dispersions comprising HOOC-PSMA$_{11}$-PBzMA$_{65}$ and H$_3$COOC-PSMA$_{11}$-PBzMA$_{65}$ worm gels up to 110 °C to induce a worm-to-sphere transition (and concomitant degelation) in each case. These two free-flowing fluids of spherical nanoparticles were then mixed together in various proportions at 110 °C to produce the desired range of carboxylic acid/methyl ester molar ratios. On cooling to 20 °C, a sphere-to-worm transition occurs *via* 1D stochastic fusion of multiple (mixed) spheres to produce 'hybrid' segmented worms comprising spatially-localized patches of steric stabilizer chains bearing carboxylic acid end-groups.[150] Figure adapted with permission from ref. 150.

1.5.1.4. Vesicles

Well-defined vesicles can be prepared in non-polar media using many of the formulations discussed above. Literature examples include PLMA-PBzMA,[46,152] PLMA-PGlyMA,[145] PSMA-PPPMA,[167,187] PSMA-PBzMA,[153,154] PSMA-PNMEP,[183] PLA-PBzA,[163] PDMS-PBzMA,[190] PDMS-PDMA,[169] PSiMA-PBzMA[157] and PhBD-PBzMA.[188] However, there are only a few reports that are focused on this particular morphology. These are briefly discussed in turn below.

Insights into the vesicle growth mechanism during PISA syntheses conducted in non-polar media was provided by Derry *et al.*[153] *In situ* SAXS studies conducted during the synthesis of PSMA$_{13}$-PBzMA$_{150}$ vesicles at 10% w/w solids in mineral oil within a capillary cell revealed a gradual evolution in copolymer morphology from molecularly-dissolved chains to spheres to

worms to vesicles (see **Figure 1.23a**). Comparing the kinetic plot obtained from this experiment with the corresponding pseudo-phase diagram constructed for $PSMA_{13}$-$PBzMA_x$ nano-objects confirmed that the critical PBzMA DP boundaries for pure morphologies (spheres, worms or vesicles) were in remarkably good agreement. DLS, TEM and *postmortem* SAXS analysis indicated that, once vesicles were formed at around 72% BzMA conversion, their membrane thickness increased monotonically with monomer conversion as the PBzMA DP increased. Furthermore, the *overall* vesicle diameter remained constant. Thus, the vesicle lumen volume must decrease during the polymerization. This implies an 'inward growth' mechanism for the vesicles. Moreover, this appears to be a generic mechanism for the growth of diblock copolymer vesicles during PISA since similar observations were reported by Warren *et al.* for PGMA-PHPMA vesicles prepared *via* aqueous PISA.[191] The same $PSMA_{13}$-$PBzMA_{150}$ vesicles were also prepared at 10% w/w solids in mineral oil on a laboratory scale to enable aliquots to be periodically extracted from the reaction mixture for TEM analysis. Intermediate morphologies such as octopi and jellyfish (see **Figure 1.23b**) were identified during the evolution from worms to vesicles, similar to observations made by Blanazs and co-workers for a $PGMA_{47}$-$PHPMA_{200}$ aqueous PISA formulation.[192]
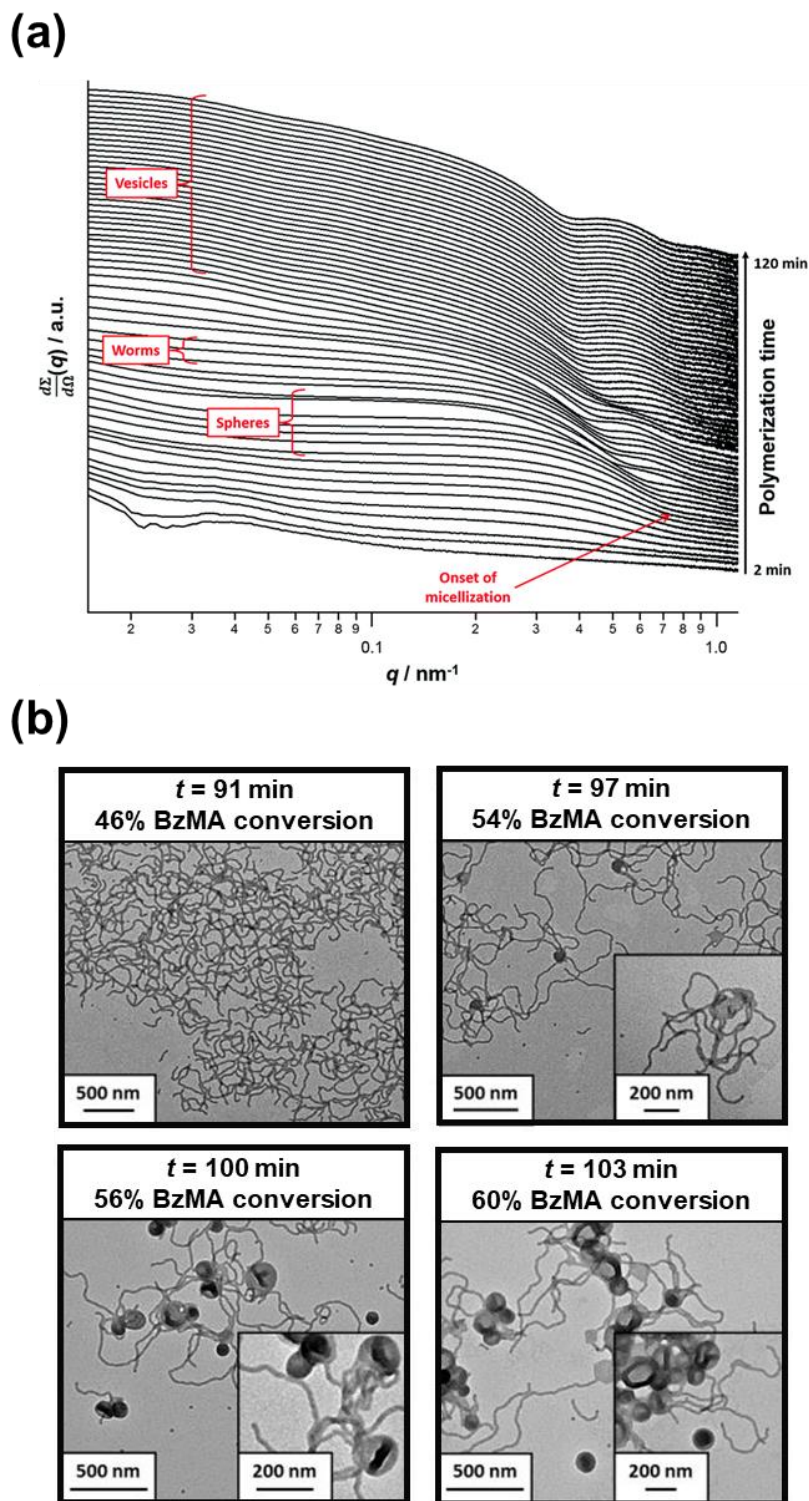
Figure 1.23. (a) *In situ* SAXS patterns recorded during the PISA synthesis of PSMA$_{13}$-PBzMA$_{150}$ diblock copolymer vesicles prepared at 90 °C in mineral oil at 10% w/w solids using a capillary cell. The onset of micellar nucleation is indicated by the red arrow. **(b)** TEM images recorded for 0.1% w/w dispersions of PSMA$_{13}$-PBzMA$_x$ nanoparticles obtained at various time points during the PISA synthesis of PSMA$_{13}$-PBzMA$_{150}$ vesicles during the equivalent laboratory-scale synthesis at 10% w/w solids in mineral oil. A pure worm morphology is observed after 91 min, worms and octopi structures are observed after 97 min and worms, vesicles, octopi and jellyfish structures are observed after 100 min and 103 min, respectively.[153] Figure adapted with permission from ref. 153.

Derry *et al*. also studied the vesicle-to-worm transition exhibited by $PSMA_{13}$-$PBzMA_{96}$ vesicles prepared in mineral oil.[154] The vesicle-to-worm transition occurred on heating from 20 to 150 °C owing to surface plasticization of the PBzMA core-forming block as discussed above for the worm-to-sphere transition exhibited by PLMA-PBzMA nanoparticles.[45] In this case, variable temperature SAXS studies were conducted to confirm the gradual change in morphology, while oscillatory rheology indicated an increase in the storage modulus (*G'*) by five orders of magnitude above 135 °C, which was determined to be the critical gelation temperature. These observations led the authors to propose that this system offers an interesting new high-temperature oil-thickening mechanism.

Dorsman *et al*. found that heating essentially the same PSMA-PBzMA vesicles up to 180 °C produced a worm-to-sphere transition after the initial vesicle-to-worm transition.[151] Moreover, statistical copolymerization of *n*-butyl methacrylate (BuMA) with BzMA to form the core-forming block enabled the temperature at which these morphology transitions occur to be finely tuned simply by adjusting the comonomer molar ratio. This is because PBuMA (T_g = 20 °C) has a relatively low T_g compared to PBzMA (T_g = 54 °C). For example, the vesicle-to-worm transition was observed at 167 °C for $PSMA_{14}$-$PBzMA_{125}$ vesicles but at 109 °C for $PSMA_{14}$-$P(0.5BzMA$-*stat*-$0.5BuMA)_{130}$ vesicles. Heating the latter dispersion further produced a mixture of short worms and spheres at 130°C and a purely spherical morphology was obtained at 180 °C. The worm-to-sphere transition led to a sharp reduction in both the storage modulus (see **Figure 1.24**) and the dispersion viscosity. Moreover, lowering the temperature at which such morphological transitions occur should in principle enable a wider range of oil-thickening applications to be explored.
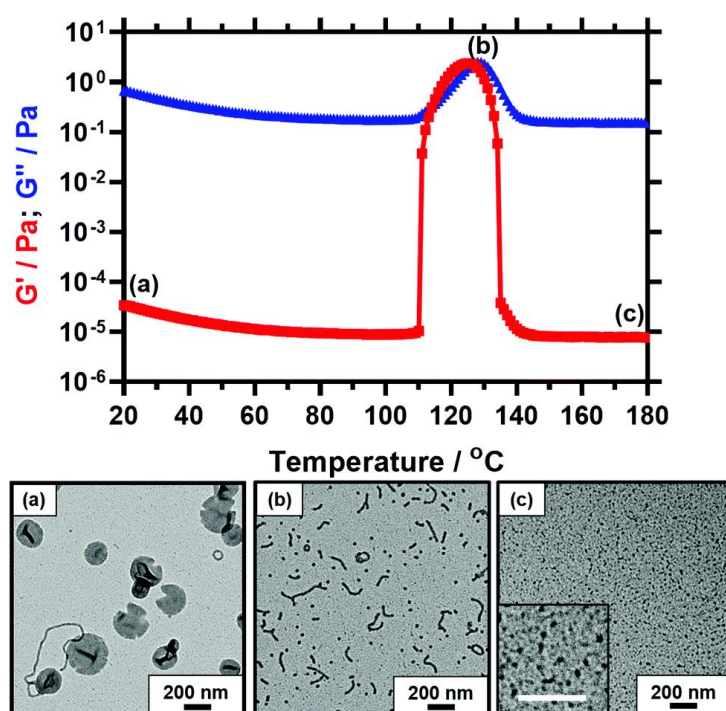
Figure 1.24. Temperature dependence of the storage modulus (G', red squares) and loss modulus (G'', blue triangles) observed for a 10% w/w dispersion of PSMA$_{14}$-P(0.5BzMA-*stat*-0.5BuMA)$_{130}$ nano-objects in mineral oil when heating from 20 °C to 180 °C at 2 °C min^{-1}. This experiment was conducted at 1.0% strain and an angular frequency of 10 rad s^{-1}. Representative TEM images recorded after drying 0.10% w/w dispersions of PSMA$_{14}$-P(0.5BzMA-*stat*-0.5BuMA)$_{130}$ nano-objects: (a) vesicles (plus worms) at 20 °C, (b) worms (plus spheres) at 130 °C, (c) spheres at 180 °C.[151] Figure adapted with permission from ref. 151.

1.6. Thesis outline

In this Thesis, sterically-stabilized methacrylic diblock copolymer nano-objects are synthesized *via* RAFT dispersion polymerization either in mineral oil or in long-chain *n*-alkanes. Such nano-objects are potentially useful additives for the design of next-generation automotive engine oils. **Chapter 2** describes the synthesis of poly(stearyl methacrylate)-poly(2-hydroxypropyl methacrylate) (PSMA-PHPMA) spheres, worms and vesicles in mineral oil. A pseudo-phase diagram is obtained when systematically varying the PHPMA DP while targeting a range of copolymer concentrations. The kinetics of polymerization during the synthesis of PSMA$_9$-PHPMA$_{150}$ vesicles is compared to that of PSMA$_9$-PBzMA$_{150}$ vesicles using *in situ* ^{1}H NMR spectroscopy. Moreover, the thermoresponsive behavior of PSMA$_9$-PHPMA$_{70}$ worms is briefly explored. In **Chapter 3**, the principle of refractive index matching is used to prepare highly transparent poly(stearyl methacrylate)-poly(2,2,2-trifluoroethyl methacrylate) (PSMA-PTFEMA) vesicles of ~240 nm diameter in *n*-dodecane at relatively

high solids. Following the approach developed by Cornel and co-workers,[155] *in situ* visible absorption spectroscopy is used to monitor chain-end fidelity during the synthesis of $PSMA_{16}$-$PTFEMA_{86}$ spheres in *n*-hexadecane using a dithiobenzoate-based RAFT agent. The synthesis of poly(lauryl methacrylate)-poly(methyl methacrylate) (PLMA-PMMA) spheres and short worms in mineral oil is discussed in **Chapter 4**. Targeting a relatively high PMMA DP results in an unexpected morphological constraint that is attributed to the high T_g of PMMA. In **Chapter 5**, this problem is addressed by statistical copolymerization of 10 mol% LMA with MMA to produce relatively long PLMA-P(MMA-*stat*-LMA) worms as well as vesicles. The thermoresponsive behavior of these nano-objects is examined at elevated temperature. **Chapter 6** compares the synthesis and post-polymerization modification of epoxy-functional poly(lauryl methacrylate)-poly(glycidyl methacrylate) (PLMA-PGlyMA) spheres, in which epoxy groups are located within the nanoparticle cores, with that of P(LMA-*stat*-GlyMA)-PMMA spheres in which epoxy groups are incorporated into the steric stabilizer chains. In **Chapter 7**, QCM-D is used to compare the adsorption of such ~30 nm diameter epoxy-functional spheres onto planar stainless steel from *n*-dodecane to that of similar-sized non-functional PLMA-PMMA spheres. QCM-D adsorption experiments are also conducted for ~50 nm diameter P(LMA-*stat*-GlyMA)-PBzMA and PLMA-PBzMA spheres and SEM is used to estimate the fractional surface coverage. Finally, such epoxy-functional and non-functional spheres are evaluated as friction modifiers in MTM tribological experiments conducted by Lubrizol scientists.

1.7. References

(1)   Kutz, M. *Applied Plastics Engineering Handbook Processing and Materials*, First Ed.; Elsevier: Oxford, 2011.

(2)   Jenkins, M. *Introduction to Polymeric Drug Delivery Systems*, First Ed.; Woodhead Publishing: Cambridge, 2007.

(3)   Wang, B.; Wang, S.; Zhang, Q.; Deng, Y.; Li, X.; Peng, L.; Zuo, X.; Piao, M.; Kuang, X.; Sheng, S.; Yu, Y. Recent Advances in Polymer-Based Drug Delivery Systems for Local Anesthetics. *Acta Biomater.* **2019**, *96*, 55–67.

(4)   Liechty, W. B.; Kryscio, D. R.; Slaughter, B. V.; Peppas, N. A. Polymers for Drug Delivery Systems. *Annu. Rev. Chem. Biomol. Eng.* **2010**, *1*, 149–173.

(5)   Hiemenz, Paul, C.; Lodge, Timothy, P. *Polymer Chemistry*, Second Ed.; CRC Press: London, 2007.

(6)   Carraher Jr., C. E. *Polymer Chemistry*, Sixth Ed.; Marcel Dekker: New York, 2003.

(7)   Debye, P. Light Scattering in Solutions. *J. Appl. Phys.* **1944**, *15*, 338–342.

(8)   Sperling, L. H. *Introduction to Physical Polymer Science*, Fourth Ed.; John Wiley &

Sons: Hoboken, 2006.

(9)   Craver, C. D.; Carraher Jr., C. E. *Applied Polymer Science: 21st Century*, First Ed.; Elsevier: Oxford, 2000.

(10)   Obi, B. E. *Polymeric Foams Structure-Property-Performance: A Design Guide*, First Ed.; Elsevier: Oxford, 2017.

(11)   Sarac, A. S. Redox Polymerization. *Prog. Polym. Sci.* **1999**, *24*, 1149–1204.

(12)   Odian, G. *Principle of Polymerization*, Fourth Ed.; John Wiley & Sons: Hoboken, 2004.

(13)   Bevington, J. C.; Melville, H. W.; Taylor, R. P. The Termination Reaction in Radical Polymerizations. Polymerizations of Methyl Methacrylate and Styrene at 25°. *J. Polym. Sci.* **1954**, *12*, 449–459.

(14)   Bevington, J. C.; Melville, H. W.; Taylor, R. P. The Termination Reaction in Radical Polymerizations. II. Polymerizations of Styrene at 60° and of Methyl Methacrylate at 0 and 60°, and the Copolymerization of These Monomers at 60°. *J. Polym. Sci.* **1954**, *14*, 463–476.

(15)   Su, W.-F. *Principles of Polymer Design and Synthesis*, First Ed.; Springer: Heidelberg, 2013.

(16)   Liu, S.; Srinivasan, S.; Grady, M. C.; Soroush, M.; Rappe, A. M. Backbiting and β-Scission Reactions in Free-Radical Polymerization of Methyl Acrylate. *Int. J. Quantum Chem.* **2014**, *114*, 345–360.

(17)   Szwarc, M. Living Polymers. *Nature* **1956**, *176*, 1168–1169.

(18)   Szwarc, M. Polymerization Initiated by Electron Transfer to Monomer. A New Method of Formation of Block Polymers. *J. Am. Chem. Soc.* **1956**, *78*, 2656–2657.

(19)   Matyjaszewski, K.; Müller, A. H. E. *Controlled and Living Polymerizations: From Mechanisms to Applications*, First Ed.; Wiley-VCH: Weinheim, 2009.

(20)   Szwarc, M. "Living" Polymers. *Nature* **1956**, *178*, 1168–1169.

(21)   Johnson, A. F.; Worsfold, D. J. Anionic Polymerization of Butadiene and Styrene. *J. Polym. Sci. Part A Gen. Pap.* **1965**, *3*, 449–455.

(22)   Johnson, A. F.; Worsfold, D. J. Anionic Copolymerization of Styrene and Butadiene. *Die Makromol. Chemie* **1965**, *85*, 273–279.

(23)   Worsfold, D. J. Anionic Copolymerization of Styrene and Isoprene in Cyclohexane. *J. Polym. Sci. Part A-1 Polym. Chem.* **1967**, *5*, 2783–2789.

(24)   Fisher, M.; Szwarc, M. Kinetics of Propagation of Living Poly-2-Vinylpyridine. *Macromolecules* **1970**, *3*, 23–27.

(25)   Lee, C. L.; Smid, J.; Szwarc, M. Kinetics of Anionic Polymerization and Copolymerization of Vinylpyridines. The Penultimate Effects. *Trans. Faraday Soc.* **1963**, *59*, 1192–1200.

(26)   Shar, J. A.; Cosgrove, T.; Obey, T. M.; Warne, M. R.; Wedlock, D. J. Adsorption Studies of Diblock Copolymers at the Cyclohexane/Carbon Black Interface. *Langmuir* **1999**, *15*, 7688–7694.

(27)   Growney, D. J.; Mykhaylyk, O. O.; Middlemiss, L.; Fielding, L. A.; Derry, M. J.; Aragrag, N.; Lamb, G. D.; Armes, S. P. Is Carbon Black a Suitable Model Colloidal Substrate for Diesel Soot? *Langmuir* **2015**, *31*, 10358–10369.

(28)   Growney, D. J.; Mykhaylyk, O. O.; Derouineau, T.; Fielding, L. A.; Smith, A. J.; Aragrag, N.; Lamb, G. D.; Armes, S. P. Star Diblock Copolymer Concentration Dictates the Degree of Dispersion of Carbon Black Particles in Nonpolar Media: Bridging Flocculation versus Steric Stabilization. *Macromolecules* **2015**, *48*, 3691–3704.

(29)   Eckert, R. J. A. Hydrogenated Star-Shaped Polymer. US Patent: 4116917, 1978.

(30)   Mark, H. F. *Encyclopedia of Polymer Science and Technology*, Third Ed.; John Wiley & Sons: Hoboken, 2003.

(31)   Braunecker, W. A.; Matyjaszewski, K. Controlled/Living Radical Polymerization: Features, Developments, and Perspectives. *Prog. Polym. Sci.* **2007**, *32*, 93–146.

(32)   Matyjaszewski, K.; Spanswick, J. Controlled/Living Radical Polymerization. *Mater. Today* **2005**, *8*, 26–33.

(33)   Kobayashi, S.; Müllen, K. *Encyclopedia of Polymeric Nanomaterials*, First Ed.; Springer: Berlin, Heidelberg, 2015.

(34)   Studer, A. The Persistent Radical Effect in Organic Synthesis. *Chem. - A Eur. J.* **2001**, *7*, 1159–1164.

(35)   Fischer, H. The Persistent Radical Effect in "Living" Radical Polymerization. *Macromolecules* **1997**, *30*, 5666–5672.

(36)   Nicolas, J.; Guillaneuf, Y.; Lefay, C.; Bertin, D.; Gigmes, D.; Charleux, B. Nitroxide-Mediated Polymerization. *Prog. Polym. Sci.* **2013**, *38*, 63–235.

(37)   Grubbs, R. B. Nitroxide-Mediated Radical Polymerization: Limitations and Versatility. *Polym. Rev.* **2011**, *51*, 104–137.

(38)   Nicolas, J.; Dire, C.; Mueller, L.; Belleney, J.; Charleux, B.; Marque, S. R. A.; Bertin, D.; Magnet, S.; Couvreur, L. Living Character of Polymer Chains Prepared via Nitroxide-Mediated Controlled Free-Radical Polymerization of Methyl Methacrylate in the Presence of a Small Amount of Styrene at Low Temperature. *Macromolecules* **2006**, *39*, 8274–8282.

(39)   Nicolas, J.; Brusseau, S.; Charleux, B. A Minimal Amount of Acrylonitrile Turns the Nitroxide-Mediated Polymerization of Methyl Methacrylate into an Almost Ideal Controlled/Living System. *J. Polym. Sci. Part A Polym. Chem.* **2010**, *48*, 34–47.

(40)   Matyjaszewski, K. Atom Transfer Radical Polymerization (ATRP): Current Status and Future Perspectives. *Macromolecules* **2012**, *45*, 4015–4039.

(41)   Lou, Q.; Shipp, D. A. Recent Developments in Atom Transfer Radical Polymerization (ATRP): Methods to Reduce Metal Catalyst Concentrations. *ChemPhysChem* **2012**, *13*, 3257–3261.

(42)   Moad, G.; Rizzardo, E.; Thang, S. H. Radical Addition-Fragmentation Chemistry in Polymer Synthesis. *Polymer* **2008**, *49*, 1079–1131.

(43)   Moad, G.; Rizzardo, E.; Thang, S. H. Toward Living Radical Polymerization. *Acc. Chem. Res.* **2008**, *41*, 1133–1142.

(44)   Barner-Kowollik, C. *Handbook of RAFT Polymerization*, First Ed.; Wiley-VCH: Weinheim, 2008.

(45)   Fielding, L. A.; Lane, J. A.; Derry, M. J.; Mykhaylyk, O. O.; Armes, S. P. Thermo-Responsive Diblock Copolymer Worm Gels in Non-Polar Solvents. *J. Am. Chem. Soc.* **2014**, *136*, 5790–5798.

(46)   Fielding, L. A.; Derry, M. J.; Ladmiral, V.; Rosselgong, J.; Rodrigues, A. M.; Ratcliffe, L. P. D.; Sugihara, S.; Armes, S. P. RAFT Dispersion Polymerization in Non-Polar Solvents: Facile Production of Block Copolymer Spheres, Worms and Vesicles in n-Alkanes. *Chem. Sci.* **2013**, *4*, 2081–2087.

(47)   Perrier, S. 50th Anniversary Perspective: RAFT Polymerization - A User Guide. *Macromolecules* **2017**, *50*, 7433–7447.

(48)   Quinn, J. F.; Barner, L.; Barner-Kowollik, C.; Rizzardo, E.; Davis, T. P. Reversible

Addition-Fragmentation Chain Transfer Polymerization Initiated with Ultraviolet Radiation. *Macromolecules* **2002**, *35*, 7620–7627.

(49) You, Y.-Z.; Hong, C.-Y.; Bai, R.-K.; Pan, C.-Y.; Wang, J. Photo-Initiated Living Free Radical Polymerization in the Presence of Dibenzyl Trithiocarbonate. *Macromol. Chem. Phys.* **2002**, *203*, 477–483.

(50) Lu, L.; Yang, N.; Cai, Y. Well-Controlled Reversible Addition-Fragmentation Chain Transfer Radical Polymerisation under Ultraviolet Radiation at Ambient Temperature. *Chem. Commun.* **2005**, 5287–5288.

(51) Muthukrishnan, S.; Pan, E. H.; Stenzel, M. H.; Barner-Kowollik, C.; Davis, T. P.; Lewis, D.; Barner, L. Ambient Temperature RAFT Polymerization of Acrylic Acid Initiated with Ultraviolet Radiation in Aqueous Solution. *Macromolecules* **2007**, *40*, 2978–2980.

(52) Carmean, R. N.; Becker, T. E.; Sims, M. B.; Sumerlin, B. S. Ultra-High Molecular Weights via Aqueous Reversible-Deactivation Radical Polymerization. *Chem* **2017**, *2*, 93–101.

(53) Carmean, R. N.; Sims, M. B.; Figg, C. A.; Hurst, P. J.; Patterson, J. P.; Sumerlin, B. S. Ultrahigh Molecular Weight Hydrophobic Acrylic and Styrenic Polymers through Organic-Phase Photoiniferter-Mediated Polymerization. *ACS Macro Lett.* **2020**, *9*, 613–618.

(54) Zhang, H.; Deng, J.; Lu, L.; Cai, Y. Ambient-Temperature RAFT Polymerization of Styrene and Its Functional Derivatives under Mild Long-Wave UV-Vis Radiation. *Macromolecules* **2007**, *40*, 9252–9261.

(55) Deng, J.; Shi, Y.; Jiang, W.; Peng, Y.; Lu, L.; Cai, Y. Facile Synthesis and Thermoresponsive Behaviors of a Well-Defined Pyrrolidone Based Hydrophilic Polymer. *Macromolecules* **2008**, *41*, 3007–3014.

(56) Li, Y.; Tang, Y.; Yang, K.; Chen, X.; Lu, L.; Cai, Y. Facile Synthesis and Photo-Tunable Properties of a Photosensitive Polymer Whose Chromophores Bound with PH-Labile Cyclic Acetal Linkages. *Macromolecules* **2008**, *41*, 4597–4606.

(57) Jiang, W.; Lu, L.; Cai, Y. Highly Efficient and Well-Controlled Ambient Temperature RAFT Polymerization under Solar Radiation. *Macromol. Rapid Commun.* **2007**, *28*, 725–728.

(58) Shi, Y.; Gao, H.; Lu, L.; Cai, Y. Ultra-Fast RAFT Polymerisation of Poly(Ethylene Glycol) Acrylate in Aqueous Media under Mild Visible Light Radiation at 25 °C. *Chem. Commun.* **2009**, 1368–1370.

(59) Yeow, J.; Sugita, O. R.; Boyer, C. Visible Light-Mediated Polymerization-Induced Self-Assembly in the Absence of External Catalyst or Initiator. *ACS Macro Lett.* **2016**, *5*, 558–564.

(60) Zhou, H.; Johnson, J. A. Photo-Controlled Growth of Telechelic Polymers and End-Linked Polymer Gels. *Angew. Chemie - Int. Ed.* **2013**, *52*, 2235–2238.

(61) Shi, Y.; Liu, G.; Gao, H.; Lu, L.; Cai, Y. Effect of Mild Visible Light on Rapid Aqueous RAFT Polymerization of Water-Soluble Acrylic Monomers at Ambient Temperature: Initiation and Activation. *Macromolecules* **2009**, *42*, 3917–3926.

(62) Tan, J.; Sun, H.; Yu, M.; Sumerlin, B. S.; Zhang, L. Photo-PISA: Shedding Light on Polymerization-Induced Self-Assembly. *ACS Macro Lett.* **2015**, *4*, 1249–1253.

(63) Otsu, T.; Yoshida, M. Role of Initiator-Transfer Agent-Terminator (Iniferter) in Radical Polymerizations: Polymer Design by Organic Disulfides as Iniferters. *Die Makromol. Chemie, Rapid Commun.* **1982**, *3*, 127–132.

(64) Otsu, T. Iniferter Concept and Living Radical Polymerization. *J. Polym. Sci. Part A*

Polym. Chem. **2000**, *38*, 2121–2136.

(65) Xu, J.; Jung, K.; Boyer, C. Oxygen Tolerance Study of Photoinduced Electron Transfer-Reversible Addition-Fragmentation Chain Transfer (PET-RAFT) Polymerization Mediated by Ru(Bpy)3Cl2. *Macromolecules* **2014**, *47*, 4217–4229.

(66) Wu, C.; Shanmugam, S.; Xu, J.; Zhu, J.; Boyer, C. Chlorophyll a Crude Extract: Efficient Photo-Degradable Photocatalyst for PET-RAFT Polymerization. *Chem. Commun.* **2017**, *53*, 12560–12563.

(67) Tucker, B. S.; Coughlin, M. L.; Figg, C. A.; Sumerlin, B. S. Grafting-From Proteins Using Metal-Free PET-RAFT Polymerizations under Mild Visible-Light Irradiation. *ACS Macro Lett.* **2017**, *6*, 452–457.

(68) Chen, M.; MacLeod, M. J.; Johnson, J. A. Visible-Light-Controlled Living Radical Polymerization from a Trithiocarbonate Iniferter Mediated by an Organic Photoredox Catalyst. *ACS Macro Lett.* **2015**, *4*, 566–569.

(69) Keddie, D. J. A Guide to the Synthesis of Block Copolymers Using Reversible-Addition Fragmentation Chain Transfer (RAFT) Polymerization. *Chem. Soc. Rev.* **2014**, *43*, 496–505.

(70) Moad, G.; Rizzardo, E.; Thang, S. H. Living Radical Polymerization by the RAFT Process. *Aust. J. Chem.* **2005**, *58*, 379–410.

(71) Moad, G.; Rizzardo, E.; Thang, S. H. End-Functional Polymers, Thiocarbonylthio Group Removal/Transformation and Reversible Addition-Fragmentation-Chain Transfer (RAFT) Polymerization. *Polym. Int.* **2011**, *60*, 9–25.

(72) Willcock, H.; O'Reilly, R. K. End Group Removal and Modification of RAFT Polymers. *Polym. Chem.* **2010**, *1*, 149–157.

(73) Ming, C.; Moad, G.; Rizzardo, E. Thiocarbonylthio End Group Removal from RAFT-Synthesized Polymers by a Radical-Induced Process. *J. Polym. Sci. Part A Polym. Chem.* **2009**, *47*, 6704–6714.

(74) Chong, Y. K.; Moad, G.; Rizzardo, E.; Thang, S. H. Thiocarbonylthio End Group Removal from RAFT-Synthesized Polymers by Radical-Induced Reduction. *Macromolecules* **2007**, *40*, 4446–4455.

(75) Jesson, C. P.; Pearce, C. M.; Simon, H.; Werner, A.; Cunningham, V. J.; Lovett, J. R.; Smallridge, M. J.; Warren, N. J.; Armes, S. P. H2O2 Enables Convenient Removal of RAFT End-Groups from Block Copolymer Nano-Objects Prepared via Polymerization-Induced Self-Assembly in Water. *Macromolecules* **2017**, *50*, 182–191.

(76) Bryztwa, A. J.; Johnson, J. Scaled Production of RAFT CTA - a STAR Performer. *Am. Chem. Soc. Polym. Prepr. Div. Polym. Chem.* **2011**, *52*, 533–534.

(77) Moad, G.; Rizzardo, E.; Thang, S. H. RAFT Polymerization and Some of Its Applications. *Chem. - An Asian J.* **2013**, *8*, 1634–1644.

(78) Arshady, R. Suspension, Emulsion, and Dispersion Polymerization: A Methodological Survey. *Colloid Polym. Sci.* **1992**, *270*, 717–732.

(79) Matyjaszewski, K.; Davis, T. P. *Handbook of Radical Polymerization*, First Ed.; John Wiley & Sons: Hoboken, 2002.

(80) Richez, A. P.; Yow, H. N.; Biggs, S.; Cayre, O. J. Dispersion Polymerization in Non-Polar Solvent: Evolution toward Emerging Applications. *Prog. Polym. Sci.* **2013**, *38*, 897–931.

(81) Okobu, M. *Advances in Polymer Science*, First Ed.; Springer: Heidelberg, 2005; Vol. 175.

(82) Osmond, D. W. J.; Thompson, H. H. Dispersion Polymerization. GB Patent: 893429, 1962.

(83) Armes, S. P.; Vincent, B. Dispersions of Electrically Conducting Polypyrrole Particles in Aqueous Media. *J. Chem. Soc. Chem. Commun.* **1987**, 288–290.

(84) Ali, A. M. I.; Pareek, P.; Sewell, L.; Schmid, A.; Fujii, S.; Armes, S. P.; Shirley, I. M. Synthesis of Poly(2-Hydroxypropyl Methacrylate) Latex Particles via Aqueous Dispersion Polymerization. *Soft Matter* **2007**, *3*, 1003–1013.

(85) Lok, K. P.; Ober, C. K. Particle Size Control in Dispersion Polymerization. *Can. J. Chem.* **1985**, *63*, 209–216.

(86) Tseng, C. M.; Lu, Y. Y.; El-Aasser, M. S.; Vanderhoff, J. W. Uniform Polymer Particles by Dispersion Polymerization in Alcohol. *J. Polym. Sci. Part A Polym. Chem.* **1986**, *24*, 2995–3007.

(87) Almog, Y.; Reich, S.; Levy, M. Monodisperse Polymeric Spheres in the Micron Size Range By a Single Step Process. *Br. Polym. J.* **1982**, *14*, 131–136.

(88) Barrett, K. E. J.; Thomas, H. R. Kinetics of Dispersion Polymerization of Soluble Monomers. I. Methyl Methacrylate. *J. Polym. Sci. Part A-1 Polym. Chem.* **1969**, *7*, 2621–2650.

(89) Barrett, K. E. J. Dispersion Polymerisation in Organic Media. *Br. Polym. J.* **1973**, *5*, 259–271.

(90) Tanford, C. The Hydrophobic Effect and the Organization of Living Matter. *Science* **1978**, *200*, 1012–1018.

(91) Israelachvili, J. N. *Intermolecular and Surface Forces*, Third Ed.; Elsevier: Amsterdam, 2011.

(92) Israelachvili, J. N.; Mitchell, D. J.; Ninham, B. W. Theory of Self-Assembly of Hydrocarbon Amphiphiles into Micelles and Bilayers. *J. Chem. Soc. Faraday Trans. 2* **1976**, *72*, 1525–1568.

(93) Nagarajan, R. Molecular Packing Parameter and Surfactant Self-Assembly: The Neglected Role of the Surfactant Tail. *Langmuir* **2002**, *18*, 31–38.

(94) Thomas, E. L.; Anderson, D. M.; Henkee, C. S.; Hoffman, D. Periodic Area-Minimizing Surfaces in Block Copolymers. *Nature* **1988**, *334*, 598–601.

(95) Bates, F. S. Polymer-Polymer Phase Behavior. *Science* **1991**, *251*, 898–905.

(96) Bates, F. S.; Fredrickson, G. H. Block Copolymers-Designer Soft Materials. *Phys. Today* **1999**, *52*, 32–38.

(97) Van Hest, J. C. M., Delnoye, D. A. P., Baars, M. W. P. L., van Genderen, M. H. P., & Meijer, E. W. Polystyrene-Dendrimer Amphiphilic Block Copolymers with a Generation-Dependent Aggregation. *Science* **1995**, *268*, 1592–1595.

(98) Zhang, L.; Eisenberg, A. Multiple Morphologies of "Crew-Cut" Aggregates of Polystyrene-b-Poly(Acrylic Acid) Block Copolymers. *Science* **1995**, *268*, 1728–1731.

(99) Zhang, L.; Yu, K.; Eisenberg, A. Ion-Induced Morphological Changes in "Crew-Cut" Aggregates of Amphiphilic Block Copolymers. *Science* **1996**, *272*, 1777–1779.

(100) Creutz, S.; Van Stam, J.; De Schryver, F. C.; Jérôme, R. Dynamics of Poly((Dimethylamino)Alkyl Methacrylate-Block-Sodium Methacrylate) Micelles. Influence of Hydrophobicity and Molecular Architecture on the Exchange Rate of Copolymer Molecules. *Macromolecules* **1998**, *31*, 681–689.

(101) Wang, Y.; Balaji, R.; Quirk, R. P.; Mattice, W. L. Detection of the Rate of Exchange of Chains between Micelles Formed by Diblock Copolymers in Aqueous Solution. *Polym.*

Bull. **1992**, *28*, 333–338.

(102) Tian, M.; Qin, A.; Ramireddy, C.; Tuzar, Z.; Munk, P. Hybridization of Block Copolymer Micelles. *Langmuir* **1993**, *9*, 1741–1748.

(103) Cameron, N. S.; Corbierre, M. K.; Eisenberg, A. Asymmetric Amphiphilic Block Copolymers in Solution: A Morphological Wonderland. *Can. J. Chem.* **1999**, *77*, 1311–1326.

(104) Jain, S.; Bates, F. S. Consequences of Nonergodicity in Aqueous Binary PEO-PB Micellar Dispersions. *Macromolecules* **2004**, *37*, 1511–1523.

(105) He, Y.; Li, Z.; Simone, P.; Lodge, T. P. Self-Assembly of Block Copolymer Micelles in an Ionic Liquid. *J. Am. Chem. Soc.* **2006**, *128*, 2745–2750.

(106) Willner, L.; Poppe, A.; Allgaier, J.; Monkenbusch, M.; Richter, D. Time-Resolved SANS for the Determination of Unimer Exchange Kinetics in Block Copolymer Micelles. *Europhys. Lett.* **2001**, *55*, 667–673.

(107) Won, Y. Y.; Davis, H. T.; Bates, F. S. Molecular Exchange in PEO-PB Micelles in Water. *Macromolecules* **2003**, *36*, 953–955.

(108) Meli, L.; Santiago, J. M.; Lodge, T. P. Path-Dependent Morphology and Relaxation Kinetics of Highly Amphiphilic Diblock Copolymer Micelles in Ionic Liquids. *Macromolecules* **2010**, *43*, 2018–2027.

(109) Bates, F. S.; Fredrickson, G. H. Block Copolymer Thermodynamics: Theory and Experiment. *Annu. Rev. Phys. Chem.* **1990**, *41*, 525–557.

(110) Mai, Y.; Eisenberg, A. Self-Assembly of Block Copolymers. *Chem. Soc. Rev.* **2012**, *41*, 5969–5985.

(111) Matsen, M. W.; Bates, F. S. Unifying Weak- and Strong-Segregation Block Copolymer Theories. *Macromolecules* **1996**, *29*, 1091–1098.

(112) Khandpur, A. K.; Förster, S.; Bates, F. S.; Hamley, I. W.; Ryan, A. J.; Bras, W.; Almdal, K.; Mortensen, K. Polyisoprene-Polystyrene Diblock Copolymer Phase Diagram near the Order-Disorder Transition. *Macromolecules* **1995**, *28*, 8796–8806.

(113) Zhang, L.; Eisenberg, A. Multiple Morphologies and Characteristics of "crew-Cut" Micelle-like Aggregates of Polystyrene-b-Poly(Acrylic Acid) Diblock Copolymers in Aqueous Solutions. *J. Am. Chem. Soc.* **1996**, *118*, 3168–3181.

(114) Zhang, L.; Eisenberg, A. Formation of Crew-Cut Aggregates of Various Morphologies from Amphiphilic Block Copolymers in Solution. *Polym. Adv. Technol.* **1998**, *9*, 677–699.

(115) Shen, H.; Eisenberg, A. Morphological Phase Diagram for a Ternary System of Block Copolymer PS310-b-PAA52/ Dioxane/H2O. *J. Phys. Chem. B* **1999**, *103*, 9473–9487.

(116) Discher, D. E.; Eisenberg, A. Polymer Vesicles. *Science* **2002**, *297*, 967–973.

(117) Yu, Y.; Zhang, L.; Eisenberg, A. Morphogenic Effect of Solvent on Crew-Cut Aggregates of Apmphiphilic Diblock Copolymers. *Macromolecules* **1998**, *31*, 1144–1154.

(118) Zhang, L.; Eisenberg, A. Morphogenic Effect of Added Ions on Crew-Cut Aggregates of Polystyrene-b-Poly(Acrylic Acid) Block Copolymers in Solutions. *Macromolecules* **1996**, *29*, 8805–8815.

(119) Charleux, B.; Delaittre, G.; Rieger, J.; D'Agosto, F. Polymerization-Induced Self-Assembly: From Soluble Macromolecules to Block Copolymer Nano-Objects in One Step. *Macromolecules* **2012**, *45*, 6753–6765.

(120) Monteiro, M. J.; Cunningham, M. F. Polymer Nanoparticles via Living Radical

Polymerization in Aqueous Dispersions: Design and Applications. *Macromolecules* **2012**, *45*, 4939–4957.

(121) Warren, N. J.; Armes, S. P. Polymerization-Induced Self-Assembly of Block Copolymer Nano-Objects via RAFT Aqueous Dispersion Polymerization. *J. Am. Chem. Soc.* **2014**, *136*, 10174–10185.

(122) Derry, M. J.; Fielding, L. A.; Armes, S. P. Polymerization-Induced Self-Assembly of Block Copolymer Nanoparticles via RAFT Non-Aqueous Dispersion Polymerization. *Prog. Polym. Sci.* **2016**, *52*, 1–18.

(123) Lowe, A. B. RAFT Alcoholic Dispersion Polymerization with Polymerization-Induced Self-Assembly. *Polymer* **2016**, *106*, 161–181.

(124) Canning, S. L.; Smith, G. N.; Armes, S. P. A Critical Appraisal of RAFT-Mediated Polymerization-Induced Self-Assembly. *Macromolecules* **2016**, *49*, 1985–2001.

(125) Lansalot, M.; Rieger, J. Polymerization-Induced Self-Assembly. *Macromol. Rapid Commun.* **2019**, *40*, 1800885.

(126) D'Agosto, F.; Rieger, J.; Lansalot, M. RAFT-Mediated Polymerization-Induced Self-Assembly. *Angew. Chemie - Int. Ed.* **2020**, *59*, 8368–8392.

(127) Cao, J.; Tan, Y.; Chen, Y.; Zhang, L.; Tan, J. Expanding the Scope of Polymerization-Induced Self-Assembly: Recent Advances and New Horizons. *Macromol. Rapid Commun.* **2021**, *42*, 2100498.

(128) Chiefari, J.; Chong, Y. K. B.; Ercole, F.; Krstina, J.; Jeffery, J.; Le, T. P. T.; Mayadunne, R. T. A.; Meijs, G. F.; Moad, C. L.; Moad, G.; Rizzardo, E.; Thang, S. H. Living Free-Radical Polymerization by Reversible Addition-Fragmentation Chain Transfer: The RAFT Process. *Macromolecules* **1998**, *31*, 5559–5562.

(129) Antonietti, M.; Förster, S. Vesicles and Liposomes: A Self-Assembly Principle Beyond Lipids. *Adv. Mater.* **2003**, *15*, 1323–1333.

(130) Penfold, N. J. W.; Yeow, J.; Boyer, C.; Armes, S. P. Emerging Trends in Polymerization-Induced Self-Assembly. *ACS Macro Lett.* **2019**, *8*, 1029–1054.

(131) D'Agosto, F.; Rieger, J.; Lansalot, M. RAFT-Mediated Polymerization-Induced Self-Assembly. *Angew. Chemie - Int. Ed.* **2020**, *59*, 8368–8392.

(132) Zaquen, N.; Azizi, W. A. A. W.; Yeow, J.; Kuchel, R. P.; Junkers, T.; Zetterlund, P. B.; Boyer, C. Alcohol-Based PISA in Batch and Flow: Exploring the Role of Photoinitiators. *Polym. Chem.* **2019**, *10*, 2406–2414.

(133) Ferguson, C. J.; Hughes, R. J.; Pham, B. T. T.; Hawkett, B. S.; Gilbert, R. G.; Serelis, A. K.; Such, C. H. Effective Ab Initio Emulsion Polymerization under RAFT Control. *Macromolecules* **2002**, *35*, 9243–9245.

(134) Manguian, M.; Save, M.; Charleux, B. Batch Emulsion Polymerization of Styrene Stabilized by a Hydrophilic Macro-RAFT Agenta. *Macromol. Rapid Commun.* **2006**, *27*, 399–404.

(135) Rieger, J.; Stoffelbach, F.; Bui, C.; Alaimo, D.; Jérôme, C.; Charleux, B. Amphiphilic Poly(Ethylene Oxide) Macromolecular RAFT Agent as a Stabilizer and Control Agent in Ab Initio Batch Emulsion Polymerization. *Macromolecules* **2008**, *41*, 4065–4068.

(136) Zhang, X.; Boissé, S.; Zhang, W.; Beaunier, P.; D'Agosto, F.; Rieger, J.; Charleux, B. Well-Defined Amphiphilic Block Copolymers and Nano-Objects Formed in Situ via RAFT-Mediated Aqueous Emulsion Polymerization. *Macromolecules* **2011**, *44*, 4149–4158.

(137) Chaduc, I.; Zhang, W.; Rieger, J.; Lansalot, M.; D'Agosto, F.; Charleux, B. Amphiphilic

Block Copolymers from a Direct and One-Pot RAFT Synthesis in Water. *Macromol. Rapid Commun.* **2011**, *32*, 1270–1276.

(138) Thompson, K. L.; Cinotti, N.; Jones, E. R.; Mable, C. J.; Fowler, P. W.; Armes, S. P. Bespoke Diblock Copolymer Nanoparticles Enable the Production of Relatively Stable Oil-in-Water Pickering Nanoemulsions. *Langmuir* **2017**, *33*, 12616–12623.

(139) Hunter, S. J.; Armes, S. P. Long-Term Stability of Pickering Nanoemulsions Prepared Using Diblock Copolymer Nanoparticles: Effect of Nanoparticle Core Crosslinking, Oil Type, and the Role Played by Excess Copolymers. *Langmuir* **2022**, *38*, 8021–8029.

(140) North, S. M.; Armes, S. P. Aqueous One-Pot Synthesis of Well-Defined Zwitterionic Diblock Copolymers by RAFT Polymerization: An Efficient and Environmentally-Friendly Route to a Useful Dispersant for Aqueous Pigments. *Green Chem.* **2021**, *23*, 1248–1258.

(141) Chan, D. H. H.; Kynaston, E. L.; Lindsay, C.; Taylor, P.; Armes, S. P. Block Copolymer Nanoparticles Are Effective Dispersants for Micrometer-Sized Organic Crystalline Particles. *ACS Appl. Mater. Interfaces* **2021**, *13*, 30235–30243.

(142) Canton, I.; Warren, N. J.; Chahal, A.; Amps, K.; Wood, A.; Weightman, R.; Wang, E.; Moore, H.; Armes, S. P. Mucin-Inspired Thermoresponsive Synthetic Hydrogels Induce Stasis in Human Pluripotent Stem Cells and Human Embryos. *ACS Cent. Sci.* **2016**, *2*, 65–74.

(143) Mable, C. J.; Canton, I.; Mykhaylyk, O. O.; Ustbas Gul, B.; Chambon, P.; Themistou, E.; Armes, S. P. Targeting Triple-Negative Breast Cancer Cells Using Dengue Virus-Mimicking PH-Responsive Framboidal Triblock Copolymer Vesicles. *Chem. Sci.* **2019**, *10*, 4811–4821.

(144) Varlas, S.; Foster, J. C.; Georgiou, P. G.; Keogh, R.; Husband, J. T.; Williams, D. S.; O'Reilly, R. K. Tuning the Membrane Permeability of Polymersome Nanoreactors Developed by Aqueous Emulsion Polymerization-Induced Self-Assembly. *Nanoscale* **2019**, *11*, 12643–12654.

(145) Docherty, P. J.; Girou, C.; Derry, M. J.; Armes, S. P. Epoxy-Functional Diblock Copolymer Spheres, Worms and Vesicles via Polymerization-Induced Self-Assembly in Mineral Oil. *Polym. Chem.* **2020**, *11*, 3332–3339.

(146) Parker, B. R.; Derry, M. J.; Ning, Y.; Armes, S. P. Exploring the Upper Size Limit for Sterically Stabilized Diblock Copolymer Nanoparticles Prepared by Polymerization-Induced Self-Assembly in Non-Polar Media. *Langmuir* **2020**, *36*, 3730–3736.

(147) Cornel, E. J.; O'Hora, P. S.; Smith, T.; Growney, D. J.; Mykhaylyk, O. O.; Armes, S. P. SAXS Studies of the Thermally-Induced Fusion of Diblock Copolymer Spheres: Formation of Hybrid Nanoparticles of Intermediate Size and Shape. *Chem. Sci.* **2020**, *11*, 4312–4321.

(148) Cornel, E. J.; Smith, G. N.; Rogers, S. E.; Hallett, J. E.; Growney, D. J.; Smith, T.; O'Hora, P. S.; Van Meurs, S.; Mykhaylyk, O. O.; Armes, S. P. Time-Resolved Small-Angle Neutron Scattering Studies of the Thermally-Induced Exchange of Copolymer Chains between Spherical Diblock Copolymer Nanoparticles Prepared via Polymerization-Induced Self-Assembly. *Soft Matter* **2020**, *16*, 3657–3668.

(149) Derry, M. J.; Mykhaylyk, O. O.; Armes, S. P. Shear-Induced Alignment of Block Copolymer Worms in Mineral Oil. *Soft Matter* **2021**, *17*, 8867–8876.

(150) Raphael, E.; Derry, M. J.; Hippler, M.; Armes, S. P. Tuning the Properties of Hydrogen-Bonded Block Copolymer Worm Gels Preparedviapolymerization-Induced Self-Assembly. *Chem. Sci.* **2021**, *12*, 12082–12091.

(151) Dorsman, I. R.; Derry, M. J.; Cunningham, V. J.; Brown, S. L.; Williams, C. N.; Armes, S. P. Tuning the Vesicle-to-Worm Transition for Thermoresponsive Block Copolymer Vesicles Prepared: Via Polymerisation-Induced Self-Assembly. *Polym. Chem.* **2021**, *12*, 1224–1235.

(152) Derry, M. J.; Fielding, L. A.; Armes, S. P. Industrially-Relevant Polymerization-Induced Self-Assembly Formulations in Non-Polar Solvents: RAFT Dispersion Polymerization of Benzyl Methacrylate. *Polym. Chem.* **2015**, *6*, 3054–3062.

(153) Derry, M. J.; Fielding, L. A.; Warren, N. J.; Mable, C. J.; Smith, A. J.; Mykhaylyk, O. O.; Armes, S. P. In Situ Small-Angle X-Ray Scattering Studies of Sterically-Stabilized Diblock Copolymer Nanoparticles Formed during Polymerization-Induced Self-Assembly in Non-Polar Media. *Chem. Sci.* **2016**, *7*, 5078–5090.

(154) Derry, M. J.; Mykhaylyk, O. O.; Armes, S. P. A Vesicle-to-Worm Transition Provides a New High-Temperature Oil Thickening Mechanism. *Angew. Chemie - Int. Ed.* **2017**, *56*, 1746–1750.

(155) Cornel, E. J.; Meurs, S. Van; Smith, T.; Hora, P. S. O.; Armes, S. P. In Situ Spectroscopic Studies of Highly Transparent Nanoparticle Dispersions Enable Assessment of Trithiocarbonate Chain-End Fidelity during RAFT Dispersion Polymerization in Nonpolar Media. *J. Am. Chem. Soc.* **2018**, *140*, 12980–12988.

(156) Docherty, P. J.; Derry, M. J.; Armes, S. P. RAFT Dispersion Polymerization of Glycidyl Methacrylate for the Synthesis of Epoxy-Functional Block Copolymer Nanoparticles in Mineral Oil. *Polym. Chem.* **2019**, *10*, 603–611.

(157) Rymaruk, M. J.; O'Brien, C. T.; Brown, S. L.; Williams, C. N.; Armes, S. P. RAFT Dispersion Polymerization of Benzyl Methacrylate in Silicone Oil Using a Silicone-Based Methacrylic Stabilizer Provides Convenient Access to Spheres, Worms, and Vesicles. *Macromolecules* **2020**, *53*, 1785–1794.

(158) Rymaruk, M. J.; O'Brien, C. T.; Brown, S. L.; Williams, C. N.; Armes, S. P. Effect of Core Cross-Linking on the Physical Properties of Poly(Dimethylsiloxane)-Based Diblock Copolymer Worms Prepared in Silicone Oil. *Macromolecules* **2019**, *52*, 6849–6860.

(159) Derry, M. J.; Smith, T.; O'Hora, P. S.; Armes, S. P. Block Copolymer Nanoparticles Prepared via Polymerization-Induced Self-Assembly Provide Excellent Boundary Lubrication Performance for Next-Generation Ultralow-Viscosity Automotive Engine Oils. *ACS Appl. Mater. Interfaces* **2019**, *11*, 33364–33369.

(160) Houillot, L.; Bui, C.; Farcet, C.; Moire, C.; Raust, J. A.; Pasch, H.; Save, M.; Charleux, B. Dispersion Polymerization of Methyl Acrylate in Nonpolar Solvent Stabilized by Block Copolymers Formed in Situ via the RAFT Process. *ACS Appl. Mater. Interfaces* **2010**, *2*, 434–442.

(161) Farcet, C. Cosmetic Composition. FR Patent: 2881648, 2006.

(162) Houillot, L.; Bui, C.; Save, M.; Charleux, B.; Farcet, C.; Moire, C.; Raust, J. A.; Rodriguez, I. Synthesis of Well-Defined Polyacrylate Particle Dispersions in Organic Medium Using Simultaneous RAFT Polymerization and Self-Assembly of Block Copolymers. A Strong Influence of the Selected Thiocarbonylthio Chain Transfer Agent. *Macromolecules* **2007**, *40*, 6500–6509.

(163) Ratcliffe, L. P. D.; McKenzie, B. E.; Le Bouëdec, G. M. D.; Williams, C. N.; Brown, S. L.; Armes, S. P. Polymerization-Induced Self-Assembly of All-Acrylic Diblock Copolymers via RAFT Dispersion Polymerization in Alkanes. *Macromolecules* **2015**, *48*, 8594–8607.

(164) Gibson, R. R.; Fernyhough, A.; Musa, O. M.; Armes, S. P. RAFT Dispersion Polymerization of: N, N -Dimethylacrylamide in a Series of n -Alkanes Using a Thermoresponsive Poly(Tert-Octyl Acrylamide) Steric Stabilizer. *Polym. Chem.* **2021**, *12*, 2165–2174.

(165) Gibson, R. R.; Fernyhough, A.; Musa, O. M.; Armes, S. P. Synthesis of Well-Defined Diblock Copolymer Nano-Objects by RAFT Non-Aqueous Emulsion Polymerization of: N -(2-Acryloyloxy)Ethyl Pyrrolidone in Non-Polar Media. *Polym. Chem.* **2021**, *12*, 3762–3774.

(166) Canning, S. L.; Cunningham, V. J.; Ratcliffe, L. P. D.; Armes, S. P. Phenyl Acrylate Is a Versatile Monomer for the Synthesis of Acrylic Diblock Copolymer Nano-Objects via Polymerization-Induced Self-Assembly. *Polym. Chem.* **2017**, *8*, 4811–4821.

(167) Pei, Y.; Sugita, O. R.; Thurairajah, L.; Lowe, A. B. Synthesis of Poly(Stearyl Methacrylate-b-3-Phenylpropyl Methacrylate) Nanoparticles in n-Octane and Associated Thermoreversible Polymorphism. *RSC Adv.* **2015**, *5*, 17636–17646.

(168) Pei, Y.; Noy, J. M.; Roth, P. J.; Lowe, A. B. Soft Matter Nanoparticles with Reactive Coronal Pentafluorophenyl Methacrylate Residues via Non-Polar RAFT Dispersion Polymerization and Polymerization-Induced Self-Assembly. *J. Polym. Sci. Part A Polym. Chem.* **2015**, *53*, 2326–2335.

(169) Rymaruk, M. J.; Hunter, S. J.; O'Brien, C. T.; Brown, S. L.; Williams, C. N.; Armes, S. P. RAFT Dispersion Polymerization in Silicone Oil. *Macromolecules* **2019**, *52*, 2822–2832.

(170) Raust, J. A.; Houillot, L.; Save, M.; Charleux, B.; Moire, C.; Farcet, C.; Pasch, H. Two Dimensional Chromatographic Characterization of Block Copolymers of 2-Ethylhexyl Acrylate and Methyl Acrylate, P2EHA-b-PMA, Produced via RAFT-Mediated Polymerization in Organic Dispersion. *Macromolecules* **2010**, *43*, 8755–8765.

(171) Blanazs, A.; Ryan, A. J.; Armes, S. P. Predictive Phase Diagrams for RAFT Aqueous Dispersion Polymerization: Effect of Block Copolymer Composition, Molecular Weight, and Copolymer Concentration. *Macromolecules* **2012**, *45*, 5099–5107.

(172) Jones, E. R.; Semsarilar, M.; Blanazs, A.; Armes, S. P. Efficient Synthesis of Amine-Functional Diblock Copolymer Nanoparticles via RAFT Dispersion Polymerization of Benzyl Methacrylate in Alcoholic Media. *Macromolecules* **2012**, *45*, 5091–5098.

(173) Zheng, R.; Liu, G.; Devlin, M.; Hux, K.; Jao, T. C. Friction Reduction of Lubricant Base Oil by Micelles and Crosslinked Micelles of Block Copolymers. *Tribol. Trans.* **2010**, *53*, 97–107.

(174) Hatton, F. L.; Lovett, J. R.; Armes, S. P. Synthesis of Well-Defined Epoxy-Functional Spherical Nanoparticles by RAFT Aqueous Emulsion Polymerization. *Polym. Chem.* **2017**, *8*, 4856–4868.

(175) Pedersen, J. S. Form Factors of Block Copolymer Micelles with Spherical, Ellipsoidal and Cylindrical Cores. *J. Appl. Crystallogr.* **2000**, *33*, 637–640.

(176) Zinn, T.; Willner, L.; Lund, R.; Pipich, V.; Richter, D. Equilibrium Exchange Kinetics in N-Alkyl-PEO Polymeric Micelles: Single Exponential Relaxation and Chain Length Dependence. *Soft Matter* **2012**, *8*, 623–626.

(177) Choi, S. H.; Lodge, T. P.; Bates, F. S. Mechanism of Molecular Exchange in Diblock Copolymer Micelles: Hypersensitivity to Core Chain Length. *Phys. Rev. Lett.* **2010**, *104*, 047802.

(178) Lu, J.; Choi, S.; Bates, F. S.; Lodge, T. P. Molecular Exchange in Diblock Copolymer Micelles: Bimodal Distribution in Core-Block Molecular Weights. *ACS Macro Lett.*

2012, *1*, 982–985.

(179) Lu, J.; Bates, F. S.; Lodge, T. P. Chain Exchange in Binary Copolymer Micelles at Equilibrium: Confirmation of the Independent Chain Hypothesis. *ACS Macro Lett.* **2013**, *2*, 451–455.

(180) Cunningham, V. J.; Alswieleh, A. M.; Thompson, K. L.; Williams, M.; Leggett, G. J.; Armes, S. P.; Musa, O. M. Poly(Glycerol Monomethacrylate)-Poly(Benzyl Methacrylate) Diblock Copolymer Nanoparticles via RAFT Emulsion Polymerization: Synthesis, Characterization, and Interfacial Activity. *Macromolecules* **2014**, *47*, 5613–5623.

(181) Mable, C. J.; Warren, N. J.; Thompson, K. L.; Mykhaylyk, O. O.; Armes, S. P. Framboidal ABC Triblock Copolymer Vesicles: A New Class of Efficient Pickering Emulsifie. *Chem. Sci.* **2015**, *6*, 6179–6188.

(182) Thompson, K. L.; Derry, M. J.; Hatton, F. L.; Armes, S. P. Long-Term Stability of n-Alkane-in-Water Pickering Nanoemulsions: Effect of Aqueous Solubility of Droplet Phase on Ostwald Ripening. *Langmuir* **2018**, *34*, 9289–9297.

(183) Cunningham, V. J.; Armes, S. P.; Musa, O. M. Synthesis, Characterisation and Pickering Emulsifier Performance of Poly(Stearyl Methacrylate)-Poly(N-2-(Methacryloyloxy)Ethyl Pyrrolidone) Diblock Copolymer Nano-Objects via RAFT Dispersion Polymerisation in n-Dodecane. *Polym. Chem.* **2016**, *7*, 1882–1891.

(184) Hunter, S. J.; Cornel, E. J.; Mykhaylyk, O. O.; Armes, S. P. Effect of Salt on the Formation and Stability of Water-in-Oil Pickering Nanoemulsions Stabilized by Diblock Copolymer Nanoparticles. *Langmuir* **2020**, *36*, 15523–15535.

(185) Rymaruk, M. J.; Thompson, K. L.; Derry, M. J.; Warren, N. J.; Ratcliffe, L. P. D.; Williams, C. N.; Brown, S. L.; Armes, S. P. Bespoke Contrast-Matched Diblock Copolymer Nanoparticles Enable the Rational Design of Highly Transparent Pickering Double Emulsions. *Nanoscale* **2016**, *8*, 14497–14506.

(186) Lovett, J. R.; Derry, M. J.; Yang, P.; Hatton, F. L.; Warren, N. J.; Fowler, P. W.; Armes, S. P. Can Percolation Theory Explain the Gelation Behavior of Diblock Copolymer Worms? *Chem. Sci.* **2018**, *9*, 7138–7144.

(187) Pei, Y.; Thurairajah, L.; Sugita, O. R.; Lowe, A. B. RAFT Dispersion Polymerization in Nonpolar Media: Polymerization of 3-Phenylpropyl Methacrylate in N-Tetradecane with Poly(Stearyl Methacrylate) Homopolymers as Macro Chain Transfer Agents. *Macromolecules* **2015**, *48*, 236–244.

(188) Darmau, B.; Rymaruk, M. J.; Warren, N. J.; Bening, R.; Armes, S. P. RAFT Dispersion Polymerization of Benzyl Methacrylate in Non-Polar Media Using Hydrogenated Polybutadiene as a Steric Stabilizer Block. *Polym. Chem.* **2020**, *11*, 7533–7541.

(189) Rymaruk, M. J.; O'Brien, C. T.; György, C.; Darmau, B.; Jennings, J.; Mykhaylyk, O. O.; Armes, S. P. Small-Angle X-Ray Scattering Studies of Block Copolymer Nano-Objects: Formation of Ordered Phases in Concentrated Solution During Polymerization-Induced Self-Assembly. *Angew. Chemie - Int. Ed.* **2021**, *60*, 12955–12963.

(190) Lopez-Oliva, A. P.; Warren, N. J.; Rajkumar, A.; Mykhaylyk, O. O.; Derry, M. J.; Doncom, K. E. B.; Rymaruk, M. J.; Armes, S. P. Polydimethylsiloxane-Based Diblock Copolymer Nano-Objects Prepared in Nonpolar Media via RAFT-Mediated Polymerization-Induced Self-Assembly. *Macromolecules* **2015**, *48*, 3547–3555.

(191) Warren, N. J.; Mykhaylyk, O. O.; Ryan, A. J.; Williams, M.; Doussineau, T.; Dugourd, P.; Antoine, R.; Portale, G.; Armes, S. P. Testing the Vesicular Morphology to Destruction: Birth and Death of Diblock Copolymer Vesicles Prepared via

Polymerization-Induced Self-Assembly. *J. Am. Chem. Soc.* **2015**, *137*, 1929–1937.

(192) Blanazs, A.; Madsen, J.; Battaglia, G.; Ryan, A. J.; Armes, S. P. Mechanistic Insights for Block Copolymer Morphologies: How Do Worms Form Vesicles? *J. Am. Chem. Soc.* **2011**, *133*, 16581–16587.

Chapter 2. Synthesis of Poly(Stearyl Methacrylate)-Poly(2-Hydroxypropyl Methacrylate) Diblock Copolymer Nanoparticles *via* RAFT Dispersion Polymerization of 2-Hydroxypropyl Methacrylate in Mineral Oil

Chapter 2. Synthesis of Poly(Stearyl Methacrylate)-Poly(2-Hydroxypropyl Methacrylate) Diblock Copolymer Nanoparticles *via* RAFT Dispersion Polymerization of 2-Hydroxypropyl Methacrylate in Mineral Oil

2.1. Introduction

Poly(2-hydroxypropyl methacrylate) (PHPMA) has been utilized for a wide range of PISA formulations.[1–11] For example, Blanazs *et al.* studied the evolution of copolymer morphology during the RAFT aqueous dispersion polymerization of HPMA, which provided important mechanistic insights regarding the worm-to-vesicle transition.[1] In closely-related work, using PHPMA as a weakly hydrophobic structure-directing block enables the rational design of thermoresponsive worms[2,4,5] and vesicles.[3] Moreover, utilizing PHPMA in conjunction with highly biocompatible steric stabilizer blocks such as poly(glycerol monomethacrylate) [PGMA][12] or poly(ethylene glycol) [PEG][6,13] enables the soft hydrogels formed by semi-concentrated worm dispersions[14] to be evaluated as novel cell storage media.[13,15–17] Zehm and co-workers demonstrated that PHPMA can also be used as a steric stabilizer block for the RAFT alcoholic dispersion polymerization of benzyl methacrylate.[11] As mentioned in **Chapter 1**, Rymaruk *et al.* reported that PHPMA could serve as a core-forming block when exploring RAFT dispersion polymerization formulations in silicone oil.[18] However, only kinetically-trapped spheres could be obtained in this latter case. As far as we are aware, there are no prior reports of the use of PHPMA as a structure-directing block to access spheres, worms or vesicles *via* RAFT-mediated PISA in non-polar media.

Herein, we report the synthesis of PSMA$_9$-PHPMA$_x$ diblock copolymer nano-objects *via* RAFT dispersion polymerization of HPMA in mineral oil at 90 °C. Using a relatively short PSMA$_9$ precursor block ensures access to spheres, worms and vesicles.[19] A pseudo-phase diagram has been constructed for a series of PSMA$_9$-PHPMA$_x$ nanoparticles by varying the copolymer concentration from 15% to 30% w/w, confirming that a pure worm phase can be obtained over a relatively narrow range of diblock copolymer compositions (x = 67 to 70). The thermoresponsive nature of such worms is briefly explored.

Chapter 2. Synthesis of Poly(Stearyl Methacrylate)-Poly(2-Hydroxypropyl Methacrylate) Diblock Copolymer Nanoparticles *via* RAFT Dispersion Polymerization of 2-Hydroxypropyl Methacrylate in Mineral Oil

2.2. Experimental

2.2.1. Materials

2-Hydroxypropyl methacrylate (HPMA) was donated by GEO Specialty Chemicals (UK) and used without further purification. Stearyl methacrylate (SMA) was purchased from Santa Cruz Biotechnology Ltd (USA) and was used without further purification. Benzyl methacrylate (BzMA, 96%) was purchased from Sigma Aldrich, passed through an inhibitor remover column to remove monomethyl ether hydroquinone (MMEHQ) and then stored at −20 °C prior to use. 2-Cyano-2-propyl dithiobenzoate (CPDB), CDCl$_3$ and *n*-dodecane were purchased from Sigma Aldrich (UK). 2,2′-Azobisisobutyronitrile (AIBN) was obtained from Molekula (UK). *tert*-Butyl peroxy-2-ethylhexanoate (T21s) was purchased from AkzoNobel (The Netherlands). CD$_2$Cl$_2$ was purchased from Goss Scientific (UK). API Group III mineral oil (viscosity = 3.1 cSt at 100 °C) was kindly provided by The Lubrizol Corporation Ltd (Hazelwood, Derbyshire, UK). All other solvents were purchased from Fisher Scientific (UK) and were used as received.

2.2.2. Methods

Synthesis of poly(stearyl methacrylate) (PSMA$_9$) precursor *via* RAFT solution polymerization

The synthesis of the PSMA$_9$ homopolymer precursor was conducted at 50% w/w solids as follows. SMA (34.0 g; 100.4 mmol), CPDB (4.40 g; 19.9 mmol; target degree of polymerization = 5), AIBN (659 mg; 4.01 mmol; CPDB/AIBN molar ratio = 5.0) and toluene (39 g) were weighed into a 250 mL round-bottomed flask. The sealed reaction vessel was purged with nitrogen for 30 min, then placed in a pre-heated oil-bath at 70 °C with stirring for 4 h. The SMA polymerization was quenched by exposing the reaction solution to air and cooling to room temperature. A final SMA conversion of 77% was determined by ^{1}H NMR spectroscopy. The crude homopolymer was purified by two consecutive precipitations into a ten-fold excess of ethanol. The mean degree of polymerization (DP) of this macro-CTA was calculated to be 9 using ^{1}H NMR spectroscopy by comparing the integrated aromatic protons from the dithiobenzoate end-group at 6.8-8.0 ppm to the two oxymethylene protons assigned to the SMA residues at 3.6-4.0 ppm. THF GPC analysis using a refractive index detector and

a series of near-monodisperse poly(methyl methacrylate) standards indicated an M_n of 4 500 g mol^{-1} and an M_w/M_n of 1.12.

Synthesis of poly(stearyl methacrylate)-poly(2-hydroxypropyl methacrylate) (PSMA$_9$-PHPMA$_x$) diblock copolymer nanoparticles *via* RAFT dispersion polymerization of HPMA in mineral oil

The protocol for the synthesis of PSMA$_9$-PHPMA$_{150}$ diblock copolymer vesicles at 15% w/w solids is representative and was conducted as follows. PSMA$_9$ (0.040 g; 12.2 µmol), HPMA (0.26 g; 1.84 mmol), T21s initiator (0.53 mg; 2.45 µmol; 10.0% v/v in mineral oil; PSMA$_9$/T21s molar ratio = 5.0) and mineral oil (1.73 g) were weighed into a vial and this reaction mixture was purged with nitrogen gas for 30 min. The sample vial was then immersed into a pre-heated oil bath at 90 °C and the reaction mixture was magnetically stirred for 5 h. ^{1}H NMR spectroscopy studies indicated indicated more than 98% HPMA monomer conversion (the integrated vinyl proton signals at 5.0-6.0 ppm were compared with the integrated polymer backbone signals at 3.5-4.0 ppm). THF GPC analysis indicated an M_n of 18 800 g mol^{-1} and an M_w/M_n of 1.37. Other diblock copolymer compositions were targeted at 15% to 30% w/w solids by using the same mass of PSMA$_9$ and adjusting the HPMA/PSMA$_9$ molar ratio and the volume of mineral oil accordingly.

^{1}H NMR spectroscopy

^{1}H NMR spectra were recorded in either CD$_2$Cl$_2$ or CDCl$_3$ using a 400 MHz Bruker Avance III spectrometer. Typically 64 scans were averaged per spectrum. *In situ* ^{1}H NMR spectra were recorded using the same spectrometer in order to study the HPMA polymerization kinetics during the synthesis of PSMA$_9$-PHPMA$_{150}$ vesicles at 15% w/w solids in mineral oil and also PSMA$_9$-PBzMA$_{150}$ vesicles at 18% w/w solids in the same solvent. A 0.20 mL aliquot of the reaction mixture was transferred into an NMR tube equipped with an inert J-Young's tap under a nitrogen atmosphere. A capillary tube containing 0.28 M toluene dissolved in d$_6$-DMSO was flame-sealed and used as an external standard (and also a solvent lock). A reference spectrum was recorded at 20 °C prior to heating the reaction mixture up to 90 °C. Spectra were recorded approximately every 2 min for the first 20 min and approximately every 6 min thereafter. Spectra were acquired in eight transients using a 30° excitation pulse and a delay time of 5 s over a spectral window of 16 kHz with 64 k data points.

Gel Permeation Chromatography (GPC)

Molecular weight distributions (MWDs) were assessed by GPC using THF eluent. The THF GPC system was equipped with two 5 µm (30 cm) Mixed C columns and a WellChrom K-2301 refractive index detector operating at 950 ± 30 nm. The THF mobile phase contained 2.0% v/v triethylamine and 0.05% w/v butylhydroxytoluene (BHT) and the flow rate was fixed at 1.0 mL min^{-1}. A series of eleven near-monodisperse poly(methyl methacrylate) standards (M_p values ranging from 800 to 988 000 g mol^{-1}) were used for column calibration.

Dynamic Light Scattering (DLS)

DLS studies were performed using a Zetasizer Nano ZS instrument (Malvern Instruments, UK) at a fixed scattering angle of 173°. Copolymer dispersions were diluted in *n*-dodecane (0.10% w/w) prior to light scattering studies at 25 °C. The intensity-average diameter and polydispersity of the diblock copolymer nanoparticles were calculated by cumulants analysis of the experimental correlation function using Dispersion Technology Software version 6.20. Data were averaged over ten runs each of thirty seconds duration. It is emphasized that DLS assumes a spherical morphology and reports intensity-average diameters. Thus, the apparent DLS diameter determined for highly anisotropic particles such as worms is neither equal to the worm length nor the worm width. Despite this limitation, DLS can be used to monitor a thermally-induced worm-to-sphere transition by determining the reduction in the apparent diameter.[20]

Transmission Electron Microscopy (TEM)

TEM studies were conducted using a FEI Tecnai G2 spirit instrument operating at 80 kV and equipped with a Gatan 1k CCD camera. Diluted diblock copolymer dispersions (0.10% w/w) were placed on carbon-coated copper grids and exposed to ruthenium(VIII) oxide vapor for 7 min at 20 °C prior to analysis.[21] This heavy metal compound acted as a positive stain for the core-forming block to improve contrast. The ruthenium(VIII) oxide was prepared as follows: ruthenium(IV) oxide (0.30 g) was added to water (50 g) to form a black slurry; addition of sodium periodate (2.0 g) with continuous stirring produced a yellow solution of ruthenium(VIII) oxide within 1 min. In order to study the thermally-induced worm-to-vesicle transition, a sample vial containing 1.0 g of a 25% w/w PSMA$_9$-PHPMA$_{70}$ dispersion in mineral oil was placed in a pre-heated oil bath at 150 °C, allowed to equilibrate for 1 h, diluted

with *n*-dodecane (preheated to the same temperature), and then a single droplet of this hot dispersion was transferred onto a TEM grid and allowed to evaporate.

Small-Angle X-ray Scattering (SAXS)

SAXS patterns were collected at a synchrotron source (Diamond Light Source, station I22, Didcot, UK) using monochromatic X-ray radiation (wavelength $\lambda = 0.100$ nm, with q ranging from 0.017 to 2.1 nm^{-1}, where $q = 4\pi.\sin\theta/\lambda$ is the length of the scattering vector and θ is one-half of the scattering angle) and a 2D Pilatus 2M pixel detector (Dectris, Switzerland). A glass capillary of 2.0 mm diameter was used as a sample holder. Scattering data were reduced using standard routines from the beamline and were further analyzed using Irena SAS macros for Igor Pro.[22]

2.3. Results and Discussion

2.3.1. Synthesis of PSMA$_9$ macro-CTA

The RAFT solution polymerization of SMA was conducted in toluene at 70 °C using CPDB as a RAFT CTA to produce the desired PSMA macro-CTA precursor (see **Scheme 2.1**). A preliminary kinetic study when targeting a PSMA$_5$ macro-CTA had indicated first-order kinetics after an initial induction period of approximately 1 h and the expected linear evolution in molecular weight with conversion (see **Figure 2.1**). In order to avoid the possible loss of RAFT chain-ends under monomer-starved conditions, the scaled-up SMA polymerization was quenched after 4 h by exposure to air, which resulted in an SMA conversion of 77%. This protocol produced approximately 26 g of PSMA homopolymer with a mean degree of polymerization (DP) of 9 and a relatively narrow molecular weight distribution ($M_w/M_n = 1.12$), indicating that good RAFT control was achieved.

Chapter 2. Synthesis of Poly(Stearyl Methacrylate)-Poly(2-Hydroxypropyl Methacrylate) Diblock Copolymer Nanoparticles *via* RAFT Dispersion Polymerization of 2-Hydroxypropyl Methacrylate in Mineral Oil
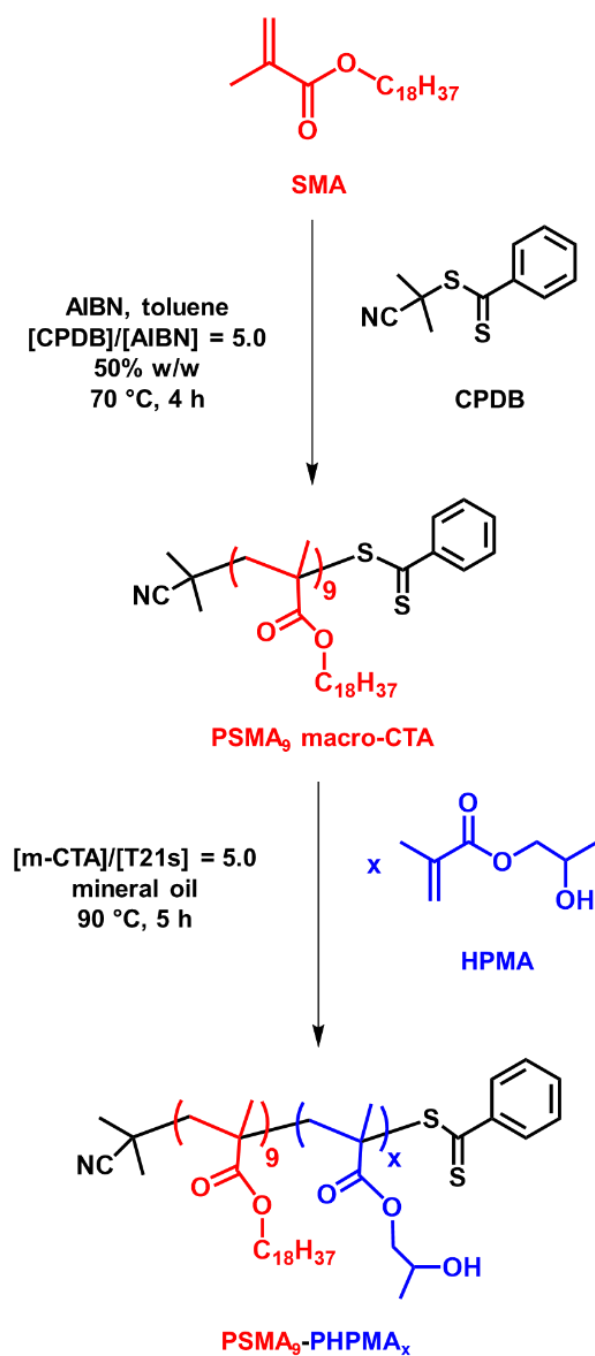
Scheme 2.1. Synthesis of a poly(stearyl methacrylate) (PSMA) precursor *via* RAFT solution polymerization in toluene using 2-cyano-2-propyl benzodithioate (CPDB) at 70 °C, followed by the RAFT dispersion polymerization of 2-hydroxypropyl methacrylate (HPMA) in mineral oil at 90 °C.
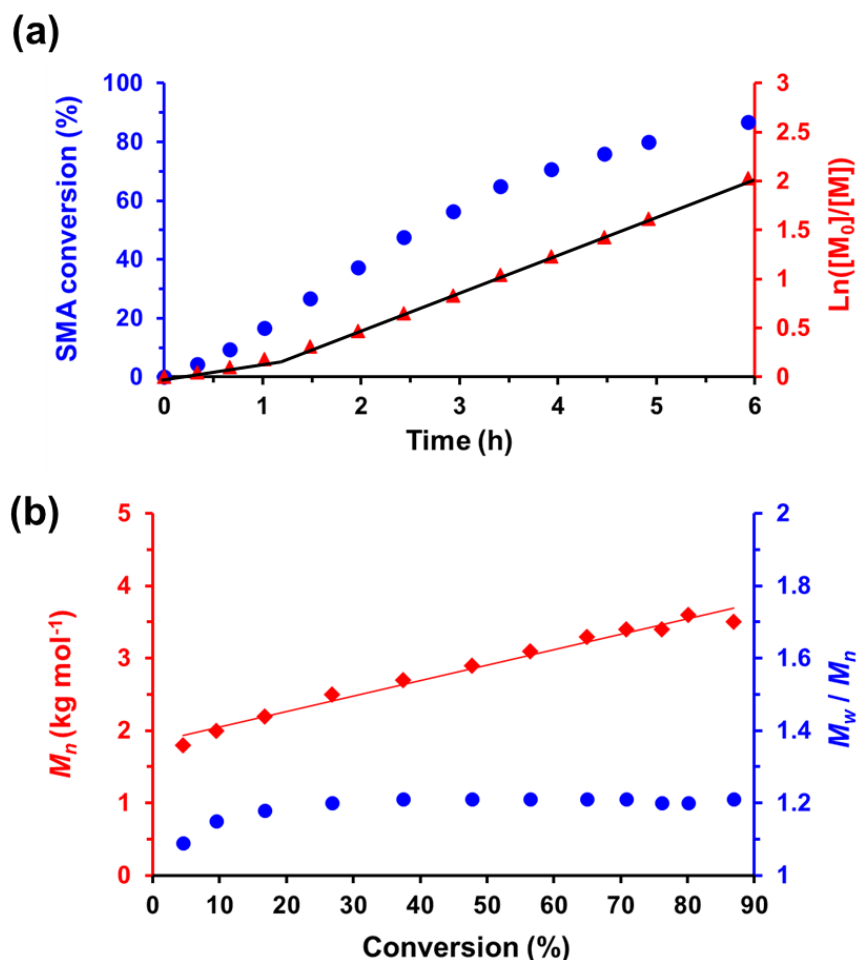
Figure 2.1. RAFT solution polymerization of SMA in toluene at 50% w/w solids and 70 °C using CPDB as a RAFT agent (target PSMA DP = 5; CPDB/initiator molar ratio = 5.0). **(a)** Conversion *vs.* time (blue circles) and corresponding $\ln([M]_0/[M])$ *vs.* time (red triangles) plots. **(b)** Evolution in M_n (red diamonds) and M_w/M_n (blue circles) obtained by THF GPC analysis using a series of near-monodisperse poly(methyl methacrylate) calibration standards.

2.3.2. Kinetic study of the RAFT dispersion polymerization of HPMA in mineral oil

In situ ^{1}H NMR spectroscopy experiments were performed to examine the kinetics of the RAFT dispersion polymerization of HPMA at 90 °C when targeting $PSMA_9$-$PHPMA_{150}$ vesicles at 15% w/w solids. HPMA conversions were determined by comparing the integrated monomer vinyl proton signals at 5.0-6.0 ppm to the three methyl protons assigned to the toluene external standard at 2.3 ppm (see **Figure 2.2a**).
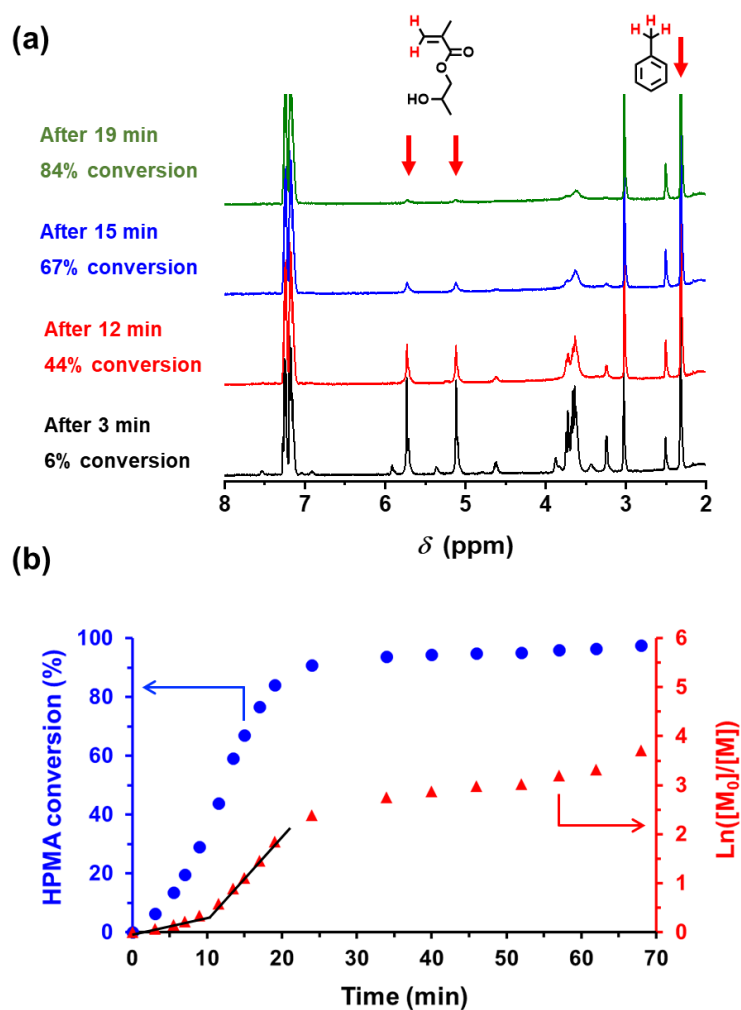
Figure 2.2. (a) Selected partial ^{1}H NMR spectra recorded during the RAFT dispersion polymerization of HPMA targeting a 15% w/w dispersion of $PSMA_9$-$PHPMA_{150}$ vesicles in mineral oil at 90 °C: after 3 min (black data), 12 min (red data), 15 min (blue data) and 19 min (green data) using toluene in d_6-DMSO as an external standard. **(b)** Conversion *vs*. time curve (blue circles) and corresponding semi-logarithmic plot (red triangles) for the same PISA synthesis.

The HPMA polymerization proceeded relatively slowly for the first 10 min prior to an approximate six-fold rate enhancement. This time point corresponded to 29% HPMA conversion or a PHPMA DP of 44 and is attributed to the onset of micellar nucleation. as the growing PHPMA chains become insoluble in the HPMA/mineral oil reaction mixture resulting in the formation of spherical micelles by *in situ* self-assembly.[1,19] Thereafter, first-order kinetics were observed up to 84% HPMA conversion, followed by a slower rate of polymerization under monomer-starved conditions (see **Figure 2.2b**). More than 98% HPMA

conversion was achieved within 70 min at 90 °C. This indicates a significantly faster polymerization than most previously studied PISA formulations in non-polar media, which is attributed to the polar nature of HPMA.[23] In order to confirm this hypothesis, we compared the kinetics of this RAFT dispersion polymerization with that for a non-polar monomer, benzyl methacrylate (BzMA), while targeting $PSMA_9$-$PBzMA_{150}$ vesicles in mineral oil under precisely the same reaction conditions (*i.e.* using identical monomer and $PSMA_9$ concentrations). For $PSMA_9$-$PHPMA_{150}$ vesicles, an HPMA conversion of 94% was achieved within 40 min whereas only 37% BzMA conversion was achieved for $PSMA_9$-$PBzMA_{150}$ vesicles on the same timescale (see **Figure 2.3a**). Moreover, the corresponding semilogarithmic plots suggested a pseudo-first order rate constant for the HPMA polymerization that was twelve-fold greater than that for the BzMA polymerization (see **Figure 2.3b**).

THF GPC analysis of the final $PSMA_9$-$PHPMA_{150}$ (98% conversion after 70 min; M_n = 19,500 g mol^{-1}, M_w/M_n = 1.24) and $PSMA_9$-$PBzMA_{150}$ diblock copolymers (97% conversion after 150 min; M_n = 17,300 g mol^{-1}, M_w/M_n = 1.11) indicated good RAFT control over each polymerization. Thus it appears that the RAFT dispersion polymerization of HPMA offers an advantage over the equivalent synthesis using BzMA.
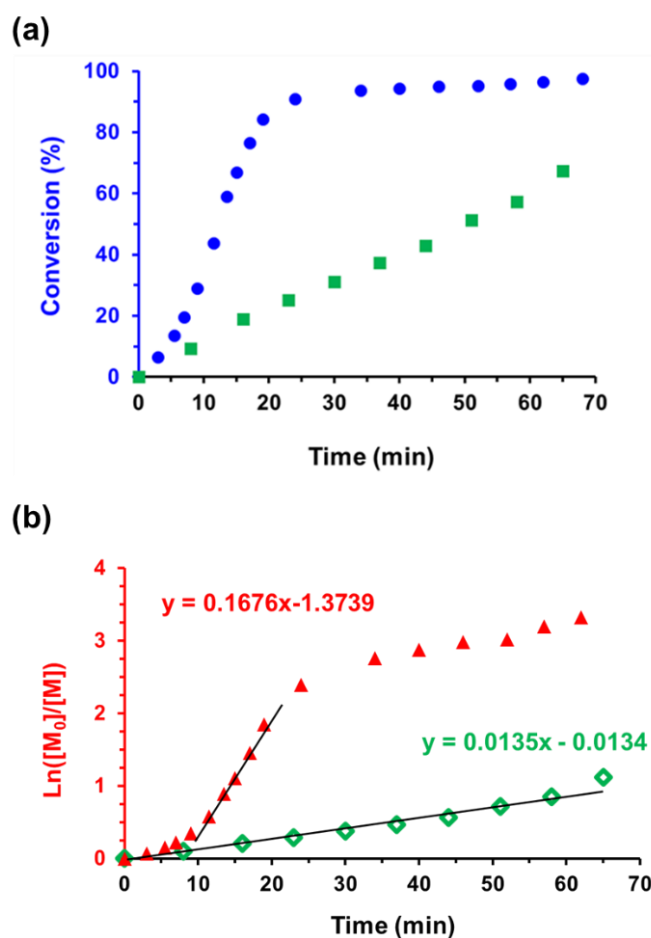
Figure 2.3. (a) Conversion *vs*. time curves obtained for the RAFT dispersion polymerization of either HPMA (blue circles) or BzMA (green squares) at 90 °C in mineral oil targeting either PSMA$_9$-PHPMA$_{150}$ vesicles at 15% w/w solids or PSMA$_9$-PBzMA$_{150}$ at 18% w/w solids, respectively. Conditions: [HPMA]$_0$ = [BzMA]$_0$ = 0.78 M; [PSMA$_9$] = 17 g dm^{-3}; [PSMA$_9$]/[T21s] molar ratio = 5.0. **(b)** Semilogarithmic plots obtained for the RAFT dispersion polymerization of either HPMA or BzMA in mineral oil at 90 °C targeting either 15% w/w PSMA$_9$-PHPMA$_{150}$ vesicles (red triangles) or 18% w/w PSMA$_9$-PBzMA$_{150}$ vesicles (open green diamonds).

2.3.3. Synthesis of PSMA$_9$-PHPMA$_x$ diblock copolymer nanoparticles

A series of PSMA$_9$-PHPMA$_x$ diblock copolymer nano-objects were then targeted *via* RAFT dispersion polymerization of HPMA in mineral oil at 90 °C. The PSMA$_9$ precursor was utilized to polymerize HPMA and PHPMA DPs from 30 to 150 were targeted while varying the overall solids content between 15% and 30% w/w. In each case, more than 98% HPMA monomer conversion was achieved within 5 h as judged by ^{1}H NMR spectroscopy. GPC analysis indicated that relatively good RAFT control was achieved in all cases ($M_w/M_n \leq 1.37$, see **Figure 2.4**). Targeting higher PHPMA DPs resulted in a systematic shift in the GPC curves

towards higher molecular weight (see **Figure 2.4a**), while minimal $PSMA_9$ precursor contamination indicated high blocking efficiencies. Moreover, a linear evolution of M_n with target PHPMA DP is observed in **Figure 2.4b** for a series of $PSMA_9\text{-}PHPMA_x$ nano-objects prepared at 15% w/w solids, although a gradual increase in M_w/M_n is discernible as higher PHPMA DPs are targeted.
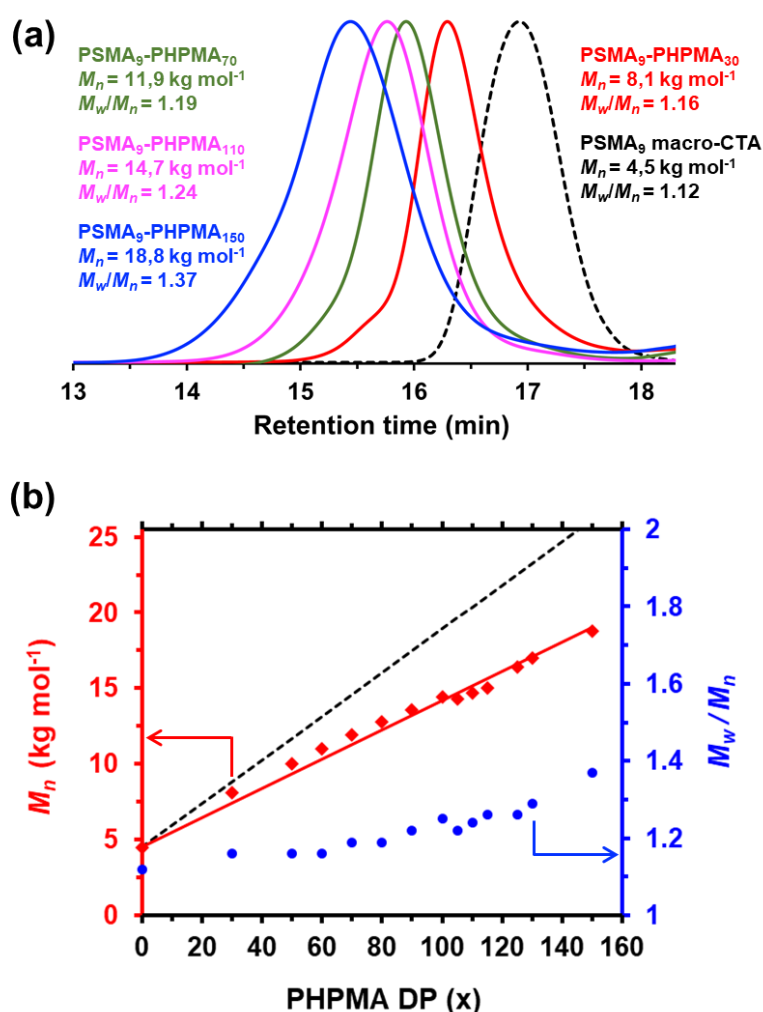
Figure 2.4. (a) THF gel permeation chromatograms (*vs.* poly(methyl methacrylate) standards) obtained for the precursor $PSMA_9$ macro-CTA (black dashed curve) and four $PSMA_9\text{-}PHPMA_x$ diblock copolymers prepared *via* RAFT dispersion polymerization of HPMA in mineral oil at 90 °C targeting 15% w/w solids. **(b)** Plots of M_n (red diamonds) and M_w/M_n (blue circles) *vs.* PHPMA DP for a series of $PSMA_9\text{-}PHPMA_x$ diblock copolymer nano-objects. The black dashed line indicates the theoretical M_n *vs.* PHPMA DP relationship for this series, with the difference being attributed to the GPC calibration error incurred by using poly(methyl methacrylate) standards.

Recently, Docherty *et al.* reported the chain extension of $PSMA_{13}$ and $PSMA_{18}$ stabilizer blocks using glycidyl methacrylate in mineral oil, but only kinetically-trapped spherical nanoparticles could be obtained.[24] In contrast, using the shorter $PSMA_9$ stabilizer block for the RAFT dispersion polymerization of HPMA provides convenient access to worms and vesicles, as well as spheres. Accordingly, a pseudo-phase diagram was constructed to facilitate the reproducible synthesis of such nano-objects (see **Tables 9.1-9.2**), with copolymer morphology assignments being made on the basis of TEM studies (see **Figure 2.5**).[6,19,25,26] Well-defined spherical nanoparticles could be obtained at all copolymer concentrations examined, with DLS studies indicating narrow size distributions (polydispersity index, PDI ≤ 0.20) and a systematic increase in the intensity-average diameter when targeting higher PHPMA DPs, as expected.[19,24] However, a pure worm phase could only be obtained at relatively high copolymer concentrations (either 25% w/w or 30% w/w solids). Derry *et al.* reported similar observations for poly(lauryl methacrylate)-poly(benzyl methacrylate) diblock copolymer nano-objects prepared in mineral oil.[25] The rather broad mixed phase observed in **Figure 2.5e** is similar to that recently reported by Rymaruk *et al.*[18] for polydimethylsiloxane-poly(2-(dimethylamino)ethyl methacrylate) nano-objects in silicone oil. This suggests that sphere-sphere fusion is not particularly efficient for such PISA formulations. Nevertheless, pure vesicles could be accessed by targeting PHPMA DPs of 115 or higher at copolymer concentrations ranging from 15% w/w to 25% w/w. Interestingly, a mixed phase comprising vesicles and lamellae was observed when increasing the copolymer concentration up to 30% w/w (see **Figure 2.5d**).

To confirm the copolymer morphologies assigned by TEM analysis, SAXS patterns were recorded for 1.0% w/w dispersions of four $PSMA_9$-$PHPMA_x$ diblock copolymers originally prepared at 25% w/w (see **Figure 2.6**).
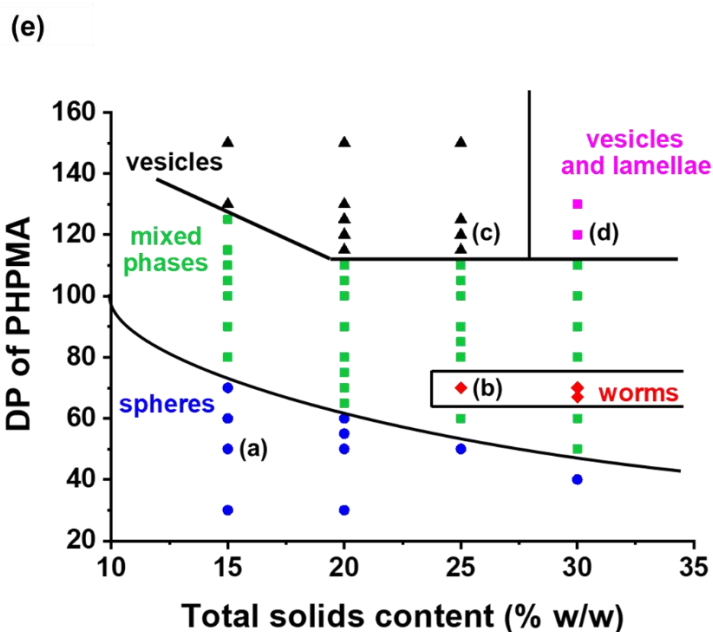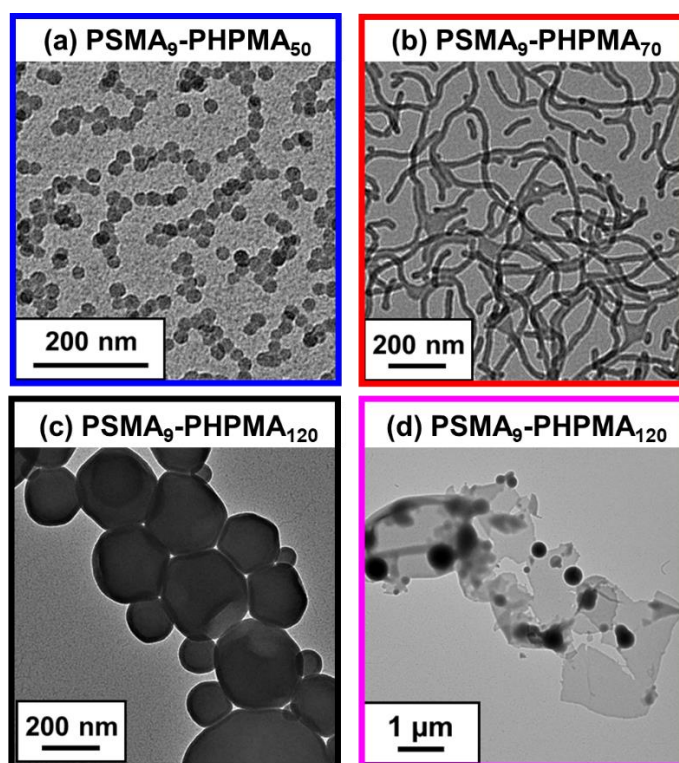
Figure 2.5. Representative TEM images obtained for **(a)** PSMA$_9$-PHPMA$_{50}$ spheres, **(b)** PSMA$_9$-PHPMA$_{70}$ worms, **(c)** PSMA$_9$-PHPMA$_{120}$ vesicles and **(d)** a mixed phase comprising PSMA$_9$-PHPMA$_{120}$ lamellae and vesicles. **(e)** Pseudo-phase diagram constructed for PSMA$_9$-PHPMA$_x$ diblock copolymer nano-objects prepared by RAFT dispersion polymerization of HPMA in mineral oil using a PSMA$_9$ precursor and T21s initiator at 90 °C ([PSMA$_9$]/[T21s] molar ratio = 5.0). [Black triangles (▲), red diamonds (◆) and blue circles (●) represent pure vesicles, worms and spheres, respectively. Green squares (■) correspond to either sphere/worm or worm/vesicle mixed phases, whereas purple squares (■) represent a vesicle/lamellae mixed phase].
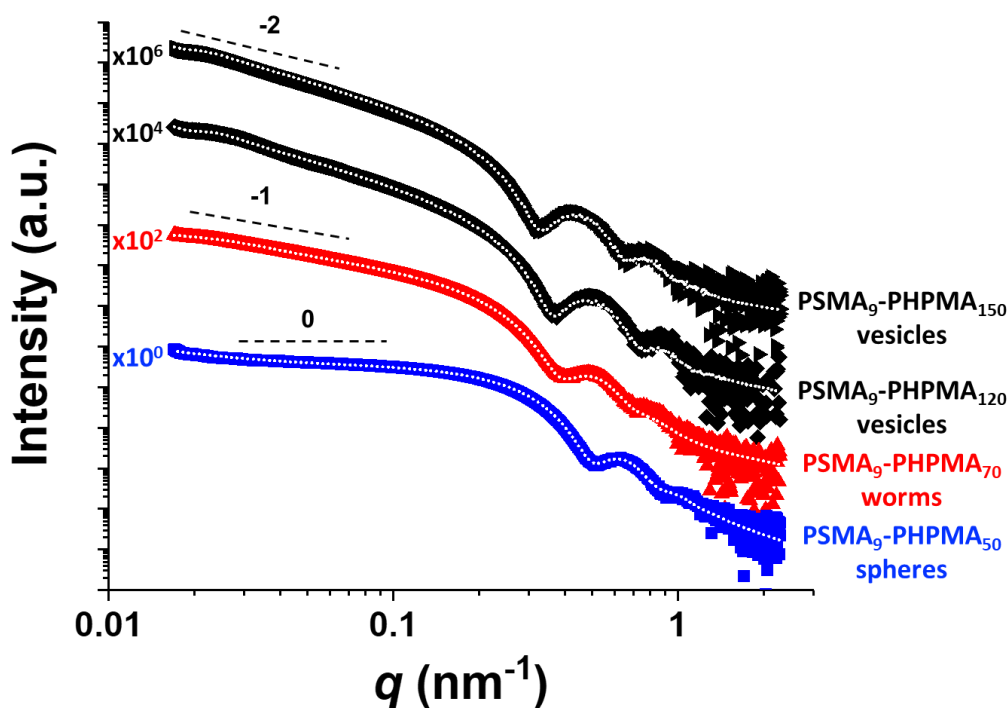
Figure 2.6. Small-angle X-ray scattering patterns recorded for 1.0% w/w dispersions of $PSMA_9$-$PHPMA_x$ diblock copolymer spheres, worms and vesicles in mineral oil. Dotted white lines indicate the data fits obtained using the relevant scattering model. In each case, these diblock copolymer nano-objects were initially synthesized at 25% w/w solids.

For $PSMA_9$-$PHPMA_{50}$, an approximate zero gradient was observed at low q as expected for spherical nanoparticles, and the local minimum in the scattering pattern at $q \sim 0.5$ nm^{-1} indicates a mean core radius of approximately 9 nm.[27] Fitting this SAXS pattern to a well-known spherical micelle model[28] indicated an overall sphere diameter (D_{sphere}) of 21.1 ± 1.9 nm and a mean aggregation number (N_{agg}, or number of copolymer chains per nanoparticle) of 200 (see **Table 2.1**). This volume-average D_{sphere} value is consistent with the intensity-average diameter of 31 nm reported by DLS for these $PSMA_9$-$PHPMA_{50}$ spheres. The SAXS pattern recorded for $PSMA_9$-$PHPMA_{70}$ exhibits a gradient of approximately -1 in the low q region, which is consistent with the worm morphology indicated by TEM analysis. In this case, the local minimum observed at $q \sim 0.4$ nm^{-1} represents the mean worm core radius.

Chapter 2. Synthesis of Poly(Stearyl Methacrylate)-Poly(2-Hydroxypropyl Methacrylate) Diblock Copolymer Nanoparticles *via* RAFT Dispersion Polymerization of 2-Hydroxypropyl Methacrylate in Mineral Oil

Table 2.1. Summary of nano-object dimensions obtained from fitting small-angle X-ray scattering patterns using either a spherical micelle,[28] worm-like micelle[28] or vesicle model.[29] D_{sphere} is the overall sphere diameter such that $D_{sphere} = 2R_s + 4R_g$, where R_s is the mean core radius and R_g is the radius of gyration of the stabilizer chains. T_{worm} is the overall worm thickness ($T_{worm} = 2R_{wc} + 4R_g$, where R_{wc} is the mean worm core radius) and L_{worm} is the mean worm contour length. $D_{vesicle}$ is the overall vesicle diameter ($D_{vesicle} = 2R_m + T_{membrane} + 4R_g$, where R_m is the distance from the centre of the vesicle to the centre of the vesicle membrane, and $T_{membrane}$ is the vesicle membrane thickness). N_{agg} is the mean aggregation number (*i.e.* the mean number of copolymer chains per nano-object).

Block copolymer	Nanoparticle Morphology	D_{sphere}	T_{worm}	L_{worm}	$D_{vesicle}$	$T_{membrane}$	N_{agg}
PSMA$_9$-PHPMA$_{50}$	Spheres	21.1 ± 1.9 nm	-	-	-	-	200
PSMA$_9$-PHPMA$_{70}$	Worms	-	22.5 ± 2.4 nm	252 nm	-	-	3800
PSMA$_9$-PHPMA$_{120}$	Vesicles	-	-	-	348 ± 54 nm	16.0 ± 1.6 nm	177,400
PSMA$_9$-PHPMA$_{150}$	Vesicles	-	-	-	366 ± 58 nm	18.1 ± 1.9 nm	177,500

Fitting this SAXS pattern to a worm-like micelle model[28] indicates an overall worm thickness (T_{worm}) of 22.5 ± 2.4 nm, a mean worm length (L_{worm}) of ~252 nm and an N_{agg} of 3800. Comparing this aggregation number with that determined for the PSMA$_9$-PHPMA$_{50}$ spheres suggests that, on average, each worm is formed by stochastic 1D fusion of no more than 19 spheres. SAXS patterns recorded for PSMA$_9$-PHPMA$_{120}$ and PSMA$_9$-PHPMA$_{150}$ both exhibit low q gradients of approximately -2, which is consistent with a vesicular morphology.[6,19] In this case, the subtle feature observed at low q ($q \sim 0.02$ nm^{-1}) indicates the overall vesicle radius while the well-defined local minimum at high q ($q \sim 0.2$-0.3 nm^{-1}) provides information regarding the vesicle membrane thickness. Fitting these patterns to a well-known vesicle model[29] indicated that PSMA$_9$-PHPMA$_{120}$ and PSMA$_9$-PHPMA$_{150}$ vesicles exhibit comparable overall diameters ($D_{vesicle}$ = 348 ± 54 nm and 366 ± 58 nm, respectively), but increasing the PHPMA DP from 120 to 150 led to a thicker vesicle membrane ($T_{membrane}$ = 16.0 ± 1.6 nm *vs.* 18.1 ± 1.9 nm, respectively). These data are consistent with the previously discussed vesicle growth mechanism proposed by Warren *et al.*[30] and later validated by Derry *et al.*[19] for PISA syntheses (see **Chapter 1**). Mean N_{agg} values for PSMA$_9$-PHPMA$_{120}$ and PSMA$_9$-PHPMA$_{150}$ vesicles were calculated to be 177,400 and 177,500, respectively. These N_{agg} values are remarkably similar, which suggests that little or no net copolymer chain exchange occurs during the latter stages of the PISA synthesis of PSMA$_9$-PHPMA$_{150}$ vesicles (*i.e.* from 80% to 100% HPMA conversion).

2.3.4. Rheological studies of a PSMA$_9$-PHPMA$_{70}$ worm gel

The PSMA$_9$-PHPMA$_{70}$ worms prepared at 25% w/w solids in mineral oil form a free-standing gel owing to multiple inter-worm contacts.[14] This worm gel was characterized by variable temperature oscillatory rheology, as described previously for other worm gel systems.[4,9,20] Degelation occurred on heating above approximately 100 °C, with this critical temperature corresponding to the cross-over point for the bulk storage modulus G' and loss modulus G'' curves (see **Figure 2.7a**). Similar thermoresponsive behavior has been reported for poly(lauryl methacrylate)-poly(benzyl methacrylate) nano-objects in *n*-dodecane and explained in terms of a *worm-to-sphere* transition owing to surface plasticization of the worm cores by ingress of hot solvent (see **Chapter 1**).[20] However, in the present case TEM studies suggest that a partial *worm-to-vesicle* transition occurs on heating. The initial pure worms – diluted at 20 °C for TEM analysis (see **Figure 2.7b**) – were transformed into a mixed phase comprising large vesicles and some remaining worms on heating up to 150 °C (see **Figure 2.7c**).

These observations are consistent with DLS studies: the sphere-equivalent intensity-average diameter determined at 20 °C for the initial dilute dispersion of pure worms (156 nm, PDI = 0.54) increased significantly after heating up to 150 °C (231 nm, PDI = 0.63). On cooling, regelation occurred at a critical gelation temperature (CGT) of approximately 100 °C, which suggests thermoreversible behavior. However, the initial G' value of ~ 6700 Pa was reduced by more than an order of magnitude to ~ 420 Pa after this single thermal cycle. Moreover, TEM analysis of the diluted copolymer dispersion revealed a mixed morphology of worms and vesicles at 20 °C, thus indicating that the original pure worm morphology had not been restored on cooling (see **Figure 2.8**).

(a)

(b) *T* = 20 °C

250 nm

(c) *T* = 150 °C

250 nm
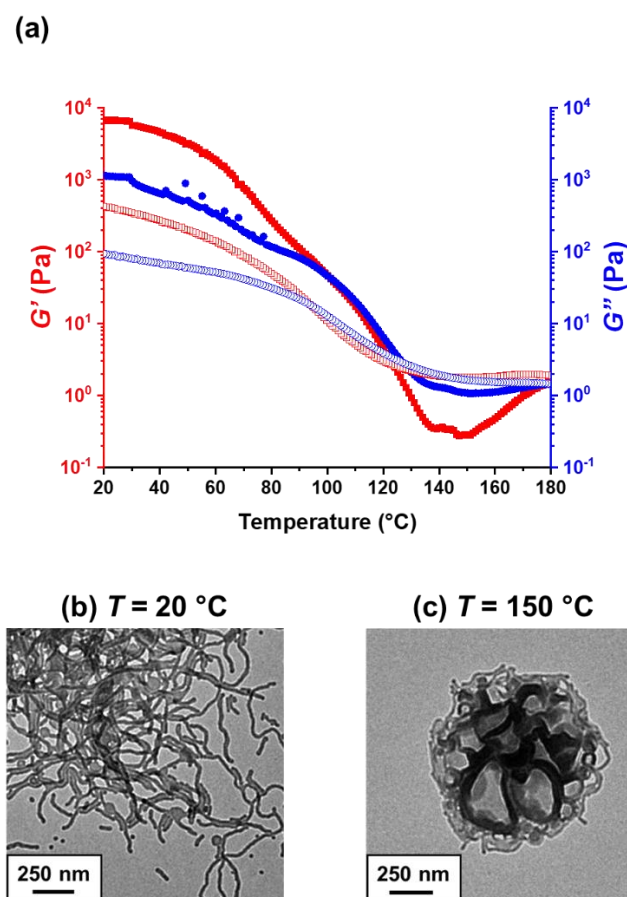
Figure 2.7. (a) Temperature dependence for the storage moduli (G', red squares) and loss moduli (G'', blue circles) observed for a PSMA$_9$-PHPMA$_{70}$ worm gel prepared at 25% w/w solids in mineral oil on heating from 20 to 180 °C (filled symbols) and cooling from 180 to 20 °C (hollow symbols) at a rate of 2.0 °C min^{-1}. Data were recorded at 1.0% strain amplitude using an angular frequency of 10 rad s^{-1}. Representative TEM images obtained for this PSMA$_9$-PHPMA$_{70}$ dispersion after dilution **(b)** at 20 °C (pure worms) and **(c)** 150 °C (mixed phase comprising vesicles and worms). This partial morphological transition accounts for the degelation that is observed above 100 °C.

200 nm
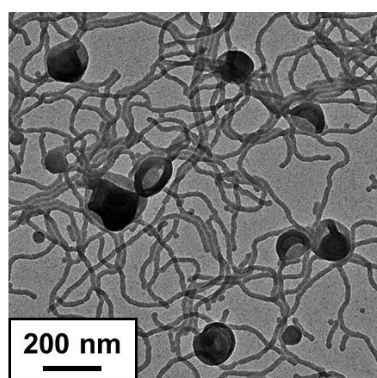
Figure 2.8. Representative TEM image recorded for a mixed phase of PSMA$_9$-PHPMA$_{70}$ vesicles and worms (prepared at 25% w/w solids) obtained after oscillatory rheology studies.

Unlike previous morphological transformations of diblock copolymer nano-objects in non-polar media,[20,31–33] this partial worm-to-vesicle transition on heating cannot be explained by surface plasticization of the PHPMA worm cores by hot solvent. This can only result in an increase in the volume of the solvophilic block relative to the solvophobic block, resulting in a reduction in the critical packing parameter (P) and thus favoring the formation of spheres. Instead, an *increase* in P is required to generate vesicles from the initial worms, which means that the volume of the solvophobic PHPMA block must increase relative to that of the solvophilic PSMA block. In principle, this could occur *via uniform solvation* of the core-forming PHPMA block. However, this seems unlikely given that even hot *n*-dodecane is likely to remain a very poor solvent for the hydroxyl-functional PHPMA chains. An alternative explanation could be that the poly(stearyl methacrylate) block becomes less solvated at elevated temperature and hence occupies a smaller volume relative to that at 20 °C. Clearly, further studies are warranted to provide a satisfactory physical explanation for this unexpected morphological transition, which serves to demonstrate that there is still much to learn about such thermoresponsive PISA formulations.

2.4. Conclusion

The PISA synthesis of PSMA-PHPMA diblock copolymer spheres, worms and vesicles was achieved *via* RAFT dispersion polymerization of HPMA at 90 °C in mineral oil. *In situ* ^{1}H NMR spectroscopy was utilized to examine the kinetics of the PISA synthesis of $PSMA_9$-$PHPMA_{150}$ vesicles, for which (more than 98%) monomer conversion was achieved within 70 min. This is a remarkably short time scale compared to most other PISA formulations conducted in non-polar media and is attributed to the relatively polar nature of the HPMA monomer. Construction of a pseudo-phase diagram enables the reproducible targeting of $PSMA_9$-$PHPMA_x$ pure spheres, worms or vesicles, as confirmed by TEM, DLS and SAXS studies. Thus this is a rare example of the use of a commercially available polar monomer for PISA syntheses in non-polar media that offers access to the full range of copolymer morphologies. The worms formed thermoresponsive free-standing gels with degelation occurring on heating above 100 °C. Unusually, such degelation is the result of a worm-to-vesicle transition, rather than a worm-to-sphere transition.

2.5. References

(1) Blanazs, A.; Madsen, J.; Battaglia, G.; Ryan, A. J.; Armes, S. P. Mechanistic Insights for Block Copolymer Morphologies: How Do Worms Form Vesicles? *J. Am. Chem. Soc.* **2011**, *133*, 16581–16587.

(2) Blanazs, A.; Verber, R.; Mykhaylyk, O. O.; Ryan, A. J.; Heath, J. Z.; Douglas, C. W. I.; Armes, S. P. Sterilizable Gels from Thermoresponsive Block Copolymer Worms. *J. Am. Chem. Soc.* **2012**, *134*, 9741–9748.

(3) Lovett, J. R.; Warren, N. J.; Armes, S. P.; Smallridge, M. J.; Cracknell, R. B. Order-Order Morphological Transitions for Dual Stimulus Responsive Diblock Copolymer Vesicles. *Macromolecules* **2016**, *49*, 1016–1025.

(4) Verber, R.; Blanazs, A.; Armes, S. P. Rheological Studies of Thermo-Responsive Diblock Copolymer Worm Gels. *Soft Matter* **2012**, *8*, 9915–9922.

(5) Warren, N. J.; Derry, M. J.; Mykhaylyk, O. O.; Lovett, J. R.; Ratcliffe, L. P. D.; Ladmiral, V.; Blanazs, A.; Fielding, L. A.; Armes, S. P. Critical Dependence of Molecular Weight on Thermoresponsive Behavior of Diblock Copolymer Worm Gels in Aqueous Solution. *Macromolecules* **2018**, *51*, 8357–8371.

(6) Warren, N. J.; Mykhaylyk, O. O.; Mahmood, D.; Ryan, A. J.; Armes, S. P. RAFT Aqueous Dispersion Polymerization Yields Poly(Ethylene Glycol)-Based Diblock Copolymer Nano-Objects with Predictable Single Phase Morphologies. *J. Am. Chem. Soc.* **2014**, *136*, 1023–1033.

(7) Deng, R.; Ning, Y.; Jones, E. R.; Cunningham, V. J.; Penfold, N. J. W.; Armes, S. P. Stimulus-Responsive Block Copolymer Nano-Objects and Hydrogels: Via Dynamic Covalent Chemistry. *Polym. Chem.* **2017**, *8*, 5374–5380.

(8) Jesson, C. P.; Pearce, C. M.; Simon, H.; Werner, A.; Cunningham, V. J.; Lovett, J. R.; Smallridge, M. J.; Warren, N. J.; Armes, S. P. H2O2 Enables Convenient Removal of RAFT End-Groups from Block Copolymer Nano-Objects Prepared via Polymerization-Induced Self-Assembly in Water. *Macromolecules* **2017**, *50*, 182–191.

(9) Ratcliffe, L. P. D.; Bentley, K. J.; Wehr, R.; Warren, N. J.; Saunders, B. R.; Armes, S. P. Cationic Disulfide-Functionalized Worm Gels. *Polym. Chem.* **2017**, *8*, 5962–5971.

(10) Penfold, N. J. W.; Lovett, J. R.; Warren, N. J.; Verstraete, P.; Smets, J.; Armes, S. P. PH-Responsive Non-Ionic Diblock Copolymers: Protonation of a Morpholine End-Group Induces an Order–Order Transition. *Polym. Chem.* **2016**, *7*, 79–88.

(11) Zehm, D.; Ratcliffe, L. P. D.; Armes, S. P. Synthesis of Diblock Copolymer Nanoparticles via RAFT Alcoholic Dispersion Polymerization: Effect of Block Copolymer Composition, Molecular Weight, Copolymer Concentration, and Solvent Type on the Final Particle Morphology. *Macromolecules* **2013**, *46*, 128–139.

(12) Rimmer, S.; Wilshaw, S.-P.; Pickavance, P.; Ingham, E. Biomaterials and Conetworks with or without Alkyl Amine Functionality. *Biomaterials* **2009**, *30*, 2468–2478.

(13) Sponchioni, M.; O'Brien, C. T.; Borchers, C.; Wang, E.; Rivolta, M. N.; Penfold, N. J. W.; Canton, I.; Armes, S. P. Probing the Mechanism for Hydrogel-Based Stasis Induction in Human Pluripotent Stem Cells: Is the Chemical Functionality of the Hydrogel Important? *Chem. Sci.* **2020**, *11*, 232–240.

(14) Lovett, J. R.; Derry, M. J.; Yang, P.; Hatton, F. L.; Warren, N. J.; Fowler, P. W.; Armes,

S. P. Can Percolation Theory Explain the Gelation Behavior of Diblock Copolymer Worms? *Chem. Sci.* **2018**, *9*, 7138–7144.

(15) Canton, I.; Warren, N. J.; Chahal, A.; Amps, K.; Wood, A.; Weightman, R.; Wang, E.; Moore, H.; Armes, S. P. Mucin-Inspired Thermoresponsive Synthetic Hydrogels Induce Stasis in Human Pluripotent Stem Cells and Human Embryos. *ACS Cent. Sci.* **2016**, *2*, 65–74.

(16) Mitchell, D. E.; Lovett, J. R.; Armes, S. P.; Gibson, M. I. Combining Biomimetic Block Copolymer Worms with an Ice-Inhibiting Polymer for the Solvent-Free Cryopreservation of Red Blood Cells. *Angew. Chem.* **2016**, *128*, 2851–2854.

(17) Simon, K. A.; Warren, N. J.; Mosadegh, B.; Mohammady, M. R.; Whitesides, G. M.; Armes, S. P. Disulfide-Based Diblock Copolymer Worm Gels : A Wholly- Synthetic Thermo-Reversible 3D Matrix for Sheet-Based Cultures Disulfide-Based Diblock Copolymer Worm Gels : A Wholly-Synthetic Thermo-Reversible 3D Matrix for Sheet-Based Cultures. *Biomacromolecules* **2015**, *16*, 3952–3958.

(18) Rymaruk, M. J.; Hunter, S. J.; O'Brien, C. T.; Brown, S. L.; Williams, C. N.; Armes, S. P. RAFT Dispersion Polymerization in Silicone Oil. *Macromolecules* **2019**, *52*, 2822–2832.

(19) Derry, M. J.; Fielding, L. A.; Warren, N. J.; Mable, C. J.; Smith, A. J.; Mykhaylyk, O. O.; Armes, S. P. In Situ Small-Angle X-Ray Scattering Studies of Sterically-Stabilized Diblock Copolymer Nanoparticles Formed during Polymerization-Induced Self-Assembly in Non-Polar Media. *Chem. Sci.* **2016**, *7*, 5078–5090.

(20) Fielding, L. A.; Lane, J. A.; Derry, M. J.; Mykhaylyk, O. O.; Armes, S. P. Thermo-Responsive Diblock Copolymer Worm Gels in Non-Polar Solvents. *J. Am. Chem. Soc.* **2014**, *136*, 5790–5798.

(21) Trent, J. S. Ruthenium Tetraoxide Staining of Polymers: New Preparative Methods for Electron Microscopy. *Macromolecules* **1984**, *17*, 2930–2931.

(22) Ilavsky, J.; Jemian, P. R. Irena: Tool Suite for Modeling and Analysis of Small-Angle Scattering. *J. Appl. Crystallogr.* **2009**, *42*, 347–353.

(23) Cunningham, V. J.; Armes, S. P.; Musa, O. M. Synthesis, Characterisation and Pickering Emulsifier Performance of Poly(Stearyl Methacrylate)-Poly(N-2-(Methacryloyloxy)Ethyl Pyrrolidone) Diblock Copolymer Nano-Objects via RAFT Dispersion Polymerisation in n-Dodecane. *Polym. Chem.* **2016**, *7*, 1882–1891.

(24) Docherty, P. J.; Derry, M. J.; Armes, S. P. RAFT Dispersion Polymerization of Glycidyl Methacrylate for the Synthesis of Epoxy-Functional Block Copolymer Nanoparticles in Mineral Oil. *Polym. Chem.* **2019**, *10*, 603–611.

(25) Derry, M. J.; Fielding, L. A.; Armes, S. P. Industrially-Relevant Polymerization-Induced Self-Assembly Formulations in Non-Polar Solvents: RAFT Dispersion Polymerization of Benzyl Methacrylate. *Polym. Chem.* **2015**, *6*, 3054–3062.

(26) Fielding, L. A.; Derry, M. J.; Ladmiral, V.; Rosselgong, J.; Rodrigues, A. M.; Ratcliffe, L. P. D.; Sugihara, S.; Armes, S. P. RAFT Dispersion Polymerization in Non-Polar Solvents: Facile Production of Block Copolymer Spheres, Worms and Vesicles in n-Alkanes. *Chem. Sci.* **2013**, *4*, 2081–2087.

(27) Glatter, O.; Kratky, O. *Small-Angle X-Ray Scattering*; Academic Press, London, 1982.

(28) Pedersen, J. S. Form Factors of Block Copolymer Micelles with Spherical, Ellipsoidal and Cylindrical Cores. *J. Appl. Crystallogr.* **2000**, *33*, 637–640.

(29)   Bang, J.; Jain, S.; Li, Z.; Lodge, T. P.; Pedersen, J. S.; Kesselman, E.; Talmon, Y. Sphere, Cylinder, and Vesicle Nanoaggregates in Poly(Styrene-b-Isoprene) Diblock Copolymer Solutions. *Macromolecules* **2006**, *39*, 1199–1208.

(30)   Warren, N. J.; Mykhaylyk, O. O.; Ryan, A. J.; Williams, M.; Doussineau, T.; Dugourd, P.; Antoine, R.; Portale, G.; Armes, S. P. Testing the Vesicular Morphology to Destruction: Birth and Death of Diblock Copolymer Vesicles Prepared via Polymerization-Induced Self-Assembly. *J. Am. Chem. Soc.* **2015**, *137*, 1929–1937.

(31)   Derry, M. J.; Mykhaylyk, O. O.; Armes, S. P. A Vesicle-to-Worm Transition Provides a New High-Temperature Oil Thickening Mechanism. *Angew. Chemie - Int. Ed.* **2017**, *56*, 1746–1750.

(32)   Pei, Y.; Sugita, O. R.; Thurairajah, L.; Lowe, A. B. Synthesis of Poly(Stearyl Methacrylate-b-3-Phenylpropyl Methacrylate) Nanoparticles in n-Octane and Associated Thermoreversible Polymorphism. *RSC Adv.* **2015**, *5*, 17636–17646.

(33)   Pei, Y.; Lowe, A. B.; Roth, P. J. Stimulus-Responsive Nanoparticles and Associated (Reversible) Polymorphism via Polymerization Induced Self-Assembly (PISA). *Macromol. Rapid Commun.* **2017**, *38*, 1600528.

Chapter 3. Synthesis of Highly Transparent Diblock Copolymer Vesicles *via* RAFT Dispersion Polymerization of 2,2,2-Trifluoroethyl Methacrylate in *n*-Alkanes

Chapter 3. Synthesis of Highly Transparent Diblock Copolymer Vesicles *via* RAFT Dispersion Polymerization of 2,2,2-Trifluoroethyl Methacrylate in N-Alkanes

3.1. Introduction

Poly(2,2,2-trifluoroethyl methacrylate) (PTFEMA) has been utilized as a core-forming block for various aqueous and non-aqueous PISA formulations.[1–9] Semsarilar and co-workers were the first to report that choosing PTFEMA as the structure-directing block offers an opportunity to study the fate of the RAFT chain-ends during RAFT dispersion polymerization. More specifically, the refractive index of PTFEMA (1.418) is close to that of ethanol (1.361), which leads to minimal turbidity for PTFEMA-core nanoparticles in this solvent. This enabled the living character of RAFT solution polymerization to be compared with that of RAFT dispersion polymerization by targeting the same diblock copolymer composition and monitoring the gradual loss of RAFT chain-ends over time by *ex situ* UV spectroscopy.[1] Akpinar *et al.* reported the RAFT aqueous emulsion polymerization of TFEMA using poly(glycerol monomethacrylate) (PGMA) as a stabilizer block to produce a series of kinetically-trapped spheres.[3] Such nanoparticles were used as Pickering emulsifiers by Thompson *et al.* to produce oil-in-water nanoemulsions with relatively high stability.[5,10] Subsequently, Rymaruk and co-workers demonstrated that highly transparent *isorefractive* n-dodecane-in-water Pickering emulsions could be prepared using PGMA-PTFEMA spherical nanoparticles. This is because the refractive index of water can be raised to that of the PTFEMA cores (and the oil droplets) by dissolution of sufficient quantities of either glycerol or sucrose.[4] Recently, Cornel *et al.* reported that careful optimization of a PISA formulation (*i.e.*, judicious choice of *n*-alkane and reaction temperature) enabled the rational design of an isorefractive dispersion of PTFEMA-core spherical nanoparticles using a poly(stearyl methacrylate) (PSMA) precursor. At the chosen reaction temperature (70 °C), the preferred *n*-alkane (*n*-tetradecane) had almost precisely the same refractive index as the growing PTFEMA block, which resulted in a highly transparent dispersion. This enabled the kinetics of the RAFT dispersion polymerization of TFEMA to be monitored by *in situ* visible absorption spectroscopy studies of the relatively weak n → π* transition for the trithiocarbonate end-group at 446 nm.[7]

Herein we report the PISA synthesis of a series of $PSMA_9$-$PTFEMA_x$ nano-objects *via* RAFT dispersion polymerization of TFEMA in *n*-dodecane at 90 °C. The use of a relatively short $PSMA_9$ precursor block ensures access to the full range of copolymer morphologies (*i.e.*, spheres, worms and vesicles). A pseudo-phase diagram is constructed for this PISA formulation by targeting PTFEMA degrees of polymerizations (DPs) ranging from 20 to 300 at 15-25% w/w solids. Copolymer morphologies are initially assigned based on DLS and TEM

studies and subsequently confirmed by SAXS analysis. *In particular, this PISA formulation provides the first example of highly transparent block copolymer vesicles owing to the close match between the refractive indices of PTFEMA and n-dodecane at 20 °C.* Moreover, the variation in refractive index with temperature enables minimization of the turbidity of PSMA$_9$-PTFEMA$_x$ nanoparticle dispersions at elevated temperature in either *n*-tetradecane or *n*-hexadecane. Such formulations enable *in situ* visible absorption spectroscopy studies to be performed during the RAFT dispersion polymerization of TFEMA when using a dithiobenzoate RAFT agent to target PSMA$_{16}$-PTFEMA$_{86}$ spheres at 15% w/w solids in *n*-hexadecane at 90 °C.

3.2. Experimental Section

3.2.1. Materials

Stearyl methacrylate (SMA) was purchased from Santa Cruz Biotechnology, Inc. (USA) and was used as received. 2,2,2-Trifluoroethyl methacrylate (TFEMA) was purchased from Fluorochem Ltd. (UK) and was used without further purification. 2-Cyano-2-propyl dithiobenzoate (CPDB), CDCl$_3$, *n*-dodecane, *n*-hexadecane and *n*-tetradecane were purchased from Merck (UK). 2,2′-Azobisisobutyronitrile (AIBN) was obtained from Molekula (UK) and *tert*-butyl peroxy-2-ethylhexanoate (T21s) was purchased from AkzoNobel (The Netherlands). CD$_2$Cl$_2$ was purchased from Goss Scientific (UK). Tetrahydrofuran and *n*-heptane were obtained from VWR Chemicals (UK). Ethanol and toluene were purchased from Fisher Scientific (UK).

3.2.2. Methods

Synthesis of poly(stearyl methacrylate) (PSMA) stabilizer blocks *via* RAFT solution polymerization in toluene

PSMA$_9$ and PSMA$_{16}$ stabilizer blocks were prepared by following a recently reported synthesis protocol.[11] The synthesis of PSMA$_9$ was conducted as follows. SMA (30.0 g; 88.6 mmol), CPDB (3.92 g; 17.7 mmol; target DP = 5.0), AIBN (582 mg; 3.55 mmol; CPDB/AIBN molar ratio = 5.0) and toluene (34.5 g) were weighed into a 250 mL round-bottomed flask. The sealed reaction vessel was purged with nitrogen for 30 min and placed in a preheated oil bath at 70 °*C*

with stirring for 4 h. The ensuing SMA polymerization was then quenched by exposing the reaction solution to air and cooling to room temperature. A final SMA conversion of 78% was determined by ^{1}H NMR spectroscopy. In order to remove residual monomer, the crude polymer was purified by three consecutive precipitations into a ten-fold excess of ethanol. The mean DP of the stabilizer block was calculated to be 9 using ^{1}H NMR analysis by comparing the aromatic protons of the dithiobenzoate end-group at 6.8-8.0 ppm to the two oxymethylene protons of PSMA at 3.6-4.0 ppm. THF GPC analysis of PSMA$_9$ using a UV detector (set at λ = 260 nm) and a series of near-monodisperse polystyrene standards indicated an M_n of 2 700 g mol^{-1} and an M_w/M_n of 1.22. GPC analysis of PSMA$_{16}$ gave M_n = 5 500 g mol^{-1} and M_w/M_n = 1.16.

Synthesis of poly(stearyl methacrylate)-poly(2,2,2-trifluoroethyl methacrylate) (PSMA-PTFEMA) diblock copolymer nanoparticles *via* RAFT dispersion polymerization of TFEMA in *n*-dodecane

A typical example is the PISA synthesis of PSMA$_9$-PTFEMA$_{294}$ diblock copolymer vesicles at 25% w/w solids, which was conducted as follows. PSMA$_9$ macro-CTA (0.05 g; 15.30 µmol), T21s initiator (1.10 mg; 5.06 µmol; 10.0% v/v in *n*-dodecane) and *n*-dodecane (2.47 g) were weighed into a sample vial and purged with nitrogen for 30 min. TFEMA monomer (0.65 mL; 4.59 mmol; target DP = 300) was degassed separately, then added to the reaction mixture *via* syringe. The vial was immersed in a preheated oil bath at 90 *°C* and the reaction mixture was magnetically stirred for 17 h. ^{19}F NMR analysis indicated 98% TFEMA monomer conversion by comparing the integrated monomer triplet signal at –74.0 ppm to the integrated polymer signal at –73.5 ppm (see **Figure 3.1**). THF GPC analysis indicated an M_n of 26 500 g mol^{-1} and an M_w/M_n of 1.31. PSMA$_9$-PTFEMA$_{294}$ diblock copolymer vesicles were also prepared at 25% w/w solids following the same protocol using either *n*-tetradecane or *n*-hexadecane instead of *n*-dodecane. To construct a pseudo-phase diagram for PSMA$_9$-PTFEMA$_x$ nano-objects prepared in *n*-dodecane, a range of diblock copolymer compositions were targeted between 15% and 25% w/w solids by adjusting the total volume of the dispersion to 2.0 mL and varying the TFEMA/PSMA$_9$ molar ratio accordingly.

NMR Spectroscopy

^{1}H NMR spectra were recorded in either CD$_2$Cl$_2$ or CDCl$_3$ using a 400 MHz Bruker Avance spectrometer. Typically, 64 scans were averaged per spectrum. ^{19}F NMR spectra were recorded

in either CD_2Cl_2 or $CDCl_3$ using a 400 MHz Bruker Avance spectrometer. Typically, 16 scans were averaged per spectrum.
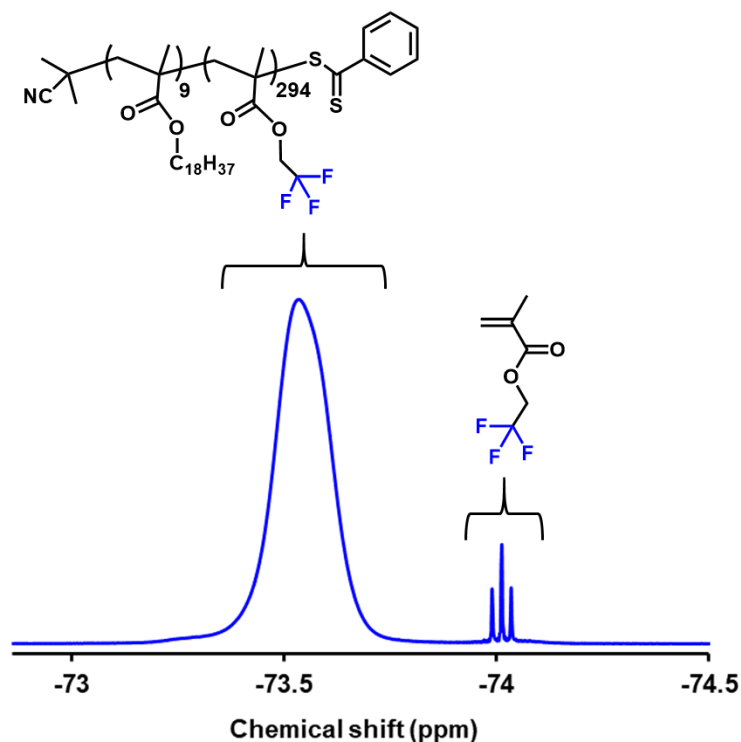
Figure 3.1. Assigned ^{19}F NMR spectrum recorded in $CDCl_3$ for the $PSMA_9$-$PTFEMA_{294}$ diblock copolymer vesicles prepared *via* RAFT dispersion polymerization of TFEMA at 25% w/w solids in *n*-dodecane at 90 °C. In this case, the target diblock copolymer composition was $PSMA_9$-$PTFEMA_{300}$, and the final TFEMA monomer conversion was 98%.

Gel Permeation Chromatography (GPC)

Molecular weight distributions (MWDs) were assessed by GPC using THF eluent. The THF GPC system was equipped with two 5 μm (30 cm) Mixed C columns and a WellChrom K-2301 refractive index detector operating at 950 ± 30 nm. The THF mobile phase contained 2.0% v/v triethylamine and 0.05% w/v butylhydroxytoluene (BHT) and the flow rate was fixed at 1.0 ml min^{-1}. A series of nine near-monodisperse polystyrene standards (M_p values ranging from 580 to 550,100 g mol^{-1}) were used for column calibration in combination with a UV detector operating at a fixed wavelength of 260 nm.

Dynamic Light Scattering (DLS)

DLS studies were performed using a Zetasizer Nano ZS instrument (Malvern Instruments, UK) at a fixed scattering angle of 173°. Copolymer dispersions were diluted in *n*-heptane (0.10% w/w) prior to light scattering studies at 25 °C. The intensity-average diameter and polydispersity of the diblock copolymer nanoparticles were calculated by cumulants analysis of the experimental correlation function using Dispersion Technology Software version 6.20. Data were averaged over ten runs each of thirty seconds duration. It is emphasized that DLS assumes a spherical morphology. Thus, the DLS diameter determined for highly anisotropic particles such as worms is a 'sphere-equivalent' value that is neither equal to the worm length nor the worm width.

Transmission Electron Microscopy (TEM)

TEM studies were conducted using a Philips CM 100 instrument operating at 100 kV and equipped with a Gatan 1k CCD camera. A single droplet of a 0.10% w/w diblock copolymer dispersion was placed onto a carbon-coated copper grid using a pipet and allowed to dry, prior to exposure to ruthenium(VIII) oxide vapor for 7 min at 20 °C.[12] This heavy metal compound acted as a positive stain for the core-forming PTFEMA block to improve contrast. The ruthenium(VIII) oxide was prepared as follows: ruthenium(IV) oxide (0.30 g) was added to water (50 g) to form a black slurry; addition of sodium periodate (2.0 g) with continuous stirring produced a yellow solution of ruthenium(VIII) oxide within 1 min at 20 °C.

Small-Angle X-ray Scattering (SAXS)

SAXS patterns were collected at a synchrotron source (Diamond Light Source, station I22, Didcot, UK; experiment number SM19852) using monochromatic X-ray radiation (wavelength $\lambda = 0.100$ nm, with q ranging from 0.015 to 1.8 nm^{-1}, where $q = 4\pi \sin \theta/\lambda$ is the length of the scattering vector and θ is one-half of the scattering angle) and a 2D Pilatus 2M pixel detector (Dectris, Switzerland). A glass capillary of 2 mm diameter was used as a sample holder. Scattering data were reduced using standard routines from the beamline[13] and were further analyzed using Irena SAS macros for Igor Pro.[14]

UV-visible spectroscopy studies of vesicle dispersions

The transmittance of vesicle dispersions prepared at 25% w/w solids in various *n*-alkanes was studied using a PC-controlled UV-1800 spectrophotometer equipped with a 10 mm pathlength quartz cell. Spectra were recorded between 200 and 800 nm from 20 °C to 90 °C by increasing the temperature at 10 °C intervals. The transmittance was determined at $\lambda = 600$ nm and corrected by the pure solvent transmittance at each temperature determined prior to analysis of the vesicle dispersions. This wavelength was chosen to avoid the absorption bands associated with the dithiobenzoate chain-ends at approximately 300 nm and 507 nm.

***In situ* UV-visible spectroscopy studies of the synthesis of PSMA$_{16}$-PTFEMA$_{90}$ spheres in *n*-hexadecane**

This experiment was conducted using an Agilent Cary 60 spectrometer equipped with a Hellma all-quartz UV-visible immersion probe, 1.8 m fiber optic cables and SMA 905 connectors. This probe has a wavelength range of 190 to 1100 nm, can operate between 5 °C and 150 °C and has a 10 mm pathlength. The baseline for pure *n*-hexadecane was recorded at 90 °C prior to the *in situ* experiment. During the PISA synthesis conducted at 90 °C, spectra were recorded between 200 and 800 nm at a spectral resolution of $\pm$ 3 nm using a scan rate of 1800 nm min^{-1} at 1 min intervals for the first 20 min of the polymerization, then at 2 min intervals for the remaining 880 min. In a final experiment, the spectral resolution was adjusted to $\pm$ 1 nm.
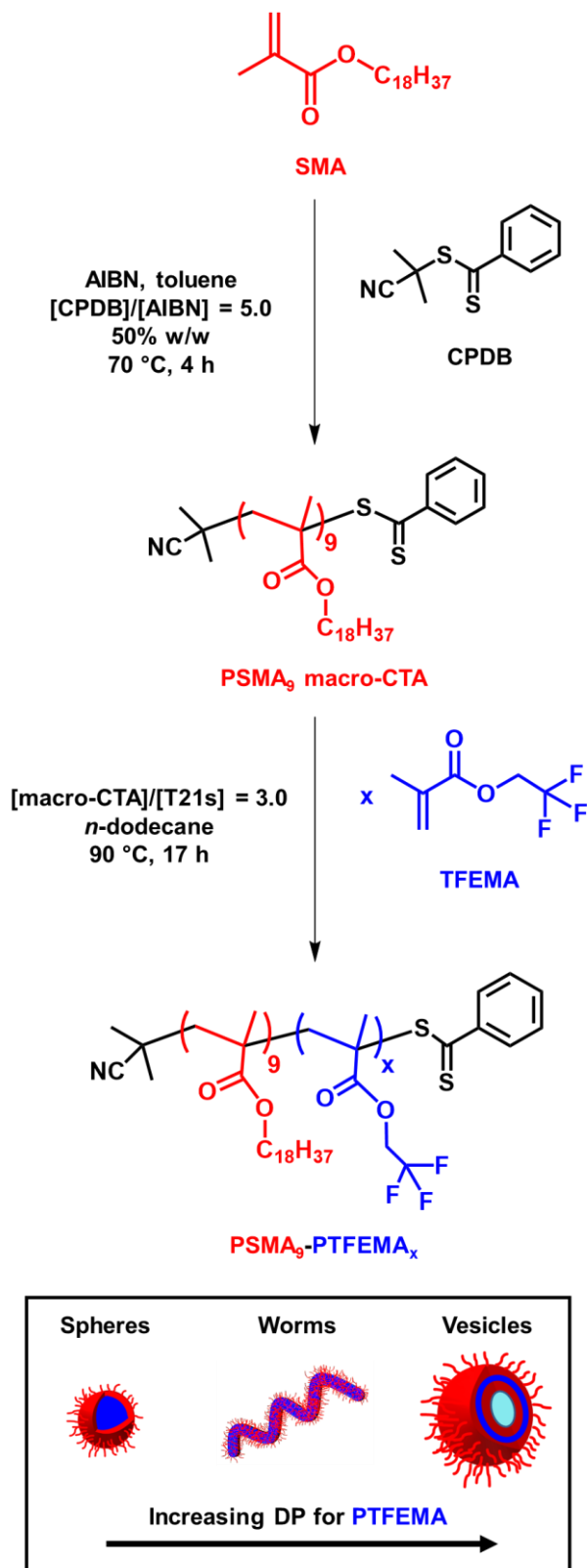
Scheme 3.1. Synthesis of poly(stearyl methacrylate) (PSMA$_9$) macro-CTA *via* RAFT solution polymerization in toluene using 2-cyano-2-propyl benzodithioate (CPDB) at 70 °C, followed by the RAFT dispersion polymerization of 2,2,2-trifluoroethyl methacrylate (TFEMA) in *n*-dodecane at 90 °C.

3.3. Results and Discussion

3.3.1. Synthesis of PSMA stabilizer precursors

Two PSMA precursors with mean DPs of either 9 (target DP = 5) or 16 (target DP = 20) were synthesized *via* RAFT solution polymerization of SMA in toluene at 70 °C using a CPDB RAFT agent, as shown in **Scheme 3.1**. To preserve the dithiobenzoate end-groups (*i.e.*, avoid monomer-starved conditions), the polymerization was quenched after 4 h in the case of PSMA$_9$ and after 5 h for PSMA$_{16}$.[15] ^{1}H NMR spectroscopy studies indicated SMA conversions of 78% (PSMA$_9$) and 60% (PSMA$_{16}$). Relatively good RAFT control ($M_w/M_n \leq 1.22$) was confirmed by THF GPC analysis in both cases.

3.3.2. Kinetic studies of the RAFT dispersion polymerization of TFEMA in *n*-dodecane

Kinetic data was obtained for the RAFT dispersion polymerization of TFEMA at 90 °C when targeting PSMA$_9$-PTFEMA$_{200}$ vesicles at 20% w/w solids in *n*-dodecane. The reaction mixture was periodically sampled and each aliquot was diluted with CD$_2$Cl$_2$ prior to ^{19}F NMR spectroscopy analysis, which enabled excellent discrimination between the TFEMA monomer and PTFEMA signals. The corresponding semilogarithmic plot indicates three distinct linear regimes (see **Figure 3.2a**). Cornel *et al.* reported similar observations for the synthesis of PSMA$_{12}$-PTFEMA$_{98}$ spheres in *n*-tetradecane.[7] The initial solution polymerization proceeds relatively slowly, then an approximate two-fold rate enhancement is observed after 1.5 h. This marks the onset of micellar nucleation for this PISA formulation[7,16–18] at approximately 22% TFEMA conversion, for which the theoretical PTFEMA DP is calculated to be around 45. A subsequent four-fold rate enhancement occurs after 2 h, which corresponds to ~34% TFEMA conversion and a PTFEMA DP of approximately 67. First-order kinetics were observed thereafter up to 93% TFEMA conversion, whereupon a slower rate of polymerization occurs under monomer-starved conditions. More than 95% TFEMA conversion was achieved within 5 h at 90 °C. THF GPC analysis indicates a linear evolution of M_n with conversion (see **Figure 3.2b**) and relatively low dispersities throughout the polymerization ($M_w/M_n \leq 1.23$), which is consistent with the pseudo-living character expected for a RAFT polymerization.[19–21]
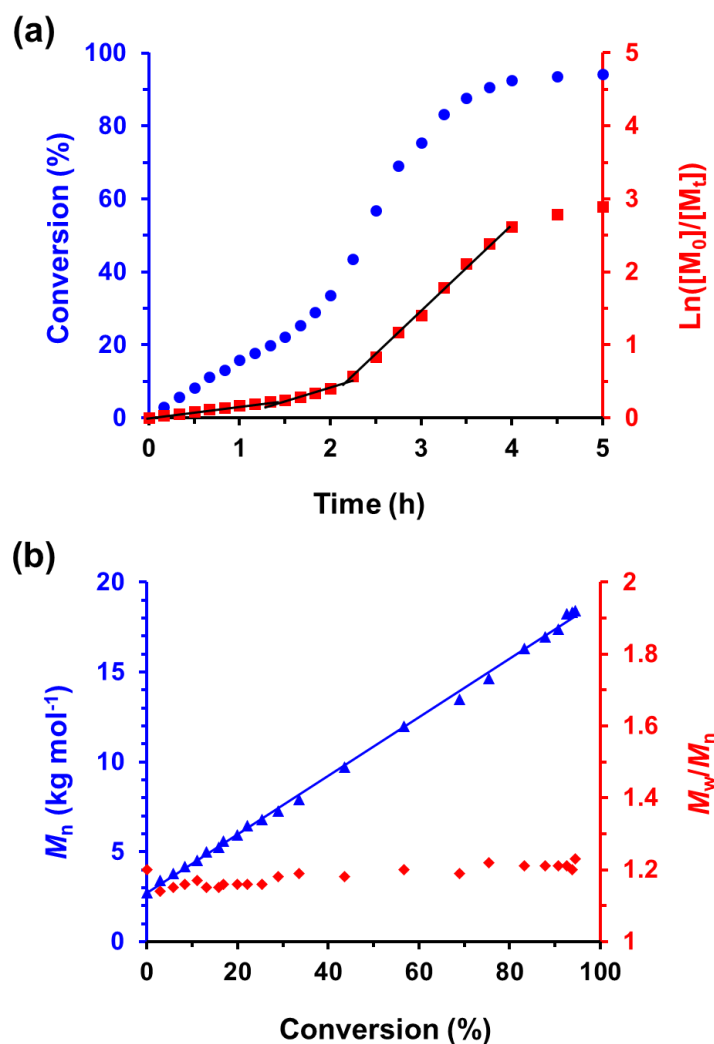
Figure 3.2. (a) Conversion *vs.* time curve (blue circles) and the corresponding $\ln([M_0]/[M_t])$ *vs.* time plot (red squares) for the RAFT dispersion polymerization of TFEMA at 90 °C targeting PSMA$_9$-PTFEMA$_{200}$ diblock copolymer vesicles at 20% w/w solids in *n*-dodecane. **(b)** Evolution of M_n (blue triangles, *vs.* polystyrene calibration standards) and M_w/M_n (red diamonds) with TFEMA monomer conversion for this PISA formulation.

3.3.3. RAFT dispersion polymerization of TFEMA in *n*-dodecane

As we have shown in **Chapter 2**, using a relatively short PSMA$_9$ stabilizer block provides access to the full range of copolymer morphologies (*i.e.*, spheres, worms or vesicles) for PSMA-PHPMA. Herein the RAFT dispersion polymerization of TFEMA was examined using such PSMA$_9$ precursor in *n*-dodecane at 90 °C.

Semsarilar *et al.* reported that GPC analysis of PTFEMA-based diblock copolymers can be problematic because of the relatively low refractive index of PTFEMA (1.418) compared to

that of most other methacrylates (1.491-1.596).[1] This means that a GPC refractive index detector tends to underestimate the signal arising from the semi-fluorinated PTFEMA block relative to the other (non-fluorinated) block. This typically produces a bimodal molecular weight distribution, which at first sight suggests significant contamination of the diblock copolymer by the non-fluorinated macro-CTA.[1] However, this is simply an experimental artefact owing to the mismatched refractive indices: the true level of macro-CTA contamination is significantly lower. Fortunately, the dithiobenzoate-capped diblock copolymer chains formed in the present study enables a UV detector to be used for GPC analysis. Chromatograms for four $PSMA_9\text{-}PTFEMA_{38\text{-}291}$ diblock copolymers prepared at 20% w/w solids recorded using a UV detector at a fixed wavelength of 260 nm are shown in **Figure 3.3a**, along with the corresponding chromatogram recorded for the $PSMA_9$ precursor. The latter has a relatively low dispersity ($M_w/M_n = 1.22$), and oligomers are partially resolved at longer retention times. Each of the four diblock copolymers exhibits a unimodal and reasonably narrow molecular weight distribution ($M_w/M_n \leq 1.31$). In contrast, GPC analysis of the $PSMA_9$-$PTFEMA_{291}$ diblock copolymer using a refractive index detector indicated a somewhat broader molecular weight distribution ($M_w/M_n = 1.49$) owing to the appearance of a low molecular weight shoulder, which is assigned to the (exaggerated) presence of the contaminating $PSMA_9$ precursor (see **Figure 3.4**). On the basis of these preliminary findings, UV GPC was preferred for the analysis of the $PSMA_9$-$PTFEMA_x$ diblock copolymers reported in this study.
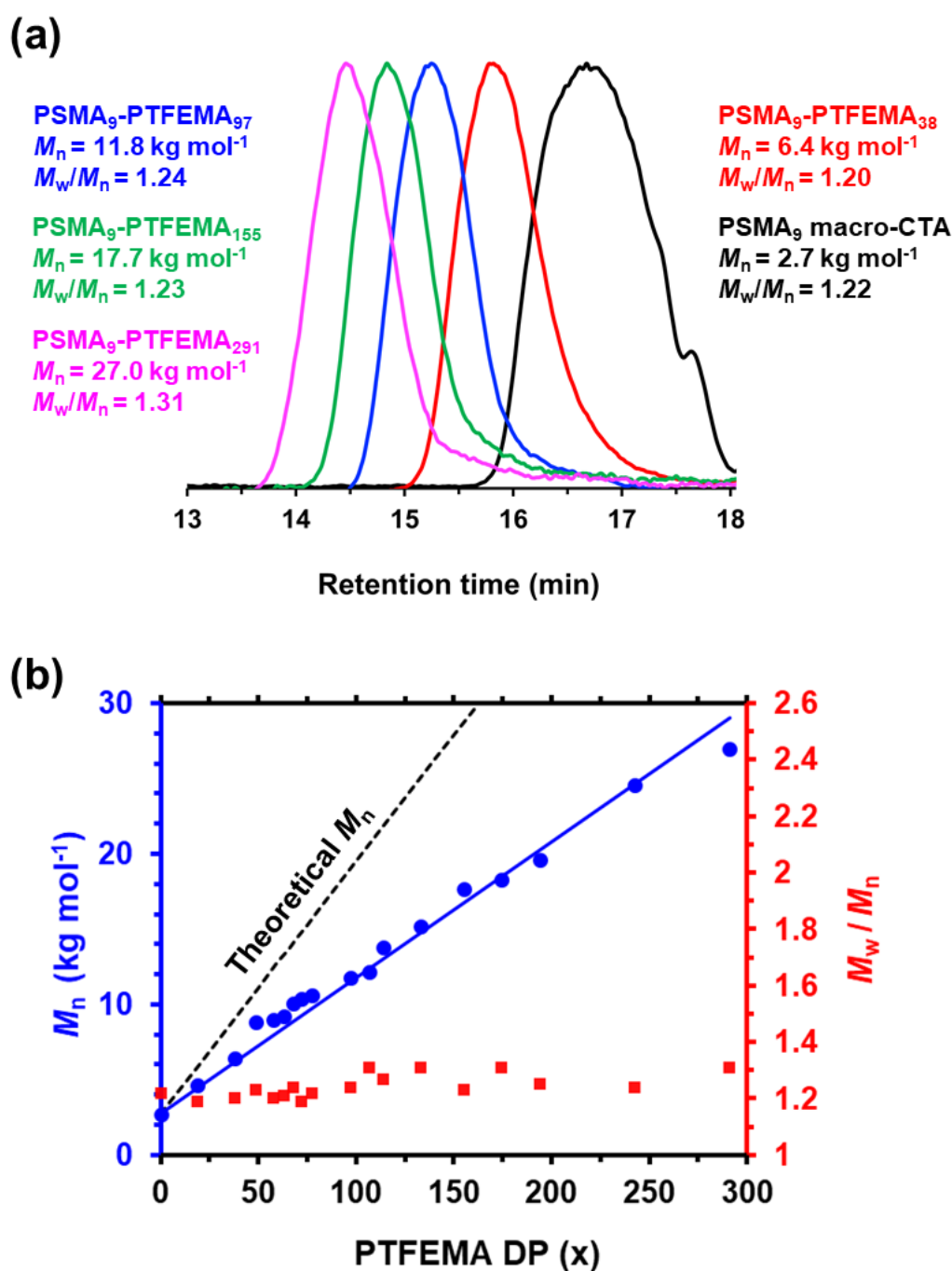
Figure 3.3. (a) Gel permeation chromatograms (*vs.* a series of near-monodisperse polystyrene calibration standards using a UV detector set at 260 nm) obtained for the PSMA$_9$ precursor (prepared in toluene at 50% w/w solids at 70 °C) and a series of four PSMA$_9$-PTFEMA$_x$ diblock copolymers prepared by RAFT dispersion polymerization of TFEMA at 90 °C at 20% w/w solids, where the mean DP of the core-forming block was 38, 97, 155 or 291, respectively. **(b)** Correlation between GPC M_n (blue circles, *vs.* polystyrene calibration standards) and actual PTFEMA DP (as determined by ^{19}F NMR) for a larger series of PSMA$_9$-PTFEMA$_x$ diblock copolymers at 20% w/w solids. The corresponding GPC M_w/M_n (red squares) are also shown.
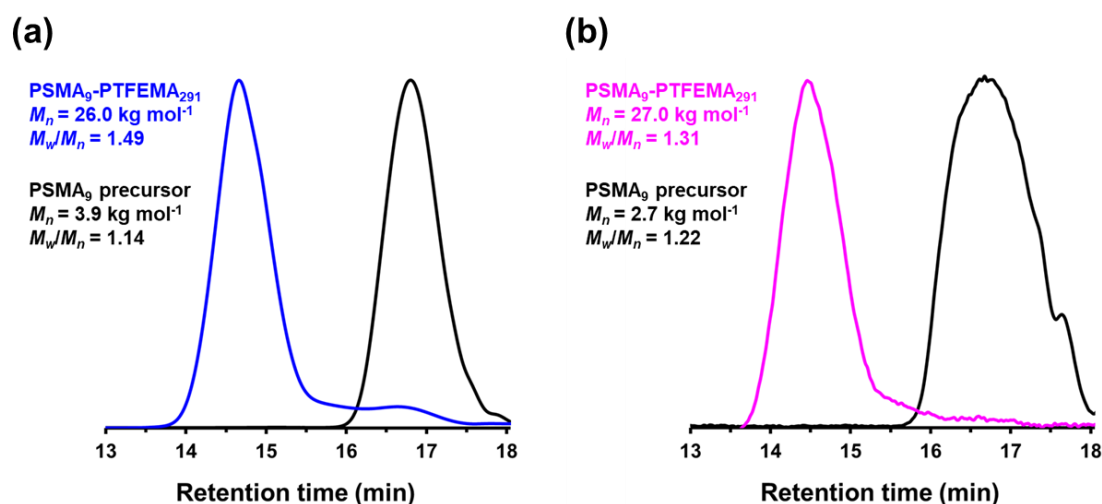
Figure 3.4. THF GPC curves recorded for the PSMA$_9$-PTFEMA$_{291}$ diblock copolymer vesicles prepared at 20% w/w solids and the corresponding PSMA$_9$ macro-CTA using **(a)** a refractive index detector *vs.* poly(methyl methacrylate) standards and **(b)** a UV detector calibrated at a fixed wavelength of 260 nm against polystyrene standards.

UV GPC data obtained for a series of PSMA$_9$-PTFEMA$_x$ nanoparticles prepared at 20% w/w solids are shown in **Figure 3.3b.** There is a linear correlation between the GPC M_n data and the actual PTFEMA DP (after correcting for the TFEMA conversion) when the latter is systematically varied from 19 to 291. Reasonably narrow molecular weight distributions ($M_w/M_n \leq$ 1.31) were obtained for mean PTFEMA DPs up to 291. This is comparable to GPC data reported by Derry *et al*. and Docherty *et al*. for similar RAFT dispersion polymerization formulations conducted in mineral oil.[11,15,17,18] The broader molecular weight distributions that are observed when targeting higher DPs are most likely the result of chain transfer to polymer.[22] The pendent methylene group in the TFEMA repeat units is expected to be particularly susceptible to this side reaction owing to the highly electronegative nature of the three neighbouring fluorine atoms.

A pseudo-phase diagram was constructed to aid the reproducible targeting of pure spheres, worms and vesicles in *n*-dodecane (see **Figure 3.5**). A series of PSMA$_9$-PTFEMA$_x$ copolymers was produced by varying the target DP for PTFEMA between 20 and 300 for formulations conducted at 15%, 20% or 25% w/w solids, respectively (see **Tables 9.3 and 9.4**).
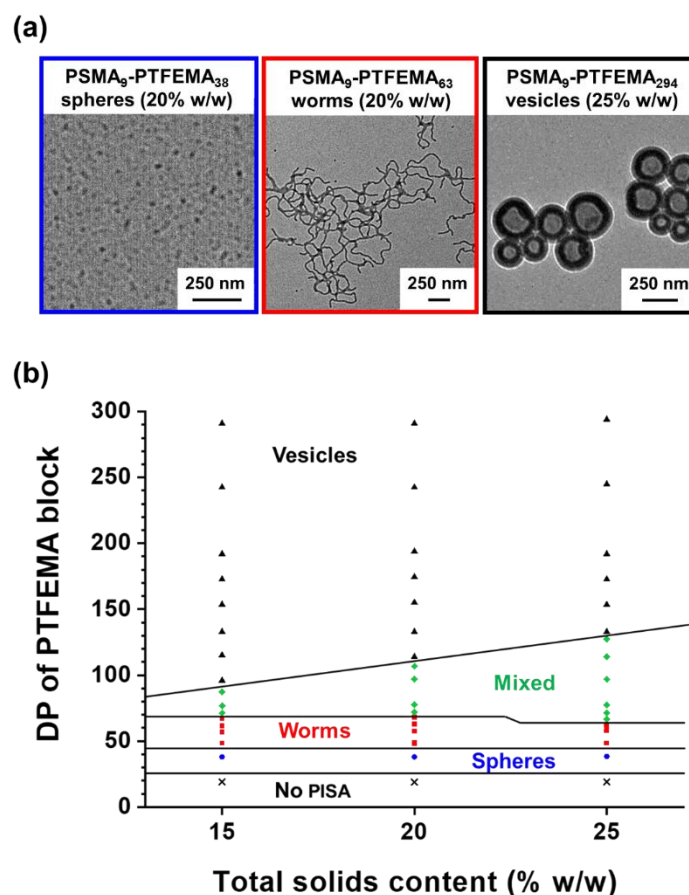
Figure 3.5. **(a)** Representative TEM images obtained for $PSMA_9$-$PTFEMA_{38}$ spheres, $PSMA_9$-$PTFEMA_{63}$ worms and $PSMA_9$-$PTFEMA_{294}$ vesicles prepared at 20%, 20% and 25% w/w solids, respectively. **(b)** Pseudo-phase diagram constructed for $PSMA_9$-$PTFEMA_x$ diblock copolymer nano-objects prepared by RAFT dispersion polymerization of TFEMA in *n*-dodecane using a $PSMA_9$ macro-CTA and T21s initiator at 90 °C ([$PSMA_9$]/[T21s] molar ratio = 3.0). Green diamonds correspond to a mixed phase comprising worms and vesicles (plus a minor population of spheres in some cases).

$PSMA_9$-$PTFEMA_{38}$ spheres could be produced at all copolymer concentrations examined, with z-average diameters of 18-21 nm (DLS polydispersity (or PDI) ≤ 0.33) as judged by DLS. Unlike $PSMA_9$-$PHPMA_x$ formulations previously examined in mineral oil (see **Chapter 2**), a relatively broad worm phase was observed with well-defined worms being obtained at copolymer concentration as low as 15% w/w. A digital photograph recorded for $PSMA_9$-$PTFEMA_{63}$ worms prepared at 20% w/w solids confirms the relatively high transparency of such free-standing gels (see **Figure 3.6**). However, similar findings have been reported for many other PISA formulations in various solvents because the mean worm width is usually so small that such nano-objects do not scatter light particularly strongly.[11,23–27] In contrast, the formation of vesicles invariably leads to highly turbid dispersions, regardless of whether such

dispersions are prepared directly *via* PISA or indirectly *via* post-polymerization processing.[11,23,25,28–33] Indeed, we are not aware of any literature reports of the synthesis of highly transparent vesicle dispersions. However, all PSMA$_9$-PTFEMA$_x$ vesicles obtained at up to 25% w/w solids in *n*-dodecane by targeting a PTFEMA DP (x) of 140 to 300 proved to be highly transparent at 20 °C.
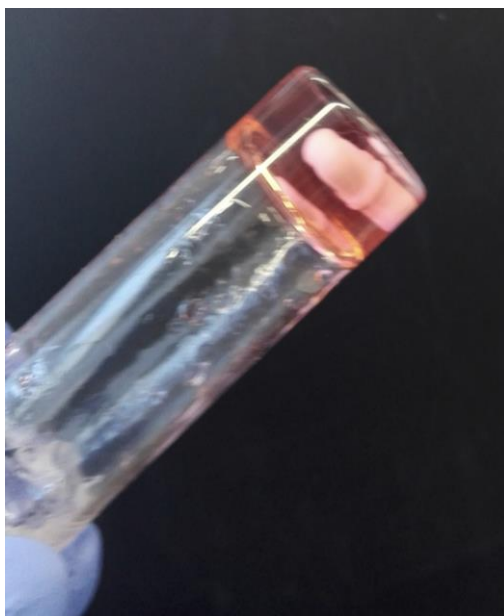
Figure 3.6. Digital photograph recorded for a 20% w/w dispersion of PSMA$_9$-PTFEMA$_{63}$ worms prepared *via* RAFT dispersion polymerization of TFEMA in *n*-dodecane at 90 °C. A highly transparent, free-standing gel is obtained for this PISA formulation.

Transmittance *vs*. wavelength plots recorded at 25 °C for 0.50% w/w dispersions of PSMA$_9$-PTFEMA$_{294}$ vesicles (DLS diameter = 237 nm, PDI = 0.10) and PSMA$_9$-PHPMA$_{294}$ vesicles (DLS diameter = 175 nm, PDI = 0.03) are compared in **Figure 3.7**. In both cases, the vesicles were originally prepared at 25% w/w in *n*-dodecane and subsequently diluted to 0.50% w/w using the same solvent. The PSMA$_9$-PHPMA$_{294}$ vesicles form a *relatively turbid* dispersion (e.g., 31% transmittance at $\lambda = 600$ nm) owing to the refractive index difference between the PHPMA block (~1.51 at 20 °C) and *n*-dodecane (1.421 at 20 °C), which leads to light scattering. In contrast, the *larger* PSMA$_9$-PTFEMA$_{294}$ vesicles form a *highly transparent* dispersion (e.g., more than 99% transmittance at $\lambda = 600$ nm) because the PTFEMA block (refractive index = 1.418 at 20 °C) is almost perfectly isorefractive with the same solvent at 20-25 °C.
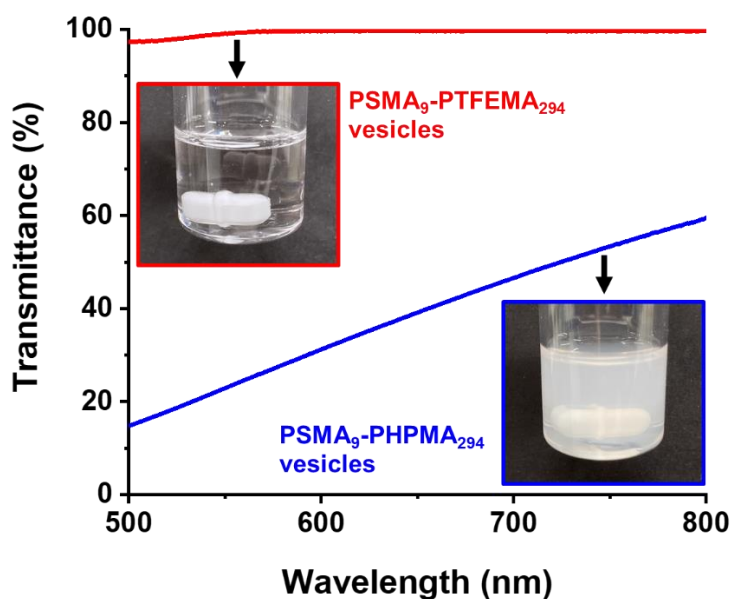
Figure 3.7. Transmittance *vs.* wavelength plots recorded at 25 °C for 0.50% w/w dispersions of PSMA$_9$-PTFEMA$_{294}$ (red data) and PSMA$_9$-PHPMA$_{294}$ (blue data) vesicles in *n*-dodecane, respectively. These vesicles were originally prepared at 25% w/w in *n*-dodecane by RAFT dispersion polymerization of either TFEMA or HPMA, respectively. Insets: digital photographs recorded for the 0.50% w/w dispersions at 25 °C to illustrate their differing turbidity.

Small-angle X-ray scattering (SAXS) patterns were recorded for 1.0% w/w dispersions of selected PSMA$_9$-PTFEMA$_x$ nano-objects originally synthesized at 20% w/w in *n*-dodecane (see **Figure 3.8**).
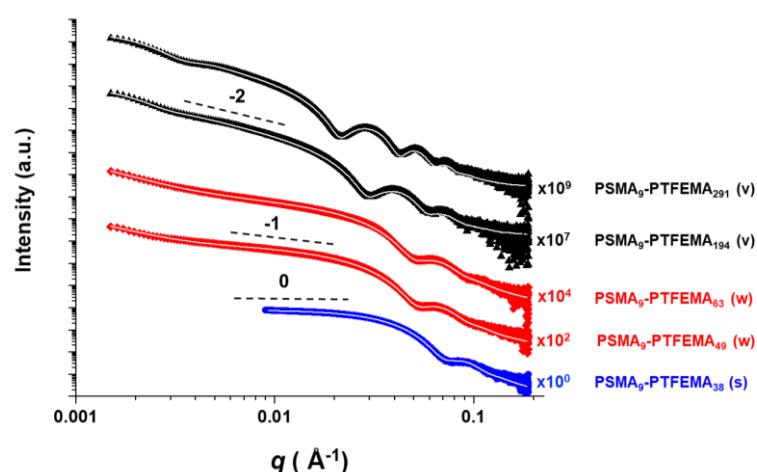
Figure 3.8. Small-angle X-ray scattering (SAXS) patterns and corresponding data fits (white lines) for 1.0% w/w dispersions of PSMA$_9$-PTFEMA$_x$ spheres, worms and vesicles in *n*-dodecane at 20 °C. These nano-objects were initially synthesized at 20% w/w solids. Black dashed lines indicate gradients of 0, –1 and –2 for guidance to the eye.

SAXS offers important advantages over TEM and DLS. Data are averaged over millions of nanoparticles in their native dispersed state, unlike the hundreds of dried nano-objects typically analyzed by TEM. Moreover, SAXS enables much more rigorous analysis of highly anisotropic nano-objects such as worms than DLS, not least because the latter technique assumes a spherical morphology. Similarly, SAXS provides additional structural information for vesicles such as the mean membrane thickness. As shown in **Chapter 2**, SAXS analysis can be used to corroborate the pseudo-phase diagram shown in **Figure 3.5b**, for which morphology assignments were based on TEM studies. Indeed, preliminary inspection of the low q region of the SAXS patterns recorded for each dispersion indicated the same morphology as that suggested by TEM. More specifically, gradients of approximately 0, –1 and –2 were observed for spheres, worms and vesicles, respectively (see **Figure 3.8**).

These initial observations were further validated by obtaining satisfactory fits to these SAXS patterns when using established spherical micelle,[34] worm-like micelle[34] or vesicle[35] models. These data fits also provided volume-average nanoparticle dimensions and the mean number of copolymer chains per nano-object, otherwise known as the aggregation number (N_{agg}), as summarized in **Table 3.1**. For example, PSMA$_9$-PTEMA$_{38}$ spheres have an overall diameter (D_{sphere}) of 14.6 ± 1.7 nm, with an N_{agg} of 110. For PSMA$_9$-PTFEMA$_{49}$ and PSMA$_9$-PTFEMA$_{63}$ worms, the overall worm thicknesses (T_{worm}) were 15.8 ± 2.0 nm and 16.4 ± 2.1 nm, respectively, with slightly thicker worms being formed as the PTFEMA DP (x) was increased, as expected. Moreover, the mean worm contour lengths (L_{worm}) were comparable (905 nm *vs.* 1040 nm respectively) and similar N_{agg} values (13,700 *vs.* 13,400) were obtained. Similarly, the vesicle membrane thickness ($T_{membrane}$) increased from 20.6 ± 4.4 nm to 28.8 ± 4.4 nm on increasing x from 194 to 291, but the overall vesicle diameter ($D_{vesicle}$) remained relatively constant (195 ± 66 nm and 190 ± 48 nm, respectively). This apparent 'inward growth' of vesicles on increasing the membrane-forming block DP[15,36] is consistent with our observations for PSMA-PHPMA vesicles in **Chapter 2**. Interestingly, N_{agg} was reduced by ~19% from 50,700 to 41,100 on increasing x from 200 to 300, which suggests that copolymer chain rearrangement/reorganization may well occur during the vesicle growth phase for this PISA formulation.[36]

Table 3.1. Summary of structural parameters obtained from fitting small-angle X-ray scattering patterns recorded for a series of PSMA$_9$-PTFEMA$_x$ nano-objects using either a spherical micelle,[34] worm-like micelle[34], or vesicle model.[35] D_{sphere} is the overall sphere diameter such that $D_{sphere} = 2R_s + 4R_g$, where R_s is the mean core radius and R_g is the radius of gyration of the stabilizer chains. T_{worm} is the overall worm thickness ($T_{worm} = 2R_{wc} + 4R_g$, where R_{wc} is the mean worm core radius) and L_{worm} is the mean worm contour length. $D_{vesicle}$ is the overall vesicle diameter ($D_{vesicle} = 2R_m + T_{membrane} + 4R_g$, where R_m is the distance from the center of the vesicle to the center of the vesicle membrane, and $T_{membrane}$ is the vesicle membrane thickness). N_{agg} is the mean aggregation number (*i.e.*, the mean number of copolymer chains per nano-object).

Block copolymer	Nanoparticle Morphology	D_{sphere} (nm)	T_{worm} (nm)	L_{worm} (nm)	$D_{vesicle}$ (nm)	$T_{membrane}$ (nm)	N_{agg}
PSMA$_9$-PTFEMA$_{38}$	Spheres	14.6 ± 1.7	-	-	-	-	110
PSMA$_9$-PTFEMA$_{49}$	Worms	-	15.8 ± 2.0	905	-	-	13,700
PSMA$_9$-PTFEMA$_{63}$	Worms	-	16.4 ± 2.1	1040	-	-	13,400
PSMA$_9$-PTFEMA$_{194}$	Vesicles	-	-	-	195 ± 66	20.6 ± 4.4	50,700
PSMA$_9$-PTFEMA$_{291}$	Vesicles	-	-	-	190 ± 48	28.8 ± 4.4	41,100

3.3.4. Transmittance of PSMA$_9$-PTFEMA$_{294}$ diblock copolymer vesicles synthesized at 25% w/w solids in various *n*-alkanes

Cornel *et al*. reported the synthesis of highly transparent PSMA$_{12}$-PTFEMA$_{98}$ spherical nanoparticles *via* RAFT dispersion polymerization of TFEMA in *n*-tetradecane at 70 °C. The minimal turbidity of this PISA formulation enabled the kinetics of the TFEMA polymerization to be monitored *in situ* using visible absorption spectroscopy.[7] Subsequently, they demonstrated that selecting *n*-dodecane rather than *n*-tetradecane enabled high transmittance to be achieved for PSMA$_{32}$-PTFEMA$_{490}$ spheres at 30 °C owing to the differing temperature dependence of the refractive index for the former solvent compared to that of the PTFEMA core-forming block.[7] Herein we extend this approach to present *various examples of highly transparent vesicles*. Block copolymer vesicles are invariably obtained as highly turbid dispersions[11,23,25,28,29,31] because their relatively large particle size scatters visible light much more strongly than that of spherical nanoparticles. Since *n*-dodecane (1.421 at 20 °C), *n*-tetradecane (1.429 at 20 °C) and *n*-hexadecane (1.434 at 20 °C) have similar refractive indices to PTFEMA (1.418 at 20 °C) using such *n*-alkanes as solvents for the synthesis of PSMA$_9$-PTFEMA$_x$ vesicles enables such light scattering to be minimized. Accordingly, PSMA$_9$-

PTFEMA$_{294}$ vesicles were synthesized at 25% w/w solids in *n*-dodecane (DLS diameter = 237 nm, PDI = 0.10), *n*-tetradecane (DLS diameter = 209 nm, PDI = 0.06) and *n*-hexadecane (DLS diameter = 193 nm, PDI = 0.03), respectively. The transmittance (λ = 600 nm) of the resulting vesicle dispersions was determined at 10 °C intervals between 20 °C and 90 °C when using either *n*-dodecane (see **Figure 3.9**) or *n*-tetradecane. However, a slightly narrower temperature range was preferred for *n*-hexadecane owing to the relatively high melting point (18 °C) of this solvent. In principle, if the same PSMA$_9$-PTFEMA$_{294}$ vesicles are synthesized at a fixed copolymer concentration, the turbidity of the dispersion should simply depend on the refractive index difference obtained between the PTFEMA-core and the *n*-alkane at any given temperature. Hence the highest transmittance is observed at the temperature where these two refractive indices are (almost) identical.[7] In **Figure 3.10**, this isorefractive temperature was determined to be 20 °C for vesicles synthesized in *n*-dodecane and either 50 °C or 90 °C when they were prepared in *n*-tetradecane or *n*-hexadecane, respectively.
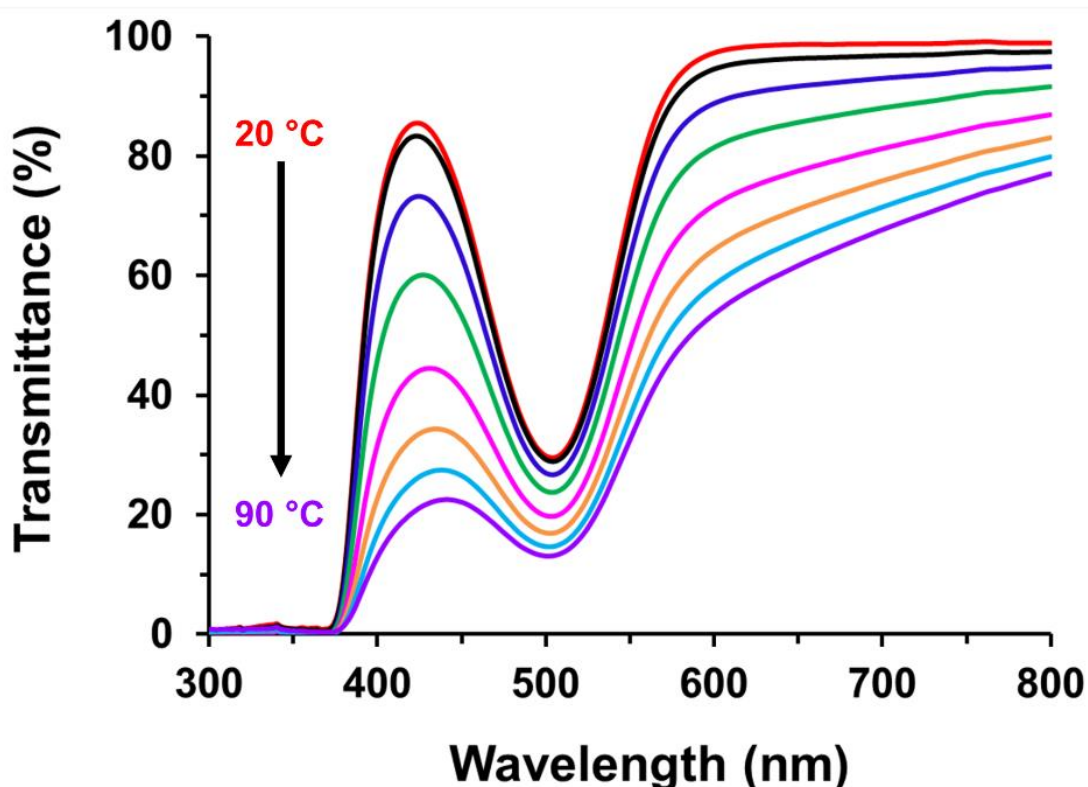
Figure 3.9. Transmittance *vs.* wavelength plots recorded between 20 and 90 °C for 25% w/w dispersions of PSMA$_9$-PTFEMA$_{294}$ vesicles in *n*-dodecane.

Figure 3.10. (a) Transmittance ($\lambda = 600$ nm) *vs*. temperature plots recorded for PSMA$_9$-PTFEMA$_{294}$ vesicles prepared by RAFT dispersion polymerization of TFEMA at 25% w/w solids in *n*-dodecane (blue circles), *n*-tetradecane (black squares) and *n*-hexadecane (red triangles), respectively. **(b)** Digital photographs recorded for these three 25 % w/w vesicle dispersions at 25 °C, 50 °C and 90 °C to illustrate their difference in visual appearance. The most transparent dispersions are obtained in *n*-dodecane (C$_{12}$H$_{26}$) at 20 °C, in *n*-tetradecane (C$_{14}$H$_{30}$) at 50 °C and in *n*-hexadecane (C$_{16}$H$_{34}$) at 90 °C, respectively. These observations informed our subsequent *in situ* visible absorption spectroscopy studies.

107

3.3.5. *In situ* visible absorption spectroscopy study during the synthesis of PSMA$_{16}$-PTFEMA$_{86}$ spherical nanoparticles in *n*-hexadecane

In order to record high-quality visible absorption spectra during the RAFT dispersion polymerization of TFEMA, three criteria must be fulfilled.[7] Firstly, nanoparticle scattering must be minimized (preferably eliminated) by obtaining an isorefractive dispersion at the reaction temperature.[7] For the current PISA formulation, this can be achieved by employing *n*-hexadecane as a solvent at 90 °C (see **Figure 3.10**) while targeting relatively small PSMA$_{16}$-PTFEMA$_{86}$ spherical nanoparticles (in this case, DLS studies indicate a z-average diameter of 26 nm and a PDI of 0.05). Ideally, the absorbance of the initial and final reaction mixture should remain below unity to ensure that the Beer–Lambert law remains valid. The former can be achieved by utilizing a longer stabilizer block (PSMA$_{16}$) to produce kinetically-trapped spheres while the latter requires the copolymer concentration to be reduced to 15% w/w solids. In principle, the kinetics of polymerization can be monitored by focusing on the relatively weak absorption band associated with the $n \rightarrow \pi^*$ transition for *dithiobenzoate* chain-ends at 515 nm in preference to the much stronger $\pi \rightarrow \pi^*$ transition that occurs at approximately 300 nm.[7] The final requirement is that the RAFT chain-ends must remain stable throughout the duration of the TFEMA polymerization.

Cornel *et al*. recorded high-quality visible absorption spectra during the synthesis of PSMA$_{12}$-PTFEMA$_{98}$ spheres at 30% w/w solids in *n*-tetradecane using a *trithiocarbonate*-based RAFT agent at $\lambda_{max} = 446$ nm.[7] In this case, the corresponding absorbance *vs*. time plot suggested that such chain-ends remained stable for at least 2 h under monomer-starved conditions (96% TFEMA conversion).[7] Thus the observed increase in absorbance could be directly related to the volumetric contraction of the reaction mixture that occurs on converting TFEMA monomer ($\rho = 1.18$ g cm^{-3}) into PTFEMA ($\rho = 1.47$ g cm^{-3}). This dilatometric effect enables the kinetics of the TFEMA polymerization to be monitored.[37] The question to be addressed in the present study is whether the same approach can be used to study the kinetics of TFEMA polymerization for a similar PISA formulation when using a *dithiobenzoate*-based RAFT agent.

An absorbance *vs*. time plot recorded during the synthesis of PSMA$_{16}$-PTFEMA$_{86}$ spheres at 15% w/w solids using 2-cyano-2-propyl dithiobenzoate (CPDB) at 90 °C in *n*-tetradecane is shown in **Figure 3.11a**. For comparison, kinetic data obtained for precisely the same PISA formulation using ^{19}F NMR spectroscopy are shown in **Figure 3.11b**.
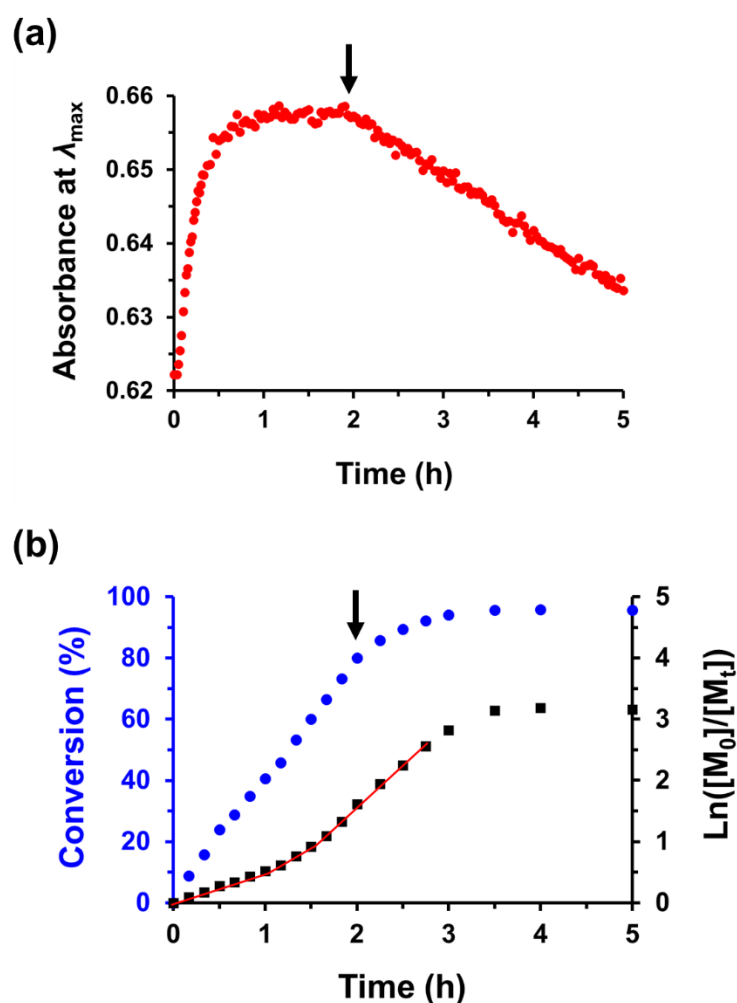
Figure 3.11. Synthesis of $PSMA_{16}$-$PTFEMA_{86}$ spherical nanoparticles at 15% w/w solids in *n*-hexadecane at 90 °C: **(a)** absorbance *vs.* time curve and **(b)** conversion *vs.* time curve (blue circles) and corresponding $ln([M_0]/[M_t])$ *vs.* time plot (black squares). These data confirm that the dithiobenzoate chain-ends do not remain stable on the timescale required for the TFEMA polymerization under such conditions. Instead, their gradual loss is observed within 2 h, which corresponds to a TFEMA conversion of only around 80%. Thus, the kinetics of polymerization for this particular PISA formulation cannot be monitored by visible absorption spectroscopy.

If it is assumed that the dithiobenzoate chain-ends remain stable for the duration of the TFEMA polymerization, then the absorbance *vs.* time data suggests that this reaction is complete within approximately 1 h. Moreover, a plateau region is observed at longer reaction times, which is similar to that reported by Cornel *et al.*[7] However, the ^{19}F NMR kinetic data indicate that only approximately 41% TFEMA conversion is achieved within the first 60 min. Indeed, 94% TFEMA conversion required a reaction time of around 3 h whereas a gradual reduction in absorbance is observed after 2 h, implying the premature loss of dithiobenzoate chain-ends. Finally, it is noteworthy that both experiments produced essentially the same copolymer chains

as judged by GPC (see **Table 3.2**) while the formation of relatively small spheres in both cases was confirmed by TEM and DLS analysis (see **Figure 3.12**).

Table 3.2. Summary of the GPC and DLS data obtained for $PSMA_{16}$-$PTFEMA_{86}$ spherical nanoparticles prepared at 15% w/w solids in *n*-hexadecane during the *in situ* visible absorption spectroscopy study and the kinetic experiments conducted using ^{19}F NMR spectroscopy.

	Target Composition	Solids content (% w/w)	M_n (kg mol^{-1})	M_w/M_n	DLS diameter (nm)	PDI
Precursor block	$PSMA_{16}$	-	5.5	1.16	-	-
In situ visible absorption spectroscopy	$PSMA_{16}$ – $PTFEMA_{86}$ spheres	15	17.7	1.13	26	0.05
Kinetics by ^{19}F NMR spectroscopy	$PSMA_{16}$ – $PTFEMA_{86}$ spheres	15	17.1	1.17	25	0.02
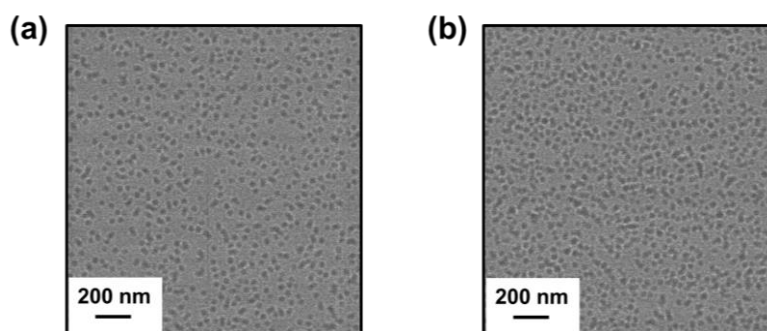
Figure 3.12. Representative TEM images recorded for $PSMA_{16}$−$PTFEMA_{86}$ spherical nanoparticles prepared at 15% w/w solids in *n*-hexadecane during **(a)** the *in situ* visible absorption spectroscopy study and **(b)** the kinetic experiment conducted using ^{19}F NMR spectroscopy. The very similar particle size indicated by these two images is consistent with the DLS data reported in **Table 3.2**.

It is well known that RAFT end-groups are prone to thermal degradation. Indeed, thermolysis can be used to remove such organosulfur functionality from various vinyl polymers in a post-polymerization derivatization step.[38–42] The chain-end stability depends on the monomer type, the precise chemical structure of the RAFT agent and the reaction conditions. The thermal decomposition of dithioesters such as cumyl dithiobenzoate (CDB) at 90-120 °C and its effect on the polymerization of styrene or methyl methacrylate was studied by both Liu *et al*.[43] and Xu and co-workers.[44] Nejad *et al*. reported the *in situ* degradation of 4-cyanopentanoic acid-4-dithiobenzoate (CPADB) during the synthesis of poly(methacrylic acid) and poly(methyl methacrylate) chains *via* RAFT solution polymerization at 80 °C in either 1,4-dioxane or toluene, leading to the formation of dithiobenzoic acid (DTBA) as a side-product.[45]

Furthermore, Zhou *et al*. observed the thermal decomposition of CPDB in *tert*-butylbenzene at 60 °C and sought to explain such degradation in terms of the molecular structure of this RAFT agent.[46]

To examine whether the dithiobenzoate chain-ends were intrinsically unstable, the absorbance of a 4.4% w/w solution of the $PSMA_{16}$ macro-CTA in *n*-hexadecane ($[PSMA_{16}]$ = 6.2 mmol dm^{-3} = 35 g dm^{-3}; this concentration corresponds to that used in the PISA formulation investigated herein) was monitored over time in an inert atmosphere at 90 °C using *in situ* visible absorption spectroscopy. The gradual reduction in absorbance that is observed during this experiment (see **Figure 3.13**) suggests that the premature loss of dithiobenzoate chain-ends may well occur during the early stages of the TFEMA polymerization. Moreover, the actual DP of the PTFEMA block in the final $PSMA_9$-$PTFEMA_x$ nano-objects is likely to be somewhat higher than that originally targeted.
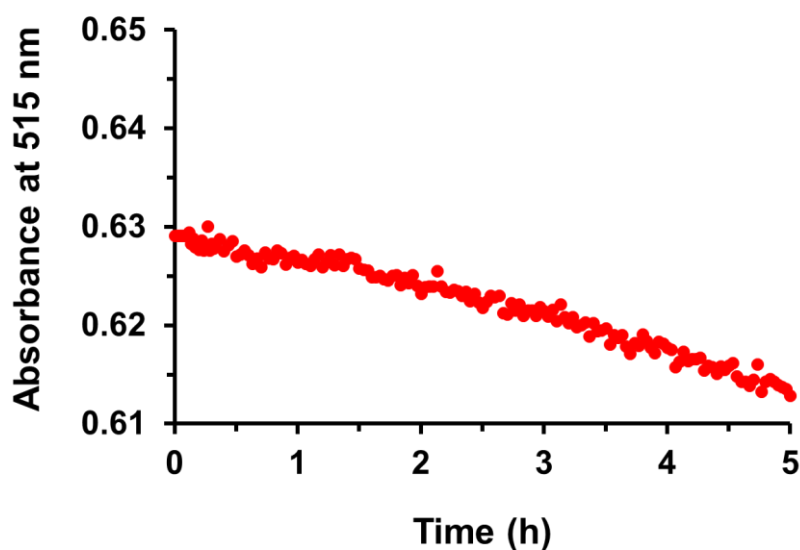
Figure 3.13. Absorbance *vs*. time curve observed for the $PSMA_{16}$ stabilizer block dissolved in *n*-hexadecane ($[PSMA_{16}]$ = 6.2 mmol dm^{-3} = 35 g dm^{-3}) on heating for 5 h at 90 °C. The monotonic reduction in absorbance under such conditions indicates the gradual loss of dithiobenzoate RAFT end-groups even in the absence of any free radical initiator.

Cornel *et al*. demonstrated that the absorbance *vs*. time data recorded during the synthesis of $PSMA_{12}$-$PTFEMA_{98}$ spherical nanoparticles could be converted into a conversion *vs*. time curve using the Beer-Lambert equation.[7] However, this approach assumes that there is no shift in λ_{max} for the trithiocarbonate absorption band at 446 nm, otherwise the implicit assumption that the molar extinction coefficient remains constant may not be valid. In this context,

Skrabania *et al*. reported that dithiobenzoate-based RAFT agents are more sensitive to the nature of the reaction medium than trithiocarbonates, with a more polar environment typically leading to a blue shift in λ_{max}.[47] The λ_{max} *vs*. time data recorded during the synthesis of PSMA$_{16}$-PTFEMA$_{86}$ spheres indicates a two-step 6 nm reduction in λ_{max} within the first 12 min of the TFEMA polymerization (see **Figure 3.14**). Moreover, a 6 nm difference was also observed for solutions of the CPDB RAFT agent in TFEMA and *n*-hexadecane (see **Figure 3.15**).
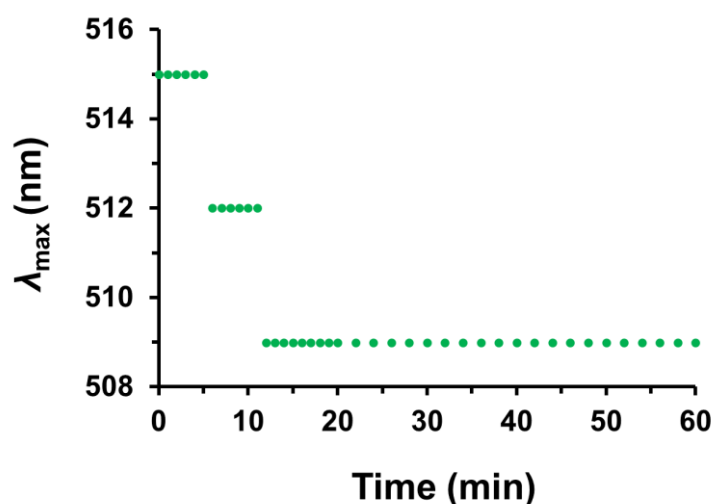
Figure 3.14. Systematic blue shift in λ_{max} observed for the relatively weak n $\rightarrow$ π^* transition of the dithiobenzoate end-group during the synthesis of PSMA$_{16}$-PTFEMA$_{86}$ spherical nanoparticles *via* RAFT dispersion polymerization of TFEMA at 15% w/w solids in *n*-hexadecane at 90 °C. Spectra were recorded between 200 and 800 nm at a resolution of ± 3 nm.
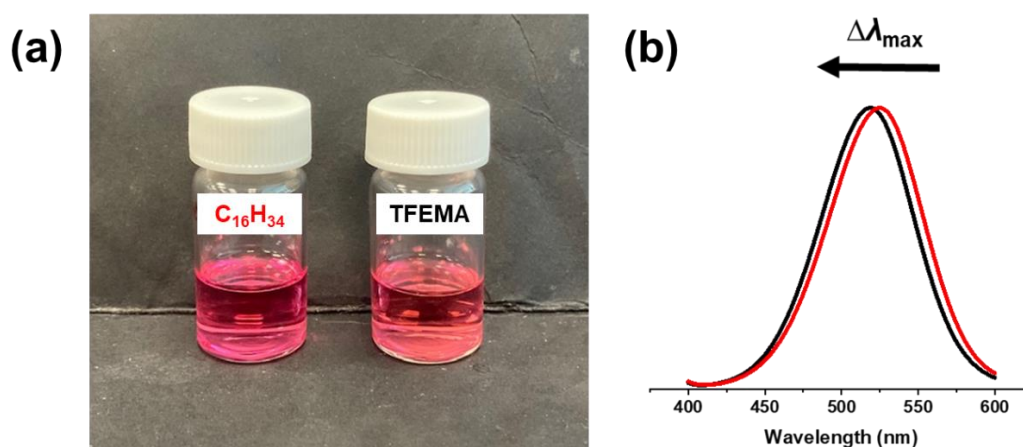
Figure 3.15. (a) Digital photograph recorded at 25 °C for an 8 mmol dm^{-3} solution of CPDB dissolved in either *n*-hexadecane (λ_{max} = 524 nm) or TFEMA monomer (λ_{max} = 518 nm), respectively. The subtle blue shift in the latter solvent is discernible to the naked eye. **(b)** Visible absorption spectra recorded at 25 °C for the same two 8 mmol dm^{-3} solutions of CPDB dissolved in either *n*-hexadecane (red data; λ_{max} = 524 nm) or TFEMA monomer (black data; λ_{max} = 518 nm), respectively.

Initially, we assumed that this blue shift in λ_{max} occurs at the onset of micellar nucleation, with diffusion of TFEMA monomer into the PTFEMA nanoparticle cores producing a more polar environment for the dithiobenzoate chain-ends. However, the kinetic data suggest that micellar nucleation only occurs after 1 h (see **Figure 3.11b**). Only 9% TFEMA conversion is achieved after a reaction time of 10 min, which corresponds to a PTFEMA DP of 8. Thus, only soluble $PSMA_{16}$-$PTFEMA_8$ oligomers are present at this time point. The λ_{max} values for molecularly-dissolved $PSMA_{16}$-$PTFEMA_9$ and $PSMA_{16}$-$PTFEMA_{19}$ copolymer chains prepared in *n*-hexadecane at 15% w/w solids were also determined at 90 °C (see **Table 3.3**).

Table 3.3. Summary of the λ_{max} data obtained at 90 °C for the $PSMA_{16}$ precursor block dissolved in either *n*-hexadecane or TFEMA, and the $PSMA_{16}$-$PTFEMA_9$ and the $PSMA_{16}$-$PTFEMA_{19}$ chains prepared at 15% w/w solids in *n*-hexadecane.

Composition	Solvent	Solids content (% w/w)	T (°C)	λ_{max} (nm)
$PSMA_{16}$	*n*-hexadecane	-	90	516
$PSMA_{16}$	TFEMA	-	90	510
$PSMA_{16} - PTFEMA_9$ chains	*n*-hexadecane	15	90	510
$PSMA_{16} - PTFEMA_{19}$ chains	*n*-hexadecane	15	90	509

Since a 5-6 nm blue shift in λ_{max} was also observed for these latter two solutions, it is presumably related to the growing PTFEMA content of the copolymer chains. UV-visible spectra were initially recorded at a spectral resolution of ± 3 nm, which accounts for the apparent two-step reduction in λ_{max}. Hence this *in situ* study was repeated using a higher spectral resolution of ± 1 nm (see **Figure 3.16**). In this case, a more gradual reduction in λ_{max} from 515 nm to 507 nm was observed within 1.5 h (60% TFEMA conversion). Because of this significant shift in λ_{max}, the molar extinction coefficient for the corresponding absorption band cannot be assumed to remain constant throughout the polymerization. Thus it would not be advisable to attempt to calculate monomer conversions from such spectroscopic data. In principle, the high transmittance observed for $PSMA_{16}$-$PTFEMA_{86}$ spheres prepared in *n*-hexadecane at 90 °C offers the opportunity to study the kinetics of TFEMA polymerization *via in situ* visible absorption spectroscopy. However, in practice the premature loss of dithiobenzoate chain-ends on the timescale of the polymerization and the significant blue shift

in λ_{max} that is observed for such RAFT groups does not allow meaningful kinetic data to be obtained using this technique. In summary, our observations suggest that such *in situ* visible absorption spectroscopy experiments are best undertaken when using trithiocarbonate RAFT agents because the corresponding end-groups exhibit much better thermal stability and do not suffer from any discernible blue shift in the λ_{max} for their relatively weak visible absorption band.
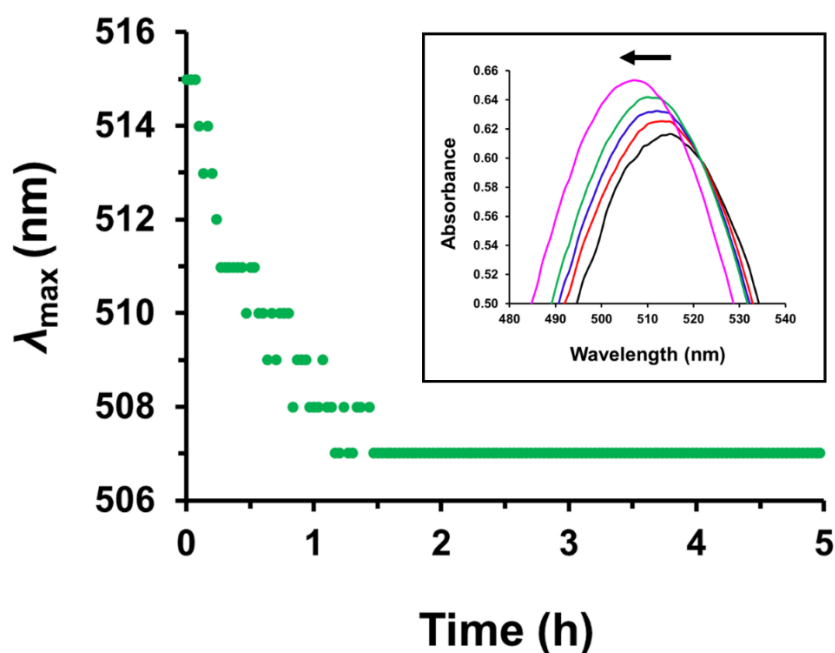
Figure 3.16. Systematic shift in λ_{max} observed for the relatively weak n $\rightarrow \pi^*$ transition of the dithiobenzoate end-group during the synthesis of PSMA$_{16}$-PTFEMA$_{86}$ spherical nanoparticles *via* RAFT dispersion polymerization of TFEMA at 15% w/w solids in *n*-hexadecane at 90 °C. Inset: visible absorption spectra recorded for the reaction mixture after 4 min (black data), 8 min (red data), 14 min (blue data), 28 min (green data) and 90 min (purple data). Spectra were recorded every 2 min at a spectral resolution of $\pm$ 1 nm.

3.4. Conclusions

A series of PSMA$_9$-PTFEMA$_x$ diblock copolymer nano-objects (spheres, worms or vesicles) can be prepared *via* RAFT dispersion polymerization of TFEMA at 90 °C in *n*-dodecane. When targeting PSMA$_9$-PTFEMA$_{200}$ vesicles, ^{19}F NMR spectroscopy studies indicated that more than 95% TFEMA conversion can be achieved within 5 h. Copolymer morphologies were assigned on the basis of TEM and DLS studies and confirmed by SAXS analysis. A pseudo-phase diagram was constructed to ensure the reproducible targeting of pure spheres, worms

and vesicles at 15-25% w/w solids. The first ever example of highly transparent block copolymer vesicles was obtained at 20 °C in *n*-dodecane; such vesicles can be prepared at up to 25% w/w solids. Similarly, transparent vesicles can be prepared in either *n*-tetradecane or *n*-hexadecane at 90 °C. *In situ* visible absorption spectroscopy studies conducted during the PISA synthesis of PSMA$_{16}$-PTFEMA$_{86}$ spheres in *n*-hexadecane revealed the premature loss of dithiobenzoate chain-ends at 90 °C. Unfortunately, this means that the kinetics of RAFT dispersion polymerization of TFEMA cannot be monitored using this technique. Nevertheless, these observations highlight the inferior thermal stability of dithiobenzoate chain-ends compared to trithiocarbonate chain-ends. Finally, an 8 nm blue shift in λ_{max} is observed for the relatively weak n → π^* transition exhibited by the dithiobenzoate chain-ends during the TFEMA polymerization relative to that of the dithiobenzoate-capped PSMA$_9$ precursor. This latter observation suggests that the problem of thermally labile RAFT chain-ends cannot be addressed by simply performing the TFEMA polymerization at a lower temperature.

3.5. References

(1)   Semsarilar, M.; Jones, E. R.; Armes, S. P. Comparison of Pseudo-Living Character of RAFT Polymerizations Conducted under Homogeneous and Heterogeneous Conditions. *Polym. Chem.* **2014**, *5*, 195–203.

(2)   Guo, L.; Jiang, Y.; Qiu, T.; Meng, Y.; Li, X. One-Pot Synthesis of Poly(Methacrylic Acid)-b-Poly(2,2,2-Trifluoroethyl Methacrylate) Diblock Copolymers via RAFT Polymerization. *Polymer* **2014**, *55*, 4601–4610.

(3)   Akpinar, B.; Fielding, L. A.; Cunningham, V. J.; Ning, Y.; Mykhaylyk, O. O.; Fowler, P. W.; Armes, S. P. Determining the Effective Density and Stabilizer Layer Thickness of Sterically Stabilized Nanoparticles. *Macromolecules* **2016**, *49*, 5160–5171.

(4)   Rymaruk, M. J.; Thompson, K. L.; Derry, M. J.; Warren, N. J.; Ratcliffe, L. P. D.; Williams, C. N.; Brown, S. L.; Armes, S. P. Bespoke Contrast-Matched Diblock Copolymer Nanoparticles Enable the Rational Design of Highly Transparent Pickering Double Emulsions. *Nanoscale* **2016**, *8*, 14497–14506.

(5)   Thompson, K. L.; Cinotti, N.; Jones, E. R.; Mable, C. J.; Fowler, P. W.; Armes, S. P. Bespoke Diblock Copolymer Nanoparticles Enable the Production of Relatively Stable Oil-in-Water Pickering Nanoemulsions. *Langmuir* **2017**, *33*, 12616–12623.

(6)   Chakrabarty, A.; Ponnupandian, S.; Kang, N. G.; Mays, J. W.; Singha, N. K. Designing Superhydrophobic Surface Based on Fluoropolymer–Silica Nanocomposite via RAFT-Mediated Polymerization-Induced Self-Assembly. *J. Polym. Sci. Part A Polym. Chem.* **2018**, *56*, 266–275.

(7)   Cornel, E. J.; Meurs, S. Van; Smith, T.; Hora, P. S. O.; Armes, S. P. In Situ Spectroscopic Studies of Highly Transparent Nanoparticle Dispersions Enable Assessment of Trithiocarbonate Chain-End Fidelity during RAFT Dispersion Polymerization in Nonpolar Media. *J. Am. Chem. Soc.* **2018**, *140*, 12980–12988.

(8)   Smith, G. N.; Derry, M. J.; Hallett, J. E.; Lovett, J. R.; Mykhaylyk, O. O.; Neal, T. J.; Prévost, S.; Armes, S. P. Refractive Index Matched, Nearly Hard Polymer Colloids. *Proc. R. Soc. A Math. Phys. Eng. Sci.* **2019**, *475*, 20180763.

(9)   Rymaruk, M. J.; Hunter, S. J.; O'Brien, C. T.; Brown, S. L.; Williams, C. N.; Armes, S. P. RAFT Dispersion Polymerization in Silicone Oil. *Macromolecules* **2019**, *52*, 2822–2832.

(10)   Thompson, K. L.; Derry, M. J.; Hatton, F. L.; Armes, S. P. Long-Term Stability of n-Alkane-in-Water Pickering Nanoemulsions: Effect of Aqueous Solubility of Droplet Phase on Ostwald Ripening. *Langmuir* **2018**, *34*, 9289–9297.

(11)   Docherty, P. J.; Girou, C.; Derry, M. J.; Armes, S. P. Epoxy-Functional Diblock Copolymer Spheres, Worms and Vesicles via Polymerization-Induced Self-Assembly in Mineral Oil. *Polym. Chem.* **2020**, *11*, 3332–3339.

(12)   Trent, J. S. Ruthenium Tetraoxide Staining of Polymers: New Preparative Methods for Electron Microscopy. *Macromolecules* **1984**, *17*, 2930–2931.

(13)   Pauw, B. R.; Smith, A. J.; Snow, T.; Terrill, N. J.; Thünemann, A. F. The Modular Small-Angle X-Ray Scattering Data Correction Sequence. *J. Appl. Crystallogr.* **2017**, *50*, 1800–1811.

(14)   Ilavsky, J.; Jemian, P. R. Irena: Tool Suite for Modeling and Analysis of Small-Angle Scattering. *J. Appl. Crystallogr.* **2009**, *42*, 347–353.

(15)   Derry, M. J.; Fielding, L. A.; Warren, N. J.; Mable, C. J.; Smith, A. J.; Mykhaylyk, O. O.; Armes, S. P. In Situ Small-Angle X-Ray Scattering Studies of Sterically-Stabilized Diblock Copolymer Nanoparticles Formed during Polymerization-Induced Self-Assembly in Non-Polar Media. *Chem. Sci.* **2016**, *7*, 5078–5090.

(16)   Blanazs, A.; Madsen, J.; Battaglia, G.; Ryan, A. J.; Armes, S. P. Mechanistic Insights for Block Copolymer Morphologies: How Do Worms Form Vesicles? *J. Am. Chem. Soc.* **2011**, *133*, 16581–16587.

(17)   Docherty, P. J.; Derry, M. J.; Armes, S. P. RAFT Dispersion Polymerization of Glycidyl Methacrylate for the Synthesis of Epoxy-Functional Block Copolymer Nanoparticles in Mineral Oil. *Polym. Chem.* **2019**, *10*, 603–611.

(18)   Derry, M. J.; Fielding, L. A.; Armes, S. P. Industrially-Relevant Polymerization-Induced Self-Assembly Formulations in Non-Polar Solvents: RAFT Dispersion Polymerization of Benzyl Methacrylate. *Polym. Chem.* **2015**, *6*, 3054–3062.

(19)   Chiefari, J.; Chong, Y. K. B.; Ercole, F.; Krstina, J.; Jeffery, J.; Le, T. P. T.; Mayadunne, R. T. A.; Meijs, G. F.; Moad, C. L.; Moad, G.; Rizzardo, E.; Thang, S. H. Living Free-Radical Polymerization by Reversible Addition-Fragmentation Chain Transfer: The RAFT Process. *Macromolecules* **1998**, *31*, 5559–5562.

(20)   Moad, G.; Rizzardo, E.; Thang, S. H. Living Radical Polymerization by the RAFT Process. *Aust. J. Chem.* **2005**, *58*, 379–410.

(21)   Moad, G.; Rizzardo, E.; Thang, S. H. Radical Addition-Fragmentation Chemistry in Polymer Synthesis. *Polymer* **2008**, *49*, 1079–1131.

(22)   Heatley, F.; Lovell, P. A.; Yamashita, T. Chain Transfer to Polymer in Free-Radical Solution Polymerization of 2-Ethylhexyl Acrylate Studied by NMR Spectroscopy. *Macromolecules* **2001**, *34*, 7636–7641.

(23)   Blanazs, A.; Verber, R.; Mykhaylyk, O. O.; Ryan, A. J.; Heath, J. Z.; Douglas, C. W. I.; Armes, S. P. Sterilizable Gels from Thermoresponsive Block Copolymer Worms. *J. Am. Chem. Soc.* **2012**, *134*, 9741–9748.

(24) Verber, R.; Blanazs, A.; Armes, S. P. Rheological Studies of Thermo-Responsive Diblock Copolymer Worm Gels. *Soft Matter* **2012**, *8*, 9915–9922.

(25) Warren, N. J.; Mykhaylyk, O. O.; Mahmood, D.; Ryan, A. J.; Armes, S. P. RAFT Aqueous Dispersion Polymerization Yields Poly(Ethylene Glycol)-Based Diblock Copolymer Nano-Objects with Predictable Single Phase Morphologies. *J. Am. Chem. Soc.* **2014**, *136*, 1023–1033.

(26) Penfold, N. J. W.; Lovett, J. R.; Warren, N. J.; Verstraete, P.; Smets, J.; Armes, S. P. PH-Responsive Non-Ionic Diblock Copolymers: Protonation of a Morpholine End-Group Induces an Order–Order Transition. *Polym. Chem.* **2016**, *7*, 79–88.

(27) Fielding, L. A.; Lane, J. A.; Derry, M. J.; Mykhaylyk, O. O.; Armes, S. P. Thermo-Responsive Diblock Copolymer Worm Gels in Non-Polar Solvents. *J. Am. Chem. Soc.* **2014**, *136*, 5790–5798.

(28) Pei, Y.; Thurairajah, L.; Sugita, O. R.; Lowe, A. B. RAFT Dispersion Polymerization in Nonpolar Media: Polymerization of 3-Phenylpropyl Methacrylate in N-Tetradecane with Poly(Stearyl Methacrylate) Homopolymers as Macro Chain Transfer Agents. *Macromolecules* **2015**, *48*, 236–244.

(29) Lovett, J. R.; Warren, N. J.; Armes, S. P.; Smallridge, M. J.; Cracknell, R. B. Order-Order Morphological Transitions for Dual Stimulus Responsive Diblock Copolymer Vesicles. *Macromolecules* **2016**, *49*, 1016–1025.

(30) Deng, R.; Ning, Y.; Jones, E. R.; Cunningham, V. J.; Penfold, N. J. W.; Armes, S. P. Stimulus-Responsive Block Copolymer Nano-Objects and Hydrogels: Via Dynamic Covalent Chemistry. *Polym. Chem.* **2017**, *8*, 5374–5380.

(31) Jesson, C. P.; Pearce, C. M.; Simon, H.; Werner, A.; Cunningham, V. J.; Lovett, J. R.; Smallridge, M. J.; Warren, N. J.; Armes, S. P. H2O2 Enables Convenient Removal of RAFT End-Groups from Block Copolymer Nano-Objects Prepared via Polymerization-Induced Self-Assembly in Water. *Macromolecules* **2017**, *50*, 182–191.

(32) Le, D.; Wagner, F.; Takamiya, M.; Hsiao, I. L.; Gil Alvaradejo, G.; Strähle, U.; Weiss, C.; Delaittre, G. Straightforward Access to Biocompatible Poly(2-Oxazoline)-Coated Nanomaterials by Polymerization-Induced Self-Assembly. *Chem. Commun.* **2019**, *55*, 3741–3744.

(33) Pham, B. T. T.; Nguyen, D.; Huynh, V. T.; Pan, E. H.; Shirodkar-Robinson, B.; Carey, M.; Serelis, A. K.; Warr, G. G.; Davey, T.; Such, C. H.; Hawkett, B. S. Aqueous Polymeric Hollow Particles as an Opacifier by Emulsion Polymerization Using Macro-RAFT Amphiphiles. *Langmuir* **2018**, *34*, 4255–4263.

(34) Pedersen, J. S. Form Factors of Block Copolymer Micelles with Spherical, Ellipsoidal and Cylindrical Cores. *J. Appl. Crystallogr.* **2000**, *33*, 637–640.

(35) Bang, J.; Jain, S.; Li, Z.; Lodge, T. P.; Pedersen, J. S.; Kesselman, E.; Talmon, Y. Sphere, Cylinder, and Vesicle Nanoaggregates in Poly(Styrene-b-Isoprene) Diblock Copolymer Solutions. *Macromolecules* **2006**, *39*, 1199–1208.

(36) Warren, N. J.; Mykhaylyk, O. O.; Ryan, A. J.; Williams, M.; Doussineau, T.; Dugourd, P.; Antoine, R.; Portale, G.; Armes, S. P. Testing the Vesicular Morphology to Destruction: Birth and Death of Diblock Copolymer Vesicles Prepared via Polymerization-Induced Self-Assembly. *J. Am. Chem. Soc.* **2015**, *137*, 1929–1937.

(37) Kwak, Y.; Goto, A.; Tsujii, Y.; Murata, Y.; Komatsu, K.; Fukuda, T. A Kinetic Study on the Rate Retardation in Radical Polymerization of Styrene with Addition-Fragmentation Chain Transfer. *Macromolecules* **2002**, *35*, 3026–3029.

(38)   Moad, G.; Rizzardo, E.; Thang, S. H. End-Functional Polymers, Thiocarbonylthio Group Removal/Transformation and Reversible Addition-Fragmentation-Chain Transfer (RAFT) Polymerization. *Polym. Int.* **2011**, *60*, 9–25.

(39)   Willcock, H.; O'Reilly, R. K. End Group Removal and Modification of RAFT Polymers. *Polym. Chem.* **2010**, *1*, 149–157.

(40)   Moad, G.; Chong, Y. K.; Postma, A.; Rizzardo, E.; Thang, S. H. Advances in RAFT Polymerization: The Synthesis of Polymers with Defined End-Groups. *Polymer* **2005**, *46*, 8458–8468.

(41)   Postma, A.; Davis, T. P.; Moad, G.; O'Shea, M. S. Thermolysis of RAFT-Synthesized Polymers. A Convenient Method for Trithiocarbonate Group Elimination. *Macromolecules* **2005**, *38*, 5371–5374.

(42)   Postma, A.; Davis, T. P.; Li, G.; Moad, G.; O'Shea, M. S. RAFT Polymerization with Phthalimidomethyl Trithiocarbonates or Xanthates. On the Origin of Bimodal Molecular Weight Distributions in Living Radical Polymerization. *Macromolecules* **2006**, *39*, 5307–5318.

(43)   Liu, Y.; He, J.; Xu, J.; Fan, D.; Tang, W.; Yang, Y. Thermal Decomposition of Cumyl Dithiobenzoate. *Macromolecules* **2005**, *38*, 10332–10335.

(44)   Xu, J.; He, J.; Fan, D.; Tang, W.; Yang, Y. Thermal Decomposition of Dithioesters and Its Effect on RAFT Polymerization. *Macromolecules* **2006**, *39*, 3753–3759.

(45)   Nejad, E. H.; Castignolles, P.; Gilbert, R. G.; Guillaneuf, Y. Synthesis of Methacrylate Derivatives Oligomers by Dithiobenzoate-RAFT-mediated Polymerization. *J. Polym. Sci. Part A Polym. Chem.* **2008**, *46*, 2277–2289.

(46)   Zhou, Y.; He, J.; Li, C.; Hong, L.; Yang, Y. Dependence of Thermal Stability on Molecular Structure of RAFT/MADIX Agents: A Kinetic and Mechanistic Study. *Macromolecules* **2011**, *44*, 8446–8457.

(47)   Skrabania, K.; Miasnikova, A.; Bivigou-Koumba, A. M.; Zehm, D.; Laschewsky, A. Examining the UV-Vis Absorption of RAFT Chain Transfer Agents and Their Use for Polymer Analysis. *Polym. Chem.* **2011**, *2*, 2074–2083.

Chapter 4. RAFT Dispersion Polymerization of Methyl Methacrylate in Mineral Oil: High Glass Transition Temperature of the Core-Forming Block Constrains the Evolution of Copolymer Morphology

Chapter 4. RAFT Dispersion Polymerization of Methyl Methacrylate in Mineral Oil: High Glass Transition Temperature of the Core-Forming Block Constrains the Evolution of Copolymer Morphology

4.1. Introduction

Methyl methacrylate (MMA) is the cheapest commodity methacrylic monomer. Indeed, it is often employed as a starting material for the preparation of a range of methacrylic monomers *via* transesterification with the appropriate alcohol. Herein we explore the RAFT dispersion polymerization of MMA in mineral oil, which is the most cost-effective PISA formulation for the synthesis of methacrylic diblock copolymer nano-objects in non-polar media. A pseudo-phase diagram has been constructed for the preparation of PLMA$_y$-PMMA$_x$ nanoparticles at 20% w/w solids in mineral oil at 90 °C by systematically varying the target DP for the PMMA block from 20 to 200 when using three PLMA precursors of varying DP. Initially, two-pot PISA syntheses were performed but subsequently a more efficient one-pot protocol was developed (see **Scheme 4.1**). To examine the effect of the reaction temperature on the copolymer morphology, these syntheses were not only conducted at 70 °C and 90 °C (*i.e.* below the T_g of the PMMA block) but also at 115 °C (*i.e.* above the T_g of the PMMA block). A series of diblock copolymer nano-objects was also synthesized at 90 °C by (i) varying the solids content, (ii) using *n*-dodecane instead of mineral oil and (iii) employing an alternative steric stabilizer. The particle size and morphology were characterized using DLS and TEM and, in some cases, by SAXS. Finally, the thermoresponsive behavior of PLMA$_{22}$-PMMA$_{69}$ short worms was briefly studied using DLS, oscillatory rheology and TEM.
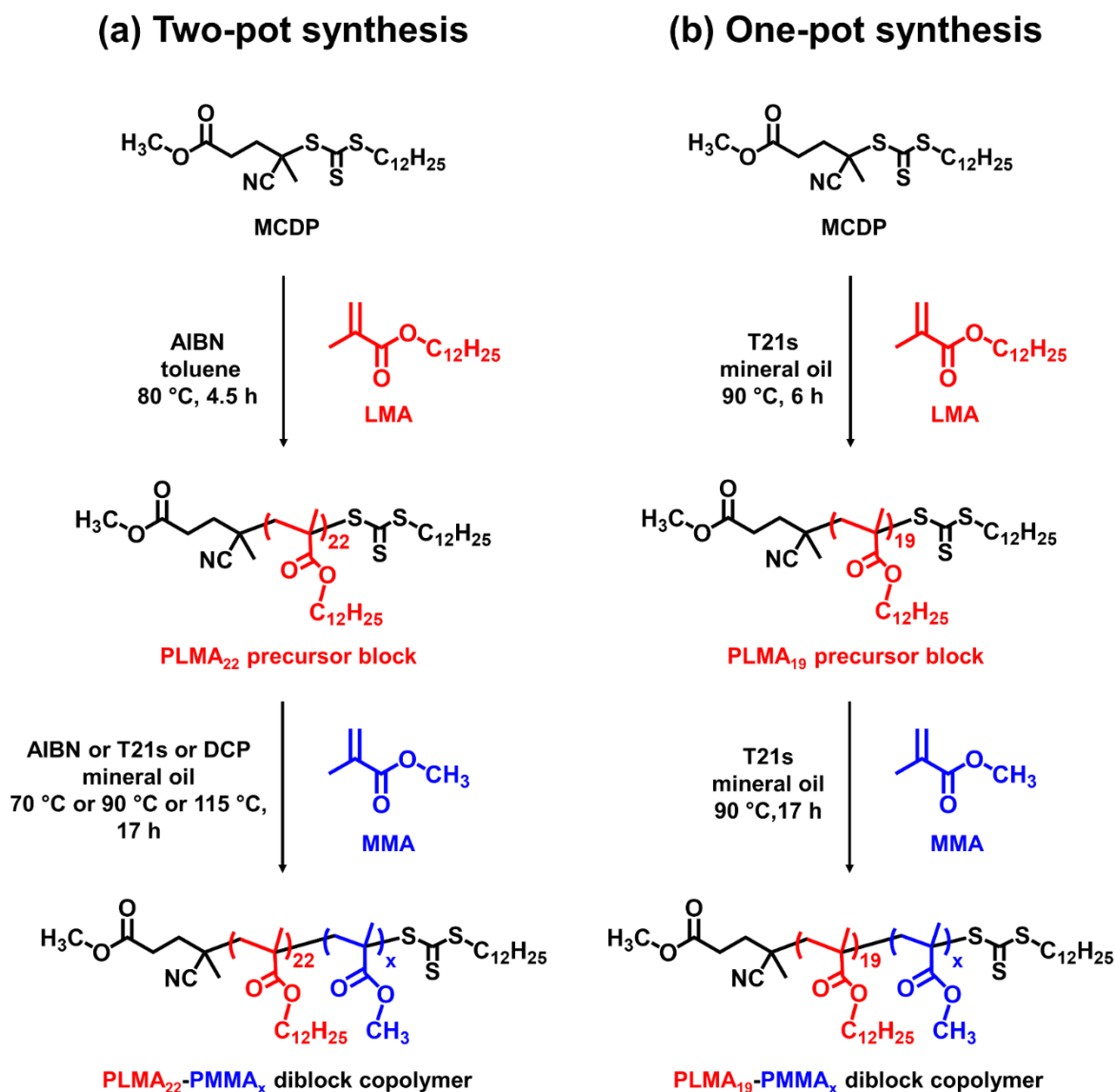
Scheme 4.1. (a) Two-pot synthesis involving the initial preparation and purification of a poly(lauryl methacrylate) ($PLMA_{22}$) precursor *via* RAFT solution polymerization of LMA in toluene at 50% w/w solids using methyl 4-cyano-4(dodecylthiocarbonothioylthio) pentanoate (MCDP) at 80 °C, followed by the RAFT dispersion polymerization of methyl methacrylate (MMA) at 70 °C (using AIBN), 90 °C (using T21s) or 115 °C (using DCP) in mineral oil at 20% w/w solids. **(b)** One-pot synthesis of $PLMA_{19}$-$PMMA_x$ nanoparticles in mineral oil at 20% w/w solids using MCDP and T21s at 90 °C. In this case, the $PLMA_{19}$ precursor was chain-extended immediately without further purification after its synthesis at 60% w/w solids. [N.B. AIBN, DCP and T21s denote 2,2′-azobisisobutyronitrile, dicumyl peroxide and *tert*-butyl peroxy-2-ethylhexanoate initiators, respectively.]

Chapter 4. RAFT Dispersion Polymerization of Methyl Methacrylate in Mineral Oil: High Glass Transition Temperature of the Core-Forming Block Constrains the Evolution of Copolymer Morphology

4.2. Experimental Section

4.2.1. Materials

Methyl methacrylate (MMA, 99%) was purchased from Alfa Aesar (Germany), passed through basic alumina to remove its inhibitor and then stored at –20 °C prior to use. Lauryl methacrylate (LMA), dicumyl peroxide (DCP), CDCl$_3$, ruthenium(IV) oxide, sodium periodate and *n*-dodecane were purchased from Merck (UK) and used as received. Stearyl methacrylate (SMA) was purchased from Santa Cruz Biotechnology, Inc. (USA). 2,2′-Azobisisobutyronitrile (AIBN) was obtained from Molekula (UK) and *tert*-butyl peroxy-2-ethylhexanoate (T21s) was purchased from AkzoNobel (The Netherlands). CD$_2$Cl$_2$ was purchased from Goss Scientific (UK). Tetrahydrofuran was obtained from VWR Chemicals (UK). Methanol and toluene were purchased from Fisher Scientific (UK). 4-Cyano-4(dodecylthiocarbonothioylthio)pentanoate (MCDP) and Group III hydroisomerized mineral oil (viscosity = 4.3 cSt at 100 °C) were kindly provided by The Lubrizol Corporation Ltd. (Hazelwood, Derbyshire, UK).

4.2.2. Methods

Synthesis of poly(lauryl methacrylate) (PLMA) precursor block *via* RAFT solution polymerization in toluene

PLMA$_{22}$, PLMA$_{30}$ and PLMA$_{41}$ precursor blocks were prepared at 50% w/w solids (see **Table S1**). A typical synthesis of PLMA$_{22}$ was conducted as follows. LMA (48.7 g; 191.5 mmol), MCDP (4.0 g; 9.6 mmol; target DP = 20), AIBN (315 mg; 1.9 mmol; MCDP/AIBN molar ratio = 5.0) and toluene (53.0 g) were weighed into a 250 mL round-bottomed flask. The sealed flask was purged with nitrogen for 30 min and immersed in a preheated oil bath at 80 °C. The reaction solution was stirred continuously and the ensuing polymerization was quenched after 4.5 h by exposing the reaction solution to air and cooling the flask to room temperature. A final LMA conversion of 91% was determined by ^{1}H NMR spectroscopy. In order to remove residual monomer, the crude polymer was purified by three consecutive precipitations into a ten-fold excess of methanol (with redissolution in THF after precipitation). The mean DP of the precursor block was calculated to be 22 by using ^{1}H NMR spectroscopy to compare the three methyl protons assigned to the trithiocarbonate end-group at 3.7 ppm to the two

oxymethylene protons attributed to PLMA at 3.80–4.20 ppm (see **Figure 4.1**). Kinetic studies for this polymerization were also performed (see **Figure 4.2**). THF GPC analysis using a refractive index detector and a series of near-monodisperse poly(methyl methacrylate) standards indicated an M_n of 6 000 g mol^{-1} and an M_w/M_n of 1.13. PSMA$_{10}$ and PSMA$_{37}$ precursor blocks were synthesized by following the previously reported synthesis protocol.[1]
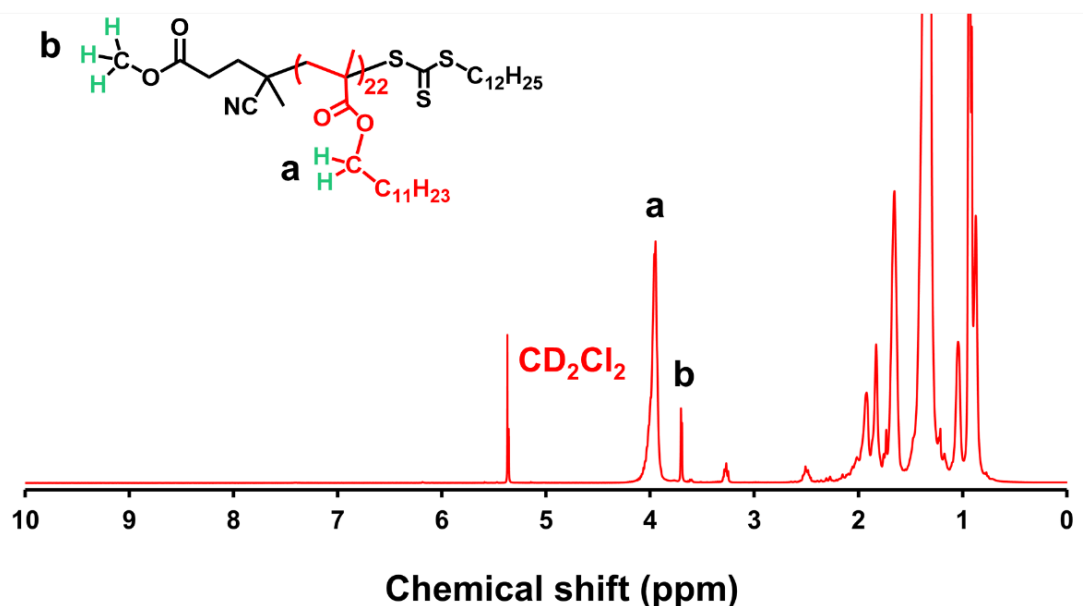
Figure 4.1. Assigned ^{1}H NMR spectrum recorded in CD$_2$Cl$_2$ for the PLMA$_{22}$ precursor prepared *via* RAFT solution polymerization in toluene using the MCDP RAFT agent.

(a)

(b)
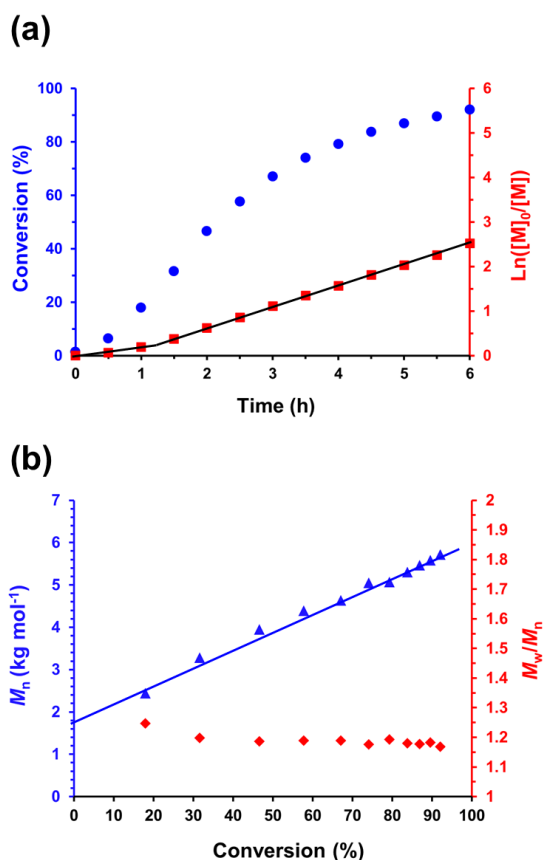
Figure 4.2. RAFT solution polymerization of LMA in toluene at 50% w/w solids and 80 °C using MCDP as a RAFT agent (target PLMA DP = 20; MCDP/initiator molar ratio = 5.0). **(a)** Conversion *vs.* time (blue circles) and corresponding $\ln([M]_0/[M])$ *vs.* time (red squares) plots. **(b)** Evolution in M_n (blue triangles) and M_w/M_n (red diamonds) obtained by THF GPC analysis using a series of near-monodisperse poly(methyl methacrylate) calibration standards.

Two-pot synthesis of poly(lauryl methacrylate)-poly(methyl methacrylate) (PLMA$_{22}$-PMMA$_{69}$) diblock copolymer nanoparticles *via* RAFT dispersion polymerization of MMA in mineral oil

The following example of a two-pot synthesis targeting PLMA$_{22}$-PMMA$_{69}$ nanoparticles at 20% w/w solids is representative and was conducted as follows. PLMA$_{22}$ precursor (0.20 g; 33.25 µmol), T21s initiator (2.40 mg; 11.08 µmol; 10.0% v/v in mineral oil) and mineral oil (1.74 g) were weighed into a glass vial and purged with nitrogen for 30 min. MMA monomer (0.25 mL; 2.33 mmol) was degassed separately then added to the reaction mixture *via* syringe. The sealed vial was immersed in a preheated oil bath at 90 °C and the reaction mixture was magnetically stirred for 17 h. ^{1}H NMR analysis indicated 98% MMA conversion by comparing the integrated methyl signal of the monomer at 3.75–3.78 ppm to the integrated methyl signal

124

of the polymer at 3.50–3.72 ppm. THF GPC analysis indicated an M_n of 14 800 g mol^{-1} and an M_w/M_n of 1.14. To construct a pseudo-phase diagram for PLMA$_y$-PMMA$_x$ nano-objects prepared in mineral oil, a range of diblock copolymer compositions were targeted using PLMA$_{22}$, PLMA$_{30}$ and PLMA$_{41}$ precursors in turn at 20% w/w solids. In each case, the same mass of PLMA$_y$ precursor was used and the MMA/PLMA$_y$ molar ratio and volume of mineral oil were adjusted accordingly. The effect of varying the synthesis temperature on the copolymer morphology was studied by using the same protocol to target diblock copolymer compositions at either 70 ℃ (with AIBN initiator) or 115 ℃ (with DCP initiator). For syntheses performed at 115 *°C, the round-bottomed flask was sealed with a plastic cap rather than a rubber septum in order to prevent evaporative loss of MMA monomer (boiling point = 101* ℃). Furthermore, a series of PSMA$_y$-PMMA$_x$ nanoparticles were prepared at 20% w/w solids in mineral oil using either a PSMA$_{10}$ or a PSMA$_{37}$ precursor at 90 ℃ using the same protocol.

One-pot synthesis of poly(lauryl methacrylate)-poly(methyl methacrylate) (PLMA$_{19}$-PMMA$_{69}$) nanoparticles

 A typical one-pot PISA synthesis of PLMA$_{19}$-PMMA$_{69}$ nanoparticles at 20% w/w solids in mineral oil was conducted as follows. LMA (2.44 g; 9.58 mmol; target 60% w/w solids), MCDP (0.20 g; 478.8 µmol; target degree of polymerization = 20) and T21s initiator (20.7 mg; 95.8 µmol; dissolved at 10% v/v in mineral oil) were dissolved in mineral oil (1.79 g). The reaction mixture was sealed in a 100 mL round-bottomed flask and deoxygenated with nitrogen gas for 30 min. The flask was then placed in a pre-heated oil bath at 90 ℃ for 6 h (final LMA conversion = 97%; M_n = 6 300 g mol^{-1}; M_w/M_n = 1.11) (see **Figure 4.3**). T21s initiator (34.5 mg; 159.6 µmol; dissolved at 10% v/v in mineral oil) was dissolved in mineral oil (22.45 g) and purged with nitrogen gas for 30 min before being added to the reaction solution at 97% LMA conversion. MMA monomer (3.57 mL; 33.52 mmol; target degree of polymerization = 70) was degassed separately and then added to the reaction solution *via* syringe. The reaction mixture was heated at 90 ℃ for a further 17 h. ^{1}H NMR studies confirmed a final MMA conversion of 99% (see **Figure 4.3**) while GPC studies indicated an M_n of 14 500 g mol^{-1} and an M_w/M_n of 1.11. A series of PLMA$_{19}$-PMMA$_x$ nanoparticles were also prepared at 30% w/w solids in mineral oil and at 20% w/w solids in *n*-dodecane using essentially the same synthesis protocol.
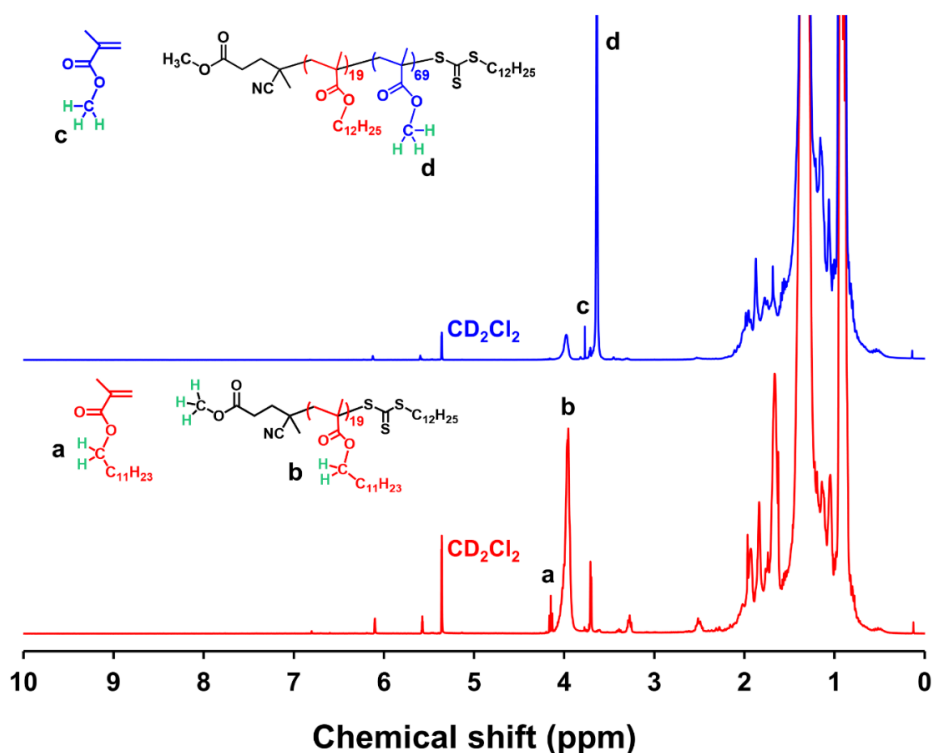
Figure 4.3. Assigned ^{1}H NMR spectra recorded in CD$_2$Cl$_2$ for the PLMA$_{19}$ precursor (red spectrum; LMA conversion = 97%) and the PLMA$_{19}$-PMMA$_{69}$ diblock copolymer (blue spectrum; MMA conversion = 99%) prepared using the one-pot synthesis protocol at 20% w/w solids in mineral oil at 90 °C.

^{1}H NMR Spectroscopy

^{1}H NMR spectra were recorded in either CD$_2$Cl$_2$ or CDCl$_3$ using a 400 MHz Bruker Avance spectrometer. Typically, 64 scans were averaged per spectrum. For the kinetic study of the synthesis of PLMA$_{19}$-PMMA$_{100}$ nano-objects at 20% w/w solids in mineral oil, aliquots were extracted from the reaction mixture every 10 min for the first 90 min then at 30 min intervals for a further 60 min. Each aliquot was diluted with CD$_2$Cl$_2$ prior to ^{1}H NMR analysis.

Gel Permeation Chromatography (GPC)

Molecular weight distributions (MWDs) were assessed by GPC using THF as an eluent. The GPC system was equipped with two 5 μm (30 cm) Mixed C columns and a WellChrom K-2301 refractive index detector operating at 950 ± 30 nm. The THF mobile phase contained 2.0% v/v triethylamine and 0.05% w/v butylhydroxytoluene (BHT) and the flow rate was fixed at 1.0 ml min^{-1}. A series of twelve near-monodisperse

poly(methyl methacrylate) standards (M_p values ranging from 800 to 2 200 000 g mol^{-1}) were used for column calibration in combination with a refractive index detector.

Dynamic Light Scattering (DLS)

DLS studies were performed using a Zetasizer Nano ZS instrument (Malvern Instruments, UK) at a fixed scattering angle of 173°. Copolymer dispersions were diluted in *n*-dodecane (0.10% w/w) prior to light scattering studies at 20 °C. The intensity-average diameter and polydispersity of the nanoparticles were calculated by cumulants analysis of the experimental correlation function using Dispersion Technology Software version 6.20. Data were averaged over ten runs each of thirty seconds duration. It is emphasized that DLS assumes a spherical morphology. Thus, the DLS diameter determined for anisotropic nanoparticles such as worms is a 'sphere-equivalent' value that does not indicate the worm length or the worm width. Nevertheless, DLS can be used to monitor a thermally-induced worm-to-sphere transition by monitoring the reduction in the apparent diameter as a function of temperature.[2]

Transmission Electron Microscopy (TEM)

TEM studies were conducted using a Philips CM 100 instrument operating at 100 kV and equipped with a Gatan 1k CCD camera. A single droplet of a 0.10% w/w copolymer dispersion was placed onto a carbon-coated copper grid and allowed to dry, prior to exposure to ruthenium(VIII) oxide vapor for 7 min at 20 °C.[3] This heavy metal compound acts as a positive stain for the core-forming PMMA block to improve contrast. The ruthenium(VIII) oxide was prepared as follows: ruthenium(IV) oxide (0.30 g) was added to water (50 g) to form a black slurry; addition of sodium periodate (2.0 g) with continuous stirring produced a yellow solution of ruthenium(VIII) oxide within 1 min at 20 °C.

Small-Angle X-ray Scattering (SAXS)

SAXS patterns were recorded using a Xeuss 2.0 laboratory beamline (Xenocs, Grenoble, France) equipped with a MetalJet X-ray source (GaK_α radiation, wavelength $\lambda = 1.34$ Å, with q ranging from 0.004 to 0.300 Å^{-1}, where $q = 4\pi.\sin\theta/\lambda$ is the length of the scattering vector and θ is one-half of the scattering angle) and a 2D Pilatus 1M pixel detector (Dectris, Baden-Daettwil, Switzerland). A glass capillary of 2.0 mm

diameter was used as a sample holder. Scattering data were reduced using software supplied by the SAXS instrument manufacturer and were further analyzed using Irena SAS macros for Igor Pro.[4]

Differential scanning calorimetry (DSC)

Measurements were performed using a TA DSC25 Discovery series instrument operating from 0 to 180 °C at a rate of 5 °C min^{-1} using aluminum T_{zero} pans and T_{zero} hermetic lids for both PMMA homopolymers and PLMA$_{22}$-PMMA$_x$ diblock copolymers. Instrument calibration was performed using an indium standard. Purified PLMA$_{22}$-PMMA$_x$ (where x is 69, 97, 139 or 194) powders were obtained after three consecutive precipitations of the as-synthesized diblock copolymer dispersion into a ten-fold excess of methanol (with redissolution in THF after each precipitation), followed by isolation *via* filtration and drying under vacuum for 24 h. For DSC analysis, each diblock copolymer (or PMMA homopolymer) was subjected to two heating/cooling cycles: the first cycle ensured removal of residual organic solvent, and the glass transition temperature was determined during the second cycle.

Oscillatory Rheology

An Anton Paar MCR 502 rheometer (equipped with TruGap functionality for online monitoring of the geometry gap), a variable-temperature Peltier plate, Peltier hood and a 50 mm 2° stainless cone was used for the rheology experiments. The storage (G') and loss (G'') moduli were determined as a function of temperature at a heating rate of 2 °C min^{-1}, a fixed strain amplitude of 1.0%, and an angular frequency of 10 rad s^{-1}. The sample gap was 207 μm.

4.3. Results and Discussion

4.3.1. Synthesis of PLMA precursors for the two-pot synthesis protocol

PLMA precursors with mean DPs of 22, 30 or 41 were prepared *via* RAFT solution polymerization of LMA in toluene at 80 °C using MCDP as a RAFT agent (see **Scheme 4.1** and **Figure 4.1**). Preliminary kinetic studies of the RAFT solution polymerization of LMA when targeting a PLMA$_{20}$ precursor indicated first-order kinetics after an initial induction period of 1 h and confirmed the linear evolution of molecular weight with conversion (see

Figure 4.2). To avoid the possible loss of RAFT chain-ends under monomer-starved conditions,[5] such polymerizations were quenched after 4.5 h for PLMA$_{22}$ and PLMA$_{30}$, and after 5.5 h for PLMA$_{41}$. ^{1}H NMR studies confirmed relatively high LMA conversions ($\geq$ 89%) (see **Table 4.1**). THF GPC analysis indicated a narrow molecular weight distribution (M_w/M_n $\leq$ 1.13) in each case, suggesting that relatively good RAFT control was achieved.

Table 4.1. Summary of the reaction times, conversions and GPC data obtained for three PLMA$_x$ precursors prepared at 50% w/w solids in toluene at 80 °C.

Target DP of PLMA precursor	Reaction time (h)	LMA Conversion (%)	THF GPC		Final DP of PLMA precursor
			M_n (g mol^{-1})	M_w/M_n	
20	4.5	91	6,000	1.13	22
40	4.5	90	8,400	1.13	30
50	5.5	89	11,300	1.12	41

4.3.2. Kinetic studies of the RAFT dispersion polymerization of MMA in mineral oil

A representative kinetic experiment was conducted for the RAFT dispersion polymerization of MMA at 90 °C when targeting PLMA$_{19}$-PMMA$_{100}$ nano-objects at 20% w/w solids in mineral oil using the one-pot protocol (see **Scheme 4.1b**). The corresponding semilogarithmic plot indicates two distinct linear regimes (see **Figure 4.4a**) as previously reported for various examples of RAFT dispersion polymerization conducted in either aqueous[6] or non-polar media.[7–10] The first regime corresponds to a relatively slow solution polymerization, followed by an approximate ten-fold rate enhancement after 30 min. This corresponds to the onset of micellar nucleation.[12,36,39] The MMA conversion was 29% at this time point, which corresponds to a critical PMMA DP of 29 (see **Figure 4.4**). Moreover, TEM studies confirm the appearance of nascent spherical nanoparticles in the reaction mixture after 30 min (see **Figure 4.5**). DLS studies indicated a z-average diameter of 16 nm (DLS polydispersity, PDI = 0.11) for such nuclei (see **Figure 4.5a**). Thereafter, first-order kinetics were observed up to 97% MMA conversion, followed by a slower rate of polymerization under monomer-starved conditions. ^{1}H NMR spectroscopy studies indicated that a final MMA conversion of 99% was

achieved after 150 min. A linear increase in M_n with conversion and relatively low dispersities ($M_w/M_n \leq 1.14$) were confirmed by THF GPC analysis, see **Figure 4.4b**.[12–14] This is consistent with the pseudo-living character expected for a well-controlled RAFT polymerization. The final copolymer morphology was a mixture of spheres and short worms (z-average diameter = 123 nm, DLS PDI = 0.22), see **Figure 4.5**.
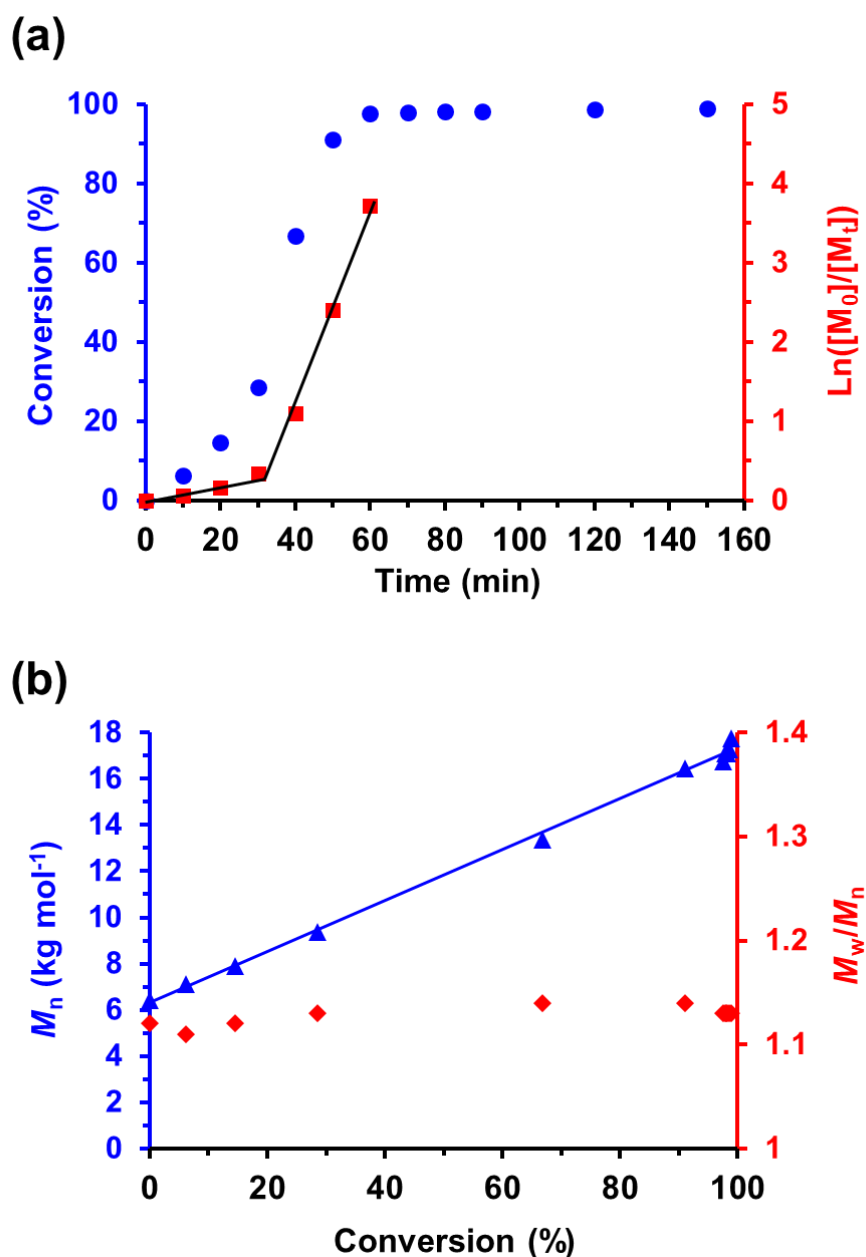
Figure 4.4. (a) Conversion *vs*. time curve (blue circles) and corresponding ln([M$_0$]/[M$_t$]) *vs*. time plot (red squares) for the RAFT dispersion polymerization of MMA at 90 °C when targeting PLMA$_{19}$-PMMA$_{100}$ spheres using the one-pot synthesis protocol (see **Scheme 4.1b**) at 20% w/w solids in mineral oil. **(b)** Evolution of M_n (blue triangles) and M_w/M_n (red diamonds) with monomer conversion for this PISA formulation.
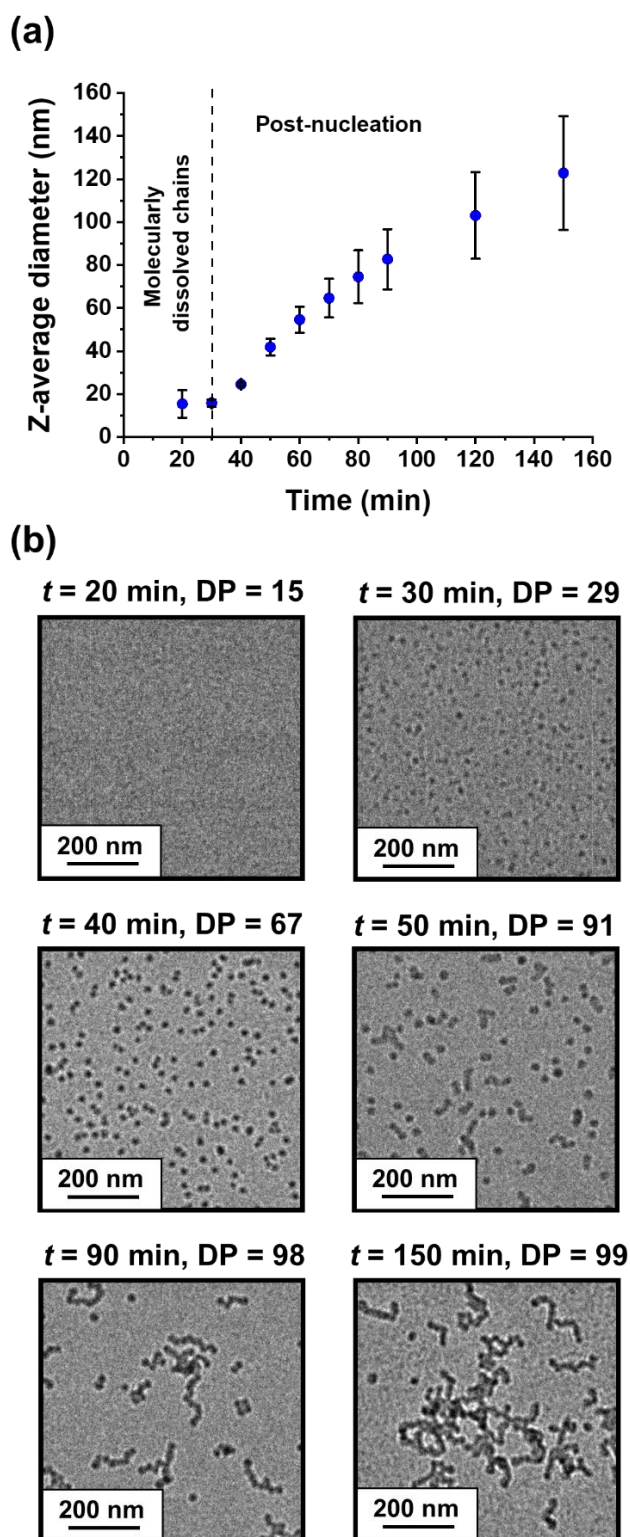
Figure 4.5. (a) Variation in z-average diameter over time obtained for aliquots periodically taken from the reaction mixture when targeting PLMA$_{19}$-PMMA$_{100}$ nano-objects using the one-pot protocol at 90 °C in mineral oil at 20% w/w solids. [N.B. Standard deviations are calculated from the DLS polydispersities and indicate the breadth of each particle size distribution, rather than the experimental error]. **(b)** Representative TEM images recorded for aliquots taken from the reaction mixture after 20, 30, 40, 50, 90 or 150 min.

4.3.3. GPC analysis of PLMA-PMMA diblock copolymers

PLMA has been previously utilized as a steric stabilizer block by Fielding *et al.* for the RAFT dispersion polymerization of benzyl methacrylate in non-polar media (see **Chapter 1**).[2,7,15] More recently, Cornel *et al.* reported the RAFT dispersion polymerization of MMA using a PLMA$_{39}$ precursor in *n*-dodecane. For this latter PISA formulation, targeting a PMMA DP of either 50 or 100 produced spherical nanoparticles.[16] In each case, GPC analysis indicated narrow molecular weight distributions ($M_w/M_n \leq 1.14$), which suggests reasonably good RAFT control. Herein the RAFT dispersion polymerization of MMA was conducted at 20% w/w solids in mineral oil at 90 °C using either a PLMA$_{22}$ precursor block in a two-pot protocol or a PLMA$_{19}$ precursor by using a one-pot protocol (see **Scheme 4.1**).

Chromatograms recorded for the purified PLMA$_{22}$ precursor and five PLMA$_{22}$-PMMA$_x$ diblock copolymers (where x ranges from 19 to 194) prepared using the traditional two-pot protocol are shown in **Figure 4.6a**. For comparison, chromatograms obtained for the PLMA$_{19}$ precursor and five PLMA$_{19}$-PMMA$_x$ diblock copolymers (where x ranges from 20 to 198) prepared by the one-pot protocol under otherwise identical conditions are shown in **Figure 4.6b**. A systematic shift towards higher molecular weight was observed in both cases when targeting higher PMMA DPs. The two-pot protocol resulted in unimodal curves for PMMA DPs of 19, 50 and 97. However, a low molecular weight shoulder became increasingly evident when higher PMMA DPs were targeted. Similar observations were reported by Fielding *et al.* for the synthesis of PLMA$_{17}$-PBzMA$_x$ nano-objects by the RAFT dispersion polymerization of benzyl methacrylate in *n*-heptane.[15] This feature indicates the presence of unreacted PLMA precursor (or prematurely terminated PLMA$_{22}$-PMMA$_x$ chains). This sub-optimal blocking efficiency inevitably leads to broader molecular weight distributions when targeting higher PMMA DPs, *e.g.* $M_w/M_n = 1.16$ for PLMA$_{22}$-PMMA$_{97}$ *vs.* $M_w/M_n = 1.36$ for PLMA$_{22}$-PMMA$_{194}$.

In contrast, the one-pot protocol was more efficient (final MMA conversions $\geq$ 98%; **Figure 4.3**) and afforded unimodal chromatograms with significantly narrower MWDs ($M_w/M_n \leq 1.21$) in all cases (see **Table 9.5**). In this case, the pseudo-living character of the RAFT dispersion polymerization is enhanced by minimizing the time for which the PLMA$_{19}$ precursor is exposed to monomer-starved conditions at elevated temperature.[5] For both synthesis protocols, a linear

relationship was observed between the GPC M_n data and the PMMA DP (corrected for the final MMA conversion), see **Figure 4.6**.
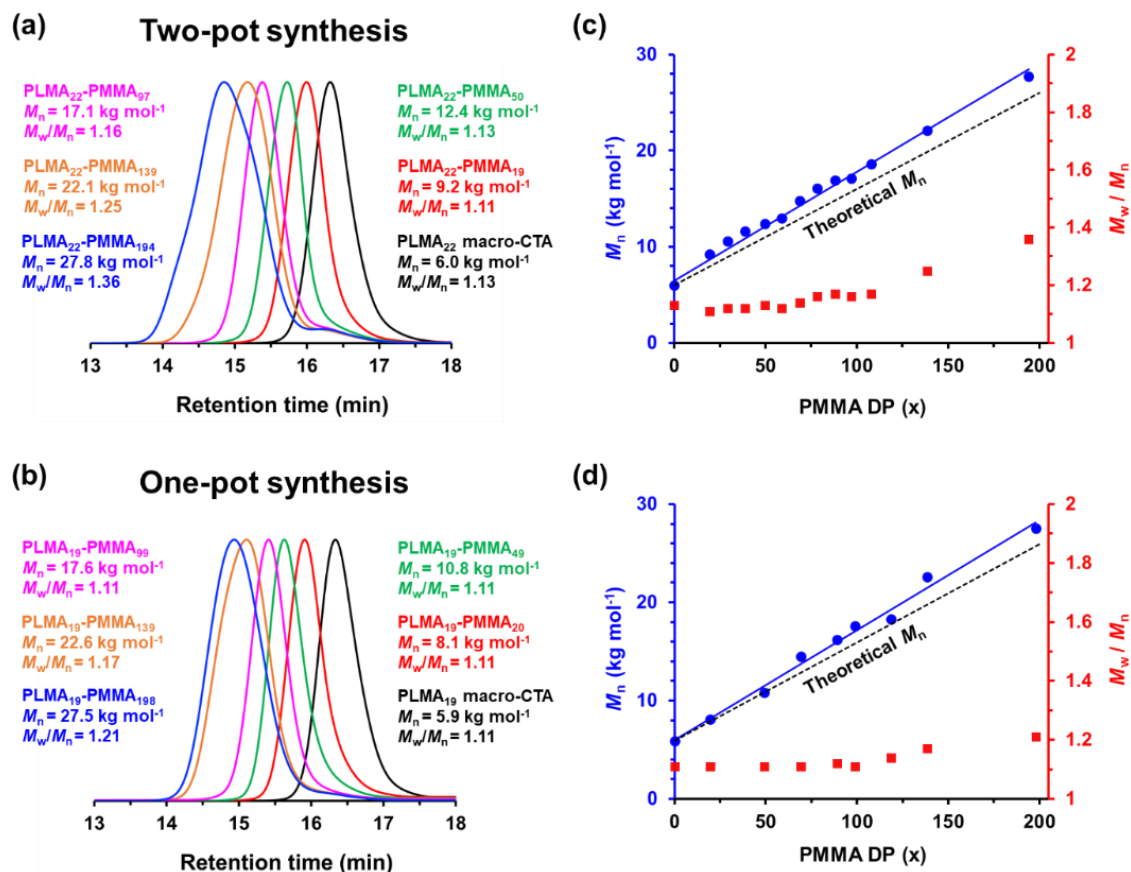
Figure 4.6. GPC curves (*vs.* a series of near-monodisperse poly(methyl methacrylate) calibration standards using a refractive index detector) recorded for: **(a)** the PLMA$_{22}$ precursor (prepared in toluene at 80 °C targeting 50% w/w solids) and a series of five PLMA$_{22}$-PMMA$_x$ diblock copolymers prepared by RAFT dispersion polymerization of MMA at 90 °C targeting 20% w/w solids using the *two-pot protocol*, where x = 19, 50, 97, 139 or 194, respectively; **(b)** the PLMA$_{19}$ precursor (prepared in mineral oil at 90 °C targeting 60% w/w solids) and a series of five PLMA$_{19}$-PMMA$_x$ diblock copolymers prepared using the *one-pot protocol* at 90 °C targeting 20% w/w solids, where x = 20, 49, 99, 139 or 198, respectively. Linear relationship between M_n (blue circles) and PMMA DP (as determined by ^{1}H NMR studies) for a series of **(c)** PLMA$_{22}$-PMMA$_x$ and **(d)** PLMA$_{19}$-PMMA$_x$ diblock copolymers prepared at 20% w/w solids. The corresponding M_w/M_n (red squares) data are also shown.

4.3.4. Pseudo-phase diagram constructed for PLMA$_y$-PMMA$_x$ nano-objects prepared in mineral oil at 90 °C using the two-pot protocol

A pseudo-phase diagram was constructed for the two-pot synthesis protocol using PLMA$_{22}$, PLMA$_{30}$ and PLMA$_{41}$ precursors by systematically varying the PMMA DP between 20 and 200 (see **Tables 9.6** and **9.7**) while targeting 20% w/w solids in mineral oil at 90 °C. Previous PISA syntheses conducted in non-polar media suggested that employing a sufficiently short steric stabilizer block should provide access to the three main copolymer morphologies (*i.e.* spheres, worms and vesicles).[1,15] In practice, vesicles were not obtained even when using the shortest stabilizer block (see **Figure 4.7**). In this case, DLS studies indicated the formation of spheres with z-average diameters of 18–30 nm (DLS PDI < 0.20) for PMMA DPs ranging between 19 and 39. Targeting PLMA$_{22}$-PMMA$_{50}$ and PLMA$_{22}$-PMMA$_{59}$ produced viscous liquids comprising mixtures of spheres and short worms. For PMMA DPs ranging between 69 and 97, mainly short worms were obtained with only a minor population of spheres; these dispersions formed transparent, free-standing gels, whereas targeting higher PMMA DPs (≥ 108) formed turbid brittle gels. Both DLS and TEM studies indicated the formation of micron-sized aggregates of spherical nanoparticles for these latter formulations.

Similar observations were made for a series of PLMA$_{19}$-PMMA$_x$ nano-objects prepared using the one-pot protocol (see **Figure 4.8**), suggesting that the synthesis route does not have a significant effect on the copolymer morphology. Well-defined spheres were produced when the PLMA$_{30}$ precursor was chain-extended with MMA. For example, z-average diameters of 24–26 nm (DLS PDI ≤ 0.06) were observed for PLMA$_{30}$-PMMA$_{29}$ and PLMA$_{30}$-PMMA$_{49}$. However, targeting higher PMMA DPs only afforded a mixture of spheres and short worms prior to the formation of colloidally unstable aggregates of spherical nanoparticles (e.g. for PLMA$_{30}$-PMMA$_{139}$).
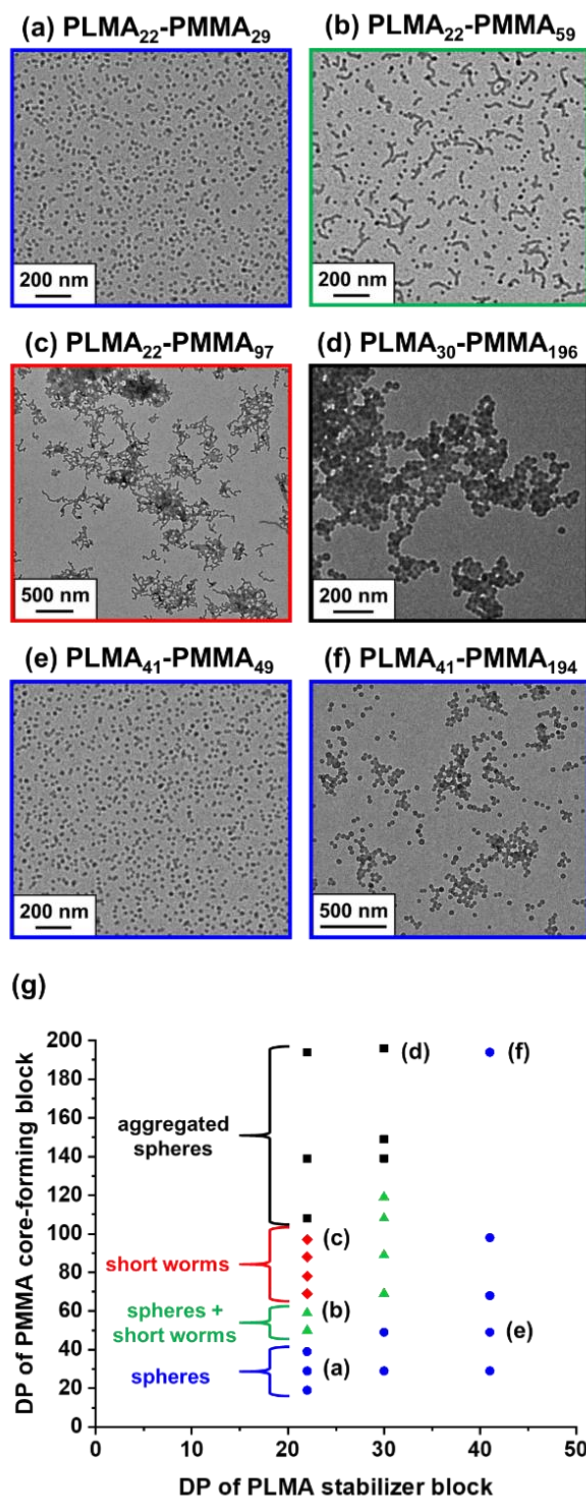
Figure 4.7. Representative TEM images obtained for **(a)** PLMA$_{22}$-PMMA$_{29}$ spheres, **(b)** a mixed phase comprising PLMA$_{22}$-PMMA$_{59}$ spheres and short worms, **(c)** PLMA$_{22}$-PMMA$_{97}$ short worms, **(d)** PLMA$_{30}$-PMMA$_{196}$ aggregated spheres, **(e)** PLMA$_{41}$-PMMA$_{49}$ spheres and **(f)** PLMA$_{41}$-PMMA$_{194}$ spheres each prepared at 20% w/w solids in mineral oil, respectively. **(g)** Pseudo-phase diagram constructed for PLMA$_y$–PMMA$_x$ diblock copolymer nano-objects prepared by RAFT dispersion polymerization of MMA in mineral oil using the two-pot protocol and employing PLMA$_{22}$, PLMA$_{30}$ or PLMA$_{41}$ precursors with T21s initiator at 90 °C ([PLMA$_y$]/[T21s] molar ratio = 3.0).

Chapter 4. RAFT Dispersion Polymerization of Methyl Methacrylate in Mineral Oil: High Glass Transition Temperature of the Core-Forming Block Constrains the Evolution of Copolymer Morphology
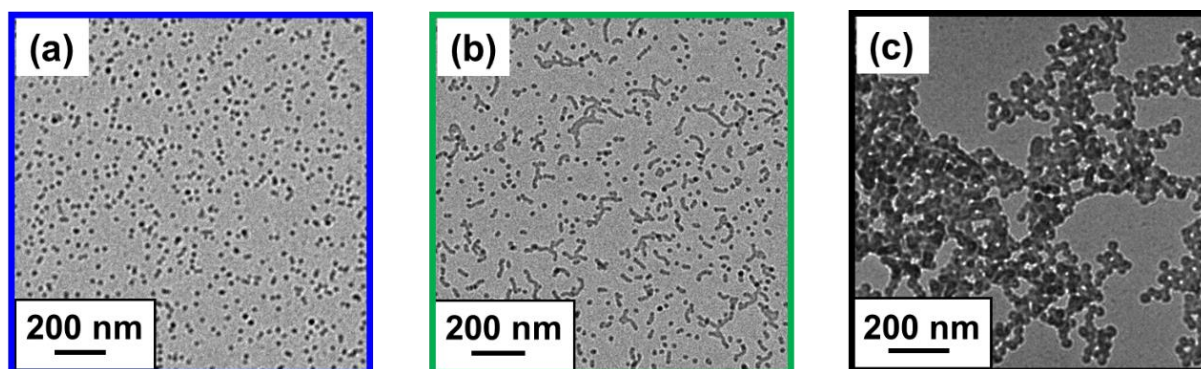
Figure 4.8. Representative TEM images of **(a)** the $PLMA_{19}$-$PMMA_{49}$ spheres **(b)** the $PLMA_{19}$-$PMMA_{69}$ mixture of short worms and spheres and **(c)** the $PLMA_{19}$-$PMMA_{198}$ large spherical aggregates prepared using the one-pot protocol at 20% w/w solids in mineral oil at 90 °C.

Employing the $PLMA_{41}$ stabilizer only allowed access to kinetically-trapped spheres. Similar morphological limitations have been reported for other PISA formulations in non-polar media.[8,15] In addition to the steric stabilizer DP, there are various other synthesis parameters that may influence the chain mobility of the PMMA block, including the solids content, the solvent composition, and the chemical nature of the steric stabilizer. Interestingly, we observed the same unexpected morphological limitation (*i.e.* no access to either long worms or vesicles) when targeting a series of $PLMA_{19}$-$PMMA_x$ nanoparticles: (i) at 30% w/w solids in mineral oil, (ii) using *n*-dodecane instead of mineral oil at 20% w/w solids or (iii) when employing poly(stearyl methacrylate) (PSMA) as a steric stabilizer instead of PLMA to target $PSMA_{10}$-$PMMA_{30-200}$ nano-objects in mineral oil at 20% w/w solids (see **Figure 4.9**, **Table 9.8** and **Table 9.9**).
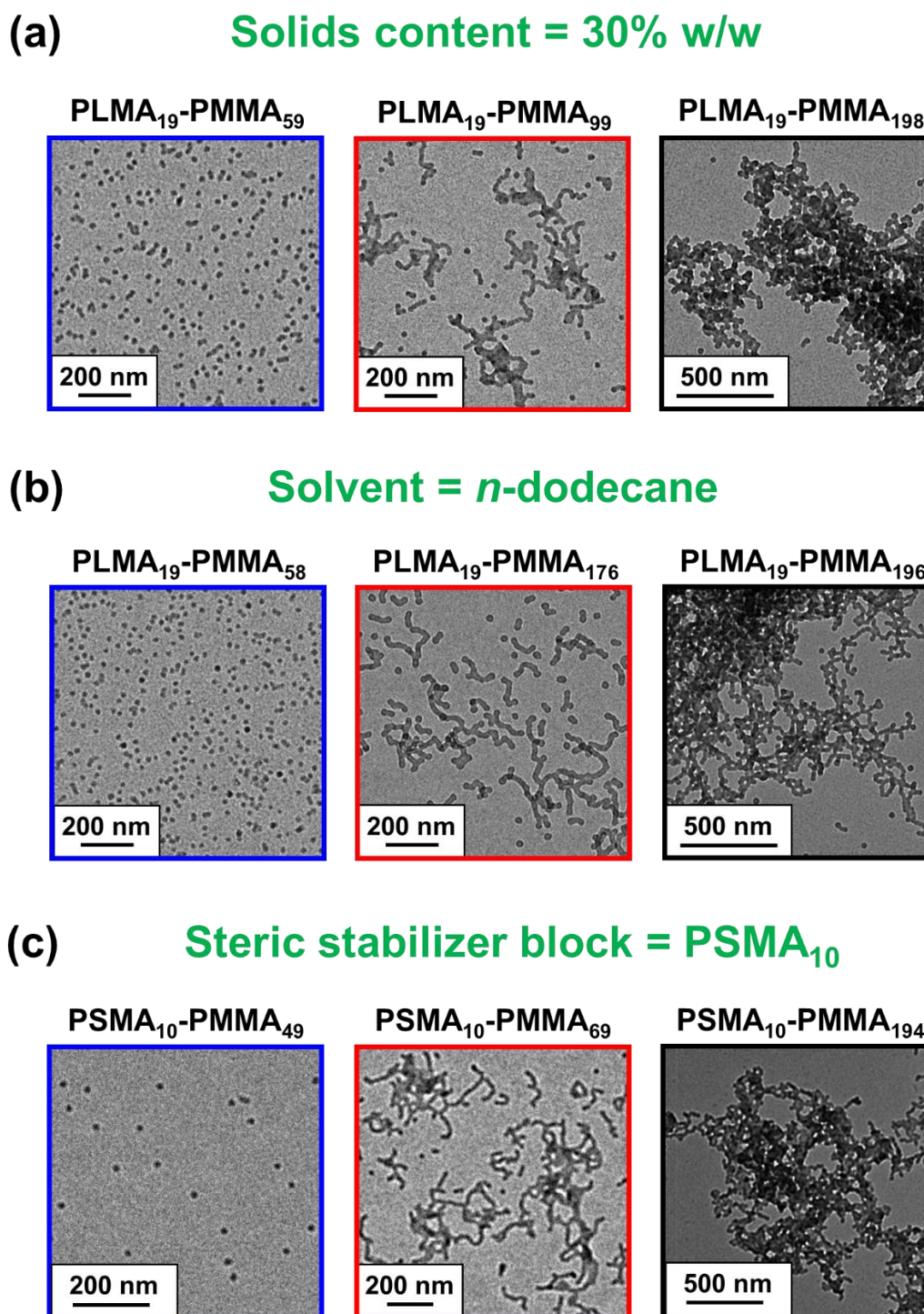
Figure 4.9. Representative TEM images recorded for: **(a)** PLMA$_{19}$-PMMA$_{59}$, PLMA$_{19}$-PMMA$_{99}$ and PLMA$_{19}$-PMMA$_{198}$ nano-objects prepared at 30% w/w solids in mineral oil using the one-pot protocol; **(b)** PLMA$_{19}$-PMMA$_{58}$, PLMA$_{19}$-PMMA$_{176}$ and PLMA$_{19}$-PMMA$_{196}$ nano-objects prepared at 20% w/w solids in n-dodecane using the one-pot protocol; **(c)** PSMA$_{10}$-PMMA$_{49}$, PSMA$_{10}$-PMMA$_{69}$ and PSMA$_{10}$-PMMA$_{194}$ nano-objects prepared at 20% w/w solids in mineral oil with a PSMA$_{10}$ precursor using the two-pot protocol. These images confirm that colloidally unstable aggregates are also obtained for various related formulations, which suggests that this is a generic problem for this PISA system.

137

4.3.5. Synthesis of PLMA$_{22}$-PMMA$_x$ diblock copolymers above the T_g of the PMMA block

The unexpected observations described above invite the following question: why does targeting higher PMMA DPs using a PLMA$_{22}$ or PLMA$_{19}$ precursor result in the formation of large spherical aggregates instead of relatively long worms or vesicles? Ideally, PISA should be performed above the effective glass transition temperature of the core-forming block: this is important because it ensures sufficient chain mobility to provide access to higher order morphologies. Conversely, if PISA syntheses are conducted below the T_g of the core-forming block this is likely to lead to the formation of kinetically-trapped spheres, since the growing solvophobic chains become increasingly stiff and immobile during the polymerization.[17,18]

Therefore, determining the T_g of the core-forming PMMA block is important for understanding the morphological limitations observed herein. The relationship between the T_g and M_n (or DP) for a homopolymer is described by the Flory-Fox equation.[19,20] To determine the molecular weight dependence for the T_g of PMMA, DSC studies were conducted on a series of near-monodisperse PMMA homopolymers with DPs ranging between 13 and 1270 (see **Figure 4.10**). For DPs above 200, the T_g is essentially constant at approximately 126 °C, which is in reasonable agreement with the literature value for PMMA.[21–23] As expected, targeting lower DPs leads to a gradual reduction in the T_g below this upper limit value. This is important because the PMMA DPs used to construct the pseudo-phase diagram shown in **Figure 4.7** range from 20 to 200. Thus the PMMA T_g is often significantly lower than the literature value and, in many cases, also below the reaction temperature (90 °C) at which these PISA syntheses are conducted. On the other hand, targeting a PMMA DP of 200 at 90 °C generates chains whose T_g exceeds the reaction temperature. However, literature precedent suggests that the effective T_g of PMMA is likely to be lower when such chains are conjugated to a well-solvated, highly mobile low T_g polymer such as PLMA.[24,25]

(a)

(b)

Flory-Fox equation:

$$T_g = T_{g,\infty} - \frac{K}{DP \cdot 100.12}$$
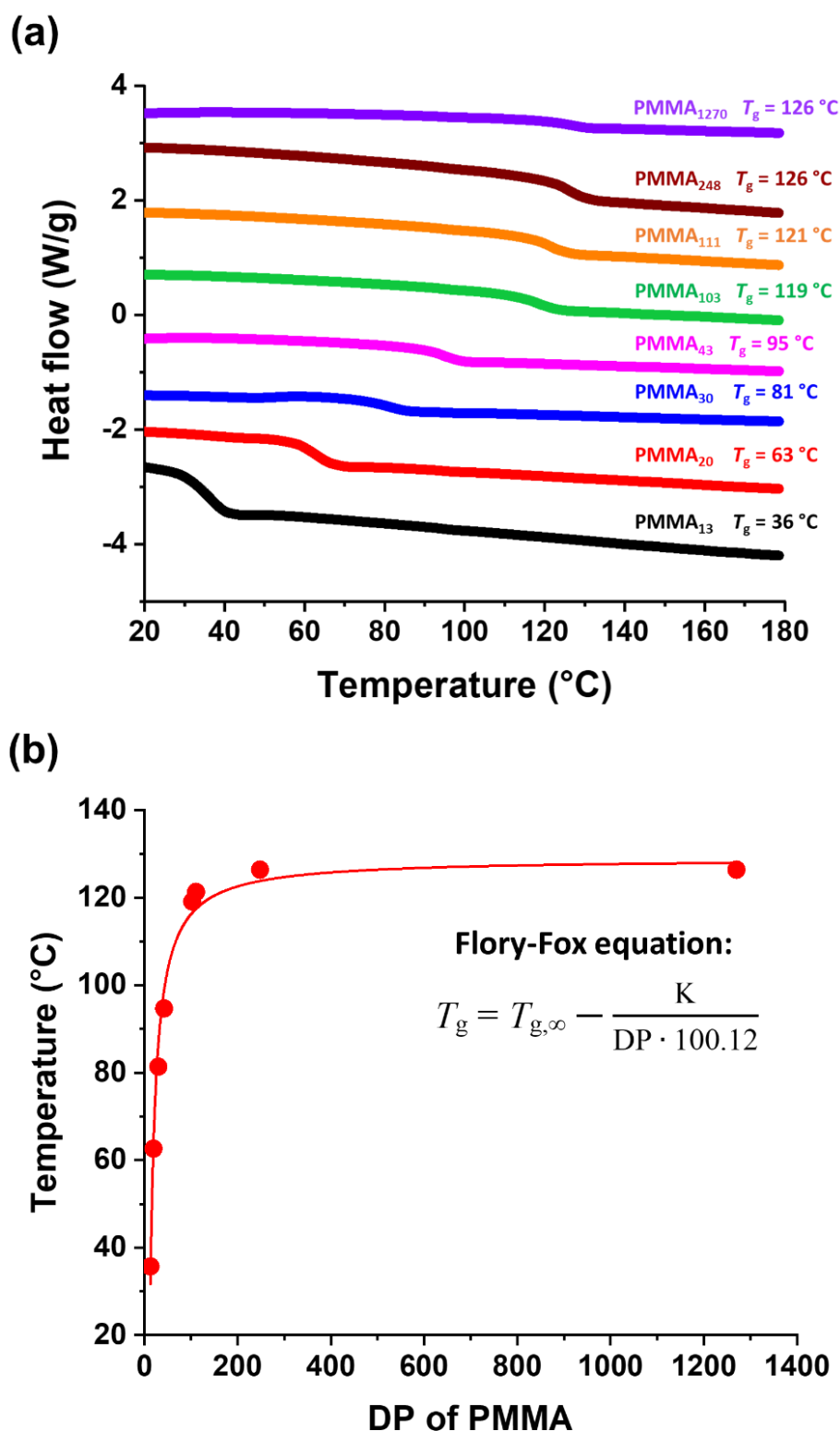
Figure 4.10. (a) DSC thermograms obtained for a series of near-monodisperse PMMA homopolymers with mean degrees of polymerization (DPs) ranging between 13 and 1270. **(b)** Plot of T_g against mean DP for the same series of PMMA homopolymers. Fitting the Fox-Flory equation to the data points (see red curve) gives $T_{g,\infty} = 129 \pm 2$ °C and $K = 127\ 700 \pm 5\ 700$ g mol^{-1}.

To examine this hypothesis, four PLMA$_{22}$-PMMA$_x$ diblock copolymers were purified by precipitation to remove residual monomer and solvent and subsequently analyzed by DSC, see **Figure 4.11**. It is perhaps worth emphasizing that the T_g of the PMMA$_x$ blocks determined by this method is almost certainly higher than the effective T_g of the growing PMMA chains during PISA. This is because the presence of unreacted MMA monomer within the nanoparticle cores most likely lowers the effective T_g. Bearing in mind this caveat, the T_g for PLMA$_{22}$-PMMA$_{69}$, which comprises mainly short worms, was determined to be 91 °C. This is very close to the reaction temperature and may explain why only rather short (as opposed to relatively long) worms could be formed. At intermediate conversions, the growing PMMA chains possess a T_g well below 90 °C and hence are relatively mobile. However, they become increasingly stiff as the MMA polymerization nears completion because (i) the higher PMMA DP leads to a higher T_g and (ii) the lower MMA concentration leads to less plasticization of the PMMA chains. This inevitably reduces the efficiency of the 1D stochastic fusion of multiple spheres that is required to generate the worm morphology.[2,11,15,26] Inspecting **Figure 4.11**, increasing the PMMA DP from 69 to 194 raises the T_g to approximately 113 °C. According to our PISA synthesis protocol, increasing the target PMMA DP also means a higher MMA concentration within the reaction mixture. Since MMA acts as a co-solvent for the diblock copolymer chains, this delays micellar nucleation until a higher critical PMMA DP is achieved. Presumably, when targeting higher PMMA DPs at 90 °C, the growing chains quickly become too immobile to allow evolution of the copolymer morphology from the spheres that are formed during micellar nucleation. It is noteworthy to mention that there are various literature reports of aqueous and alcoholic PISA formulations in which nanoparticles with higher order morphologies have been obtained when employing polystyrene as a core-forming block.[27–31] The T_g of polystyrene is comparable to that of PMMA, which suggests that there are likely to be further as-yet-unidentified synthesis parameters that may also influence the evolution in copolymer morphology.
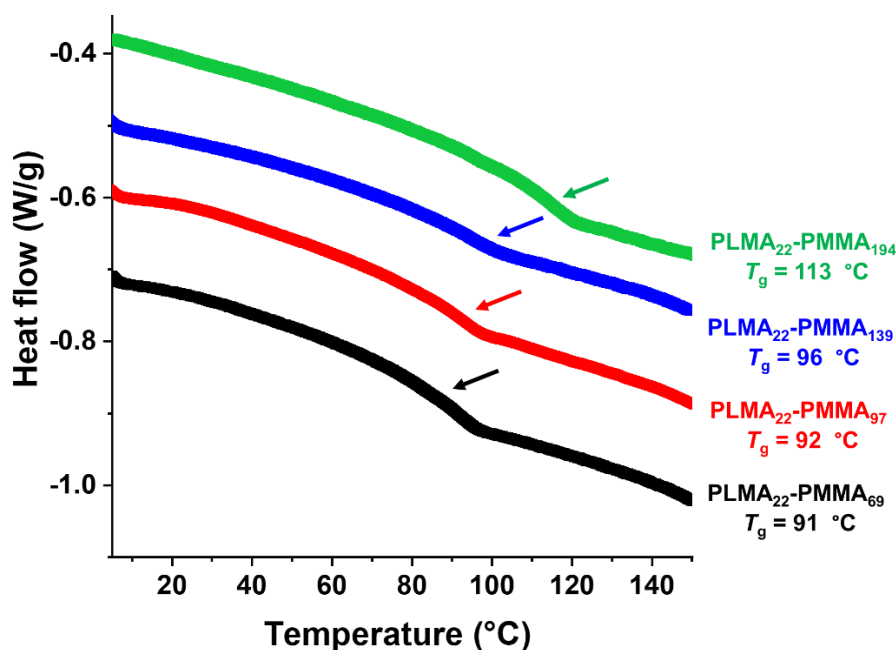
Figure 4.11. DSC curves recorded for dried PLMA$_{22}$-PMMA$_{69}$, PLMA$_{22}$-PMMA$_{97}$, PLMA$_{22}$-PMMA$_{139}$ and PLMA$_{22}$-PMMA$_{194}$ diblock copolymers (after purification to remove residual monomer and solvent). Clearly, longer PMMA blocks (*i.e.*, higher DPs) lead to higher T_g values.

For the present PISA formulation, targeting x $\geq$ 108 for PLMA$_{22}$-PMMA$_x$ nano-objects invariably produced colloidally unstable micron-sized aggregates comprising kinetically-trapped spheres (see **Figure 4.7g**). Furthermore, DLS studies of a series of PLMA$_{41}$-PMMA$_x$ spheres revealed a linear relationship between the z-average diameter and PMMA DPs of 29 to 118 when the data are plotted on a log-log scale (see **Figure 4.12**).

This enables fine control to be achieved over the particle size over this compositional range. However, the pronounced upturn in apparent particle size indicated by DLS studies suggests incipient nanoparticle flocculation when targeting higher PMMA DPs (x $\geq$ 137). This interpretation is consistent with selected TEM images of such nanoparticles shown in **Figure 4.7e** and **4.7f**. We are currently unable to explain these unexpected observations. It seems that the longer PLMA chains are unable to confer effective steric stabilization under such conditions.
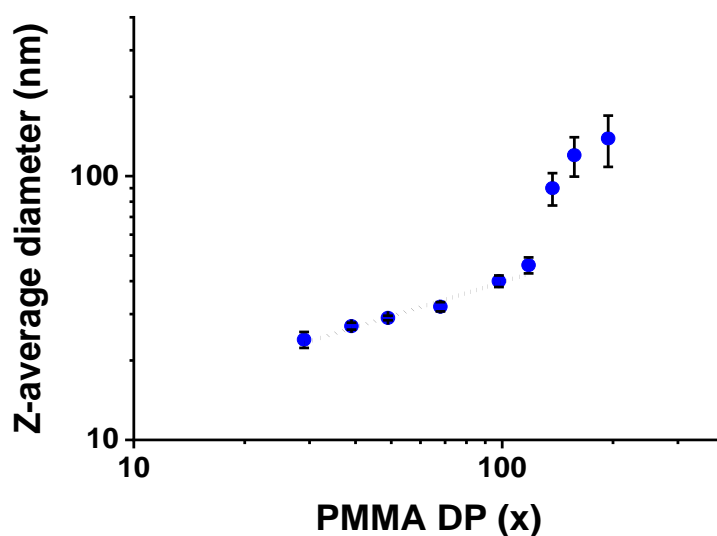
Figure 4.12. Double logarithmic plot for the relationship between z-average diameter *vs*. PMMA DP (x) for a series of PLMA$_{41}$-PMMA$_x$ (ranging x from 29 to 194) spheres prepared by RAFT dispersion polymerization of MMA at 90 °C in mineral oil targeting 20% w/w solids using the two-pot protocol (see **Table 9.7**). [N.B. Standard deviations are calculated from the DLS polydispersities and thus indicate the breadth of the particle size distributions, rather than the experimental error].

However, this is rather surprising given that significantly higher core-forming block DPs can be targeted for comparable PISA formulations conducted in non-polar media. For example, Derry *et al.* used a PLMA$_{47}$ precursor to grow core-forming blocks with a mean DP of up to 495 for the RAFT dispersion polymerization of benzyl methacrylate (BzMA) at 90 °C in mineral oil.[7] In this case, well-defined colloidally stable spherical nanoparticles were obtained at up to 50% w/w solids. In closely-related work, Derry *et al.* also used a relatively short poly(stearyl methacrylate) (PSMA$_{31}$) precursor to target a PBzMA DP of up to 2000 in mineral oil.[32] In a follow-up study, Parker and co-workers were able to target PBzMA DPs of up to 3500 using a PSMA$_{54}$ precursor.[33] Similarly, Docherty *et al.* utilized a PSMA$_{13}$ precursor to grow poly(glycidyl methacrylate) chains with DPs of up to 400 in mineral oil without any loss of colloidal stability for the resulting sterically-stabilised spheres.[8] Moreover, the colloidal instability observed in the present study does not seem to be related to the polymerization kinetics. For example, using 2-hydroxypropyl methacrylate (HPMA) leads to a significantly faster rate of RAFT dispersion polymerization compared to less polar methacrylic monomers (e.g. BzMA or MMA), yet PHPMA DPs of up to 150 can be targeted using an oligomeric PSMA$_9$ precursor to generate a vesicular morphology without any loss in colloidal stability.[34]

Bearing in mind these prior studies, we conducted a series of PISA syntheses using a longer PSMA block, since this was expected to confer more effective steric stabilization. More specifically, we targeted $PSMA_{37}$-$PMMA_{30-400}$ nano-objects at 20% w/w solids in mineral oil using an alternative trithiocarbonate-based RAFT agent at 90 °C (see **Figure 4.13** and **Table 9.10**).
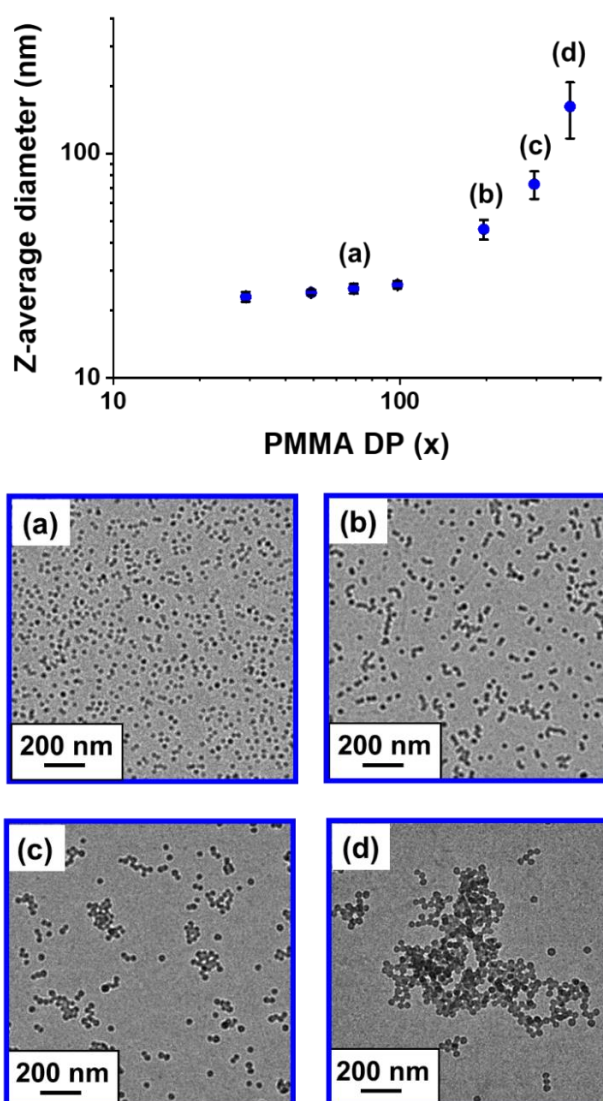
Figure 4.13. Double logarithmic plot for the relationship between z-average diameter and PMMA DP (x) for a series of $PSMA_{37}$-$PMMA_x$ (ranging x from 29 to 392) spheres prepared by RAFT dispersion polymerization of MMA at 90 °C in mineral oil targeting 20% w/w solids using the two-pot protocol. [N.B. Standard deviations are calculated from the DLS polydispersities and thus indicate the breadth of the particle size distributions, rather than the experimental error]. Representative TEM images obtained for **(a)** $PSMA_{37}$-$PMMA_{69}$ **(b)** $PSMA_{37}$-$PMMA_{196}$ **(c)** $PSMA_{37}$-$PMMA_{294}$ and **(d)** $PSMA_{37}$-$PMMA_{392}$ spherical nanoparticles. The apparent aggregation observed in (c) and (d) is consistent with the upturn in the DLS diameter observed above a PMMA DP of 100 and indicates incipient flocculation for these larger spheres.

Interestingly, DLS studies of these diluted dispersions indicated that colloidally stable spheres were obtained up to a PMMA DP of 100 but only colloidally unstable aggregates were formed when targeting higher DPs. These observations, combined with the results obtained for the series of PSMA$_{10}$-PMMA$_x$ nano-objects (see **Figure 4.9c**), suggest that the morphological constraints reported herein are independent of the nature of the steric stabilizer block.

We recently observed that a remarkably similar constraint also applies to the RAFT aqueous emulsion polymerization of MMA at 70 °C.[35] Thus, targeting PMMA DPs up to 80–100 using a non-ionic hydrophilic stabilizer block produced well-defined spheres at 10% w/w solids yet colloidally unstable aggregates were invariably formed when targeting a PMMA DP of 130. This latter observation implies that this phenomenon is likely to be a specific problem associated with the growth of PMMA core-forming blocks below their effective T_g.

Yang *et al*. reported the PISA synthesis of poly(methacrylic acid)-poly(styrene-*alt*-*N*-phenylmaleimide) diblock copolymer nano-objects in a binary mixture of ethanol and 1,4-dioxane at 70 °C. This reaction temperature is well below the T_g of 219 °C for the core-forming block so vesicles cannot be produced under such conditions. Indeed, this observation was explained in terms of the stiff, inflexible nature of the diblock copolymer chains under the synthesis conditions.[36] Similarly, Wang *et al*. reported that the copolymer morphology strongly depends on the polymerization temperature for the PISA synthesis of poly(oligo(ethylene oxide) methyl ether methacrylate)-poly(benzyl methacrylate) diblock copolymer nanoparticles in ethanol.[18] More specifically, worms or vesicles could be accessed when the BzMA polymerization was conducted at 65 °C (*i.e.* above the T_g of the insoluble PBzMA block), whereas only spheres or spherical aggregates could be obtained for syntheses conducted at 25 °C. Similarly, Sobotta *et al*. examined the synthesis of poly(*N*-acryloylmorpholine)-poly(*N*-acryloylthiomorpholine) (PNAM-PNAT) diblock copolymer nano-objects in aqueous solution. Despite the high T_g of the core-forming PNAT block, the copolymer morphology could be varied from spheres to lamellae when targeting the same diblock copolymer composition (PNAM$_{25}$-PNAT$_{25}$) simply by increasing the synthesis temperature.[37]

In view of these encouraging literature precedents, we decided to examine the PISA synthesis of PLMA$_{22}$-PMMA$_x$ nano-objects above the T_g of PMMA. Since the T_g of the diblock copolymer with the highest PMMA DP (PLMA$_{22}$-PMMA$_{194}$) was 113 °C, we selected the reaction temperature to be 115 °C and chose DCP (whose 10 h half-life is 114 °C) as a suitable

initiator. There are two potential technical problems to consider: (i) the thermal stability of the RAFT chain-ends at this elevated temperature and (ii) the potential loss of MMA during the polymerization as its boiling point (101 °C) is below the reaction temperature. For RAFT dispersion polymerizations conducted in non-polar media, our prior studies indicated that trithiocarbonates are much more resistant to thermal degradation than dithiobenzoates (see **Chapter 3**).[5] Moreover, GPC analysis of diblock copolymers prepared at 115 °C resulted in M_n and M_w/M_n data comparable to those observed for the same diblock composition prepared at 90 °C (see **Table 9.6** and **9.11**). A pseudo-phase diagram was constructed (see **Figure 4.14**) to compare the PLMA$_{22}$-PMMA$_x$ nano-objects prepared at 90 °C to those synthesized at 70 °C and 115 °C, respectively (see **Table 9.11**). A similar evolution in morphology from spheres, short worms to colloidally unstable aggregates was observed for PISA syntheses conducted at either 70 °C or 90 °C. However, targeting the same diblock copolymers at 115 °C merely led to the formation of kinetically-trapped spheres of increasing size when targeting PMMA DPs of 50–400 (see **Figure 4.14a-d**). This was a wholly unexpected observation, because selecting this higher temperature was meant to facilitate the evolution in morphology, rather than suppress it.

Recently, Cornel *et al*. used time-resolved small-angle neutron scattering to demonstrate rapid exchange of individual copolymer chains for a binary mixture of PLMA$_{39}$-PMMA$_{55}$ and PLMA$_{39}$-d$_8$PMMA$_{57}$ spheres on heating to 150 °C for 3 min.[16] Copolymer chain exchange (which produces hybrid nanoparticle cores comprising both PMMA$_{55}$ and d$_8$PMMA$_{57}$ blocks) was observed even at 80 °C, which is below the effective T_g for these relatively short core-forming blocks. Given that only spherical nanoparticles were formed during PISA syntheses conducted at 115 °C (**Figure 4.14e**), these findings suggest that a chain expulsion/insertion mechanism[16,38–47] most likely occurs under such conditions. In contrast, a micelle fusion/fission mechanism[39,45–47] appears to be favored at either 70 °C or 90 °C, since such conditions enable the formation of short worms.
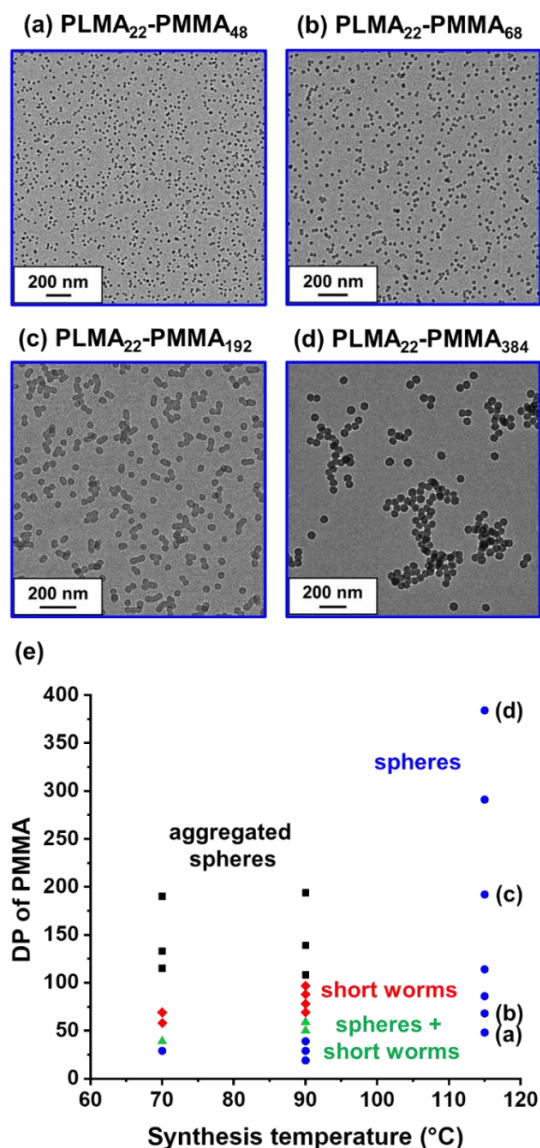
Figure 4.14. Representative TEM images recorded for the following spherical nanoparticles prepared at 20% w/w solids in mineral oil at 115 °C: **(a)** $PLMA_{22}$-$PMMA_{48}$, **(b)** $PLMA_{22}$-$PMMA_{68}$, **(c)** $PLMA_{22}$-$PMMA_{192}$ and **(d)** $PLMA_{22}$-$PMMA_{384}$. **(e)** Pseudo-phase diagram constructed for three series of $PLMA_{22}$-$PMMA_x$ nano-objects prepared by RAFT dispersion polymerization of MMA in mineral oil using the two-pot protocol employing a $PLMA_{22}$ precursor and AIBN initiator at 70 °C, T21s initiator at 90 °C or DCP initiator at 115 °C ([$PLMA_{22}$]/[initiator] molar ratio = 3.0).

4.3.6. SAXS analysis of PLMA-PMMA diblock copolymer nanoparticles

The pseudo-phase diagrams for $PLMA_y$-$PMMA_x$ nano-objects shown in **Figures 4.7** and **4.14** were constructed using TEM.[15,48,49] However, this imaging technique invariably suffers from poor statistics. Thus, small-angle X-ray scattering (SAXS) patterns were also recorded for 1.0%

w/w dispersions of four examples of PLMA$_{22}$-PMMA$_x$ nano-objects originally synthesized at 20% w/w solids in mineral oil (see **Figure 4.15**).
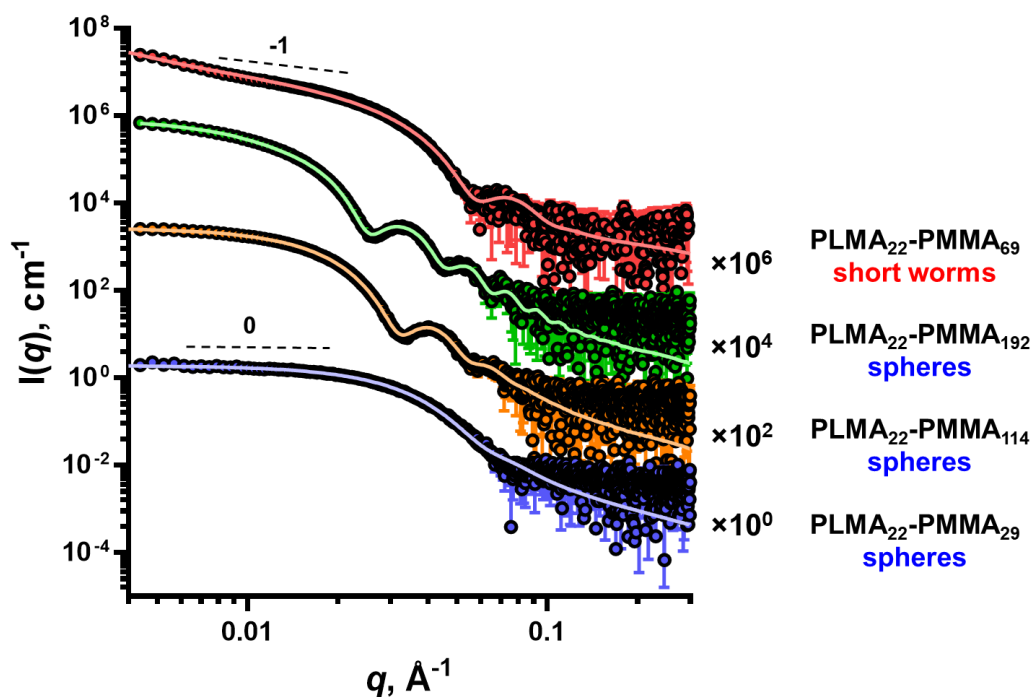
Figure 4.15. Small-angle X-ray scattering (SAXS) patterns and data fits (solid lines) obtained for 1.0% w/w dispersions of PLMA$_{22}$-PMMA$_{29}$, PLMA$_{22}$-PMMA$_{114}$ and PLMA$_{22}$-PMMA$_{192}$ spheres and PLMA$_{22}$-PMMA$_{69}$ short worms in mineral oil at 20 °C. The PLMA$_{22}$-PMMA$_{29}$ spheres and PLMA$_{22}$-PMMA$_{69}$ short worms were originally prepared at 90 °C at 20% w/w solids in mineral oil using the two-pot protocol while PLMA$_{22}$-PMMA$_{114}$ and PLMA$_{22}$-PMMA$_{192}$ spheres were prepared under the same conditions at 115 °C. Dashed lines indicate gradients of 0 and –1 for guidance.

It is well-known that the low q gradient provides morphological information.[50] Thus a zero gradient indicates spherical particles, whereas a gradient of –1 or –2 indicates worms or vesicles, respectively. Data were recorded for PLMA$_{22}$-PMMA$_{29}$ spheres and PLMA$_{22}$-PMMA$_{69}$ short worms prepared at 90 °C and also for PLMA$_{22}$-PMMA$_{114}$ and PLMA$_{22}$-PMMA$_{192}$ spheres synthesized at 115 °C. The low q gradients observed for these four samples (see **Figure 4.15**) are consistent with the morphologies assigned by TEM (see **Figures 4.7, 4.14** and **4.16**). Fitting the SAXS pattern obtained for PLMA$_{22}$-PMMA$_{29}$ using a well-known spherical micelle model[51] indicated an overall diameter (D_{sphere}) of 14.4 ± 2.6 nm with a mean aggregation number (N_{agg}, or number of copolymer chains per nanoparticle) of 190 (see **Table 4.2**).

Similarly, satisfactory data fits to the SAXS patterns recorded for PLMA$_{22}$-PMMA$_{114}$ and PLMA$_{22}$-PMMA$_{192}$ spheres were obtained using the same spherical model. In the former case $D_{sphere} = 29.2 \pm 2.8$ nm and $N_{agg} = 570$, while in the latter case $D_{sphere} = 39.2 \pm 4.4$ nm and $N_{agg} = 900$. These volume-average diameters are consistent with the z-average diameters of 36 ± 1.1 nm for PLMA$_{22}$-PMMA$_{114}$ and 50 ± 2.0 nm for PLMA$_{22}$-PMMA$_{192}$ indicated by DLS studies.

Table 4.2. Summary of the structural parameters obtained from fitting SAXS patterns recorded for a series of PLMA$_{22}$-PMMA$_x$ nano-objects using either a spherical micelle or a worm-like micelle model.[51] D_{sphere} is the overall sphere diameter such that $D_{sphere} = 2R_s + 4R_g$, where R_s is the mean core radius and R_g is the radius of gyration of the stabilizer chains. T_{worm} is the overall worm thickness ($T_{worm} = 2R_{wc} + 4R_g$, where R_{wc} is the mean worm core radius) and L_{worm} is the mean worm contour length. N_{agg} is the mean aggregation number (*i.e.* the mean number of copolymer chains per nano-object).

Block copolymer	Copolymer Morphology	D_{sphere} (nm)	T_{worm} (nm)	L_{worm} (nm)	N_{agg}
PLMA$_{22}$-PMMA$_{29}$	Spheres	14.4 ± 2.6	-	-	190
PLMA$_{22}$-PMMA$_{69}$	Worms	-	14.2 ± 1.4	200	540
PLMA$_{22}$-PMMA$_{114}$	Spheres	29.2 ± 2.8	-	-	570
PLMA$_{22}$-PMMA$_{192}$	Spheres	39.2 ± 4.4	-	-	900

Unfortunately, the restricted q range used to record the SAXS pattern for PLMA$_{22}$-PMMA$_{69}$ did not enable precise determination of the worm contour length. However, a satisfactory data fit could be obtained using a worm-like micelle model[51] by fixing the worm contour length at 200 nm (as estimated by TEM analysis). This pragmatic approach indicated an overall cross-sectional worm diameter or worm thickness (T_{worm}) of 14.2 ± 1.4 nm and an N_{agg} of 540.

4.3.7. Thermo-responsive behavior of PLMA$_{22}$-PMMA$_{69}$ short worms

The thermoresponsive behavior of PLMA$_{22}$-PMMA$_{69}$ short worms was examined. This diblock copolymer was selected because this PMMA DP was the lowest for which a soft, free-standing gel was obtained. Moreover, our prior studies suggested that thermally-induced morphology transitions were more likely to occur for diblock compositions that lie close to the phase boundary.[52] For DLS analysis, the 20% w/w dispersion of PLMA$_{22}$-PMMA$_{69}$ short worms in

mineral oil was diluted to 0.1% w/w using *n*-dodecane. This solvent was preferred as the diluent because it evaporates much faster than mineral oil and does not leave any involatile residues during TEM grid preparation. The resulting dilute dispersion was heated from 20 °C to 150 °C, with an annealing time of 30 min at each intermediate temperature. An aliquot of this dispersion was extracted at each temperature and cooled to 20 °C prior to DLS measurements. This unusual protocol was adopted because the upper limit temperature for our DLS instrument was only 90 °C, which is insufficient to observe the worm-to-sphere transition for this system. The implicit assumption here is that the dilute nature of the dispersion ensures that the evolving copolymer morphology is always quenched on cooling to 20 °C after each successive thermal annealing step. The initial apparent sphere-equivalent z-average diameter was determined to be 273 nm (DLS PDI = 0.63), see **Figure 4.16a**.
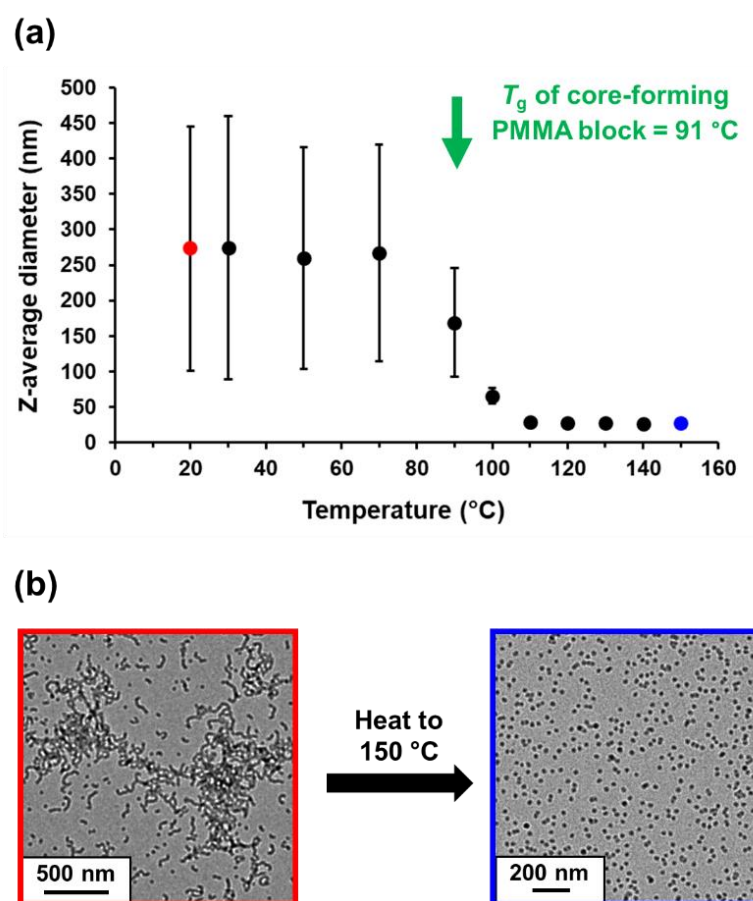
Figure 4.16. (a) DLS studies showing the variation in apparent hydrodynamic diameter for a 0.1 % w/w PLMA$_{22}$-PMMA$_{69}$ dispersion prepared by dilution using *n*-dodecane on heating from 20 to 150 °C [N.B. Standard deviations were calculated from the DLS polydispersity data and indicate the breadth of the particle size distribution, rather than the experimental error]. **(b)** Representative TEM images obtained for the initial short worms (red frame) and the final spheres that are formed after heating to 150 °C (blue frame).

This data is consistent with the polydisperse short worms (plus a minor population of spheres) observed by TEM studies (see **Figure 4.16b**). Heating led to a gradual reduction in the apparent hydrodynamic diameter from 267 nm at 70 °C to 169 nm at 90 °C to 66 nm at 100 °C. There is also a significant reduction in the PDI from 0.57 to 0.17 over this temperature range. These observations correlate well with the T_g of the core-forming block, which is 91 °C for $PLMA_{22}$-$PMMA_{69}$ (see **Figure 4.11**). On further heating to 110 °C, a z-average diameter of 29 nm and a PDI of 0.05 were observed, which is consistent with the presence of well-defined spherical nanoparticles. Indeed, TEM analysis of the nano-objects formed after thermal equilibration at 150 °C confirmed this morphology, see **Figure 4.16b**. Given that this dilute dispersion was cooled to 20 °C prior to DLS analysis, these observations suggest that this thermally-induced morphological transition is essentially irreversible under such conditions. Similar observations were reported by Fielding *et al*. for a dilute dispersion of $PLMA_{16}$-$PBzMA_{37}$ worms in *n*-dodecane (see **Chapter 1**).[2] Clearly, the probability of 1D stochastic fusion of multiple spheres to reform the original short worms is very low at 20 °C, not least because this quenching temperature is well below the T_g of the PMMA block.

The gel comprising $PLMA_{22}$-$PMMA_{69}$ short worms that is formed at 20% w/w solids was characterized by variable temperature oscillatory rheology. This technique has been previously used to study worm-to-sphere[2] and vesicle-to-worm[52,53] transitions for various diblock copolymer systems. As discussed in **Chapter 2**, the critical gelation temperature (CGT) is indicated by the intersection of the storage modulus (G') and loss modulus (G'') curves and was determined to be 103 °C for the $PLMA_{22}$-$PMMA_{69}$ gel (see **Figure 4.17a**). This is consistent with DLS studies, which indicated that only spheres can be obtained above 100 °C (see **Figure 4.16a**). Fielding *et al*. reported a similar rheology study of a $PLMA_{16}$-$PBzMA_{37}$ worm gel prepared in *n*-dodecane. [2] In that case, the morphology transition was more or less reversible because the CGT determined during the heating run was close to that observed on cooling (see **Chapter 1**). However, the storage modulus for the reconstituted worm gel was reduced from 2300 Pa to 67 Pa, which suggests that significantly shorter worms were formed on the timescale of the experiment. In the present study, intersection of the G' and G'' curves indicated a CGT of approximately 103 °C and the initial and final G' values were 2900 Pa and 65 Pa, respectively. This significant reduction in G' is comparable to that reported by Fielding *et al*.[2] However, in our case, only a highly viscous fluid was obtained after the thermal cycle instead of a free-standing gel. TEM analysis of the final copolymer dispersion revealed mainly spheres

and only a minor population of short worms. Moreover, the mean contour length of the latter nano-objects was significantly shorter than that of the original sample (compare the two TEM images shown in **Figure 4.17**).
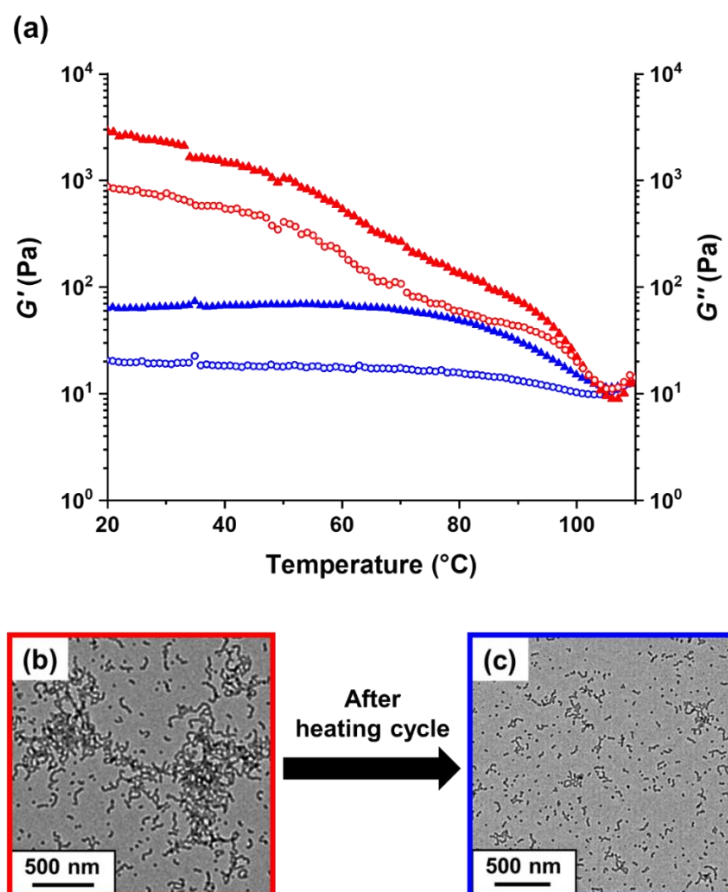
Figure 4.17. (a) Variation in storage moduli (G', filled triangles) and loss moduli (G'', hollow circles) observed for a 20% w/w dispersion of PLMA$_{22}$-PMMA$_{69}$ short worms in mineral oil on heating from 20 to 110 °C (red symbols) and cooling from 110 to 20 °C (blue symbols) at 2.0 °C min^{-1}. Data were recorded at 1.0% strain amplitude using an angular frequency of 10 rad s^{-1}. Representative TEM images recorded for **(b)** the initial PLMA$_{22}$-PMMA$_{69}$ short worms and **(c)** the mixed phase of PLMA$_{22}$-PMMA$_{69}$ short worms and spheres obtained after this oscillatory rheology study.

As discussed for PLMA$_{16}$-PBzMA$_{37}$ worms[2] in **Chapter 1**, this worm-to-sphere transition is driven *via* surface plasticization of the worms by ingress of hot solvent. This leads to an increase in the volume fraction of the PLMA$_{22}$ stabilizer block relative to the PMMA$_{69}$ core-forming block, which results in a reduction in the critical packing parameter (P) and thus favors the formation of spheres. It is perhaps noteworthy that the synthesis temperature of 115 °C examined in **Figure 4.14** exceeds the CGT observed for the 20% w/w dispersion of PLMA$_{22}$-

151

PMMA$_{69}$ nano-objects (see **Figure 4.17**). Given that this CGT is associated with a worm-to-sphere transition, this explains why worms cannot be produced at this relatively high temperature: this morphology is simply thermodynamically unstable with respect to spheres under such conditions.

TEM was used to assess the reversibility of the worm-to-sphere transition for the original 20% w/w dispersion of PLMA$_{22}$-PMMA$_{69}$ worms in the absence of applied shear. This worm gel was equilibrated at 150 °C for 1 h, then a small aliquot was extracted and immediately diluted to 0.1% w/w using hot *n*-dodecane to assess the copolymer morphology. Thereafter, the concentrated dispersion was allowed to cool to 20 °C and then stored at this temperature for 24 h prior to dilution with *n*-dodecane for TEM analysis. Unlike the PLMA$_{16}$-PBzMA$_{37}$ worms reported by Fielding *et al.*,[2] the original gel was not reformed. Instead, a highly viscous fluid was obtained after this thermal cycle. As shown in **Figure 4.18a**, a worm-to-sphere transition was observed on heating but only partial worm reconstitution occurred on cooling to 20 °C. This thermal annealing experiment was repeated but this time the copolymer dispersion was maintained at 90 °C (*i.e.* around the T_g of the PMMA$_{69}$ chains) for 24 h, instead of simply cooling to 20 °C. However, after ageing for a further 24 h at 20 °C, TEM studies indicated an irreversible worm-to-sphere transition in this case (see **Figure 4.18b**).
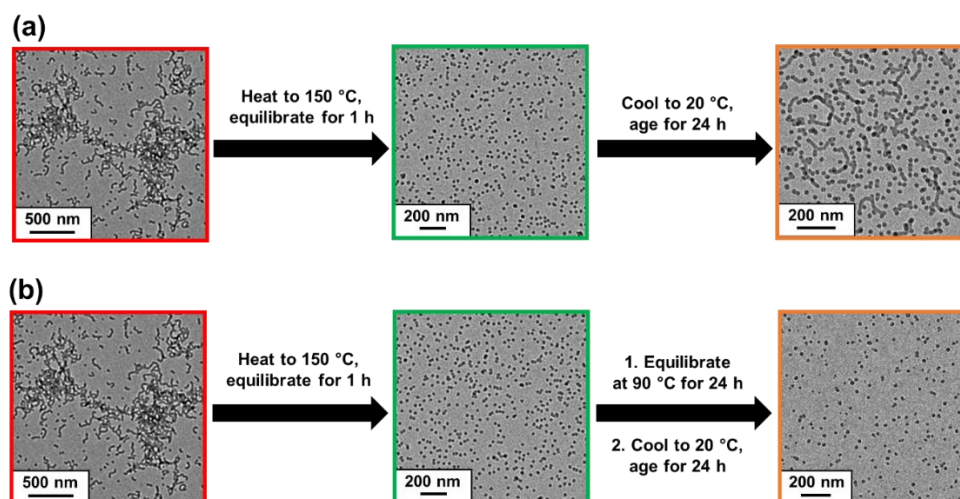
Figure 4.18. Representative TEM images recorded during the worm-to-sphere transition for the PLMA$_{22}$-PMMA$_{69}$ short worms prepared at 20% w/w solids in mineral oil. **(a)** This initial copolymer dispersion (red frame) was heated to 150 °C and equilibrated for 1 h at this temperature, prior to dilution with hot *n*-dodecane (green frame) and finally aged for 24 h at 20 °C (orange frame). **(b)** The same copolymer dispersion (red frame) was heated to 150 °C and equilibrated for 1 h at this temperature, prior to dilution with hot *n*-dodecane (green frame) followed by further equilibration at 90 °C for 24 h, cooling to 20 °C and ageing for 24 h (orange frame).

4.4. Conclusions

A series of PLMA$_y$-PMMA$_x$ nano-objects were prepared *via* RAFT dispersion polymerization of MMA using a PLMA$_{22}$, PLMA$_{30}$ or PLMA$_{41}$ precursor at 90 °C in mineral oil at 20% w/w solids. ^{1}H NMR spectroscopy studies indicated that more than 97% MMA conversion was achieved for such PISA syntheses, while THF GPC confirmed relatively narrow molecular weight distributions ($M_w/M_n \leq 1.39$). An efficient one-pot protocol for the synthesis of PLMA$_{19}$-PMMA$_x$ nano-objects enabled higher blocking efficiencies and narrower molecular weight distributions to be achieved compared to the traditional two-pot protocol using a purified PLMA$_{22}$ precursor. DLS, TEM and SAXS were used to assess the copolymer morphology. Surprisingly, we were unable to access vesicles, even when using the shortest PLMA$_{22}$ precursor. Instead, only spherical or relatively short worms could be obtained. Moreover, micron-sized colloidally unstable aggregates of spheres were invariably produced when targeting higher PMMA DPs (e.g. PLMA$_{22}$-PMMA$_{139}$ or PLMA$_{22}$-PMMA$_{194}$). Such morphological constraints were also observed when performing PISA syntheses (i) at 30% w/w solids in mineral oil, (ii) at 20% w/w solids in *n*-dodecane, or (iii) when employing an alternative steric stabilizer block. The experimental evidence presented herein suggests that these unexpected limitations are related to the high T_g of the core-forming PMMA block. In an attempt to overcome this problem, the synthesis of PLMA$_{22}$-PMMA$_x$ nano-objects was also studied at 115 °C (above the T_g of PMMA). However, only kinetically-trapped spheres were obtained, which suggests that a chain expulsion/insertion mechanism may operate under such conditions. In contrast, the formation of short worms at 70–90 °C suggests a micelle fusion mechanism. Finally, the thermoresponsive behavior of PLMA$_{22}$-PMMA$_{69}$ short worms was assessed by DLS, TEM and oscillatory rheology. A worm-to-sphere transition occurred on heating above 100 °C, which proved to be only partially reversible on cooling. This is consistent with the observation of kinetically-trapped spheres at 115 °C because short worms are thermodynamically unstable with respect to spheres at this temperature.

4.5. References

(1)   Docherty, P. J.; Girou, C.; Derry, M. J.; Armes, S. P. Epoxy-Functional Diblock Copolymer Spheres, Worms and Vesicles via Polymerization-Induced Self-Assembly in Mineral Oil. *Polym. Chem.* **2020**, *11*, 3332–3339.

(2)   Fielding, L. A.; Lane, J. A.; Derry, M. J.; Mykhaylyk, O. O.; Armes, S. P. Thermo-Responsive Diblock Copolymer Worm Gels in Non-Polar Solvents. *J. Am. Chem. Soc.* **2014**, *136*, 5790–5798.

(3)   Trent, J. S. Ruthenium Tetraoxide Staining of Polymers: New Preparative Methods for Electron Microscopy. *Macromolecules* **1984**, *17*, 2930–2931.

(4)   Ilavsky, J.; Jemian, P. R. Irena: Tool Suite for Modeling and Analysis of Small-Angle Scattering. *J. Appl. Crystallogr.* **2009**, *42*, 347–353.

(5)   Cornel, E. J.; Meurs, S. Van; Smith, T.; Hora, P. S. O.; Armes, S. P. In Situ Spectroscopic Studies of Highly Transparent Nanoparticle Dispersions Enable Assessment of Trithiocarbonate Chain-End Fidelity during RAFT Dispersion Polymerization in Nonpolar Media. *J. Am. Chem. Soc.* **2018**, *140*, 12980–12988.

(6)   Cunningham, V. J.; Derry, M. J.; Fielding, L. A.; Musa, O. M.; Armes, S. P. RAFT Aqueous Dispersion Polymerization of N-(2-(Methacryloyloxy)Ethyl)Pyrrolidone: A Convenient Low Viscosity Route to High Molecular Weight Water-Soluble Copolymers. *Macromolecules* **2016**, *49*, 4520–4533.

(7)   Derry, M. J.; Fielding, L. A.; Armes, S. P. Industrially-Relevant Polymerization-Induced Self-Assembly Formulations in Non-Polar Solvents: RAFT Dispersion Polymerization of Benzyl Methacrylate. *Polym. Chem.* **2015**, *6*, 3054–3062.

(8)   Docherty, P. J.; Derry, M. J.; Armes, S. P. RAFT Dispersion Polymerization of Glycidyl Methacrylate for the Synthesis of Epoxy-Functional Block Copolymer Nanoparticles in Mineral Oil. *Polym. Chem.* **2019**, *10*, 603–611.

(9)   Rymaruk, M. J.; Hunter, S. J.; O'Brien, C. T.; Brown, S. L.; Williams, C. N.; Armes, S. P. RAFT Dispersion Polymerization in Silicone Oil. *Macromolecules* **2019**, *52*, 2822–2832.

(10)   Darmau, B.; Rymaruk, M. J.; Warren, N. J.; Bening, R.; Armes, S. P. RAFT Dispersion Polymerization of Benzyl Methacrylate in Non-Polar Media Using Hydrogenated Polybutadiene as a Steric Stabilizer Block. *Polym. Chem.* **2020**, *11*, 7533–7541.

(11)   Blanazs, A.; Madsen, J.; Battaglia, G.; Ryan, A. J.; Armes, S. P. Mechanistic Insights for Block Copolymer Morphologies: How Do Worms Form Vesicles? *J. Am. Chem. Soc.* **2011**, *133*, 16581–16587.

(12)   Chiefari, J.; Chong, Y. K. B.; Ercole, F.; Krstina, J.; Jeffery, J.; Le, T. P. T.; Mayadunne, R. T. A.; Meijs, G. F.; Moad, C. L.; Moad, G.; Rizzardo, E.; Thang, S. H. Living Free-Radical Polymerization by Reversible Addition-Fragmentation Chain Transfer: The RAFT Process. *Macromolecules* **1998**, *31*, 5559–5562.

(13)   Moad, G.; Rizzardo, E.; Thang, S. H. Living Radical Polymerization by the RAFT Process. *Aust. J. Chem.* **2005**, *58*, 379–410.

(14)   Moad, G.; Rizzardo, E.; Thang, S. H. Radical Addition-Fragmentation Chemistry in Polymer Synthesis. *Polymer* **2008**, *49*, 1079–1131.

(15)   Fielding, L. A.; Derry, M. J.; Ladmiral, V.; Rosselgong, J.; Rodrigues, A. M.; Ratcliffe, L. P. D.; Sugihara, S.; Armes, S. P. RAFT Dispersion Polymerization in Non-Polar Solvents:

Facile Production of Block Copolymer Spheres, Worms and Vesicles in n-Alkanes. *Chem. Sci.* **2013**, *4*, 2081–2087.

(16)   Cornel, E. J.; Smith, G. N.; Rogers, S. E.; Hallett, J. E.; Growney, D. J.; Smith, T.; O'Hora, P. S.; Van Meurs, S.; Mykhaylyk, O. O.; Armes, S. P. Time-Resolved Small-Angle Neutron Scattering Studies of the Thermally-Induced Exchange of Copolymer Chains between Spherical Diblock Copolymer Nanoparticles Prepared via Polymerization-Induced Self-Assembly. *Soft Matter* **2020**, *16*, 3657–3668.

(17)   Zhou, J.; Zhang, W.; Hong, C.; Pan, C. Promotion of Morphology Transition of Di-Block Copolymer Nano-Objects: Via RAFT Dispersion Copolymerization. *Polym. Chem.* **2016**, *7*, 3259–3267.

(18)   Wang, G.; Schmitt, M.; Wang, Z.; Lee, B.; Pan, X.; Fu, L.; Yan, J.; Li, S.; Xie, G.; Bockstaller, M. R.; Matyjaszewski, K. Polymerization-Induced Self-Assembly (PISA) Using ICAR ATRP at Low Catalyst Concentration. *Macromolecules* **2016**, *49*, 8605–8615.

(19)   Fox, T. G.; Flory, P. J. Second-Order Transition Temperatures and Related Properties of Polystyrene. I. Influence of Molecular Weight. *J. Appl. Phys.* **1950**, *21*, 581–591.

(20)   Fox, T. G.; Flory, P. J. The Glass Temperature and Related Properties of Poly-Styrene. Influence of Molecular Weight. *J. Polym. Sci.* **1954**, *14*, 315–319.

(21)   Faivre, A.; David, L.; Vassoille, R.; Vigier, G.; Etienne, S.; Geissler, E. Electronic Density Fluctuations in Disordered Systems. 1. Effect of Thermal Treatments on the Dynamics and Local Microstructure of Poly(Methyl Methacrylate). *Macromolecules* **1996**, *29*, 8387–8390.

(22)   Porter, C. E.; Blum, F. D. Thermal Characterization of PMMA Thin Films Using Modulated Differential Scanning Calorimetry. *Macromolecules* **2000**, *33*, 7016–7020.

(23)   Brandrup, J.; Immergut, E. H.; McDowell, W. *Polymer Handbook*, 2nd ed.; Wiley: New York, 1975.

(24)   Lejars, M.; Margaillan, A.; Bressy, C. Well-Defined Graft Copolymers of Tert-Butyldimethylsilyl Methacrylate and Poly(Dimethylsiloxane) Macromonomers Synthesized by RAFT Polymerization. *Polym. Chem.* **2013**, *4*, 3282–3292.

(25)   Wang, W. W.; Jiang, L.; Ren, W. Y.; Zhang, C. M.; Man, C. Z.; Nguyen, T. P.; Dan, Y. The Crystallinity, Thermal Properties and Microscopic Morphology of Di-Block Copolymers of l-Lactide and Several Acrylates. *RSC Adv.* **2016**, *6*, 31934–31946.

(26)   Zhang, X.; Rieger, J.; Charleux, B. Effect of the Solvent Composition on the Morphology of Nano-Objects Synthesized via RAFT Polymerization of Benzyl Methacrylate in Dispersed Systems. *Polym. Chem.* **2012**, *3*, 1502–1509.

(27)   Pham, B. T. T.; Nguyen, D.; Huynh, V. T.; Pan, E. H.; Shirodkar-Robinson, B.; Carey, M.; Serelis, A. K.; Warr, G. G.; Davey, T.; Such, C. H.; Hawkett, B. S. Aqueous Polymeric Hollow Particles as an Opacifier by Emulsion Polymerization Using Macro-RAFT Amphiphiles. *Langmuir* **2018**, *34*, 4255–4263.

(28)   Rieger, J.; Zhang, W.; Stoffelbach, F.; Charleux, B. Surfactant-Free RAFT Emulsion Polymerization Using Poly(N,N -Dimethylacrylamide) Trithiocarbonate Macromolecular Chain Transfer Agents. *Macromolecules* **2010**, *43*, 6302–6310.

(29)   Huang, C. Q.; Pan, C. Y. Direct Preparation of Vesicles from One-Pot RAFT Dispersion Polymerization. *Polymer* **2010**, *51*, 5115–5121.

(30)   He, W. D.; Sun, X. L.; Wan, W. M.; Pan, C. Y. Multiple Morphologies of PAA-b-PSt Assemblies throughout RAFT Dispersion Polymerization of Styrene with PAA Macro-CTA.

Macromolecules **2011**, *44*, 3358–3365.

(31)   Wan, W. M.; Sun, X. L.; Pan, C. Y. Morphology Transition in RAFT Polymerization for Formation of Vesicular Morphologies in One Pot. *Macromolecules* **2009**, *42*, 4950–4952.

(32)   Derry, M. J.; Fielding, L. A.; Warren, N. J.; Mable, C. J.; Smith, A. J.; Mykhaylyk, O. O.; Armes, S. P. In Situ Small-Angle X-Ray Scattering Studies of Sterically-Stabilized Diblock Copolymer Nanoparticles Formed during Polymerization-Induced Self-Assembly in Non-Polar Media. *Chem. Sci.* **2016**, *7*, 5078–5090.

(33)   Parker, B. R.; Derry, M. J.; Ning, Y.; Armes, S. P. Exploring the Upper Size Limit for Sterically Stabilized Diblock Copolymer Nanoparticles Prepared by Polymerization-Induced Self-Assembly in Non-Polar Media. *Langmuir* **2020**, *36*, 3730–3736.

(34)   György, C.; Hunter, S. J.; Girou, C.; Derry, M. J.; Armes, S. P. Synthesis of Poly(Stearyl Methacrylate)-Poly(2-Hydroxypropyl Methacrylate) Diblock Copolymer Nanoparticles via RAFT Dispersion Polymerization of 2-Hydroxypropyl Methacrylate in Mineral Oil. *Polym. Chem.* **2020**, *11*, 4579–4590.

(35)   Chan, D. H. H.; Cockram, A. A.; Gibson, R. R.; Kynaston, E. L.; Lindsay, C.; Taylor, P.; Armes, S. P. RAFT Aqueous Emulsion Polymerization of Methyl Methacrylate: Observation of Unexpected Constraints When Employing a Non-Ionic Steric Stabilizer Block. *Polym. Chem.* **2021**, *12*, 5760–5769.

(36)   Yang, P.; Ratcliffe, L. P. D.; Armes, S. P. Efficient Synthesis of Poly(Methacrylic Acid)-Block-Poly(Styrene-Alt-N-phenylmaleimide) Diblock Copolymer Lamellae Using RAFT Dispersion Polymerization. *Macromolecules* **2013**, *46*, 8545–8556.

(37)   Sobotta, F. H.; Kuchenbrod, M.; Hoeppener, S.; Brendel, J. C. One Polymer Composition, Various Morphologies: The Decisive Influence of Conditions on the Polymerization-Induced Self-Assembly (PISA) of N-Acryloyl Thiomorpholine. *Nanoscale* **2020**, *12*, 20171–20176.

(38)   Choi, S. H.; Lodge, T. P.; Bates, F. S. Mechanism of Molecular Exchange in Diblock Copolymer Micelles: Hypersensitivity to Core Chain Length. *Phys. Rev. Lett.* **2010**, *104*, 047802.

(39)   Cornel, E. J.; O'Hora, P. S.; Smith, T.; Growney, D. J.; Mykhaylyk, O. O.; Armes, S. P. SAXS Studies of the Thermally-Induced Fusion of Diblock Copolymer Spheres: Formation of Hybrid Nanoparticles of Intermediate Size and Shape. *Chem. Sci.* **2020**, *11*, 4312–4321.

(40)   Choi, S. H.; Bates, F. S.; Lodge, T. P. Molecular Exchange in Ordered Diblock Copolymer Micelles. *Macromolecules* **2011**, *44*, 3594–3604.

(41)   Lu, J.; Bates, F. S.; Lodge, T. P. Remarkable Effect of Molecular Architecture on Chain Exchange in Triblock Copolymer Micelles. *Macromolecules* **2015**, *48*, 2667–2676.

(42)   Zhao, D.; Ma, Y.; Lodge, T. P. Exchange Kinetics for a Single Block Copolymer in Micelles of Two Different Sizes. *Macromolecules* **2018**, *51*, 2312–2320.

(43)   Zinn, T.; Willner, L.; Pipich, V.; Richter, D.; Lund, R. Molecular Exchange Kinetics of Micelles: Corona Chain Length Dependence. *ACS Macro Lett.* **2016**, *5*, 884–888.

(44)   Wang, Y.; Kausch, C. M.; Chun, M.; Quirk, R. P.; Mattice, W. L. Exchange of Chains between Micelles of Labeled Polystyrene-Block-Poly(Oxyethylene) As Monitored by Nonradiative Singlet Energy Transfer. *Macromolecules* **1995**, *28*, 904–911.

(45)   Haliloğlu, T.; Bahar, I.; Erman, B.; Mattice, W. L. Mechanisms of the Exchange of Diblock Copolymers between Micelles at Dynamic Equilibrium. *Macromolecules* **1996**, *29*, 4764–4771.

(46)   Dormidontova, E. E. Micellization Kinetics in Block Copolymer Solutions: Scaling Model. *Macromolecules* **1999**, *32*, 7630–7644.

(47)   Halperin, A.; Alexander, S. Polymeric Micelles: Their Relaxation Kinetics. *Macromolecules* **1989**, *22*, 2403–2412.

(48)   Blanazs, A.; Ryan, A. J.; Armes, S. P. Predictive Phase Diagrams for RAFT Aqueous Dispersion Polymerization: Effect of Block Copolymer Composition, Molecular Weight, and Copolymer Concentration. *Macromolecules* **2012**, *45*, 5099–5107.

(49)   Warren, N. J.; Mykhaylyk, O. O.; Mahmood, D.; Ryan, A. J.; Armes, S. P. RAFT Aqueous Dispersion Polymerization Yields Poly(Ethylene Glycol)-Based Diblock Copolymer Nano-Objects with Predictable Single Phase Morphologies. *J. Am. Chem. Soc.* **2014**, *136*, 1023–1033.

(50)   Glatter, O.; Kratky, O. *Small-Angle X-Ray Scattering*; Academic Press, London, 1982.

(51)   Pedersen, J. S. Form Factors of Block Copolymer Micelles with Spherical, Ellipsoidal and Cylindrical Cores. *J. Appl. Crystallogr.* **2000**, *33*, 637–640.

(52)   Derry, M. J.; Mykhaylyk, O. O.; Armes, S. P. A Vesicle-to-Worm Transition Provides a New High-Temperature Oil Thickening Mechanism. *Angew. Chemie - Int. Ed.* **2017**, *56*, 1746–1750.

(53)   Dorsman, I. R.; Derry, M. J.; Cunningham, V. J.; Brown, S. L.; Williams, C. N.; Armes, S. P. Tuning the Vesicle-to-Worm Transition for Thermoresponsive Block Copolymer Vesicles Prepared: Via Polymerisation-Induced Self-Assembly. *Polym. Chem.* **2021**, *12*, 1224–1235.

Chapter 5. Tuning the Glass Transition Temperature of a Core-Forming Block during Polymerization-Induced Self-Assembly: Statistical Copolymerization of Lauryl Methacrylate with Methyl Methacrylate Provides Access to Spheres, Worms, and Vesicles

Chapter 5. Tuning the Glass Transition Temperature of a Core-Forming Block during Polymerization-Induced Self-Assembly: Statistical Copolymerization of Lauryl Methacrylate with Methyl Methacrylate Provides Access to Spheres, Worms, and Vesicles

5.1. Introduction

As discussed in **Chapter 1**, the final copolymer morphology (e.g. spheres, worms or vesicles) obtained *via* PISA can often simply depend on the relative volume fractions of the soluble and insoluble blocks, as defined by the fractional packing parameter, P.[1,2] Indeed, there are many PISA formulations for which targeting a sufficiently asymmetric diblock composition (*i.e.* a relatively long insoluble block) leads to a progressive evolution in copolymer morphology from spheres to worms to vesicles. This is because the DP of the soluble block remains constant, so P must gradually increase during the growth of the insoluble block.[3,4] However, certain synthesis parameters can lead to morphological constraints. For example, it is well-known that kinetically-trapped spheres are usually obtained if the steric stabilizer precursor is relatively long[5–8] or has polyelectrolytic character (in the case of aqueous PISA formulations).[9,10] This is because strong inter-particle repulsive forces inhibit sphere-sphere fusion, which is the critical step in the evolution of the copolymer morphology. Another important parameter can be the glass transition temperature (T_g) of the insoluble structure-directing block. For example, Yang *et al*. found that the vesicle morphology was inaccessible for the poly(methacrylic acid)-poly(styrene-*alt*-*N*-phenylmaleimide) PISA formulation because of the high T_g of the core-forming block relative to the reaction temperature.[11] In **Chapter 4**, we discussed the synthesis of PLMA-PMMA diblock copolymer nano-objects *via* RAFT dispersion polymerization in mineral oil.[12] For this PISA formulation, only kinetically-trapped spheres or relatively short worms could be obtained. This was attributed to the high T_g of the structure-directing PMMA block (126 °C) relative to the synthesis temperature (70-115°C). This is actually a rather subtle effect because the T_g also depends on the DP, as indicated by the Flory-Fox equation.[13,14] Thus, the T_g is initially low when the insoluble block is relatively short but increases significantly during the polymerization as the PMMA chains grow longer.

Herein we demonstrate that the PLMA-PMMA PISA formulation can be readily modified to provide convenient access to spheres, worms or vesicles. This involves conducting a two-pot synthesis protocol whereby lauryl methacrylate is statistically copolymerized with methyl methacrylate during the second-stage polymerization (see **Scheme 5.1**). Dispersion polymerization conditions can be maintained if the former comonomer constitutes a minor component (up to ~ 10 mol%) relative to the latter. Importantly, this approach is sufficient to

lower the effective T_g of the structure-directing block, which provides convenient access to well-defined spheres, highly anisotropic worms and vesicles.
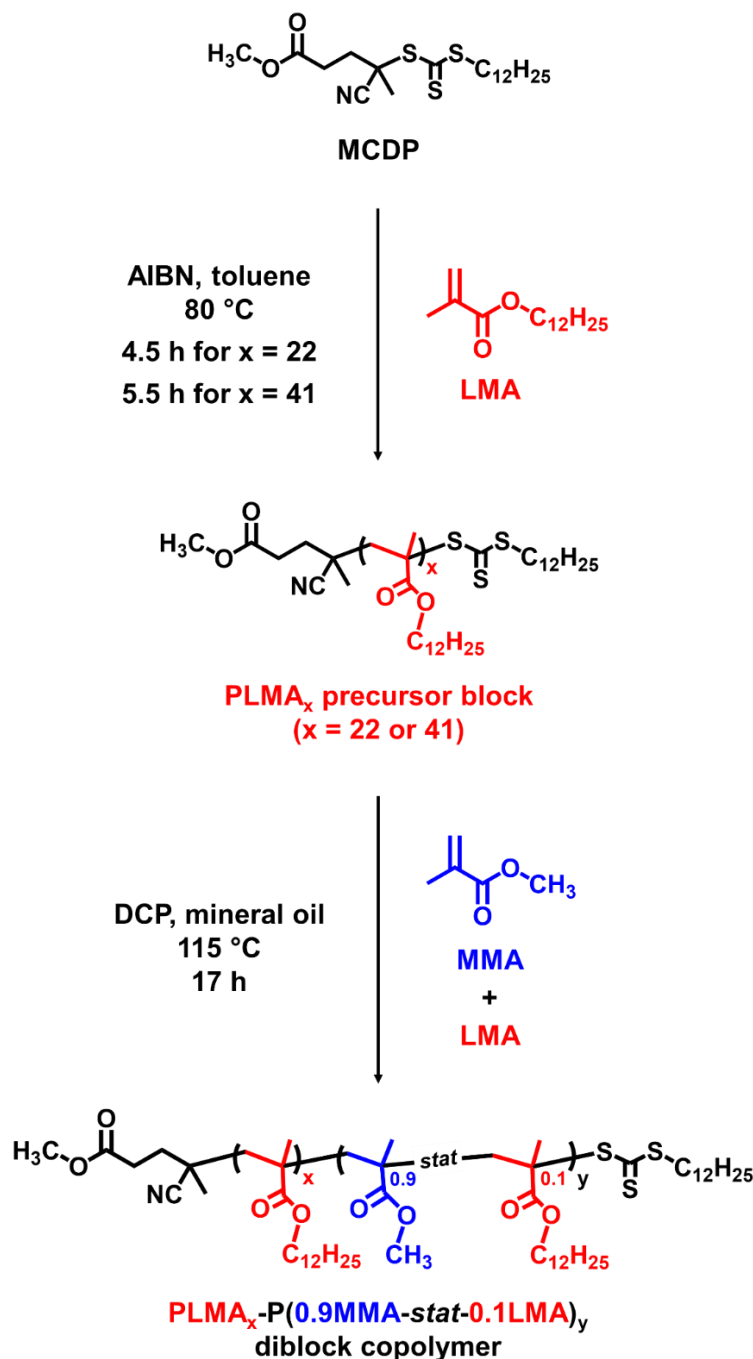
Scheme 5.1. Synthesis of a poly(lauryl methacrylate) (PLMA$_x$; x = 22 or 41) precursor *via* RAFT solution polymerization of LMA in toluene at 50% w/w solids using methyl 4-cyano-4(dodecylthiocarbonothioylthio)-pentanoate (MCDP) at 80 °C (AIBN denotes 2-2'-azoisobutyronitrile), followed by the RAFT dispersion copolymerization of methyl methacrylate (MMA) with LMA at 115 °C in mineral oil at 20% w/w solids using a dicumyl peroxide (DCP) initiator.

Chapter 5. Tuning the Glass Transition Temperature of a Core-Forming Block during Polymerization-Induced Self-Assembly: Statistical Copolymerization of Lauryl Methacrylate with Methyl Methacrylate Provides Access to Spheres, Worms, and Vesicles

5.2. Experimental Section

5.2.1. Materials

The various sources for the materials used herein have been provided in **Chapter 4**.

5.2.2. Methods

Synthesis of PLMA precursors *via* RAFT solution polymerization in toluene

The synthesis of PLMA$_{22}$ and PLMA$_{41}$ has been previously discussed in **Chapter 4**.

Synthesis of poly(lauryl methacrylate)-poly(methyl methacrylate-*stat*-lauryl methacrylate) (PLMA$_{22}$-P(0.9MMA-*stat*-0.1LMA)$_{282}$) diblock copolymer nanoparticles *via* RAFT dispersion copolymerization of LMA with MMA in mineral oil

The following example is representative for targeting PLMA$_{22}$-P(0.9MMA-*stat*-0.1LMA)$_{300}$ nanoparticles at 20% w/w solids. PLMA$_{22}$ precursor (0.20 g; 33.25 µmol), LMA monomer (0.25 g; 997.55 µmol), DCP initiator (3.0 mg; 11.08 µmol) and mineral oil (5.42 g) were weighed into a glass vial and purged with nitrogen for 30 min. MMA monomer (0.96 mL; 8.98 mmol) was degassed separately then added to the reaction mixture *via* syringe. The sealed vial was immersed in a preheated oil bath at 115 °C and the reaction mixture was magnetically stirred for 17 h. ^{1}H NMR analysis indicated an overall comonomer conversion of 94% by comparing the integrated vinyl signals observed for the final reaction mixture to the methoxy signals assigned to the MMA and PMMA at 3.50-3.79 ppm while allowing for the initial [MMA]/[LMA] molar ratio of 9:1 (see **Figure 5.1**). An MMA conversion of 96% was determined by comparing the integrated methyl signal assigned to MMA monomer at 3.75–3.79 ppm to that of the copolymer at 3.50–3.72 ppm at the end of the copolymerization. An LMA conversion of 76% was determined by comparing the integrated methylene signal for LMA monomer at 4.12–4.19 ppm to the combined methoxy signal for both MMA and PMMA according to the initial [MMA]/[LMA] molar ratio. THF GPC analysis indicated an M_n of 34 800 g mol^{-1} and an M_w/M_n of 1.25. To construct a pseudo-phase diagram for PLMA$_x$-P(0.9MMA-*stat*-0.1LMA)$_y$ nano-objects, a range of diblock copolymer compositions were targeted using PLMA$_{22}$ and PLMA$_{41}$ precursors in mineral oil at 20% w/w solids (see **Table**

9.12 and **9.13**). In each case, the same mass of PLMA$_x$ precursor was employed and the [0.9MMA-*stat*-0.1LMA]/[PLMA$_x$] molar ratio and the volume of mineral oil were adjusted accordingly. Since these copolymerizations were performed at 115 °C, *the round-bottomed flask was sealed with a plastic cap rather than a rubber septum in order to prevent evaporative loss of MMA monomer* (boiling point = 101 ℃). It is important to note that conducting polymerizations above the boiling point of the MMA monomer can be potentially hazardous: scale-up syntheses of these nanoparticles would most likely require a pressurized reactor. PLMA$_{22}$-PMMA$_{300}$ and PLMA$_{22}$-P(0.9MMA-*stat*-0.1LMA)$_{300}$ diblock copolymers were also targeted at 90 °C using T21s initiator (dissolved at 10% v/v in mineral oil; [T21s]/[PLMA$_{22}$] = 3.0) at 20% w/w solids in mineral oil.
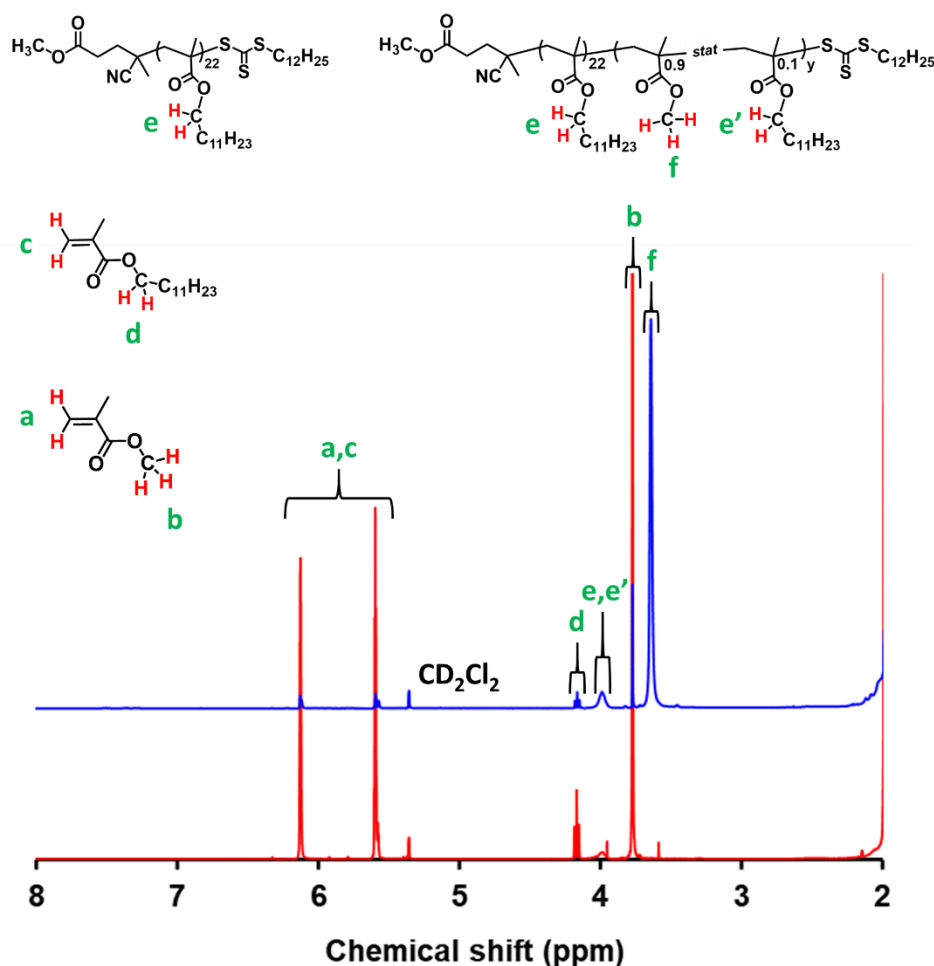
Figure 5.1. Assigned ^{1}H NMR spectra recorded in CD$_2$Cl$_2$ for targeting PLMA$_{22}$-P(0.9MMA-*stat*-0.1LMA)$_{300}$ copolymer composition at 20% w/w solids in mineral oil at t_0 (red spectrum) and after 17 h at 115 °C (blue spectrum). The overall comonomer conversion was determined to be 94% while the final MMA and LMA conversions were 96% and 76%, respectively.

^{1}H NMR Spectroscopy

^{1}H NMR spectra were recorded in either CD_2Cl_2 or $CDCl_3$ using a 400 MHz Bruker Avance spectrometer. Typically, 64 scans were averaged per spectrum. *In situ* ^{1}H NMR spectra were recorded using the same spectrometer to study the kinetics of the synthesis of P(0.9MMA-*stat*-0.1LMA)$_{282}$ vesicles at 20% w/w solids in mineral oil. A 0.20 mL aliquot of the reaction mixture was transferred into an NMR tube equipped with a J-Young's tap under an inert nitrogen atmosphere. A capillary tube containing 0.17 M benzylamine dissolved in d$_6$-DMSO was flame-sealed and used as an external standard (and also a solvent lock). A reference spectrum was recorded at 20 °C prior to heating the reaction mixture to 115 °C. Spectra were acquired in 16 transients using a 30° excitation pulse and a delay time of 1 s over a spectral window of 8 kHz with 64 k data points and recorded approximately every 10 min for 2.5 h.

Gel Permeation Chromatography (GPC)

Molecular weight distributions (MWDs) were assessed by GPC using THF as an eluent. The GPC system was equipped with two 5 μm (30 cm) Mixed C columns and a WellChrom K-2301 refractive index detector operating at 950 ± 30 nm. The THF mobile phase contained 2.0% v/v triethylamine and 0.05% w/v butylhydroxytoluene (BHT) and the flow rate was fixed at 1.0 ml min^{-1}. A series of twelve near-monodisperse poly(methyl methacrylate) standards (M_p values ranging from 800 to 2 200 000 g mol^{-1}) were used for column calibration in combination with a refractive index detector.

Dynamic Light Scattering (DLS)

DLS studies were performed using a Zetasizer Nano ZS instrument (Malvern Instruments, UK) at a fixed scattering angle of 173°. Copolymer dispersions were diluted in *n*-dodecane (0.10% w/w) prior to light scattering studies at 20 °C. The intensity-average diameter and polydispersity of the nanoparticles were calculated by cumulants analysis of the experimental correlation function using Dispersion Technology Software version 6.20. Data were averaged over ten runs each of thirty seconds duration. It is emphasized that DLS assumes a spherical morphology. Thus, the DLS diameter calculated for anisotropic nanoparticles such as worms is a 'sphere-equivalent' value that indicates neither the worm length nor the worm width. Nevertheless, DLS can be used to monitor a thermally-induced worm-to-sphere transition by determining the reduction in the apparent diameter as a function of temperature.[7]

Chapter 5. Tuning the Glass Transition Temperature of a Core-Forming Block during Polymerization-Induced Self-Assembly: Statistical Copolymerization of Lauryl Methacrylate with Methyl Methacrylate Provides Access to Spheres, Worms, and Vesicles

Transmission Electron Microscopy (TEM)

TEM studies were conducted using a Philips CM 100 instrument operating at 100 kV and equipped with a Gatan 1k CCD camera. A single droplet of a 0.10% w/w copolymer dispersion was placed onto a carbon-coated copper grid and allowed to dry, prior to exposure to ruthenium(VIII) oxide vapor for 7 min at 20 °C.[15] This heavy metal compound acts as a positive stain for the core-forming PMMA block to improve contrast. The ruthenium(VIII) oxide was prepared as follows: ruthenium(IV) oxide (0.30 g) was added to water (50 g) to form a black slurry; addition of sodium periodate (2.0 g) with continuous stirring produced a yellow solution of ruthenium(VIII) oxide within 1 min at 20 °C.

Small-Angle X-ray Scattering (SAXS)

SAXS patterns were collected at a synchrotron source (ESRF, beamline ID02, Grenoble, France; experiment number SC-5109) using a monochromatic X-ray radiation (wavelength $\lambda = 0.0995$ nm, with q ranging from 0.0021 to 2.0 nm^{-1}, where $q = (4\pi/\lambda)$. $\sin\theta$ is the length of the scattering vector and θ is the one-half of the scattering angle) and a Ravonix MX-170HS CCD detector. A glass capillary of 2 mm diameter was used as a sample holder. Scattering data were reduced using standard routines from the beamline[16] and were further analyzed using Irena SAS macros for Igor Pro.[17]

Differential scanning calorimetry (DSC)

Measurements were performed using a TA DSC25 Discovery series instrument operating from -90 to 180 °C at a rate of 5 °C min^{-1} using aluminum T_{zero} pans and T_{zero} hermetic lids for $PLMA_{22}$, $PLMA_{22}$-$PMMA_{192}$, $PLMA_{22}$-P(0.95MMA-*stat*-0.05LMA)$_{188}$, $PLMA_{22}$-P(0.9MMA-*stat*-0.1LMA)$_{188}$ and $PLMA_{22}$-P(0.8MMA-*stat*-0.2LMA)$_{186}$. Instrument calibration was performed using an indium standard. Purified copolymer powders were obtained after three consecutive precipitations of the as-synthesized diblock copolymer dispersion into a ten-fold excess of methanol (with redissolution in THF after each precipitation), followed by isolation *via* filtration and drying under vacuum for 24 h. For DSC analysis, the $PLMA_{22}$ precursor and each diblock copolymer were subjected to two heating/cooling cycles: the first cycle ensured removal of residual organic solvent, and the glass transition temperature was determined during the second cycle.

5.3. Results and Discussion

5.3.1. Optimizing the synthesis of PLMA$_{22}$-P(MMA-*stat*-LMA)$_y$ diblock copolymer nano-objects

In **Chapter 4**, when preparing PLMA$_{22}$-PMMA$_y$ diblock copolymer nano-objects in mineral oil,[12] we found that only spheres and short worms (y < 108) could be accessed even when using a relatively short steric stabilizer block (PLMA$_{22}$). Targeting relatively high DPs (y ≥ 108) for the core-forming PMMA block invariably resulted in colloidally unstable micron-sized spherical aggregates (see **Figure 5.2a** for an example when targeting PLMA$_{22}$-PMMA$_{300}$). The same morphology constraint was also observed when particles were targeted (i) at higher solids, (ii) in an alternative solvent (*n*-dodecane) or (iii) when an alternative poly(stearyl methacrylate) (PSMA$_{10}$) precursor block was utilized (see **Chapter 4**). Varying the PISA synthesis conditions did not resolve this problem thus we hypothesized that it was most likely related to the relatively high T_g of the core-forming PMMA block. According to the PISA literature, access to higher order morphologies can be restricted when the synthesis temperature is relatively low compared to the T_g of the core-forming polymer, which has been explained in terms of insufficient chain mobility.[11,18,19] In principle, this problem might be eliminated by conducting the PISA synthesis of PLMA$_{22}$-PMMA$_y$ nanoparticles at a higher temperature.[18,20] However, only spherical nanoparticles were obtained when targeting PMMA DPs between 50 and 400 at 115 °C, rather than 90 °C (see **Figure 5.2b** and **Chapter 4**).

Chapter 5. Tuning the Glass Transition Temperature of a Core-Forming Block during Polymerization-Induced Self-Assembly: Statistical Copolymerization of Lauryl Methacrylate with Methyl Methacrylate Provides Access to Spheres, Worms, and Vesicles
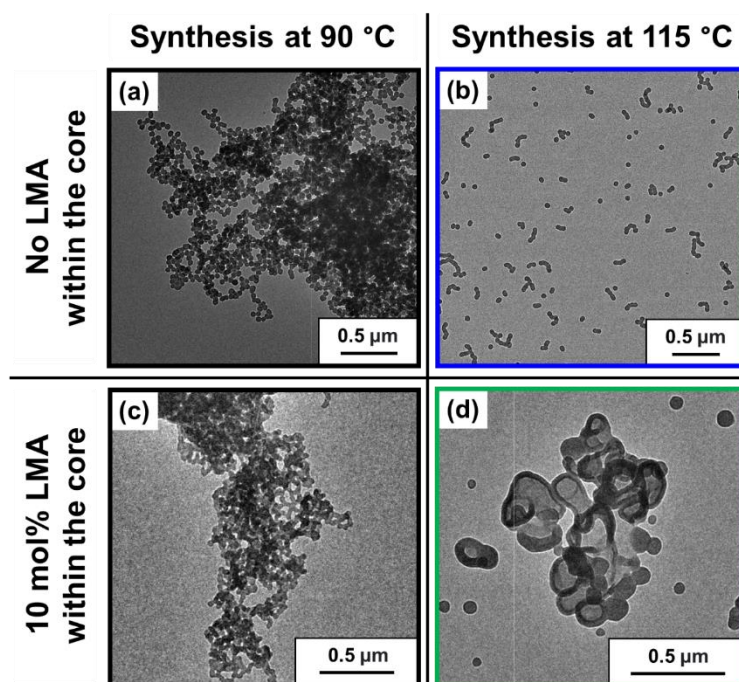
Figure 5.2. Representative TEM images obtained when targeting **(a)** PLMA$_{22}$-PMMA$_{300}$ at 90 °C, **(b)** PLMA$_{22}$-PMMA$_{300}$ at 115 °C, **(c)** PLMA$_{22}$-P(0.9MMA-*stat*-0.1LMA)$_{300}$ at 90 °C and **(d)** PLMA$_{22}$-P(0.9MMA-*stat*-0.1LMA)$_{300}$ at 115 °C using a two-pot synthesis protocol at 20% w/w solids in mineral oil.

Several research groups have demonstrated that introducing a small amount of a solvophilic comonomer into the core-forming block *via* statistical copolymerization can greatly influence the nanoparticle morphology obtained during PISA.[19,21–25] The solvophilic comonomer enhances plasticization of the growing insoluble chains, which results in a higher packing parameter and hence promotes the evolution in morphology from spheres to worms to vesicles. For example, Shi *et al*. reported the dispersion copolymerization of styrene (S) and 4-vinylpyridine (4VP) using a PEG$_{45}$ precursor block in a methanol/water mixture. In this case, the nanoparticle morphology could be tuned by varying either the DP of the statistical core-forming P(S-*stat*-4VP) block or by adjusting the [S]/[4VP] molar ratio.[22] Similarly, Zhou *et al*. studied a poly(2-hydroxyethyl acrylate)-poly(styrene-*stat*-methyl methacrylate) PISA formulation. Only kinetically-trapped spheres were obtained when targeting PHEA$_{21}$-PS$_y$ diblock copolymer nano-objects (where y = 50, 70 or 100) at 20% w/w solids in methanol. In contrast, replacing 25 mol% of the styrene with MMA provided access to spheres, worms or vesicles when targeting the same overall core-forming block DP.[19] Figg *et al*. reported some degree of control over the mean worm length by adjusting the hydrophobic character of the core-forming block. In this aqueous PISA formulation, a poly(*N,N'*-dimethylacrylamide)

Chapter 5. Tuning the Glass Transition Temperature of a Core-Forming Block during Polymerization-Induced Self-Assembly: Statistical Copolymerization of Lauryl Methacrylate with Methyl Methacrylate Provides Access to Spheres, Worms, and Vesicles

(PDMAC) precursor was chain-extended using both diacetone acrylamide (DAAm) and *N,N'*-dimethylacrylamide (DMAC).[24] Similarly, Tan *et al*. used the same monomer (acrylic acid) to both prepare the stabilizer block and act as a suitable comonomer for the core-forming block to promote the formation of higher order morphologies for poly(acrylic acid)-block-poly(acrylic acid-*stat*-styrene) nano-objects in ethanol/water mixtures.[25]

Inspired by these literature examples, we decided to explore replacing a small amount of MMA (ca. 10 mol%) with LMA when generating the core-forming block. TEM images recorded when targeting PLMA$_{22}$-PMMA$_{300}$ nanoparticles at **(a)** 90 °C and **(b)** 115 °C respectively are shown in **Figure 5.2**. Targeting PLMA$_{22}$-P(0.9MMA-*stat*-0.1LMA)$_{300}$ nano-objects at 90 °C resulted in large, highly polydisperse spherical aggregates (see **Figure 5.2c**) with an apparent z-average diameter of 1703 nm as judged by DLS, much like that produced during the attempted synthesis of PLMA$_{22}$-PMMA$_{300}$ nanoparticles (z-average diameter = 957 nm) at 90 °C. However, when the same PLMA$_{22}$-P(0.9MMA-*stat*-0.1LMA)$_{300}$ composition was targeted at 115 °C (see **Figure 5.1**), well-defined vesicles (z-average diameter = 148 nm; polydispersity index (PDI) = 0.08) were obtained as a pure phase, see **Figure 5.2d**. Thus it appears that such nano-objects must be prepared at 115 °C to ensure sufficient mobility for the growing diblock copolymer chains to access higher order morphologies.

Next, we examined the effect of varying the LMA content of the core-forming block (from 0 to 10 mol%) on the copolymer morphology when targeting an overall core-forming DP of 200. Targeting PLMA$_{22}$-PMMA$_{200}$ at 115 °C produced PLMA$_{22}$-PMMA$_{192}$ spheres at 96% conversion (see **Figure 5.3a**).[12] Introducing 5 mol% LMA into the core-forming block was insufficient to produce a higher order morphology, merely resulting in PLMA$_{22}$-P(0.95MMA-*stat*-0.05LMA)$_{188}$ spheres (see **Figure 5.3b**). However, employing 10 mol% LMA led to a mixed phase comprising mainly vesicles and worms with a minor population of spheres (see **Figure 5.3c**). Clearly, a relatively high synthesis temperature of 115 °C is a necessary but not sufficient condition: incorporation of at least 10 mol% LMA within the core-forming block is also required to access higher order morphologies for the current PISA formulation.

In **Chapter 4**, we stated that the morphology constraint observed for PLMA$_{22}$-PMMA$_y$ nano-objects was related to the relatively high T_g of the core-forming PMMA block.[12] Flory and Fox derived a well-known equation for calculating the T_g for statistical copolymers.[13,26] Since PLMA has a relatively low T_g of –38 °C (see **Figure 5.4**), incorporating LMA comonomer *via*

statistical copolymerization must lead to a reduction in the T_g of the core-forming block. To examine this hypothesis, three diblock copolymers prepared with a common target core-forming block DP of 200 were purified and subsequently analyzed by DSC. Increasing the LMA content from 0 mol% to 10 mol% led to a gradual T_g reduction from 111 °C to 82 °C, see **Figure 5.3d**. Thus, introducing LMA comonomer significantly enhances the mobility of the core-forming block at 115 °C by both lowering its T_g and also increasing its degree of plasticization by hot solvent (mineral oil).
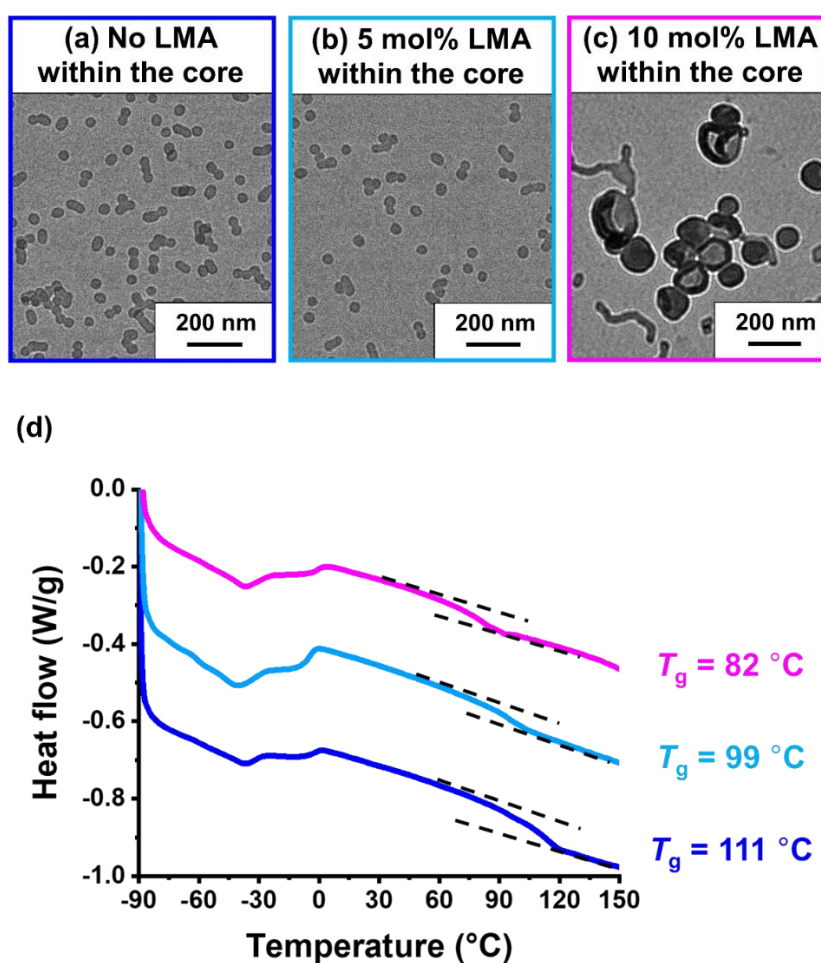
Figure 5.3. Representative transmission electron microscopy (TEM) images obtained when targeting **(a)** PLMA$_{22}$-PMMA$_{200}$, **(b)** PLMA$_{22}$-P(0.95MMA-*stat*-0.05LMA)$_{200}$ or **(c)** PLMA$_{22}$-P(0.9MMA-*stat*-0.1LMA)$_{200}$ at 20% w/w solids in mineral oil at 115 °C. **(d)** DSC curves and corresponding calculated core-forming block T_g values for PLMA$_{22}$-PMMA$_{192}$ (dark blue curve), the PLMA$_{22}$-P(0.95MMA-*stat*-0.05LMA)$_{188}$ (light blue curve) and the PLMA$_{22}$-P(0.9MMA-*stat*-0.1LMA)$_{188}$ (pink curve). Copolymers were purified by three consecutive precipitations into excess methanol (with redissolution in THF) followed by filtration and drying under vacuum.
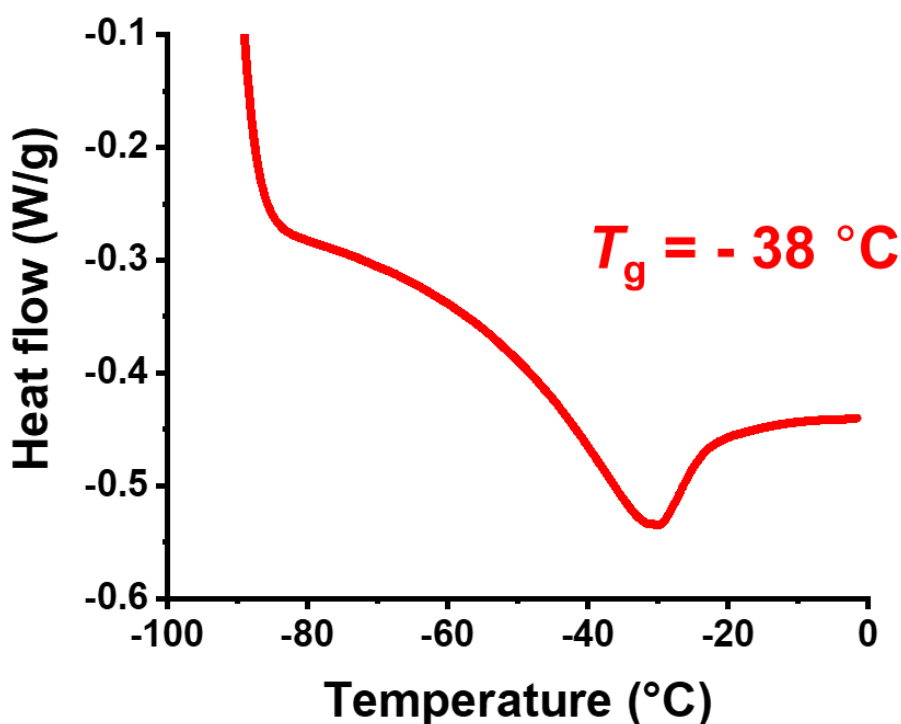
Figure 5.4. DSC curve recorded for the PLMA$_{22}$ precursor, for which the T_g was determined to be -38 °C.

5.3.2. RAFT dispersion copolymerization of MMA with 10% mol LMA comonomer at 115 °C

Kinetic studies were performed during the synthesis of PLMA$_{22}$-P(0.9MMA-*stat*-0.1LMA)$_{282}$ vesicles at 20% w/w solids in mineral oil at 115 °C using *in situ* ^{1}H NMR spectroscopy. Unfortunately, the vinyl signals for the LMA and MMA monomers overlap, so only the overall comonomer conversion could be determined over time. This was achieved by comparing the integrated vinyl signals at 4.5-6.0 ppm to the integrated aromatic signals assigned to an external standard (benzylamine) at 6.5-7.6 ppm, see **Figure 5.5a**. Initially, the polymerization proceeded slowly followed by an approximate five-fold rate enhancement after 50 min (see **Figure 5.5b**) which corresponds to the micellar nucleation.[6,10,27]
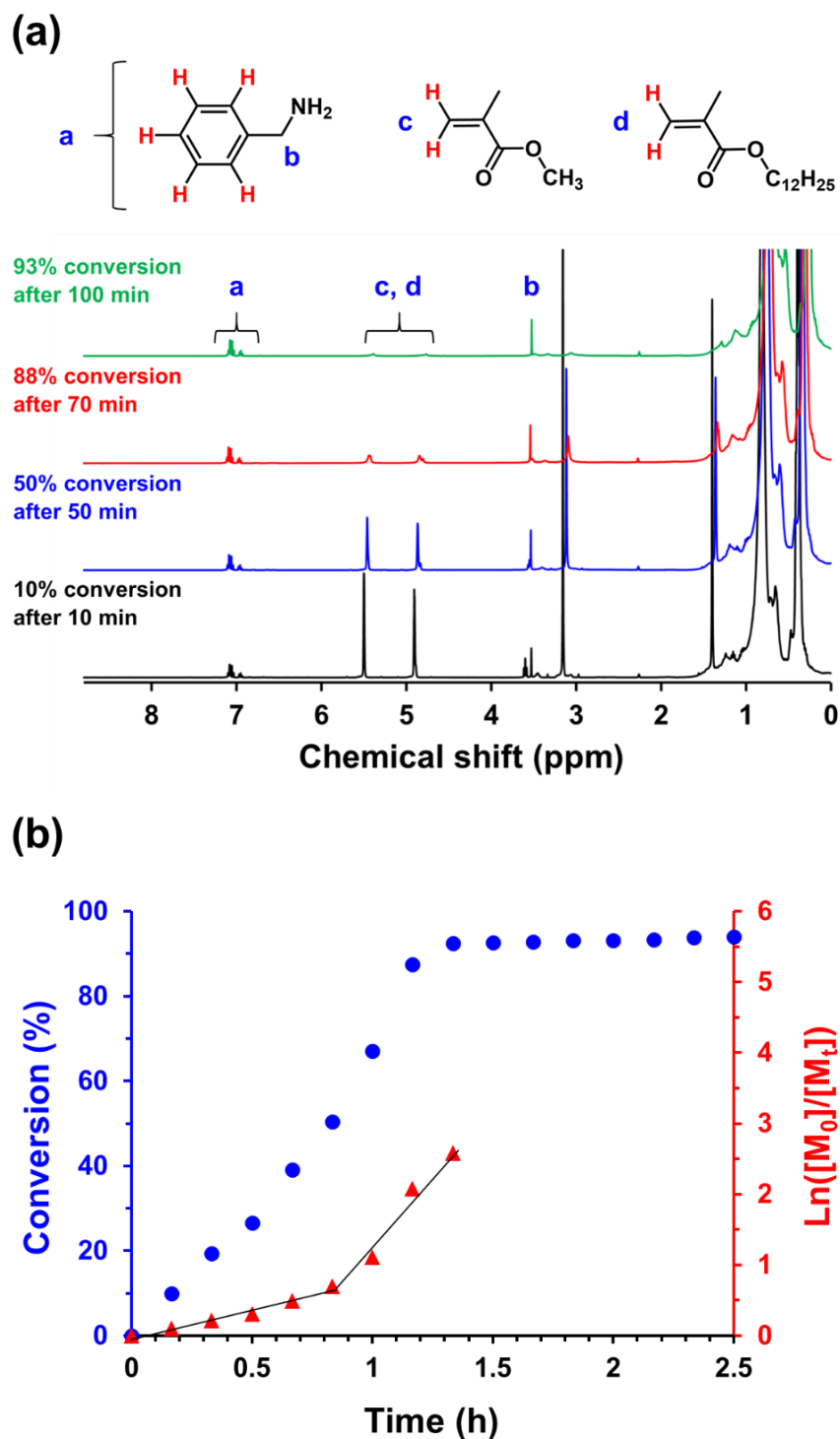
Figure 5.5. (a) Selected ^{1}H NMR spectra recorded during the RAFT dispersion copolymerization of MMA with LMA at 115 °C when targeting $PLMA_{22}$-P(0.9MMA-*stat*-0.1LMA)$_{300}$ vesicles at 20% w/w solids in mineral oil: $t = 10$ min (black spectrum), $t = 50$ min (blue spectrum), $t = 70$ min (red spectrum) and $t = 100$ min (green spectrum) using benzylamine in d$_6$-DMSO as an external standard. **(b)** Conversion *vs.* time curve (blue circles) and corresponding $\ln([M_0]/[M_t])$ *vs.* time plot (red triangles) obtained for the same PISA formulation.

Chapter 5. Tuning the Glass Transition Temperature of a Core-Forming Block during Polymerization-Induced Self-Assembly: Statistical Copolymerization of Lauryl Methacrylate with Methyl Methacrylate Provides Access to Spheres, Worms, and Vesicles

The instantaneous comonomer conversion was 50% at this point, which is equivalent to a mean core-forming block DP of 150. Following nucleation, this statistical copolymerization followed first-order kinetics and attained an overall conversion of 92%. Then a slower rate of polymerization occurred under monomer-starved conditions. A final monomer conversion of 94% was achieved within 2.5 h. THF GPC analysis indicated a relatively narrow molecular weight distribution for the final diblock copolymer (M_n = 34,800 g mol^{-1}; M_w/M_n = 1.25) and the vesicle morphology was confirmed by TEM analysis (see **Figure 5.6**). Subsequently, DLS studies indicated a z-average diameter of 148 nm (PDI = 0.08).
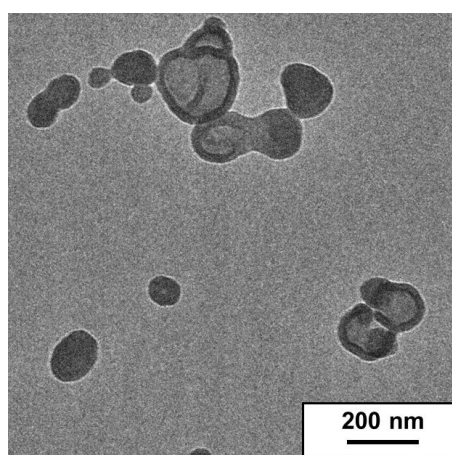
Figure 5.6. Representative TEM image obtained for the final PLMA$_{22}$-P(0.9MMA-*stat*-0.1LMA)$_{282}$ vesicles after 3 h when targeting 20% w/w solids in mineral oil at 115 °C during the *in situ* ^{1}H NMR kinetic experiment.

It is worth asking whether the incomplete monomer conversion (6% unreacted comonomer overall, estimated to be ~3.6% MMA and ~2.4% LMA) contributes to the formation of higher order morphologies *via* plasticization of the statistical core-forming block at 115 °C. In this context, it is notable that targeting PLMA$_{22}$-PMMA$_y$ (y = 50 to 400) nano-objects at 20% w/w solids in mineral oil invariably resulted in the formation of kinetically-trapped spherical nanoparticles despite MMA conversions remaining incomplete ($\geq$ 95%) after 17 h at 115 °C (see **Table 9.11**). Herein, a 20% w/w dispersion of PLMA$_{22}$-PMMA$_{291}$ spherical nanoparticles (previously prepared at 115 °C in mineral oil; final MMA conversion = 97% (see **Table 9.11**)) was heated at 115 °C for 17 h in the presence of a large excess amount of LMA monomer ([LMA]/[PLMA$_{22}$-PMMA$_{291}$] molar ratio = 50). The reaction mixture was sealed to prevent evaporative loss of LMA (plus residual MMA comonomer) and was not degassed prior to heating to prevent further copolymerization. The ^{1}H NMR spectrum shown in **Figure 5.7**

confirms the continued presence of unreacted comonomers after such thermal annealing. Moreover, the GPC trace recorded for the $PLMA_{22}$-$PMMA_{291}$ prior ($M_n = 35,000$ g mol^{-1}; $M_w/M_n = 1.27$) was essentially identical to that obtained after this experiment ($M_n = 34,900$ g mol^{-1}; $M_w/M_n = 1.27$), confirming that no further copolymerization had occurred. Importantly, TEM images recorded for the $PLMA_{22}$-$PMMA_{291}$ nanoparticles after heating in the presence of LMA indicated the same morphology as the original spheres (see **Figure 5.7**). Thus, there is no evidence that LMA monomer can plasticize PMMA cores under such conditions. This is consistent with our observation that LMA is a non-solvent for PMMA homopolymer at 20 °C. In summary, the relatively low residual LMA content that remains after the PISA synthesis of $PLMA_{22}$-P(0.9MMA-*stat*-0.1LMA)$_{282}$ vesicles do not appear to be sufficient to account for the observed evolution in copolymer morphology.

Cornel *et al.* was the first to examine PLMA-PMMA formulations, with such PISA syntheses utilizing a relatively long $PLMA_{39}$ precursor to target spherical nanoparticles in *n*-dodecane.[28] When revisiting this PLMA-PMMA formulation, we employed $PLMA_{22}$, $PLMA_{30}$ or $PLMA_{41}$ precursors to target PMMA DPs of 20-200 at 70, 90 or 115 °C in mineral oil, see **Chapter 4**. In all cases, THF GPC analysis confirmed relatively narrow molecular weight distributions ($M_w/M_n \leq 1.39$), suggesting reasonably good RAFT control.[6,7,12,28,29] Moreover, we also compared the relative merits of a two-pot synthesis with a one-pot synthesis in **Chapter 4**. A low molecular weight shoulder corresponding to unreacted PLMA precursor[6,12] became increasingly prominent when targeting higher PMMA DPs using the former protocol. Hence the one-pot protocol always resulted in narrower molecular weight distributions.
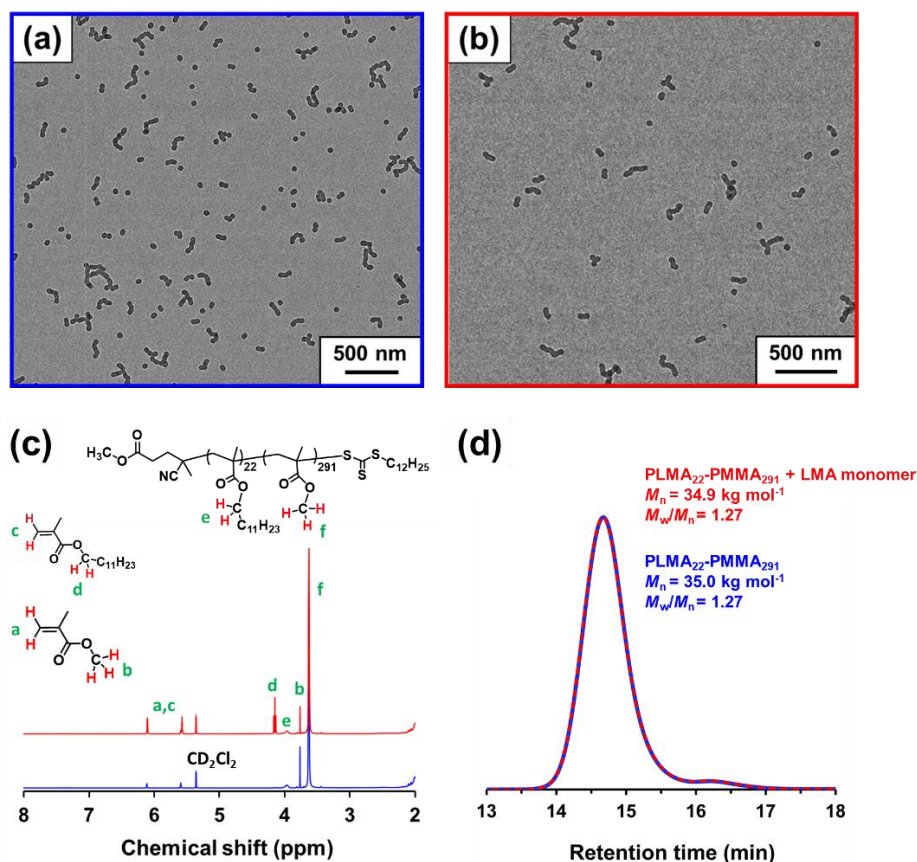
Figure 5.7. Representative TEM images obtained for **(a)** PLMA$_{22}$-PMMA$_{291}$ nano-objects prepared at 20% w/w solids in mineral oil at 115 °C and **(b)** the same diblock copolymer after heating the 20% w/w dispersion at 115 °C for 17 h in the presence of a large excess of LMA monomer ([LMA]/[PLMA$_{22}$-PMMA$_{291}$] molar ratio = 50). **(c)** Assigned ^{1}H NMR spectra recorded in CD$_2$Cl$_2$ for the initial PLMA$_{22}$-PMMA$_{291}$ diblock copolymer (blue spectrum) and that obtained after thermal annealing at 115 °C for 17 h (red spectrum). **(d)** GPC traces recorded using a refractive index detector (and expressed relative to a series of near-monodisperse poly(methyl methacrylate) calibration standards) for the initial PLMA$_{22}$-PMMA$_{291}$ diblock copolymer (blue curve) and the copolymer obtained after thermal annealing at 115 °C for 17 h (red data). Clearly, no LMA polymerization occurs during thermal annealing.

In principle, either synthetic route could be employed to produce the PLMA$_{22}$-P(0.9MMA-*stat*-0.1LMA)$_y$ nanoparticles reported herein. Thus, a two-pot protocol would simply involve the chain extension of a PLMA$_{22}$ precursor *via* statistical copolymerization of 10 mol% LMA with 90 mol% MMA. This approach has been previously reported by several research groups.[19,22,23] Alternatively, a one-pot protocol could be utilized in which either MMA or an MMA/LMA mixture was added at a specific (known) LMA conversion. Thus, any unreacted LMA remaining from the first step becomes statistically copolymerized within the insoluble structure-directing block during the subsequent chain extension. This approach was demonstrated for the synthesis of poly(acrylic acid)-poly(acrylic acid-*stat*-styrene) nano-

objects by Tan *et al.*[25] As indicated in **Figure 5.3**, the PLMA$_{22}$-P(MMA-*stat*-LMA)$_y$ formulation requires incorporation of at least 10 mol% LMA into the insoluble block to access higher order morphologies. Unfortunately, in our hands the kinetics of LMA homopolymerization during the first step was not sufficiently reproducible to ensure precisely the same intermediate LMA conversion after a given reaction time. Rather than produce diblock copolymers with slightly differing stabilizer DPs (and hence introduce corresponding uncertainty regarding the comonomer composition of the insoluble block), we chose to use the two-pot synthesis protocol despite its imperfect blocking efficiency (which is presumably the result of a minor fraction of trithiocarbonate chain-ends being lost during isolation and purification of the PLMA$_{22}$ precursor).

GPC traces recorded for the PLMA$_{22}$ precursor and a series of five PLMA$_{22}$-P(0.9MMA-*stat*-0.1LMA)$_y$ diblock copolymers prepared using the two-pot protocol are shown in **Figure 5.8a** when targeting a core-forming block DP (y) of 70, 120, 160, 240 or 300. For each of these copolymers, the overall comonomer conversion is at least 94% (see **Table 9.12**). In this case, the low molecular weight shoulder assigned to PLMA precursor is relatively small and narrow molecular weight distributions are obtained ($M_w/M_n \leq 1.25$). Moreover, a linear correlation between the GPC M_n and the actual core-forming block DP (corrected for the final comonomer conversion) is evident in **Figure 5.8b**. In summary, a two-pot synthesis leads to acceptable results under the stated conditions.
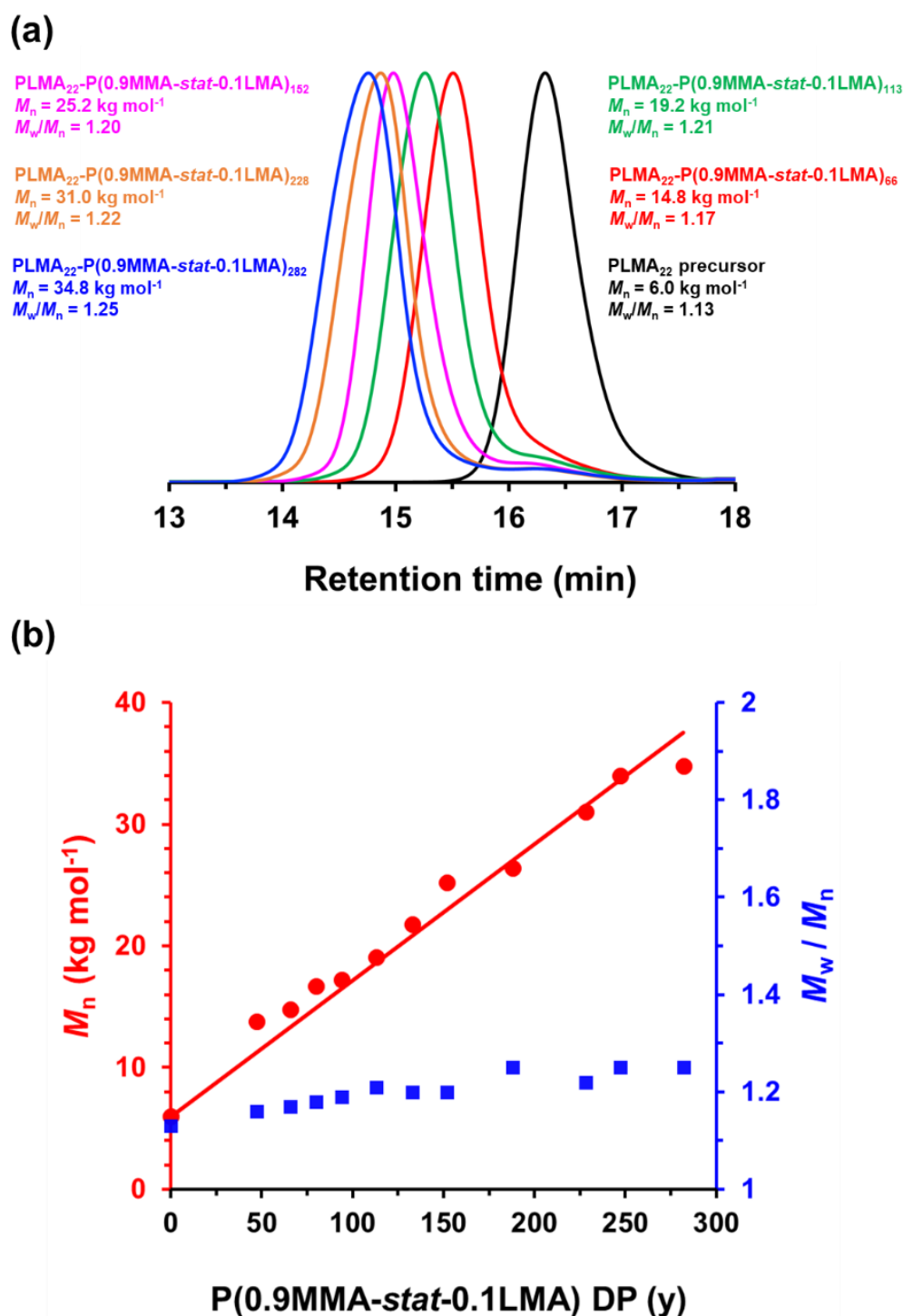
Figure 5.8. (a) GPC traces (using a series of near-monodisperse poly(methyl methacrylate) calibration standards) recorded using a refractive index detector for a PLMA$_{22}$ precursor (prepared in toluene at 50% w/w solids at 80 °C) and a series of five PLMA$_{22}$-P(0.9MMA-*stat*-0.1LMA)$_y$ diblock copolymers prepared by RAFT dispersion copolymerization of MMA with LMA comonomer at 115 °C at 20% w/w solids in mineral oil, targeting y = 70, 120, 160, 240 or 300, respectively. **(b)** Linear relationship between GPC M_n (red circles) and P(0.9MMA-*stat*-0.1LMA) DP (as determined by ^{1}H NMR studies) for a series of PLMA$_{22}$-P(0.9MMA-*stat*-0.1LMA)$_y$ diblock copolymers prepared at 20% w/w solids. The corresponding M_w/M_n (blue squares) data are also shown.

5.3.3. Construction of a pseudo-phase diagram for a series of PLMA$_x$-P(0.9MMA-*stat*-0.1LMA)$_y$ diblock copolymer nano-objects

As shown in **Chapter 2** and **3,** using a relatively short stabilizer block aids the formation of higher order morphologies (worms, or vesicles).[8,30] In **Chapter 4**, a pseudo-phase diagram constructed for a series of PLMA$_{22}$-PMMA$_y$ nano-objects prepared at 20% solids in mineral oil showed that vesicles could not be accessed.[12] Herein, the same PLMA$_{22}$ precursor was used to target P(0.9MMA-*stat*-0.1LMA) DPs of 50-300 at 20% w/w solids in mineral oil at 115 °C (**Figure 5.9**, **Table 9.12** and **9.13**).
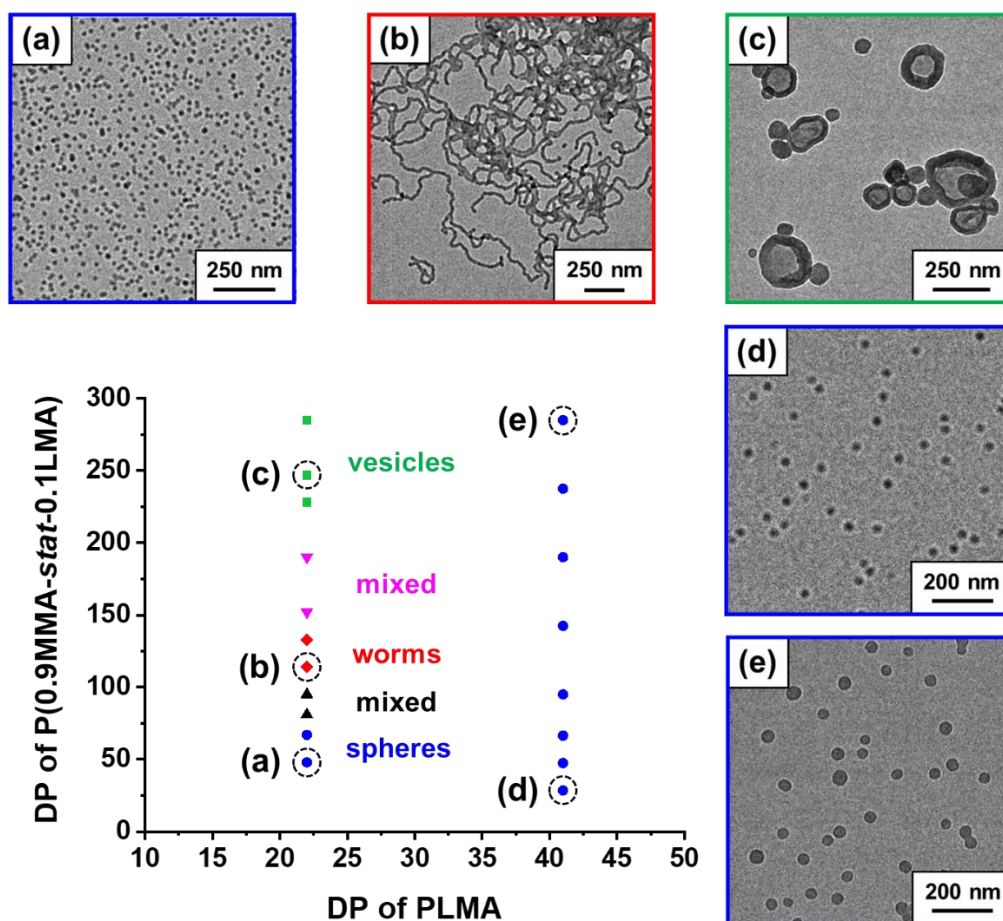
Figure 5.9. Pseudo-phase diagram constructed for PLMA$_x$-P(0.9MMA-*stat*-0.1LMA)$_y$ diblock copolymer nano-objects prepared by RAFT dispersion copolymerization of MMA with LMA ([MMA]/[LMA] molar ratio = 9.0) in mineral oil using either a PLMA$_{22}$ or a PLMA$_{41}$ precursor with DCP initiator at 115 °C ([PLMA$_x$]/[DCP] molar ratio = 3.0). Representative TEM images obtained for **(a)** PLMA$_{22}$-P(0.9MMA-*stat*-0.1LMA)$_{47}$, **(b)** PLMA$_{22}$-P(0.9MMA-*stat*-0.1LMA)$_{113}$, **(c)** PLMA$_{22}$-P(0.9MMA-*stat*-0.1LMA)$_{247}$, **(d)** PLMA$_{41}$-P(0.9MMA-*stat*-0.1LMA)$_{28}$ and **(e)** PLMA$_{41}$-P(0.9MMA-*stat*-0.1LMA)$_{282}$ diblock copolymers at 20% w/w solids in mineral oil, respectively.

Chapter 5. Tuning the Glass Transition Temperature of a Core-Forming Block during Polymerization-Induced Self-Assembly: Statistical Copolymerization of Lauryl Methacrylate with Methyl Methacrylate Provides Access to Spheres, Worms, and Vesicles

Well-defined spheres with z-average diameters of 24 (PDI = 0.01) and 29 nm (PDI = 0.02) were obtained for P(0.9MMA-*stat*-0.1LMA) DPs of 47 or 66 (see **Figure 5.9a**). Transparent, free-standing gels were produced for DPs of 113 and 133, suggesting the presence of worms (see **Figure 5.9b**). At DPs of 228 or above, vesicles were obtained in the form of highly turbid, free-flowing fluids, with z-average diameters ranging from 140 nm (PDI = 0.12) to 148 nm (PDI = 0.08), see **Figure 5.9c**.

In contrast, only kinetically-trapped spheres of increasing size were obtained when using a PLMA$_{41}$ precursor to target a series of PLMA$_{41}$-P(0.9MMA-*stat*-0.1LMA)$_y$ nano-objects (y = 30 to 300), see **Figure 5.9d and e**, **Figure 5.10** (red data set) and **Table 9.13**.
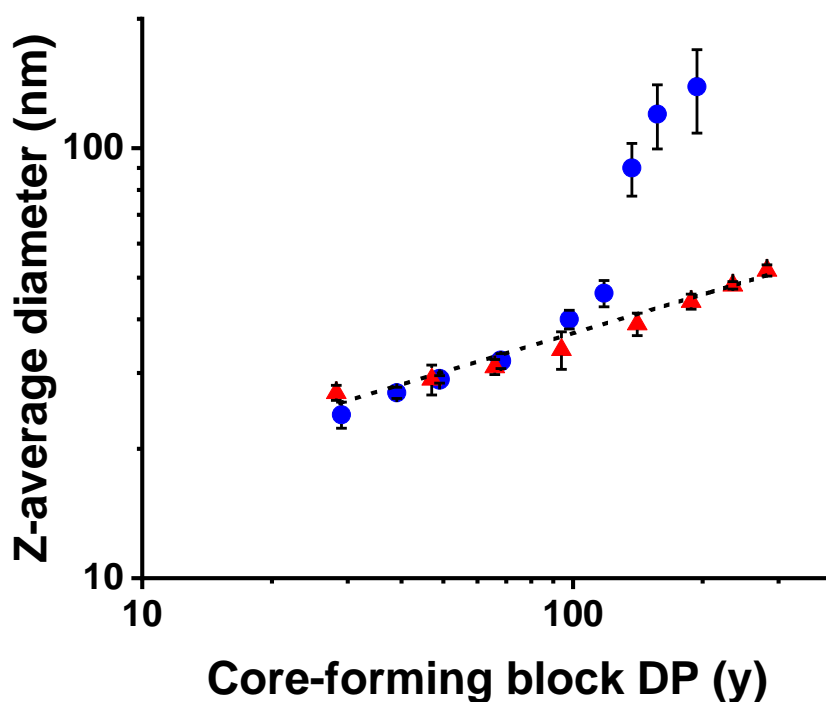
Figure 5.10. Double-logarithmic plot for the relationship between z-average diameter and core-forming block DP (y) for a series of PLMA$_{41}$-PMMA$_y$ (targeting y = 30-200) spheres prepared by RAFT dispersion polymerization of MMA at 90 °C (blue data) and a series of PLMA$_{41}$-P(0.9MMA-*stat*-0.1LMA)$_y$ (targeting y = 30-300) spheres prepared by RAFT dispersion copolymerization of LMA with MMA at 115 °C (red data) at 20% w/w solids in mineral oil. [N.B. Standard deviations are calculated from DLS polydispersities and thus indicate the breadth of the particle size distributions, rather than the experimental error]. Blue data are taken from **Chapter 4**.

We have reported similar observations for various PISA syntheses conducted in non-polar media.[31,32] For the analogous $PLMA_{41}$-$PMMA_y$ formulation, a linear relationship was initially observed between the DLS z-average diameter and PMMA DP (see **Chapter 4**). However, colloidally unstable aggregates were invariably obtained for PMMA DPs $\geq$ 137, as indicated by the substantial increase in particle size and PDI, see **Figure 5.10** (blue data set).

In order to confirm the copolymer morphology assigned on the basis of TEM analysis (see **Figure 5.9**), small-angle X-ray scattering (SAXS) patterns were recorded for 1.0% w/w dispersions of five examples of $PLMA_x$-$P(0.9MMA$-*stat*-$LMA)_y$ nano-objects (see **Figure 5.11**). As discussed in previous **Chapters**, the low q gradient in a SAXS pattern is diagnostic of the predominant copolymer morphology.[33] Thus, spheres have a zero gradient, while worms and vesicles exhibit gradients of –1 and –2, respectively. Inspecting **Figure 5.11**, a low q gradient of zero was observed for $PLMA_{22}$-$P(0.9MMA$-*stat*-$0.1LMA)_{47}$, $PLMA_{41}$-$P(0.9MMA$-*stat*-$0.1LMA)_{28}$, $PLMA_{41}$-$P(0.9MMA$-*stat*-$0.1LMA)_{282}$, while low q gradients of –1 and –2 were obtained for $PLMA_{22}$-$P(0.9MMA$-*stat*-$0.1LMA)_{113}$ and $PLMA_{22}$-$P(0.9MMA$-*stat*-$0.1LMA)_{247}$, respectively. Fitting the first three patterns (see **Figure 5.11a**) using a spherical micelle model[34] indicated an overall volume-average diameter (D_{sphere}) of 18.9 $\pm$ 1.9 nm and a mean aggregation number (N_{agg}) of 200 for $PLMA_{22}$-$P(0.9MMA$-*stat*-$0.1LMA)_{47}$, a D_{sphere} of 19.8 $\pm$ 1.1 nm and an N_{agg} of 140 for $PLMA_{41}$-$P(0.9MMA$-*stat*-$0.1LMA)_{28}$ and a D_{sphere} of 43.0 $\pm$ 4.5 nm and an N_{agg} of 510 for $PLMA_{41}$-$P(0.9MMA$-*stat*-$0.1LMA)_{282}$ (see **Table 9.14**). These data are consistent with the corresponding z-average diameters reported by DLS, which were 24 nm (PDI = 0.01) for $PLMA_{22}$-$P(0.9MMA$-*stat*-$0.1LMA)_{47}$, 27 nm (PDI = 0.04) for $PLMA_{41}$-$P(0.9MMA$-*stat*-$0.1LMA)_{28}$ and 52 nm (PDI = 0.03) for $PLMA_{41}$-$P(0.9MMA$-*stat*-$0.1LMA)_{282}$ provided by DLS (see **Tables 9.12** and **9.13**).
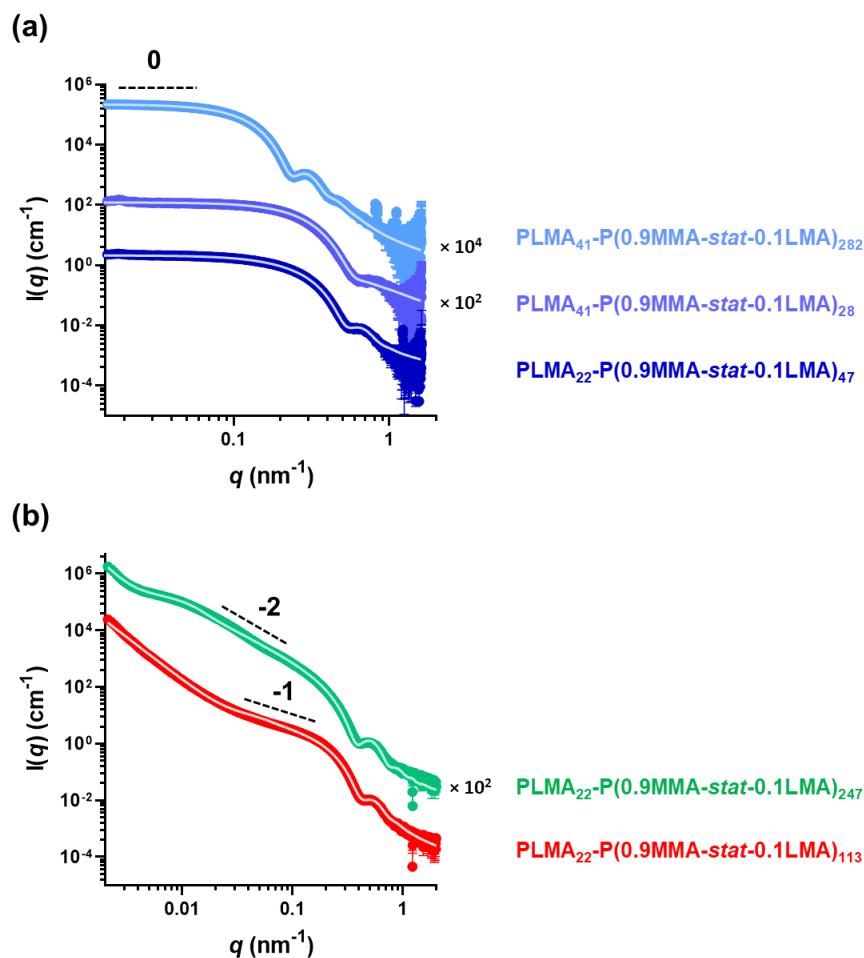
Figure 5.11. Small-angle X-ray scattering (SAXS) patterns and corresponding data fits (solid white lines) recorded for 1.0% w/w dispersions of **(a)** PLMA$_{22}$-P(0.9MMA-*stat*-0.1LMA)$_{47}$, PLMA$_{41}$-P(0.9MMA-*stat*-0.1LMA)$_{28}$ and PLMA$_{41}$-P(0.9MMA-*stat*-0.1LMA)$_{282}$ spheres and **(b)** PLMA$_{22}$-P(0.9MMA-*stat*-0.1LMA)$_{113}$ worms and PLMA$_{22}$-P(0.9MMA-*stat*-0.1LMA)$_{247}$ vesicles in mineral oil at 20 °C. These nano-objects were originally prepared at 115 °C targeting 20% w/w solids in mineral oil. Dashed lines are provided for guidance to the eye and indicate low q gradients of 0, –1 and –2.

SAXS patterns recorded for PLMA$_{22}$-P(0.9MMA-*stat*-0.1LMA)$_{113}$ and PLMA$_{22}$-P(0.9MMA-*stat*-0.1LMA)$_{247}$ are shown in **Figure 5.11b**. A satisfactory fit to the former pattern was obtained using a worm-like micelle model,[34] which indicated a mean worm cross-sectional diameter of 20.0 ± 2.4 nm. The upturn in the scattering intensity observed in the low q region most likely indicates worm branching and/or clustering: unfortunately, this feature prevents determination of the mean contour length and a reliable N_{agg} for these worms. The pattern obtained for PLMA$_{22}$-P(0.9MMA-*stat*-0.1LMA)$_{247}$ could be satisfactorily fitted using a vesicle model,[35] which indicated an overall volume-average diameter of 172 ± 126 nm, a mean vesicle

membrane thickness of 15.4 ± 1.6 nm and an N_{agg} of 25,600. Comparing this aggregation number to that determined for the PLMA$_{22}$-P(0.9MMA-*stat*-0.1LMA)$_{47}$ spheres, we calculate that the mean number of spheres that must undergo fusion to form a single vesicle is 128.[36]

5.3.4. Thermoresponsive behavior of PLMA$_{22}$-P(0.9MMA-*stat*-0.1LMA)$_{113}$ worms and PLMA$_{22}$-P(0.9MMA-*stat*-0.1LMA)$_{228}$ vesicles

The PISA literature contains examples of thermoresponsive diblock copolymer nano-objects prepared in non-polar media, with both worm-to-sphere transitions[7,12,37,38] and vesicle-to-worm transitions[36,39] being observed at elevated temperature (see **Chapter 1**). Such transitions can be explained in terms of surface plasticization of the insoluble block by ingress of hot solvent.[7,36] The worm-to-sphere transition is typically reversible for a concentrated copolymer dispersion (e.g. 5-20% solids) but becomes irreversible at the relatively high dilution (e.g. 0.1% w/w) typically used for DLS experiments (see **Chapter 1**).[7]

In **Chapter 4**, we used DLS to examine the thermoresponsive behavior of PLMA$_{22}$-PMMA$_{69}$ short worms, which exhibited an irreversible worm-to-sphere transition on heating above 110 °C. For this system, only partial reversibility was observed by TEM at 20% w/w solids after a 20 °C to 150 °C to 20 °C thermal cycle.[12] Herein, we explore the thermoresponsive behavior of PLMA$_{22}$-P(0.9MMA-*stat*-0.1LMA)$_{113}$ worms and PLMA$_{22}$-P(0.9MMA-*stat*-0.1LMA)$_{228}$ vesicles (see **Table 9.12**) *via* DLS and TEM studies.[12] These compositions were selected because they lie close to the phase boundaries indicated in **Figure 5.9**, which should enhance the probability of observing the expected thermal transition.[36] For DLS experiments (see **Figure 5.12**), the as-synthesized 20% w/w dispersions of PLMA$_{22}$-P(0.9MMA-*stat*-0.1LMA)$_{113}$ worms and PLMA$_{22}$-P(0.9MMA-*stat*-0.1LMA)$_{228}$ vesicles in mineral oil were diluted to 0.1% w/w using *n*-dodecane and the 'cumulative thermal annealing' protocol was adapted from **Chapter 4**.
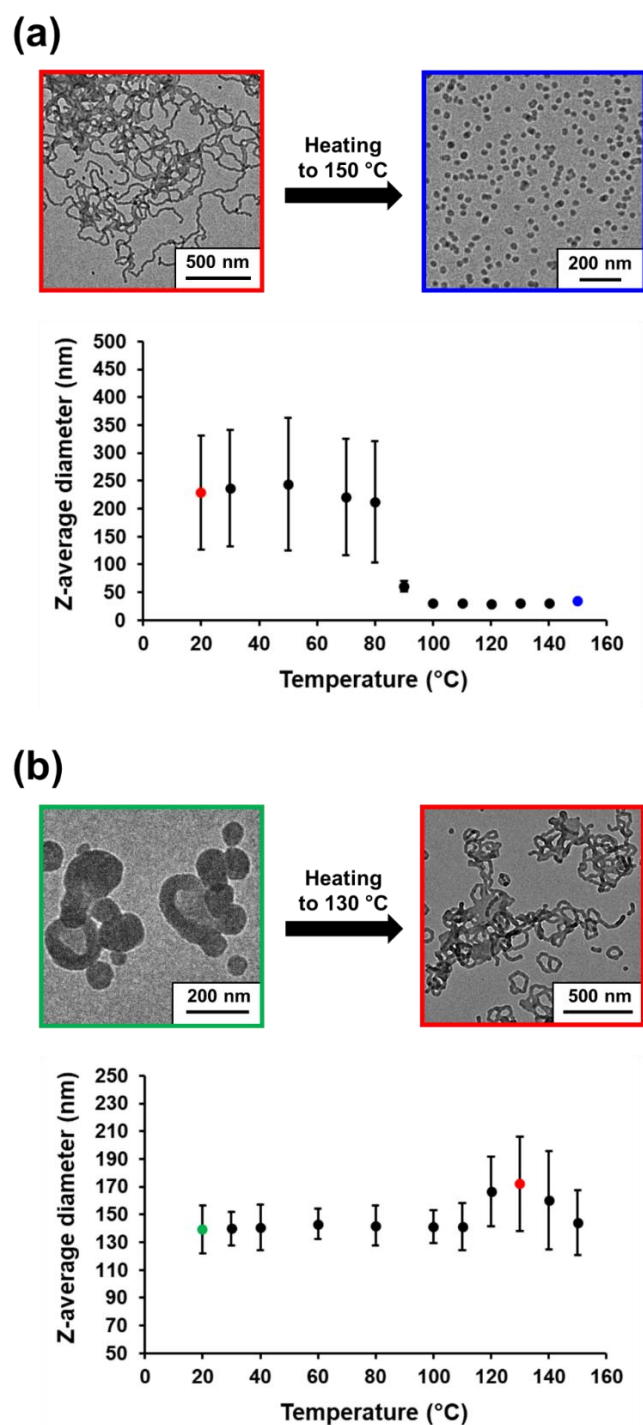
Figure 5.12. (a) Variation in DLS z-average diameter observed for a 0.1% w/w dispersion of PLMA$_{22}$-P(0.9MMA-*stat*-0.1LMA)$_{113}$ nano-objects (prepared using *n*-dodecane as a diluent) on heating from 20 to 150 °C. Representative TEM images obtained for the initial worms (red frame) and the final spheres that are formed after heating to 150 °C (blue frame). **(b)** Variation in DLS z-average diameter for a 0.1% w/w PLMA$_{22}$-P(0.9MMA-*stat*-0.1LMA)$_{228}$ nano-objects (prepared using *n*-dodecane as a diluent) on heating from 20 to 150 °C. Representative TEM images obtained for the initial vesicles (green frame) and the worms formed after heating to 130 °C (red frame). [N.B. Standard deviations are calculated from the DLS polydispersity data and indicate the breadth of the particle size distribution, rather than the experimental error].

Chapter 5. Tuning the Glass Transition Temperature of a Core-Forming Block during Polymerization-Induced Self-Assembly: Statistical Copolymerization of Lauryl Methacrylate with Methyl Methacrylate Provides Access to Spheres, Worms, and Vesicles

The sphere-equivalent z-average diameter observed for PLMA$_{22}$-P(0.9MMA-*stat*-0.1LMA)$_{113}$ worms remained almost unchanged between 20 °C and 80 °C with minimal variation in the associated DLS polydispersity (PDI), see **Figure 5.12a**. A substantial reduction in both parameters occurs on further heating from 80 °C (213 nm; PDI = 0.51) to 100 °C (31 nm; PDI = 0.05). These data suggest a worm-to-sphere transition within this temperature range, which was confirmed by TEM analysis (see **Figure 5.12a**). For the PLMA$_{22}$-P(0.9MMA-*stat*-0.1LMA)$_{228}$ vesicles, an apparent increase in the z-average diameter and PDI was observed on raising the temperature from 110 °C (141 nm; PDI = 0.12) to 130 °C (172 nm; PDI = 0.20), see **Figure 5.12b**. TEM analysis indicated the formation of branched worms (see **Figure 5.12b**).[36] Further heating up to 140 °C led to a modest reduction in the z-average diameter (160 nm; PDI = 0.22) and the formation of mainly worms plus a minor population of spheres (see **Figure 5.13**).
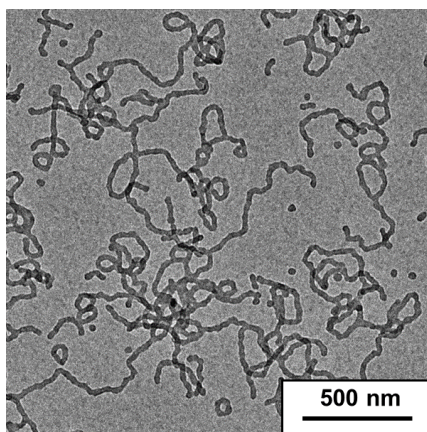
Figure 5.13. Representative TEM image obtained for the PLMA$_{22}$-P(0.9MMA-*stat*-0.1LMA)$_{228}$ worms that are formed after heating a 0.1% w/w dispersion of PLMA$_{22}$-P(0.9MMA-*stat*-0.1LMA)$_{228}$ vesicles (originally prepared in mineral oil but then diluted with *n*-dodecane) to 140 °C.

TEM was used to study the reversibility of these thermal transitions for 20% w/w copolymer dispersions. Accordingly, PLMA$_{22}$-P(0.9MMA-*stat*-0.1LMA)$_{113}$ worms and PLMA$_{22}$-P(0.9MMA-*stat*-0.1LMA)$_{228}$ vesicles were each heated in turn to 150 °C and equilibrated for 1 h. Then a small aliquot was extracted in each case and immediately diluted to 0.1% w/w using hot *n*-dodecane (preheated to 150 °C) to assess the copolymer morphology. The PLMA$_{22}$-P(0.9MMA-*stat*-0.1LMA)$_{113}$ worms were converted into spheres on heating (see **Figure 5.14a**). Only 'jellyfish' structures were formed on heating the PLMA$_{22}$-P(0.9MMA-*stat*-0.1LMA)$_{228}$ vesicles to 150 °C (see **Figure 5.15**) but further heating to 170 °C generated a pure

worm morphology (see **Figure 5.14b**). Thereafter, both 20% w/w copolymer dispersions were allowed to cool to 20 °C and stored at this temperature for 24 h prior to dilution with *n*-dodecane.[12] Subsequent TEM analysis confirmed that both thermal transitions were more or less reversible for such concentrated dispersions (**Figure 5.14**) with the corresponding DLS data supporting these observations (**Table 5.1**).
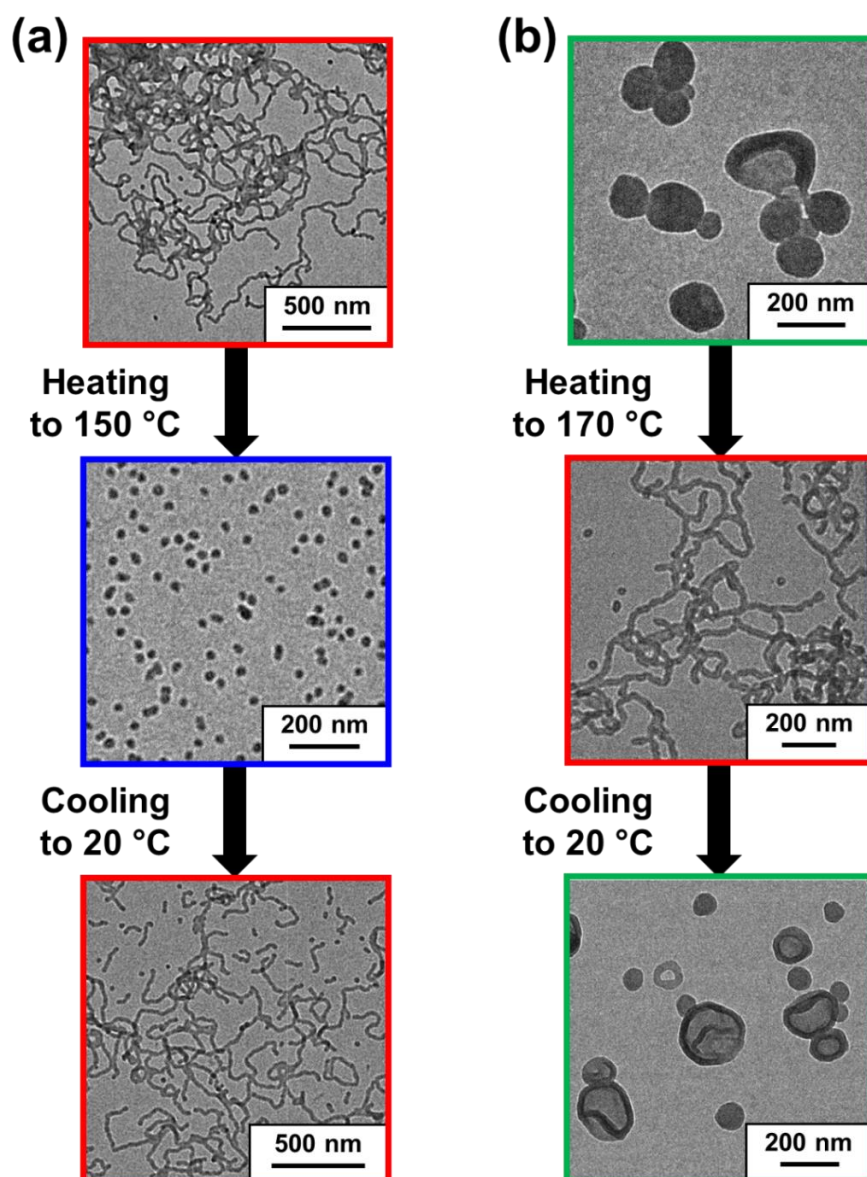
Figure 5.14. (a) Representative TEM images recorded during the worm-to-sphere transition for PLMA$_{22}$-P(0.9MMA-*stat*-0.1LMA)$_{113}$ worms prepared at 20% w/w solids in mineral oil. The initial copolymer dispersion (red frame) was heated to 150 °C and equilibrated for 30 min at this temperature, prior to dilution with hot *n*-dodecane (blue frame) and finally aged for 24 h at 20 °C (red frame). **(b)** Representative TEM images recorded during the vesicle-to-worm transition for PLMA$_{22}$-P(0.9MMA-*stat*-0.1LMA)$_{228}$ vesicles prepared at 20% w/w solids in mineral oil. The initial copolymer dispersion (green frame) was heated to 170 °C and equilibrated for 30 min at this temperature, prior to dilution with hot *n*-dodecane (red frame) and finally aged for 24 h at 20 °C (green frame).
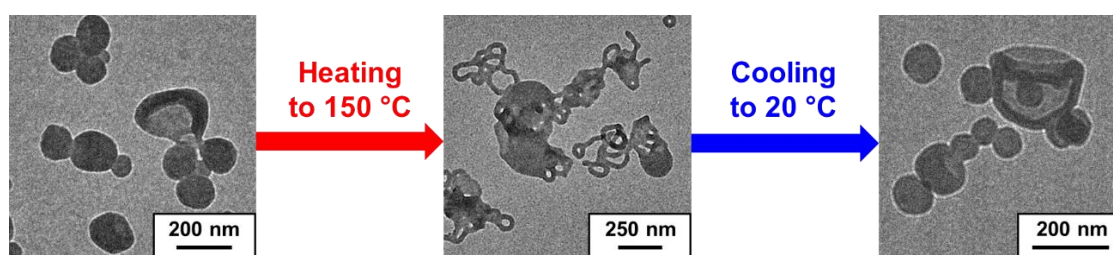
Figure 5.15. Representative TEM images recorded for the morphology transition exhibited by PLMA$_{22}$-P(0.9MMA-*stat*-0.1LMA)$_{228}$ vesicles prepared at 20% w/w solids in mineral oil. The initial copolymer dispersion was heated to 150 °C and equilibrated for 30 min at this temperature, prior to dilution with hot *n*-dodecane, cooling from 150 °C to 20 °C and ageing for 24 h at 20 °C.

Table 5.1. Summary of DLS data obtained for thermoresponsive PLMA$_{22}$-P(0.9MMA-*stat*-0.1LMA)$_{113}$ worms and PLMA$_{22}$-P(0.9MMA-*stat*-0.1LMA)$_{228}$ vesicles prepared at 20% w/w solids in mineral oil at 115 °C. The 20% w/w worm dispersion was heated to 150 °C, equilibrated for 1 h, then cooled to 20 °C and stored at this temperature for 24 h before DLS analysis. The vesicle dispersion was treated similarly, except that it was heated to 170 °C rather than 150 °C.

Target Copolymer Composition	Experimental Conditions	DLS		TEM Morphology
		D_h (nm)	PDI	
PLMA$_{22}$-P(0.9MMA-*stat*-0.1LMA)$_{113}$	Original	229	0.45	Worms
PLMA$_{22}$-P(0.9MMA-*stat*-0.1LMA)$_{113}$	Heated to 150 °C	35	0.04	Spheres
PLMA$_{22}$-P(0.9MMA-*stat*-0.1LMA)$_{113}$	Cooled to 20 °C	166	0.32	Worms
PLMA$_{22}$-P(0.9MMA-*stat*-0.1LMA)$_{228}$	Original	140	0.12	Vesicles
PLMA$_{22}$-P(0.9MMA-*stat*-0.1LMA)$_{228}$	Heated to 170 °C	104	0.16	Worms
PLMA$_{22}$-P(0.9MMA-*stat*-0.1LMA)$_{228}$	Cooled to 20 °C	129	0.09	Vesicles

5.4. Conclusions

In **Chapter 4**, we reported the synthesis of PLMA$_{22}$-PMMA$_y$ diblock copolymer nanoparticles in mineral oil but only spheres, short worms or micron-sized spherical aggregates could be produced. To overcome this unexpected morphological constraint, a series of PLMA$_x$-P(0.9MMA-*stat*-0.1LMA)$_y$ diblock copolymer nanoparticles were prepared *via* RAFT dispersion copolymerization of MMA with 10 mol% LMA at 20% solids in mineral oil using either PLMA$_{22}$ or PLMA$_{41}$ precursors at 115 °C. *In situ* ^{1}H NMR studies indicated an overall comonomer conversion of 94% within 2.5 h when targeting a core-forming block DP of 300. A narrow molecular weight distribution ($M_w/M_n \leq 1.35$) was confirmed for each diblock copolymer. Systematic variation of the LMA content from 0 to 10 mol % resulted in a gradual reduction in the T_g of the core-forming block. Empirically, it was found that at least 10 mol% LMA was required to promote the formation of higher order morphologies for syntheses performed at 115 °C. Using the relatively short PLMA$_{22}$ precursor enabled pure spheres, worms or vesicles to be obtained, as judged by TEM, DLS and SAXS analysis. Furthermore, a worm-to-sphere transition was observed for PLMA$_{22}$-P(0.9MMA-*stat*-0.1LMA)$_{113}$ worms at elevated temperature while PLMA$_{22}$-P(0.9MMA-*stat*-0.1LMA)$_{228}$ vesicles underwent a vesicle-to-worm transition on heating. DLS studies indicated that such morphology transitions were irreversible for 0.1 % w/w dispersions but good reversibility was observed for 20% w/w dispersions according to TEM and DLS analysis.

5.5. References

(1)   Israelachvili, J. N.; Mitchell, D. J.; Ninham, B. W. Theory of Self-Assembly of Hydrocarbon Amphiphiles into Micelles and Bilayers. *J. Chem. Soc. Faraday Trans. 2* **1976**, *72*, 1525–1568.

(2)   Antonietti, M.; Förster, S. Vesicles and Liposomes: A Self-Assembly Principle Beyond Lipids. *Adv. Mater.* **2003**, *15*, 1323–1333.

(3)   Warren, N. J.; Armes, S. P. Polymerization-Induced Self-Assembly of Block Copolymer Nano-Objects via RAFT Aqueous Dispersion Polymerization. *J. Am. Chem. Soc.* **2014**, *136*, 10174–10185.

(4)   Canning, S. L.; Smith, G. N.; Armes, S. P. A Critical Appraisal of RAFT-Mediated Polymerization-Induced Self-Assembly. *Macromolecules* **2016**, *49*, 1985–2001.

(5)   Blanazs, A.; Ryan, A. J.; Armes, S. P. Predictive Phase Diagrams for RAFT Aqueous

Dispersion Polymerization: Effect of Block Copolymer Composition, Molecular Weight, and Copolymer Concentration. *Macromolecules* **2012**, *45*, 5099–5107.

(6) Fielding, L. A.; Derry, M. J.; Ladmiral, V.; Rosselgong, J.; Rodrigues, A. M.; Ratcliffe, L. P. D.; Sugihara, S.; Armes, S. P. RAFT Dispersion Polymerization in Non-Polar Solvents: Facile Production of Block Copolymer Spheres, Worms and Vesicles in n-Alkanes. *Chem. Sci.* **2013**, *4*, 2081–2087.

(7) Fielding, L. A.; Lane, J. A.; Derry, M. J.; Mykhaylyk, O. O.; Armes, S. P. Thermo-Responsive Diblock Copolymer Worm Gels in Non-Polar Solvents. *J. Am. Chem. Soc.* **2014**, *136*, 5790–5798.

(8) Derry, M. J.; Fielding, L. A.; Warren, N. J.; Mable, C. J.; Smith, A. J.; Mykhaylyk, O. O.; Armes, S. P. In Situ Small-Angle X-Ray Scattering Studies of Sterically-Stabilized Diblock Copolymer Nanoparticles Formed during Polymerization-Induced Self-Assembly in Non-Polar Media. *Chem. Sci.* **2016**, *7*, 5078–5090.

(9) Semsarilar, M.; Ladmiral, V.; Blanazs, A.; Armes, S. P. Anionic Polyelectrolyte-Stabilized Nanoparticles via RAFT Aqueous Dispersion Polymerization. *Langmuir* **2012**, *28*, 914–922.

(10) Semsarilar, M.; Ladmiral, V.; Blanazs, A.; Armes, S. P. Cationic Polyelectrolyte-Stabilized Nanoparticles via RAFT Aqueous Dispersion Polymerization. *Langmuir* **2013**, *29*, 7416–7424.

(11) Yang, P.; Ratcliffe, L. P. D.; Armes, S. P. Efficient Synthesis of Poly(Methacrylic Acid)-Block-Poly(Styrene-Alt-N-phenylmaleimide) Diblock Copolymer Lamellae Using RAFT Dispersion Polymerization. *Macromolecules* **2013**, *46*, 8545–8556.

(12) György, C.; Verity, C.; Neal, T. J.; Rymaruk, M. J.; Cornel, E. J.; Smith, T.; Growney, D. J.; Armes, S. P. RAFT Dispersion Polymerization of Methyl Methacrylate in Mineral Oil: High Glass Transition Temperature of the Core-Forming Block Constrains the Evolution of Copolymer Morphology. *Macromolecules* **2021**, *54*, 9496–9509.

(13) Fox, T. G.; Flory, P. J. Second-Order Transition Temperatures and Related Properties of Polystyrene. I. Influence of Molecular Weight. *J. Appl. Phys.* **1950**, *21*, 581.

(14) Fox, T. G.; Flory, P. J. The Glass Temperature and Related Properties of Poly-Styrene. Influence of Molecular Weight. *J. Polym. Sci.* **1954**, *14*, 315–319.

(15) Trent, J. S. Ruthenium Tetraoxide Staining of Polymers: New Preparative Methods for Electron Microscopy. *Macromolecules* **1984**, *17*, 2930–2931.

(16) Pauw, B. R.; Smith, A. J.; Snow, T.; Terrill, N. J.; Thünemann, A. F. The Modular Small-Angle X-Ray Scattering Data Correction Sequence. *J. Appl. Crystallogr.* **2017**, *50*, 1800–1811.

(17) Ilavsky, J.; Jemian, P. R. Irena: Tool Suite for Modeling and Analysis of Small-Angle Scattering. *J. Appl. Crystallogr.* **2009**, *42*, 347–353.

(18) Wang, G.; Schmitt, M.; Wang, Z.; Lee, B.; Pan, X.; Fu, L.; Yan, J.; Li, S.; Xie, G.; Bockstaller, M. R.; Matyjaszewski, K. Polymerization-Induced Self-Assembly (PISA) Using ICAR ATRP at Low Catalyst Concentration. *Macromolecules* **2016**, *49*, 8605–8615.

(19) Zhou, J.; Zhang, W.; Hong, C.; Pan, C. Promotion of Morphology Transition of Di-Block Copolymer Nano-Objects: Via RAFT Dispersion Copolymerization. *Polym. Chem.* **2016**, *7*, 3259–3267.

(20) Sobotta, F. H.; Kuchenbrod, M.; Hoeppener, S.; Brendel, J. C. One Polymer

Composition, Various Morphologies: The Decisive Influence of Conditions on the Polymerization-Induced Self-Assembly (PISA) of N-Acryloyl Thiomorpholine. *Nanoscale* **2020**, *12*, 20171–20176.

(21) Yoshida, E. Morphology Control of Giant Vesicles by Manipulating Hydrophobic-Hydrophilic Balance of Amphiphilic Random Block Copolymers through Polymerization-Induced Self-Assembly. *Colloid Polym. Sci.* **2014**, *292*, 763–769.

(22) Shi, P.; Zhou, H.; Gao, C.; Wang, S.; Sun, P.; Zhang, W. Macro-RAFT Agent Mediated Dispersion Copolymerization: A Small Amount of Solvophilic Co-Monomer Leads to a Great Change. *Polym. Chem.* **2015**, *6*, 4911–4920.

(23) Huang, C.; Tan, J.; Xu, Q.; He, J.; Li, X.; Liu, D.; Zhang, L. Adding a Solvophilic Comonomer to the Polymerization-Induced Self-Assembly of Block Copolymer and Homopolymer: A Cooperative Strategy for Preparing Large Compound Vesicles. *RSC Adv.* **2017**, *7*, 46069–46081.

(24) Figg, C. A.; Carmean, R. N.; Bentz, K. C.; Mukherjee, S.; Savin, D. A.; Sumerlin, B. S. Tuning Hydrophobicity To Program Block Copolymer Assemblies from the Inside Out. *Macromolecules* **2017**, *50*, 935–943.

(25) Tan, M.; Shi, Y.; Fu, Z.; Yang, W. In Situ Synthesis of Diblock Copolymer Nano-Assemblies via Dispersion RAFT Polymerization Induced Self-Assembly and Ag/Copolymer Composite Nanoparticles Thereof. *Polym. Chem.* **2018**, *9*, 1082–1094.

(26) Fox, T. G. Influence of Diluent and of Copolymer Composition on the Glass Temperature of a Polymer System. *Bull. Am. Phys. Soc.* **1956**, *1*, 123.

(27) Rymaruk, M. J.; Hunter, S. J.; O'Brien, C. T.; Brown, S. L.; Williams, C. N.; Armes, S. P. RAFT Dispersion Polymerization in Silicone Oil. *Macromolecules* **2019**, *52*, 2822–2832.

(28) Cornel, E. J.; Smith, G. N.; Rogers, S. E.; Hallett, J. E.; Growney, D. J.; Smith, T.; O'Hora, P. S.; Van Meurs, S.; Mykhaylyk, O. O.; Armes, S. P. Time-Resolved Small-Angle Neutron Scattering Studies of the Thermally-Induced Exchange of Copolymer Chains between Spherical Diblock Copolymer Nanoparticles Prepared via Polymerization-Induced Self-Assembly. *Soft Matter* **2020**, *16*, 3657–3668.

(29) Derry, M. J.; Fielding, L. A.; Armes, S. P. Industrially-Relevant Polymerization-Induced Self-Assembly Formulations in Non-Polar Solvents: RAFT Dispersion Polymerization of Benzyl Methacrylate. *Polym. Chem.* **2015**, *6*, 3054–3062.

(30) Docherty, P. J.; Girou, C.; Derry, M. J.; Armes, S. P. Epoxy-Functional Diblock Copolymer Spheres, Worms and Vesicles via Polymerization-Induced Self-Assembly in Mineral Oil. *Polym. Chem.* **2020**, *11*, 3332–3339.

(31) Docherty, P. J.; Derry, M. J.; Armes, S. P. RAFT Dispersion Polymerization of Glycidyl Methacrylate for the Synthesis of Epoxy-Functional Block Copolymer Nanoparticles in Mineral Oil. *Polym. Chem.* **2019**, *10*, 603–611.

(32) Parker, B. R.; Derry, M. J.; Ning, Y.; Armes, S. P. Exploring the Upper Size Limit for Sterically Stabilized Diblock Copolymer Nanoparticles Prepared by Polymerization-Induced Self-Assembly in Non-Polar Media. *Langmuir* **2020**, *36*, 3730–3736.

(33) Glatter, O.; Kratky, O. *Small-Angle X-Ray Scattering*; Academic Press, London, 1982.

(34) Pedersen, J. S. Form Factors of Block Copolymer Micelles with Spherical, Ellipsoidal and Cylindrical Cores. *J. Appl. Crystallogr.* **2000**, *33*, 637–640.

(35) Bang, J.; Jain, S.; Li, Z.; Lodge, T. P.; Pedersen, J. S.; Kesselman, E.; Talmon, Y.

Sphere, Cylinder, and Vesicle Nanoaggregates in Poly(Styrene-b-Isoprene) Diblock Copolymer Solutions. *Macromolecules* **2006**, *39*, 1199–1208.

(36)   Derry, M. J.; Mykhaylyk, O. O.; Armes, S. P. A Vesicle-to-Worm Transition Provides a New High-Temperature Oil Thickening Mechanism. *Angew. Chemie - Int. Ed.* **2017**, *56*, 1746–1750.

(37)   Pei, Y.; Thurairajah, L.; Sugita, O. R.; Lowe, A. B. RAFT Dispersion Polymerization in Nonpolar Media: Polymerization of 3-Phenylpropyl Methacrylate in N-Tetradecane with Poly(Stearyl Methacrylate) Homopolymers as Macro Chain Transfer Agents. *Macromolecules* **2015**, *48*, 236–244.

(38)   Pei, Y.; Sugita, O. R.; Thurairajah, L.; Lowe, A. B. Synthesis of Poly(Stearyl Methacrylate-b-3-Phenylpropyl Methacrylate) Nanoparticles in n-Octane and Associated Thermoreversible Polymorphism. *RSC Adv.* **2015**, *5*, 17636–17646.

(39)   Dorsman, I. R.; Derry, M. J.; Cunningham, V. J.; Brown, S. L.; Williams, C. N.; Armes, S. P. Tuning the Vesicle-to-Worm Transition for Thermoresponsive Block Copolymer Vesicles Prepared: Via Polymerisation-Induced Self-Assembly. *Polym. Chem.* **2021**, *12*, 1224–1235.

Chapter 6. Synthesis and Derivatization of Epoxy-Functional Sterically-Stabilized Diblock Copolymer Spheres in Non-Polar Media: Does the Spatial Location of the Epoxy Groups Matter?

Chapter 6. Synthesis and Derivatization of Epoxy-Functional Sterically-Stabilized Diblock Copolymer Spheres in Non-Polar Media: Does the Spatial Location of the Epoxy Groups Matter?

6.1. Introduction

Over the past two decades or so, RAFT polymerization has proven to be a powerful radical-based technique for the synthesis of a wide range of *functional* vinyl polymers.[1–4] It is particularly useful in the context of polymerization-induced self-assembly (PISA).

Given the exceptional tolerance of RAFT polymerization towards monomer functionality, many examples of functional nanoparticles have been prepared using PISA.[5–14] Of particular relevance to this Thesis Chapter is the use of glycidyl methacrylate (GlyMA) to design epoxy-functional nanoparticles.[15–33] In principle, such nanoparticles can be derivatized by ring-opening the epoxy groups using nucleophiles such as water,[34–36] amines,[23,29,33,36–39] thiols[19,23,29,36,39,40] carboxylic acids,[41,42] azides[33,36,43] or organosilyl reagents.[44]

The preparation of epoxy-functional spheres, worms or vesicles *via* RAFT aqueous emulsion polymerization of GlyMA has been reported by both Armes and co-workers and Tan *et al*.[18,20,22,24,25,33,45] For such PISA formulations, premature loss of the epoxy groups *via* ring-opening attack by water can be minimized by choosing appropriate mild reaction conditions (e.g. neutral pH, moderate reaction temperatures of 20-50 °C) and ensuring short reaction times. Similarly, Docherty *et al*. reported the facile synthesis of epoxy-functional diblock copolymer nano-objects directly in mineral oil.[15,16] In this case, the survival of the epoxy groups is much less sensitive to the reaction conditions. Nevertheless, trace amounts of protic impurities can lead to intermolecular branching/crosslinking during the long-term storage of such copolymer dispersions at ambient temperature.[15] Typically, the epoxy groups are located within the nanoparticle cores but an alternative strategy is to incorporate the epoxy groups within the steric stabilizer chains. In principle, this can be achieved either by using an appropriate epoxy-functional RAFT agent[19] or by statistical copolymerization of a small amount of GlyMA with a suitable oil-soluble methacrylic comonomer.[19,29,30]

Herein we use PISA to prepare epoxy-functional sterically-stabilized diblock copolymer spheres directly in mineral oil whereby the epoxy groups are located either (i) within the nanoparticle cores or (ii) within the steric stabilizer chains, see **Scheme 6.1**. Both types of nanoparticles are characterized by ¹H NMR spectroscopy, THF GPC, TEM and DLS. Subsequently, model epoxy ring-opening reactions are conducted using either benzylamine or

water. In particular, we demonstrate that the reaction conditions required to achieve high extents of reaction are highly dependent on the spatial location of the epoxy groups.
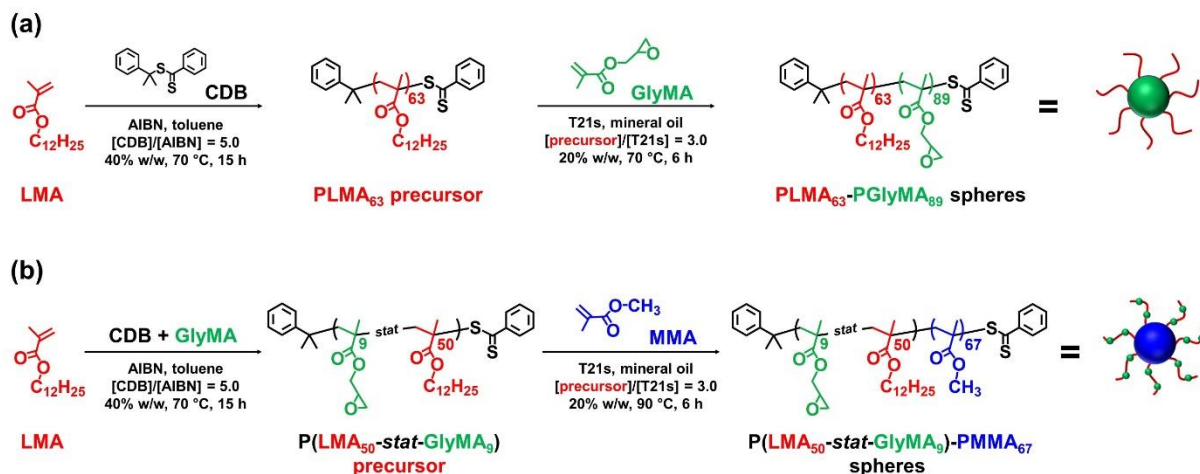
Scheme 6.1. (a) Synthesis of poly(lauryl methacrylate) (PLMA$_{63}$) *via* RAFT solution polymerization of LMA in anhydrous toluene at 40% w/w solids using cumyl dithiobenzoate (CDB) RAFT agent and 2,2′-azobisisobutyronitrile (AIBN) initiator at 70 °C. This precursor was then chain-extended by RAFT dispersion polymerization of glycidyl methacrylate (GlyMA) using a *tert*-butyl peroxy-2-ethylhexanoate (T21s) initiator at 70 °C in mineral oil and targeting 20% w/w solids. **(b)** Synthesis of a poly(lauryl methacrylate-*stat*-glycidyl methacrylate) [P(LMA$_{50}$-*stat*-GlyMA$_9$)] precursor *via* RAFT solution copolymerization of LMA with GlyMA in anhydrous toluene at 40% w/w solids using a CDB RAFT agent and AIBN initiator at 70 °C, followed by the RAFT dispersion polymerization of methyl methacrylate (MMA) at 90 °C in mineral oil using T21s initiator and targeting 20% w/w solids.

6.2. Experimental

6.2.1. Materials

Methyl methacrylate (MMA, 99%) was purchased from Alfa Aesar (Germany), passed through basic alumina to remove its inhibitor and then stored at –20 °C prior to use. Lauryl methacrylate (LMA, 96%), glycidyl methacrylate (GlyMA, 97%), cumyl dithiobenzoate (CDB), benzylamine (99%), *N*-methylaniline (99%), 2-(dimethylamino)propylamine (99%), triethylenetetramine (≥ 97%), 1-butanethiol (99%), CDCl$_3$ and *n*-dodecane were purchased from Merck (UK) and used as received. 2,2′-Azobisisobutyronitrile (AIBN) was obtained from Molekula (UK) and *tert*-butyl peroxy-2-ethylhexanoate (T21s) was purchased from AkzoNobel (The Netherlands). CD$_2$Cl$_2$ was purchased from Goss Scientific (UK).

Chapter 6. Synthesis and Derivatization of Epoxy-Functional Sterically-Stabilized Diblock Copolymer Spheres in Non-Polar Media: Does the Spatial Location of the Epoxy Groups Matter?

Tetrahydrofuran was obtained from VWR Chemicals (UK). Methanol, acetic acid (99%) and toluene were purchased from Fisher Scientific (UK). Group III hydroisomerized mineral oil (viscosity = 4.3 cSt at 100 °C) was kindly provided by Lubrizol Ltd. (Hazelwood, Derbyshire, UK).

6.2.2. Methods

Synthesis of PLMA$_{63}$ precursor *via* RAFT solution polymerization in toluene

A PLMA$_{63}$ precursor was synthesized at 40% w/w solids according to a previously reported synthesis protocol.[46] Briefly, this synthesis was conducted as follows. LMA (77.0 g; 302.8 mmol), CDB (1.50 g; 5.5 mmol; target DP = 55), AIBN (181 mg; 1.10 mmol; CDB/AIBN molar ratio = 5.0) and anhydrous toluene (118.1 g) were weighed into a 250 mL round-bottomed flask. The sealed flask was purged with nitrogen for 30 min and immersed in a preheated oil bath at 70 °C. The reaction solution was stirred continuously, and the ensuing polymerization was quenched after 15 h by exposing the reaction solution to air while cooling the flask to room temperature. A final LMA conversion of 90% was determined by ^{1}H NMR spectroscopy. The crude polymer was purified by three consecutive precipitations into a ten-fold excess of methanol (with redissolution in THF after each precipitation). The mean DP of this PLMA precursor was calculated to be 63 using ^{1}H NMR spectroscopy by comparing the ten aromatic protons assigned to the cumyl and dithiobenzoate end-groups at 7.10-8.00 ppm to the two oxymethylene protons attributed to PLMA at 3.75–4.20 ppm. THF GPC analysis using a refractive index detector and a series of near-monodisperse poly(methyl methacrylate) calibration standards indicated an M_n of 12 600 g mol^{-1} and an M_w/M_n of 1.19.

Synthesis of P(LMA$_{50}$-*stat*-GlyMA$_9$) precursor *via* RAFT solution polymerization in toluene

The P(LMA$_{50}$-*stat*-GlyMA$_9$) precursor was synthesized at 40% w/w solids as follows. LMA (63.0 g; 247.8 mmol), GlyMA (5.5 g; 38.5 mmol), CDB (1.50 g; 5.50 mmol; target DP = 52), AIBN (181 mg; 1.10 mmol; CDB/AIBN molar ratio = 5.0) and anhydrous toluene (105.3 g) were weighed into a 250 mL round-bottomed flask. Anhydrous

toluene was used to minimize the potential loss of epoxy groups *via* ring-opening with water. The sealed flask was purged with nitrogen for 30 min and immersed in a preheated oil bath at 70 °C. The reaction solution was stirred continuously, and the ensuing polymerization was quenched after 15 h by exposing the reaction solution to air while cooling the flask to room temperature. An overall comonomer conversion of 90% was determined by ^{1}H NMR spectroscopy. The crude copolymer was purified by three consecutive precipitations into a ten-fold excess of methanol (with redissolution in THF after each precipitation). The overall mean DP of this P(LMA-*stat*-GlyMA) precursor was calculated to be 59 (with 50 LMA units and 9 GlyMA units per copolymer chain), by using ^{1}H NMR spectroscopy to compare the ten aromatic protons assigned to the cumyl and dithiobenzoate end-groups at 7.10-8.00 ppm to the two oxymethylene protons attributed to the LMA repeat units at 3.85–4.20 ppm and the methine proton corresponding to the epoxide ring at 3.10-3.30 ppm, respectively. THF GPC analysis using a refractive index detector and a series of near-monodisperse poly(methyl methacrylate) calibration standards indicated an M_n of 12 300 g mol^{-1} and an M_w/M_n of 1.19.

Synthesis of poly(lauryl methacrylate)-poly(glycidyl methacrylate) (PLMA$_{63}$-PGlyMA$_{89}$) spherical nanoparticles *via* RAFT dispersion polymerization of GlyMA in mineral oil

PLMA$_{63}$-PGlyMA$_{89}$ spherical nanoparticles were synthesized at 20% w/w solids using the following protocol. PLMA$_{63}$ precursor (1.50 g; 92.0 µmol), GlyMA (1.18 g; 8.28 mmol; target DP = 90), T21s initiator (6.64 mg; 30.7 µmol; precursor/T21s molar ratio = 3.0; 10.0% v/v in mineral oil) and mineral oil (10.74 g) were weighed into a glass vial and purged with nitrogen for 30 min. The sealed vial was immersed in a preheated oil bath at 70 °C and the reaction mixture was magnetically stirred for 6 h. ^{1}H NMR analysis indicated 99% GlyMA conversion by comparing the integrated monomer vinyl signal at 6.17 ppm to the integrated epoxy methine signals corresponding to both PGlyMA and GlyMA at 3.20–3.33 ppm. THF GPC analysis using a refractive index detector and a series of near-monodisperse poly(methyl methacrylate) calibration standards indicated an M_n of 22 000 g mol^{-1} and an M_w/M_n of 1.18.

Chapter 6. Synthesis and Derivatization of Epoxy-Functional Sterically-Stabilized Diblock Copolymer Spheres in Non-Polar Media: Does the Spatial Location of the Epoxy Groups Matter?

Synthesis of poly(lauryl methacrylate-*stat*-glycidyl methacrylate)-poly(methyl methacrylate) (P(LMA$_{50}$-*stat*-GlyMA$_9$)-PMMA$_{67}$) spherical nanoparticles *via* RAFT dispersion polymerization of MMA in mineral oil

P(LMA$_{50}$-*stat*-GlyMA$_9$)-PMMA$_{67}$ spherical nanoparticles were synthesized at 20% w/w solids as follows. P(LMA$_{50}$-*stat*-GlyMA$_9$) precursor (2.00 g; 140.13 µmol), T21s initiator (10.10 mg; 46.71 µmol; precursor/T21s molar ratio = 3.0; 10.0% v/v in mineral oil) and mineral oil (11.97 g) were weighed into a glass vial and purged with nitrogen for 30 min. MMA monomer (1.04 mL; 9.81 mmol; target DP = 70) was degassed separately then added to the reaction mixture *via* syringe. The sealed vial was immersed in a preheated oil bath at 90 °C and the reaction mixture was magnetically stirred for 6 h. ^{1}H NMR analysis indicated 95% MMA conversion by comparing the integrated methyl signal assigned to MMA at 3.77 ppm to the integrated methyl signal corresponding to PMMA at 3.55–3.72 ppm. THF GPC analysis using a refractive index detector and a series of near-monodisperse poly(methyl methacrylate) calibration standards indicated an M_n of 21 100 g mol^{-1} and an M_w/M_n of 1.17.

Derivatization of PLMA$_{63}$-PGlyMA$_{89}$ spherical nanoparticles with benzylamine

A typical protocol for functionalization of PLMA$_{63}$-PGlyMA$_{89}$ spheres with benzylamine was conducted as follows: benzylamine (67.6 µL, 0.619 mmol; [amine]/[epoxy] molar ratio = 1.0) was added to 1.0 g of a 20% w/w dispersion of PLMA$_{63}$-PGlyMA$_{89}$ spheres in mineral oil *via* micropipet. The sealed vial was immersed in a preheated oil bath at 70 °C and the reaction mixture was magnetically stirred for 17 h. Unfortunately, the final copolymer proved to be insoluble in various deuterated solvents, which prevented its analysis by ^{1}H NMR spectroscopy. Thus the extent of functionalization was assessed by FT-IR spectroscopy. The core-crosslinked copolymer nanoparticles were purified by three consecutive precipitations into a ten-fold excess of methanol (with redispersion in THF after each precipitation) and then dried under vacuum for 24 h prior to analysis.

Chapter 6. Synthesis and Derivatization of Epoxy-Functional Sterically-Stabilized Diblock Copolymer Spheres in Non-Polar Media: Does the Spatial Location of the Epoxy Groups Matter?

Derivatization of P(LMA$_{50}$-*stat*-GlyMA$_9$)-PMMA$_{67}$ spherical nanoparticles using various amines

A typical protocol for functionalization of P(LMA$_{50}$-*stat*-GlyMA$_9$)-PMMA$_{67}$ spheres with benzylamine was conducted as follows: benzylamine (9.2 µL, 84.58 µmol; [amine]/[epoxy] molar ratio = 1.0) was added to 1.0 g of a 20% w/w dispersion of P(LMA$_{50}$-*stat*-GlyMA$_9$)-PMMA$_{67}$ spheres in mineral oil *via* micropipet. The sealed vial was immersed in a preheated oil bath at 70 °C and the reaction mixture was magnetically stirred for 17 h. The reduction in epoxy groups (Y%) was determined using ^{1}H NMR spectroscopy by comparing the satellite signal of the PMMA backbone at 3.43-3.47 ppm to the integrated epoxy methine signal at 3.12-3.30 ppm. The same reaction was also studied using a 2, 5, 10, 20 or 50-fold excess of benzylamine under otherwise identical conditions. In addition, when using an equimolar amount of amine, the reaction time was varied from 17 h to 88 h, the solids content was adjusted from 20 to 35% w/w solids and the reaction temperature ranged from 20 to 90 °C. Furthermore, alternative nucleophiles such as *N*-methylaniline, 2-(dimethylamino)propylamine or triethylenetetramine (using an [amine]/[epoxy] molar ratio = 1.0 in each case) were also examined at 20% w/w solids in mineral oil for 17 h at 70 °C. Finally, 1-butanethiol ([thiol]/[epoxy] molar ratio = 50) was also examined at 20% w/w solids in mineral oil for 17 h at 70 °C.

Epoxy ring-opening reactions of PLMA$_{63}$-PGlyMA$_{89}$ and P(LMA$_{50}$-*stat*-GlyMA$_9$)-PMMA$_{67}$ spherical nanoparticles using water

A typical protocol for reacting the epoxy groups of PLMA$_{63}$-PGlyMA$_{89}$ and P(LMA$_{50}$-*stat*-GlyMA$_9$)-PMMA$_{67}$ spheres with water was conducted as follows. A 20% w/w nanoparticle dispersion in mineral oil (1.0 g) was weighed into a glass vial. The sealed vial was immersed in a preheated oil bath at 110 °C and the reaction mixture was magnetically stirred for 17 h. The reduction in epoxy groups (Y%) for the P(LMA$_{50}$-*stat*-GlyMA$_9$)-PMMA$_{67}$ spheres was determined by using ^{1}H NMR spectroscopy to compare the satellite signal of the PMMA backbone at 3.43-3.47 ppm to the integrated epoxy methine signal at 3.12-3.30 ppm. The extent of epoxy ring-opening for the PLMA$_{63}$-PGlyMA$_{89}$ spheres was assessed by FT-IR spectroscopy. The core-crosslinked copolymer nanoparticles were purified by three consecutive precipitations into a ten-

fold excess of methanol (with redispersion in THF after each precipitation) and then dried under vacuum for 24 h prior to analysis.

Epoxy ring-opening reactions of PLMA$_{63}$-PGlyMA$_{89}$ spherical nanoparticles using 50% v/v acetic acid

A typical protocol for ring-opening the epoxy groups of PLMA$_{63}$-PGlyMA$_{89}$ spherical nanoparticles using 50% v/v acetic acid was conducted as follows: 4.0 g of a 20% w/w nanoparticle dispersion in mineral oil was weighed into a 10 mL round-bottomed flask. This flask was then immersed in a preheated oil bath at 110 °C and connected *via* plastic tubing to a second round-bottomed flask (also immersed in an oil bath set to 110 °C) containing 10 mL of 50% v/v aqueous acetic acid (see **Figure 6.1**). The latter flask was connected to a stream of N$_2$ gas to generate acidic vapor. Both flasks were magnetically stirred for 17 h whereby essentially all of the 50% v/v aqueous acetic acid had evaporated. The epoxy ring-opening reaction for the PLMA$_{63}$-PGlyMA$_{89}$ spheres was analyzed by FT-IR spectroscopy. The copolymer was purified by three consecutive precipitations into a ten-fold excess of methanol (with redispersion in THF after each precipitation) then dried under vacuum for 24 h prior to analysis.
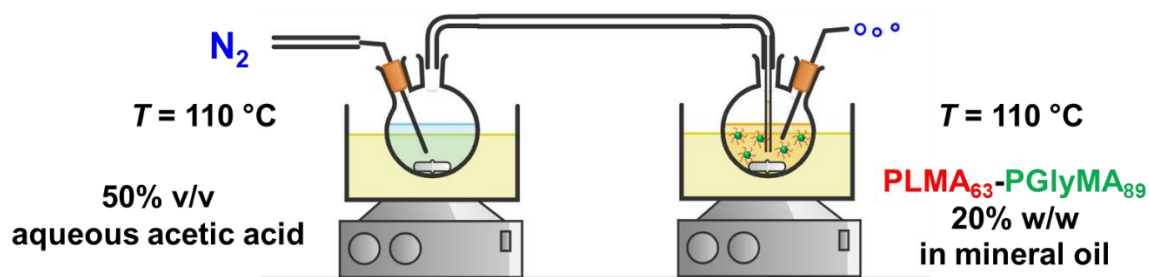
Figure 6.1. Experimental setup when reacting a 20% w/w dispersion of PLMA$_{63}$-PGlyMA$_{89}$ nanoparticles in mineral oil with 50% v/v aqueous acetic acid at 110 °C.

^{1}H NMR spectroscopy

^{1}H NMR spectra were recorded in either CD$_2$Cl$_2$ or CDCl$_3$ using a 400 MHz Bruker Avance spectrometer. Typically, 64 scans were averaged per spectrum.

Gel Permeation Chromatography (GPC)

Molecular weight distributions (MWDs) were assessed by GPC using THF as an eluent. The GPC system was equipped with two 5 μm (30 cm) Mixed C columns and a WellChrom K-2301 refractive index detector operating at 950 ± 30 nm. The THF mobile phase contained 2.0% v/v triethylamine and 0.05% w/v butylhydroxytoluene (BHT) and the flow rate was fixed at 1.0 ml min^{-1}. A series of twelve near-monodisperse poly(methyl methacrylate) standards (M_p values ranging from 800 to 2 200 000 g mol^{-1}) were used for column calibration in combination with a refractive index detector.

Dynamic Light Scattering (DLS)

DLS studies were performed using a Zetasizer Nano ZS instrument (Malvern Instruments, UK) at a fixed scattering angle of 173°. Copolymer dispersions were diluted to 0.10% w/w solids using n-dodecane prior to analysis at 20 °C. The z-average diameter and polydispersity of the nanoparticles were calculated by cumulants analysis of the experimental correlation function using Dispersion Technology Software version 6.20. Data were averaged over ten runs each of thirty seconds duration.

Transmission Electron Microscopy (TEM)

TEM studies were conducted using a FEI Tecnai G2 spirit instrument operating at 80 kV and equipped with a Gatan 1k CCD camera. A single droplet of a 0.10% w/w copolymer dispersion was placed onto a carbon-coated copper grid and allowed to dry, prior to exposure to ruthenium(VIII) oxide vapor for 7 min at 20 °C.[47] This heavy metal compound acts as a positive stain for the core-forming PGlyMA or PMMA block to improve contrast. The ruthenium(VIII) oxide was prepared as follows: ruthenium(IV) oxide (0.30 g) was added to water (50 g) to form a black slurry; addition of sodium periodate (2.0 g) with continuous stirring produced a yellow solution of ruthenium(VIII) oxide within 1 min at 20 °C.

Fourier Transform Infrared (FT-IR) Spectroscopy

FT-IR spectra were recorded for the PLMA$_{63}$-PGlyMA$_{89}$ precursor and derivatized PLMA$_{63}$-PGlyMA$_{89}$ diblock copolymers at 20 °C using a Thermo-Scientific Nicolet

iS10 FT-IR spectrometer equipped with a Golden Gate Diamond ATR accessory. The spectral resolution was 4 cm^{-1} and 96 scans were averaged per spectrum.

6.3. Results and Discussion

6.3.1. Synthesis of PLMA$_{63}$-PGlyMA$_{89}$ and P(LMA$_{50}$-*stat*-GlyMA$_{9}$)-PMMA$_{67}$ spherical nanoparticles

A PLMA$_{63}$ precursor was synthesized *via* RAFT solution polymerization of LMA in anhydrous toluene at 70 °C using CDB as a RAFT agent (see **Scheme 6.1**). A P(LMA$_{50}$-*stat*-GlyMA$_{9}$) precursor was prepared by copolymerization of LMA with GlyMA using the same reaction conditions. Since LMA and GlyMA are both methacrylic monomers, they should exhibit similar comonomer reactivity ratios. Thus an approximately statistical distribution of GlyMA groups along the steric stabilizer chains is expected for this second precursor.

For both syntheses, the polymerization was quenched after 15 h, with ^{1}H NMR spectroscopy studies indicating 90% LMA conversion for PLMA$_{63}$ and an overall comonomer conversion of 90% for P(LMA$_{50}$-*stat*-GlyMA$_{9}$). THF GPC analysis indicated an M_{n} of 12 600 g mol^{-1} (M_{w}/M_{n} = 1.19) for PLMA$_{63}$ and an M_{n} of 12 300 g mol^{-1} (M_{w}/M_{n} = 1.19) for P(LMA$_{50}$-*stat*-GlyMA$_{9}$) (see **Figure 6.2**). In order to produce nanoparticles of comparable size, the PLMA$_{63}$ precursor was chain-extended *via* RAFT dispersion polymerization of GlyMA in mineral oil targeting a degree of polymerization (DP) of 90 for the PGlyMA block while the P(LMA$_{50}$-*stat*-GlyMA$_{9}$) precursor was chain-extended using MMA targeting a mean PMMA DP of 70. ^{1}H NMR analysis indicated a GlyMA conversion of 99% to afford PLMA$_{63}$-PGlyMA$_{89}$ nanoparticles while 95% MMA conversion produced P(LMA$_{50}$-*stat*-GlyMA$_{9}$)-PMMA$_{67}$ nanoparticles. ^{1}H NMR analysis also confirmed that essentially all the epoxy groups remained intact under these synthesis conditions (the ten aromatic protons assigned to the cumyl and dithiobenzoate end-groups at 7.10-8.00 ppm were compared to the epoxy methine proton at 3.12-3.33 ppm, see **Figure 6.3**). Similar observations were reported by Docherty *et al*. for the synthesis of PSMA-PGlyMA spherical nanoparticles in mineral oil.[15] A relatively high blocking efficiency and narrow molecular weight

distribution ($M_w/M_n \leq 1.18$) was confirmed in each case by THF GPC analysis (see **Figure 6.2**). The PLMA$_{63}$-PGlyMA$_{89}$ nanoparticles had a z-average diameter of 28 nm (polydispersity index (PDI) = 0.03) while the P(LMA$_{50}$-*stat*-GlyMA$_9$)-PMMA$_{67}$ nanoparticles exhibited a z-average diameter of 26 nm (PDI = 0.05), see **Figure 6.4**. In summary, these nanoparticles were deemed suitable for studying the post-polymerization modification of their epoxy groups using various nucleophiles.
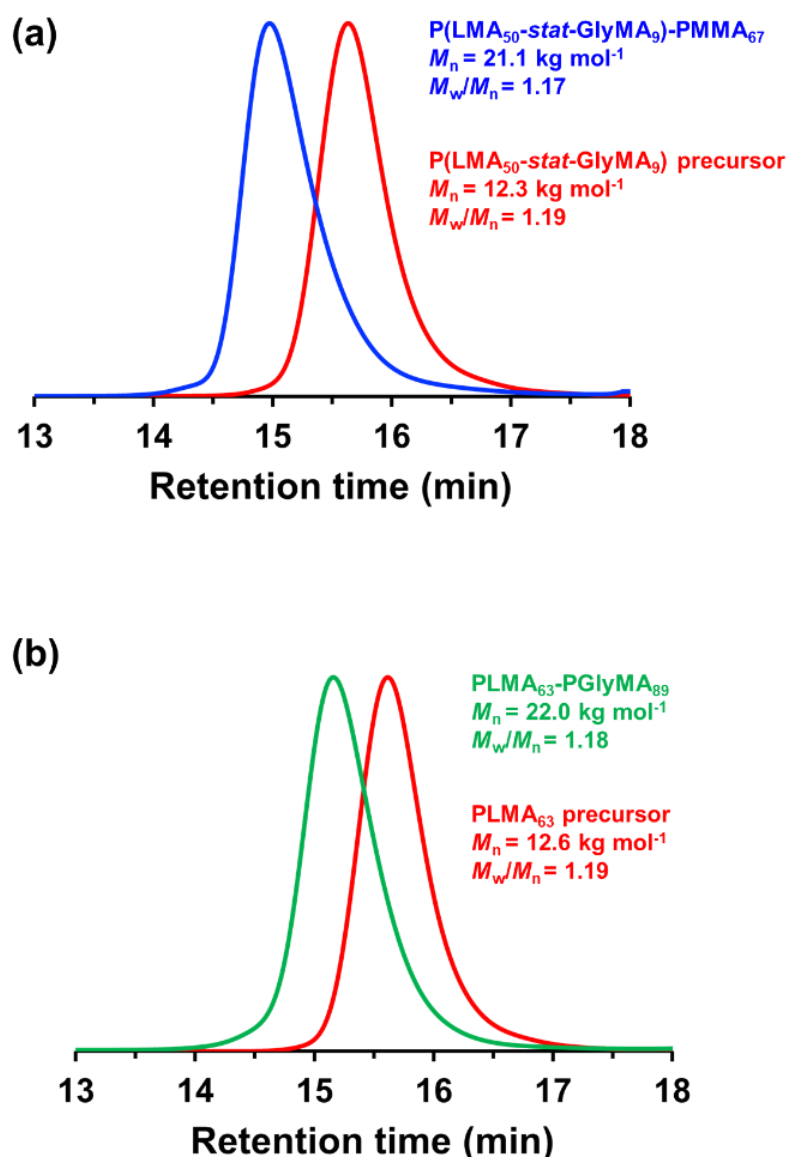
Figure 6.2. THF GPC curves (refractive index detector; *vs.* a series of near-monodisperse poly(methyl methacrylate) calibration standards) recorded for: **(a)** the P(LMA$_{50}$-*stat*-GlyMA$_9$) precursor and the corresponding P(LMA$_{50}$-*stat*-GlyMA$_9$)-PMMA$_{67}$ diblock copolymer; **(b)**.the PLMA$_{63}$ precursor and the corresponding PLMA$_{63}$-GlyMA$_{89}$ diblock copolymer.
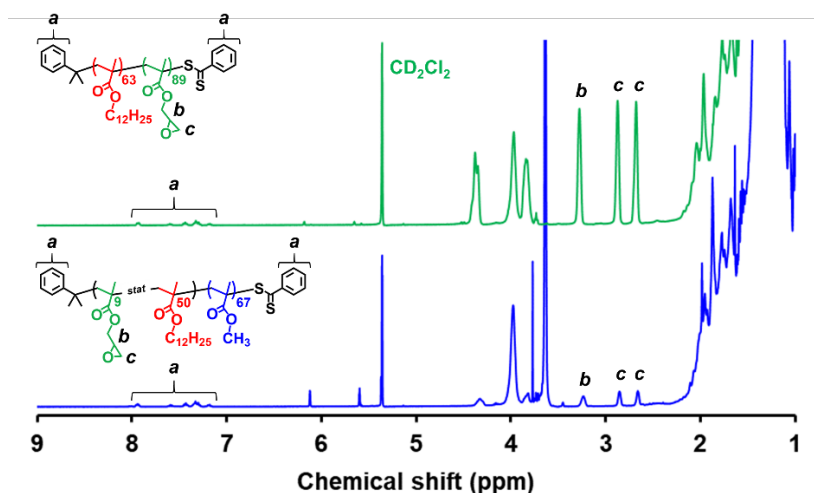
Figure 6.3. ^{1}H NMR spectra recorded in CD_2Cl_2 for the PLMA$_{63}$-PGlyMA$_{89}$ (green spectrum) and P(LMA$_{50}$-*stat*-GlyMA$_9$)-PMMA$_{67}$ (blue spectrum) diblock copolymers. To determine the degree of retention of the epoxy groups, the integrated aromatic proton signals *a* assigned to the copolymer end-groups at 7.10-8.00 ppm were compared to the intensity of the methine proton *b* assigned to the epoxy rings at 3.12-3.33 ppm.
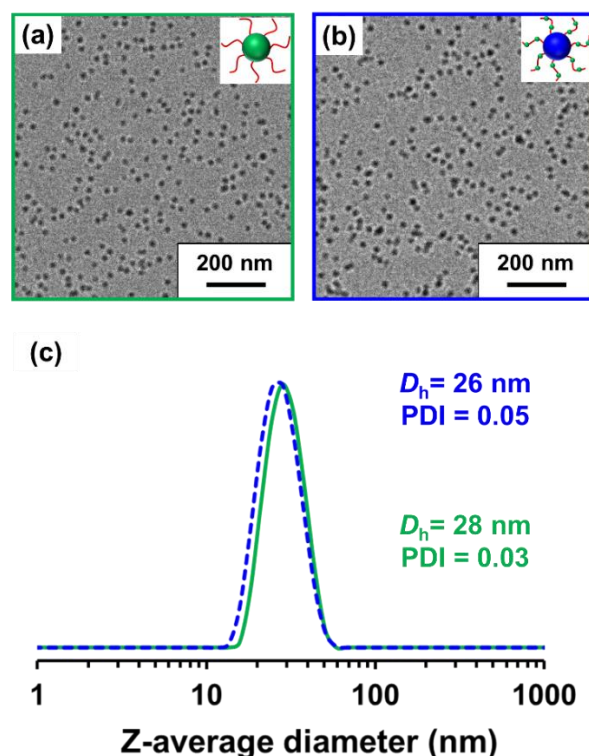
Figure 6.4. Representative TEM images obtained for **(a)** PLMA$_{63}$-PGlyMA$_{89}$ (green frame) and **(b)** P(LMA$_{50}$-*stat*-GlyMA$_9$)-PMMA$_{67}$ (blue frame) nanoparticles prepared at 20% w/w solids in mineral oil. **(c)** DLS data recorded for 0.1% w/w dispersions of PLMA$_{63}$-PGlyMA$_{89}$ nanoparticles (green trace) and P(LMA$_{50}$-*stat*-GlyMA$_9$)-PMMA$_{67}$ nanoparticles (blue trace) in mineral oil. A z-average hydrodynamic diameter (D_h) of 28 nm (DLS PDI = 0.03) was determined for the PLMA$_{63}$-PGlyMA$_{89}$ nanoparticles and 26 nm (DLS PDI = 0.05) for the P(LMA$_{50}$-*stat*-GlyMA$_9$)-PMMA$_{67}$ nanoparticles.

6.3.2. Post-polymerization modification of the epoxy groups within PLMA$_{63}$-PGlyMA$_{89}$ nanoparticles and P(LMA$_{50}$-*stat*-GlyMA$_{9}$)-PMMA$_{67}$ nanoparticles using benzylamine

The post-polymerization modification of epoxy-functional diblock copolymer nanoparticles by amines has been previously studied for various aqueous PISA formulations.[22,27,29,33] In such cases, epoxy-amine chemistry was used to introduce either disulfide[29] or TEMPO[22] functionalities or cationic character,[22,27,29,33] with intra- or inter-nanoparticle crosslinking often being observed. Recently, the reaction of epoxy groups with *N*-methylaniline has been reported for PSMA-PGlyMA nanoparticles in mineral oil.[15]

Herein we examine the derivatization of epoxy-functional PLMA$_{63}$-PGlyMA$_{89}$ and P(LMA$_{50}$-*stat*-GlyMA$_{9}$)-PMMA$_{67}$ nanoparticles using benzylamine. This is a useful model compound because aromatic amines such as *p*-phenylenediamine can serve as anti-knock agents[48] and/or anti-oxidants[49,50] for automotive engine oil formulations. Initially, the reaction between the P(LMA$_{50}$-*stat*-GlyMA$_{9}$)-PMMA$_{67}$ nanoparticles and benzylamine was examined using an [amine]/[epoxy] molar ratio of unity at 20% w/w solids in mineral oil at 70 °C. Subsequent studies involved using excess amine (ranging from two-fold to fifty-fold) under the same conditions. To identify the precise chemical shift for the new azamethylene signal produced by the epoxy ring-opening reaction, a model reaction between GlyMA monomer and benzylamine was examined in mineral oil (see **Figure 6.5**). Unfortunately, this new azamethylene signal overlaps with the original methylene signal arising from the epoxy ring at 2.60-2.90 ppm.
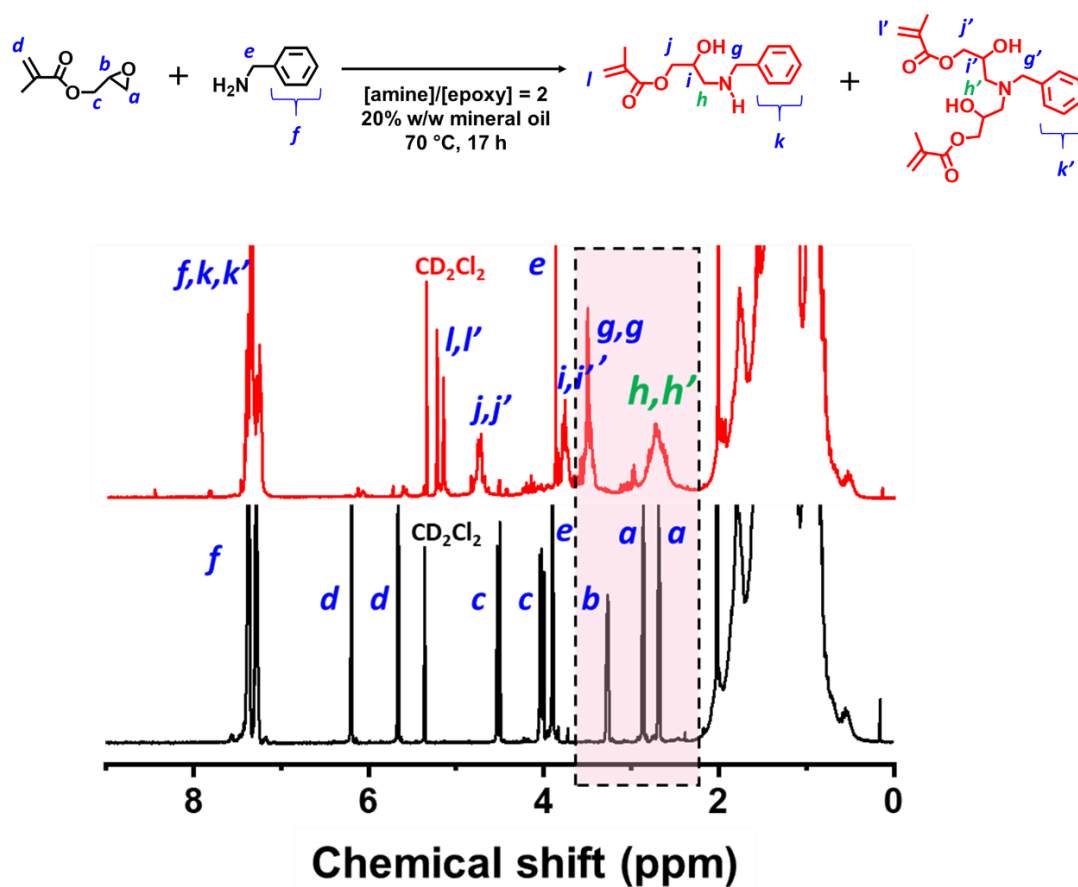
Figure 6.5. Assigned ¹H NMR spectra recorded in CD₂Cl₂ for the reaction between GlyMA and benzylamine: initial mixture (black spectrum) and after heating for 17 h at 70 °C (red spectrum). This reaction was conducted at 20% w/w solids in mineral oil using an [amine]/[epoxy] molar ratio of 2.0.

Nevertheless, epoxy group consumption could be monitored by comparing the intensity of the (constant) satellite signal assigned to the PMMA backbone at 3.43-3.47 ppm to the methine signal of the epoxy ring at 3.12-3.30 ppm (see **Figure 6.6**). Loss of 16% of the original epoxy groups was observed after 17 h at 70 °C when using a stoichiometric amount of benzylamine. In fact, complete loss of the epoxy groups (99%) was only achieved when using a 50-fold excess of benzylamine (see **Figure 6.6**).
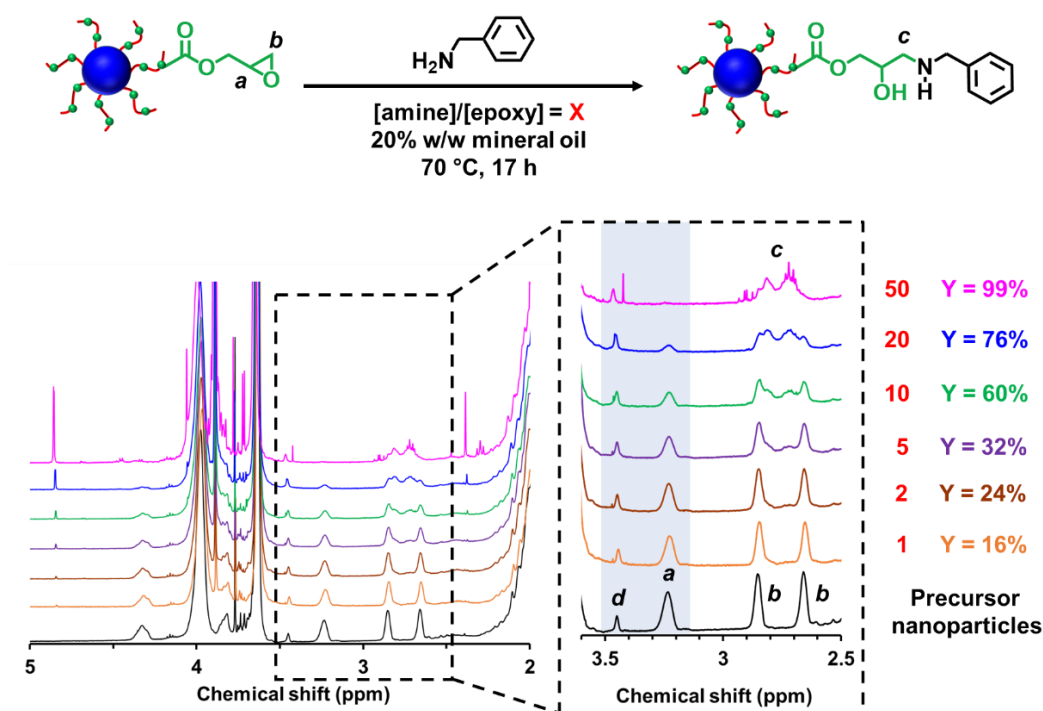
Figure 6.6. ^{1}H NMR spectra recorded in CD_2Cl_2 for P(LMA$_{50}$-*stat*-GlyMA$_9$)-PMMA$_{67}$ before (black spectrum) and after reaction with benzylamine at 70 °C for 17 h at 20% w/w solids when using an [amine]/[epoxy] molar ratio (X) of 1 (orange spectrum), 2 (brown spectrum), 5 (purple spectrum), 10 (green spectrum), 20 (blue spectrum) and 50 (pink spectrum), respectively. Expansion of the 2.5-3.6 ppm region confirms the systematic loss of epoxy groups (note the gradual attenuation of methine signal *a* and the evolution of a new methylene signal *c* on increasing the [amine]/[epoxy] molar ratio. In each case, the epoxy loss (Y%) was determined by comparing the satellite signal *d* assigned to the PMMA backbone at 3.43-3.47 ppm to the methine signal *a* corresponding to the epoxide ring at 3.12-3.30 ppm.

In an attempt to enhance this sluggish epoxy-amine reaction, the reaction time, solids content and temperature were systematically varied while using an [amine]/[epoxy] molar ratio of unity. As shown in **Table 6.1**, an extended reaction time of 88 h resulted in a 30% reduction in the original epoxy group signal. In contrast, derivatizing the nanoparticles at 35% w/w solids only led to 23% of epoxy groups reacting with the benzylamine. Similar results (21%) were achieved when heating a 20% w/w nanoparticle dispersion to 90 °C for 17 h.

203

Chapter 6. Synthesis and Derivatization of Epoxy-Functional Sterically-Stabilized Diblock Copolymer Spheres in Non-Polar Media: Does the Spatial Location of the Epoxy Groups Matter?

Table 6.1. Summary of the loss of epoxy groups (Y%) determined by ^{1}H NMR analysis of P(LMA$_{50}$-stat-GlyMA$_9$)-PMMA$_{67}$ after reaction with benzylamine using a constant [amine]/[epoxy] molar ratio of unity while systematically varying (i) the reaction time (a-d), (ii) the solids content (e-g) or (iii) the reaction temperature (h-j). In each case, the loss of epoxy groups (Y%) was determined by comparing a satellite signal assigned to the PMMA backbone at 3.43-3.47 ppm to the methine signal corresponding to the epoxide ring at 3.12-3.30 ppm.

Reaction Code	Reaction Time (h)	Solids content (%)	Reaction Temperature (°C)	Y (%)
a	17	20	70	16
b	40	20	70	23
c	64	20	70	28
d	88	20	70	30
e	17	25	70	19
f	17	30	70	21
g	17	35	70	23
h	17	20	25	9
i	17	20	50	13
j	17	20	90	21

Alternative aromatic amines such as *N*-methylaniline, 2-(dimethylamino)propylamine or triethylenetetramine were also examined but a discernible difference (*i.e.* 68% loss of the original epoxy groups) was only observed in the latter case (see **Figure 6.7**).
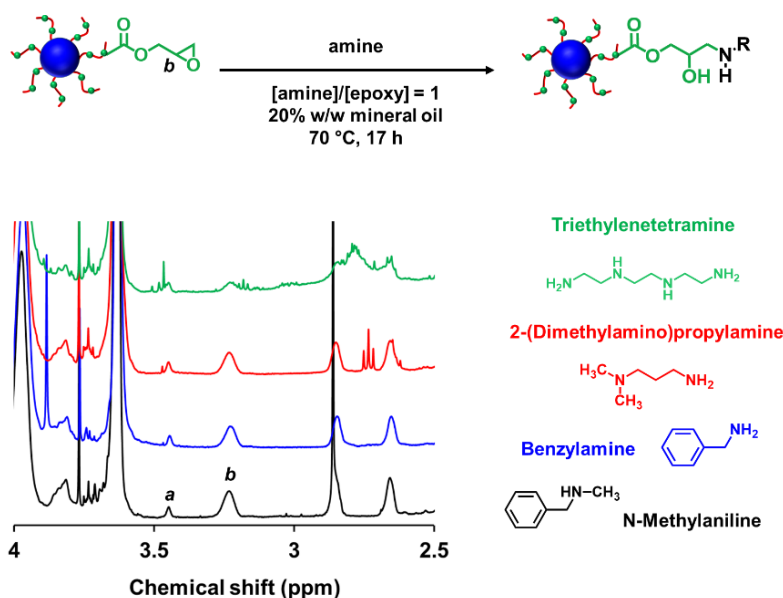
Figure 6.7. ^{1}H NMR spectra recorded in CD$_2$Cl$_2$ for a P(LMA$_{50}$-stat-GlyMA$_9$)-PMMA$_{67}$ diblock copolymer after reacting a 20% w/w dispersion of such nanoparticles in mineral oil with each of the following four amines in turn: *N*-methylaniline (black spectrum), benzylamine (blue spectrum), 2-(dimethylamino)propylamine (red spectrum) or triethylenetetramine (green spectrum). Conditions: 70 °C for 17 h, [thiol]/[epoxy] molar ratio = 1.0. By comparing satellite signal *a* assigned to the PMMA backbone at 3.43-3.47 ppm to the integrated methine signal *b* of the epoxy ring at 3.12-3.30 ppm, the approximate loss of the original epoxy groups was estimated to be 12%, 16%, 23% or 68% when using *N*-methylaniline, benzylamine, 2-(dimethylamino)propylamine or triethylenetetramine, respectively.

Chapter 6. Synthesis and Derivatization of Epoxy-Functional Sterically-Stabilized Diblock Copolymer Spheres in Non-Polar Media: Does the Spatial Location of the Epoxy Groups Matter?

Triethylenetetramine contains two primary and two secondary amine groups, which means that it can react with up to six epoxy groups. This leads to a high degree of inter-nanoparticle crosslinking: the apparent z-average diameter increased up to 59 nm, while the corresponding DLS PDI of 0.24 suggested significant broadening of the particle size distribution. Furthermore, using an alternative nucleophile such as 1-butanethiol only resulted in a 13% reduction of the epoxy groups even when using a 50-fold excess of this reagent, see **Figure 6.8**.
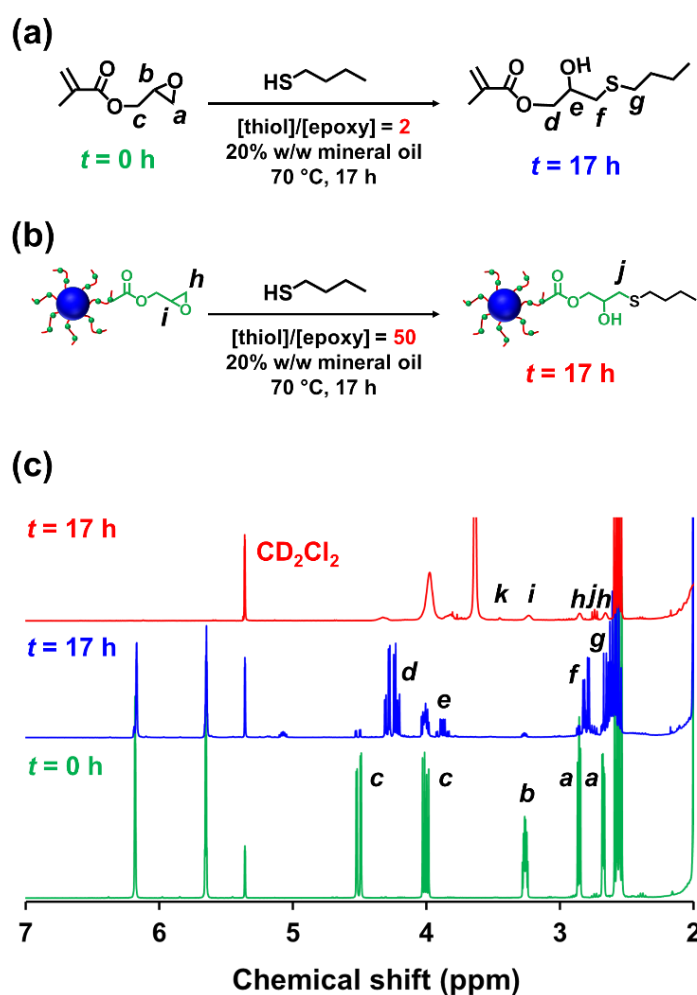
Figure 6.8. Schematic reaction of 1-butanethiol with **(a)** GlyMA monomer or **(b)** P(LMA$_{50}$-*stat*-GlyMA$_9$)-PMMA$_{67}$ nanoparticles. **(c)** Assigned ^{1}H NMR spectra recorded in CD$_2$Cl$_2$ for a reaction mixture containing GlyMA and 1-butanethiol at 20% w/w solids in mineral oil at 0 h (green spectrum) and after heating at 70 °C for 17 h (blue spectrum) when using an [amine]/[epoxy] molar ratio of 2.0. The red spectrum was obtained for a P(LMA$_{50}$-*stat*-GlyMA$_9$)-PMMA$_{67}$ diblock copolymer after heating the corresponding 20% w/w copolymer dispersion in mineral oil at 70 °C for 17 h using a [thiol]/[epoxy] molar ratio of 50. A % loss of epoxy groups of 13% was determined by comparing the satellite signal *k* assigned to the PMMA backbone at 3.43-3.47 ppm to the methine signal *i* corresponding to the epoxide ring at 3.12-3.30 ppm.

These data suggest that a high degree of derivatization for the epoxy-functionalized P(LMA$_{50}$-*stat*-GlyMA$_9$)-PMMA$_{67}$ nanoparticles can only be achieved when using a large excess of amine. This problem is most likely related to the relatively low epoxy group concentration (~ 0.07 mol dm^{-3}) under the reaction conditions. Indeed, similar observations were reported by Ratcliffe *et al.* for the derivatization of an aqueous dispersion of P(GMA$_{65}$-*stat*-GlyMA$_{1.7}$)-PHPMA$_{140}$ worms *via* epoxy-amine chemistry using cystamine. In this prior study, a 20-fold excess of diamine was required to obtain primary amine-functionalized thermoresponsive worms.[29]

Since benzylamine is a primary amine, there are various side-reactions that can occur during the attempted functionalization of P(LMA$_{50}$-*stat*-GlyMA$_9$)-PMMA$_{67}$ nanoparticles (see **Scheme 6.2**).[51]
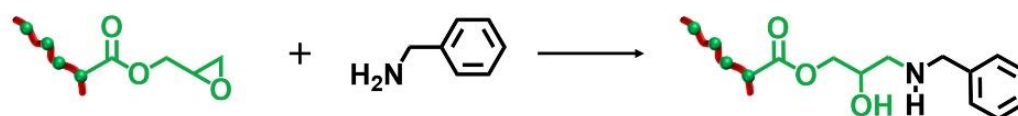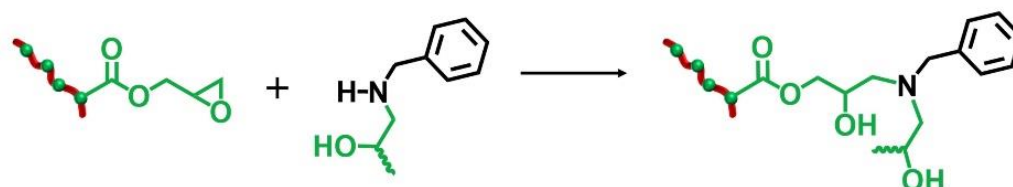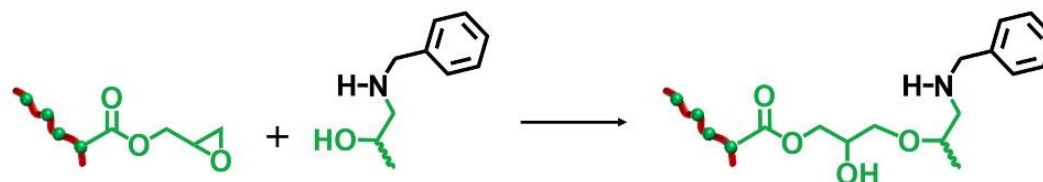
Scheme 6.2. Summary of the three possible reactions that can occur when reacting P(LMA$_{50}$-*stat*-GlyMA$_9$)-PMMA$_{67}$ nanoparticles with benzylamine. **(a)** Epoxy ring-opening results in the formation of a secondary amine and a hydroxyl group. **(b)** This secondary amine can then react with remaining epoxy groups. **(c)** Alternatively, the hydroxyl group can react with epoxy groups. Side-reactions (b) and (c) can lead cross-linking between and/or within stabilizer chains. In practice, the rate of reaction for (c) is expected to be slower than for (b).

The initial epoxy ring-opening reaction produces a hydroxyl and a secondary amine. In principle, these nucleophilic groups can react further with the remaining epoxy groups, which inevitably results in intra-chain and inter-chain cross-linking. Indeed, THF GPC analysis indicates the appearance of a high molecular weight shoulder, which provides evidence for such crosslinking (see **Figure 6.9**). Using an [amine]/[epoxy] molar ratio of unity resulted in an M_n of 24 900 g mol^{-1} with an M_w/M_n of 1.79, and the latter value being a significant increase on that observed for the linear precursor nanoparticles (M_n = 21 100 g mol^{-1}; M_w/M_n =1.17). However, systematically increasing the amount of excess benzylamine led to a gradual reduction in the high molecular weight shoulder (e.g., using a 50-fold excess of benzylamine afforded M_n = 23 100 g mol^{-1}; M_w/M_n = 1.31) (see **Figure 6.9**). These data suggest that using a sufficiently large excess of amine can minimize crosslinking between the copolymer chains.
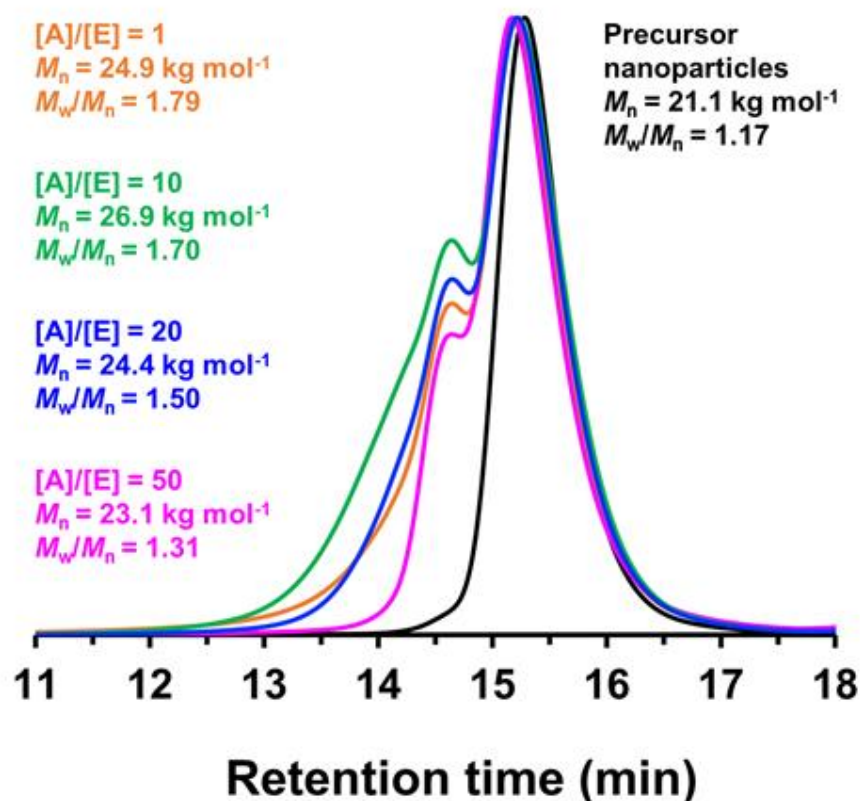
Figure 6.9. GPC curves (*vs.* a series of near-monodisperse poly(methyl methacrylate) calibration standards) recorded using a refractive index detector for P(LMA$_{50}$-*stat*-GlyMA$_9$)-PMMA$_{67}$ (prepared in mineral oil at 20% w/w solids at 90 °C) (black curve) and the benzylamine-derivatized P(LMA$_{50}$-*stat*-GlyMA$_9$)-PMMA$_{67}$ produced when using an [amine]/[epoxy] molar ratio of 1 (orange curve), 10 (green curve), 20 (blue curve) or 50 (pink curve). A systematic reduction in M_w/M_n was observed when increasing the [amine]/[epoxy] molar ratio.

The derivatization of PLMA$_{63}$-GlyMA$_{89}$ nanoparticles with benzylamine could not be assessed by ^{1}H NMR spectroscopy. In this case, the epoxy groups are much more closely located to each other within the nanoparticle cores. Thus using an [amine]/[epoxy] molar ratio of unity inevitably led to extensive core-crosslinking, which rendered the derivatized copolymer chains insoluble in deuterated solvents and hence precluded ^{1}H NMR analysis. Instead, copolymer powders were analyzed by FT-IR spectroscopy (after extended purification to remove the unreacted amine and mineral oil) to determine the extent of reaction of the epoxy groups. When using a stoichiometric amount of benzylamine, the asymmetric/symmetric ring deformation bands assigned to the epoxy groups at 850 and 910 cm^{-1} are fully attenuated while a new strong band corresponding to the out-of-plane aromatic C-H bending of the conjugated benzylamine is evident at 699 cm^{-1} (see **Figure 6.10**).
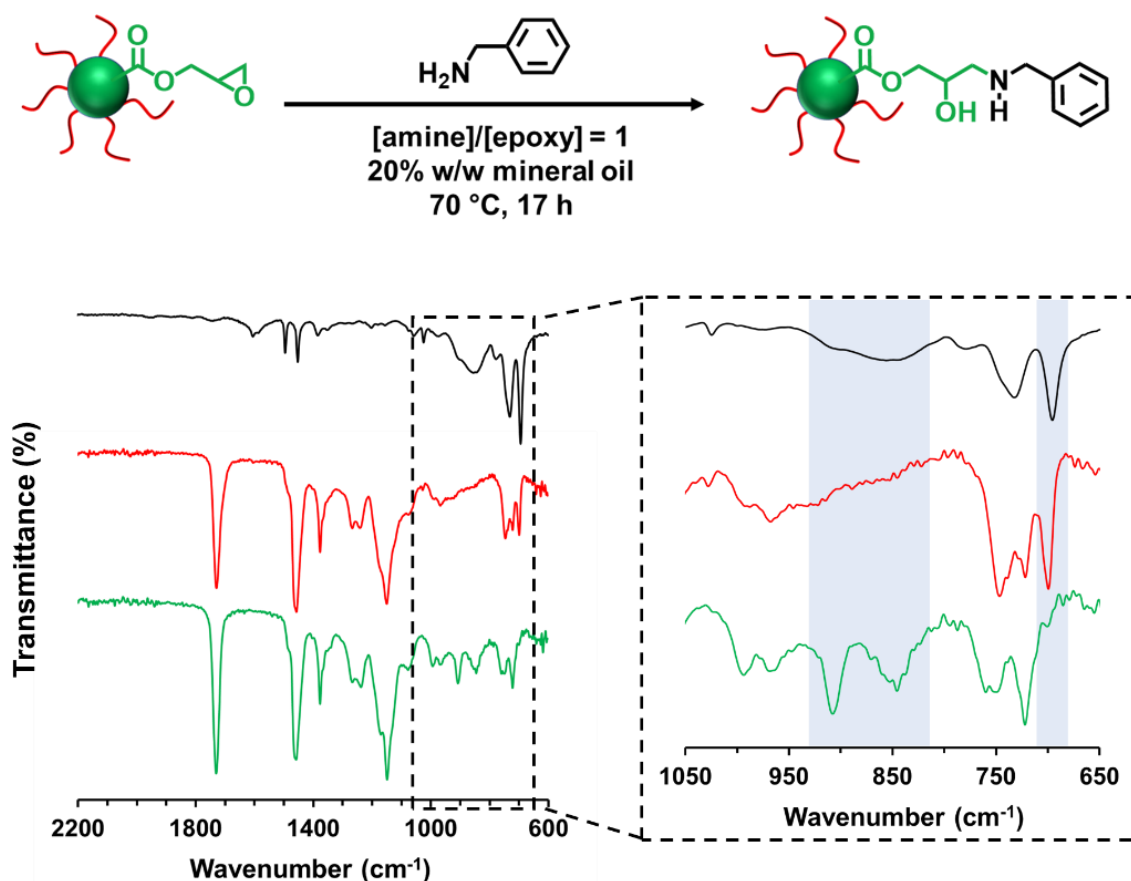
Figure 6.10. FT-IR spectra recorded for PLMA$_{63}$-PGlyMA$_{89}$ diblock copolymer prior to functionalization (green spectrum), PLMA$_{63}$-PGlyMA$_{89}$ diblock copolymer after functionalization with benzylamine (red spectrum) and benzylamine alone (black spectrum). The reaction conditions used are summarized in the corresponding chemical reaction.

6.3.3. Ring-opening of epoxy groups in PLMA$_{63}$-PGlyMA$_{89}$ and P(LMA$_{50}$-*stat*-GlyMA$_9$)-PMMA$_{67}$ nanoparticles by reaction with water

Zheng *et al.* and Derry *et al.* reported that core-crosslinked diblock copolymer spherical nanoparticles significantly reduced the friction between metal surfaces within the boundary lubrication regime.[52,53] In principle, such nanoparticles could be potentially useful for the formulation of next-generation, ultralow-viscosity automotive engine oils.[53]

Wan *et al.*[54] and Yuan *et al.*[55] demonstrated that ultrafine magnetite nanoparticles are produced by coprecipitation of ferric and ferrous salts in the presence of poly(glycerol monomethacrylate) (PGMA) homopolymer or PGMA-based diblock copolymers on addition of ammonium hydroxide. The PGMA chains adsorb strongly onto the magnetite nanoparticles because their pendent *cis*-diol groups can act as a bidentate chelating ligand for the surface Fe atoms.[54,55] In the context of the present study, ring-opening of the epoxy groups with water should produce the same GMA repeat units.[35] In principle, such GMA-functionalized nanoparticles may exhibit enhanced adsorption onto stainless steel, which might be expected to reduce friction between moving parts within an automotive engine.[53]

Ratcliffe *et al.* reported that GlyMA monomer can be readily converted into GMA by reaction with water at 80 °C.[35] Accordingly, the ring-opening of epoxy groups within the steric stabilizer chains of P(LMA$_{50}$-*stat*-GlyMA$_9$)-PMMA$_{67}$ nanoparticles was examined by simply heating a 20% w/w dispersion of such nanoparticles in mineral oil up to 110 °C. ^{1}H NMR analysis enabled the loss of epoxy groups over time to be monitored as they reacted with trace amounts of water. This approach indicated an extent of reaction of 72% within 17 h and 100% after 40 h (see **Figure 6.11a**).
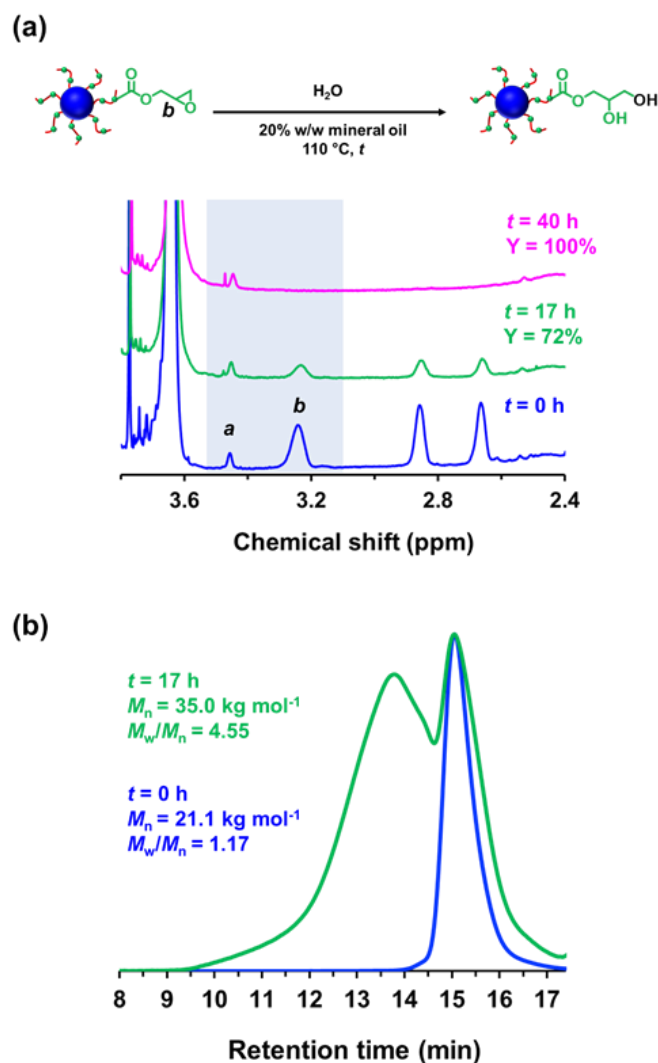
Figure 6.11. (a) ^{1}H NMR spectra recorded in CD_2Cl_2 for P(LMA$_{50}$-*stat*-GlyMA$_9$)-PMMA$_{67}$ chains before ($t = 0$ h; blue spectrum) and after heating the corresponding 20% w/w nanoparticle dispersion at 110 °C for either 17 h (green spectrum) or 40 h (pink spectrum). The epoxy loss (Y%) was determined by comparing the satellite signal *a* assigned to the PMMA backbone at 3.43-3.47 ppm to the methine signal *b* corresponding to the epoxide ring at 3.12-3.30 ppm. **(b)** GPC curves (refractive index detector *vs*. a series of near-monodisperse poly(methyl methacrylate) calibration standards) recorded for the P(LMA$_{50}$-*stat*-GlyMA$_9$)-PMMA$_{67}$ chains prior to heating (blue trace) and after heating to 110 °C for 17 h (green trace). The prominent high molecular weight shoulder indicates that extensive inter-chain crosslinking occurs under such conditions.

However, the initial free-flowing 20% w/w dispersion was transformed into a highly viscous gel (see **Figure 6.12**). Moreover, the z-average diameter of the nanoparticles increased from 26 nm (PDI = 0.05) to 117 nm (PDI = 0.43), which indicated extensive crosslinking between neighboring nanoparticles (see **Figure 6.13a**). TEM analysis also provided direct evidence for

210

such nanoparticle aggregation (see arrows in **Figure 6.13c**). Moreover, THF GPC analysis indicated the appearance of a high molecular weight shoulder after 17 h (see **Figure 6.11b**).

Figure 6.12. Digital photograph recorded for the original free-flowing 20% w/w dispersion of P(LMA$_{50}$-*stat*-GlyMA$_9$)-PMMA$_{67}$ nanoparticles (left-hand vial) and the viscous gel that is obtained after heating the same dispersion to 110 °C for 40 h (right-hand vial).
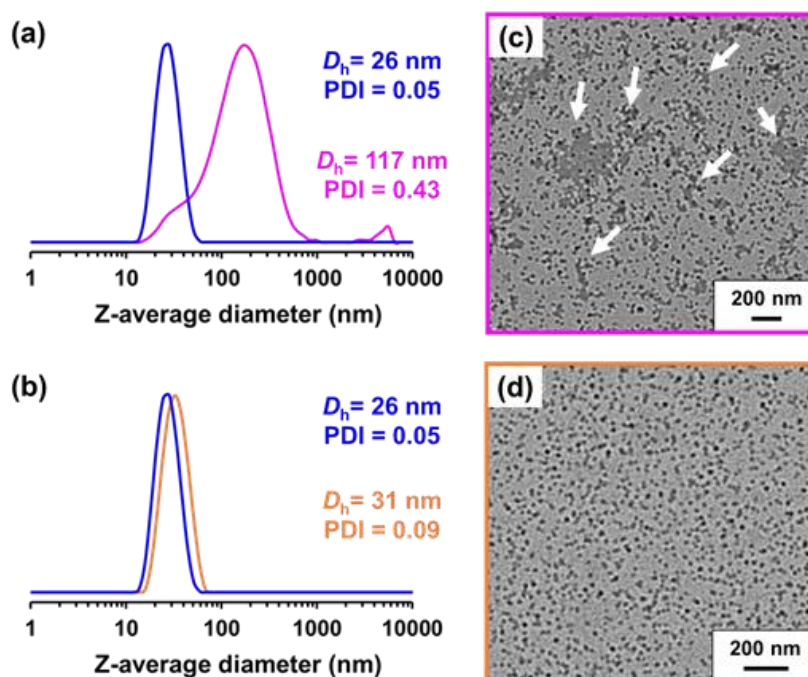
Figure 6.13. DLS particle size distributions recorded for P(LMA$_{50}$-*stat*-GlyMA$_9$)-PMMA$_{67}$ nanoparticles both prior to heating (blue trace) and after heating to 110 °C for 40 h at **(a)** 20% w/w solids (pink trace) or **(b)** 1.0% w/w solids (orange trace). Corresponding TEM images obtained for **(c)** the 20% w/w dispersion and **(d)** the 1.0% w/w dispersion after heating to 110 °C for 40 h.

Chapter 6. Synthesis and Derivatization of Epoxy-Functional Sterically-Stabilized Diblock Copolymer Spheres in Non-Polar Media: Does the Spatial Location of the Epoxy Groups Matter?

In principle, water can either originate from the mineral oil itself (which contains $\leq 0.004\%$ water) or from the atmosphere ($\leq 4\%$, depending on the relative humidity). To identify the source, the heating experiment was repeated under a N_2 atmosphere after deoxygenating the dispersion for 30 min using a stream of dry N_2 gas prior to heating. In this case, only $\sim 21\%$ of the original epoxy groups were lost within 88 h at 110 °C, which suggests that the major source of water is from the atmosphere (see **Figure 6.14**).
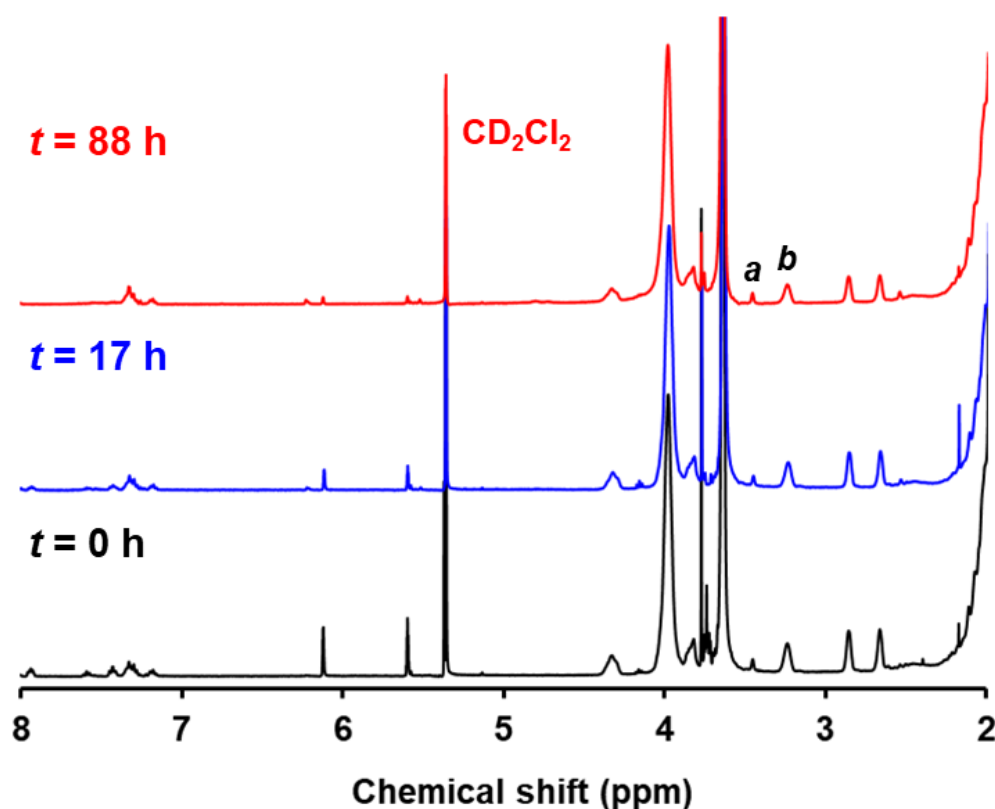
Figure 6.14. ^{1}H NMR spectra recorded in CD_2Cl_2 for the P(LMA$_{50}$-*stat*-GlyMA$_9$)-PMMA$_{67}$ diblock copolymer at t_0 (black spectrum) and after heating to 110 °C for either 17 h (blue spectrum) or 88 h (red spectrum). Prior to the heating experiment, the 20% w/w copolymer dispersion was deoxygenated using a stream of N_2 gas for 30 min. A % loss of epoxy groups of 21% was determined by comparing the satellite signal *a* assigned to the PMMA backbone at 3.43-3.47 ppm to the methine signal *b* corresponding to the epoxy ring at 3.12-3.30 ppm.

Moreover, using a relatively high reaction temperature appears to be essential because similar experiments conducted at 40 °C, 70 °C or 90 °C did not result in any discernible loss of the epoxy groups. In such cases, the GPC curves recorded for the copolymer chains before and after heating overlapped, which suggests that no ring-opening occurred under these milder conditions (see **Figure 6.15**).

(a) $T = 40\ °C$

t = 17 h
$M_n = 20.9$ kg mol^{-1}
$M_w/M_n = 1.17$

t = 0 h
$M_n = 21,1$ kg mol^{-1}
$M_w/M_n = 1.17$

(b) $T = 70\ °C$

t = 17 h
$M_n = 20.3$ kg mol^{-1}
$M_w/M_n = 1.17$

t = 0 h
$M_n = 21,1$ kg mol^{-1}
$M_w/M_n = 1.17$

(c) $T = 90\ °C$

t = 17 h
$M_n = 21.4$ kg mol^{-1}
$M_w/M_n = 1.21$

t = 0 h
$M_n = 21,1$ kg mol^{-1}
$M_w/M_n = 1.17$
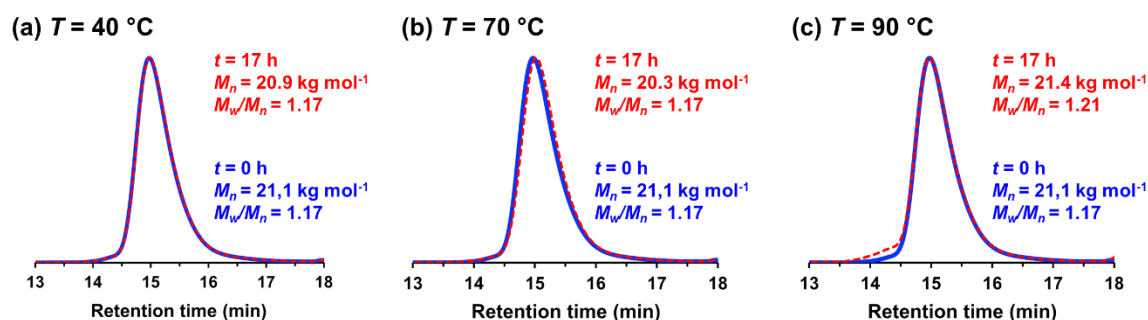
Figure 6.15. Comparison of the THF GPC curve recorded for the P(LMA$_{50}$-*stat*-GlyMA$_9$)-PMMA$_{67}$ diblock copolymer (prepared as a 20% w/w dispersion of nanoparticles in mineral oil at 90 °C; blue curves) with that obtained for the same copolymer (red data) after heating the 20% w/w dispersion for 17 h at **(a)** 40 °C, **(b)** 70 °C or **(c)** 90 °C, respectively.

As discussed above, hydroxyl groups produced *via* epoxy ring-opening can react further with the remaining epoxy groups. Such reactions can either occur between chains within an individual nanoparticle to produce intra-chain and/or inter-chain crosslinking or between two or more nanoparticles to produce incipient aggregation (see **Scheme 6.3**).

Crosslinking between stabilizer chains
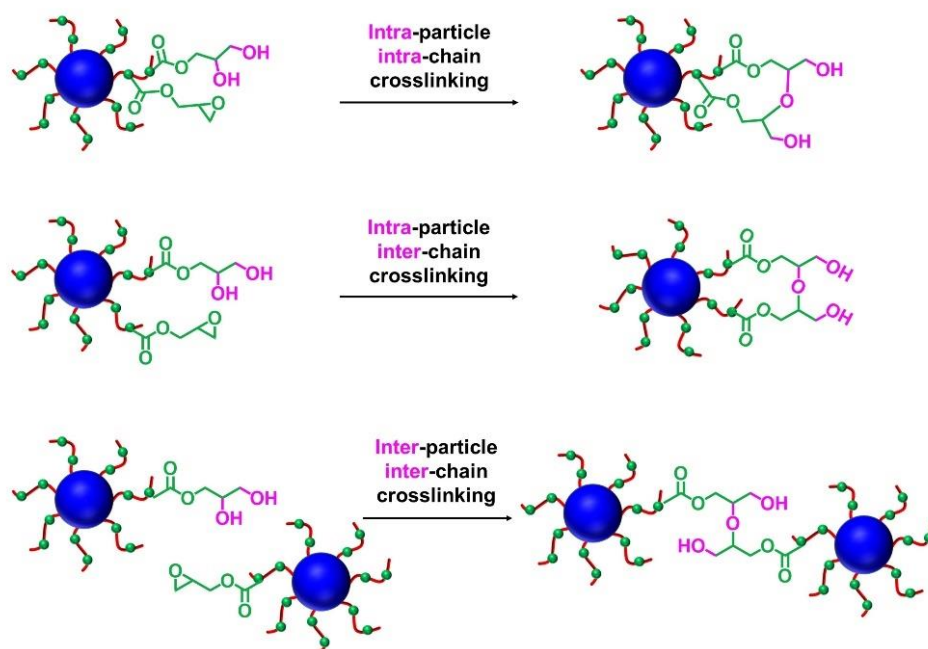
Scheme 6.3. Schematic representation of the various reactions that can occur when reacting P(LMA$_{50}$-*stat*-GlyMA$_9$)-PMMA$_{67}$ nanoparticles with trace water by heating a 20% w/w copolymer dispersion in mineral oil to 110 °C. Following the initial epoxy ring-opening reaction, the resulting hydroxyl groups can react with the remaining epoxy groups. This leads to both intra-particle and/or inter-particle crosslinking.

In order to minimize the latter problem, the heating protocol was also conducted at a much lower nanoparticle concentration. As expected, heating a 1.0% w/w dispersion of P(LMA$_{50}$-stat-GlyMA$_9$)-PMMA$_{67}$ nanoparticles in mineral oil led to ring-opening of all the epoxy groups within 17 h at 110 °C (see **Figure 6.16a**). THF GPC analysis of the resulting copolymer chains produced a similar chromatogram to that recorded for the 20% w/w dispersion after heating (see **Figure 6.16b** and **6.11b**).
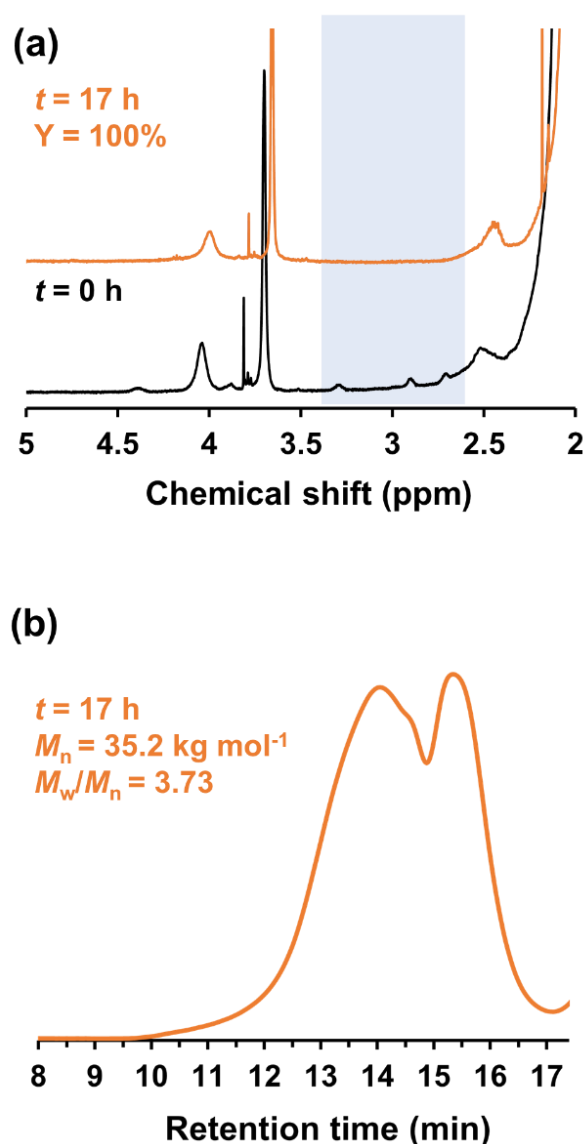
Figure 6.16. (a) ^{1}H NMR spectra recorded in CD$_2$Cl$_2$ for a 1.0% w/w dispersion of P(LMA$_{50}$-stat-GlyMA$_9$)-PMMA$_{67}$ nanoparticles at t_0 (black spectrum) and after heating the same dispersion to 110 °C for 17 h (orange spectrum). **(b)** THF GPC curve recorded for the P(LMA$_{50}$-stat-GlyMA$_9$)-PMMA$_{67}$ diblock copolymer chains after this heating protocol.

However, in this case DLS studies indicated only relatively minor changes in the nanoparticle size distribution (D_h = 31 nm; PDI = 0.09), while TEM analysis confirmed a well-defined spherical morphology for the final nanoparticles (see **Figure 6.13b** and **6.13d**).

Heating a 20% w/w dispersion of PLMA$_{63}$-PGlyMA$_{89}$ nanoparticles up to 70 °C for 17 h led to no discernible change in the epoxy NMR signals, see **Figure 6.17.** Significant loss of epoxy groups was observed at 90 °C but the copolymer remained soluble in CD$_2$Cl$_2$ for ^{1}H NMR analysis. Raising the reaction temperature to 110 °C resulted in core-crosslinking and hence insoluble copolymer chains, which precluded ^{1}H NMR analysis.
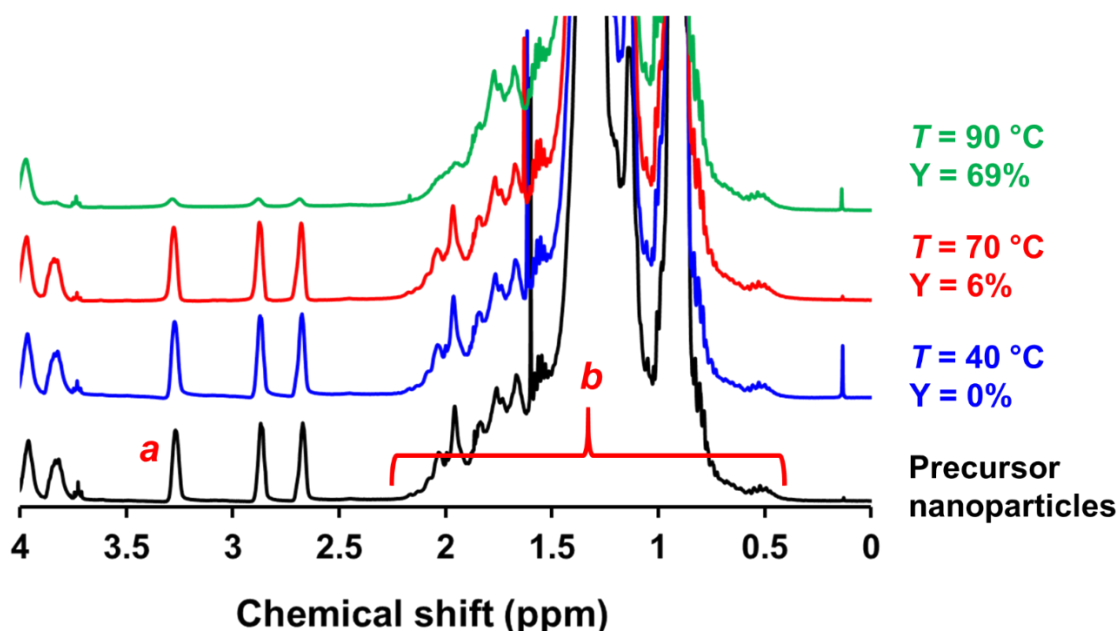
Figure 6.17. ^{1}H NMR spectra recorded in CD$_2$Cl$_2$ for PLMA$_{63}$-PGlyMA$_{89}$ diblock copolymer (black spectrum), the same copolymer after heating a 20% w/w copolymer dispersion in mineral oil for 17 h at 40 °C (blue spectrum), 70 °C (red spectrum) or 90 °C (green spectrum), respectively. In each case, the % loss of the original epoxy groups (Y%) was determined by comparing the aliphatic copolymer backbone at 0.30-2.30 ppm (see signal *b*) to the methine signal *a* corresponding to the epoxy ring at 3.20-3.33 ppm.

However, FT-IR spectroscopy studies of the purified copolymer isolated after heating to 110 °C for 17 h indicated a relatively small amount of residual epoxy groups, as judged by the weak asymmetric/symmetric ring deformation bands at 850 and 910 cm^{-1} (see **Figure 6.18**).
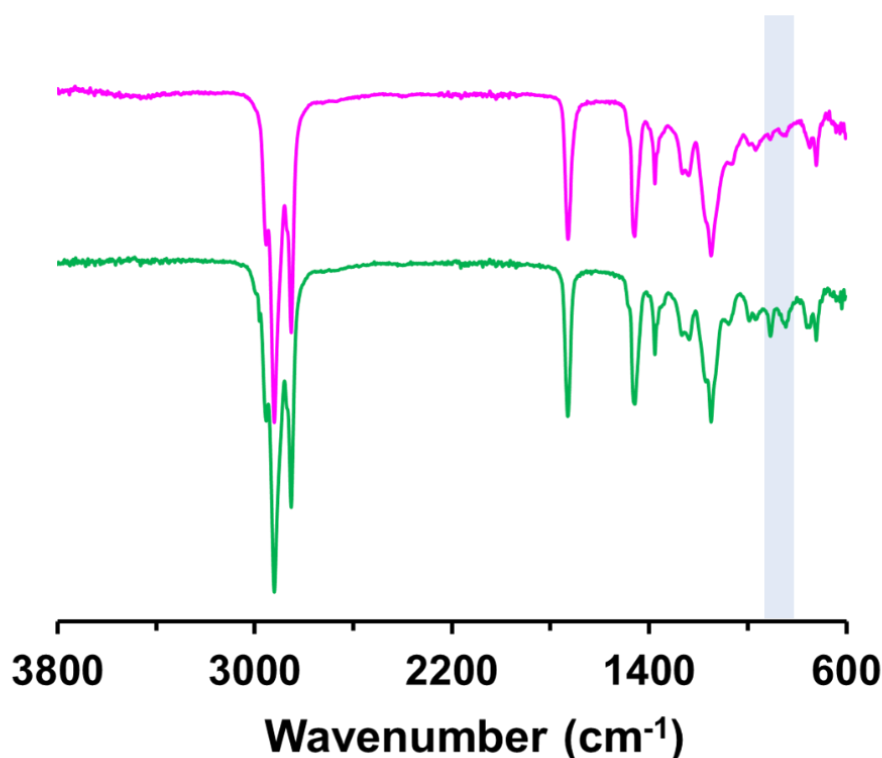
Figure 6.18. FT-IR spectra recorded for PLMA$_{63}$-PGlyMA$_{89}$ diblock copolymer (green spectrum) and the same copolymer after heating a 20% w/w copolymer dispersion in mineral oil for 17 h at 110 °C (pink spectrum).

6.3.4. Ring-opening of epoxy groups on PLMA$_{63}$-PGlyMA$_{89}$ by reaction with 50% v/v aqueous acetic acid

It is well-known that carboxylic acids can act as nucleophiles in epoxy ring-opening reactions to produce a β-hydroxypropyl ester.[41,56–58] Such reactions are often catalyzed by base. However, carboxylic acids can also be employed as acid catalysts to promote epoxy ring-opening by water.[59] Herein, the ring-opening of the epoxy groups in PLMA$_{63}$-PGlyMA$_{89}$ nanoparticles was examined by heating a 50% v/v aqueous acetic acid solution at 110 °C and passing the resulting hot vapor through a 20% w/w copolymer dispersion (also heated to 110 °C) using the experimental setup shown in **Figure 6.1** under a N$_2$ atmosphere. Disappearance of the characteristic epoxy bands at 850 and 910 cm^{-1} shown in **Figure 6.19** suggests that complete loss of the epoxy groups can be achieved within 17 h. Moreover, the appearance of a broad band corresponding to a hydroxyl stretch at 3000-3650 cm^{-1} plus a primary alcohol C-O stretch at 1041cm^{-1} confirmed the presence of hydroxyl groups within the final copolymer.

216
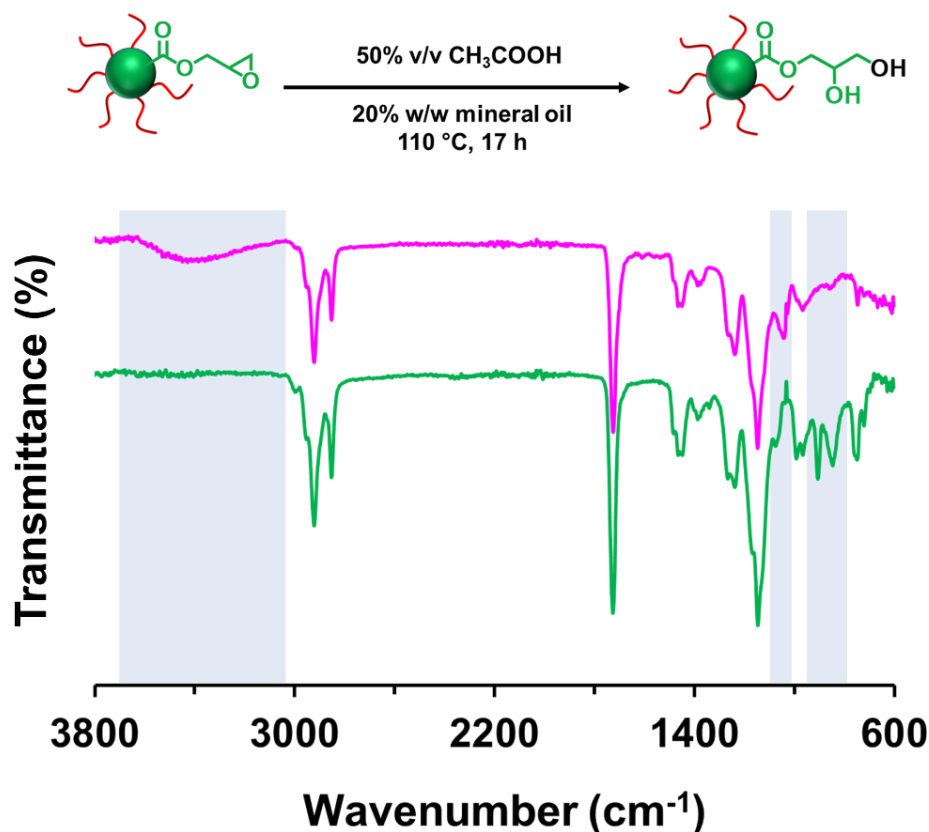
Figure 6.19. FT-IR spectra recorded for PLMA$_{63}$-PGlyMA$_{89}$ prior to (green spectrum) and after reacting with 50% v/v aqueous acetic acid at 110 °C for 17 h (pink spectrum). In principle, this simply involves acid-catalyzed epoxy ring-opening with water but in practice side-reactions also occur, which leads to extensive core-crosslinking of the nanoparticles.

A z-average diameter of 38 nm (DLS PDI = 0.31) was determined for the derivatized PLMA$_{63}$-PGlyMA$_{89}$ nanoparticles after dilution with *n*-dodecane. This increase in nanoparticle size and polydispersity indicated some degree of inter-particle crosslinking. Furthermore, DLS analysis after dilution with THF (z-average diameter = 43 nm; PDI = 0.28) confirmed core-crosslinking of these nanoparticles because THF is a good solvent for the linear diblock copolymer precursor. Apart from the addition of water to the epoxy ring and the subsequent hydroxyl-epoxy reaction, there are two further side-reactions that can occur: (i) epoxy ring-opening by acetic acid and (ii) esterification between acetic acid and the pendent hydroxyl groups (see **Scheme 6.4**).[41,58] However, the presence of 50% v/v water appears to minimize such side-reactions.[59]

217

(a) Carboxylic acid-epoxy addition
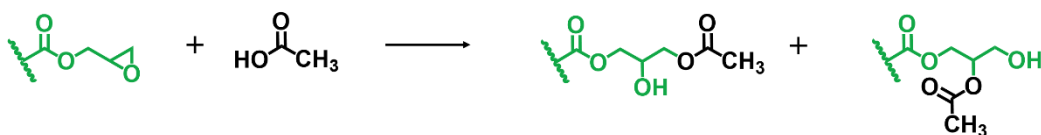
(b) Carboxylic acid-hydroxyl esterification
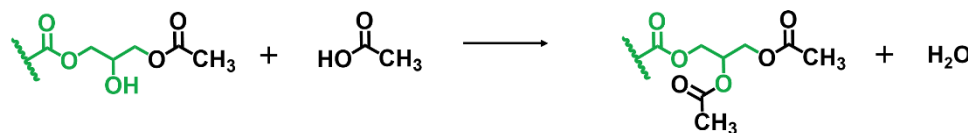
Scheme 6.4. Possible side-reactions that might occur when reacting PLMA$_{63}$-PGlyMA$_{89}$ nanoparticles with 50% v/v aqueous acetic acid: **(a)** epoxy ring-opening with acetic acid and **(b)** esterification between acetic acid and the pendent hydroxyl groups.

6.4. Conclusions

Epoxy-functional P(LMA$_{50}$-*stat*-GlyMA$_9$)-PMMA$_{67}$ and PLMA$_{63}$-PGlyMA$_{89}$ spherical nanoparticles of comparable size were prepared at 20% w/w solids in mineral oil *via* RAFT-mediated PISA. Both types of nanoparticles were characterized using ^{1}H NMR spectroscopy, THF GPC, DLS and TEM. Post-polymerization modification of these nanoparticles was studied using benzylamine as a model compound. Using a stoichiometric amount of amine relative to the epoxy groups was sufficient for complete derivatization of the PLMA$_{63}$-PGlyMA$_{89}$ nanoparticles. However, achieving a similar extent of reaction for the P(LMA$_{50}$-*stat*-GlyMA$_9$)-PMMA$_{67}$ nanoparticles required a 50-fold excess of benzylamine. This is attributed to the relatively low molar concentration of the epoxy groups (0.07 mol dm^{-3} *vs*. 0.52 mol dm^{-3}) in the latter case. Furthermore, the epoxy ring-opening reaction of these spheres using a trace amount of water was also studied. Complete loss of epoxy groups was observed for the P(LMA$_{50}$-*stat*-GlyMA$_9$)-PMMA$_{67}$ nanoparticles on heating a 20% w/w dispersion at 110 °C for 17 h. This protocol led to crosslinking between neighboring nanoparticles but this problem could be minimized by diluting the nanoparticles to 1.0% w/w solids prior to heating. On simply heating a 20% w/w dispersion of PLMA$_{63}$-PGlyMA$_{89}$ nanoparticles to 110 °C for 17 h, a minor fraction of unreacted epoxy groups was observed by FT-IR spectroscopy. However, when using 50% v/v aqueous acetic acid instead of water, complete loss of epoxy

groups was achieved under the same conditions. In the case of the $PLMA_{63}$-$PGlyMA_{89}$ spheres, derivatization always led to core-crosslinking owing to the ring-opening of epoxy groups by neighboring hydroxyl groups. In principle, such epoxy-functional nanoparticles may be useful additives for designing next-generation ultralow-viscosity engine oils.

6.5. References

(1)   Chiefari, J.; Chong, Y. K. B.; Ercole, F.; Krstina, J.; Jeffery, J.; Le, T. P. T.; Mayadunne, R. T. A.; Meijs, G. F.; Moad, C. L.; Moad, G.; Rizzardo, E.; Thang, S. H. Living Free-Radical Polymerization by Reversible Addition-Fragmentation Chain Transfer: The RAFT Process. *Macromolecules* **1998**, *31*, 5559–5562.

(2)   Moad, G.; Rizzardo, E.; Thang, S. H. Toward Living Radical Polymerization. *Acc. Chem. Res.* **2008**, *41*, 1133–1142.

(3)   Keddie, D. J. A Guide to the Synthesis of Block Copolymers Using Reversible-Addition Fragmentation Chain Transfer (RAFT) Polymerization. *Chem. Soc. Rev.* **2014**, *43*, 496–505.

(4)   Perrier, S. 50th Anniversary Perspective: RAFT Polymerization - A User Guide. *Macromolecules* **2017**, *50*, 7433–7447.

(5)   Blanazs, A.; Ryan, A. J.; Armes, S. P. Predictive Phase Diagrams for RAFT Aqueous Dispersion Polymerization: Effect of Block Copolymer Composition, Molecular Weight, and Copolymer Concentration. *Macromolecules* **2012**, *45*, 5099–5107.

(6)   Rosselgong, J.; Blanazs, A.; Chambon, P.; Williams, M.; Semsarilar, M.; Madsen, J.; Battaglia, G.; Armes, S. P. Thiol-Functionalized Block Copolymer Vesicles. *ACS Macro Lett.* **2012**, *1*, 1041–1045.

(7)   Semsarilar, M.; Jones, E. R.; Armes, S. P. Comparison of Pseudo-Living Character of RAFT Polymerizations Conducted under Homogeneous and Heterogeneous Conditions. *Polym. Chem.* **2014**, *5*, 195–203.

(8)   Karagoz, B.; Esser, L.; Duong, H. T.; Basuki, J. S.; Boyer, C.; Davis, T. P. Polymerization-Induced Self-Assembly (PISA)-Control over the Morphology of Nanoparticles for Drug Delivery Applications. *Polym. Chem.* **2014**, *5*, 350–355.

(9)   Zhou, W.; Qu, Q.; Yu, W.; An, Z. Single Monomer for Multiple Tasks: Polymerization Induced Self-Assembly, Functionalization and Cross-Linking, and Nanoparticle Loading. *ACS Macro Lett.* **2014**, *3*, 1220–1224.

(10)   Pei, Y.; Noy, J. M.; Roth, P. J.; Lowe, A. B. Thiol-Reactive Passerini-Methacrylates and Polymorphic Surface Functional Soft Matter Nanoparticles via Ethanolic RAFT Dispersion Polymerization and Post-Synthesis Modification. *Polym. Chem.* **2015**, *6*, 1928–1931.

(11)   Figg, C. A.; Simula, A.; Gebre, K. A.; Tucker, B. S.; Haddleton, D. M.; Sumerlin, B. S. Polymerization-Induced Thermal Self-Assembly (PITSA). *Chem. Sci.* **2015**, *6*, 1230–1236.

(12)   Zhou, W.; Qu, Q.; Xu, Y.; An, Z. Aqueous Polymerization-Induced Self-Assembly for the Synthesis of Ketone-Functionalized Nano-Objects with Low Polydispersity. *ACS Macro Lett.* **2015**, *4*, 495–499.

(13)   Zhao, W.; Ta, H. T.; Zhang, C.; Whittaker, A. K. Polymerization-Induced Self-Assembly (PISA) - Control over the Morphology of 19F-Containing Polymeric Nano-Objects for Cell Uptake and Tracking. *Biomacromolecules* **2017**, *18*, 1145–1156.

(14)   Zhang, W. J.; Hong, C. Y.; Pan, C. Y. Efficient Fabrication of Photosensitive Polymeric Nano-Objects via an Ingenious Formulation of RAFT Dispersion Polymerization and Their Application for Drug Delivery. *Biomacromolecules* **2017**, *18*, 1210–1217.

(15)   Docherty, P. J.; Derry, M. J.; Armes, S. P. RAFT Dispersion Polymerization of Glycidyl Methacrylate for the Synthesis of Epoxy-Functional Block Copolymer Nanoparticles in Mineral Oil. *Polym. Chem.* **2019**, *10*, 603–611.

(16)   Docherty, P. J.; Girou, C.; Derry, M. J.; Armes, S. P. Epoxy-Functional Diblock Copolymer Spheres, Worms and Vesicles via Polymerization-Induced Self-Assembly in Mineral Oil. *Polym. Chem.* **2020**, *11*, 3332–3339.

(17)   Penfold, N. J. W.; Parnell, A. J.; Molina, M.; Verstraete, P.; Smets, J.; Armes, S. P. Layer-By-Layer Self-Assembly of Polyelectrolytic Block Copolymer Worms on a Planar Substrate. *Langmuir* **2017**, *33*, 14425–14436.

(18)   Xu, Q.; Zhang, Y.; Li, X.; He, J.; Tan, J.; Zhang, L. Enzyme Catalysis-Induced RAFT Polymerization in Water for the Preparation of Epoxy-Functionalized Triblock Copolymer Vesicles. *Polym. Chem.* **2018**, *9*, 4908–4916.

(19)   György, C.; Lovett, J. R.; Penfold, N. J. W.; Armes, S. P. Epoxy-Functional Sterically Stabilized Diblock Copolymer Nanoparticles via RAFT Aqueous Emulsion Polymerization: Comparison of Two Synthetic Strategies. *Macromol. Rapid Commun.* **2018**, *40*, 1800289.

(20)   Dai, X.; Yu, L.; Zhang, Y.; Zhang, L.; Tan, J. Polymerization-Induced Self-Assembly via RAFT-Mediated Emulsion Polymerization of Methacrylic Monomers. *Macromolecules* **2019**, *52*, 7468–7476.

(21)   Hunter, S. J.; Thompson, K. L.; Lovett, J. R.; Hatton, F. L.; Derry, M. J.; Lindsay, C.; Taylor, P.; Armes, S. P. Synthesis, Characterization, and Pickering Emulsifier Performance of Anisotropic Cross-Linked Block Copolymer Worms: Effect of Aspect Ratio on Emulsion Stability in the Presence of Surfactant. *Langmuir* **2019**, *35*, 254–265.

(22)   Hatton, F. L.; Park, A. M.; Zhang, Y.; Fuchs, G. D.; Ober, C. K.; Armes, S. P. Aqueous One-Pot Synthesis of Epoxy-Functional Diblock Copolymer Worms from a Single Monomer: New Anisotropic Scaffolds for Potential Charge Storage Applications. *Polym. Chem.* **2019**, *10*, 194–200.

(23)   Dai, X.; Zhang, Y.; Yu, L.; Li, X.; Zhang, L.; Tan, J. Seeded Photoinitiated Polymerization-Induced Self-Assembly: Cylindrical Micelles with Patchy Structures Prepared via the Chain Extension of a Third Block. *ACS Macro Lett.* **2019**, *8*, 955–961.

(24)   Hatton, F. L.; Derry, M. J.; Armes, S. P. Rational Synthesis of Epoxy-Functional Spheres, Worms and Vesicles by RAFT Aqueous Emulsion Polymerisation of Glycidyl Methacrylate. *Polym. Chem.* **2020**, *11*, 6343–6355.

(25)   Cao, J.; Tan, Y.; Dai, X.; Chen, Y.; Zhang, L.; Tan, J. In Situ Cross-Linking in RAFT-Mediated Emulsion Polymerization: Reshaping the Preparation of Cross-Linked Block Copolymer Nano-Objects by Polymerization-Induced Self-Assembly. *Polymer* **2021**, *230*, 124095.

(26)   Chambon, P.; Blanazs, A.; Battaglia, G.; Armes, S. P. How Does Cross-Linking Affect the Stability of Block Copolymer Vesicles in the Presence of Surfactant? *Langmuir* **2012**, *28*, 1196–1205.

(27)   Lovett, J. R.; Ratcliffe, L. P. D.; Warren, N. J.; Armes, S. P.; Smallridge, M. J.; Cracknell, R. B.; Saunders, B. R. A Robust Cross-Linking Strategy for Block Copolymer Worms Prepared via Polymerization-Induced Self-Assembly. *Macromolecules* **2016**, *49*, 2928–2941.

(28)   Penfold, N. J. W.; Ning, Y.; Verstraete, P.; Smets, J.; Armes, S. P. Cross-Linked Cationic Diblock Copolymer Worms Are Superflocculants for Micrometer-Sized Silica Particles. *Chem. Sci.* **2016**, *7*, 6894–6904.

(29)   Ratcliffe, L. P. D.; Bentley, K. J.; Wehr, R.; Warren, N. J.; Saunders, B. R.; Armes, S. P. Cationic Disulfide-Functionalized Worm Gels. *Polym. Chem.* **2017**, *8*, 5962–5971.

(30)   Yao, H.; Ning, Y.; Jesson, C. P.; He, J.; Deng, R.; Tian, W.; Armes, S. P. Using Host-Guest Chemistry to Tune the Kinetics of Morphological Transitions Undertaken by Block Copolymer Vesicles. *ACS Macro Lett.* **2017**, *6*, 1379–1385.

(31)   Sadrearhami, Z.; Yeow, J.; Nguyen, T. K.; Ho, K. K. K.; Kumar, N.; Boyer, C. Biofilm Dispersal Using Nitric Oxide Loaded Nanoparticles Fabricated by Photo-PISA: Influence of Morphology. *Chem. Commun.* **2017**, *53*, 12894–12897.

(32)   Tan, J.; Liu, D.; Huang, C.; Li, X.; He, J.; Xu, Q.; Zhang, L. Photoinitiated Polymerization-Induced Self-Assembly of Glycidyl Methacrylate for the Synthesis of Epoxy-Functionalized Block Copolymer Nano-Objects. *Macromol. Rapid Commun.* **2017**, *38*, 1–7.

(33)   Hatton, F. L.; Lovett, J. R.; Armes, S. P. Synthesis of Well-Defined Epoxy-Functional Spherical Nanoparticles by RAFT Aqueous Emulsion Polymerization. *Polym. Chem.* **2017**, *8*, 4856–4868.

(34)   Jones, M. C.; Tewari, P.; Blei, C.; Hales, K.; Pochan, D. J.; Leroux, J. C. Self-Assembled Nanocages for Hydrophilic Guest Molecules. *J. Am. Chem. Soc.* **2006**, *128*, 14599–14605.

(35)   Ratcliffe, L. P. D.; Ryan, A. J.; Armes, S. P. From a Water-Immiscible Monomer to Block Copolymer Nano-Objects via a One-Pot RAFT Aqueous Dispersion Polymerization Formulation. *Macromolecules* **2013**, *46*, 769–777.

(36)   Muzammil, E. M.; Khan, A.; Stuparu, M. C. Post-Polymerization Modification Reactions of Poly(Glycidyl Methacrylate)S. *RSC Adv.* **2017**, *7*, 55874–55884.

(37)   Gao, H.; Elsabahy, M.; Giger, E. V.; Li, D.; Prud'Homme, R. E.; Leroux, J. C. Aminated Linear and Star-Shape Poly(Glycerol Methacrylate)s: Synthesis and Self-Assembling Properties. *Biomacromolecules* **2010**, *11*, 889–895.

(38)   Xu, F. J.; Chai, M. Y.; Li, W. B.; Ping, Y.; Tang, G. P.; Yang, W. T.; Ma, J.; Liu, F. S. Well-Defined Poly(2-Hydroxyl-3-(2-Hydroxyethylamino)Propyl Methacrylate) Vectors with Low Toxicity and High Gene Transfection Efficiency. *Biomacromolecules* **2010**, *11*, 1437–1442.

(39)   Benaglia, M.; Alberti, A.; Giorgini, L.; Magnoni, F.; Tozzi, S. Poly(Glycidyl Methacrylate): A Highly Versatile Polymeric Building Block for Post-Polymerization Modifications. *Polym. Chem.* **2013**, *4*, 124–132.

(40)   De, S.; Khan, A. Efficient Synthesis of Multifunctional Polymers via Thiol-Epoxy "Lick" Chemistry. *Chem. Commun.* **2012**, *48*, 3130–3132.

(41)   Blank, W. J.; He, Z. A.; Picci, M. Catalysis of the Epoxy-Carboxyl Reaction. *J. Coatings Technol.* **2002**, *74*, 33–41.

(42)   Tsyalkovsky, V.; Klep, V.; Ramaratnam, K.; Lupitskyy, R.; Minko, S.; Luzinov, I. Fluorescent Reactive Core-Shell Composite Nanoparticles with a High Surface Concentration

of Epoxy Functionalities. *Chem. Mater.* **2008**, *20*, 317–325.

(43) Tsarevsky, N. V.; Bencherif, S. A.; Matyjaszewski, K. Graft Copolymers by a Combination of ATRP and Two Different Consecutive Click Reactions. *Macromolecules* **2007**, *40*, 4439–4445.

(44) Safa, K. D.; Nasirtabrizi, M. H. Ring Opening Reactions of Glycidyl Methacrylate Copolymers to Introduce Bulky Organosilicon Side Chain Substituents. *Polym. Bull.* **2006**, *57*, 293–304.

(45) Cao, J.; Tan, Y.; Chen, Y.; Zhang, L.; Tan, J. How the Reactive End Group of Macro-RAFT Agent Affects RAFT-Mediated Emulsion Polymerization-Induced Self-Assembly. *Macromol. Rapid Commun.* **2021**, *42*, 2100333.

(46) Fielding, L. A.; Derry, M. J.; Ladmiral, V.; Rosselgong, J.; Rodrigues, A. M.; Ratcliffe, L. P. D.; Sugihara, S.; Armes, S. P. RAFT Dispersion Polymerization in Non-Polar Solvents: Facile Production of Block Copolymer Spheres, Worms and Vesicles in n-Alkanes. *Chem. Sci.* **2013**, *4*, 2081–2087.

(47) Trent, J. S. Ruthenium Tetraoxide Staining of Polymers: New Preparative Methods for Electron Microscopy. *Macromolecules* **1984**, *17*, 2930–2931.

(48) Brown, J. E.; Markley, F. X.; Shapiro, H. Mechanism Aromatic Action. *Ind. Eng. Chem.* **1955**, *47*, 2141–2146.

(49) Varatharajan, K.; Cheralathan, M.; Velraj, R. Mitigation of NOx Emissions from a Jatropha Biodiesel Fuelled DI Diesel Engine Using Antioxidant Additives. *Fuel* **2011**, *90*, 2721–2725.

(50) Balaji, G.; Cheralathan, M. Experimental Reduction of NOx and HC Emissions in a CI Engine Fuelled with Methyl Ester of Neem Oil Using P-Phenylenediamine Antioxidant. *J. Sci. Ind. Res.* **2014**, *73*, 177–180.

(51) Acocella, M. R.; Corcione, C. E.; Giuri, A.; Maggio, M.; Maffezzoli, A.; Guerra, G. Graphene Oxide as a Catalyst for Ring Opening Reactions in Amine Crosslinking of Epoxy Resins. *RSC Adv.* **2016**, *6*, 23858–23865.

(52) Zheng, R.; Liu, G.; Devlin, M.; Hux, K.; Jao, T. C. Friction Reduction of Lubricant Base Oil by Micelles and Crosslinked Micelles of Block Copolymers. *Tribol. Trans.* **2010**, *53*, 97–107.

(53) Derry, M. J.; Smith, T.; O'Hora, P. S.; Armes, S. P. Block Copolymer Nanoparticles Prepared via Polymerization-Induced Self-Assembly Provide Excellent Boundary Lubrication Performance for Next-Generation Ultralow-Viscosity Automotive Engine Oils. *ACS Appl. Mater. Interfaces* **2019**, *11*, 33364–33369.

(54) Wan, S.; Zheng, Y.; Liu, Y.; Yan, H.; Liu, K. Fe3O4 Nanoparticles Coated with Homopolymers of Glycerol Mono(Meth)Acrylate and Their Block Copolymers. *J. Mater. Chem.* **2005**, *15*, 3424–3430.

(55) Yuan, J. J.; Armes, S. P.; Takabayashi, Y.; Prassides, K.; Leite, C. A. P.; Galembeck, F.; Lewis, A. L. Synthesis of Biocompatible Poly[2-(Methacryloyloxy)Ethyl Phosphorylcholine]-Coated Magnetite Nanoparticles. *Langmuir* **2006**, *22*, 10989–10993.

(56) Shechter, L.; Wynstra, J.; Kurkjy, R. P. Chemistry of Styrene Oxide Comparison with Phenyl Glycidyl Ether in Model Compound Reactions. *Ind. Eng. Chem.* **1957**, *49*, 1107–1109.

(57) Chang, S. C.; Chiu, S. J.; Hsu, C. Y.; Chang, Y.; Liu, Y. L. White-Light Fluorescent Nanoparticles from Self-Assembly of Rhodamine B-Anchored Amphiphilic Poly(Poly(Ethylene Glycol)Methacrylate)-b-Poly(Glycidyl Methacrylate) Block Copolymer.

Polymer **2012**, *53*, 4399–4406.

(58)   Jang, K. S.; Eom, Y. S.; Choi, K. S.; Bae, H. C. Crosslinkable Deoxidizing Hybrid Adhesive of Epoxy–Diacid for Electrical Interconnections in Semiconductor Packaging. *Polym. Int.* **2018**, *67*, 1241–1247.

(59)   Kalal, J.; Svec, F.; Marousek, V. Reactions of Epoxide Groups of Glycidyl Methacrylate Copolymers. *J Polym Sci Part C, Polym Symp* **1974**, *47*, 155–166.

Chapter 7. Enhanced Adsorption of Epoxy-Functional Nanoparticles onto Stainless Steel Significantly Reduces Friction in Tribological Studies

7.1. Introduction

It is well-documented that the addition of oil-soluble polymers to automotive engine oils confers various benefits. For example, polyolefins or poly(*n*-alkyl methacrylates) confer superior lubrication performance,[1–4] polystyrene-based diblock copolymers can act as effective diesel soot dispersants[5] and star diblock copolymers can be used to control the viscosity-temperature profile of engine oils.[6]

In 2010, Zheng and co-workers reported that core-crosslinked acrylic diblock copolymer nanoparticles reduced friction within the boundary lubrication regime as judged by mini-traction machine (MTM) studies.[7] Such nanoparticles were postulated to provide a physical barrier between the planar stainless steel surface and the stainless steel ball bearing that was placed in direct contact with it. However, these acrylic nanoparticles were prepared by a multi-step process that involved protecting group chemistry and self-assembly in dilute solution *via* solvent transfer from THF to mineral oil.[7] Thus they are not readily amenable to industrial scale-up. In contrast, in 2019 Derry *et al*. reported an efficient, scalable route for the preparation of methacrylic core-crosslinked nanoparticles directly in mineral oil[8] by the judicious combination of reversible addition-fragmentation chain transfer (RAFT) polymerization[9,10] with polymerization-induced self-assembly (PISA).[11–18] Importantly, such sterically-stabilized poly(stearyl methacrylate-poly(benzyl methacrylate)-poly(ethylene glycol dimethacrylate) ($PSMA_{31}$-$PBzMA_{200}$-$PEGDMA_{20}$) nanoparticles also significantly reduced friction within the boundary lubrication regime in tribological experiments.[8]

Herein we demonstrate that introducing epoxy groups into similar methacrylic nanoparticles significantly enhances their adsorption from *n*-dodecane onto planar stainless steel. This is achieved simply by statistical copolymerization of glycidyl methacrylate (GlyMA) with lauryl methacrylate (LMA) when preparing the steric stabilizer precursor block, prior to its chain extension using either MMA or BzMA. Quartz crystal microbalance with dissipation (QCM-D) and scanning electron microscopy (SEM) are used to compare the adsorption of such epoxy-functional nanoparticles onto a model planar stainless steel substrate with that of (i) nanoparticles containing epoxy groups located within the cores and (ii) unfunctionalized nanoparticles. Finally, tribological experiments are conducted to assess whether nanoparticle adsorption leads to lower friction within the boundary lubrication regime.

7.2. Experimental

7.2.1. Materials

Methyl methacrylate (MMA, 99%) was purchased from Alfa Aesar (Germany), passed through basic alumina to remove its inhibitor and then stored at –20 °C prior to use. Lauryl methacrylate (LMA, 96%), glycidyl methacrylate (GlyMA, 97%), benzyl methacrylate (BzMA, 96%) cumyl dithiobenzoate (CDB), CDCl$_3$ and n-dodecane were purchased from Merck (UK) and used as received. 2,2′-Azobisisobutyronitrile (AIBN) was obtained from Molekula (UK) and $tert$-butyl peroxy-2-ethylhexanoate (T21s) was purchased from AkzoNobel (The Netherlands). CD$_2$Cl$_2$ was purchased from Goss Scientific (UK). Tetrahydrofuran was obtained from VWR Chemicals (UK). Methanol and toluene were purchased from Fisher Scientific (UK). Group III hydroisomerized mineral oil (viscosity = 4.3 cSt at 100 °C) was kindly provided by Lubrizol Ltd. (Hazelwood, Derbyshire, UK).

7.2.2. Methods

Synthesis of poly(lauryl methacrylate) (PLMA$_{63}$) and poly(lauryl methacrylate-$stat$-glycidyl methacrylate) (P(LMA$_{50}$-$stat$-GlyMA$_9$)) precursors via RAFT solution polymerization in toluene

The synthesis of PLMA$_{63}$ and of P(LMA$_{50}$-$stat$-GlyMA$_9$) precursors has been previously discussed in **Chapter 6**.

Synthesis of poly(lauryl methacrylate)-poly(glycidyl methacrylate) (PLMA$_{63}$-PGlyMA$_{89}$) spherical nanoparticles via RAFT dispersion polymerization of GlyMA in mineral oil

The synthesis of PLMA$_{63}$-PGlyMA$_{89}$ spheres has been previously discussed in **Chapter 6**.

Synthesis of poly(lauryl methacrylate-$stat$-glycidyl methacrylate)-poly(methyl methacrylate) (P(LMA$_{50}$-$stat$-GlyMA$_9$)-PMMA$_{67}$) spherical nanoparticles via RAFT dispersion polymerization of MMA in mineral oil

The synthesis of P(LMA$_{50}$-*stat*-GlyMA$_9$)-PMMA$_{67}$ spheres has been previously discussed in **Chapter 6**.

Synthesis of poly(lauryl methacrylate)-poly(methyl methacrylate) (PLMA$_{63}$-PMMA$_{67}$) diblock copolymer spheres *via* RAFT dispersion polymerization of MMA in mineral oil

PLMA$_{63}$-PMMA$_{67}$ spheres were synthesized at 20% w/w solids as follows. PLMA$_{63}$ precursor (1.40 g; 85.89 µmol), T21s initiator (6.19 mg; 28.63 µmol; precursor/T21s molar ratio = 3.0; 10.0% v/v in mineral oil) and mineral oil (8.04 g) were weighed into a glass vial and purged with nitrogen for 30 min. MMA monomer (0.64 mL; 6.01 mmol; target DP = 70) was degassed separately, then added to the reaction mixture *via* syringe. The sealed vial was immersed in a preheated oil bath at 90 °C and the reaction mixture was magnetically stirred for 6 h. ^{1}H NMR analysis indicated 95% MMA conversion by comparing the integrated methyl signal of the monomer at 3.76 ppm to the integrated methyl signal of the polymer at 3.55–3.70 ppm. THF GPC analysis indicated an M_n of 21 200 g mol^{-1} and an M_w/M_n of 1.14. A hydrodynamic diameter (D_h) of 27 nm (polydispersity index = 0.05) was determined by DLS.

Synthesis of poly(lauryl methacrylate)-poly(benzyl methacrylate) (PLMA$_{63}$-PBzMA$_{245}$) diblock copolymer spheres *via* RAFT dispersion polymerization of BzMA in mineral oil

PLMA$_{63}$-PBzMA$_{245}$ spheres were synthesized at 20% w/w solids as follows. PLMA$_{63}$ precursor (0.27 g; 16.56 µmol), BzMA (0.73 g; 4.14 mmol; target DP = 250), T21s initiator (1.19 mg; 5.52 µmol; precursor/T21s molar ratio = 3.0; 10.0% v/v in mineral oil) and mineral oil (4.00 g) were weighed into a glass vial and purged with nitrogen for 30 min. The sealed vial was immersed in a preheated oil bath at 90 °C and the reaction mixture was magnetically stirred for 6 h. ^{1}H NMR analysis indicated 98% BzMA conversion by comparing the integrated methylene signal of the monomer at 5.25 ppm to the integrated methylene signal of the polymer at 4.80–5.10 ppm. THF GPC analysis indicated an M_n of 38 700 g mol^{-1} and an M_w/M_n of 1.18. A hydrodynamic diameter (D_h) of 48 nm (polydispersity index = 0.03) was determined by DLS.

Synthesis of poly(lauryl methacrylate-*stat*-glycidyl methacrylate)-poly(benzyl methacrylate) (P(LMA$_{50}$-*stat*-GlyMA$_9$)-PBzMA$_{245}$) diblock copolymer spheres *via* RAFT dispersion polymerization of BzMA in mineral oil

P(LMA$_{50}$-*stat*-GlyMA$_9$)-PBzMA$_{245}$ spheres were synthesized at 20% w/w solids as follows. P(LMA$_{50}$-*stat*-GlyMA$_9$) precursor (0.25 g; 17.52 µmol), BzMA (0.77 g; 4.38 mmol; target DP

= 250), T21s initiator (1.26 mg; 5.84 µmol; precursor/T21s molar ratio = 3.0; 10.0% v/v in mineral oil) and mineral oil (4.09 g) were weighed into a glass vial and purged with nitrogen for 30 min. The sealed vial was immersed in a preheated oil bath at 90 °C and the reaction mixture was magnetically stirred for 6 h. ^{1}H NMR analysis indicated 98% BzMA conversion by comparing the integrated methylene signal of the monomer at 5.25 ppm to the integrated methylene signal of the polymer at 4.80–5.10 ppm. THF GPC analysis indicated an M_n of 39 500 g mol^{-1} and an M_w/M_n of 1.18. A hydrodynamic diameter (D_h) of 56 nm (polydispersity index = 0.04) was determined by DLS.

^{1}H NMR Spectroscopy

^{1}H NMR spectra were recorded in either CD_2Cl_2 or $CDCl_3$ using a 400 MHz Bruker Avance spectrometer. Typically, 64 scans were averaged per spectrum.

Gel Permeation Chromatography (GPC)

Molecular weight distributions (MWDs) were assessed by GPC using THF as an eluent. The GPC system was equipped with two 5 µm (30 cm) Mixed C columns and a WellChrom K-2301 refractive index detector operating at 950 ± 30 nm. The THF mobile phase contained 2.0% v/v triethylamine and 0.05% w/v butylhydroxytoluene (BHT) and the flow rate was fixed at 1.0 ml min^{-1}. A series of twelve near-monodisperse poly(methyl methacrylate) standards (M_p values ranging from 800 to 2 200 000 g mol^{-1}) were used for column calibration in combination with a refractive index detector.

Dynamic Light Scattering (DLS)

DLS studies were performed using a Zetasizer Nano ZS instrument (Malvern Instruments, UK) at a fixed scattering angle of 173°. Copolymer dispersions were diluted to 0.10% w/w solids using n-dodecane prior to analysis at 20 °C. The z-average diameter and polydispersity of the nanoparticles were calculated by cumulants analysis of the experimental correlation function using Dispersion Technology Software version 6.20. Data were averaged over ten runs each of thirty seconds duration.

Transmission Electron Microscopy (TEM)

TEM studies were conducted using a FEI Tecnai G2 spirit instrument operating at 80 kV and equipped with a Gatan 1k CCD camera. A single droplet of a 0.10% w/w copolymer dispersion was placed onto a carbon-coated copper grid and allowed to dry, prior to exposure to

ruthenium(VIII) oxide vapor for 7 min at 20 °C.[19] This heavy metal compound acts as a positive stain for the core-forming PGlyMA or PMMA block to improve contrast. The ruthenium(VIII) oxide was prepared as follows: ruthenium(IV) oxide (0.30 g) was added to water (50 g) to form a black slurry; addition of sodium periodate (2.0 g) with continuous stirring produced a yellow solution of ruthenium(VIII) oxide within 1 min at 20 °C.

Small-angle X-ray scattering (SAXS)

SAXS patterns were recorded using a Xeuss 2.0 laboratory beamline (Xenocs, Grenoble, France) equipped with a MetalJet X-ray source (Ga$K\alpha$ radiation, wavelength $\lambda = 1.34$ Å, with q ranging from 0.03 to 2.00 nm^{-1}, where $q = 4\pi.\sin\theta/\lambda$ is the length of the scattering vector and θ is one-half of the scattering angle) and a 2D Pilatus 1M pixel detector (Dectris, Baden-Daettwil, Switzerland). A glass capillary of 2.0 mm diameter was used as a sample holder. Scattering data were reduced using software supplied by the SAXS instrument manufacturer (Xenocs) and were further analyzed using Irena SAS macros for Igor Pro.[20] SAXS patterns were fitted by fixing the radius of gyration (R_g) for the PLMA$_{63}$ and P(LMA$_{50}$-$stat$-GlyMA$_9$) precursors at 2.70 nm and 2.61 nm, respectively.

Scanning Electron Microscopy (SEM)

SEM images were obtained using an FEI Inspect-F instrument operating at an accelerating voltage of 10 kV. Stainless steel substrates were dried and then sputter-coated with a thin overlayer of gold prior to imaging. The MTM disks were immersed in n-hexane to remove mineral oil before drying and subsequent sputter-coating with gold.

Quartz Crystal Microbalance with Dissipation (QCM-D)

QCM-D measurements were performed using an openQCM NEXT instrument (Novatech Srl., Italy) equipped with a temperature-controlled cell connected to a Masterflex Digital Miniflex peristaltic pump (Cole-Parmer Instrument Company, UK). The stainless steel substrates (SS2343, 5 MHz) were supplied by Q-Sense AB (Sweden). Prior to adsorption, the substrates were thoroughly cleaned by sonication in DMF, ethanol and acetone in turn (for 10 min in each solvent), followed by exposure to UV/ozone for 10 min and finally dried with compressed air. The substrates were initially equilibrated with n-dodecane, followed by the introduction of the nanoparticle dispersion (1.0% w/w solids, prepared by dilution with n-dodecane) then

equilibrated with *n*-dodecane again. Measurements were performed at 20 and 40 °C with a continuous flow rate of 0.5 mL min^{-1} to ensure that fresh solution was always present within the cell.

Lubrication testing using a Mini-Traction Machine (MTM)

The nanoparticle dispersion was diluted to 2.5% w/w solids using an API Group III mineral base oil at 20 °C (with no other additives present) then magnetically stirred while heating up to 65 °C, held for a further 5 min at 65 °C with stirring, then allowed to cool to 20 °C before addition to the mini-traction machine (MTM, PCS Instruments, UK). MTM was used to evaluate the lubricating performance of each nanoparticle dispersion in turn. The MTM ball and disk were each made from AISI 52100 steel, and had a surface roughness of less than 0.02 µm Ra. The disk had a mean diameter of 46 mm and the ball had a mean diameter of 19.05 mm. Stribeck curves were recorded for each nanoparticle dispersion at entrainment speeds ranging from 3000 to 30 mm s^{-1} with a slide-to-roll ratio (SRR) of 50% under constant load (37 N) at 40, 60 and 80 °C. The applied load was 37 N, which equates to a contact pressure of 1 GPa. Nanoparticle dispersions were evaluated at a constant load (37 N) and entrainment speed while increasing the temperature at a linear ramp rate (heating rate = 1.33 °C min^{-1}) from 40 to 120 °C. In this latter set of experiments, the entrainment speed was set at 200 mm s^{-1} with an SRR of 50%.

7.3. Results and Discussion

7.3.1. Synthesis and characterization of spherical nanoparticles

RAFT dispersion polymerization in mineral oil was used to produce ~27 nm diameter epoxy-functional PLMA$_{63}$-PGlyMA$_{89}$ and P(LMA$_{50}$-*stat*-GlyMA$_9$)-PMMA$_{67}$ nanoparticles, as well as the corresponding non-functional PLMA$_{63}$-PMMA$_{67}$ nanoparticles (see **Scheme 7.1**). Similarly, both epoxy-functional P(LMA$_{50}$-*stat*-GlyMA$_9$)-PBzMA$_{245}$ and non-functional PLMA$_{63}$-PBzMA$_{245}$ spheres of approximately 50 nm diameter were also prepared in mineral oil (see **Scheme 7.1**). In each case, a high final monomer conversion (≥ 95%) was achieved within 6 h. THF GPC analysis indicated comparable M_n values for similar copolymer

compositions, as shown in **Figure 7.1**. A narrow molecular weight distribution ($M_w/M_n \leq 1.18$)

and a high blocking efficiency was obtained for each synthesis (see **Figure 7.1**).
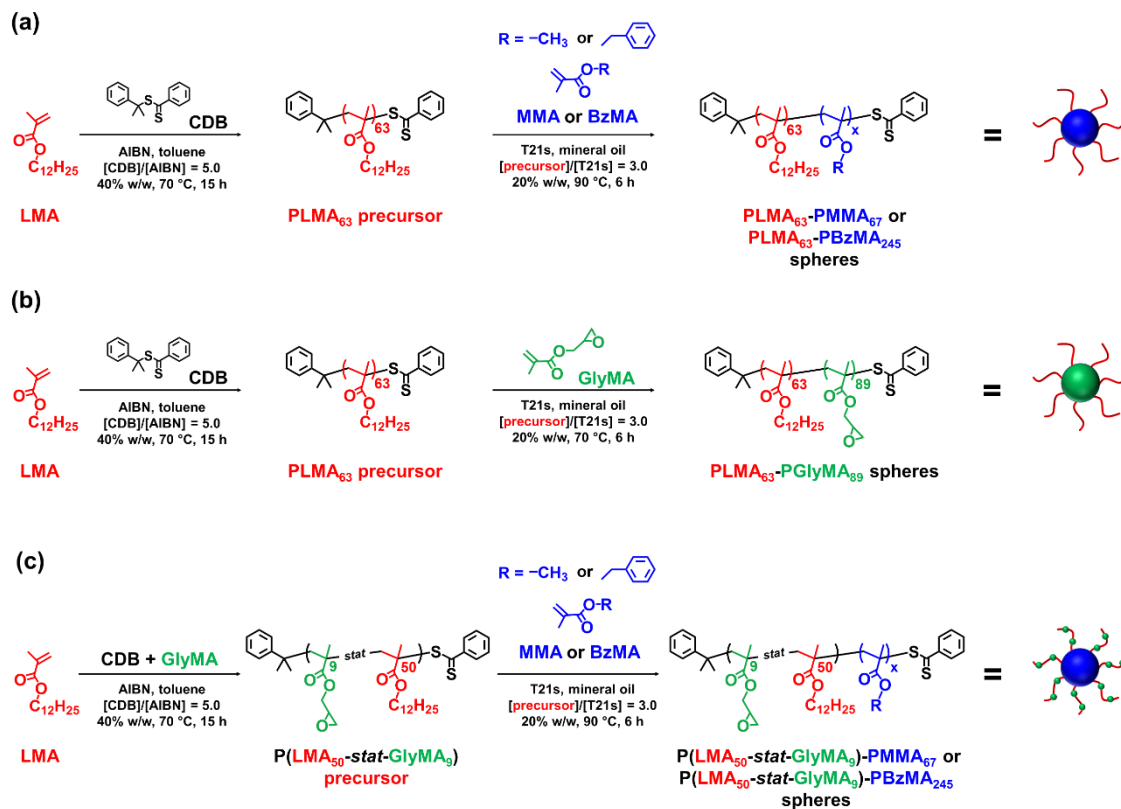
Scheme 7.1. Synthesis of **(a)** poly(lauryl methacrylate)-poly(methyl methacrylate) (PLMA$_{63}$-PMMA$_{67}$) and poly(lauryl methacrylate)-poly(benzyl methacrylate) (PLMA$_{63}$-PBzMA$_{245}$), **(b)** poly(lauryl methacrylate)-poly(glycidyl methacrylate) (PLMA$_{63}$-PGlyMA$_{89}$), **(c)** poly(lauryl methacrylate-*stat*-glycidyl methacrylate)-poly(methyl methacrylate) [P(LMA$_{50}$-*stat*-GlyMA$_{9}$)-PMMA$_{67}$] and poly(lauryl methacrylate-*stat*-glycidyl methacrylate)-poly(benzyl methacrylate) [P(LMA$_{50}$-*stat*-GlyMA$_{9}$)-PBzMA$_{245}$] spheres *via* RAFT dispersion polymerization of methyl methacrylate (MMA), benzyl methacrylate (BzMA) or glycidyl methacrylate (GlyMA) in mineral oil at 20% w/w solids.
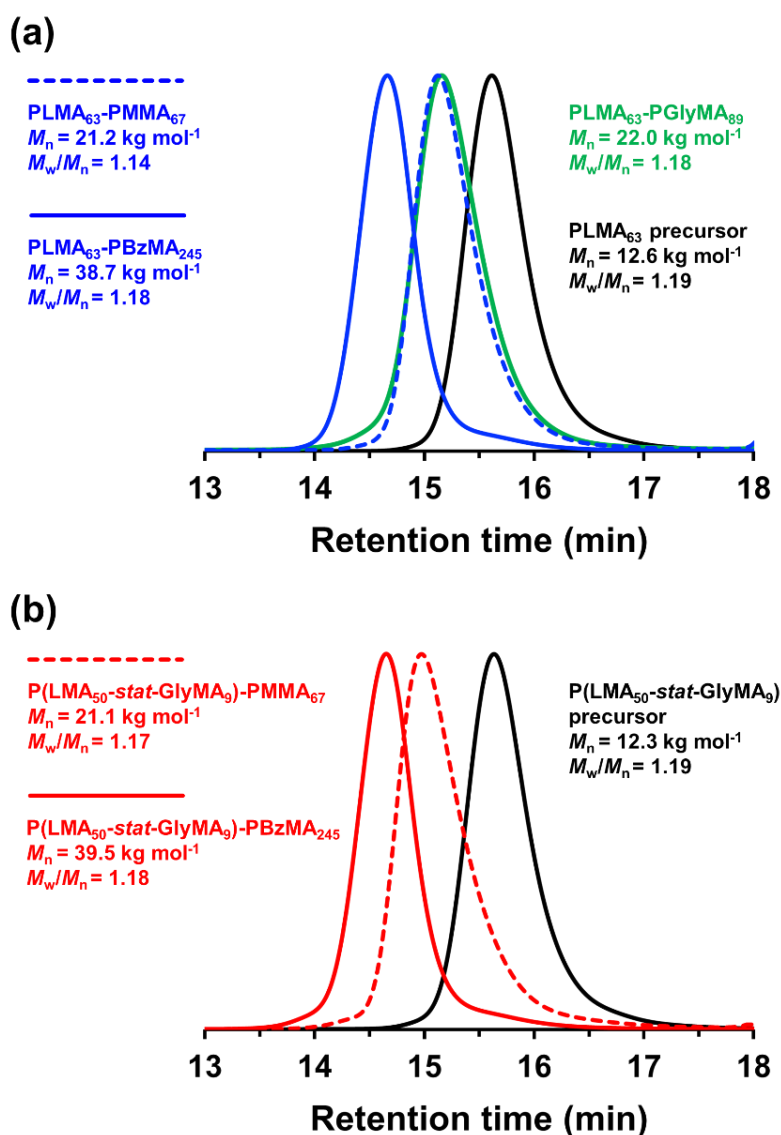
Figure 7.1. THF GPC curves (*vs.* a series of near-monodisperse poly(methyl methacrylate) calibration standards; refractive index detector) recorded for: **(a)** the PLMA$_{63}$ precursor and the corresponding PLMA$_{63}$-PGlyMA$_{89}$, PLMA$_{63}$-PMMA$_{67}$, and PLMA$_{63}$-PBzMA$_{245}$ diblock copolymers; **(b)** the P(LMA$_{50}$-*stat*-GlyMA$_9$) precursor and the corresponding P(LMA$_{50}$-*stat*-GlyMA$_9$)-PMMA$_{67}$ and P(LMA$_{50}$-*stat*-GlyMA$_9$)-PBzMA$_{245}$ diblock copolymers.

The spherical morphology was confirmed in each case *via* TEM analysis (see **Figure 7.2a-e**). Particle size distributions were assessed by DLS and SAXS. The former technique indicated a hydrodynamic diameter (D_h) of 27 nm with a polydispersity index (PDI) of 0.05 for PLMA$_{63}$-PMMA$_{67}$ nanoparticles, 28 nm (PDI = 0.03) for PLMA$_{63}$-PGlyMA$_{89}$ nanoparticles, and 26 nm (PDI= 0.05) for P(LMA$_{50}$-*stat*-GlyMA$_9$)-PMMA$_{67}$ nanoparticles (see **Figure 7.2f**). A D_h of 48 nm (PDI = 0.03) was determined for PLMA$_{63}$-PBzMA$_{245}$ nanoparticles while the P(LMA$_{50}$-*stat*-GlyMA$_9$)-PBzMA$_{245}$ nanoparticles had a D_h of 56 nm (PDI = 0.04), see **Figure 7.2f**.

SAXS is a powerful characterization technique that can provide detailed information regarding a wide range of polymer colloids.[18,21–23] SAXS patterns recorded for PLMA$_{63}$-PMMA$_{67}$, PLMA$_{63}$-PGlyMA$_{89}$, P(LMA$_{50}$-*stat*-GlyMA$_9$)-PMMA$_{67}$, PLMA$_{63}$-PBzMA$_{245}$ and P(LMA$_{50}$-*stat*-GlyMA$_9$)-PBzMA$_{245}$ nanoparticles are shown in **Figure 7.2g**. It is well-known that the nanoparticle morphology can be inferred from the low q gradient of an $I(q)$ *vs.* q plot.[24] For each nanoparticle formulation, a low q gradient of zero was observed (see **Figure 7.2g**), which is consistent with a spherical morphology. Fitting such patterns using a spherical micelle model[25] provides the volume-average particle diameter and the mean aggregation number, N_{agg}. Overall volume-average diameters of 21.6 ± 0.4 nm ($N_{agg} = 140$), 23.0 ± 0.2 nm ($N_{agg} = 130$) and 21.6 ± 0.4 nm ($N_{agg} = 150$) were determined for the PLMA$_{63}$-PMMA$_{67}$, PLMA$_{63}$-PGlyMA$_{89}$ and P(LMA$_{50}$-*stat*-GlyMA$_9$)-PMMA$_{67}$ nanoparticles, respectively. Satisfactory fits to SAXS patterns recorded for the PLMA$_{63}$-PBzMA$_{245}$ and P(LMA$_{50}$-*stat*-GlyMA$_9$)-PBzMA$_{245}$ nanoparticles resulted in volume-average diameters of 40.6 ± 2.7 nm ($N_{agg} = 390$) and 46.8 ± 3.9 nm ($N_{agg} = 620$), respectively. In all cases, these diameters are slightly lower than the corresponding D_h values determined by DLS (see **Table 7.1**). This difference is not unexpected since DLS reports a z-average diameter, so this technique should always oversize relative to SAXS.
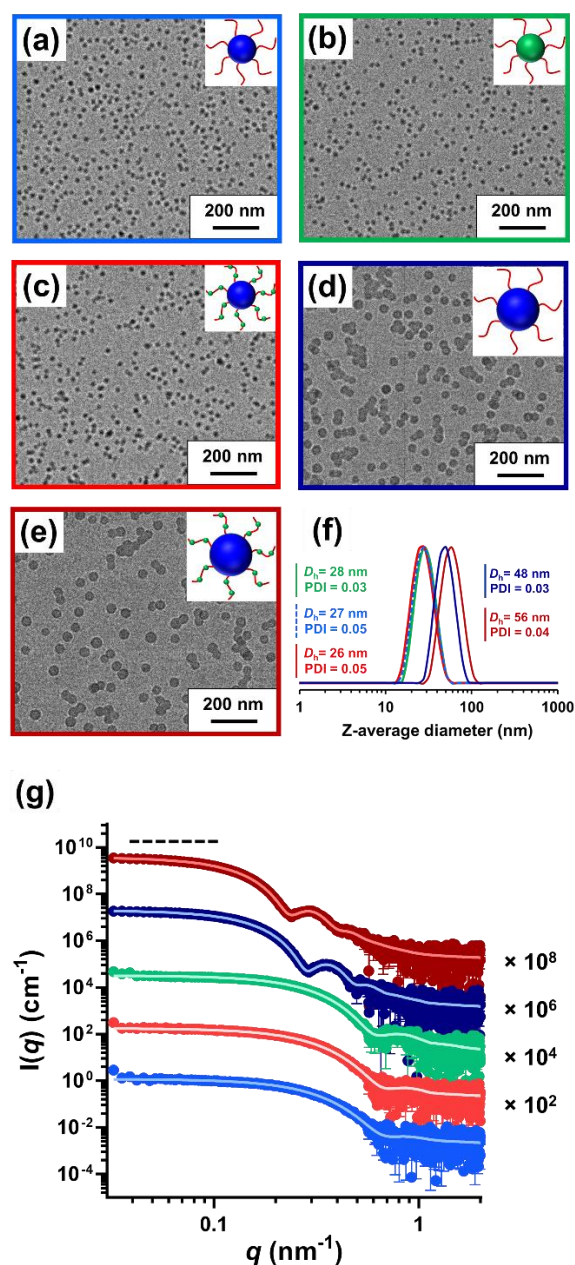
Figure 7.2. Representative TEM images obtained for **(a)** PLMA$_{63}$-PMMA$_{67}$ nanoparticles (light blue frame), **(b)** PLMA$_{63}$-PGlyMA$_{89}$ nanoparticles (green frame), **(c)** P(LMA$_{50}$-*stat*-GlyMA$_9$)-PMMA$_{67}$ nanoparticles (red frame), **(d)** PLMA$_{63}$-PBzMA$_{245}$ nanoparticles (dark blue frame) and **(e)** P(LMA$_{50}$-*stat*-GlyMA$_9$)-PBzMA$_{245}$ nanoparticles (dark red frame) prepared at 20% w/w solids in mineral oil. **(f)** DLS data recorded for 0.1% w/w dispersion of PLMA$_{63}$-PMMA$_{67}$ nanoparticles (light blue dashed trace), PLMA$_{63}$-PGlyMA$_{89}$ nanoparticles (green trace), P(LMA$_{50}$-*stat*-GlyMA$_9$)-PMMA$_{67}$ nanoparticles (red trace), PLMA$_{63}$-PBzMA$_{245}$ nanoparticles (dark blue trace) and P(LMA$_{50}$-*stat*-GlyMA$_9$)-PBzMA$_{245}$ nanoparticles (dark red trace). **(g)** SAXS patterns and corresponding data fits (solid lines) recorded for 1.0% w/w dispersions of PLMA$_{63}$-PMMA$_{67}$ nanoparticles (light blue data), PLMA$_{63}$-PGlyMA$_{89}$ nanoparticles (green data), P(LMA$_{50}$-*stat*-GlyMA$_9$)-PMMA$_{67}$ nanoparticles (red data), PLMA$_{63}$-PBzMA$_{245}$ nanoparticles (dark blue data) and P(LMA$_{50}$-*stat*-GlyMA$_9$)-PBzMA$_{245}$ nanoparticles (dark red data) prepared at 20% w/w solids in mineral oil at 20 °C. Dashed line is for guidance to the eye and indicates a low *q* gradient of zero in each case.

Table 7.1. Summary of the structural parameters obtained by fitting SAXS patterns for the $PLMA_{63}$-$PMMA_{67}$, $PLMA_{63}$-$GlyMA_{89}$, $P(LMA_{50}$-*stat*-$GlyMA_9)$-$PMMA_{67}$, $PLMA_{63}$-$PBzMA_{245}$ and $P(LMA_{50}$-*stat*-$GlyMA_9)$-$PBzMA_{245}$ nanoparticles using a spherical micelle model.[4] D_v is the overall volume-average sphere diameter such that $D_v = D_c + 4R_g$, where D_c is the mean core diameter and R_g is the radius of gyration of the stabilizer chains. N_{agg} is the mean aggregation number. The corresponding hydrodynamic diameter (D_h) and polydispersity (PDI) reported by DLS are also included.

Copolymer Composition	SAXS			DLS	
	D_c (nm)	D_v (nm)	N_{agg}	D_h (nm)	PDI
$PLMA_{63}$-$PMMA_{67}$	10.8 ± 0.4	21.6 ± 0.4	140	27	0.05
$PLMA_{63}$-$PGlyMA_{89}$	12.2 ± 0.2	23.0 ± 0.2	130	28	0.03
$P(LMA_{50}$-*stat*-$GlyMA_9)$-$PMMA_{67}$	11.2 ± 0.4	21.6 ± 0.4	150	26	0.05
$PLMA_{63}$-$PBzMA_{245}$	29.8 ± 2.7	40.6 ± 2.7	390	48	0.03
$P(LMA_{50}$-*stat*-$GlyMA_9)$-$PBzMA_{245}$	36.4 ± 3.9	46.8 ± 3.9	620	56	0.04

7.3.2. QCM-D studies of nanoparticle adsorption onto a planar stainless steel substrate

QCM-D has been used by many research groups to study the physical adsorption of nanoparticles from aqueous solution onto various model planar substrates.[26–32]

There are also various QCM-D studies of the adsorption of small-molecule surfactants, such as glyceryl monooleate (GMO),[33] fatty amines (e.g., octadecylamine, *N*-tallowalkyl-1,3-propanediamine)[33,34] or fatty acids (e.g., stearic-, oleic- or linoleic acids)[35,36] onto stainless steel, iron oxide or silica substrates from *n*-alkanes. Such compounds are friction-reducing agents,[37,38] which is believed to be a direct result of their enhanced adsorption onto metal surfaces *via* the chelate effect, hydrogen bonding or van der Waals interactions.[33,38–40] Recently, Gmür *et al.* used QCM-D to study the adsorption of a series of poly(lauryl methacrylate)-based diblock copolymers onto a planar iron oxide substrate from hexadecane. Such copolymers were prepared by RAFT solution polymerization using pentafluorophenyl methacrylate as reactive repeat units to enable introduction of nitrodopamine functional groups. The resulting anchor block led to a relatively high adsorbed mass in the form of a *brush-like* surface layer and excellent friction reduction in tribological experiments.[3] Similar observations

were reported by the same team for poly(lauryl methacrylate)-based diblock copolymers bearing a carboxylic acid-based anchoring block.[4] Herein we report the first QCM-D study of the adsorption of epoxy-functional diblock copolymer *nanoparticles* onto planar stainless steel from a non-polar solvent (*n*-dodecane).

First, adsorption of the ~27 nm epoxy-functional $PLMA_{63}$-$PGlyMA_{89}$ nanoparticles, $P(LMA_{50}$-*stat*-$GlyMA_9)$-$PMMA_{67}$ nanoparticles and non-functional $PLMA_{63}$-$PMMA_{67}$ nanoparticles were compared *via* QCM-D experiments performed at 20 °C. Initially, pure *n*-dodecane was introduced into the QCM-D cell to obtain a baseline (see **Figure 7.3**), followed by switching to a 1.0% w/w nanoparticle dispersion. Nanoparticle adsorption occurred at this stage (see **Figure 7.3a**, first red arrow) and subsequently returning to a flow of pure *n*-dodecane enabled removal of weakly adsorbed nanoparticles from the surface (see **Figure 7.3a**, second red arrow). Typical dissipation data obtained during adsorption of the $P(LMA_{50}$-*stat*-$GlyMA_9)$-$PMMA_{67}$ nanoparticles is shown in **Figure 7.4**.
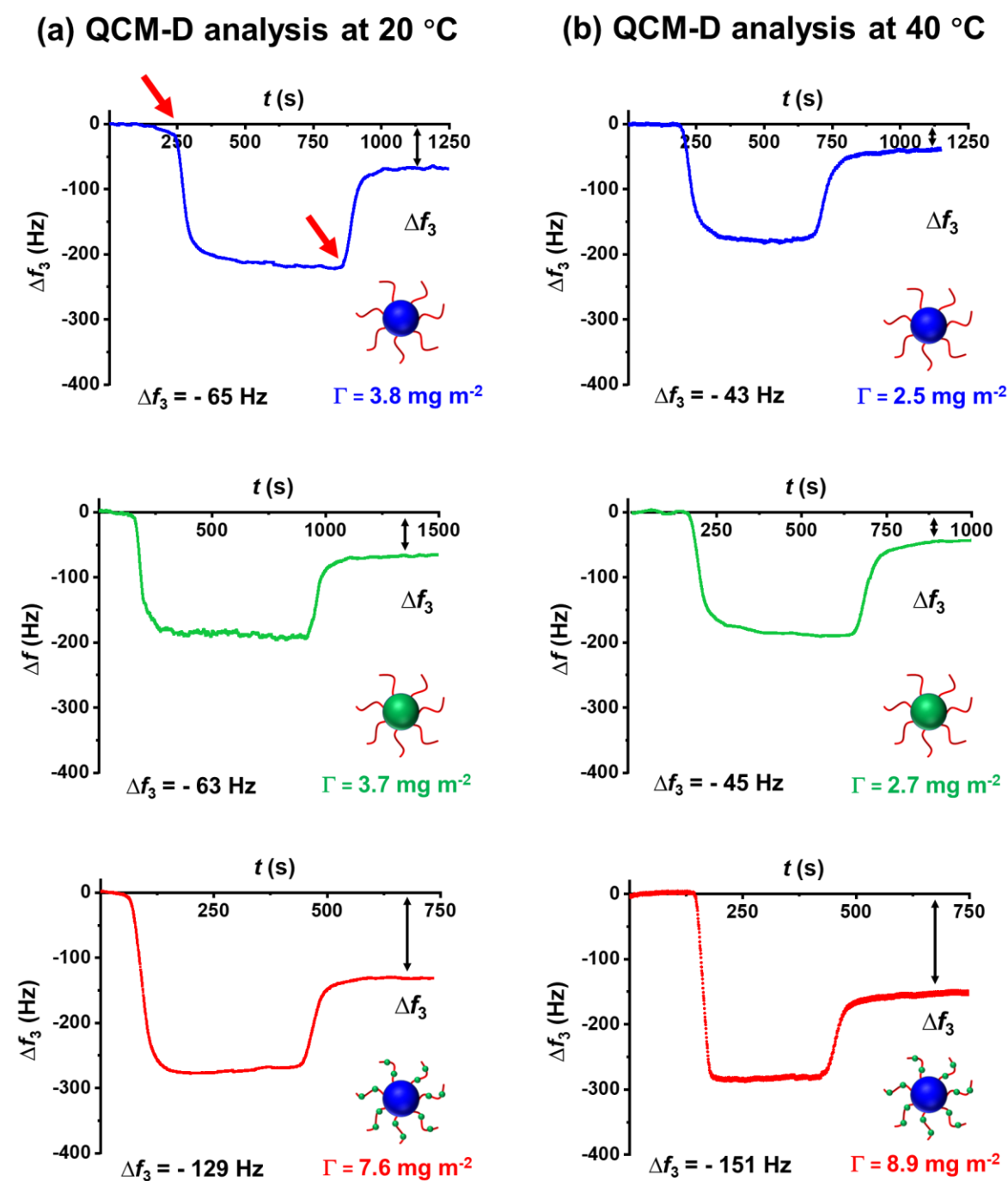
Figure 7.3. QCM-D analysis showing the change in frequency (Δf_3) observed during the adsorption of PLMA$_{63}$-PMMA$_{67}$ nanoparticles (blue data), PLMA$_{63}$-PGlyMA$_{89}$ nanoparticles (green data) or P(LMA$_{50}$-*stat*-GlyMA$_9$)-PMMA$_{67}$ nanoparticles (red data) in turn from 1.0% w/w copolymer dispersions in *n*-dodecane onto a stainless steel substrate at a flow rate of 0.5 mL min^{-1}: **(a)** at 20 °C and **(b)** at 40 °C. In part **(a)**, the first red arrow indicates when the nanoparticle dispersion was first introduced into the QCM cell while the second arrow corresponds to the rinsing step with pure *n*-dodecane. Each curve is shown for a single measurement, but it is chosen to be representative of the average of two consistent experiments. Black double-headed arrows indicate the final change in frequency (Δf_3) in each case, from which the adsorbed mass can be calculated.
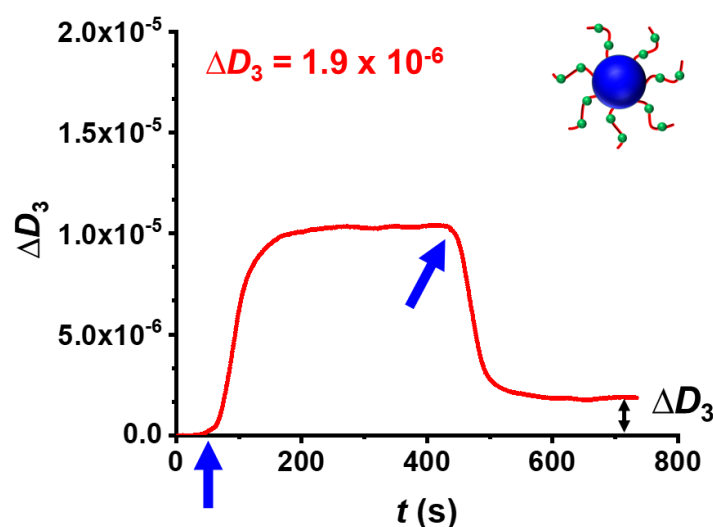
Figure 7.4. The change in dissipation (ΔD_3) recorded during the adsorption of a 1.0% w/w dispersion of P(LMA$_{50}$-*stat*-GlyMA$_9$)-PMMA$_{67}$ nanoparticles from *n*-dodecane onto a stainless steel substrate at a flow rate of 0.50 mL min^{-1} at 20 °C. The curve is shown for a single measurement but it is representative of the average of two experiments. Blue arrows indicate (i) the introduction of the nanoparticles into the QCM cell and (ii) the rinsing step with pure *n*-dodecane. The black double-headed arrow indicates the final change in dissipation (ΔD_3).

According to **Figure 7.3a**, employing the P(LMA$_{50}$-*stat*-GlyMA$_9$)-PMMA$_{67}$ nanoparticles resulted in a significantly higher change in frequency (Δf_3 = -129 Hz) relative to that recorded for either the PLMA$_{63}$-PGlyMA$_{89}$ nanoparticles (Δf_3 = -63 Hz) or the non-functional PLMA$_{63}$-PMMA$_{67}$ nanoparticles (Δf_3 = -65 Hz). In each case, the Δf_3 data provided in **Figure 7.3** were average values obtained from two consistent measurements (see **Table 7.2**). The adsorbed mass per unit area can be calculated from Δf_3 (see **Figure 7.3**, black double-headed arrows) using the Sauerbrey equation:[41]

$$\Delta m = - C \cdot (\Delta f \cdot n^{-1}) \qquad (1)$$

where C is a mass sensitivity constant, which is equal to 0.177 (mg (m^2 Hz)$^{-1}$) for a 5 MHz crystal,[42] and *n* is the overtone number. To determine the final adsorbed mass of nanoparticles in mg m^{-2}, we chose to use the third harmonic (n = 3) of the resonance frequency. This is because the fundamental frequency (n = 1) is rather sensitive to experimental artifacts.[43,44]

It is emphasized that the Sauerbrey model assumes a rigid adsorbed layer and hence neglects viscoelastic effects. If the layer is appreciably viscoelastic, employing the Sauerbrey equation leads to an underestimate of the mass of the adsorbed layer.[31,45] Monitoring the dissipation (D) in real time provides useful information regarding the viscoelasticity of the adsorbed nanoparticle layer.[46,47] In principle, the adsorbed layer can be assumed to be rigid provided that the change in dissipation (ΔD) is relatively small compared to Δf.[48,49] Furthermore, Reviakine *et al*. reported that the Sauerbrey equation can be safely used if $\Delta D_n/(-\Delta f_n/n) << 4 \times 10^{-7}$ Hz^{-1} for a 5 MHz sensor.[45,49] As shown in **Table 7.2**, all $\Delta D_3/(-\Delta f_3/3)$ data were well below this threshold value. Thus the Sauerbrey equation should be valid for the nanoparticle adsorption experiments performed herein. Accordingly, adsorbed amounts of 7.6, 3.7 and 3.8 mg m^{-2} were calculated for the P(LMA$_{50}$-*stat*-GlyMA$_9$)-PMMA$_{67}$, PLMA$_{63}$-PGlyMA$_{89}$ and PLMA$_{63}$-PMMA$_{67}$ nanoparticles, respectively.

Table 7.2. Summary of Δf_3, ΔD_3, $\Delta D_3/(-\Delta f_3/3)$, Γ, Γ_t and Θ data obtained from the QCM-D analysis of the surface adsorption of ~27 nm PLMA$_{63}$-PMMA$_{67}$, PLMA$_{63}$-PGlyMA$_{89}$ and P(LMA$_{50}$-*stat*-GlyMA$_9$)-PMMA$_{67}$ nanoparticles onto a model stainless steel substrate. Γ was calculated from Δf_3 using the Sauerbrey equation (**Equation 1**). Γ_t was calculated using **Equation 2**. Θ was obtained by dividing Γ by Γ_t.

Nanoparticle Dispersion	T (°C)	Δf_3 (Hz)	Mean Δf_3 (Hz)	Mean Γ (mg m^{-2})	Γ_t (mg)	Θ	ΔD_3 (10^{-6})	Mean ΔD_3 (10^{-6})	$\Delta D_3/(-\Delta f_3/3)$ (10^{-8})
PLMA$_{63}$-PMMA$_{67}$	20	-63	-65	3.8	31.9	0.12	1.1	1.1	5.2
	20	-67					1.2		
	40	-42	-43	2.5	31.9	0.08	0.2	0.2	1.3
	40	-44					0.1		
PLMA$_{63}$-PGlyMA$_{89}$	20	-65	-63	3.7	28.9	0.13	0.2	0.3	1.7
	20	-61					0.5		
	40	-44	-45	2.7	28.9	0.09	0.3	0.3	2.0
	40	-46					0.3		
P(LMA$_{50}$-*stat*-GlyMA$_9$)-PMMA$_{67}$	20	-126	-129	7.6	31.9	0.24	1.7	1.8	4.2
	20	-131					1.9		
	40	-147	-151	8.9	31.9	0.28	1.0	1.6	3.2
	40	-154					2.1		
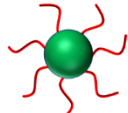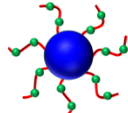
Thus, introducing epoxy groups into the steric stabilizer block resulted in almost a two-fold increase in the adsorbed mass compared to the non-functional PLMA$_{63}$-PMMA$_{67}$ nanoparticles. However, introducing almost ten times more epoxy groups into the nanoparticle cores produced no discernible increase in adsorbed amount relative to these reference nanoparticles. Hence the precise spatial location of the epoxy groups within the nanoparticles is of critical importance for achieving their enhanced adsorption onto stainless steel. Moreover, our preliminary experiments (data not shown) suggest that placing a *single* epoxy group at the end of each steric stabilizer chain using an epoxy-functional RAFT agent[50] is not sufficient to promote greater nanoparticle adsorption. Thus it seems that *multiple* epoxy groups per copolymer chain are required to achieve this objective. In future work, it would be interesting to establish the *optimum* number of epoxy groups per copolymer chain that are required for *maximum* nanoparticle adsorption.

To estimate the corresponding fractional surface coverage (Θ) in each case, the QCM-D adsorbed amount (Γ) was compared to the theoretical adsorbed mass (Γ_t) estimated for a fully-coated substrate of unit surface area. Γ_t was calculated using **Equation 2**:

$$\Gamma_t = A \cdot D \cdot \rho \qquad\qquad (2)$$

where A is equal to 1 m^2, D is the overall nanoparticle diameter (~27 nm in this case) and ρ is the density of either the PGlyMA core ($\rho \sim 1.07$ g cm^{-3} at 20 °C) or the PMMA core ($\rho = 1.18$ g cm^{-3} at 20 °C). Accordingly, a Θ of 0.24 was determined for P(LMA$_{50}$-*stat*-GlyMA$_9$)-PMMA$_{67}$ nanoparticles, 0.13 for PLMA$_{63}$-PGlyMA$_{89}$ nanoparticles and 0.12 for PLMA$_{63}$-PMMA$_{67}$ nanoparticles.

There are two possible explanations for the significantly higher surface coverage obtained for the epoxy-functional P(LMA$_{50}$-*stat*-GlyMA$_9$)-PMMA$_{67}$ nanoparticles. In principle, the surface hydroxyl (i.e., Fe-OH) groups on the stainless steel substrate can simply form hydrogen bonds with the polar epoxy groups. Alternatively, such surface hydroxyl groups can ring-open the epoxy groups to form covalent bonds. It is important to note that physical adsorption *via* hydrogen bonding should be less favorable at higher temperature. In contrast, such conditions should promote chemical adsorption.

To distinguish between these two adsorption mechanisms, the QCM-D experiments were repeated at 40 °C (which is the upper limit temperature for our instrument set-up) (see **Figure 7.3b**). This higher temperature led to a modest but discernible increase in adsorbed amount for

the P(LMA$_{50}$-*stat*-GlyMA$_9$)-PMMA$_{67}$ nanoparticles ($\Gamma = 8.9$ mg m^{-2}; $\Theta = 0.28$) whereas a significant reduction was observed for both the PLMA$_{63}$-PGlyMA$_{89}$ nanoparticles ($\Gamma = 2.7$ mg m^{-2}; $\Theta = 0.09$) and the PLMA$_{63}$-PMMA$_{67}$ nanoparticles ($\Gamma = 2.5$ mg m^{-2}; $\Theta = 0.08$). Thus these experiments suggest that a chemical reaction between the epoxy and hydroxyl groups occurs when employing the P(LMA$_{50}$-*stat*-GlyMA$_9$)-PMMA$_{67}$ nanoparticles, whereas the other two types of nanoparticles merely undergo physical adsorption (most likely *via* hydrogen bonding interactions between the methacrylic ester groups on the PLMA chains and the Fe-OH groups present at the surface of the stainless steel). This is consistent with our recent observation that higher temperature enhances the ring-opening of epoxy groups by water.[51] Moreover, both Hatton *et al*. and Docherty *et al*. reported that hydroxyl groups can ring-open epoxy groups *via* nucleophile substitution even at ambient temperature.[52,53] Furthermore, Xu and co-workers recently used sum-frequency generation (SFG) vibrational spectroscopy to study the chemical reaction between epoxy rings and surface Al-OH groups when curing an epoxy adhesive on sapphire.[54] Moreover, the same team reported enhanced adhesion for an epoxy-amine adhesive when cured in contact with a stainless steel substrate. Again, direct spectroscopic evidence was provided for a chemical reaction between the epoxy rings and the Fe-OH groups.[55]

Next, the adsorption of ~50 nm diameter epoxy-functional P(LMA$_{50}$-*stat*-GlyMA$_9$)-PBzMA$_{245}$ nanoparticles onto stainless steel was compared to that obtained for non-functional PLMA$_{63}$-PBzMA$_{245}$ nanoparticles of similar size. To produce larger spheres in mineral oil, PBzMA was chosen as a core-forming block instead of PMMA. This is because targeting higher PMMA DPs leads to the formation of colloidally unstable aggregates.[56] As shown in **Figure 7.5**, increasing the particle size only resulted in a modest increase in adsorbed amount ($\Gamma = 6.4$ mg m^{-2}) when using the PLMA$_{63}$-PBzMA$_{245}$ nanoparticles. In contrast, an approximate *five-fold* increase in adsorbed amount ($\Gamma = 31.3$ mg m^{-2}) was obtained for the P(LMA$_{50}$-*stat*-GlyMA$_9$)-PBzMA$_{245}$ nanoparticles (see **Table 7.3**). Using **Equation 2**, assuming an overall nanoparticle diameter of 50 nm and taking the density of PBzMA to be 1.179 g cm^{-3}, fractional surface coverages of 0.11 and 0.53 were calculated for the non-functional and epoxy-functional nanoparticles, respectively.
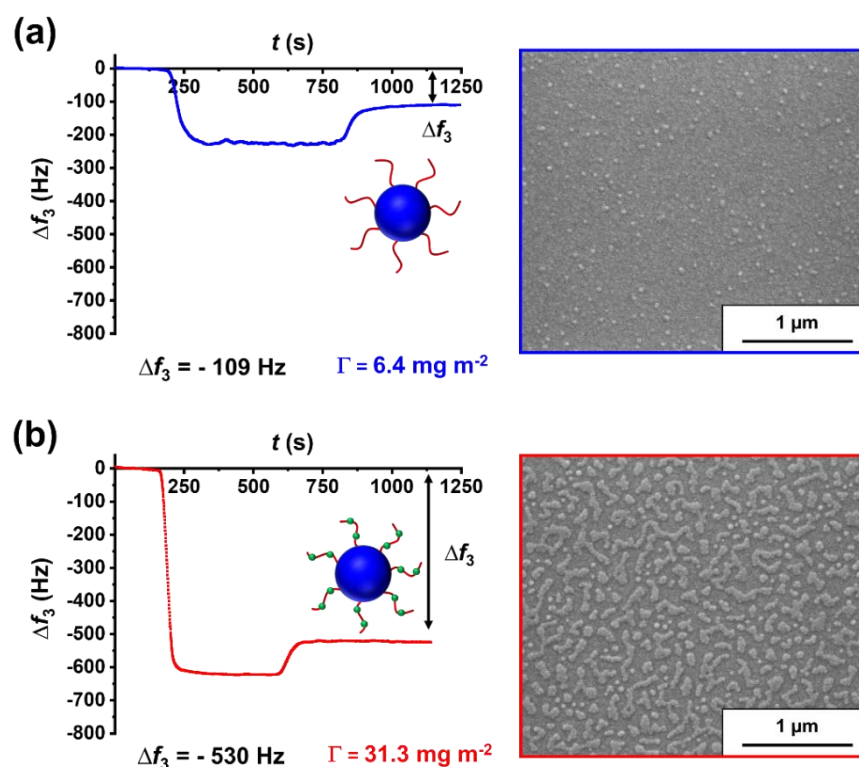
Figure 7.5. QCM-D data obtained for the adsorption of **(a)** PLMA$_{63}$-PBzMA$_{245}$ nanoparticles and **(b)** P(LMA$_{50}$-*stat*-GlyMA$_9$)-PBzMA$_{245}$ nanoparticles in turn from 1.0% w/w copolymer dispersions in *n*-dodecane onto a stainless steel substrate at a flow rate of 0.50 mL min^{-1} at 20 °C. Each curve is shown for a single measurement but has been selected to be representative of the mean of two experiments. The corresponding SEM images recorded for each nanoparticle-coated stainless steel substrate after these QCM-D experiments are also shown. The black double-headed arrows indicate the final change in frequency (Δf_3).

This remarkable difference is consistent with the observations made for the ~27 nm nanoparticles. Moreover, this indicates that nanoparticle adsorption is independent of the chemical nature of the core-forming block (i.e., PMMA *vs*. PBzMA). Furthermore, the ~50 nm diameter nanoparticles are sufficiently large to be imaged *via* SEM after their adsorption onto stainless steel (see **Figure 7.5**). Such SEM images can be used to estimate surface coverage (Θ) using *ImageJ* software. This approach enabled Θ values of ~0.10 and ~0.50 to be calculated for PLMA$_{63}$-PBzMA$_{245}$ and P(LMA$_{50}$-*stat*-GlyMA$_9$)-PBzMA$_{245}$ nanoparticles, respectively. These fractional coverages are comparable to the corresponding Θ data determined from QCM-D studies (see **Table 7.3**).

Table 7.3. Summary of Δf_3, ΔD_3, $\Delta D_3/(-\Delta f_3/3)$, Γ, Γ_t and Θ data obtained from the QCM-D analysis of the surface adsorption of ~50 nm PLMA$_{63}$-PBzMA$_{245}$ and P(LMA$_{50}$-*stat*-GlyMA$_9$)-PBzMA$_{245}$ nanoparticles onto a model stainless steel substrate. Γ was calculated from Δf_3 using the Sauerbrey equation (**Equation 1**). Γ_t was calculated using **Equation 2**. Θ was obtained by dividing Γ by Γ_t.

Nanoparticle Dispersion	T (°C)	Δf_3 (Hz)	Mean Δf_3 (Hz)	Mean Γ (mg m^{-2})	Γ_t (mg)	Θ	ΔD_3 (10^{-6})	Mean ΔD_3 (10^{-6})	$\Delta D_3/(-\Delta f_3/3)$ (10^{-8})
PLMA$_{63}$-PBzMA$_{245}$	20	-110					1.1		
	20	-107	-109	6.4	59.0	0.11	2.6	1.9	5.2
P(LMA$_{50}$-*stat*-GlyMA$_9$)-PBzMA$_{245}$	20	-524					2.9		
	20	-536	-530	31.3	59.0	0.53	3.3	3.1	1.8

7.3.3. Tribology experiments using 50 nm nanoparticles

Previously, Zheng *et al.*[7] and Derry *et al.*[8] reported excellent lubrication performance for acrylic and methacrylic core-crosslinked diblock copolymer nanoparticles, respectively (see **Chapter 1**). In these prior studies, Stribeck curves suggested a dramatic reduction in the friction coefficient at low entrainment speeds (i.e. within the boundary lubrication regime) compared to glycerol monooleate (GMO), which is a well-known friction-reducing agent. Zheng *et al.*[7] postulated that this was the result of elastic deformation of the nanoparticles once they diffused within the asperity contact area.[7,8] Herein, we sought to determine whether there is a direct relation between lubrication performance and nanoparticle adsorption. Accordingly, we compared the lubrication performance of the ~50 nm epoxy-functional P(LMA$_{50}$-*stat*-GlyMA$_9$)-PBzMA$_{245}$ nanoparticles with that of the non-functional PLMA$_{63}$-PBzMA$_{245}$ nanoparticles.

Initially, Stribeck curves were recorded for 2.5% w/w nanoparticle dispersions at 40, 60 and 80 °C while reducing the entrainment speed (v_e) from 3000 to 30 mm s^{-1} using a slide-to-roll ratio (SRR) of 50% under a constant applied load of 37 N (see **Figure 7.6**). At 40 °C, very similar data were obtained for the two nanoparticle dispersions (see **Figure 7.6c**). Moreover, these experiments indicate that a v_e of approximately 200 mm s^{-1} lies within the so-called

'mixed lubrication' regime at this temperature. This intermediate regime lies between the hydrodynamic (full fluid film) and boundary (metal-on-metal contact) lubrication regimes.[57] In principle, lowering the entrainment speed reduces the film thickness created by the oil between the metal surfaces, which should lead a higher number of asperity contacts and hence a higher friction coefficient (see **Figure 7.6**).
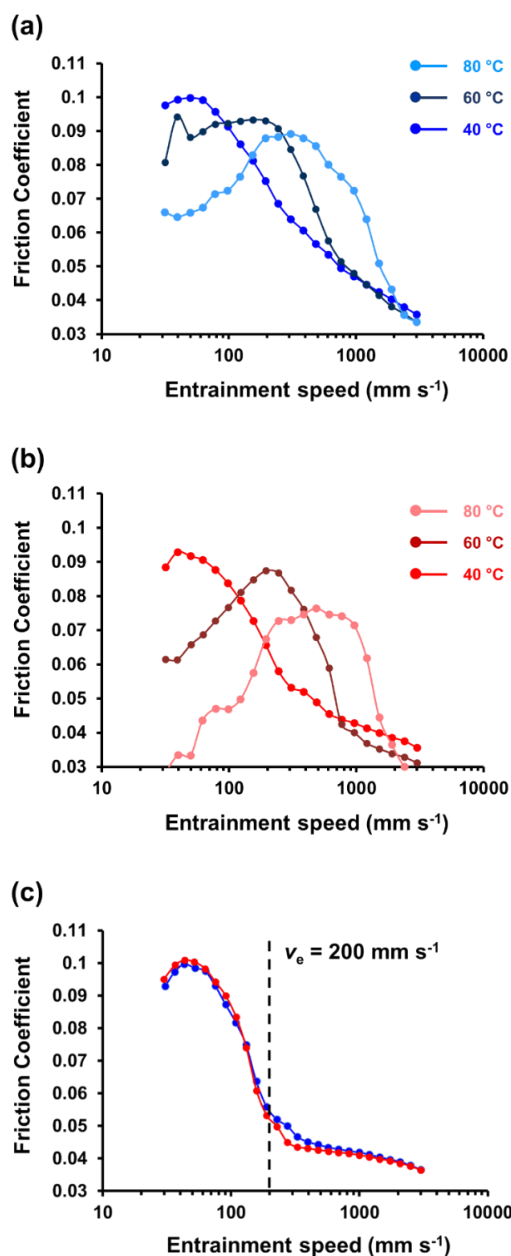
Figure 7.6. Stribeck curves showing the change in friction coefficient with entrainment speed for 2.5% w/w dispersions of **(a)** PLMA$_{63}$-PBzMA$_{245}$ and **(b)** P(LMA$_{50}$-*stat*-GlyMA$_9$)-PBzMA$_{245}$ nanoparticles at 40, 60 and 80 °C. **(c)** Comparison of the Stribeck curves obtained for PLMA$_{63}$-PBzMA$_{245}$ (blue data) and P(LMA$_{50}$-*stat*-GlyMA$_9$)-PBzMA$_{245}$ (red data) nanoparticles at 40 °C. Data were recorded at a 50% slide-to-roll ratio (SRR) under an applied load of 37 N.

Since the QCM-D data suggests enhanced adsorption for the epoxy-functional nanoparticles at higher temperature (see **Figure 7.3**), we examined more demanding MTM test conditions. Thus, the entrainment speed was fixed at 200 mm s^{-1} and a slide-to-roll ratio (SRR) of 50% was employed under an applied load of 37 N while heating from 40 to 120 °C. In principle, the viscosity of the nanoparticle dispersion should be lower at higher temperature, which means that the onset of the 'mixed lubrication' regime should occur at a higher entrainment speed (see **Figure 7.6a**-**b**). Hence additional asperity contacts and a higher friction coefficient were expected at elevated temperature.

For the 40-60 °C regime, the two sets of data are essentially identical. A gradual increase in friction coefficient is observed for both the epoxy-functional P(LMA$_{50}$-*stat*-GlyMA$_9$)-PBzMA$_{245}$ nanoparticles and the non-functional PLMA$_{63}$-PBzMA$_{245}$ nanoparticles (see **Figure 7.7a**). Above 60 °C (which corresponds to the boundary lubrication regime at a v_e of 200 mm s^{-1}; see Stribeck curves shown in **Figure 7.6a-b**), a significant reduction in the friction coefficient from 0.09 to 0.04 was observed for the epoxy-functional nanoparticles, whereas there is almost no change in this parameter for the non-functional nanoparticles. This suggests that higher temperatures lead to more epoxy-functional nanoparticles becoming located within the asperity contact area, despite the relatively harsh experimental conditions. Indeed, inspecting the surface of the MTM disks (within the test area) after these tribology experiments by SEM revealed a significant difference in the nanoparticle surface coverage, see **Figure 7.7b**. Digital image analysis using *ImageJ* software indicated a relatively high fractional surface coverage of 0.45 for the epoxy-functional P(LMA$_{50}$-*stat*-GlyMA$_9$)-PBzMA$_{245}$ nanoparticles but only 0.09 for the corresponding non-functional nanoparticles. In the former case, it is perhaps worth emphasizing that the chemically-adsorbed nanoparticles remain intact given the relatively harsh conditions to which they were subjected during the tribological experiments. These MTM studies and SEM observations are consistent with our QCM-D findings and provides further (albeit indirect) evidence for the likely chemical adsorption of the nanoparticles onto stainless steel, see **Figure 7.7c**.
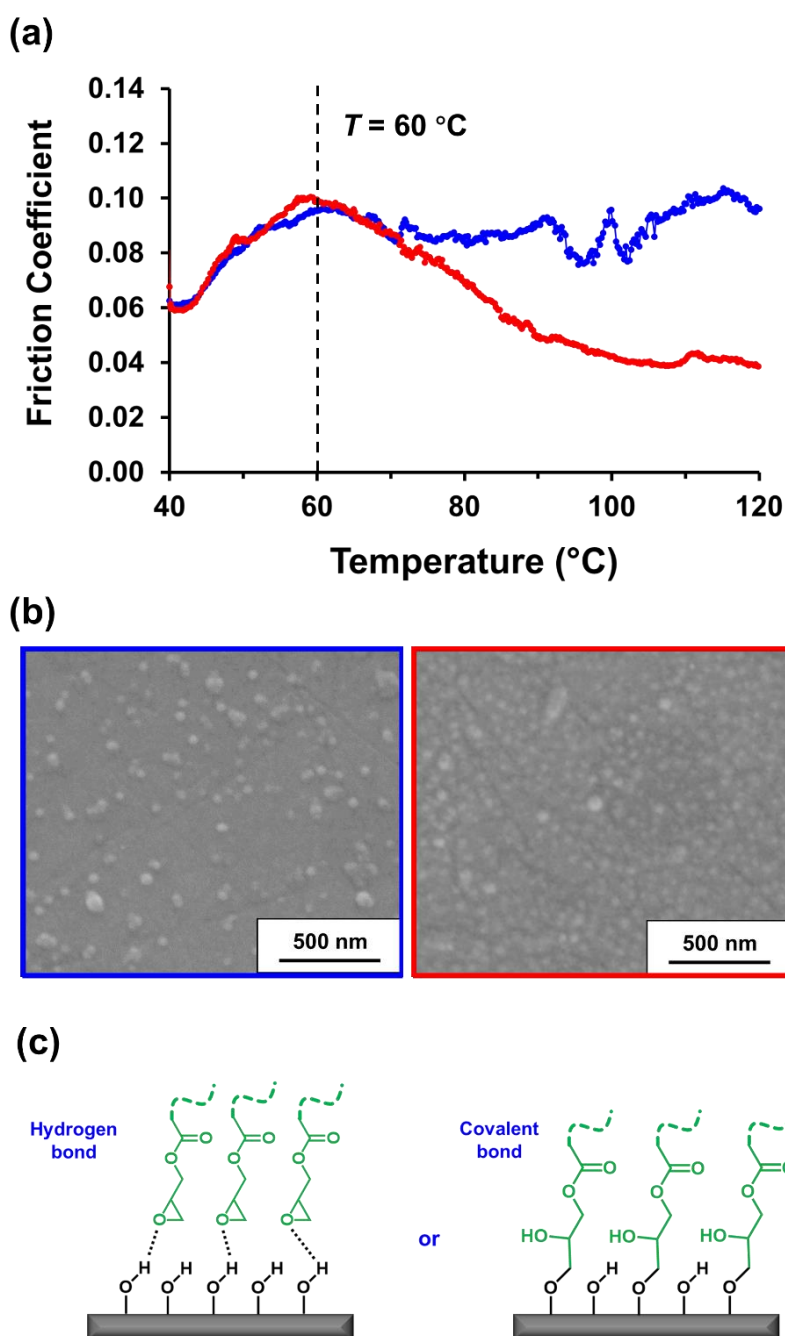
Figure 7.7. (a) Friction coefficient *vs*. temperature data obtained for a 2.5% w/w dispersion of PLMA$_{63}$-PBzMA$_{245}$ nanoparticles (blue data) and P(LMA$_{50}$-*stat*-GlyMA$_9$)-PBzMA$_{245}$ nanoparticles (red data). Data were recorded at an entrainment speed of 200 mm s^{-1} with a slide-to-roll ratio (SRR) of 50% under an applied load of 37 N. **(b)** SEM images recorded for the MTM disks following these tribology experiments when using the PLMA$_{63}$-PBzMA$_{245}$ nanoparticles (blue frame) and the P(LMA$_{50}$-*stat*-GlyMA$_9$)-PBzMA$_{245}$ nanoparticles (red frame), respectively. The epoxy groups clearly promote much stronger nanoparticle adsorption, which correlates with the significant reduction in friction coefficient observed above 60 °C. **(c)** Two possible mechanisms for the enhanced adsorption of epoxy-functional P(LMA$_{50}$-*stat*-GlyMA$_9$)-PBzMA$_{245}$ nanoparticles onto stainless steel: (i) hydrogen bond formation between the polar epoxy rings and the surface hydroxyl groups (i.e., Fe-OH) or (ii) epoxy ring-opening reaction with the same surface hydroxyl groups to produce covalent bonds. The experimental evidence reported herein supports the latter interaction, for which there is also some literature precedent.[54,55]

246

7.4. Conclusions

The adsorption of ~27 nm epoxy-functional P(LMA$_{50}$-*stat*-GlyMA$_9$)-PMMA$_{67}$, PLMA$_{63}$-PGlyMA$_{89}$ and non-functional PLMA$_{63}$-PMMA$_{67}$ nanoparticles onto stainless steel from *n*-dodecane was assessed using QCM-D at 20 °C. The highest adsorbed amount was obtained when epoxy groups were incorporated within the steric stabilizer chains, rather than being located within the nanoparticle cores. Conducting these QCM-D experiments at 40 °C led to a significantly higher adsorbed amount for the epoxy-functional P(LMA$_{50}$-*stat*-GlyMA$_9$)-PMMA$_{67}$ nanoparticles. For purely physical adsorption, a lower adsorbed amount should be obtained under such conditions. Thus, such temperature-dependent studies suggest that nanoparticle adsorption involves a chemical reaction between the epoxy groups and the Fe-OH groups located at the stainless steel surface. Indeed, there is some recent literature precedent for such surface chemistry.[54,55] Increasing the nanoparticle diameter from ~27 nm to ~50 nm resulted in an approximate five-fold increase in the adsorbed amount for P(LMA$_{50}$-*stat*-GlyMA$_9$)-PBzMA$_{245}$ nanoparticles compared to that for the non-functional PLMA$_{63}$-PBzMA$_{245}$ nanoparticles, with the corresponding QCM-D fractional surface coverages estimated to be 0.53 and 0.11, respectively. Furthermore, replacing the core-forming PMMA block with PBzMA confirmed that the enhanced adsorption of such epoxy-functional spheres is independent of the nature of the core-forming block.

The ~50 nm diameter nanoparticles were then examined for tribology experiments using an MTM set-up. When heating from 60 °C to 120 °C at a constant entrainment speed and slide-to-roll ratio, the epoxy-functional P(LMA$_{50}$-*stat*-GlyMA$_9$)-PBzMA$_{245}$ nanoparticles reduced the friction coefficient dramatically compared to the corresponding non-functional PLMA$_{63}$-PBzMA$_{245}$ nanoparticles. In this case, *postmortem* SEM studies indicated a significantly higher surface coverage for the adsorbed epoxy-functional nanoparticles. Such studies provide strong evidence for chemical adsorption of such nanoparticles *via* an epoxy-hydroxyl ring-opening reaction at elevated temperature.

Finally, given their relative ease of synthesis directly in mineral oil using potentially scalable chemistry, such epoxy-functional nanoparticles appear to offer important advantages compared to other polymer-based lubricating systems reported in the literature such as polymer brushes.[58,59]

7.5. References

(1)   Gisser, H.; Petronio, M. Friction of Poly(n–Alkyl Methacrylates). *ASLE Trans.* **1973**, *16*, 197–202.

(2)   Robinson, J. W.; Zhou, Y.; Qu, J.; Bays, J. T.; Cosimbescu, L. Highly Branched Polyethylenes as Lubricant Viscosity and Friction Modifiers. *React. Funct. Polym.* **2016**, *109*, 52–55.

(3)   Gmür, T. A.; Mandal, J.; Cayer-Barrioz, J.; Spencer, N. D. Towards a Polymer-Brush-Based Friction Modifier for Oil. *Tribol. Lett.* **2021**, *69*, 124.

(4)   Delamarre, S.; Gmür, T.; Spencer, N. D.; Cayer-Barrioz, J. Polymeric Friction Modifiers: Influence of Anchoring Chemistry on Their Adsorption and Effectiveness. *Langmuir* **2022**, *38*, 11451–11458.

(5)   Growney, D. J.; Mykhaylyk, O. O.; Middlemiss, L.; Fielding, L. A.; Derry, M. J.; Aragrag, N.; Lamb, G. D.; Armes, S. P. Is Carbon Black a Suitable Model Colloidal Substrate for Diesel Soot? *Langmuir* **2015**, *31*, 10358–10369.

(6)   Eckert, R. J. A. Hydrogenated Star-Shaped Polymer. US Patent: 4116917, 1978.

(7)   Zheng, R.; Liu, G.; Devlin, M.; Hux, K.; Jao, T. C. Friction Reduction of Lubricant Base Oil by Micelles and Crosslinked Micelles of Block Copolymers. *Tribol. Trans.* **2010**, *53*, 97–107.

(8)   Derry, M. J.; Smith, T.; O'Hora, P. S.; Armes, S. P. Block Copolymer Nanoparticles Prepared via Polymerization-Induced Self-Assembly Provide Excellent Boundary Lubrication Performance for Next-Generation Ultralow-Viscosity Automotive Engine Oils. *ACS Appl. Mater. Interfaces* **2019**, *11*, 33364–33369.

(9)   Chiefari, J.; Chong, Y. K. B.; Ercole, F.; Krstina, J.; Jeffery, J.; Le, T. P. T.; Mayadunne, R. T. A.; Meijs, G. F.; Moad, C. L.; Moad, G.; Rizzardo, E.; Thang, S. H. Living Free-Radical Polymerization by Reversible Addition-Fragmentation Chain Transfer: The RAFT Process. *Macromolecules* **1998**, *31*, 5559–5562.

(10)   Perrier, S. 50th Anniversary Perspective: RAFT Polymerization - A User Guide. *Macromolecules* **2017**, *50*, 7433–7447.

(11)   Houillot, L.; Bui, C.; Save, M.; Charleux, B.; Farcet, C.; Moire, C.; Raust, J. A.; Rodriguez, I. Synthesis of Well-Defined Polyacrylate Particle Dispersions in Organic Medium Using Simultaneous RAFT Polymerization and Self-Assembly of Block Copolymers. A Strong Influence of the Selected Thiocarbonylthio Chain Transfer Agent. *Macromolecules* **2007**, *40*, 6500–6509.

(12)   Houillot, L.; Bui, C.; Farcet, C.; Moire, C.; Raust, J. A.; Pasch, H.; Save, M.; Charleux, B. Dispersion Polymerization of Methyl Acrylate in Nonpolar Solvent Stabilized by Block Copolymers Formed in Situ via the RAFT Process. *ACS Appl. Mater. Interfaces* **2010**, *2*, 434–442.

(13)   Pei, Y.; Sugita, O. R.; Thurairajah, L.; Lowe, A. B. Synthesis of Poly(Stearyl Methacrylate-b-3-Phenylpropyl Methacrylate) Nanoparticles in n-Octane and Associated Thermoreversible Polymorphism. *RSC Adv.* **2015**, *5*, 17636–17646.

(14)   Pei, Y.; Noy, J. M.; Roth, P. J.; Lowe, A. B. Soft Matter Nanoparticles with Reactive Coronal Pentafluorophenyl Methacrylate Residues via Non-Polar RAFT Dispersion Polymerization and Polymerization-Induced Self-Assembly. *J. Polym. Sci. Part A Polym. Chem.* **2015**, *53*, 2326–2335.

(15)   Derry, M. J.; Fielding, L. A.; Armes, S. P. Polymerization-Induced Self-Assembly of Block Copolymer Nanoparticles via RAFT Non-Aqueous Dispersion Polymerization. *Prog. Polym. Sci.* **2016**, *52*, 1–18.

(16)   Lansalot, M.; Rieger, J. Polymerization-Induced Self-Assembly. *Macromol. Rapid Commun.* **2019**, *40*, 1800885.

(17)   D'Agosto, F.; Rieger, J.; Lansalot, M. RAFT-Mediated Polymerization-Induced Self-Assembly. *Angew. Chemie - Int. Ed.* **2020**, *59*, 8368–8392.

(18)   Hakkinen, S.; Tanaka, J.; Garcia Macet, R.; Hall, S.; Huband, S.; Rho, J.; Song, Q.; Perrier, S. Polymerisation-Induced Self-Assembly of Graft Copolymers. *Angew. Chemie Int. Ed.* **2022**, e202210518.

(19)   Trent, J. S. Ruthenium Tetraoxide Staining of Polymers: New Preparative Methods for Electron Microscopy. *Macromolecules* **1984**, *17*, 2930–2931.

(20)   Ilavsky, J.; Jemian, P. R. Irena: Tool Suite for Modeling and Analysis of Small-Angle Scattering. *J. Appl. Crystallogr.* **2009**, *42*, 347–353.

(21)   Fielding, L. A.; Lane, J. A.; Derry, M. J.; Mykhaylyk, O. O.; Armes, S. P. Thermo-Responsive Diblock Copolymer Worm Gels in Non-Polar Solvents. *J. Am. Chem. Soc.* **2014**, *136*, 5790–5798.

(22)   Derry, M. J.; Fielding, L. A.; Warren, N. J.; Mable, C. J.; Smith, A. J.; Mykhaylyk, O. O.; Armes, S. P. In Situ Small-Angle X-Ray Scattering Studies of Sterically-Stabilized Diblock Copolymer Nanoparticles Formed during Polymerization-Induced Self-Assembly in Non-Polar Media. *Chem. Sci.* **2016**, *7*, 5078–5090.

(23)   Docherty, P. J.; Girou, C.; Derry, M. J.; Armes, S. P. Epoxy-Functional Diblock Copolymer Spheres, Worms and Vesicles via Polymerization-Induced Self-Assembly in Mineral Oil. *Polym. Chem.* **2020**, *11*, 3332–3339.

(24)   Glatter, O.; Kratky, O. *Small-Angle X-Ray Scattering*; Academic Press, London, 1982.

(25)   Pedersen, J. S. Form Factors of Block Copolymer Micelles with Spherical, Ellipsoidal and Cylindrical Cores. *J. Appl. Crystallogr.* **2000**, *33*, 637–640.

(26)   Serizawa, T.; Kamimura, S.; Akashi, M. Electrostatic Adsorption of Polystyrene Particles with Different Surface Charges onto the Surface of an Ultrathin Polymer Film. *Colloids Surfaces A Physicochem. Eng. Asp.* **2000**, *164*, 237–245.

(27)   Yan, Y.; Zhou, X.; Ji, J.; Yan, L.; Zhang, G. Adsorption of Polymeric Micelles and Vesicles on a Surface Investigated by Quartz Crystal Microbalance. *J. Phys. Chem. B* **2006**, *110*, 21055–21059.

(28)   Xu, D.; Hodges, C.; Ding, Y.; Biggs, S.; Brooker, A.; York, D. A QCM Study on the Adsorption of Colloidal Laponite at the Solid/Liquid Interface. *Langmuir* **2010**, *26*, 8366–8372.

(29)   Sigolaeva, L. V.; Günther, U.; Pergushov, D. V.; Gladyr, S. Y.; Kurochkin, I. N.; Schacher, F. H. Sequential PH-Dependent Adsorption of Ionic Amphiphilic Diblock Copolymer Micelles and Choline Oxidase onto Conductive Substrates: Toward the Design of Biosensors. *Macromol. Biosci.* **2014**, *14*, 1039–1051.

(30)   Engström, J.; Benselfelt, T.; Wågberg, L.; D'Agosto, F.; Lansalot, M.; Carlmark, A.; Malmström, E. Tailoring Adhesion of Anionic Surfaces Using Cationic PISA-Latexes-towards Tough Nanocellulose Materials in the Wet State. *Nanoscale* **2019**, *11*, 4287–4302.

(31)   Engström, J.; Reid, M. S.; Brotherton, E. E.; Malmström, E.; Armes, S. P.; Hatton, F. L.

Investigating the Adsorption of Anisotropic Diblock Copolymer Worms onto Planar Silica and Nanocellulose Surfaces Using a Quartz Crystal Microbalance. *Polym. Chem.* **2021**, *12*, 6088–6100.

(32) Brotherton, E. E.; Josland, D.; György, C.; Johnson, E. C.; Chan, D. H. H.; Smallridge, M. J.; Armes, S. P. Histidine-Functionalized Diblock Copolymer Nanoparticles Exhibit Enhanced Adsorption onto Planar Stainless Steel. **2023**, *2200903*.

(33) Fry, B. M.; Moody, G.; Spikes, H. A.; Wong, J. S. S. Adsorption of Organic Friction Modifier Additives. *Langmuir* **2020**, *36*, 1147–1155.

(34) Nalam, P. C.; Pham, A.; Castillo, R. V.; Espinosa-marzal, R. M. Adsorption Behavior and Nanotribology of Amine-Based Friction Modifiers on Steel Surfaces. *J. Phys. Chem. C* **2019**, *123*, 13672–13680.

(35) Lundgren, S. M.; Persson, K.; Mueller, G.; Kronberg, B.; Clarke, J.; Chtaib, M.; Claesson, P. M. Unsaturated Fatty Acids in Alkane Solution : Adsorption to Steel Surfaces. *Langmuir* **2007**, *23*, 10598–10602.

(36) Jaishankar, A.; Jusu, A.; Vreeland, J. L.; Deighton, S.; Pellettiere, J.; Schilowitz, A. M. Adsorption of Stearic Acid at the Iron Oxide/Oil Interface: Theory, Experiments, and Modeling. *Langmuir* **2019**, *35*, 2033–2046.

(37) Studt, P. Boundary Lubrication: Adsorption of Oil Additives on Steel and Ceramic Surfaces and Its Influence on Friction and Wear. *Tribol. Int.* **1989**, *22*, 111–119.

(38) Spikes, H. Friction Modifier Additives. *Tribol. Lett.* **2015**, *60*, 5.

(39) Salem, L. Attractive Forces between Long Saturated Chains at Short Distances. *J. Chem. Phys.* **1962**, *37*, 2100–2113.

(40) Beltzer, M.; Jahanmir, S. Role of Dispersion Interactions between Hydrocarbon Chains in Boundary Lubrication. *ASLE Trans.* **1987**, *30*, 47–54.

(41) Sauerbrey, G. Verwendung von Schwingquarzen Zur Wägung Dünner Schichten Und Zur Mikrowägung. *Zeitschrift für Phys.* **1959**, *155*, 206–222.

(42) Malmström, J.; Agheli, H.; Kingshott, P.; Sutherland, D. S. Viscoelastic Modeling of Highly Hydrated Laminin Layers at Homogeneous and Nanostructured Surfaces: Quantification of Protein Layer Properties Using QCM-D and SPR. *Langmuir* **2007**, *23*, 9760–9768.

(43) Dutta, A. K.; Belfort, G. Adsorbed Gels versus Brushes: Viscoelastic Differences. *Langmuir* **2007**, *23*, 3088–3094.

(44) Saftics, A.; Prósz, G. A.; Türk, B.; Peter, B.; Kurunczi, S.; Horvath, R. In Situ Viscoelastic Properties and Chain Conformations of Heavily Hydrated Carboxymethyl Dextran Layers: A Comparative Study Using OWLS and QCM-I Chips Coated with Waveguide Material. *Sci. Rep.* **2018**, *8*, 11840.

(45) Chandrasekaran, N.; Dimartino, S.; Fee, C. J. Study of the Adsorption of Proteins on Stainless Steel Surfaces Using QCM-D. *Chem. Eng. Res. Des.* **2013**, *91*, 1674–1683.

(46) Vogt, B. D.; Lin, E. K.; Wu, W.; White, C. C. Effect of Film Thickness on the Validity of the Sauerbrey Equation for Hydrated Polyelectrolyte Films. *J. Phys. Chem. B* **2004**, *108*, 12685–12690.

(47) Easley, A. D.; Ma, T.; Eneh, C. I.; Yun, J.; Thakur, R. M.; Lutkenhaus, J. L. A Practical Guide to Quartz Crystal Microbalance with Dissipation Monitoring of Thin Polymer Films. *J. Polym. Sci.* **2022**, *60*, 1090–1107.

(48) Irwin, E. F.; Ho, J. E.; Kane, S. R.; Healy, K. E. Analysis of Interpenetrating Polymer

Networks via Quartz Crystal Microbalance with Dissipation Monitoring. *Langmuir* **2005**, *21*, 5529–5536.

(49) Reviakine, I.; Johannsmann, D.; Richter, R. P. Hearing What You Cannot See and Visualizing What You Hear: Interpreting Quartz Crystal Microbalance Data from Solvated Interfaces. *Anal. Chem.* **2011**, *83*, 8838–8848.

(50) György, C.; Lovett, J. R.; Penfold, N. J. W.; Armes, S. P. Epoxy-Functional Sterically Stabilized Diblock Copolymer Nanoparticles via RAFT Aqueous Emulsion Polymerization: Comparison of Two Synthetic Strategies. *Macromol. Rapid Commun.* **2018**, *40*, 1800289.

(51) György, C.; Smith, T.; Growney, D. J.; Armes, S. P. Synthesis and Derivatization of Epoxy-Functional Sterically-Stabilized Diblock Copolymer Spheres in Non-Polar Media: Does the Spatial Location of the Epoxy Groups Matter? *Polym. Chem.* **2022**, *13*, 3619–3630.

(52) Hatton, F. L.; Lovett, J. R.; Armes, S. P. Synthesis of Well-Defined Epoxy-Functional Spherical Nanoparticles by RAFT Aqueous Emulsion Polymerization. *Polym. Chem.* **2017**, *8*, 4856–4868.

(53) Docherty, P. J.; Derry, M. J.; Armes, S. P. RAFT Dispersion Polymerization of Glycidyl Methacrylate for the Synthesis of Epoxy-Functional Block Copolymer Nanoparticles in Mineral Oil. *Polym. Chem.* **2019**, *10*, 603–611.

(54) Xu, Z.; Zhang, Y.; Wu, Y.; Lu, X. Molecular-Level Correlation between Spectral Evidence and Interfacial Bonding Formation for Epoxy Adhesives on Solid Substrates. *Langmuir* **2022**, *38*, 5847–5856.

(55) Xu, Z.; Zhang, Y.; Wu, Y.; Lu, X. Spectroscopically Detecting Molecular-Level Bonding Formation between an Epoxy Formula and Steel. *Langmuir* **2022**, *38*, 13261–13271.

(56) György, C.; Verity, C.; Neal, T. J.; Rymaruk, M. J.; Cornel, E. J.; Smith, T.; Growney, D. J.; Armes, S. P. RAFT Dispersion Polymerization of Methyl Methacrylate in Mineral Oil: High Glass Transition Temperature of the Core-Forming Block Constrains the Evolution of Copolymer Morphology. *Macromolecules* **2021**, *54*, 9496–9509.

(57) Spikes, H. A. Mixed Lubrication - An Overview. *Lubr. Sci.* **1997**, *9*, 221–253.

(58) Munirasu, S.; Karunakaran, R. G.; Rühe, J.; Dhamodharan, R. Synthesis and Morphological Study of Thick Benzyl Methacrylate-Styrene Diblock Copolymer Brushes. *Langmuir* **2011**, *27*, 13284–13292.

(59) Bielecki, R. M.; Benetti, E. M.; Kumar, D.; Spencer, N. D. Lubrication with Oil-Compatible Polymer Brushes. *Tribol. Lett.* **2012**, *45*, 477–487.

8. Conclusions and Future Work

Conclusions and Future Work

RAFT polymerization is an industrially viable technique, as demonstrated by Lubrizol's exploitation of such chemistry for the industrial scale synthesis and commercialization of methacrylic star copolymers as viscosity modifiers for automotive engine oils.[1] In this Thesis, various all-methacrylic diblock copolymer nano-objects were prepared *via* RAFT-mediated PISA in non-polar solvents. According to the literature, such spheres, worms and vesicles offer potential applications as effective friction modifiers[2] or oil thickeners.[3,4]

In **Chapters 2** and **3**, the chain extension of a relatively short PSMA$_9$ precursor is examined using either HPMA in mineral oil or TFEMA in *n*-dodecane, respectively. Using a sufficiently short precursor as a steric stabilizer aids the formation of higher order morphologies, such as worms and vesicles.[5,6] Pseudo-phase diagrams for PSMA$_9$-PHPMA$_x$ and PSMA$_9$-PTFEMA$_x$ nano-objects were constructed by systematically varying the target PHPMA/PTFEMA DP for a range of copolymer concentrations. For the PSMA$_9$-PHPMA$_x$ system, a very narrow worm phase was identified, with this elusive morphology only being accessible at or above 25% w/w solids in mineral oil. Similar observations have been reported for related non-polar PISA formulations, e.g., PLMA-PBzMA or PhBD–PBzMA.[5,7] In contrast, the PSMA$_9$-PTFEMA$_x$ system enabled worms to be obtained at 15% w/w solids in *n*-dodecane.

The PSMA$_9$-PHPMA$_x$ system also exhibited relatively fast polymerization kinetics. For example, 94% HPMA conversion was achieved within 40 min when targeting PSMA$_9$-PHPMA$_{150}$ vesicles at 15% w/w solids at 90 °C, whereas only 37% BzMA conversion was achieved within the same timescale when targeting the corresponding PSMA$_9$-PBzMA$_{150}$ vesicles under the same conditions. The remarkably fast polymerization of HPMA is attributed to the relatively high polarity of this hydroxyl-functional monomer. Indeed, similar kinetic data were reported by Cunningham *et al.* for the RAFT dispersion polymerization of NMEP in *n*-dodecane.[8] However, for the synthesis of PSMA$_9$-PTFEMA$_{200}$ vesicles at 20% w/w solids in *n*-dodecane at 90 °C, only 11% TFEMA conversion was obtained after 40 min.

Cornel *et al.* reported that matching the refractive index (RI) of the core-forming block to that of the *n*-alkane solvent enabled the preparation of a highly transparent dispersion of 33 nm diameter PSMA$_9$-PTFEMA$_{98}$ spheres.[9] Utilizing the same approach, a highly transparent dispersion of 240 nm diameter PSMA$_9$-PTFEMA$_{294}$ vesicles (97% transmittance at $\lambda = 600$ nm) was prepared at 25% w/w solids in *n*-dodecane at 20 °C. As a comparison, a much more

dilute (0.5% w/w) dispersion of ~180 nm diameter $PSMA_9$-$PHPMA_{294}$ vesicles in *n*-dodecane exhibited a transmittance of just 31% at 600 nm. Taking advantage of the temperature dependence of the RI of *n*-alkanes, isorefractive $PSMA_9$-$PTFEMA_{294}$ vesicles could be obtained either at 50 °C in *n*-tetradecane or at 90 °C in *n*-hexadecane. Cornel *et al*. also reported that the fate of the trithiocarbonate RAFT agent within highly transparent $PSMA_{12}$-$PTFEMA_{98}$ spheres could be assessed in real time by monitoring its n → π* absorption band (λ = 446 nm) using *in situ* visible absorption spectroscopy. Extending this concept to include a dithiobenzoate-based RAFT agent, the synthesis of 26 nm diameter $PSMA_{16}$-$PTFEMA_{86}$ spheres was monitored using the same approach for the RAFT dispersion polymerization of TFEMA conducted with a CPDB-capped $PSMA_{16}$ precursor in *n*-hexadecane at 90 °C. Such experiments revealed the premature loss of such RAFT chain-ends, which precluded the acquisition of reliable kinetic data. In contrast, Cornel *et al*. observed that trithiocarbonate-based chain-ends remained stable for up to 2 h at 70 °C under monomer-starved conditions,[9] which indicates much higher chemical stability for trithiocarbonates compared to dithiobenzoates. In **Chapter 4** and **5**, this enhanced stability was exploited for the synthesis of a series of PLMA-PMMA and PLMA-P(0.9MMA-*stat*-0.1LMA) nano-objects at 115 °C with reasonably good RAFT control using a trithiocarbonate-based RAFT agent (MCDP). In the future, it would be worth monitoring the synthesis of transparent vesicles using *in situ* visible absorption spectroscopy at lower temperatures (say 70 °C) using various alternative dithiobenzoate- and trithiocarbonate-based RAFT agents to examine whether subtle differences in chemical structure and reaction conditions had any beneficial effect on chain-end fidelity.

Fielding *et al*. reported that $PLMA_{16}$-$PBzMA_{37}$ worms exhibited a worm-to-sphere transition on heating, which was rationalized in terms of surface plasticization of the core-forming PBzMA block.[10] However, for the $PSMA_9$-$PHPMA_{70}$ worms reported in **Chapter 2**, TEM analysis indicated that a partial worm-to-*vesicle* transition occurs when heating to 150 °C. Interestingly, Docherty *et al*. reported similar behavior for $PSMA_9$-$PGlyMA_{75}$ worms. In both cases, this thermal transition suggests *uniform* plasticization of the core-forming block at high temperature.[11] Alternatively, the $PSMA_9$ stabilizer chains may become less solvated at 150 °C. Further research is warranted to distinguish these two possible explanations.

In **Chapter 4**, a series of PLMA-PMMA nanoparticles were prepared in mineral oil using either a traditional two-step approach or a more convenient one-pot protocol. MMA is a commodity monomer, which makes this PISA formulation particularly relevant for industrial scale-up. The

one-pot protocol resulted in higher monomer conversions with narrower molecular weight distributions. A pseudo-phase diagram was constructed in which the target PMMA DP was systematically varied when using a PLMA$_{22}$, PLMA$_{30}$ or a PLMA$_{41}$ precursor at 20% w/w solids at 90 °C. Unfortunately, only spheres and short worms could be accessed. Moreover, targeting relatively high core-forming block DPs when using the PLMA$_{22}$ precursor merely produced colloidally unstable spherical aggregates, rather than long worms or vesicles. Similar limitations on the evolution in copolymer morphology were observed when using an alternative solvent (*n*-dodecane) or when employing a PSMA$_{10}$ precursor instead of PLMA$_{22}$ in mineral oil. This unexpected morphological constraint is directly related to the high T_g of the PMMA chains. Synthesis of such PLMA-PMMA nanoparticles at 115 °C (*i.e.*, above the T_g of PMMA) only resulted in spheres. This suggests that nanoparticles are formed by a chain expulsion-insertion mechanism at this relatively high temperature. In contrast, a micelle fusion/fission mechanism appears to be responsible for the formation of short worms at lower synthesis temperatures (*i.e.*, 70 or 90 °C). In **Chapter 5**, the introduction of just 10 mol% LMA into the core-forming block provided access to PLMA$_{22}$-(0.9MMA-*stat*-0.1LMA)$_x$ long worms and vesicles. The LMA comonomer enhances the mobility of the core-forming block by (i) lowering its effective T_g and (ii) increasing its degree of solvent plasticization at 115 °C. Both the PLMA$_{22}$-PMMA$_{69}$ short worms and PLMA$_{22}$-(0.9MMA-*stat*-0.1LMA)$_{113}$ long worms undergo a worm-to-sphere transition on heating to 150 °C. When conducted at 20% w/w solids, this thermally-induced transition proved to be partially reversible for the former nano-objects and fully reversible for the latter.[10] Similarly, a vesicle-to-worm transition was observed on heating PLMA$_{22}$-(0.9MMA-*stat*-0.1LMA)$_{113}$ vesicles, which is consistent with observations reported by Derry *et al*. for PSMA$_{13}$-PBzMA$_{96}$ vesicles.[3] During this PhD project, we initiated a new informal collaboration with Prof. A. Shen and Dr. V. Calabrese of the Okinawa Institute of Science and Technology in Japan. These workers have conducted a series of microfluidic experiments to study the fundamental difference in rheological behavior exhibited by short, stiff PSMA$_{10}$-PMMA$_{83}$ worms and long, flexible PSMA$_{10}$-PBzMA$_{49}$ worms (both prepared in our laboratory) when such nano-objects are subjected to either shear or extensional flow.[12] Moreover, Lubrizol successfully scaled-up the in-house synthesis of PLMA$_{22}$-PMMA$_{70}$ short worms for on-site testing to investigate the potential oil-thickening effect of such nanoparticles. Thus the new data generated in this Thesis have stimulated both academic and industrial interest. In principle, introducing EGDMA as a third block to produce core-crosslinked PLMA-PMMA short worms should ensure their morphological stability at elevated temperatures.

In **Chapter 6**, the post-polymerization modification of ~30 nm diameter epoxy-functional PLMA$_{63}$-PGlyMA$_{89}$ spheres was compared to that of ~30 nm diameter P(LMA$_{50}$-*stat*-GlyMA$_9$)-PMMA$_{67}$. For a 20% w/w dispersion of P(LMA$_{50}$-*stat*-GlyMA$_9$)-PMMA$_{67}$ spheres, a fifty-fold excess of benzylamine ([benzylamine]/[epoxy] = 50) was required to react all the epoxy groups within the stabilizer chains, whereas for PLMA$_{63}$-PGlyMA$_{89}$ spheres only an equimolar amount of amine ([benzylamine]/[epoxy] = 1.0) was required to fully react all the epoxy groups located within the nanoparticle cores. This was rationalized in terms of the low molar concentration of epoxy groups for the P(LMA$_{50}$-*stat*-GlyMA$_9$)-PMMA$_{67}$ spheres (0.07 mol dm^{-3}) relative to that of the PLMA$_{63}$-PGlyMA$_{89}$ spheres (0.52 mol dm^{-3}). For the P(LMA$_{50}$-*stat*-GlyMA$_9$)-PMMA$_{67}$ spheres, epoxy ring-opening when *via* water required heating up to 110 °C at a relatively low copolymer concentration (1.0% w/w solids) to avoid cross-linking between neighboring nanoparticles. Epoxy ring-opening for the PLMA$_{63}$-PGlyMA$_{89}$ spheres was achieved using 50% v/v acetic acid at 110 °C with the aid of a bespoke experimental set-up. Since all the epoxy groups are in close proximity within the PLMA$_{63}$-PGlyMA$_{89}$ cores, their ring-opening by reaction with either benzylamine or water inevitably led to core cross-linking. Hence ^{1}H NMR spectroscopy could be used to assess the degree of functionalization of P(LMA$_{50}$-*stat*-GlyMA$_9$)-PMMA$_{67}$ spheres, whereas FT-IR spectroscopy (which does not require copolymer solubilization) was required for the characterization of the derivatized PLMA$_{63}$-PGlyMA$_{89}$ spheres.

In **Chapter 7**, the adsorption of ~27 nm diameter epoxy-functional PLMA$_{63}$-PGlyMA$_{89}$ or P(LMA$_{50}$-*stat*-GlyMA$_9$)-PMMA$_{67}$ spheres onto stainless steel from *n*-dodecane was compared to that of similar-sized non-functional PLMA$_{63}$-PMMA$_{67}$ spheres using QCM-D at both 20 °C and 40 °C. A significantly higher adsorbed mass was determined for P(LMA$_{50}$-*stat*-GlyMA$_9$)-PMMA$_{67}$ spheres (~7.6 mg m^{-2}) relative to PLMA$_{63}$-PGlyMA$_{89}$ (~3.7 mg m^{-2}) and PLMA$_{63}$-PMMA$_{67}$ (~3.8 mg m^{-2}) spheres at 20 °C. This indicates that the precise spatial location of the epoxy groups within the nanoparticles is of critical importance in promoting their adhesion. When conducting such nanoparticle adsorption experiments at 40 °C, QCM-D studies indicated a moderate increase in adsorbed mass for the P(LMA$_{50}$-*stat*-GlyMA$_9$)-PMMA$_{67}$ spheres, whereas a reduction in adsorbed mass was observed for the PLMA$_{63}$-PGlyMA$_{89}$ and PLMA$_{63}$-PMMA$_{67}$ spheres. These experiments suggest that the epoxy groups within the P(LMA$_{50}$-*stat*-GlyMA$_9$)-PMMA$_{67}$ spheres most likely react with the surface hydroxyl groups on the stainless steel surface to form covalent bonds. In contrast, the lower extent of adsorption observed for the other two types of spheres indicates a physical adsorption mechanism in this case. The

adsorption of ~50 nm diameter P(LMA$_{50}$-*stat*-GlyMA$_9$)-PBzMA$_{245}$ and PLMA$_{63}$-PBzMA$_{245}$ spheres onto stainless steel was also conducted at 20 °C. An adsorbed mass of ~31.3 mg m^{-2} was determined for P(LMA$_{50}$-*stat*-GlyMA$_9$)-PBzMA$_{245}$ spheres, whereas a much lower adsorbed mass of only ~6.4 mg m^{-2} was obtained for PLMA$_{63}$-PBzMA$_{245}$ spheres. This significant difference was confirmed by SEM studies of the nanoparticle-coated stainless steel disks after the QCM-D experiments, with a significantly higher surface coverage being observed for the epoxy-functional nanoparticles. In tribological experiments, Derry *et al.* reported that 48 nm diameter PSMA$_{31}$-PBzMA$_{200}$-PEGDMA$_{20}$ spheres reduced the friction coefficient significantly within the boundary lubrication regime. Thus the ~50 nm epoxy-functional and non-functional spheres were evaluated as friction modifiers by Lubrizol scientists using an industry-standard MTM test. A significant reduction in friction coefficient was observed for the P(LMA$_{50}$-*stat*-GlyMA$_9$)-PBzMA$_{245}$ spheres within the mixed lubrication regime on heating from 60 to 120 °C, whereas almost no change in friction coefficient was obtained for the corresponding non-functional spheres. This suggests that introducing epoxy functionality within sterically-stabilized nanoparticles is likely to offer potential benefits (e.g. greater fuel efficiency, lower CO$_2$ emissions and reduced long-term engine wear) in the context of automotive engine oils. These studies could be extended by investigating the adsorption of epoxy-functional worms or vesicles onto stainless steel. In principle, XPS studies may provide direct evidence for the proposed chemical reaction between the epoxy groups on the nanoparticles and the surface hydroxyl groups on the stainless steel. Finally, the synthesis of fluorescent nanoparticles may aid quantification of their interfacial adsorption onto stainless steel by *in situ* reflectance measurements, which might be more convenient and more informative than *postmortem* SEM analysis.

References

(1) Bryztwa, A. J.; Johnson, J. Scaled Production of RAFT CTA - a STAR Performer. *Am. Chem. Soc. Polym. Prepr. Div. Polym. Chem.* **2011**, *52*, 533–534.

(2) Derry, M. J.; Smith, T.; O'Hora, P. S.; Armes, S. P. Block Copolymer Nanoparticles Prepared via Polymerization-Induced Self-Assembly Provide Excellent Boundary Lubrication Performance for Next-Generation Ultralow-Viscosity Automotive Engine Oils. *ACS Appl. Mater. Interfaces* **2019**, *11*, 33364–33369.

(3) Derry, M. J.; Mykhaylyk, O. O.; Armes, S. P. A Vesicle-to-Worm Transition Provides a New High-Temperature Oil Thickening Mechanism. *Angew. Chemie - Int. Ed.* **2017**, *56*, 1746–1750.

(4)   Rymaruk, M. J.; Hunter, S. J.; O'Brien, C. T.; Brown, S. L.; Williams, C. N.; Armes, S. P. RAFT Dispersion Polymerization in Silicone Oil. *Macromolecules* **2019**, *52*, 2822–2832.

(5)   Fielding, L. A.; Derry, M. J.; Ladmiral, V.; Rosselgong, J.; Rodrigues, A. M.; Ratcliffe, L. P. D.; Sugihara, S.; Armes, S. P. RAFT Dispersion Polymerization in Non-Polar Solvents: Facile Production of Block Copolymer Spheres, Worms and Vesicles in n-Alkanes. *Chem. Sci.* **2013**, *4*, 2081–2087.

(6)   Rymaruk, M. J.; O'Brien, C. T.; Brown, S. L.; Williams, C. N.; Armes, S. P. RAFT Dispersion Polymerization of Benzyl Methacrylate in Silicone Oil Using a Silicone-Based Methacrylic Stabilizer Provides Convenient Access to Spheres, Worms, and Vesicles. *Macromolecules* **2020**, *53*, 1785–1794.

(7)   Darmau, B.; Rymaruk, M. J.; Warren, N. J.; Bening, R.; Armes, S. P. RAFT Dispersion Polymerization of Benzyl Methacrylate in Non-Polar Media Using Hydrogenated Polybutadiene as a Steric Stabilizer Block. *Polym. Chem.* **2020**, *11*, 7533–7541.

(8)   Cunningham, V. J.; Armes, S. P.; Musa, O. M. Synthesis, Characterisation and Pickering Emulsifier Performance of Poly(Stearyl Methacrylate)-Poly(N-2-(Methacryloyloxy)Ethyl Pyrrolidone) Diblock Copolymer Nano-Objects via RAFT Dispersion Polymerisation in n-Dodecane. *Polym. Chem.* **2016**, *7*, 1882–1891.

(9)   Cornel, E. J.; Meurs, S. Van; Smith, T.; Hora, P. S. O.; Armes, S. P. In Situ Spectroscopic Studies of Highly Transparent Nanoparticle Dispersions Enable Assessment of Trithiocarbonate Chain-End Fidelity during RAFT Dispersion Polymerization in Nonpolar Media. *J. Am. Chem. Soc.* **2018**, *140*, 12980–12988.

(10)   Fielding, L. A.; Lane, J. A.; Derry, M. J.; Mykhaylyk, O. O.; Armes, S. P. Thermo-Responsive Diblock Copolymer Worm Gels in Non-Polar Solvents. *J. Am. Chem. Soc.* **2014**, *136*, 5790–5798.

(11)   Byard, S. J.; O'Brien, C. T.; Derry, M. J.; Williams, M.; Mykhaylyk, O. O.; Blanazs, A.; Armes, S. P. Unique Aqueous Self-Assembly Behavior of a Thermoresponsive Diblock Copolymer. *Chem. Sci.* **2020**, *11*, 396–402.

(12)   Calabrese, V.; György, C.; Haward, S. J.; Neal, T. J.; Armes, S. P.; Shen, A. Q. Microstructural Dynamics and Rheology of Worm-like Diblock Copolymer Nanoparticle Dispersions under a Simple Shear and a Planar Extensional Flow. *Macromolecules* **2022**, Manuscript accepted for publication.

9. Appendix

Table 9.1. Summary of the GPC, DLS and TEM data obtained for a series of PSMA$_9$-PHPMA$_x$ diblock copolymer nano-objects prepared at either 15% or 20% w/w in mineral oil, respectively. The PSMA$_9$ precursor is also included as a reference.

Target Composition	Solids Content (% w/w)	THF GPC		DLS		TEM Morphology
		M_n (g mol^{-1})	M_w/M_n	D (nm)	PDI	
PSMA$_9$ macro-CTA	-	4,500	1.12	-	-	-
PSMA$_9$-PHPMA$_{30}$	15	8,100	1.16	23	0.20	Spheres
PSMA$_9$-PHPMA$_{50}$	15	10,000	1.16	26	0.09	Spheres
PSMA$_9$-PHPMA$_{60}$	15	11,000	1.16	34	0.18	Spheres
PSMA$_9$-PHPMA$_{70}$	15	11,900	1.19	40	0.12	Spheres
PSMA$_9$-PHPMA$_{80}$	15	12,800	1.19	57	0.12	Mixed
PSMA$_9$-PHPMA$_{90}$	15	13,600	1.22	104	0.11	Mixed
PSMA$_9$-PHPMA$_{100}$	15	14,400	1.25	153	0.25	Mixed
PSMA$_9$-PHPMA$_{105}$	15	14,300	1.22	170	0.16	Mixed
PSMA$_9$-PHPMA$_{110}$	15	14,700	1.24	204	0.28	Mixed
PSMA$_9$-PHPMA$_{115}$	15	15,000	1.26	156	0.11	Mixed
PSMA$_9$-PHPMA$_{125}$	15	16,400	1.26	156	0.05	Mixed
PSMA$_9$-PHPMA$_{130}$	15	17,000	1.29	162	0.03	Vesicles
PSMA$_9$-PHPMA$_{150}$	15	18,800	1.37	170	0.07	Vesicles
PSMA$_9$-PHPMA$_{30}$	20	7,700	1.15	19	0.12	Spheres
PSMA$_9$-PHPMA$_{50}$	20	10,100	1.16	27	0.10	Spheres
PSMA$_9$-PHPMA$_{55}$	20	10,500	1.18	30	0.12	Spheres
PSMA$_9$-PHPMA$_{60}$	20	12,000	1.24	34	0.12	Spheres
PSMA$_9$-PHPMA$_{65}$	20	11,500	1.19	53	0.14	Mixed
PSMA$_9$-PHPMA$_{70}$	20	12,400	1.31	76	0.16	Mixed
PSMA$_9$-PHPMA$_{75}$	20	12,300	1.20	87	0.16	Mixed
PSMA$_9$-PHPMA$_{80}$	20	13,600	1.30	148	0.22	Mixed
PSMA$_9$-PHPMA$_{90}$	20	14,400	1.34	420	0.73	Mixed
PSMA$_9$-PHPMA$_{100}$	20	14,200	1.23	162	0.17	Mixed
PSMA$_9$-PHPMA$_{105}$	20	14,300	1.24	176	0.13	Mixed
PSMA$_9$-PHPMA$_{110}$	20	15,700	1.25	177	0.14	Mixed
PSMA$_9$-PHPMA$_{115}$	20	16,300	1.26	169	0.11	Vesicles
PSMA$_9$-PHPMA$_{120}$	20	16,700	1.27	182	0.14	Vesicles
PSMA$_9$-PHPMA$_{125}$	20	17,100	1.32	233	0.22	Vesicles
PSMA$_9$-PHPMA$_{130}$	20	17,600	1.28	211	0.14	Vesicles
PSMA$_9$-PHPMA$_{150}$	20	20,100	1.37	573	0.11	Vesicles

Table 9.2. Summary of the GPC, DLS and TEM data obtained for a series of PSMA$_9$-PHPMA$_x$ diblock copolymer nano-objects prepared at either 25% w/w or 30% w/w in mineral oil, respectively.

Target Composition	Solids Content (% w/w)	THF GPC		DLS		TEM Morphology
		M_n (g mol^{-1})	M_w/M_n	D (nm)	PDI	
PSMA$_9$-PHPMA$_{50}$	25	9,900	1.15	31	0.19	Spheres
PSMA$_9$-PHPMA$_{60}$	25	11,000	1.17	85	0.42	Mixed
PSMA$_9$-PHPMA$_{70}$	25	12,600	1.19	156	0.54	Worms
PSMA$_9$-PHPMA$_{80}$	25	12,700	1.19	1715	0.80	Mixed
PSMA$_9$-PHPMA$_{85}$	25	13,000	1.22	437	0.75	Mixed
PSMA$_9$-PHPMA$_{90}$	25	13,300	1.21	276	0.40	Mixed
PSMA$_9$-PHPMA$_{100}$	25	14,700	1.23	256	0.35	Mixed
PSMA$_9$-PHPMA$_{105}$	25	15,000	1.24	210	0.16	Mixed
PSMA$_9$-PHPMA$_{110}$	25	15,700	1.24	189	0.16	Mixed
PSMA$_9$-PHPMA$_{115}$	25	16,000	1.25	318	0.35	Vesicles
PSMA$_9$-PHPMA$_{120}$	25	16,000	1.25	246	0.24	Vesicles
PSMA$_9$-PHPMA$_{125}$	25	17,200	1.26	445	0.19	Vesicles
PSMA$_9$-PHPMA$_{150}$	25	18,700	1.28	448	0.27	Vesicles
PSMA$_9$-PHPMA$_{40}$	30	9,000	1.15	22	0.15	Spheres
PSMA$_9$-PHPMA$_{50}$	30	9,900	1.16	26	0.07	Mixed
PSMA$_9$-PHPMA$_{60}$	30	10,200	1.16	46	0.12	Mixed
PSMA$_9$-PHPMA$_{67}$	30	11,400	1.18	157	0.58	Worms
PSMA$_9$-PHPMA$_{70}$	30	12,100	1.21	736	0.91	Worms
PSMA$_9$-PHPMA$_{80}$	30	12,300	1.22	471	0.60	Mixed
PSMA$_9$-PHPMA$_{90}$	30	14,300	1.24	715	0.66	Mixed
PSMA$_9$-PHPMA$_{100}$	30	15,000	1.27	923	1.00	Mixed
PSMA$_9$-PHPMA$_{110}$	30	16,000	1.26	219	0.21	Mixed
PSMA$_9$-PHPMA$_{120}$	30	16,900	1.31	1400	0.97	Mixed
PSMA$_9$-PHPMA$_{130}$	30	17,800	1.35	764	0.26	Mixed

Table 9.3. Summary of the GPC, DLS, and TEM data obtained for a series of PSMA$_9$-PTFEMA$_x$ diblock copolymer nano-objects prepared at either 15% w/w or 20% w/w in *n*-dodecane. The PSMA$_9$ precursor block is also included as a reference.

Target Composition	Solids Content (% w/w)	TFEMA Conversion (%)	THF GPC		DLS		TEM Morphology
			M_n (g mol^{-1})	M_w/M_n	D_h (nm)	PDI	
PSMA$_9$ macro-CTA	-	-	2,700	1.22	-	-	-
PSMA$_9$-PTFEMA$_{20}$	15	95	4,200	1.17	-	-	No particles
PSMA$_9$-PTFEMA$_{40}$	15	95	5,900	1.19	19	0.12	Spheres
PSMA$_9$-PTFEMA$_{50}$	15	97	8,800	1.21	138	0.22	Worms
PSMA$_9$-PTFEMA$_{60}$	15	95	9,900	1.17	140	0.23	Worms
PSMA$_9$-PTFEMA$_{65}$	15	95	10,300	1.27	246	0.37	Worms
PSMA$_9$-PTFEMA$_{70}$	15	96	10,100	1.27	143	0.34	Worms
PSMA$_9$-PTFEMA$_{75}$	15	95	10,600	1.18	90	0.18	Mixed phase
PSMA$_9$-PTFEMA$_{80}$	15	96	11,200	1.18	92	0.19	Mixed phase
PSMA$_9$-PTFEMA$_{90}$	15	97	11,500	1.29	95	0.07	Mixed phase
PSMA$_9$-PTFEMA$_{100}$	15	96	12,900	1.24	100	0.08	Vesicles
PSMA$_9$-PTFEMA$_{120}$	15	96	14,500	1.24	108	0.09	Vesicles
PSMA$_9$-PTFEMA$_{140}$	15	95	16,200	1.19	125	0.22	Vesicles
PSMA$_9$-PTFEMA$_{160}$	15	96	18,400	1.32	188	0.24	Vesicles
PSMA$_9$-PTFEMA$_{180}$	15	96	17,600	1.29	165	0.24	Vesicles
PSMA$_9$-PTFEMA$_{200}$	15	96	21,200	1.28	169	0.16	Vesicles
PSMA$_9$-PTFEMA$_{250}$	15	97	23,200	1.29	153	0.04	Vesicles
PSMA$_9$-PTFEMA$_{300}$	15	97	28,500	1.32	158	0.05	Vesicles
PSMA$_9$-PTFEMA$_{20}$	20	95	4,600	1.19	-	-	No particles
PSMA$_9$-PTFEMA$_{40}$	20	95	6,400	1.20	21	0.33	Spheres
PSMA$_9$-PTFEMA$_{50}$	20	97	8,800	1.23	55	0.22	Worms
PSMA$_9$-PTFEMA$_{60}$	20	96	9,000	1.20	171	0.24	Worms
PSMA$_9$-PTFEMA$_{65}$	20	97	9,200	1.21	162	0.29	Worms
PSMA$_9$-PTFEMA$_{70}$	20	97	10,100	1.24	257	0.39	Worms
PSMA$_9$-PTFEMA$_{75}$	20	96	10,400	1.19	141	0.15	Mixed phase
PSMA$_9$-PTFEMA$_{80}$	20	97	10,600	1.22	128	0.16	Mixed phase
PSMA$_9$-PTFEMA$_{100}$	20	97	11,800	1.24	98	0.07	Mixed phase
PSMA$_9$-PTFEMA$_{110}$	20	97	12,200	1.31	309	0.41	Mixed phase
PSMA$_9$-PTFEMA$_{120}$	20	95	13,800	1.27	110	0.07	Vesicles
PSMA$_9$-PTFEMA$_{140}$	20	95	15,200	1.31	136	0.08	Vesicles
PSMA$_9$-PTFEMA$_{160}$	20	97	17,700	1.23	178	0.14	Vesicles
PSMA$_9$-PTFEMA$_{180}$	20	97	18,300	1.31	186	0.12	Vesicles
PSMA$_9$-PTFEMA$_{200}$	20	97	19,600	1.25	206	0.13	Vesicles
PSMA$_9$-PTFEMA$_{250}$	20	97	24,600	1.24	222	0.19	Vesicles
PSMA$_9$-PTFEMA$_{300}$	20	97	27,000	1.31	216	0.06	Vesicles

Table 9.4. Summary of the GPC, DLS, and TEM data obtained for a series of PSMA$_9$-PTFEMA$_x$ diblock copolymer nano-objects prepared at 25% w/w in *n*-dodecane.

Target Composition	Solids Content (% w/w)	TFEMA Conversion (%)	THF GPC		DLS		TEM Morphology
			M_n (g mol^{-1})	M_w/M_n	D (nm)	PDI	
PSMA$_9$-PTFEMA$_{20}$	25	95	4,500	1.19	-	-	No particles
PSMA$_9$-PTFEMA$_{40}$	25	96	6,800	1.20	18	0.11	Spheres
PSMA$_9$-PTFEMA$_{50}$	25	97	6,900	1.34	1170	0.53	Worms
PSMA$_9$-PTFEMA$_{60}$	25	97	7,300	1.26	58	0.19	Worms
PSMA$_9$-PTFEMA$_{65}$	25	95	8,900	1.23	403	0.47	Worms
PSMA$_9$-PTFEMA$_{70}$	25	95	9,600	1.25	298	0.23	Mixed phase
PSMA$_9$-PTFEMA$_{75}$	25	95	10,400	1.21	158	0.21	Mixed phase
PSMA$_9$-PTFEMA$_{80}$	25	97	10,200	1.20	345	0.23	Mixed phase
PSMA$_9$-PTFEMA$_{100}$	25	97	11,200	1.21	115	0.07	Mixed phase
PSMA$_9$-PTFEMA$_{120}$	25	95	14,600	1.31	245	0.46	Mixed phase
PSMA$_9$-PTFEMA$_{130}$	25	98	15,700	1.20	756	0.41	Mixed phase
PSMA$_9$-PTFEMA$_{140}$	25	95	16,200	1.19	185	0.13	Vesicles
PSMA$_9$-PTFEMA$_{160}$	25	96	17,000	1.26	192	0.28	Vesicles
PSMA$_9$-PTFEMA$_{180}$	25	96	18,300	1.17	186	0.11	Vesicles
PSMA$_9$-PTFEMA$_{200}$	25	96	20,300	1.21	194	0.28	Vesicles
PSMA$_9$-PTFEMA$_{250}$	25	98	24,200	1.25	214	0.13	Vesicles
PSMA$_9$-PTFEMA$_{300}$	25	98	26,500	1.31	237	0.10	Vesicles

Table 9.5. Summary of the GPC, DLS and TEM data obtained for a series of PLMA$_{19}$-PMMA$_x$ nano-objects prepared using the one-pot protocol at 20% w/w solids in mineral oil at 90 °C.

Target Composition	LMA Conversion (%)	THF GPC		MMA Conversion (%)	THF GPC		Final Composition	DLS		TEM Morphology
		M_n (g mol^{-1})	M_w/M_n		M_n (g mol^{-1})	M_w/M_n		D_h (nm)	PDI	
PLMA$_{20}$-PMMA$_{20}$	97	6,000	1.11	98	8,100	1.11	PLMA$_{19}$-PMMA$_{20}$	15	0.37	Chains and Spheres
PLMA$_{20}$-PMMA$_{50}$	97	5,900	1.11	98	10,800	1.11	PLMA$_{19}$-PMMA$_{49}$	21	0.09	Spheres
PLMA$_{20}$-PMMA$_{70}$	97	6,300	1.11	99	14,500	1.11	PLMA$_{19}$-PMMA$_{69}$	41	0.11	Spheres and Short Worms
PLMA$_{20}$-PMMA$_{90}$	97	6,000	1.11	99	16,200	1.12	PLMA$_{19}$-PMMA$_{89}$	272	0.65	Spheres and Short Worms
PLMA$_{20}$-PMMA$_{100}$	97	6,300	1.11	99	17,600	1.11	PLMA$_{19}$-PMMA$_{99}$	123	0.22	Spheres and Short Worms
PLMA$_{20}$-PMMA$_{120}$	97	5,900	1.11	99	18,300	1.14	PLMA$_{19}$-PMMA$_{119}$	549	0.66	Aggregated Spheres
PLMA$_{20}$-PMMA$_{140}$	97	6,000	1.11	99	22,600	1.17	PLMA$_{19}$-PMMA$_{139}$	658	0.61	Aggregated Spheres
PLMA$_{20}$-PMMA$_{200}$	97	6,200	1.11	99	27,500	1.21	PLMA$_{19}$-PMMA$_{198}$	586	0.54	Aggregated Spheres

Table 9.6. Summary of the GPC, DLS and TEM data obtained for two series of PLMA$_{22}$-PMMA$_x$ and PLMA$_{30}$-PMMA$_x$ nano-objects prepared at 20% w/w solids in mineral oil at 90 °C using the two-pot protocol.

Target Composition	Synthesis Temperature (°C)	MMA Conversion (%)	THF GPC		DLS		TEM Morphology
			M_n (g mol^{-1})	M_w/M_n	D_h (nm)	PDI	
PLMA$_{22}$-PMMA$_{20}$	90	97	9,200	1.11	18	0.15	Spheres
PLMA$_{22}$-PMMA$_{30}$	90	97	10,600	1.12	21	0.05	Spheres
PLMA$_{22}$-PMMA$_{40}$	90	97	11,600	1.12	30	0.19	Spheres
PLMA$_{22}$-PMMA$_{50}$	90	99	12,400	1.13	37	0.10	Spheres and Short Worms
PLMA$_{22}$-PMMA$_{60}$	90	98	13,000	1.12	54	0.14	Spheres and Short Worms
PLMA$_{22}$-PMMA$_{70}$	90	98	14,800	1.14	260	0.73	Short Worms
PLMA$_{22}$-PMMA$_{80}$	90	98	16,200	1.16	782	0.93	Short Worms
PLMA$_{22}$-PMMA$_{90}$	90	98	16,900	1.17	452	0.64	Short Worms
PLMA$_{22}$-PMMA$_{100}$	90	97	17,100	1.16	973	0.65	Short Worms
PLMA$_{22}$-PMMA$_{110}$	90	98	18,700	1.17	1236	0.84	Aggregated Spheres
PLMA$_{22}$-PMMA$_{140}$	90	99	22,100	1.25	1991	1.00	Aggregated Spheres
PLMA$_{22}$-PMMA$_{200}$	90	97	27,800	1.36	6094	0.68	Aggregated Spheres
PLMA$_{30}$-PMMA$_{30}$	90	98	15,700	1.11	24	0.06	Spheres
PLMA$_{30}$-PMMA$_{50}$	90	98	17,200	1.12	26	0.03	Spheres
PLMA$_{30}$-PMMA$_{70}$	90	98	19,500	1.13	39	0.07	Spheres and Short Worms
PLMA$_{30}$-PMMA$_{90}$	90	99	21,600	1.16	54	0.11	Spheres and Short Worms
PLMA$_{30}$-PMMA$_{110}$	90	98	22,100	1.17	55	0.11	Spheres and Short Worms
PLMA$_{30}$-PMMA$_{120}$	90	99	24,500	1.19	107	0.20	Spheres and Short Worms
PLMA$_{30}$-PMMA$_{140}$	90	99	26,700	1.20	145	0.24	Aggregated Spheres
PLMA$_{30}$-PMMA$_{150}$	90	99	28,200	1.23	362	0.59	Aggregated Spheres
PLMA$_{30}$-PMMA$_{200}$	90	98	32,600	1.28	892	0.45	Aggregated Spheres

Table 9.7. Summary of the GPC, DLS and TEM data obtained for a series of PLMA$_{41}$-PMMA$_x$ nano-objects prepared at 20% w/w solids in mineral oil at 90 °C using the two-pot protocol.

Target Composition	Synthesis Temperature (°C)	MMA Conversion (%)	THF GPC		DLS		TEM Morphology
			M_n (g mol^{-1})	M_w/M_n	D_h (nm)	PDI	
PLMA$_{41}$-PMMA$_{30}$	90	97	17,400	1.23	24	0.07	Spheres
PLMA$_{41}$-PMMA$_{40}$	90	97	18,900	1.15	27	0.03	Spheres
PLMA$_{41}$-PMMA$_{50}$	90	98	21,200	1.17	29	0.02	Spheres
PLMA$_{41}$-PMMA$_{70}$	90	97	23,400	1.17	32	0.04	Spheres
PLMA$_{41}$-PMMA$_{100}$	90	98	24,400	1.39	40	0.05	Spheres
PLMA$_{41}$-PMMA$_{120}$	90	98	26,700	1.20	46	0.07	Spheres
PLMA$_{41}$-PMMA$_{140}$	90	98	29,700	1.39	90	0.14	Spheres
PLMA$_{41}$-PMMA$_{160}$	90	98	31,500	1.38	120	0.17	Spheres
PLMA$_{41}$-PMMA$_{200}$	90	97	36,500	1.20	139	0.22	Spheres

Table 9.8. Summary of the GPC, DLS and TEM data obtained for a series of PLMA$_{19}$-PMMA$_x$ nano-objects prepared using the one-pot protocol at 90 °C targeting either 30% w/w solids in mineral oil or 20% w/w solids in *n*-dodecane.

Target Composition	Solvent	MMA Conversion (%)	THF GPC		DLS		TEM Morphology
			M_n (g mol^{-1})	M_w/M_n	D_h (nm)	PDI	
PLMA$_{19}$	Mineral oil	-	6,400	1.12	-	-	-
PLMA$_{19}$-PMMA$_{30}$	Mineral oil	97	9,900	1.12	18	0.03	Spheres
PLMA$_{19}$-PMMA$_{60}$	Mineral oil	98	11,700	1.13	28	0.05	Spheres
PLMA$_{19}$-PMMA$_{100}$	Mineral oil	99	17,600	1.16	199	0.38	Short Worms and Spheres
PLMA$_{19}$-PMMA$_{200}$	Mineral oil	99	27,200	1.35	470	0.56	Aggregated Spheres
PLMA$_{19}$	*n*-dodecane	-	6,500	1.12	-	-	-
PLMA$_{19}$-PMMA$_{30}$	*n*-dodecane	96	11,200	1.15	19	0.03	Spheres
PLMA$_{19}$-PMMA$_{60}$	*n*-dodecane	97	14,200	1.15	24	0.03	Spheres
PLMA$_{19}$-PMMA$_{100}$	*n*-dodecane	98	17,400	1.16	29	0.03	Spheres
PLMA$_{19}$-PMMA$_{130}$	*n*-dodecane	98	18,400	1.19	44	0.08	Spheres and Short Worms
PLMA$_{19}$-PMMA$_{160}$	*n*-dodecane	98	21,500	1.21	84	0.14	Spheres and Short Worms
PLMA$_{19}$-PMMA$_{180}$	*n*-dodecane	98	21,800	1.23	133	0.24	Short Worms and Spheres
PLMA$_{19}$-PMMA$_{200}$	*n*-dodecane	98	26,300	1.23	1090	0.97	Aggregated Spheres

Table 9.9. Summary of the GPC, DLS and TEM data obtained for a series of PSMA$_{10}$-PMMA$_x$ nano-objects prepared using the two-pot protocol at 20% w/w solids in mineral oil at 90 °C.

Target Composition	Synthesis Temperature (°C)	MMA Conversion (%)	THF GPC		DLS		TEM Morphology
			M_n (g mol^{-1})	M_w/M_n	D_h (nm)	PDI	
PSMA$_{10}$	70	-	4,400	1.13	-	-	-
PSMA$_{10}$-PMMA$_{30}$	90	97	8,500	1.12	18	0.04	Spheres
PSMA$_{10}$-PMMA$_{50}$	90	98	10,600	1.14	26	0.04	Spheres
PSMA$_{10}$-PMMA$_{70}$	90	98	12,300	1.17	104	0.23	Short Worms
PSMA$_{10}$-PMMA$_{90}$	90	98	17,000	1.29	742	0.61	Spheres and Short Worms
PSMA$_{10}$-PMMA$_{110}$	90	98	16,900	1.24	678	0.49	Spheres and Short Worms
PSMA$_{10}$-PMMA$_{140}$	90	97	19,800	1.29	783	0.82	Aggregated Spheres
PSMA$_{10}$-PMMA$_{200}$	90	97	23,700	1.77	416	0.62	Aggregated Spheres

Table 9.10. Summary of the GPC, DLS and TEM data obtained for a series of PSMA$_{37}$-PMMA$_x$ nano-objects prepared using the two-pot protocol at 20% w/w solids in mineral oil at 90 °C.

Target Composition	Synthesis Temperature (°C)	MMA Conversion (%)	THF GPC		DLS		TEM Morphology
			M_n (g mol^{-1})	M_w/M_n	D_h (nm)	PDI	
PSMA$_{37}$	70	-	10,900	1.11	-	-	-
PSMA$_{37}$-PMMA$_{30}$	90	97	16,600	1.12	23	0.05	Spheres
PSMA$_{37}$-PMMA$_{50}$	90	97	18,800	1.13	24	0.03	Spheres
PSMA$_{37}$-PMMA$_{70}$	90	98	20,800	1.13	25	0.05	Spheres
PSMA$_{37}$-PMMA$_{100}$	90	98	21,600	1.14	26	0.04	Spheres
PSMA$_{37}$-PMMA$_{200}$	90	98	27,000	1.28	46	0.10	Spheres
PSMA$_{37}$-PMMA$_{300}$	90	98	37,300	1.38	73	0.14	Spheres
PSMA$_{37}$-PMMA$_{400}$	90	98	39,000	1.49	162	0.28	Spheres

Table 9.11. Summary of the GPC, DLS and TEM data obtained for a series of PLMA$_{22}$-PMMA$_x$ nano-objects prepared at 20% w/w solids in mineral oil at either 70 °C or 115 °C using the two-pot protocol.

Target Composition	Synthesis Temperature (°C)	MMA Conversion (%)	THF GPC		DLS		TEM Morphology
			M_n (g mol^{-1})	M_w/M_n	D_h (nm)	PDI	
PLMA$_{22}$-PMMA$_{30}$	70	98	9,600	1.11	19	0.10	Spheres
PLMA$_{22}$-PMMA$_{40}$	70	98	11,200	1.12	61	0.16	Spheres and Short Worms
PLMA$_{22}$-PMMA$_{60}$	70	96	12,300	1.14	250	0.58	Short Worms
PLMA$_{22}$-PMMA$_{70}$	70	98	14,400	1.16	470	0.60	Short Worms
PLMA$_{22}$-PMMA$_{120}$	70	96	19,000	1.30	1064	0.67	Aggregated Spheres
PLMA$_{22}$-PMMA$_{140}$	70	95	20,600	1.32	1932	0.99	Aggregated Spheres
PLMA$_{22}$-PMMA$_{200}$	70	95	24,000	1.37	1906	0.22	Aggregated Spheres
PLMA$_{22}$-PMMA$_{50}$	115	95	11,600	1.16	26	0.04	Spheres
PLMA$_{22}$-PMMA$_{70}$	115	97	14,000	1.16	29	0.02	Spheres
PLMA$_{22}$-PMMA$_{90}$	115	95	16,200	1.17	32	0.02	Spheres
PLMA$_{22}$-PMMA$_{120}$	115	95	19,700	1.17	36	0.03	Spheres
PLMA$_{22}$-PMMA$_{200}$	115	96	25,400	1.19	50	0.04	Spheres
PLMA$_{22}$-PMMA$_{300}$	115	97	33,100	1.24	123	0.19	Spheres
PLMA$_{22}$-PMMA$_{400}$	115	96	35,200	1.29	150	0.19	Spheres

Table 9.12. Summary of the overall comonomer conversion (determined by ^{1}H NMR analysis), GPC, DLS and TEM data obtained for a series of PLMA$_{22}$-P(0.9MMA-*stat*-0.1LMA)$_y$ nano-objects prepared at 20% w/w solids in mineral oil at 115 °C. The PLMA$_{22}$ precursor block is also included as a reference.

Target Composition	Comonomer Conversion (%)	THF GPC		DLS		TEM Morphology
		M_n (g mol^{-1})	M_w/M_n	D_h (nm)	PDI	
PLMA$_{22}$ precursor	-	6 000	1.13	-	-	-
PLMA$_{22}$-P(0.9MMA-*stat*-0.1LMA)$_{50}$	94	13 800	1.16	24	0.01	Spheres
PLMA$_{22}$-P(0.9MMA-*stat*-0.1LMA)$_{70}$	94	14 800	1.17	29	0.02	Spheres
PLMA$_{22}$-P(0.9MMA-*stat*-0.1LMA)$_{85}$	94	16 700	1.18	54	0.14	Spheres and Worms
PLMA$_{22}$-P(0.9MMA-*stat*-0.1LMA)$_{100}$	94	17 200	1.19	82	0.15	Spheres and Worms
PLMA$_{22}$-P(0.9MMA-*stat*-0.1LMA)$_{120}$	94	19 200	1.21	229	0.45	Worms
PLMA$_{22}$-P(0.9MMA-*stat*-0.1LMA)$_{140}$	95	21 800	1.20	269	0.44	Worms
PLMA$_{22}$-P(0.9MMA-*stat*-0.1LMA)$_{160}$	95	25 200	1.20	2169	0.80	Worms and Vesicles
PLMA$_{22}$-P(0.9MMA-*stat*-0.1LMA)$_{200}$	94	26 400	1.25	142	0.14	Worms and Vesicles
PLMA$_{22}$-P(0.9MMA-*stat*-0.1LMA)$_{240}$	95	31 000	1.22	140	0.12	Vesicles
PLMA$_{22}$-P(0.9MMA-*stat*-0.1LMA)$_{260}$	95	34 000	1.25	141	0.11	Vesicles
PLMA$_{22}$-P(0.9MMA-*stat*-0.1LMA)$_{300}$	94	34 800	1.25	148	0.08	Vesicles
PLMA$_{22}$-P(0.95MMA-*stat*-0.05LMA)$_{200}$	94	25 000	1.20	54	0.04	Spheres

Table 9.13. Summary of the overall comonomer conversion (determined by ^{1}H NMR analysis), GPC, DLS and TEM data obtained for a series of PLMA$_{41}$-P(0.9MMA-*stat*-0.1LMA)$_y$ nano-objects prepared at 20% w/w solids in mineral oil at 115 °C. The PLMA$_{41}$ precursor block is also included as a reference.

Target Composition	Comonomer Conversion (%)	THF GPC		DLS		TEM Morphology
		M_n (g mol^{-1})	M_w/M_n	D_h (nm)	PDI	
PLMA$_{41}$ precursor	-	11 300	1.12	-	-	-
PLMA$_{41}$-P(0.9MMA-*stat*-0.1LMA)$_{30}$	94	17 400	1.17	27	0.04	Spheres
PLMA$_{41}$-P(0.9MMA-*stat*-0.1LMA)$_{50}$	94	18 900	1.19	29	0.08	Spheres
PLMA$_{41}$-P(0.9MMA-*stat*-0.1LMA)$_{70}$	94	20 000	1.21	31	0.04	Spheres
PLMA$_{41}$-P(0.9MMA-*stat*-0.1LMA)$_{100}$	94	21 700	1.21	34	0.10	Spheres
PLMA$_{41}$-P(0.9MMA-*stat*-0.1LMA)$_{150}$	94	27 500	1.30	39	0.06	Spheres
PLMA$_{41}$-P(0.9MMA-*stat*-0.1LMA)$_{200}$	94	32 900	1.35	44	0.04	Spheres
PLMA$_{41}$-P(0.9MMA-*stat*-0.1LMA)$_{250}$	94	37 400	1.33	48	0.02	Spheres
PLMA$_{41}$-P(0.9MMA-*stat*-0.1LMA)$_{300}$	94	40 000	1.35	52	0.03	Spheres

Table 9.14. Summary of the structural parameters obtained from fitting SAXS patterns recorded for a series of PLMA$_x$-P(0.9MMA-*stat*-0.1LMA)$_y$ nano-objects using a spherical micelle[6], a worm-like micelle model[6] or a vesicle model[7]. D_{sphere} is the overall sphere diameter such that $D_{sphere} = 2R_s + 4R_g$, where R_s is the mean core radius and R_g is the radius of gyration of the stabilizer chains. T_{worm} is the overall worm thickness ($T_{worm} = 2R_{wc} + 4R_g$, where R_{wc} is the mean worm core radius) and L_{worm} is the mean worm contour length. $D_{vesicle}$ is the overall vesicle diameter ($D_{vesicle} = 2R_m + T_{membrane} + 4R_g$, where R_m is the distance from the centre of the vesicle to the centre of the vesicle membrane, and $T_{membrane}$ is the vesicle membrane thickness). N_{agg} is the mean aggregation number (*i.e.* the mean number of copolymer chains per nano-object).

Block Copolymer	Nanoparticle Morphology	D_{sphere} (nm)	T_{worm} (nm)	L_{worm} (nm)	$D_{vesicle}$ (nm)	$T_{membrace}$ (nm)	N_{agg}
PLMA$_{22}$-P(0.9MMA-*stat*-0.1LMA)$_{47}$	Spheres	18.9 ± 1.9	-	-	-	-	200
PLMA$_{22}$-P(0.9MMA-*stat*-0.1LMA)$_{113}$	(Branched) Worms	-	20.0 ± 2.4	120	-	-	340
PLMA$_{22}$-P(0.9MMA-*stat*-0.1LMA)$_{247}$	Vesicles	-	-	-	172 ± 126	15.4 ± 1.6	25,600
PLMA$_{41}$-P(0.9MMA-*stat*-0.1LMA)$_{28}$	Spheres	19.8 ± 1.1	-	-	-	-	140
PLMA$_{41}$-P(0.9MMA-*stat*-0.1LMA)$_{282}$	Spheres	43.0 ± 4.5	-	-	-	-	510